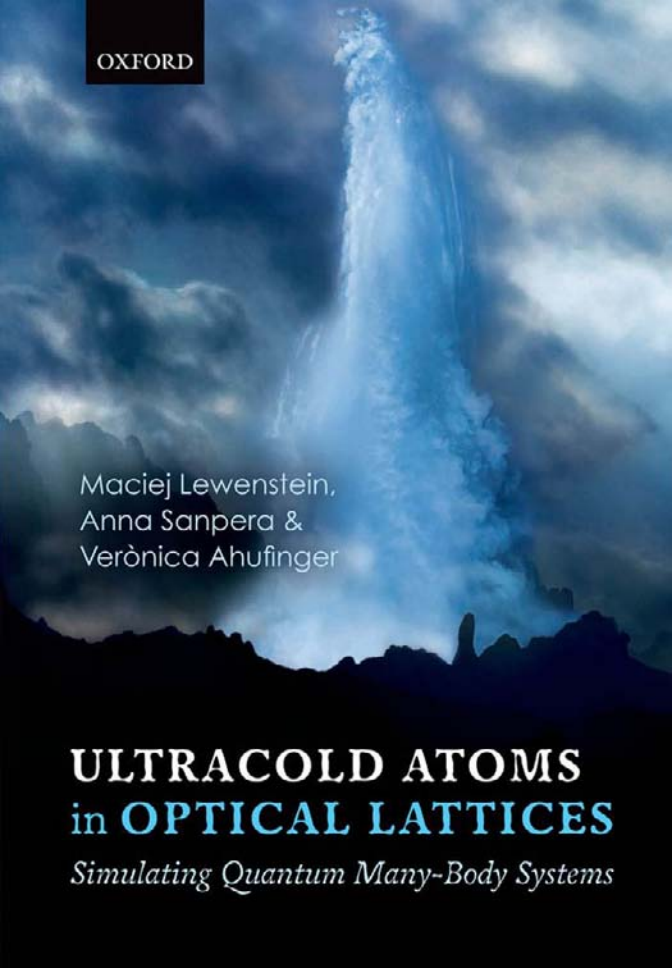


OXFORD



Maciej Lewenstein,
Anna Sanpera &
Verònica Ahufinger

ULTRACOLD ATOMS in OPTICAL LATTICES

Simulating Quantum Many-Body Systems

Ultracold Atoms in Optical Lattices

This page intentionally left blank

Ultracold Atoms in Optical Lattices

Simulating quantum many-body systems

Maciej Lewenstein

*ICREA-Institució Catalana de Recerca i Estudis Avançats and
ICFO-Institut de Ciències Fotòniques, Mediterranean Technology Park,
Castelldefels, Spain*

Anna Sanpera

*ICREA-Institució Catalana de Recerca i Estudis Avançats and Departament de Física,
Universitat Autònoma de Barcelona, Bellaterra, Spain*

and

Verònica Ahufinger

Departament de Física, Universitat Autònoma de Barcelona, Bellaterra, Spain

OXFORD
UNIVERSITY PRESS



Great Clarendon Street, Oxford, OX2 6DP
United Kingdom

Oxford University Press is a department of the University of Oxford.
It furthers the University's objective of excellence in research, scholarship,
and education by publishing worldwide. Oxford is a registered trade mark of
Oxford University Press in the UK and in certain other countries

© Maciej Lewenstein, Anna Sanpera, and Verònica Ahufinger 2012

The moral rights of the authors have been asserted

First Edition published in 2012

Impression: 1

All rights reserved. No part of this publication may be reproduced, stored in
a retrieval system, or transmitted, in any form or by any means, without the
prior permission in writing of Oxford University Press, or as expressly permitted
by law, by licence or under terms agreed with the appropriate reprographics
rights organization. Enquiries concerning reproduction outside the scope of the
above should be sent to the Rights Department, Oxford University Press, at the
address above

You must not circulate this work in any other form
and you must impose this same condition on any acquirer

British Library Cataloguing in Publication Data
Data available

Library of Congress Cataloging in Publication Data
Data available

ISBN 978-0-19-957312-7

Printed and bound by
CPI Group (UK) Ltd, Croydon, CR0 4YY

Links to third party websites are provided by Oxford in good faith and
for information only. Oxford disclaims any responsibility for the materials
contained in any third party website referenced in this work.

*To our parents and our kids Patrick, Julian, and Jan
To Minerva, Encarna, and Andreu*

This page intentionally left blank

Acknowledgements

This book could not have been written without the numerous collaborations, discussions and interactions with our friends and colleagues working in the areas of ultracold atoms, quantum information, quantum optics, and condensed matter in the last few years.

We would like to thank Antonio Acín, Gerardo Adesso, Matthieu Alloing, the late Daniel Amit, Jan Arlt, Alain Aspect, Remigiusz Augusiak, Emili Bagan, Mari-Carmen Bañuls, Michael Baranov, Nuria Barberán, Christoph Becker, Albert Benseny, Alejandro Bermudez, Gerhard Birkl, Rainer Blatt, Immanuel Bloch, Kai Bongs, Albert Bramon, Sibylle Braungardt, Dagmar Bruß, John Calsamiglia, Valentina Caprara, Alessio Celi, Marcelo Ciappina, Lukasz Cincio, Ignacio Cirac, Ramón Corbalán, Fernando Cucchietti, Danny Dagnino, Jean Dalibard, Rafał Demkowicz-Dobrzański, Eugene Demler, Ivan Deutsch, Gabriele De Chiara, Lukasz Dobrek, François Dubin, Omjyoti Dutta, Jacek Dziarmaga, André Eckardt, Kai Eckert, Jürgen Eschner, Philipp Hauke, Ulrich Elbing, Wolfgang Ertmer, Uli Everts, Henning Fehrmann, Mariusz Gajda, Roy Glauber, Nathan Goldman, Krzysztof Góral, Tobias Grass, Markus Greiner, Montse Guilleumas, Philipp Hauke, Zbigniew Idziaszek, Massimo Inguscio, Bruno Julia Díaz, Gediminas Juzeliūnas, Jarosław Korbicz, Anna Kubasiak, Marek Kuś, Thierry Lahaye, G. John Lapeyre, Jonas Larson, José-Ignacio Latorre, Luca Lepori, Mikko Juhani Leskinen, W. Vincent Liu, Yuri Loika, Dirk-Sören Lühmann, Chiara Macchiavello, Boris Malomed, Miguel Angel Martin-Delgado, Lluis Masanes, Pietro Massignan, Leonardo Mazza, Alem Mebrahtu, Ricard Menchón, Piotr Migdał, Morgan Mitchell, Klaus Mølmer, Jordi Mompart, Giovanna Morigi, Ramon Muñoz-Tapia, Armand Niederberger, Andrzej Nowak, Gaspar Orriols, Andreas Osterloh, Klaus Osterloh, Simone Paganelli, Belen Paredes, Sébastien Perseguers, Daniela Pfannkuche, Bill Phillips, Artur Polls, Eugene Polzik, Marisa Pons, Trey Porto, Guido Pupillo, Marek Rams, Matteo Rizzi, Carles Rodó, Mirta Rodriguez, Javier Rodriguez Laguna, Oriol Romero-Isart, Tomasso Roscilde, Kazimierz Rzążewski, Krzysztof Sacha, Jan Samsonowicz, Laurent Sanchez-Palencia, Klaus Sengstock, Gora Shlyapnikov, Thomas Schulte, Parvis Soltan-Panahi, Tomasz Sowiński, Ian Spielman, Julia Stasińska, Julian Struck, Edina Szirmai, Gergely Szirmai, Luca Tagliacozzo, Marek Trippenbach, Lluis Torner, Daniel Viscor, Janek Wehr, Patrick Windpassinger, Congjun Wu, Christoph Wunderlich, Jakub Zakrzewski, Alejandro Zamora, Łukasz Zawitkowski, Erhai Zhao, and Peter Zoller.

The basic structure of this book is built on a review article we published with Aditi Sen De, Ujjwal Sen, and Bogdan Damski in 2007 (Lewenstein *et al.*, 2007). We have also used material from some reviews we wrote on ultracold dipolar gases together with Thierry Lahaye, Chiara Menotti, Tilman Pfau and Luis Santos (Lahaye *et al.*, 2009) and also with Christian Trefzger and Barbara Capogrosso-Sansone. To all of them we are particularly grateful.

Finally, we acknowledge support from ICFO, Universitat Autònoma de Barcelona, ICREA, Generalitat de Catalunya Grants: SGR2009-00985, SGR2009-00347; Spanish Government (Ministerio de Ciencia e Innovación) projects: FIS2008:00784 (TOQATA),

viii *Acknowledgements*

FIS2008-01236 (QIUCSUAP), FIS2008-02425, Consolider Ingenio 2010 QOIT; European Community projects: EU-STREP NAMEQUAM, EU-IP AQUTE, ESF-MINCIN EU-ROQUAM FerMix, ERC Advanced Grant QUAGATUA, as well as the Alexander von Humboldt Foundation, the Kavli Institute for Theoretical Physics, University of California (Santa Barbara), the University of Hamburg, and the Joachim Hertz Foundation.

Barcelona-Bellaterra-Sabadell-Obrock-Santa Barbara-Barcelona, 2009–2011

Contents

Abbreviations	xiii
1 Introduction	1
1.1 The third quantum revolution	1
1.2 Cold atoms from a historical perspective	2
1.3 Cold atoms and the challenges of condensed matter physics	5
1.4 Plan of the book	11
2 Statistical physics of condensed matter: basic concepts	13
2.1 Classical phase transitions	13
2.2 Bose–Einstein condensation in non-interacting systems	21
2.3 Quantum phase transitions	23
2.4 One-dimensional systems	27
2.5 Two-dimensional systems	32
3 Ultracold gases in optical lattices: basic concepts	36
3.1 Optical potentials	36
3.2 Control of parameters in cold atom systems	38
3.3 Non-interacting particles in periodic lattices: band structure	41
3.4 Bose–Einstein condensates in optical lattices: weak interacting limit	45
3.5 From weakly interacting to strongly correlated regimes	48
4 Quantum simulators of condensed matter	51
4.1 Quantum simulators	51
4.2 Hubbard models	53
4.3 Spin models and quantum magnetism	56
5 Bose–Hubbard models: methods of treatment	60
5.1 Introduction	60
5.2 Weak interactions limit: the Bogoliubov approach	62
5.3 Strong interactions limit: strong coupling expansion	64
5.4 Perturbative mean-field approach	68
5.5 Gutzwiller approach	69
5.6 Exact diagonalization and the Lanczos method	72
5.7 Quantum Monte Carlo: path integral and worm algorithms	75
5.8 Phase-space methods	81
5.9 Analytic one-dimensional methods	84
5.10 Renormalization approaches in one dimension: DMRG and MPS	89
5.11 Renormalization approaches in two dimension: PEPS, MERA, and TNS	94
6 Fermi and Fermi–Bose Hubbard models: methods of treatment	98
6.1 Introduction	98
6.2 Fermi Hubbard model and BCS theory	99

6.3	Balanced BCS–BEC crossover	101
6.4	Mean-field description of imbalanced BCS–BEC crossover	106
6.5	Fermi Hubbard model and strongly correlated fermions	109
6.6	Hubbard models and effective Hamiltonians	118
6.7	Fermi–Bose Hubbard models	121
7	Ultracold spinor atomic gases	125
7.1	Introduction	125
7.2	Spinor interactions	126
7.3	Spinor Bose–Einstein condensates: mean-field phases	128
7.4	Spin textures and topological defects	133
7.5	Bosonic spinor gases in optical lattices	137
7.6	Spinor Fermi gases	156
8	Ultracold dipolar gases	165
8.1	Introduction	165
8.2	Properties of dipole–dipole interaction	167
8.3	Ultracold dipolar systems	169
8.4	Ultracold trapped dipolar gases	171
8.5	Dipolar gas in a lattice: extended Hubbard models	182
8.6	Dipolar bosons in a 2D optical lattice	187
8.7	Quantum Monte Carlo studies of dipolar gases	196
8.8	Further dipole effects	202
9	Disordered ultracold atomic gases	205
9.1	Introduction	205
9.2	Disorder in condensed matter	206
9.3	Realization of disorder in ultracold atomic gases	224
9.4	Disordered Bose–Einstein condensates	228
9.5	Disordered ultracold fermionic systems	246
9.6	Disordered ultracold Bose–Fermi and Bose–Bose mixtures	248
9.7	Spin glasses	251
9.8	Disorder-induced order	258
10	Frustrated ultracold atom systems	264
10.1	Introduction	264
10.2	Quantum antiferromagnets	265
10.3	Physics of frustrated quantum antiferromagnets	270
10.4	Realization of frustrated models with ultracold atoms	282
11	Ultracold atomic gases in ‘artificial’ gauge fields	293
11.1	Introduction	293
11.2	Ultracold atoms in rapidly rotating microtraps	294
11.3	Gauge symmetry in the lattice	304
11.4	Lattice gases in ‘artificial’ Abelian gauge fields	310
11.5	Lattice gases in ‘artificial’ non-Abelian gauge fields	314
11.6	Integer quantum Hall effect and emergence of Dirac fermions	316
11.7	Fractional quantum Hall effect in non-Abelian fields	322

11.8 Ultracold gases and lattice gauge theories	326
11.9 Generation of ‘artificial’ gauge fields	328
12 Many-body physics from a quantum information perspective	340
12.1 Introduction	340
12.2 Crash course on quantum information	341
12.3 Quantum phase transitions and entanglement	355
12.4 Area laws	363
12.5 The world according to tensor networks	374
13 Quantum information with lattice gases	384
13.1 Introduction	384
13.2 Quantum circuit model in optical lattices	386
13.3 One-way quantum computer with lattice gases	394
13.4 Topological quantum computing in optical lattices	398
13.5 Distributed quantum information	409
14 Detection of quantum systems realized with ultracold atoms	412
14.1 Introduction	412
14.2 Time of flight: first-order correlations	415
14.3 Time of flight and noise correlations: higher-order correlations	417
14.4 Bragg spectroscopy	418
14.5 Optical Bragg diffraction	421
14.6 Single-atom detectors	423
14.7 Quantum polarization spectroscopy	424
15 Perspectives: beyond standard optical lattices	427
15.1 Introduction	427
15.2 Beyond standard optical lattices: new trends	428
15.3 Standard optical lattices: what’s new?	432
Bibliography	439
Index	471

This page intentionally left blank

Abbreviations

AKLT	Affleck–Kennedy–Lieb–Tasaki
ARPES	angle-resolved photoemission spectroscopy
AF	antiferromagnetic
BCS	Bardeen–Cooper–Schrieffer
BdG	Bogoliubov–de Gennes
BOPTILATT	Beyond Standard Optical Lattices
BEC	Bose–Einstein condensation
BG	Bose glass
CB	checkerboard
CEGF	classical external gauge field
CMTM	coherent momentum transfer mapping
CFT	conformal field theory
CDOS	cumulative density of states
DMRG	density matrix renormalization group
DOS	density of states
DW	density wave
DS	devil’s staircase
DNLSE	discrete non-linear Schrödinger equation
FL	Fermi liquid
FB	Fermi–Bose
FBH	Fermi–Bose Hubbard
F	ferromagnetic
FQHE	fractional quantum Hall effect
FFLO	Fulde–Ferrell–Larkin–Ovchinnikov
GHZ	Greenberger–Horne–Zeilinger
GPE	Gross–Pitaevskii equation
HWHM	half-width at half maximum
HVBS	honeycomb valence-bond solid
IQHE	integer quantum Hall effect
KTB	Kosterlitz–Thouless–Berezinskii
LS	Lifshits states
LE	localizable entanglement
MPS	matrix product state
MFP	mean-field parameters
MBQC	measurement-based quantum computation
MI	Mott insulator
MERA	multiscale entanglement renormalization ansatz
NN	nearest neighbor
PM	Parisi–Mézard

xiv *Abbreviations*

PDF	probability density function
PEPS	projected entangled pair state
QFT	quantum field theory
QMC	quantum Monte Carlo
QPT	quantum phase transitions
QPS	quantum polarization spectroscopy
RG	renormalization group
RVB	resonating valence-bond
SPDM	single-particle density matrix
SVD	singular value decomposition
SR	star
STIRAP	stimulated Raman adiabatic passage
SMFT	stochastic mean-field theory
ST	stripe
SF	superfluid
SS	supersolid
TNS	tensor network states
TEBD	time evolving block decimation
TOF	time of flight
TDGPE	time-dependent non-linear Schrödinger (Gross–Pitaevskii) equation
VBC	valence-bond crystal
VBS	valence-bond solid
VHS	van Hove singularities

1

Introduction

1.1. The third quantum revolution

The achievement of Bose–Einstein condensation (BEC) in dilute gases in 1995 (Anderson *et al.*, 1995; Bradley *et al.*, 1995; Davis *et al.*, 1995) marks the beginning of a new era. For the so-called AMO community—comprising atomic, molecular, optics, and quantum optics scientists—it soon became evident that condensed-matter physics, i.e. degenerate quantum many-body systems, could be in reach. The condensed-matter community were much more sceptical at that stage. They argued that, in the end, what had been achieved experimentally was a regime of weakly interacting Bose gases: a domain that had been thoroughly investigated by condensed-matter theorists in the 1950s and 1960s (Fetter and Walecka, 1971; Mahan, 1993). For solid state/condensed matter experts the fact that the AMO experiments dealt with confined systems of finite size and typically inhomogeneous densities was a technical issue rather than a question of fundamental importance. Nonetheless, the Nobel foundation awarded its yearly prize for physics in 2001 to E. A. Cornell, C. E. Wieman, and W. Ketterle ‘for the achievement of BEC in dilute gases of alkali atoms, and for early fundamental studies of the properties of the condensates’ (Cornell and Wieman, 2002; Ketterle, 2002). However, today we can see that, due to the efforts of the whole community, these fundamental studies have enriched the standard ‘condensed matter’ understanding of the static and dynamical properties of weakly interacting Bose gases (Pitaevskii and Stringari, 2003).

From the very beginning the AMO community pushed BEC physics towards new regimes and new challenges. Progress was spectacular, and at the beginning of the third millennium it was clear, both for the AMO and condensed-matter communities, that they were entering a truly new quantum era, with unprecedented possibilities for the control of many-body systems. In particular, it became clear that the regime of strongly correlated systems might be reached with ultracold atoms and/or molecules. In 1999, a few years after the first observation of BEC, atomic degenerate Fermi gases were achieved (De Marco and Jin, 1999; Schreck *et al.*, 2001; Truscott *et al.*, 2001) paving the way toward the observations of Fermi superfluidity. This is described, in the weak interaction limit, by the Bardeen–Cooper–Schrieffer theory (BCS) (Fetter and Walecka, 1971) and the so called BEC–BCS crossover in the limit of strong correlations. For recent reviews reporting the intense activity in this field see Giorgini *et al.* (2008) and Bloch *et al.* (2008). Earlier, following the seminal proposal by Jaksch *et al.* (1998), Greiner *et al.* (2002) had observed the signatures of the quantum phase transition from the superfluid to the so-called Mott-insulator (MI) state for bosons confined in an optical lattice.

2 Introduction

Nowadays, ultracold atomic and molecular systems are at the frontiers of modern quantum physics, and are considered to provide the most controllable systems for the study of many-body physics. It is believed that these systems will also find highly non-trivial applications in quantum information and quantum metrology and will serve as powerful quantum simulators. At the theory level, the broadness of the different fields touched by ultracold atoms has led to a ‘grand unification’, where AMO, condensed-matter, nuclear-physics, and even high-energy physics theorists are involved. For reviews see Lewenstein *et al.* (2007) and Bloch *et al.* (2008).

After the first quantum revolution at the beginning of the twentieth century came a second one associated with the name of John Bell and the experimental quest for non-locality of quantum mechanics and experimental control over single-, or few-particle systems—see in particular Alain Aspect’s introduction to the famous Bell’s book (Bell, 2004). Now we are witnessing the third one: the quantum revolution associated with control over macroscopic quantum systems and the rise of quantum technologies.

1.2. Cold atoms from a historical perspective

The third quantum revolution has not arrived completely unexpectedly: the developments of atomic physics and quantum optics in the last 30 years made it inevitable. In the 1970s and 1980s, atomic physics was a very well established and respected area of physics. It was, however, by no means a ‘hot’ area. On the theory side, even though one had to deal with complex problems of many-electron systems, most of the methods and techniques had already been developed. The major problems that were considered mainly concerned optimization of these methods and reflected an evolutionary progress rather than a revolutionary search for totally new phenomena. On the experimental side, quantum optics was entering its golden age. The development of laser physics and non-linear optics led in 1981 to the awarding of the Nobel prize to A. L. Schawlow and N. Bloembergen ‘for their contribution to the development of laser spectroscopy’. Meanwhile, studies of quantum systems at the single-particle level culminated in 1989 with a Nobel prize for H. G. Dehmelt and W. Paul ‘for the development of the ion trap technique’, their award being shared with N. F. Ramsey ‘for the invention of the separated oscillatory fields method and its use in the hydrogen maser and other atomic clocks’.

Theoretical quantum optics was born in the 1960s with the work on quantum coherence theory by the 2005 Nobel prize winner, R. J. Glauber (1963*a, b*), and with the development of the laser theory in the late 1960s by H. Haken and by M. O. Scully and W. E. Lamb, a Nobel laureate of 1955. In the 1970s and 1980s, however, theoretical quantum optics was not considered to be a separate, established area of theoretical physics. One of the reasons for this situation was that quantum optics at that time was primarily dealing with single-particle problems. Most of the many-body problems of quantum optics, such as laser theory or, more generally, optical instabilities (Walls and Milburn, 2006), could have been solved either using linear models or by employing relatively simple versions of the mean-field approach. Perhaps the most sophisticated theoretical contributions concerned understanding of quantum fluctuations and quantum noise (Gardiner and Zoller, 2004; Walls and Milburn, 2006).

This situation has drastically changed due to the unprecedented level of *quantum engineering*, i.e. preparation, manipulation, control, and detection of quantum systems developed and achieved by atomic physics and quantum optics. There have been several seminal discoveries that have triggered these changes:

- The cooling and trapping of atoms, ions, and molecules is now possible in regimes of low temperature (today down to nanokelvin levels) and precision that were considered unattainable just two decades ago. These developments were recognized by the Nobel Foundation in 1997, when they awarded their prize to S. Chu (1998), C. Cohen-Tannoudji (1998), and W. D. Phillips (1998) ‘for the development of methods to cool and trap atoms with laser light’. Laser cooling and mechanical manipulations of particles with light (Metcalf and van der Straten, 2001) was essential for the development of completely new areas of atomic physics and quantum optics, such as atom optics (Meystre, 2001), and for reaching new territories of precision metrology and quantum engineering.
- In 1995, laser cooling combined with evaporative cooling allowed the experimental observation of BEC (Anderson *et al.*, 1995; Bradley *et al.*, 1995; Davis *et al.*, 1995), a phenomenon predicted by Bose and Einstein more than 70 years earlier. As we mentioned above, these experiments marked the beginning of a new era. E. Cornell and C. Wieman (2002) and W. Ketterle (2002) received the Nobel Prize in 2001 ‘for the achievement of BEC in dilute gases of alkali atoms, and for early fundamental studies of the properties of the condensates’. This was truly a breakthrough moment, in which ‘atomic physics and quantum optics has met condensed matter physics’ (Ketterle, 2002). The condensed-matter community at that time remained, however, very cautious. After all, BEC was observed in weakly interacting dilute gases, where it was very well described by the mean-field Bogoliubov–de Gennes theory (Pitaevskii and Stringari, 2003), developed for homogeneous systems in the 1950s.
- The study of quantum correlations and entanglement. The seminal theoretical works of the late A. Peres (1993, 1996), the proposals of quantum cryptography by C. H. Bennett and G. Brassard (1984) and A. K. Ekert (1991), the quantum communication proposals by C. H. Bennett and S. J. Wiesner (1992) and C. H. Bennett *et al.* (1993), the discovery of the quantum factorizing algorithm by P. Shor (1994), and the quantum computer proposal by J. I. Cirac and P. Zoller (1995) gave birth to the field of quantum information (Bouwmeester *et al.*, 2000; Zoller *et al.*, 2005a). These studies, together with the rapid development of the theory have led to enormous progress in our understanding of quantum correlations and entanglement and, in particular, how to prepare and use entangled states as a resource. The ideas from quantum information nowadays constantly impact upon the physics of cold atoms, molecules, and ions, and stimulate new approaches. It is very probable that the first quantum computers will be, as has already been suggested by Feynman (1986), special purpose computers—quantum simulators (Cirac and Zoller, 2004) that will efficiently simulate quantum many-body systems that where this cannot be done using ‘classical’ computers (Zoller *et al.*, 2005a).
- Optical lattices and Feshbach resonances. The physics of ultracold atoms entered the area of strongly correlated systems with the seminal proposal of Jaksch *et al.* (1998)

4 Introduction

on how to achieve the transition superfluid–Mott-insulator (SF–MI) in cold atoms using optical lattices. The proposal was based on the bosonic MI transition suggested in condensed matter (Fisher *et al.*, 1989), but the authors of this paper were in fact motivated by the possibility of realizing quantum computing with cold atoms in a lattice. Transition to the MI state was supposed to be an efficient method of preparation of a quantum register with a fixed number of atoms per lattice site. Entanglement between atoms could be achieved via controlled collisions (Jaksch *et al.*, 1999). The experimental observation of the SF–MI transition by the Bloch–Hänsch group (Greiner *et al.*, 2002) was without doubt a benchmark for studies of strongly correlated systems with ultracold atoms (Bloch, 2004). Several other groups have observed bosonic SF–MI transitions in pure Bose systems (Köhl *et al.*, 2005), in disordered Bose systems (Fallani *et al.*, 2007), and in Bose–Fermi (Ospelkaus *et al.*, 2006; Günter *et al.*, 2006) and Bose–Bose mixtures (Thalhammer *et al.*, 2008). The possibility of changing the collision properties of ultracold atoms by means of tuning the Feschbach resonances of the atomic species has been another tool of inestimable value, and has led to the fermionic MI (Jördens *et al.*, 2008; Schneider *et al.*, 2008). MI states of molecules have been created (Volz *et al.*, 2006) and bound repulsive pairs of atoms (i.e. pairs of atoms at a site that cannot release their repulsive energy due to the band structure of the spectrum in the lattice) have been observed (Winkler *et al.*, 2006).

- Cold trapped ions were initially investigated to realize the Cirac–Zoller quantum gate (1995), in an attempt to build an scalable quantum computer using a bottom-up approach (Schmidt-Kaler *et al.*, 2003; Home *et al.*, 2009). A stream of new ideas for using cold ions for quantum simulators has recently appeared. The first results have shown that ion–ion interactions mediated by phonons can be manipulated to implement various spin models (Mintert and Wunderlich, 2001; Wunderlich, 2002; Porras and Cirac, 2004a) where the spin states correspond to internal states of the ion. In tight linear traps, one can realize spin chains with interactions decaying as $(\text{distance})^{-3}$, i.e. as in the case of dipole–dipole interactions. Such spin chains may serve as quantum neural network models and may be used for adiabatic quantum information processing (Pons *et al.*, 2007; Braungardt *et al.*, 2007). More interestingly, ions can be employed as quantum simulators, in both one and two dimensions, the ions forming self-assembled Coulomb crystals (Porras and Cirac, 2006). The first steps towards the experimental realization of these ideas have recently been reported (Friedenauer *et al.*, 2008). Alternatively to spins, one could look at phonons in ion self-assembled crystals; these are also predicted to exhibit interesting collective behavior, from Bose condensation to strongly correlated states (Porras and Cirac, 2004b; Deng *et al.*, 2008). Trapped ions may also be used to simulate mesoscopic spin–boson models (Porras *et al.*, 2008). Combined with optical traps or ion microtrap arrays, these methods can be used to simulate a whole variety of spin models with tunable interactions in a wide range of spatial dimensions and geometries (Schmied *et al.*, 2008). Finally, they are promising candidates for the realization of many-body interactions (Bermudez *et al.*, 2009). All these theoretical proposals and the spectacular progress of the experimental trapped-ion community pushes trapped-ions physics towards more widespread use of cold atoms to mimic condensed-matter physics and to areas beyond.

1.3. Cold atoms and the challenges of condensed matter physics

The physics of cold atoms has frontiers with several other areas, such as condensed-matter physics and quantum field theory. In particular, many important challenges of the latter two disciplines can be addressed with cold atoms:

- *One-dimensional (1D) systems.* The role of quantum fluctuations and correlations is particularly important in one dimension. The theory of 1D systems is well developed due to the existence of exact methods such as the Bethe ansatz and quantum inverse scattering theory (see Essler *et al.* (2005)), powerful approximate approaches such as bosonization or conformal field theory (see Giamarchi (2004)), and efficient computational methods such as the density matrix renormalization group (DMRG) technique (see Schollwöck (2005)). There are, however, many open experimental challenges that have so far not been directly and clearly realized in condensed matter, and which can be addressed with cold atoms—for a review see Cazalilla (2004). Examples include atomic Fermi or Bose analogs of spin–charge separation or, more generally, observations of microscopic properties of Luttinger liquids (Recati *et al.*, 2003; Paredes and Cirac, 2003; Kollath *et al.*, 2005). Experimental observations of the 1D gas in the deep Tonks–Girardeau regime by Paredes *et al.* (2004) (see also Moritz *et al.* (2003), Kinoshita *et al.* (2004), Laburthe Tolra *et al.* (2004), and Stöferle *et al.* (2004a)) were the first steps in this direction. The achievement in 2008 of the Tonks regime by employing dissipative processes (two-body losses) is perhaps the first experimental example of how to control a system by making use of its coupling to the environment (Dürr *et al.*, 2008, 2009; García-Ripoll *et al.*, 2009; Syassen *et al.*, 2008). See also the recent progress towards the deep Tonks–Girardeau regime in Haller *et al.* (2010).
- *Spin-boson model.* A two-level system coupled to a bosonic reservoir is a paradigmatic model, both in quantum dissipation theory in quantum optics and in quantum phase transitions in condensed matter, where it is termed the ‘spin-boson model’—for a review see Leggett *et al.* (1987). It has also been proposed (Recati *et al.*, 2005) that an atomic quantum dot, i.e. a single atom in a tight optical trap coupled to a superfluid reservoir via laser transitions, may realize this model. In particular, atomic quantum dots embedded in a 1D Luttinger liquid of cold bosonic atoms accomplishes a spin-boson model with Ohmic coupling, which exhibits a dissipative phase transition and allows direct measurement of atomic Luttinger parameters.
- *Two-dimensional (2D) systems.* According to the celebrated Mermin–Wagner–Hohenberg theorem, 2D systems with continuous symmetry do not exhibit long-range order at temperatures $T > 0$. 2D systems may, however, undergo a Kosterlitz–Thouless–Berezinskii transition (KTB) to a state in which the correlations’ decay is algebraic rather than exponential. Although KTB transition has been observed in liquid helium (Bishop and Reppy 1978, 1980), its microscopic nature (binding of vortex pairs) has never been seen. A recent experiment (Hadzibabic *et al.*, 2006, 2008; Hadzibabic and Dalibard, 2010; Hung *et al.*, 2011) makes an important step in this direction.
- *Kondo effect and Kondo physics.* The Kondo effect is one of the paradigmatic examples of strongly correlated behavior in electronic systems. Electrical resistance diverges as

6 Introduction

the temperature approaches 0 K due to the interaction between the localized magnetic impurities and the itinerant electrons—for a review see Shiba and Kuramoto (2005). Carrying this effect over to fermionic atoms using superlattice techniques should be possible (Paredes *et al.*, 2005*a*). The challenge is to find a bosonic analog of the Kondo effect.

- *Hubbard and spin models.* Many important examples of strongly correlated states in condensed-matter physics are realized in various types of Hubbard model (Auerbach, 1994; Essler *et al.*, 2005). While Hubbard models in condensed matter are ‘reasonable caricatures’ of real systems, ultracold atomic gases in optical lattices allow practically perfect realizations of a whole variety of Hubbard models (Jaksch and Zoller, 2005). Similarly, in certain limits Hubbard models reduce to various spin models; cold atoms and ions again allow for practically perfect realizations of such spin models—see for instance Dorner *et al.* (2003), Duan *et al.* (2003), García-Ripoll *et al.* (2004), and Santos *et al.* (2004). Specifically, spin–spin interactions between neighboring atoms can be implemented by bringing the atoms together on a single site and carrying out controlled collisions (Sørensen and Mølmer, 1999; Jaksch *et al.*, 1999; Mandel *et al.*, 2003), on-site exchange interactions (Anderlini *et al.*, 2007), or superexchange interactions (Trotzky *et al.*, 2008). Moreover, one can use such realizations as quantum simulators to mimic specific condensed-matter models.
- *Disordered systems: interplay localization interactions.* Disorder plays a central role in condensed matter physics and its presence leads to various novel effects and phenomena. One of the most prominent quantum signatures of disorder is Anderson localization (Anderson, 1958) of the wave function of single particles in a random potential. In cold gases, controlled disorder or pseudo-disorder might be created in atomic traps or optical lattices by adding an optical potential created by speckle radiation or by superposing several lattices with incommensurate periods of spatial oscillation (Damski *et al.*, 2003*b*; Roth and Burnett, 2003*a*). Other proposed methods are the admixture of different atomic species randomly trapped in sites distributed across the sample and acting as impurities (Gavish and Castin, 2005) or the use of an inhomogeneous magnetic field close to a Feshbach resonance that randomly modifies the scattering length of atoms (Gimperlein *et al.*, 2005). In fact, very recently experimental realization of Anderson localization of matter waves has been reported in a non-interacting BEC of ^{39}K in a pseudo-random potential (Roati *et al.*, 2008) and also in a small condensate of ^{87}Rb in a truly random potential in the course of expansion in a 1D waveguide (Billy *et al.*, 2008). The results of the latter experiment, as well as the appearance of an effective mobility edge due to the finite correlation length of the speckle-induced disorder, were precisely predicted in Sanchez-Palencia *et al.*, 2007. The interplay between disorder and interactions is also a very active research area in ultracold gases. For attractive interactions, disorder might destroy the possibility of a superfluid transition (‘dirty’ superconductors). Weak repulsive interactions play a delocalizing role whereas very strong ones lead to Mott-type localization (Mott, 1968*a*) and insulating behavior. In the intermediate situations there exists a possibility of delocalized ‘metallic’ phases. Cold atoms in optical lattices should allow study of the crossover between Anderson-like (Anderson glass) to Mott-type (Bose glass) localization. The first experimental signals of a Bose glass (Fallani *et al.*, 2007; Pasienski *et al.*, 2010) and of the Anderson glass crossover (Deissler *et al.*, 2010)

have been reported. Theoretical predictions (Kuhn *et al.*, 2005; Bilas and Pavloff, 2006; Paul *et al.*, 2005; Schulte *et al.*, 2006) indicate signals of Anderson localization in the presence of weak non-linear interactions and quasi-disorder in a BEC. One expects in such systems the appearance of a novel Lifshits glass phase (Lugan *et al.*, 2007), where bosons condense in a finite number of states from the low-energy tail of the single-particle spectrum.

- *Disordered systems: spin glasses.* Since the seminal papers of Edwards and Anderson (1975) and Sherrington and Kirkpatrick (1975) the question of the nature of spin-glass ordering has attracted a lot of attention (Fisher and Huse, 1986; Bray and Moore, 1987; Mézard *et al.*, 1987). The two competing pictures—the replica symmetry-breaking picture of G. Parisi and the droplet model of D. S. Fisher and D. A. Huse—are probably applicable in some situations and not applicable in others. Ultracold atoms in optical lattices might resolve this controversy by, for instance, studying independent copies with the same disorder—so-called ‘replicas’. A measurement scheme for the determination of the disorder-induced correlation function between the atoms of two independent replicas with the same disorder has been proposed (Morrison *et al.*, 2008). Cold atomic physics might also add understanding of some quantum aspects, such as the behavior of Ising spin glasses in transverse fields, i.e. in a truly quantum mechanical situation (Sanpera *et al.*, 2004; Ahufinger *et al.*, 2005).
- *Disordered systems: large effects from small disorder.* There are many examples of such situations. In classical statistical physics a paradigmatic example is the random-field Ising model in two dimensions, which loses spontaneous magnetization at arbitrarily small disorder. In quantum physics the paradigmatic example is Anderson localization, which occurs at arbitrarily small disorder in one dimension and should also occur at arbitrarily small disorder in two dimensions. Cold atomic physics may address these questions and, in fact, much more (see Wehr *et al.* (2006), Niederberger *et al.*, (2008, 2009), where disorder breaks the continuous symmetry in a spin system and thus allows for long-range ordering).
- *High- T_c superconductivity.* Despite many years of research, opinions on the nature of high- T_c superconductivity still vary quite appreciably (Claeson and Delsing, 2003). It is, however, quite established—see the contribution of P. W. Anderson in Claeson and Delsing (2003)—that understanding of the 2D Hubbard model in the so-called $t - J$ limit (Spalek and Oleś, 1977; Chao *et al.*, 1977; Auerbach, 1994; Spalek, 2007) for two-component (spin- $\frac{1}{2}$) fermions provides at least part of the explanation. The simulation of these models is very hard and numerical results are also full of contradictions. Cold fermionic atoms with spin (or pseudospin) $\frac{1}{2}$ in optical lattices might provide a quantum simulator to resolve these problems (see Hofstetter *et al.* (2002) and also Koetsier *et al.* (2006)). The first experiments with both ‘spinless’, i.e. polarized, and spin- $\frac{1}{2}$ unpolarized ultracold fermions (Köhl *et al.*, 2005; Stöferle *et al.*, 2006) have been realized; particularly spectacular are the recent observations of a fermionic MI state (Jördens *et al.*, 2008; Schneider *et al.*, 2008). It is also worth noticing that Bose–Fermi mixtures in optical lattices have already been intensively studied (Günter *et al.*, 2006; Ospelkaus *et al.*, 2006; Best *et al.*, 2009). These systems may exhibit superconductivity due to boson-mediated fermion–fermion interactions. Superexchange interactions, demonstrated very recently in the context of ultracold atoms in optical lattices (Trotzky *et al.*, 2008), are

also believed to play an important role in the context of high- T_c superconductivity (Lee *et al.*, 2006).

- *BCS–BEC crossover.* The physics of high T_c superconductivity can be also addressed with trapped ultracold gases. Weakly attracting spin- $\frac{1}{2}$ fermions in such situations undergo at (very) low temperatures the BCS transition to a superfluid state of loosely bounded Cooper pairs. Weakly repulsing fermions, on the other hand, may form bosonic molecules, which in turn may form a BEC at very low temperatures. Strongly interacting fermions also undergo a transition to the superfluid state, but at much higher T . Several groups have employed the technique of Feshbach resonances (Inouye *et al.*, 1998; Timmermans *et al.*, 1999; Cornish *et al.*, 2000) to observe such BCS–BEC crossover. For a recent review on this technique see Chin *et al.* (2010) and for the recent status of experiments of the spin-balanced case see references in Bloch *et al.* (2008) and Giorgini *et al.* (2008). There are many more controversies regarding imbalanced spin mixtures (Partridge *et al.*, 2006; Zwierlein *et al.*, 2006). The first experimental signatures supporting pairing with finite momentum in spin-imbalance mixtures, the so-called FFLO state (Fulde and Ferrell, 1964; Larkin and Ovchinnikov, 1965), have been observed in 1D Fermi gases (Liao *et al.*, 2010).
- *Frustrated antiferromagnets and spin liquids.* The rule of thumb in this area says that everywhere in the vicinity of a high T_c superconducting phase there exists a (frustrated) antiferromagnetic phase. Frustrated antiferromagnets have thus been at the centre of interest in condensed matter physics for decades. Particularly challenging here is the possibility of creating novel, exotic quantum phases, such as valence-bond solids, resonating valence-bond states, and various kinds of quantum spin liquids—spin liquids of kind I and II according to C. Lhuillier (Lhuillier, 2005; Misguich and Lhuillier, 2003), and topological and critical spin liquids according to M. P. A. Fisher (Alet *et al.*, 2006; Sachdev, 2008). In this respect, cold atoms also offer opportunities to create various frustrated spin models in triangular or even kagomé lattices (Santos *et al.*, 2004). In the latter case, it has been proposed by Damski *et al.* (2005a, 2005b) that cold dipolar Fermi gases or Bose–Fermi mixtures might allow realization of a novel state of quantum matter: a *quantum spin-liquid crystal*, characterized by Néel-like order at low T (see Honecker *et al.* (2007)), accompanied by extravagantly high, liquid-like density of low-energy excited states.
- *Topological order and quantum computation.* Several very ‘exotic’ spin systems with topological order have been proposed recently (Douçot *et al.*, 2005; Kitaev, 2006) as candidates for robust quantum computing (for a recent review see Nayak *et al.* (2008)). Despite their unusual form, some of these models can be realized with cold atoms (Duan *et al.*, 2003; Micheli *et al.*, 2006). Particularly interesting (Lewenstein, 2006) is the recent proposal by Micheli *et al.* (2006), who proposed using heteronuclear polar molecules in a lattice, exciting them using microwaves to the lowest rotational level, and employing strong dipole–dipole interactions in the resulting spin model. The method provides an universal ‘toolbox’ for spin models with designable range and spatial anisotropy of couplings. Experimental achievements in cooling heteronuclear molecules that may have a large electric dipole moment (Ospelkaus *et al.*, 2006, 2009) have opened up the possibilities in this direction. Very recently, a gas of ultracold ground-state potassium–rubidium molecules was realized (Ni *et al.*, 2008).

- *Systems with higher spins.* Lattice Hubbard models, or spin systems with higher spins, are also related to many open challenges; perhaps the most famous being the Haldane conjecture concerning the existence of a gap or the lack of one for 1D antiferromagnetic spin chains with integer or half-integer spins, respectively. Ultracold spinor gases (Stamper-Kurn and Ketterle, 2001) might help study of these questions. Of particular interest in this context are spinor gases in optical lattices (Imambekov *et al.*, 2003; Yip, 2003a, 2003b; Eckert *et al.*, 2007), where in the strongly interacting limit the Hamiltonian reduces to a generalized Heisenberg Hamiltonian. Using Feshbach resonances (Chin *et al.*, 2010) and varying the lattice geometry, one should be able to generate a variety of regimes and quantum phases in such systems, including the most interesting antiferromagnetic regime. García-Ripoll *et al.* (2004) proposed to use a duality between the antiferromagnetic (AF) and ferromagnetic (F) Hamiltonians, $H_{\text{AF}} = -H_{\text{F}}$, which implies that minimal energy states of H_{AF} are maximal energy states of H_{F} and vice versa. Since dissipation and decoherence are practically negligible in such systems and affect both ends of the spectrum equally, one can study antiferromagnetic physics with H_{F} , preparing adiabatically antiferromagnetic states of interest.
- *Fractional quantum Hall states.* Since the famous work of Laughlin (1983), there has been enormous progress in our understanding of the fractional quantum Hall effect (FQHE) (Jacak *et al.*, 2003). Nevertheless, many challenges remain, such as the direct observation of the anyonic character of excitations and the observation of other kinds of strongly correlated states. FQHE states might be studied with trapped ultracold rotating gases (Wilkin and Gunn, 2000; Cooper *et al.*, 2001). Rotation induces effects equivalent to an ‘artificial’ constant magnetic field directed along the rotation axis. There are proposals about how to directly detect fractional excitations in such systems (Paredes *et al.*, 2001). Optical lattices might help in this task in two ways. First, FQHE states of small systems of atoms could be observed in a lattice with rotating site potentials or an array of rotating microtraps (see Popp *et al.* (2004), Barberán *et al.* (2006), Dagnino *et al.* (2007), and Osterloh *et al.*, 2007). Second, an ‘artificial’ magnetic field might be directly created in lattices via appropriate control of the tunneling (hopping) matrix element in the corresponding Hubbard model (Jaksch and Zoller, 2003). Such systems will also allow creation of FQHE-type states (Mueller, 2004; Sørensen *et al.*, 2005; Palmer and Jaksch, 2006; Palmer *et al.*, 2008). Klein and Jaksch (2009) recently proposed to immerse a lattice gas in a rotating Bose condensate; tunneling in the lattice then becomes partially mediated by the phonon excitations of the BEC and mimics the artificial magnetic field effects. Last, but not least, a direct approach employing lattice rotation has been developed both in theory (Bhar *et al.*, 2006, 2007), and in experiment (Tung *et al.*, 2006). The recent wave of very successful experiments creating artificial or synthetic magnetic fields employing laser-induced gauge fields (Lin *et al.*, 2009a, 2009b) were achieved by using spatially dependent optical coupling between different internal states of atoms. Such an approach is free from rotational restrictions.
- *Lattice gauge fields.* Gauge theories, and in particular lattice gauge theories (LGTs) (Montvay and Münster, 1997), are fundamental for both high-energy physics and condensed-matter physics, and despite the progress in our understanding of LGTs, many questions in this area remain (see e.g. Dalibard *et al.* (2010)). The physics

of cold atoms might help in this area in two ways: ‘artificial’ non-Abelian magnetic fields may be created in lattice gases via appropriate control of the hopping matrix elements (Osterloh *et al.*, 2005) or in trapped gases using effects of electromagnetically induced transparency (Ruseckas *et al.*, 2005). One of the most challenging tasks in this context concerns the possibility of realizing generalizations of Laughlin states with possibly non-Abelian fractional excitations. Another challenge concerns the possibility of ‘mimicking’ the dynamics of gauge fields. In fact, dynamical realizations of $U(1)$ Abelian gauge theory, which involve ring-exchange interaction in a square lattice (Büchler *et al.*, 2005) or three-particle interactions in a triangular lattice (Pachos and Rico, 2004; Tewari *et al.*, 2006) have been recently proposed.

- *Superchemistry.* This is a challenge of quantum chemistry, rather than of condensed matter physics: to perform a chemical reaction in a controlled way, using photoassociation or Feshbach resonances, from a desired initial state to a desired final quantum state. Jaksch *et al.* (2002) proposed to use an MI with two identical atoms to create via photoassociation, first an MI of homonuclear molecules and then a molecular superfluid via ‘quantum melting’. A similar idea was applied to heteronuclear molecules (Damski *et al.*, 2003a) in order to achieve molecular superfluids. Bloch’s group have indeed observed photoassociation of ^{87}Rb molecules in a MI with two atoms per site (Rom *et al.*, 2004), while Rempe’s group has realized the first molecular MI using Feshbach resonances (Volz *et al.*, 2006). Formation of three-body Efimov trimer states was observed in trapped caesium atoms by Grimm’s group (Kraemer *et al.*, 2006). This process could be even more efficient in optical lattices (Stoll and Köhler, 2005). An overview of the subject of cold chemistry can be found in Krems *et al.* (2009) and, in particular on the subject of cold Feshbach molecules, in Ferlaino *et al.* (2009). Control and creation of deeply bound molecules in the presence of an optical lattice has been reported in Danzl *et al.* (2009).
- *Ultracold dipolar gases.* Some of the most fascinating experimental and theoretical challenges of modern atomic and molecular physics concern ultracold dipolar quantum gases (see Baranov *et al.* (2002), Baranov (2008), and Lahaye *et al.* (2009)). The recent experimental realization of a dipolar Bose gas of chromium (Griesmaier *et al.*, 2005) and progress in trapping and cooling dipolar molecules (Ni *et al.*, 2008) have opened the path towards ultracold quantum gases with dominant dipole interactions. Dipolar BECs and BCS states of trapped gases are expected to exhibit very interesting dependence on the trap geometry. Dipolar ultracold gases in optical lattices, described by extended Hubbard models, should allow realization of various quantum insulating ‘solid’ phases, such as phase checkerboard and superfluid phases such as the supersolid (SS) phase (Góral *et al.*, 2002; Menotti *et al.*, 2007; Trefzger *et al.*, 2008). Of particular interest in this context are the *rotating dipolar gases*. Bose–Einstein condensates of rotating dipolar gases exhibit novel forms of vortex lattice: square, ‘stripe crystal’, and ‘bubble crystal’ forms (Cooper *et al.*, 2005). Baranov *et al.* (2005) have demonstrated that the pseudo-hole gap survives the large N limit for the Fermi rotating dipolar gases, making them perfect candidates to achieve the strongly correlated regime and to realize a Laughlin liquid at filling $\nu = \frac{1}{3}$ and a quantum Wigner crystal at $\nu \leq \frac{1}{7}$ using a mesoscopic number of atoms $N \simeq 50\text{--}100$ (Baranov *et al.*, 2008).

- *Wigner crystals or self-assembled lattices.* Wigner or Coulomb-type crystals are predicted to be formed due to long-range repulsive dipolar atom–atom or molecule–molecule interactions (Astrakharchik *et al.*, 2007, 2008a; Büchler *et al.*, 2007a) or ion–ion Coulomb interactions in the absence of a lattice (Porras and Cirac, 2006).

Many of these challenges will be discussed in the pages of this book.

1.4. Plan of the book

The aim of this book is to give an overview of the different domains covered by the physics of ultracold atoms in optical lattices. It reviews the possibilities that quantum gases in optical lattices offer with regard to exploration of an extensive range of many-body phenomena at the quantum level. The book places special emphasis on current challenges and open problems in condensed-matter and high-energy physics and quantum information that might be addressed with ultracold gases. It presents, in addition, the achievements so far. We stress here that this book does not contain a systematic course in quantum many-body systems or quantum-field theory. For such a purpose we refer the reader to the excellent books of Pitaevskii and Stringari (2003) and Pethick and Smith (2008) on Bose–Einstein condensation in the weakly interacting regime, and also to the books of Fetter and Walecka (2003) and X. G. Wen (2004) for many-body and quantum-field theory. This book offers only an introduction to this vast subject, focusing particularly on what can be studied with ultracold atoms in optical lattices.

The first part of the book (Chapters 1–6) aims to give a comprehensible introduction to ultracold atoms in optical lattices and to the condensed-matter physics that can be addressed with ultracold atoms, ions, or molecules. The intention of this part is to introduce the reader to the state of the art of working with ultracold gases in optical lattices, together with the fundamental formalism associated with it. We start in Chapter 2 with a very general consideration of classical and quantum phase transitions in statistical and condensed-matter physics, and also look at the phenomenon of condensation. We draw particular attention here to low-dimensional systems. Chapter 3 deals with basic concepts on periodic systems, introduces the physics of ultracold atomic gases in optical potentials in the weakly interacting regime, and ends up with the transition to the strongly correlated regime. Chapter 4 explains the sense in which ultracold atom can mimic condensed matter; we introduce here the concept of quantum simulators and list the condensed-matter systems of interest that may be addressed with ultracold atoms in optical lattices. In Chapters 5 and 6 we present the methodologies and formalisms to deal on one hand with bosonic ultracold lattice gases, and on the other with fermions and with fermion–boson mixtures in the strongly correlated regime.

In the second part of the book (Chapters 7–14) we present an overview of specific open problems of modern physics that can be investigated using the new paradigm of ultracold lattice gases. Although spin models have been constructed as idealizations or toy models of real systems, ultracold atoms allow for an almost perfect realization of many. The design and properties of magnetic models involving spin–spin interactions are reported in Chapter 7. Dipolar ultracold gases constitute some of the most exciting experimental and theoretical challenges of modern atomic and molecular physics, and are

12 *Introduction*

analysed in Chapter 8. The theory of disordered interacting particles is very complex and, in general, there are no exact solutions. Nonetheless, disorder plays a fundamental role in condensed-matter systems and the physics that stems from it is not only fascinating but also fundamental. Chapter 9 reports on the effects of disorder in the weakly and strongly correlated regimes and explores the possibilities of completely new exotic quantum phases. The understanding of non-disordered but nevertheless frustrated systems remains elusive, although their importance in many of the open challenges of modern physics is broadly recognized. Again, ultracold gases could be used to simulate and maybe to gain a deeper understanding of such systems (Chapter 10). Lattice gauge theories are fundamental issues in condensed-matter and high-energy physics. Ultracold atoms can be used to simulate and study Abelian and non-Abelian LGTs, as discussed in Chapter 11. The relations displayed between entanglement and quantum phase transitions stimulated the use of quantum information tools, giving a fresh perspective in the study of condensed-matter systems. Chapter 12 develops this connection in the area of ultracold gases, while Chapter 13 is devoted to quantum information processing, i.e. implementations of various quantum computation and communication protocols with ultracold atoms. Although the book is written by theorists, the last chapter of the second part (Chapter 14) is devoted to one of the most fundamental experimental challenges in this field, which is the detection of quantum many-body systems. The summary and future perspectives that we foresee for this fascinating field are discussed in Chapter 15.

2

Statistical physics of condensed matter: basic concepts

This chapter has a general introductory character, and presents, with some details, foundations of the subjects discussed in the later parts of the book. In particular we ask the question: which are the interesting phenomena that one can mimic with ultracold atoms? Here the basic concepts of condensed matter physics are sketched: classical phase transitions, quantum phase transitions, low-dimensional (1D and 2D) systems and their peculiarities. Most of the ideas are illustrated with the help of spin models, or quantum Bose gases. This chapter is mostly directed to AMO readers, and provides a reminder and a background in condensed matter and statistical physics.

2.1. Classical phase transitions

Before specifying the systems that we are going to mimic with ultracold atoms let us turn first to basic phenomena. Obviously, one of the most fascinating subjects is the investigation of the various quantum phases and phase transitions in the systems of interest. Before we discuss quantum phase transitions, we will take the reader on a ‘crash-course’ in classical phase transitions. Deeper understanding can be gained from many textbooks (for example Amit (2005), Binney *et al.* (1992), Lavis *et al.* (1999), Lavis and Bell (1999), and Mussardo (2010)). We concentrate here on second order (continuous) phase transitions and illustrate the theory with the paradigmatic example of the ferromagnetic phase transition in classical spin systems and classical ϕ^4 field theory.

In the ‘standard’ scenario of Ginsburg and Landau, classical systems order at low temperature and the order is manifested by a non-zero expectation value of the so-called *order parameter*. Temperature is, in this context, a *control parameter*. Order parameter vanishes (continuously) at and above the critical temperature. In this sense classical phase transitions are driven by thermal fluctuations. They occur, strictly speaking, when the number of constituents of the system, N , and its volume, V , tend to infinity, $N \rightarrow \infty$, $V \rightarrow \infty$, but N/V remains finite (thermodynamic limit). Phase transitions manifest themselves as non-analytic singularities of the free energy of the systems.

2.1.1 Ferromagnetic transition in classical spin systems

Let us illustrate these points using ferromagnetic spin models with nearest neighbors couplings, $J \geq 0$, for which the energy is given by

$$H = -J \sum_{\langle i,j \rangle} s_i s_j, \quad (2.1)$$

with $s_i = \pm 1$ in the Ising case (with discrete Z_2 symmetry), and

$$H = -J \sum_{\langle i,j \rangle} \mathbf{s}_i \mathbf{s}_j, \quad (2.2)$$

with $|\mathbf{s}_i| = 1$ for the *XY* (the spins \mathbf{s}_i lie in the *XY* plane, and have $U(1)$ symmetry), or Heisenberg (the spins have full rotational $SU(2)$ symmetry) models, respectively. The symbol $\langle \dots \rangle$ indicates here that the sum in the Hamiltonian is restricted to nearest neighbors only.

The thermal state is described by the canonical ensemble and the Boltzmann–Gibbs distribution $P(s) = \exp(-\beta H(s))/Z$, with Z being the partition function $\beta = 1/k_B T$, k_B denoting the Boltzmann constant, and T the temperature. The order parameter is the magnetization $m = \langle s_i \rangle$ ($m = \langle \mathbf{s}_i \rangle$). Denoting $\beta J = \kappa$, we have that for $\kappa < \kappa_c$ the system is in a *paramagnetic state*, which respects the symmetry of the Hamiltonian. For lower temperatures, i.e. for $\kappa > \kappa_c$, the symmetry is spontaneously broken in the infinite system (thermodynamic) limit, and the system enters a *ferromagnetic state*. Mathematically, this is achieved either using a ‘Bogoliubov’ trick, i.e. adding an infinitesimal symmetry-breaking magnetic field h to the Hamiltonian, or by considering fixed boundary conditions of the bulk of the system with fully polarized spins, and going with the size of the bulk to infinity. The latter method is preferred by mathematical physicists.

In Figure 2.1 we show the schematic phase diagram for a slightly more complex model: the d -dimensional Ising model in the transverse field. We do this in order to compare it with the quantum results of the next section. The Hamiltonian of this model is

$$H = -J \sum_{\langle i,j \rangle} s_i^z s_j^z - \tilde{h} \sum_i s_i^x, \quad (2.3)$$

with $(s_i^z)^2 + (s_i^x)^2 = 1$. This model has also two phases for $d \geq 2$: a magnetized ferromagnetic phase in which both $m_z = \langle s_i^z \rangle \neq 0$ and $m_x = \langle s_i^x \rangle \neq 0$, and a magnetized paramagnetic one with $m_z = 0$, whereas $m_x \neq 0$. The transition is of second order. In one dimension the ferromagnetic region shrinks to the case $T = 0$, achieved when $\kappa \rightarrow \infty$, $h \rightarrow \infty$, and $h/\kappa = \text{constant}$; the transition remains continuous there. Figure 2.1 was obtained using the mean-field theory, i.e. an approximation consisting of replacing $\beta H \rightarrow \beta H_{MF} = -2d\kappa \sum_i s_i^z m_z - h \sum_i s_i^x$, and calculating self-consistently $m_z = \langle s_i^z \rangle_{MF}$ and $m_x = \langle s_i^x \rangle_{MF}$, with $h = \beta \tilde{h}$. Within the mean-field approximation the magnetized ferromagnetic phase occurs for

$$2d\kappa \geq h I_0(h)/I_1(h), \quad (2.4)$$

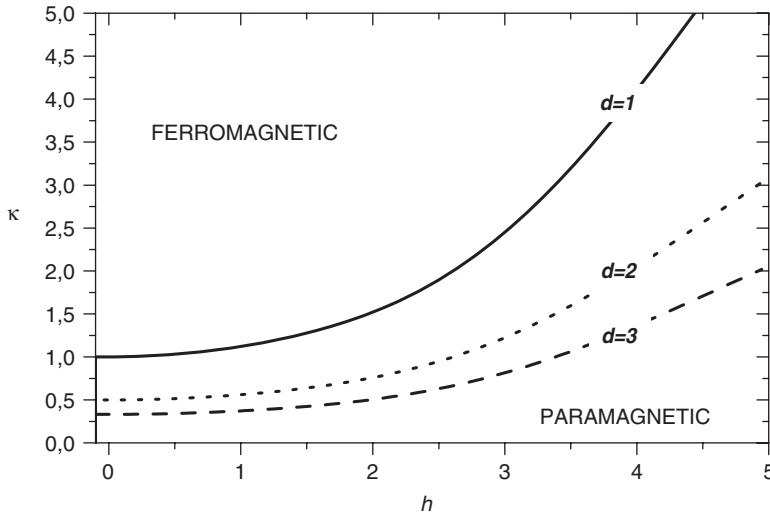


Figure 2.1 Mean-field phase diagram for the Ising model in the transverse field. Mean-field results at $d = 1$ are incorrect, since the long-range order there is destroyed by thermal fluctuations; the solid line thus describes qualitatively a crossover between paramagnetic-like and ferromagnetic-like (dominated by large domains) behavior.

where the functions $I_n(\cdot)$ denote the modified Bessel functions. There is a critical point $d\kappa_c = 1$ at $h = 0$. Note that the mean-field theory is incorrect in one dimension, as it predicts the existence of phase transition at non-zero T . The solid line in Figure 2.1 should be thus interpreted as a crossover line.

At $T = 0$ an elementary direct calculation shows that $m_z \neq 0$ for $g = h/2d\kappa = \tilde{h}/2dJ < g_c = 1$. The latter result can also be obtained from eqn (2.4) by taking the limit $h, \kappa \rightarrow \infty$ with $h/\kappa = \text{const}$. The criticality at $T = 0$ and $g_c = 1$ is correctly predicted by the mean-field theory and occurs at any $d = 1, 2, 3, \dots$. It can be regarded as a classical analog of the quantum phase transition in the quantum version of the model.

2.1.2 Critical exponents

At criticality, physical quantities exhibit *scaling behavior*, i.e. power dependence with $\tau = |\kappa - \kappa_c|$. The exponents of these power laws are called *critical exponents*. For the second-order continuous phase transitions, there is a particular importance in the exponents describing the behavior of:

- the correlation length ξ , defined by analysing the exponential decay of the spin–spin correlation functions close to criticality

$$\langle s_i s_j \rangle - \langle s_i \rangle \langle s_j \rangle \propto \exp(-|\mathbf{r}_i - \mathbf{r}_j|/\xi), \quad (2.5)$$

and which diverges as $\xi \propto \tau^{-\nu}$

16 Statistical physics of condensed matter: basic concepts

- the correlation functions, which at criticality decay algebraically,

$$\langle s_i s_j \rangle - \langle s_i \rangle \langle s_j \rangle \propto |\mathbf{r}_i - \mathbf{r}_j|^{-d+2-\eta} \quad (2.6)$$

- the magnetization near criticality, which tends to zero as the temperature tends to the critical one from below as $m = \tau^\beta$
- the magnetization at criticality, which scales for small h as $m \propto h^{1/\delta}$
- the specific heat per particle (spin), $C = \partial u / \partial T$, where $u = \langle H \rangle / N$, diverges as $C \propto \tau^{-\alpha}$
- the magnetic susceptibility, $\chi \propto \partial m / \partial h$ diverges as $\tau^{-\gamma}$.

In principle, the critical exponents of the same physical quantities could be different above and below the critical point. Due to the *scaling laws*, this is not the case (Amit, 2005). Similarly, various scaling relations hold: $\bar{\beta} = \gamma / (\delta - 1)$, $\nu = \gamma / (2 - \eta)$, etc.

2.1.3 Universality and real space renormalization group

The physical picture of the transition is as follows: as we approach the transition from above, the correlation length grows. Islands (domains) of correlated (ordered) spins appear, whose size grows. The snapshots of the system look the same for different τ s; only the length scale ξ changes. It is natural then to try to describe the systems at longer and longer length scales. One way to do this, going back to Kadanoff (Binney *et al.*, 1992, Kadanoff, 2000, Amit, 2005), is to divide the system into blocks, introduce block spins and calculate the new Hamiltonian for the *renormalized* length. In practice this procedure can be realized using various kinds of perturbative approaches and it works remarkably well for Ising models (Niemeijer and van Leeuwen, 1973). The result of such calculations is a transformation of the Hamiltonian parameters as we change the length scale. Attractive fixed points of this flow define the relevant thermodynamic phases. For the ferromagnetic problem we have two attractive fixed points corresponding to $T = 0$ (all spins ordered) and $T \rightarrow \infty$ (disordered phase). There exists one non-trivial unstable fixed point, called the *infrared fixed point*, which describes the criticality. Linearizing the renormalization transformation close to this point allows us to calculate critical exponents. This picture explains the universality: various microscopic Hamiltonians undergo the same renormalization flow and have the same exponents, which are essentially determined by the dimensionality and symmetries of the models, the range of interactions (short versus slow power law) etc. In contrast, critical values of the temperature are not universal (they are determined by the initial point of the flow, and whether it converges to $T = 0$ or $T = \infty$).

Let us illustrate this for the case of the 2D Ising model, described by the Hamiltonian

$$H = -J \sum_{\langle i,j \rangle} s_i s_j, \quad (2.7)$$

but now in a triangular lattice. We introduce block spins by grouping triples of spins in shaded cells as shown in Figure 2.2, and define for each block the new Ising spin variable

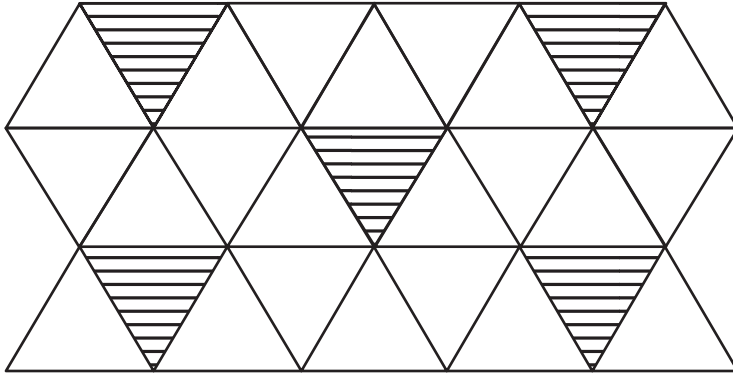


Figure 2.2 Real-space renormalization group transformation on a triangular lattice. The lattice is divided into cells (triangles) having an odd (three) number of sites such that the lattice of cells is again triangular (reproduced after Niemeijer and van Leeuwen (1973)).

$s' = \text{sign}(s_1 + s_2 + s_3)$. The real-space renormalization group transformation consists of the calculation of the new Hamiltonian for the block spins

$$\exp(-\beta'H'(s'))/Z' = \sum_{s=\pm 1} \prod_{\text{blocks}} \delta(s' - \text{sign}(s_1 + s_2 + s_3)) \exp(-\beta H(s))/Z \quad (2.8)$$

where Z and Z' are the old and new partition functions, respectively. This transformation is in practice realized using various versions of the perturbation theory in the inter-block couplings. In the most simple approach, defining $\kappa = \beta J$ we obtain for neighboring blocks a and b , linked by the bond $\langle i, j \rangle$

$$\langle s'_a s'_b \rangle = 2 \langle s_a^a s_j^b \text{sign}(s_1^a + s_2^a + s_3^a) \text{sign}(s_1^b + s_2^b + s_3^b) \rangle, \quad (2.9)$$

where $\langle . \rangle$ denotes the average, calculated exactly with respect to the (zeroth order) block Hamiltonians, and perturbatively with respect to the inter-block couplings. The factor 2 on the left-hand side comes from the fact that there are in fact two equivalent bonds connecting blocks a and b . The result of this simple calculation gives

$$\tanh(\kappa') \simeq \kappa' = 2\kappa \left(\frac{\cosh(2\kappa)}{2\cosh(2\kappa) - \sinh(2\kappa)} \right)^2. \quad (2.10)$$

It is elementary to check that this map has indeed three fixed points:

- a trivial stable (attractive) fixed point $\kappa = 0$, corresponding to the high-temperature disordered phase;
- another trivial fixed point at $\kappa = \infty$, corresponding to the low-temperature ferromagnetic phase;
- a non-trivial unstable fixed point for $\kappa^* \simeq 0.3$, which should be associated with criticality, i.e. within this calculation $\kappa_c = \kappa^*$.

Close to the criticality, one can linearize the map. Denoting $\tau = \kappa - \kappa^*$, we obtain

$$\tau' = \lambda_T \tau.$$

The fact that the fixed point is unstable implies that $\lambda_T > 1$. Note that the renormalization transformation corresponds to the change of length scale by a factor l ; in the present case $l = \sqrt{3} = 1.73\dots$. The correlation length scales thus changes as

$$\xi' = \xi/l.$$

Since, close to the criticality, the correlation length scales as $\xi \propto (\tau)^{-\nu}$, we immediately obtain $(\tau')^{-\nu} = l^{-1}(\tau)^{-\nu}$, or equivalently

$$\tau' = l^{1/\nu} \tau,$$

so that we see that

$$\lambda_T = l^{1/\nu},$$

which gives the direct relation of λ_T to the critical exponent ν .

Generalization of this calculation to include the longitudinal field $h = \beta \tilde{h}$ is straightforward. We again obtain one non-trivial unstable fixed point $\kappa = \kappa^*, h = 0$. Linearizing close to the criticality leads to

$$\tau' = \lambda_T \tau, \quad h' = \lambda_h h,$$

where both λ_T and λ_h are greater than 1. Since at the criticality the magnetization scales as $m \propto h^{1/\delta}$, whereas below the critical temperature and for $h = 0$ it tends to zero as $m \propto \tau^{\bar{\beta}}$, we obtain that $h \propto \tau^{\bar{\beta}\delta}$, and therefore

$$h' = l^{\bar{\beta}\delta/\nu} h.$$

This implies that $\lambda_h = l^{\bar{\beta}\delta/\nu}$, and thus relates λ_h to critical exponents $\bar{\beta}$, δ , and ν . Since for the 2D Ising model critical exponents, as well as the value of $\kappa_c = 0.27$, are known exactly, $\nu = 1$, $\delta = 15$, $\bar{\beta} = 1/8$, the exact values of λ_s read $\lambda_T = \sqrt{3} \simeq 1.73$, and $\lambda_h = \sqrt{3}^{15/8} = 3^{15/16} \simeq 2.80$. Direct calculation of λ_s within our real-space renormalization group method gives $\lambda_T = 1.63$, $\lambda_h = 3.04$, and the critical point $\kappa_c = 0.34$ (Niemeijer and van Leeuwen, 1973). Taking into account the ‘effort/precision’ ratio, these results are indeed amazingly good.

For the short-range spin models we have general results as follows.

- For $d \geq 4$, the (Landau–Ginsburg) mean-field theory (which consists of replacing H by $H_{MF} = Jz \sum_i s_i m$ for the Ising case, and $H_{MF} = Jz \sum_i \mathbf{s}_i \cdot \mathbf{m}$ in general, where z is the coordination number, i.e. the number of nearest neighbors in the lattice) is valid, and the mean-field exponents are $\alpha = 0$, $\bar{\beta} = 1/2$, $\gamma = 1$, $\delta = 3$, $\eta = 0$, and $\nu = 1/2$. Exactly at $d = 4$ there are logarithmic corrections to these power laws. $d = 4$ is called the *upper critical dimension*.

- For the Ising model the transition still occurs in two dimensions, which is then called the *lower critical dimension*. The exponents in two dimension, as well as critical temperatures for a variety of lattices, are known exactly from the famous exact solution of Onsager (Onsager, 1944, McCoy and Wu, 1973, Baxter, 1982): $\alpha = 0$, $\bar{\beta} = 1/8$, $\gamma = 7/4$, $\delta = 15$, $\eta = 1/4$, and $\nu = 1$. In three dimensions the exponents are known only approximately or numerically with values of $\alpha = 0.110(1)$, $\bar{\beta} = 0.3265(3)$, $\gamma = 1.2372(5)$, $\delta = 4.789(2)$, $\eta = 0.0364(5)$, and $\nu = 0.6304(1)$ (Pelissetto and Vicari, 2002).
- For the XY model, the lower critical dimension is two. As follows from the famous Mermin–Wagner–Hohenberg theorem (Mermin and Wagner, 1966, Hohenberg, 1967), the spin models with continuous symmetry cannot order (ferromagnetically) at $T > 0$. However, the XY model in two dimensions exhibits a phase transition: the celebrated Berezinskii–Kosterlitz–Thouless (BKT) transition (Berezinskii, 1972, Kosterlitz and Thouless, 1972, Kosterlitz and Thouless, 1973), in which the correlation functions at low T change their decay law from exponential to algebraic. We discuss BKT in more detail in Section 2.5.2. In three dimensions, the XY model orders but the exponents are known only approximately or numerically.
- For the Heisenberg model the situation is similar to that for the XY model. No ordering is possible for $T > 0$ in two dimensions, but there is no BKT transition. In three dimensions exponents are known approximately or numerically.

2.1.4 Ferromagnetic transition in classical ϕ^4 models

We restrict ourselves here to the ϕ^4 models with the real Z_2 or complex $U(1)$ symmetries. The energy functional has the famous Landau–Ginsburg–Wilson form. One way to derive this is to consider a spin model in a d -dimensional hypercubic lattice, with nearest neighbor couplings and arbitrary continuous values of the spin vectors, with length peaked at 1. This can be achieved by introducing into the spin Hamiltonian on the lattice a large quartic term of the form $\sum_i(s_i^2 - 1)^2$, which clearly leads to large energy costs if $s_i \neq \pm 1$. We then take the continuous limit of the lattice constant $a \rightarrow 0$, and obtain

$$H = \int \frac{d^d \mathbf{x}}{a^d} \left[Jda^2 |\nabla \phi|^2 / 2 - \mu |\phi|^2 + \frac{g}{2} |\phi|^4 - (\tilde{h}\phi + c.c.) / 2 \right]. \quad (2.11)$$

The thermal state is, as before, the Boltzmann–Gibbs state $\exp(-\beta H)/Z$, and the partition function Z is defined as a functional integral over configurations of the classical fields $\phi(\mathbf{x})$. If the fields are restricted to be real, we deal with an Ising-like system; if they are complex this corresponds to XY -like systems. Note that by introducing an auxiliary time variable and writing $\phi(\mathbf{x}, \tau) = \phi(\mathbf{x})$, we can replace βH in the partition function by

$$H = \int \frac{d^{d+1} \mathbf{x}}{a^{d+1}} \left[Jda^2 |\nabla \phi|^2 / 2 - \mu |\phi|^2 + \frac{g}{2} |\phi|^4 - (\tilde{h}\phi + c.c.) / 2 \right], \quad (2.12)$$

where the ∇ acts now in the $d + 1$ dimensional space, and the configurations of $\phi(\mathbf{x}, \tau)$ are periodic in τ , with period β . This now corresponds to the functional integral that one considers in $d + 1$ Euclidean quantum field theory, i.e. d -dimensional quantum field theory with the imaginary time variable (see Montvay and Münster (1997)).

The functional integral can be evaluated using the semiclassical approximation, i.e. Laplace's saddle point method (see Auerbach (1994)). To this end we look at the minima of the energy functional. For $\mu > 0$ the minimum (for \tilde{h}) is at zero configuration and there is no order. For $\mu < 0$, we get for the Ising case $\phi = \pm\sqrt{\mu/g}$, and for the XY case $\phi = \sqrt{\mu/g} \exp(i\theta)$, where θ is arbitrary (it corresponds to spontaneous symmetry breaking).

2.1.5 Universality and momentum space renormalization group

The concepts of renormalization group and universality classes can also be studied using the functional formulation. To this end we first rescale the field as

$$|\phi|^2 \rightarrow (a^{d-2}/Jd)|\phi|^2, \quad (2.13)$$

and the Hamiltonian eqn (2.11) reads

$$H = \int d^d \mathbf{x} \left[|\nabla \phi|^2/2 + ta^{-2}|\phi|^2 + ua^{d-4}|\phi|^4 + (ha^{-d/2-1}\phi + c.c.)/2 \right], \quad (2.14)$$

where the dimensionless parameters are $t = -\mu/Jd$, $u = g/2(Jd)^2$, and $h = -\tilde{h}/\sqrt{Jd}$. In this case, however, it is much more convenient to work in the momentum space, as pointed out in the seminal works of Wilson (Wilson, 1970a,b,c, 1975, Cardy, 1996). The Hamiltonian then reads

$$H = \int d^d \mathbf{k} \left[|\mathbf{k} \cdot \phi(\mathbf{k})|^2/2 + ta^{-2}|\phi(\mathbf{k})|^2 + ua^{d-4}|\phi(\mathbf{k})|^4 + ha^{-d/2-1}\phi(\mathbf{k}) + c.c.)/2 \right]. \quad (2.15)$$

The theory makes sense only if one introduces an ultraviolet (high-energy, high-momentum) cut-off, $\Lambda = 1/a$. The renormalization transformation consists of introducing a new cut-off $\Lambda' = \Lambda/b < \Lambda$, with $b > 1$, integrating out the contributions from large momenta $\Lambda' \leq |\mathbf{k}| \leq \Lambda$, and then rescaling Λ' back to the original value. In practice this is done using perturbation theory in g , but fairly soon it turns out that this approach corresponds in fact to the expansion in the famous dimensional parameter $\epsilon = 4 - d$ (Wilson, 1975). This is so because of the triviality of the ϕ^4 theory in 4D (Montvay and Münster, 1997), where the solutions of the renormalization group equations are dragged toward the vanishing g region. For the scalar Ising-like theory the renormalization group equations in the zeroth order (making eqn (2.14) invariant) read (Cardy, 1996, Amit, 2005, Binney *et al.*, 1992):

$$\begin{aligned} t &= b^{y_t} t = b^2 t, \\ h &= b^{y_h} h = b^{d/2+1} h, \\ u &= b^{4-d} u. \end{aligned} \quad (2.16)$$

Here we did not in fact do any expansion. We just integrated out the high energy/momentum modes, neglecting their coupling to the low energy/momentum ones. These renormalization group equations have the following meaning: when we change the cut-off we have to trivially rescale the momenta and the parameters of the theory to recover the same theory.

Scaling theory (see Cardy (1996) and the discussion in the previous section) tells us that the critical exponents are given by $\alpha = 2 - d/y_t$, $\beta = (d - y_h)/y_t$, $\gamma = (2y_h - d)/y_t$, $\delta = y_h/(d - y_h)$, and, last but not least, $\nu = 1/y_t$. As one can easily see, the renormalization group equations have a ‘trivial’ Gaussian fixed point $t = h = u = 0$. It is called Gaussian since the fixed point Hamiltonian is just $H^* = \int d^d\mathbf{k}|\mathbf{k}\phi(\mathbf{k})|^2/2$, i.e. it describes a simple Gaussian theory. For $d > 4$, the interactions are irrelevant, since $u \rightarrow 0$. The critical exponents at $d = 4$ attain their mean-field values. For $d < 4$ one has to be more careful, since we expect that a new non-Gaussian fixed point should appear. Indeed, the renormalization group equations in the next order give (Cardy, 1996):

$$\begin{aligned} dt/dl &= 2t - h^2 - 4t^2 - 24tu - 96u^2 + \dots, \\ dh/dl &= (d/2 + 1)h - 4ht + \dots, \\ du/dl &= \epsilon u - t^2 - 16tu - 72u^2 + \dots, \end{aligned} \quad (2.17)$$

where $l = \ln b$ for $b \simeq 1$, and $\epsilon = 4 - d$. Here we have done some of the work already: we used perturbation theory in u in order to treat the coupling between the high momentum modes that were integrated out and the low momentum ones. The Gaussian part of the theory was treated exactly. As can readily be seen, apart from the Gaussian fixed point there is another one for $h = 0$, $u = \epsilon/72 + O(\epsilon^2)$, $t = O(\epsilon^2)$. This is the celebrated Wilson–Fisher fixed point, which gives $y_t = 2 - (24/27)\epsilon + O(\epsilon^2)$ and $\nu = 1/2 + \epsilon/12 + O(\epsilon^2)$. The epsilon expansion expansion is quite accurate and the comparison of the approximate values of exponents and the numerical ones is quite satisfactory (Wilson, 1975, Cardy, 1996). For example, for the 2D Ising model, the exact value of $\nu = 1$ and the approximate value in the first order of the expansion is $\nu = 0.67$, but in the fifth order is $\nu = 0.99 \pm 0.04$.

2.2. Bose–Einstein condensation in non-interacting systems

Before turning to the discussion of quantum phase transitions that occur at $T = 0$ let us discuss a thermal phase transition that plays a particularly important role in the quantum world: Bose–Einstein condensation (BEC). Below a certain critical temperature T_c bosons tend to accumulate in a single one-particle state, described by the so-called condensate wave function. The critical temperature T_c is of the order of the temperature at which the interparticle distance becomes comparable to the particles’ thermal de Broglie wavelength (a detailed description of which can be found, for instance, in Pitaevskii and Stringari (2003)). The latter is defined by equating thermal energy with kinetic energy $k_B T/2 = \hbar^2 k^2/2m$, where k_B is the Boltzmann constant, m is the particle mass, and the wavevector k is related to the thermal de Broglie wavelength via $k = 2\pi/\lambda_{dB}(T)$.

2.2.1 Bose–Einstein condensation in a box

Amazingly, the phenomenon of BEC also occurs for non-interacting systems and is a direct consequence of quantum statistics (Pitaevskii and Stringari, 2003, Pethick and Smith, 2008). For a gas of N bosons trapped in a potential $V(x)$, BEC consists of condensation of a macroscopic number of bosons in the ground state of the trap for temperatures much higher than the trap excitation energy; in this sense BEC is a ‘high-temperature effect’. Let us first

consider the case of a box of a linear size L in d dimensions, in the thermodynamic limit, $N \rightarrow \infty$, $N/V = N/L^d = \text{const}$. In order to check whether the condensation takes place, we need to calculate the number of particles in the excited states of the box. To this end it is useful to consider the density of states $n(\epsilon)$, given in the semiclassical limit (consistent with large L) by

$$n(\epsilon) = \left(\frac{2\pi}{\hbar}\right)^d \int d^d x \int d^d p \delta(\epsilon - p^2/2m) = \left(\frac{2\pi}{\hbar}\right)^d 2mL^d S_d (2m\epsilon)^{(d-2)/2}, \quad (2.18)$$

where S_d is the surface of a d -dimensional sphere. According to Bose–Einstein statistics the number of particles at energy level ϵ at temperature T is $ze^{-\beta\epsilon}/(1 - ze^{-\beta\epsilon})$, where $z = e^{\beta\mu}$ is the so-called ‘fugacity’ and μ is the chemical potential. The total number of excited particles can be calculated as

$$N_{\text{exc}} = \int_{0^+} n(\epsilon) \frac{ze^{-\beta\epsilon} d\epsilon}{(1 - ze^{-\beta\epsilon})} \quad (2.19)$$

where 0^+ means that the integration takes place from 0 to ∞ excluding the ground state. The condensation occurs as $z \rightarrow 1$. The integrand decays exponentially for large ϵ , but for $z = 1$ might be divergent at $\epsilon \rightarrow 0$, where it behaves as $\propto \epsilon^{(d-4)/2}$. We immediately see that for:

- $d = 1$, the integral is divergent for any $\beta \neq \infty$, ($T \neq 0$), i.e. an infinite number of particles may occupy excited states, or, in other words, the density of excited particles can be arbitrarily large; there is no condensation, except for $T = 0$
- $d = 2$ is a marginal case in which the integral is divergent logarithmically for any $\beta \neq \infty$, ($T \neq 0$); there is no condensation, except for $T = 0$
- $d = 3$ gives a finite integral, the number of excited particles and their density are bounded from above and a macroscopic number of particles must condense in the ground state; BEC takes place.

Adding weak interactions does not change the situation in three dimensions—the BEC persists. In two dimensions the condensate exists only at $T = 0$ and is destroyed by phase fluctuations at any $T > 0$, as we shall see in later sections. The gas exhibits, however, a novel type of order: the Berezinskii–Kosterlitz–Thouless (BKT) phase. In one dimension the BEC is destroyed by phase fluctuations even at $T = 0$.

2.2.2 Bose–Einstein condensation in a trap

As we have seen in the previous section, the existence of BEC depends in the first place on the density of states. Since this quantity depends of the form of the trapping potential, the form of the trap potential decides whether there is condensation or not (de Groot *et al.*, 1950, Bagnato *et al.*, 1987, Bagnato and Kleppner, 1991). Let us consider here radially

symmetric traps with potentials $V(x) \propto |x|^s$. The density of states is given now by the expression:

$$n(\epsilon) = \left(\frac{2\pi}{\hbar}\right)^d \int d^d x \int d^d p \delta(\epsilon - p^2/2m - V(x)) \propto \epsilon^{(\frac{d-2}{2} + \frac{d}{s})}. \quad (2.20)$$

For the most commonly used harmonic traps, with $s = 2$, this implies:

- $d = 1$. The integral of eqn (2.20) is logarithmically divergent, i.e. there is no condensation except at $T = 0$. For weakly interacting gases in a harmonic trap one observes two crossovers: first to a phase-fluctuating quasi-condensate with suppressed density fluctuations, and then to a ‘true’ BEC, when the phase correlation length becomes larger than the cloud size. This will be discussed in the sections below.
- $d = 2$. In harmonic traps there is condensation in two dimensions. For weakly interacting gases the BEC transition is preceded at higher T , or even substituted by a BKT transition. Again, there is a crossover to a ‘true’ BEC when the phase correlation length becomes larger than the size of the cloud.
- $d = 3$. Similarly to the situation in the box, the BEC takes place in harmonic traps in three dimensions and obviously persists in the case of a weakly interacting gas.

2.3. Quantum phase transitions

Quantum phase transitions (QPT) occur in quantum systems at $T = 0$ (Sachdev, 1999). One can thus say that they are driven exclusively by quantum fluctuations. They happen at the non-analytic points of the ground state energy.

2.3.1 Ferromagnetic transition in a transverse field

A paradigmatic example of a quantum phase transition is provided by the spin- $\frac{1}{2}$ Ising model in the transverse field, described by the Hamiltonian

$$H = -J \sum_{\langle i,j \rangle} \hat{s}_i^z \hat{s}_j^z - h \sum_i \hat{s}_i^x, \quad (2.21)$$

where \hat{s}_i^z, \hat{s}_i^x denote the quantum spin operators. This model is exactly soluble in one dimension with the help of the Jordan–Wigner transformation (see Chapter 5). Here we just point out that it has (similarly to the classical case above) two phases: magnetized ferromagnetic for $J \gg h$ and magnetized paramagnetic otherwise. For systems of large but finite size, there are two quasi-degenerate ground states in the ferromagnetic phase ($J \gg h$), being the linear combinations of all spins up and all down, symmetric and anti-symmetric with respect to the flip of all spins. The z -component of the magnetization m_z is zero, but the states are of the Schrödinger’s cat type: any local measurement of \hat{s}_i^z projects them onto states with non-zero m_z . Apart from these two quasi-degenerate states the spectrum is gapped and excitations cost at least energy of order J . In the other limit, $J \ll h$, the ground state is non-degenerate and the spectrum exhibits a gap of order h . The gap vanishes at the criticality. Similarly to the classical case, one can introduce critical exponents here,

24 Statistical physics of condensed matter: basic concepts

and also the concepts related to universality. Renormalization group analysis is technically more involved, but there are no fundamental obstacles in realizing it.

2.3.2 Bose–Einstein condensation in interacting Bose systems

BEC (Pitaevskii and Stringari, 2003, Pethick and Smith, 2008) is typically regarded as a thermal phase transition. One can, however, look at BEC as a quantum phase transition occurring at $T = 0$ as a function of the chemical potential, μ . For negative μ there are very few particles, and the mean value of the atomic field operators is zero. In contrast, for positive μ atomic field operators attain a non-zero mean, and we have the condensation of a macroscopic number of atoms.

There are several ways of describing this physics, but the Bogoliubov–de Gennes (BdG) approach is the more direct one: we consider the Hamiltonian in the second quantized form

$$\hat{H} = \int d^d \mathbf{x} \left[+\frac{\hbar^2}{2m} \partial_{\mathbf{x}} \hat{\phi}^\dagger \partial_{\mathbf{x}} \hat{\phi} - \mu \hat{\phi}^\dagger \hat{\phi} + \frac{g}{2} \hat{\phi}^\dagger \hat{\phi}^\dagger \hat{\phi} \hat{\phi} \right], \quad (2.22)$$

and replace the fields by their average values plus quantum fluctuations $\hat{\phi} = \phi + \delta\hat{\phi}$, where the fluctuations fields now fulfill the canonical bosonic commutation relations. One inserts this ansatz into eqn (2.22) and keeps only up to quadratic terms in fluctuations. In effect, the Hamiltonian becomes a sum of ‘classical’ energy $E[\phi]$ (given by eqn (2.28) below) and a Hermitian form of $\delta\hat{\phi}$ and $\delta\hat{\phi}^\dagger$, describing the BdG quasiparticles:

$$H_{BdG} = E[\phi] + \int d^d \mathbf{x} \left[\frac{\hbar^2}{2m} \partial_{\mathbf{x}} \delta\hat{\phi}^\dagger \partial_{\mathbf{x}} \delta\hat{\phi} - \mu \delta\hat{\phi}^\dagger \delta\hat{\phi} + \frac{g}{2} (4|\phi|^2 \delta\hat{\phi}^\dagger \delta\hat{\phi} + \phi^2 \delta\hat{\phi}^\dagger \delta\hat{\phi}^\dagger + (\phi^*)^2 \delta\hat{\phi} \delta\hat{\phi}) \right]. \quad (2.23)$$

The linear terms in $\delta\hat{\phi}$ vanish provided ϕ fulfills the famous (stationary) Gross–Pitaevskii equation,

$$\mu\phi = \left[-\frac{\hbar^2}{2m} \nabla_{\mathbf{x}}^2 \phi + g\phi^*\phi\phi \right]. \quad (2.24)$$

The quadratic Hamiltonian (2.23) can easily be diagonalized in the homogenous case by using the Fourier and Bogoliubov transforms. In the non-homogeneous case, such as in a trap, the diagonalization is typically technically much more involved. The corresponding eigenmodes describe quasiparticles, in the sense that creation of such quasiparticles is a superposition of the creation of a real particle and the annihilation of a real particle accompanied by the creation of two condensate particles. Since the Bogoliubov approach breaks the $U(1)$ symmetry of the model, one of the BdG modes corresponds to a gapless Nambu–Goldstone mode, which restores the symmetry in a finite system (see discussion below).

Another way of describing the quantum field theory of interacting many-body systems, and perhaps one of the best, makes use of the Feynman’s path integrals. The generating

functional for the correlation functions for the interacting Bose system is given by (see Wen (2004)):

$$Z[j] = \int D[\phi(\mathbf{x}, t)] D[\phi^*(\mathbf{x}, t)] \exp[iS/\hbar + i \int d^d \mathbf{x} dt (\phi(\mathbf{x}, t)j(\mathbf{x}, t) + c.c.)/\hbar], \quad (2.25)$$

where the $D[\phi(\mathbf{x}, t)]$ is the measure and the action is:

$$S = \int d^d \mathbf{x} dt \left[\frac{i\hbar}{2} (\phi^* \partial_t \phi - \phi \partial_t \phi^*) - \frac{\hbar^2}{2m} \partial_{\mathbf{x}} \phi^* \partial_{\mathbf{x}} \phi + \mu |\phi|^2 - \frac{g}{2} |\phi|^4 \right]. \quad (2.26)$$

The partition function is then given by $Z[0]$. One can try to evaluate the functional integrals by using a *semiclassical* approximation, i.e. applying the *stationary action principle* to the action (eqn (2.26)). The stationary configurations of the fields then fulfill the time-dependent non-linear Schrödinger (Gross–Pitaevskii) equation (TDGPE) (Pitaevskii and Stringari, 2003),

$$i\hbar \frac{\partial \phi}{\partial t} = \left[-\frac{\hbar^2}{2m} \nabla_{\mathbf{x}}^2 \phi + g \phi^* \phi \phi \right]. \quad (2.27)$$

This fact is the basis of a powerful dynamical variational approach to solve the TDGPE: one parametrizes the solutions with few time-dependent functions, calculates the action, and derives equations for these functions (Pérez-García *et al.*, 1996, 1997). If one assumes that ϕ is time-independent (or alternatively that it oscillates in time with some frequency, and that this then modifies the value of μ), the stationary action principle reduces to the minimization of the energy given by:

$$E = \int d^d \mathbf{x} \left[\frac{\hbar^2}{2m} \partial_{\mathbf{x}} \phi^* \partial_{\mathbf{x}} \phi - \mu |\phi|^2 + \frac{g}{2} |\phi|^4 \right]. \quad (2.28)$$

The minimum occurs for $\phi = 0$, for $\mu < 0$, and is given by $\phi = \sqrt{\mu/g} \exp(i\theta)$ for $\mu > 0$, with θ being completely arbitrary. This change of ground state marks the phase transition to the Bose condensed or superfluid state, and spontaneous $U(1)$ symmetry breaking. Spontaneous symmetry breaking is necessarily connected with the appearance of a gapless excitation in the system: the so-called Nambu–Goldstone mode. Physically, this mode corresponds to excitations that try to restore the $U(1)$ (or actually broken) symmetry. In infinite systems the quantum phase diffusion becomes infinitely slow; in finite systems this is not the case and the phase symmetry restoring time is long but finite (see Blaizot and Ripka (1985) and Wen (2004)); for the BEC in a harmonic trap see Wright *et al.* (1996), Lewenstein and You (1996), and Imamoğlu *et al.* (1997). Quantum fluctuations, and in particular those associated with the Nambu–Goldstone mode, may destroy the superfluid order. This is particularly important in low dimensions, as we shall see in the next sections.

Before going to low d , let us derive a general description of the low-energy excitations for Bose systems, anticipating that the most important role at low energies is played by the phase fluctuations. To this end we can use either the BdG theory or the functional integral approach. For pedagogical reasons we shall outline both approaches.

2.3.3 BdG approach

We choose ϕ real and positive, and write the field $\hat{\phi} = \sqrt{\rho_0 + \delta\rho} \exp(i\hat{\theta}) \simeq \sqrt{\rho_0}(1 + \delta\hat{\rho}/2\rho_0 + i\hat{\theta})$, with $\rho_0 = \mu/g = \phi^2$, so that $\delta\hat{\phi} = \delta\hat{\rho}/2\sqrt{\rho_0} + i\sqrt{\rho_0}\hat{\theta}$. Inserting this into the BdG Hamiltonian (eqn (2.23)), we may easily derive the Heisenberg equations of motion for $\delta\hat{\rho}$ and $\hat{\theta}$, which take the form (Pitaevskii and Stringari, 2003):

$$\begin{aligned}\frac{d}{dt}\hat{\theta} &= -\frac{\hbar\nabla^2\delta\hat{\rho}}{4m\rho_0} - \frac{\mu\delta\hat{\rho}}{2\rho_0} - g\delta\hat{\rho}, \\ \frac{d}{dt}\delta\hat{\rho} &= +\frac{\rho_0\nabla\hat{\theta}}{m}.\end{aligned}\quad (2.29)$$

Eliminating the ‘fast’ density fluctuations and neglecting the second spatial derivative of ρ , we arrive at the hydrodynamic equation:

$$\frac{d^2}{dt^2}\theta = -\frac{\mu}{m}\nabla\theta. \quad (2.30)$$

It is easy to see that the eigenmodes of the above equation, i.e. eigenmodes of the phase fluctuations, fulfill a hydrodynamic or phonon dispersion relation $\omega = uk$, where $u = \sqrt{\mu/m} = \sqrt{g\rho_0/m}$ is the sound velocity.

The above derivation of hydrodynamic equations is valid in any dimension; it is practically always valid for low energies when the density fluctuations are small and vary slowly in space. Typically, this will happen in the so-called Thomas–Fermi limit (Pitaevskii and Stringari, 2003).

2.3.4 Path integral approach

We consider the partition function $Z[0]$ defined in eqn (2.25), and write $\phi = \sqrt{\rho_0 + \delta\rho} \exp(i\theta)$. We obtain (Wen, 2004)

$$\begin{aligned}Z[0] &= \int D^2[\phi(\mathbf{x}, t)] \exp[i \int d^d\mathbf{x} dt \left[-(\rho_0 + \delta\rho)\dot{\theta} - \frac{\hbar\rho_0}{2m} ((\partial_{\mathbf{x}}\theta)^2 \right. \\ &\quad \left. + (\partial_{\mathbf{x}}\delta\rho)^2/\rho_0) + \mu(\rho_0 + \delta\rho)/\hbar - \frac{g}{2\hbar}(\rho_0 + \delta\rho)^2 \right]].\end{aligned}\quad (2.31)$$

The terms that are derivatives (such as, for instance, the term $\propto \rho_0\dot{\theta}$) do not contribute to the action, since we expect that θ vanishes at the boundaries of the action integral. Moreover, we can assume that the integral of $\delta\rho$ vanishes, i.e. ρ_0 is the exact mean density. We neglect terms that are higher than second order in $\delta\rho$, and perform the remaining Gaussian integral in $\delta\rho$ exactly. The resulting functional integral and action read:

$$Z[0] = \int D[\theta(\mathbf{x}, t)] \exp \left[i \int d^d\mathbf{x} dt \left[\dot{\theta} \frac{1}{2g + (\partial_{\mathbf{x}}\theta)^2/2m\rho_0} \dot{\theta} - \frac{\rho_0}{2m} (\partial_{\mathbf{x}}\theta)^2 \right] \right]. \quad (2.32)$$

We neglect the terms originating from the spatial variations of the density fluctuations, i.e. proportional to $+(\partial_{\mathbf{x}})^2/2m\rho_0$, and end up at the hydrodynamic action

$$S = \int d^d \mathbf{x} dt \left[\frac{\dot{\theta}^2}{2g} - \frac{\rho_0}{2m} (\partial_{\mathbf{x}} \theta)^2 \right]. \quad (2.33)$$

The stationary action principle leads thus to the same result as eqn (2.30). This equation will be the basis of our further analysis of BEC in low dimensions. Note that this action describes an XY model; letting $z = \exp(i\theta)$, it can be rewritten as:

$$S = \int d^d \mathbf{x} dt \left[\frac{|\dot{z}|^2}{2g} - \frac{\rho_0}{2m} |\partial_{\mathbf{x}} z|^2 \right]. \quad (2.34)$$

2.4. One-dimensional systems

2.4.1 Phase fluctuations

As noted above, hydrodynamic theory is valid in any dimension but its consequences are particularly dramatic in low dimensions. In one dimension in particular, phase fluctuations destroy the superfluid order. In order to see this, we neglect completely density fluctuations and calculate the ground state correlation function:

$$\langle \hat{\phi}^\dagger(x, t) \hat{\phi}(0, 0) \rangle = \rho_0 \langle \exp(-i\hat{\theta}(x, t)) \exp(i\hat{\theta}(0, 0)) \rangle. \quad (2.35)$$

Again, this can be done using the Heisenberg equations or the functional integral approach. It is useful to introduce the canonical fields $\hat{\theta}(x, t)$ and $\hat{\Pi}(x, t) = \dot{\hat{\theta}}(x, t)/g\pi$, which fulfill the canonical position-momentum equal time commutation relations:

$$[\hat{\theta}(x, t), \hat{\Pi}(x', t)] = i\delta(x - x'), \quad (2.36)$$

and Heisenberg equations:

$$\dot{\hat{\theta}}(x, t) = \pi g \hat{\Pi}(x, t) = \pi u K \hat{\Pi}(x, t) \quad (2.37)$$

$$\dot{\hat{\Pi}}(x, t) = -\frac{u}{\pi K} \partial_x \hat{\theta}(x, t). \quad (2.38)$$

The ground-state correlation function can be directly derived from the Hamiltonian

$$\hat{H} = \frac{1}{2} \int dx \left[u K (\pi \hat{\Pi}(x))^2 + \frac{u}{K} (\partial_x \hat{\theta})^2 \right], \quad (2.39)$$

where $u = \sqrt{g\rho_0/m}$ is the sound velocity and $K = \sqrt{gm/\rho_0}$, the so-called Luttinger parameter, is dimensionless.

Perhaps the simplest way of calculating the correlation function (eqn (2.35)) is to observe that the Hamiltonian (eqn (2.39)) is a quadratic form, so that $\hat{\theta}(x, t)$ and $\hat{\Pi}(x, t)$ constitute

quantum Gaussian stochastic processes with zero average. The average is then trivially given by the Gaussian function of the corresponding two-point correlation function. To obtain its form, we expand the average into a Taylor series in $\hat{\theta}(x, t)$ up to second order, and collect the result to the exponent. This gives:

$$\langle \hat{\phi}^\dagger(x, t)\hat{\phi}(0, 0) \rangle = \rho_0 \exp\left(-\frac{1}{2}\langle \mathcal{T}(\hat{\theta}(x, t) - \hat{\theta}(0, 0))^2 \rangle\right), \quad (2.40)$$

where \mathcal{T} denotes the time ordering, i.e. operators are placed in time-descending order from the left to the right. This correlation is easily expressed in terms of the Green function for the phase $iG_\theta(x, t) = \langle \mathcal{T}[\hat{\theta}(x, t)\hat{\theta}(0, 0)] \rangle$ as:

$$\langle \hat{\phi}^\dagger(x, t)\hat{\phi}(0, 0) \rangle = \rho_0 \exp(iG_\theta(x, t)) \exp(iG_\theta(0, 0)). \quad (2.41)$$

The phase correlation function is, of course, most easily calculated in the Fourier representation, due to the time and translational invariance of the Hamiltonian (2.39):

$$G_\theta(k, \omega) = \frac{g/\hbar}{(\omega^2 - u^2 k^2 + i0^+)}. \quad (2.42)$$

The inverse Fourier transform in ω can easily be calculated using Cauchy's residuum method; the remaining integrations over k for finite systems are conveniently replaced by the summation over $k = 2\pi n/L$, where L is the size of the system and n is an integer, with the standard substitution $\int dk/2\pi = \sum_k 1/L$. The result is:

$$G_\theta(x, t) = \frac{g\pi}{\hbar L} \sum_k \frac{-i}{2u|k|} \exp(i(-u|kt| + kx)). \quad (2.43)$$

The term corresponding to $k = 0$ is infinite, but depends neither on x nor on t . One can thus regularize it and drop it away, since it does not affect the form of the correlation function. The remaining sums of $|k| \neq 0$ can be summed up analytically, since they correspond to the Taylor expansion of $\log(1 + x)$. We then obtain:

$$G_\theta(x, t) = \frac{ig}{4\pi\hbar u} [\log(1 - \exp(2\pi i(-u|t| + x)/L - 0^+)) + \log(1 - \exp(2\pi i(-u|t| - x)/L - 0^+))]. \quad (2.44)$$

In the limit of large L we recover the famous result (see for instance Wen (2004) and Giamarchi (2004)):

$$G_\theta(x, t) = \frac{ig}{4\pi\hbar u} \log\left(4\pi^2 \frac{(x^2 - u^2 t^2 + i0^+)}{L^2}\right). \quad (2.45)$$

To conclude the calculations of the correlation function (eqn (2.35)) we still need to evaluate $G_\theta(0, 0)$ which, similarly to the $k = 0$ term, is divergent. This divergence is, however, easily removed, since the present theory is valid only in the low energy/long wavelength limit.

We should therefore introduce the short distance cut-off l , and replace $G_\theta(0, 0)$ by $G_\theta(l, 0)$, calculated at the length scale l . The final result then reads (taking $L \rightarrow \infty$ in (eqn (2.44)):

$$\langle \phi^\dagger(x, t)\phi(0, 0) \rangle = \rho_0 \left(\frac{l^2}{(x^2 - u^2 t^2 + i0^+)} \right)^{K/4\pi}. \quad (2.46)$$

This result has profound consequences, since it implies that a 1D Bose gas does not exhibit long-range order, even at zero temperature. The long-range order is washed out by the phase fluctuations, and the condensate is replaced by a so-called ‘quasi-condensate’ with negligible density fluctuations but significant phase fluctuations. At any finite temperature algebraic decay of correlations becomes exponential. In practice, in quasi-1D Bose gases in elongated traps, one expects three regimes to appear. Firstly, non-condensed gas for temperatures $T \geq T_\theta$. Secondly, quasi-condensate with fluctuating phase but weakly fluctuating density for $T_\theta \geq T \geq T_c$; here correlations decay exponentially, with the correlation length being essentially equal to the phase coherence length L_θ , which in this regime is smaller than the size of the system L . Finally, the regime of true condensate is obtained when $T_c \geq T$ and $L_\theta \geq L$. This scenario was predicted by Petrov *et al.* (2000b, 2001) and has been demonstrated in the experiments of the Hannover group (Dettmer *et al.*, 2001).

2.4.2 Luttinger liquids

Most of the 1D systems, Fermi or Bose, can be described in the low-energy limit by a theory of similar form to the one given by the Hamiltonian (eqn (2.39)). This is achieved by applying a powerful technique called bosonization (Giamarchi, 2004, Gogolin *et al.*, 2004). The application of this technique to a 1D polarized Fermi gas is discussed in Chapter 5, where the derivation of the Hamiltonian is presented. The method can be easily generalized to the case of a spin $S = \frac{1}{2}$ Fermi gas, where one of the most important properties is the separation of density and spin dynamics, so that the density and spin excitations fulfill independent hydrodynamic equations. Moreover, depending on the concrete model, the hydrodynamic spin excitations may propagate with a completely different sound velocity to the density (charge for electrons) excitations—this is a well known spin–charge separation effect.

2.4.3 Tonks–Girardeau gas

Funnily enough, while 1D Fermi gases may be conveniently bosonized, a 1D Bose gas in the strongly correlated regime is well described by an effective theory that can be termed ‘fermionization’. The Bose gas in this limit is a gas of *impenetrable* or *hard-core* bosons, and was studied many years ago by Tonks (1936) and more recently by Girardeau (Girardeau, 1960, Girardeau and Wright, 2000, Girardeau *et al.*, 2001); it is thus called a Tonks–Girardeau gas. Its Hamiltonian, described by eqn (2.22), takes the form, in the first quantization picture:

$$H_{\text{Tonks}} = -\frac{\hbar^2}{2m} \sum_{j=1}^N \frac{\partial^2}{\partial x_j^2} + g_{1D} \sum_{i=1}^N \sum_{j=i+1}^N \delta(x_i - x_j) + \sum_{j=1}^N V(x_j, t), \quad (2.47)$$

where the 1D coupling derived from 3D theory (Olshanii, 1998) is $g_{1D} = -2\hbar^2/m a_{1D}$, and $a_{1D} = -(l_\rho^2/a_s)/(1 - Ca_s/l_\rho)$, where a_s is the 3D scattering length, l_ρ is the radial oscillator length, and $C \simeq 1.4603$. In order to treat the Tonks limit it is useful to introduce the Tonks parameter, which is defined as

$$\gamma = 2/n|a_{1D}| = mg_{1D}/\hbar^2 n, \quad (2.48)$$

where n is the particle density. The Tonks parameter is small in the weakly interacting regime, where the Gross–Pitaevskii theory is valid, provided one accounts for the phase fluctuations discussed above. For large γ the mean-field description breaks down. In principle, the model described by eqn (2.47) admits exact solutions (Lieb and Liniger, 1963), which are very useful for various analyses (see Öhberg and Santos (2002), Gangardt and Shlyapnikov (2003a), and Gangardt and Shlyapnikov (2003b)) but very complex. Girardeau proposed approximating the ground state wave function of the Tonks gas by the wave function of the 1D Fermi gas, with the additional constraint of taking the absolute value of the wave function to ensure the proper bosonic statistics. More precisely the Fermi–Bose mapping takes any many-body (in general time-dependent) wave function for N fermions $\Psi_F(x_1, \dots, x_N)$, and multiplies it by the ‘unit antisymmetric function’:

$$A(x_1, \dots, x_N) = \prod_{1 \leq j < k \leq N} \text{sign}(x_j - x_k), \quad (2.49)$$

so that the many-body bosonic wave function becomes

$$\Psi_B(x_1, \dots, x_N) = A(x_1, \dots, x_N) \Psi_F(x_1, \dots, x_N). \quad (2.50)$$

In the Tonks limit (low density, large scattering length) the fermionic function can be well approximated in the spirit of time-dependent Hartree–Fock approximation by a Slater determinant $\Psi_F(x_1, \dots, x_N) \propto \det \hat{M}$, where the $N \times N$ matrix \hat{M} has the elements $\hat{M}_{ij} = \varphi_i(x_j, t)$, where $\varphi_i(x, t)$ are the single-particle wave functions obtained by solving the Schrödinger equation

$$i\hbar \frac{\partial \varphi_i(x, t)}{\partial t} = \left[-\frac{\hbar^2}{2m} \frac{\partial^2}{\partial x^2} + V(x, t) \right] \varphi_i(x, t).$$

In particular, the ground state wave function for the Tonks gas with periodic boundary conditions (i.e. in a toroidal trap) or for a Tonks gas in a loose harmonic trap, read

$$\Psi_{Tonks}(z_1, \dots, z_N) \propto \prod_{i < j} |z_i - z_j|, \quad (2.51)$$

$$\Psi_{Tonks}(x_1, \dots, x_N) \propto \left(\prod_{i < j} |x_i - x_j| \right) \exp \left(-\sum_k x_k^2/l^2 \right), \quad (2.52)$$

where $z_j = e^{i\phi_j}$ is an atomic coordinate on a 1D torus S_1 , and l is the harmonic oscillator length scale. The Fermi–Bose mapping implies that the density–density correlations in the

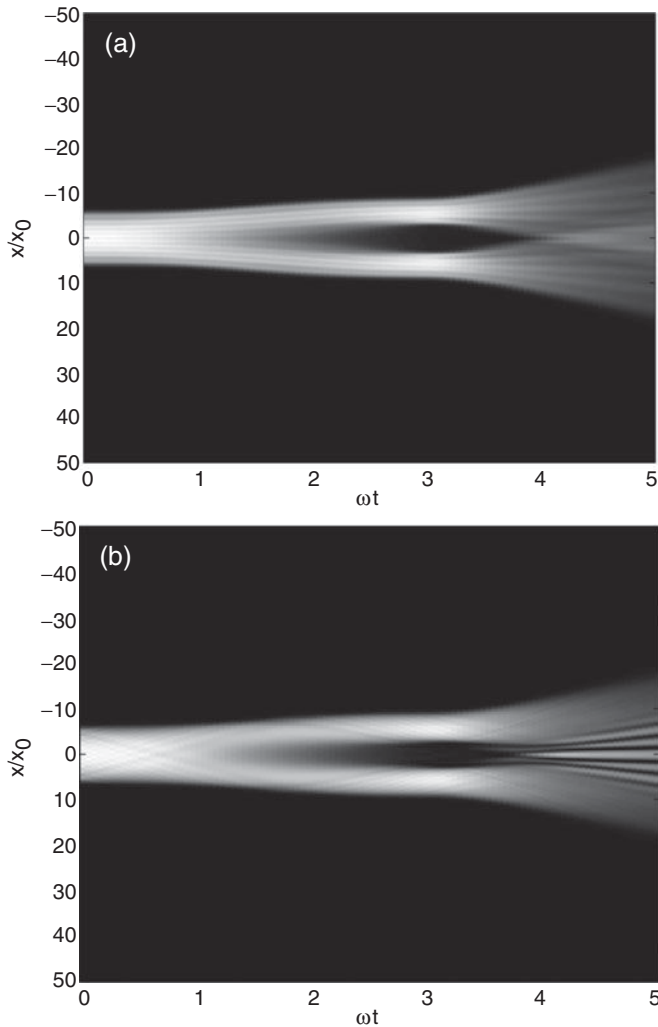


Figure 2.3 Particle density after recombination of the two 1D hard core gases as function of time (horizontal axis) and position (vertical axis) obtained by (a) exact many body theory (b) mean field time-dependent non-linear Schrödinger equation. From Girardeau and Wright, 2000.

Tonks gas are exactly the same as in the related polarized Fermi gas. This is not true for general correlation functions, such as momentum distributions, which have a sharp peak at zero momentum (Vaidya and Tracy, 1979, Olshanii, 1998), implying that there is a certain level of coherence in the Tonks limit. At the same time, a Tonks-Girardeau gas generally cannot be described by a mean field theory which predicts unphysical coherence (see Figure 2.3).

In order to achieve the Tonks limit in experiments, one needs to either increase the 1D coupling constant or go to the ultra-dilute limit, as been done in the experiments reported

in Kinoshita *et al.* (2004) and Stöferle *et al.* (2004*a*, 2004*b*). Note, however, that at fixed g_{1D} , γ depends also on the atomic mass. Paredes *et al.* (2004) used this observation, and changed the effective mass of atoms by placing the 1D gas in an optical lattice, so that values of $\gamma \simeq 5 - 200$ could be achieved.

The description of the gas in the conditions of the experiment of Paredes *et al.* (2004) allows use of the tight-binding approximation and the so-called Bose–Hubbard model, which will be introduced in Chapter 3. Interestingly, in the impenetrable bosons limit, the 1D Bose–Hubbard model reduces to a so-called spin XX model and is exactly soluble using the Jordan–Wigner transformation (for details see Chapter 5).

2.5. Two-dimensional systems

In order to understand the effect of phase fluctuations in two dimensions, we will again derive the hydrodynamics from the BdG equations at $T = 0$. Here we follow closely the approach given by Cheneau (2008). We start by substituting the atomic annihilation and creation field operators by $\hat{\phi}(\mathbf{x}) = \psi_0 + \delta\hat{\phi}(\mathbf{x})$, $\hat{\phi}^\dagger(\mathbf{x}) = \psi_0 + \delta\hat{\phi}^\dagger(\mathbf{x})$, with $\int |\psi_0|^2 = n_0$. The BdG equations for fluctuations follow from the Hamiltonian (eqn (2.23)):

$$i\hbar\dot{\hat{\phi}}(\mathbf{x}, t) = \left[-\frac{\hbar^2}{2m}\nabla^2 + 2g_{2D}n_0 - \mu \right] \delta\hat{\phi}(\mathbf{x}, t) + g_{2D}\psi_0^2\delta\hat{\phi}^\dagger(\mathbf{x}, t). \quad (2.53)$$

In the case of homogeneous gas, the solution is immediately found using the Fourier transform and reads

$$\delta\hat{\phi}(\mathbf{x}, t) = e^{-i\mu t / } \sum_{\mathbf{k}} \left[u_{\mathbf{k}}(\mathbf{x})\hat{a}_{\mathbf{k}}e^{-i\epsilon_{\mathbf{k}}t / } - v_{\mathbf{k}}^*(\mathbf{x})\hat{a}_{\mathbf{k}}^\dagger e^{+i\epsilon_{\mathbf{k}}t / } \right], \quad (2.54)$$

where $\epsilon_{\mathbf{k}} = \sqrt{E_{\mathbf{k}}^2 + 2\mu E_{\mathbf{k}}}$, and $E_{\mathbf{k}} = \hbar^2 k^2 / 2m$. The operators $\hat{a}_{\mathbf{k}}$ and $\hat{a}_{\mathbf{k}}^\dagger$ annihilate and create BdG quasiparticles, respectively. The wave function of the BdG quasiparticles are given by:

$$u_{\mathbf{k}}(\mathbf{x}) \pm v_{\mathbf{k}}(\mathbf{x}) = \frac{1}{V} \left(\frac{\epsilon_{\mathbf{k}}}{E_{\mathbf{k}}} \right)^{\pm 1/2} e^{i\mathbf{k} \cdot \mathbf{x}}. \quad (2.55)$$

The number of excited particles at $T = 0$ (quantum depletion) can then be calculated as

$$N_{\text{exc}} = \int d^2\mathbf{x} \langle \delta\hat{\phi}^\dagger(\mathbf{x})\delta\hat{\phi}(\mathbf{x}) \rangle = \frac{V}{(2\pi)^2} \int d^2\mathbf{k} v_{\mathbf{k}}^2 = \frac{mg_{2D}}{4\pi\hbar^2} n_0. \quad (2.56)$$

In situations typically encountered in experiments, the 2D coupling g_{2D} is given by $g = 4\pi\hbar^2 a_s / m$, averaged over the axial (Gaussian) profile of the 2D gas. This gives $g_{2D} = \sqrt{8\pi\hbar^2 a_s / ml_z}$, where l_z is the axial harmonic oscillator length. This means that for a weakly interacting gas the relative quantum depletion $N_{\text{exc}}/N_0 = n_{\text{exc}}/n_0 = a_s/\sqrt{2\pi}l_z \ll 1$ is small, which implies that the BdG theory is self-consistent. On the other hand, quantum depletion is non-negligible, especially in the vicinity of a Feschbach resonance, when a_s is larger, and a more careful description of the scattering processes has to be used (for reviews see Petrov *et al.* (2000*a*) and Petrov and Shlyapnikov (2001)).

2.5.1 Algebraic order at low T

As we have seen from BdG theory, the condensate survives in two dimensions at $T = 0$. We will now see that phase fluctuations destroy it at any $T > 0$. To this end we use the BdG theory for the density and phase fluctuations. At low temperatures, in the low energy limit the solutions of the BdG equations can be rewritten as:

$$\hat{\theta}(\mathbf{x}, t) = -i \sum_{\mathbf{k}} \left(\frac{mu}{2V\hbar\bar{n}k} \right)^{1/2} \hat{a}_{\mathbf{k}} e^{i(\mathbf{k}\cdot\mathbf{x} - \epsilon_{\mathbf{k}}t)} + h.c., \quad (2.57)$$

$$\delta\hat{n}(\mathbf{x}, t) = \sum_{\mathbf{k}} \left(\frac{m\hbar\bar{n}k}{2V} \right)^{1/2} \hat{a}_{\mathbf{k}} e^{i(\mathbf{k}\cdot\mathbf{x} - \epsilon_{\mathbf{k}}t)} + h.c., \quad (2.58)$$

with the speed of sound $u = \sqrt{\mu/m}$, and $\epsilon_{\mathbf{k}} = \hbar ck$, i.e. taken in the low-energy phonon regime. We have assumed $\hat{n}(\mathbf{x}) = \bar{n}(\mathbf{x}) + \delta\hat{n}(\mathbf{x})$. If density fluctuations are suppressed, the atomic field operator can be safely approximated as:

$$\hat{\phi}(\mathbf{x}) = \sqrt{\bar{n}} \exp(i\hat{\theta}(\mathbf{x})), \quad (2.59)$$

where $\bar{n} = \langle \hat{n} \rangle$ is the mean density, which includes the thermal excitations. Similarly to the 1D section we employ:

$$\langle \hat{\phi}^\dagger(x, 0) \hat{\phi}(0, 0) \rangle = \bar{n} \exp \left(-\frac{1}{2} \langle \mathcal{T}(\hat{\theta}(x, 0) - \hat{\theta}(0, 0))^2 \rangle \right). \quad (2.60)$$

Explicit use of the eqn (2.57) gives:

$$\frac{1}{2} \left\langle (\hat{\theta}(x, 0) - \hat{\theta}(0, 0))^2 \right\rangle = \frac{mu}{V\hbar\bar{n}} \sum_{\mathbf{k}} \frac{(1 - \cos(\mathbf{k}\cdot\mathbf{x}))}{k} (n_{\mathbf{k}} + 1/2), \quad (2.61)$$

where $n_{\mathbf{k}} = \langle a_{\mathbf{k}}^\dagger a_{\mathbf{k}} \rangle$ is the occupation of the BdG modes. For low-energy modes (long wavelength) we may approximate $n_{\mathbf{k}} \simeq k_B T / \hbar ck \gg \frac{1}{2}$. We then get

$$\frac{1}{2} \left\langle (\hat{\theta}(x, 0) - \hat{\theta}(0, 0))^2 \right\rangle \simeq \frac{1}{\bar{n}\lambda^2} \int_k d^2\mathbf{k} \frac{(1 - \cos(\mathbf{k}\cdot\mathbf{x}))}{k^2}. \quad (2.62)$$

For large \mathbf{k} this integral has to be cut off at $1/\xi$, where ξ is the healing length, defined as $\xi = \hbar/\sqrt{m\mu}$. Observing that the Laplacian of the integrand is a 2D Dirac delta function, we obtain that at large distances the leading part of the integral is

$$\frac{1}{2} \langle (\hat{\theta}(x, 0) - \hat{\theta}(0, 0))^2 \rangle \simeq \frac{1}{\bar{n}\lambda^2} \log(\mathbf{x}/\xi), \quad (2.63)$$

which, inserting in eqn (2.60), gives :

$$\langle \hat{\phi}^\dagger(x, 0) \hat{\phi}(0, 0) \rangle = \rho_0 \exp \left[-\frac{1}{2} \langle (\hat{\theta}(x, 0) - \hat{\theta}(0, 0))^2 \rangle \right] \simeq \bar{n} \left(\frac{\xi}{\mathbf{x}} \right)^{1/\bar{n}\lambda^2}. \quad (2.64)$$

34 Statistical physics of condensed matter: basic concepts

This result shows that for any $T > 0$ (i.e. $\lambda < \infty$) the correlation functions decay to zero at large distance, i.e. there is no long-range order, and no BEC. At the same time, the correlations at $T = 0$ have a non-zero limit at $r \rightarrow \infty$, which is in agreement with the results of the previous section: there is BEC at $T = 0$ although the condensate is quantum depleted. Last but not least, this result is related to the famous Hohenberg–Mermin–Wagner theorem (Mermin and Wagner, 1966, Hohenberg, 1967), which states that homogeneous systems with continuous symmetry cannot exhibit long-range order in dimensions smaller than or equal to 2. At the same time the result is very remarkable, since it predicts very slow, algebraic decay of the correlations, which indicates much stronger coherence than a thermal gas. This unusual phase is called the Berezinskii–Kosterlitz–Thouless (BKT) phase, and one expects that it ceases to exist at high temperatures.

2.5.2 Berezinskii–Kosterlitz–Thouless transition

The BKT phase ceases to exist at high temperatures but the mechanism of its instability is related to vortex excitations. In fact the BKT phase is superfluid and typically contains many bounded vortex–antivortex pairs. At high T these pairs break up and free vortices appear in the gas at low (free) energy cost.

To better understand this mechanism, we remind the reader that the vortex (anti-vortex) corresponds to a BEC with order parameter given by

$$\psi = \sqrt{n_s} \exp(\pm i\phi), \quad (2.65)$$

where n_s is the superfluid fraction density far from the vortex core, which has a size of healing length, ξ . At distances of order ξ , the density in the vortex decreases and goes exactly to zero at the core. The vortex solution induces a velocity field

$$\mathbf{v} = \pm \frac{\hbar}{m} \nabla \phi = \pm \frac{\hbar}{mr} \mathbf{e}_\phi. \quad (2.66)$$

The proliferation of free vortices will occur when the free energy associated with a vortex becomes negative. Thus the critical temperature for the BKT transition corresponds to $F(T_c) = E - T_c S = 0$. The vortex energy is simply calculated by integrating the kinetic energy density corresponding to the velocity field induced by the vortex:

$$E = \int d^2 \mathbf{x} n_s \frac{m \mathbf{v}^2}{2} \simeq n_s \frac{\pi \hbar^2}{2m} \log(V/\xi^2). \quad (2.67)$$

The contributions of the vortex core are neglected here. The entropy is determined by the log of the number of possible vortex configurations, i.e. ratio of the vortex size to the system size,

$$S \simeq k_B \log(V/\xi^2). \quad (2.68)$$

Combining the above two equations we obtain the estimate for the critical temperature

$$k_B T_c = n_s \frac{\pi \hbar^2}{2m}, \quad (2.69)$$

or $n_s \lambda^2 = 4|_{\text{at crit}}$. This last equation implies that at the BKT transition the superfluid density is not continuous, and it jumps from 0 to $4/\lambda^2$ as the temperature approaches the critical one from above (Kosterlitz, 1974, Nelson and Kosterlitz, 1977).

Note, that eqn (2.69) does not yet determine the critical temperature since it relates it to the (unknown) superfluid density, and not the total density, n . The critical point is given by the relation (Popov, 1983, Fisher and Hohenberg, 1988):

$$k_B T_c = \frac{2\pi\hbar^2}{m} \frac{n}{\log(\gamma/\sqrt{8\pi}(a_s/l_z))}, \quad (2.70)$$

where γ is dimensionless and has to be determined numerically. Extensive quantum Monte Carlo simulations reported in Prokof'ev *et al.* (2001) yield $\gamma = 380 \pm 3$.

The first observation of BKT transition goes back to the seminal work of Bishop and Reppy (1978) on liquid helium films. It is worth noticing, however, that direct observations of the microscopic nature of the BKT transition (such as proliferation of vortices) only recently became possible with the advent of ultracold gases (Hadzibabic *et al.*, 2006).

3

Ultracold gases in optical lattices: basic concepts

This chapter deals with the basic concepts of ultracold gases in optical lattices. We start with the fundamental principle of optical trapping of neutral atoms, and discuss the so-called dipole potentials. These are the potentials generated by an off-resonant laser shining on a neutral atom. Optical lattices—periodic structures made of light—are just an straightforward consequence of the dipole potential and are discussed at length in Section 3.1. The possibilities they offer to engineer the atomic systems under consideration are listed in Section 3.2. Optical lattices simulate periodic systems, and weakly interacting atoms in such potentials display the well known band structure. In Sections 3.3 and Section 3.4 we stress the similarities between periodic electronic systems and ultracold lattice gases. The latter reproduce solid-state physics such as Bloch oscillations, Landau–Zener tunneling or Josephson tunneling. In Section 3.5 we explain how, using optical lattices, it is possible to push a weakly interacting system, such as a BEC, into the strongly correlated regime, and we derive the appropriate description of the system in this regime.

3.1. Optical potentials

Ultracold atoms loaded in optical lattices are systems closely related to condensed matter and solid-state physics. The basic tools to generate ultracold lattice gases are optical potentials. An electron in an atom in the presence of an oscillating electric field $\mathbf{E}(\mathbf{r}, t)$ of a laser attains a time-dependent dipole moment \mathbf{d} . When the field frequency is far off resonance, i.e. it does not cause any real transition in the atom, the induced dipole moment follows the laser field oscillations

$$d_i^{(\pm)}(t) = \sum_{j=x,y,z} \alpha_{ij}(\omega_L) E_j^{(\pm)}(\mathbf{r}, t), \quad (3.1)$$

where $d_i^{(\pm)}$ ($i = x, y, z$) is the corresponding complex, positive (negative) frequency component of \mathbf{d} , ω_L is the laser frequency, and $\alpha_{ij}(\omega_L)$ denotes the matrix elements of the complex polarizability tensor, which fully characterizes the response of the atom at the applied electric field. Note that in general the polarizability is a tensor, which means that the induced dipole moment is not necessarily in the direction of the applied field. Such a situation occurs in anisotropic media. The time dependence here accounts for the slow modulations of the laser field.

The polarizability depends in general on the laser frequency and on the energies of the non-resonant excited states of the atom. One of these states—with excitation energy, say, $E_1 = \hbar\omega_1$ —is usually much closer to the resonance than the others; in such cases the polarizability becomes inversely proportional to the laser detuning from the resonance, $\Delta = \omega_L - \omega_1$. In this situation the electronic energy undergoes a shift, $\Delta E = \mathbf{d} \cdot \mathbf{E}$, which is nothing more than an AC version of the standard quadratic Stark effect. The energy shift is proportional to:

$$\Delta E(\mathbf{r}, t) = -2 \sum_{i,j=x,y,z} \operatorname{Re} \left(\alpha_{ij}(\omega_L) E_i^{(-)}(\mathbf{r}, t) E_j^{(+)}(\mathbf{r}, t) \right). \quad (3.2)$$

Note that this expression is automatically time averaged over the fast optical oscillations. When the polarizability is a scalar, independent of the direction, i.e. when the response of the media to the applied electric field is isotropic, the induced dipole moment and the field are parallel, that is, $\alpha_{ij} = \alpha \delta_{ij}$, and the AC shift reads:

$$\Delta E(\mathbf{r}, t) = -2 \operatorname{Re}(\alpha) I(\mathbf{r}, t) \propto \frac{I(\mathbf{r}, t)}{\Delta} \quad (3.3)$$

where $I(\mathbf{r}, t)$ is the laser beam intensity, in general slowly dependent on time.¹

The consequences of the above simple formula are enormous. The atom feels an optical potential that follows the spatial pattern of the laser field intensity—which can be considered time independent—and its sign depends on the atomic detuning

$$V_{opt}(\mathbf{r}) = \Delta E(\mathbf{r}) \propto \frac{I(\mathbf{r})}{\Delta}. \quad (3.4)$$

This is the basis for optical manipulations and trapping of atoms (see Grimm *et al.* (2000)). If the laser is red-detuned ($\Delta < 0$), the atoms are attracted towards the regions of high intensity corresponding to the potential minima. Conversely, a blue-detuned laser ($\Delta > 0$) pushes the atoms out of these regions since the potential minima are at the positions of minimum intensity. Note that in order to reduce heating caused by inelastic scattering, i.e. photon absorption and spontaneous emission processes, a large detuning is required because the photon scattering rate, which is proportional to the imaginary part of the polarizability, scales as $I(\mathbf{r})/\Delta^2$.

Adding two or more laser fields of the same frequency leads, in general, to interference. Correspondingly there is also an interference pattern of the intensity. In particular, two counter-propagating laser waves of the same polarization will create a standing wave and thus a spatially periodic potential for atoms of the form:

$$V(x) = V_0 \sin^2(kx) \quad (3.5)$$

with $k = 2\pi/\lambda$, λ being the wavelength of the lasers that form the standing wave, and V_0 the depth of the optical lattice proportional to the intensity of the laser beams. The potential

¹The proportional constant can be calculated using a semiclassical model and corresponds to $\frac{3\pi^2 c^2 D}{2\omega_1^3}$, where D denotes the dipole matrix element between the ground state and the state close to resonance.

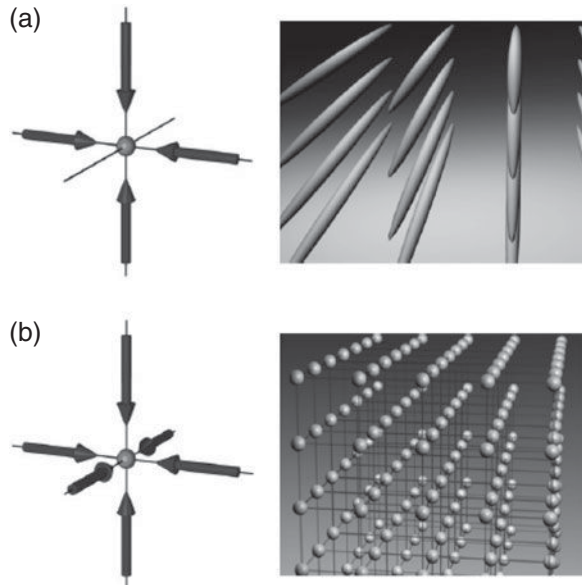


Figure 3.1 Schematic pictures of optical lattice potentials created by counter-propagating lasers: (a) 2D array of quasi-1D tubes and (b) 3D simple cubic lattice. From Bloch (2004).

depth is often expressed in units of the recoil energy $E_R = \hbar^2 k^2 / 2m$, m being the mass of the atom. Thus three pairs of counter-propagating laser beams in three orthogonal directions will form a three-dimensional (3D) optical lattice like the one represented schematically in Figure 3.1(b). One can easily avoid interference when adding more and more laser fields by using laser fields with orthogonal polarizations. An alternative way to avoid interference on demand is to use slightly, but sufficiently different frequencies. In this case, time averaging over the ‘sufficiently’ different frequencies washes out the interference effects. Similarly, one can use laser beams with polarizations rotating at different frequencies to avoid interference.

Optical lattices thus provide *ideal* periodic potentials in which the atoms can move, i.e. the lattices contain no defects and are rigid, and do not support phonon excitations unless some special circumstances are met (Larson *et al.*, 2008). The high degree of control over the optical lattice parameters permits the use of ultracold atoms in a very versatile way and exploration of various situations encountered in condensed matter systems.

3.2. Control of parameters in cold atom systems

Atomic physics and quantum optics offer many new methods to quantum engineer ultracold atoms in optical lattices. ‘*Toutes proportions gardées*’, there are instances in which atomic physics and quantum optics not only meets, but rather ‘beats’ condensed matter physics. One of the reasons is the high degree of control that experiments with cold atoms in optical lattices provide. Here we list some of these controllable parameters.

- *Lattice geometry and dimensionality.* By engineering the direction, polarization, intensity, phase, and frequency of the laser beams, practically any lattice geometry may be achieved with optical potentials. Also the dimensionality of the system can be modified. Square and cubic lattices in two and three dimensions have been created using counterpropagating laser beams along the corresponding directions. For instance, using a 1D (2D) optical lattice in a 3D system, an array of 2D (1D) systems is generated. For reviews see Petrov *et al.* (2004), Bloch *et al.* (2008), and Hadzibabic and Dalibard (2010). In each subsystem the dynamics in two (one) of the three initial dimensions are frozen by using a sufficiently strong confining potential in these dimensions such that all the relevant energies of the system are below the first excited state of the trap (Pitaevskii and Stringari, 2003). Recently, the possibility of implementing mixed dimensionalities has been also reported (Lamporesi *et al.*, 2010). The spacing between adjacent wells can also be modified—from $d = \lambda/2$, where λ is the wavelength of the counter-propagating beams forming the lattice, to $d = (\lambda/2) \sin(\theta/2)$ —by making the beams interfere at a certain angle θ . This method can also be used to address individual lattice wells. The method of superlattices, consisting of adding a new lattice of different frequency on top of the existing one, is also very well developed. This method allows creation of double well lattices, i.e. the unit cell of a lattice contains two sites. It also permits creation of quasiperiodic or even random systems by either superposing lattices with incommensurate frequencies or by adding a speckle radiation to the lattice. For reviews see Fallani *et al.* (2008), Bouyer (2009), and Sanchez-Palencia and Lewenstein (2010). More involved geometries, such as triangular (Becker *et al.*, 2010), hexagonal (Soltan-Panahi *et al.*, 2011), or kagomé may also be implemented. Periodic boundary conditions can be realized in ring-shaped optical lattices.
- *Phonons.* Optical lattices are rigid and robust: they do not support phonons. An interesting situation arises when the lattice is formed in an optical cavity: in these circumstances, atom–light coupling might suffice to shift the cavity resonance. The cavity will affect the atoms but the atoms will perform a back action, and can create ‘phonon’-like excitations (Maschler and Ritsch, 2005), which lead to a superfluid–Mott insulator (SF–MI) crossover (Larson *et al.*, 2008). On the other hand, phonons obviously play a role in ion traps, where they provide the major mechanism for ion–ion interactions (Mintert and Wunderlich, 2001; Porras and Cirac, 2004a).
- *Tunneling.* Tunneling can be controlled to a great extent using a combination of pure tunneling, laser assisted coherent transitions, and lattice tilting (acceleration) techniques. Prominent examples of such control are the proposals for creating artificial magnetic fields in lattices (Jaksch and Zoller, 2003), as detailed in Chapter 11.
- *On-site interactions.* Although quantum gases are very dilute systems, with densities typically ranging from 10^{13} to 10^{15} cm^{-3} , many of their properties are governed by the interactions between particles. These interactions are characterized by scattering lengths, which can be modified using Feshbach resonances in magnetic fields (Inouye *et al.*, 1998; Timmermans *et al.*, 1999; Cornish *et al.*, 2000) or optical Feshbach resonances. For explanations of the theory see Fedichev *et al.* (1996) and Papoular *et al.* (2010). For experimental details see Theis *et al.* (2004) and Thalhammer *et al.* (2005). In the original proposal for optical Feshbach resonances, the laser non-resonantly

couples the ground state of scattered atoms with an excited molecular state. Such a method typically leads to large non-elastic losses. Very recently, Rempe's group has proposed (Bauer *et al.*, 2009) coupling resonant molecular levels with excited molecular states. In this way a novel control that is remarkably free of losses is achieved. On-site interactions can be set to zero in dipolar gases by changing the shape of the on-site potential (Góral *et al.*, 2002).

- *Next neighbor and long-range interactions.* Effective models obtained by calculating the effect of tunneling (t) in the MI phases typically contain next-neighbor interactions of energies $\propto t^2/U$, where U denotes the on-site interactions. Long-range interactions can be achieved using dipolar forces, as discussed in recent reviews (Baranov *et al.*, 2002; Baranov, 2008; Lahaye *et al.*, 2009). The group of Pfau has recently realized the first experimental observation of ultracold dipolar gas (Griesmaier *et al.*, 2005) by condensing bosonic chromium. Dipolar interactions are mediated here by magnetic dipoles of the chromium atoms; they are weak but nevertheless lead to observable effects (Stuhler *et al.*, 2005). Much stronger electric dipole-dipole interactions can be achieved with polar molecules in their ground states (Ni *et al.*, 2008). In Bose-Fermi mixtures, bosons may mediate the interaction between fermions, providing stronger interactions. Long-range interactions can also be achieved in trapped ion systems, where they are mediated via phonon vibrations of the equilibrium ionic configuration.
- *Spin-dependent optical lattices.* Spin-dependent optical lattices can be created in a lin∠lin configuration, i.e. two counterpropagating laser beams with linear polarization forming a certain angle. By exploiting this type of control, atoms with different internal hyperfine states (spin) can experience different lattice potentials. In this way the atoms can be made to move to one direction, or the opposite one, simply by manipulating their spin (Jaksch *et al.*, 1999; Mandel *et al.*, 2003). Such a technique is often used to control interactions between atoms.
- *Multiparticle (plaquette) interactions.* The way in which effective three-body interactions can be generated has also been demonstrated (Pachos and Rico, 2004; Mazza *et al.*, 2010). These interactions result from the possibility of atoms tunneling along two different paths. Similarly, ring-exchange interactions in a square optical lattice can be generated by employing the correlated hopping of two bosons (Büchler *et al.*, 2005). Various types of three-particle interaction can be achieved with polar molecules (Büchler *et al.*, 2007a; Pupillo *et al.*, 2008), or Rydberg atoms (using the so-called Rydberg blockade effect; see Weimer *et al.* (2010)).
- *Potentials.* Different types of external potential can also be applied to the atoms. One can use magnetic potentials whose shape can currently be controlled on the scale of few microns. Magnetic potentials with larger gradients can be created on atom chips (see della Pietra *et al.* (2007)). The most flexible type are, however, optical potentials. Apart from limitations set by the diffraction limit, they can have practically any desired shape and can form any kind of optical lattice: regular, disordered, modulated, etc. Great possibilities are offered by the so-called radio frequency potentials (Hofferberth *et al.*, 2006) and holographic masks (Bakr *et al.*, 2009).
- *Temperatures.* Typical critical temperatures of trapped ultracold condensed Bose gases are of order of few tens of nanokelvins (nK). Using evaporative cooling, however, one can reach lower temperatures, although methods to reliably determine the temperature

in this range are lacking. For recent advances see Gati *et al.* (2006). Similarly, the temperature of superfluid Fermi gases are in the range of few tens of nK. Thus, temperatures in the range of few tens of nK are nowadays becoming standard. The quantum phase transition from superfluid to MI also occurs in a range of accessible temperatures. However, many strongly correlated phases achievable with ultracold atoms in optical lattices demand a tunneling (t) much smaller than on-site interactions (U), implying temperatures of the order $k_B T \simeq t^2/U$, i.e. 10–20 nK or even less—at the limit of current possibilities. There are many proposals for reaching even lower temperatures, employing additional cooling and filtering procedures (Rabl *et al.*, 2003; Griessner *et al.*, 2005; Popp *et al.*, 2006a,b) or entropy control (Bernier *et al.*, 2009; Ho and Zhou, 2009). The progress in cooling and quantum engineering techniques allow us to believe that these limitations will be overcome very soon.

- *Time dependencies.* The time scale of dynamics for these systems is typically in the millisecond range. This implies that, in contrast to condensed matter systems, all of the controls discussed above can be made time dependent, adiabatic, or diabatic, on demand. Some of the fascinating possibilities include changes of lattice geometry, switching-on of disorder in real time, or the study of the sudden quench of the Hamiltonian parameters.

3.3. Non-interacting particles in periodic lattices: band structure

As is well known from solid state theory, the spectrum of a non-interacting single particle in a periodic potential consists of bands separated by energy gaps. Thus a neutral atom in a periodic potential is described by Bloch wave functions, just like electrons in a solid-state crystal. In this section we review the basic physics of a single particle (Ashcroft and Mermin, 1976) subject to a 1D periodic potential. Generalization to higher dimensions is straightforward.

A particle of mass m in a periodic potential $V(x) = V(x + d)$ with periodicity d is described by the Schrödinger equation:

$$\left[\frac{p^2}{2m} + V(x) \right] \Phi_q^{(n)}(x) = E_q^{(n)} \Phi_q^{(n)}(x). \quad (3.6)$$

The solutions of this equation are the so-called Bloch functions, which, according to Bloch's theorem (Ashcroft and Mermin, 1976), can be written as the product of a plane wave times a function with the same periodicity as the potential:

$$\Phi_q^{(n)}(x) = e^{iqx} u_q^{(n)}(x), \quad (3.7)$$

where:

$$u_q^{(n)}(x + d) = u_q^{(n)}(x). \quad (3.8)$$

Introducing eqn (3.7) into eqn (3.6) leads to the Schrödinger equation for $u_q^{(n)}(x)$:

$$\left[\frac{(p + \hbar q)^2}{2m} + V(x) \right] u_q^{(n)}(x) = E_q^{(n)} u_q^{(n)}(x), \quad (3.9)$$

where q , introduced by the Bloch's theorem, is the quasimomentum, a quantum number characteristic of the translational symmetry of the periodic potential. Due to the periodicity, q can be confined to the first Brillouin zone, i.e. $-\pi/d < q < \pi/d$, where $k_B = \pi/d$ is defined as the Bragg momentum. The index n (positive integer) appears in Bloch's theorem because for a given q there are many solutions of the Schrödinger equation; it simply labels the band. In fact, eqn (3.9) can be seen as a set of eigenvalue problems, one for each q , with an infinite number of solutions. These solutions have a discretely spaced spectrum, the well-known band structure. Note that in an infinite periodic potential the energy eigenvalues for a fixed n , $E^{(n)}(q)$, vary continuously with q . The n th band is separated from the $(n+1)$ th band by an energy gap that depends on the lattice structure and on the quasimomentum. For a 1D optical lattice, the potential reads $V(x) = V_0 \sin^2(kx)$, with $k = \pi/d$, d being the periodicity of the potential. For two counter-propagating laser beams forming a standing wave pattern in a collinear case $d = \lambda/2$ or, if the two laser beams interfere at an angle θ , then $d = (\lambda/2)\sin(\theta/2)$. The potential strength V_0 is proportional to the beam intensities and corresponds to the maximum depth of the lattice potential. In this situation the band structure is obtained by solving the following 1D Mathieu equation (Abramowitz and Stegun, 1964):

$$-\frac{d^2}{dy^2} \Phi_q^{(n)}(x) + \frac{V_0}{4E_R} (2 - 2\cos(2y)) \Phi_q^{(n)}(x) = \frac{E_q^{(n)}}{E_R} \Phi_q^{(n)}(x), \quad (3.10)$$

where $E_R = \hbar^2 k^2 / 2m$ is the atomic recoil energy and $y = kx$.

Analogously, the band structure can also be obtained by expressing the periodic functions $V(x)$ and $u_q^{(n)}(x)$ as discrete Fourier sums:

$$V(x) = -(V_0/4)(e^{2ik_B x} + e^{-2ik_B x} + 2) \quad (3.11)$$

$$u_q^{(n)}(x) = \sum_l c_l^{(n,q)} e^{2ilk_B x}, \quad (3.12)$$

and, inserting the above expressions into eqn (3.9), one obtains:

$$\sum_l H_{l,l'} c_l^{(n,q)} = E_q^{(n)} c_{l'}^{(n,q)}, \quad (3.13)$$

where $H_{l,l'}$ reads:

$$\begin{cases} (2l + q/\hbar k)^2 E_R & \text{if } l = l', \\ -V_0/4 & \text{if } |l - l'| = 1, \\ 0 & \text{otherwise.} \end{cases} \quad (3.14)$$

The eigenvalues and eigenvectors can then be calculated by truncating the Hamiltonian for large positive and negative l . Figure 3.2 shows the band structure for a sinusoidal potential

for different potential depths. For a vanishing lattice depth, there are no gaps and the spectrum consists of the free-particle energy momentum parabola, i.e. it is quadratic in q . When the lattice depth increases, the dispersion relation is no longer quadratic with the quasimomentum; the band gaps become larger and the band widths decrease. For very deep lattices, the spectrum is almost degenerate in q . Experimentally, in the context of ultracold bosons and fermions, the probing of the band structure has been performed by adiabatic mapping (Greiner *et al.*, 2001; Köhl *et al.*, 2005), by band spectroscopy (Denschlag *et al.*, 2002), and by Bragg spectroscopy (Ernst *et al.*, 2010).

Analytical expressions for the band structure can be obtained from eqn (3.10) in two limits: (i) weak potential limit and (ii) tight-binding regime. A comparison between numerics and analytics can be found in the recent review of Morsch and Oberthaler (2006).

Regarding the eigenvectors, it is worthwhile noting that Bloch functions are extended over the whole lattice. Nevertheless, an alternative single-particle basis for each band, n , is formed by the so-called Wannier functions. Wannier functions are localized around each lattice site and are related to the Bloch functions through the following relationship:

$$w_n(x - x_i) = \frac{1}{\sqrt{M}} \sum_q e^{-iqx_i} \Phi_q^{(n)}(x), \quad (3.15)$$

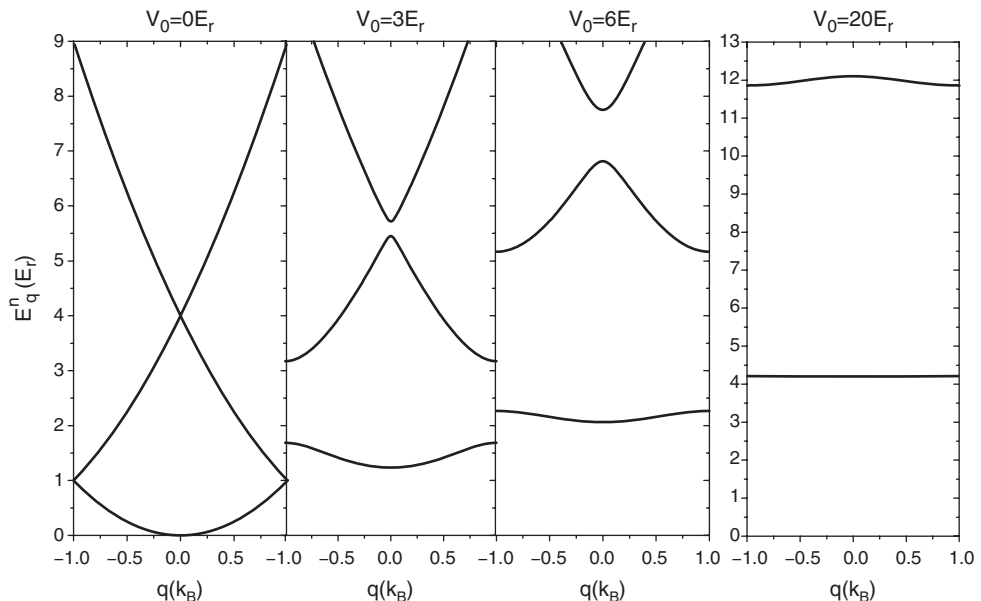


Figure 3.2 Band structure of a 1D optical lattice for different potential depths given in units of the recoil energy. The energy of the bands is plotted as a function of the quasimomentum in the first Brillouin zone. Gaps between bands increase as the potential depth increases. For sufficiently deep potentials the band structure tends to be flat.

where x_i is the position of the i th lattice site and M is a normalization constant. The Wannier functions are orthogonal for different bands as well as for different sites.

The existence of a band structure strongly modifies the motion of a single particle with respect to free propagation, as it is well known in solid state physics (Ashcroft and Mermin, 1976). If the momentum distribution of the particle wave function, centered at \tilde{q} , involves only a small range of quasimomenta, the semiclassical approximation applies and the energy dispersion can be Taylor expanded:

$$E(q) = E(\tilde{q}) + (q - \tilde{q}) \frac{\partial E(q)}{\partial q} \Big|_{\tilde{q}} + \frac{(q - \tilde{q})^2}{2} \frac{\partial^2 E(q)}{\partial q^2} \Big|_{\tilde{q}} + \dots, \quad (3.16)$$

where one can define the group velocity of the wavepacket as:

$$v_g(\tilde{q}) = \frac{1}{\hbar} \frac{\partial E(q)}{\partial q} \Big|_{\tilde{q}}, \quad (3.17)$$

and the effective mass is:

$$m_{eff}(\tilde{q}) = \hbar^2 \left(\frac{\partial^2 E(q)}{\partial q^2} \Big|_{\tilde{q}} \right)^{-1}, \quad (3.18)$$

Therefore the particle moves in the periodic potential with a group velocity given by eqn (3.17), as if it has an effective mass given by eqn (3.18). Figure 3.3 shows the group velocity as a function of the quasimomentum for different potential depths. For $q = 0$ and $q = \pi/d$, i.e. at the center and at the edges of the first Brillouin zone, the velocity vanishes while it is negative (positive) for negative (positive) quasimomentum. Regarding the effective mass, its value is given by the curvature of the bands; it is negative (positive) at the edges (center) of the first Brillouin zone for the lowest band. In this situation, under the influence of an external constant force F , weak enough to avoid interband transitions, a given Bloch state with well-determined quasimomentum q_0 will evolve into a state with time-varying quasimomentum $q(t) = q_0 + Ft/\hbar$. This evolution is periodic, with a period given by $T = \hbar|F|/d$, corresponding to the time needed to scan the first Brillouin zone. As the quasimomentum varies across the first Brillouin zone, the group velocity changes sign. As a consequence, a wave packet prepared with a well-defined quasimomentum will oscillate in position space with an amplitude fixed by the energy width of the first band. This behavior is known as Bloch oscillation (Ashcroft and Mermin, 1976). If the applied force is sufficiently strong, atoms cannot follow adiabatically the variation of energy with quasimomentum in the lowest band, and at the edge of the first Brillouin zone there is a finite probability of tunneling to the second band. This effect is known as Landau–Zener tunneling. Both Bloch oscillations and Landau–Zener tunneling have been reported for constant forces applied to ultracold atoms optical lattices, Bose–Einstein condensates, and degenerate Fermi gases. Possible applications of Bloch oscillations to high precision measurements have been also explored; for a review see Morsch and Oberthaler (2006). Very recently, the possibility of ‘in vivo’ observation of Bloch oscillations of atoms inside an optical cavity has also been proposed (Venkatesh *et al.*, 2009).

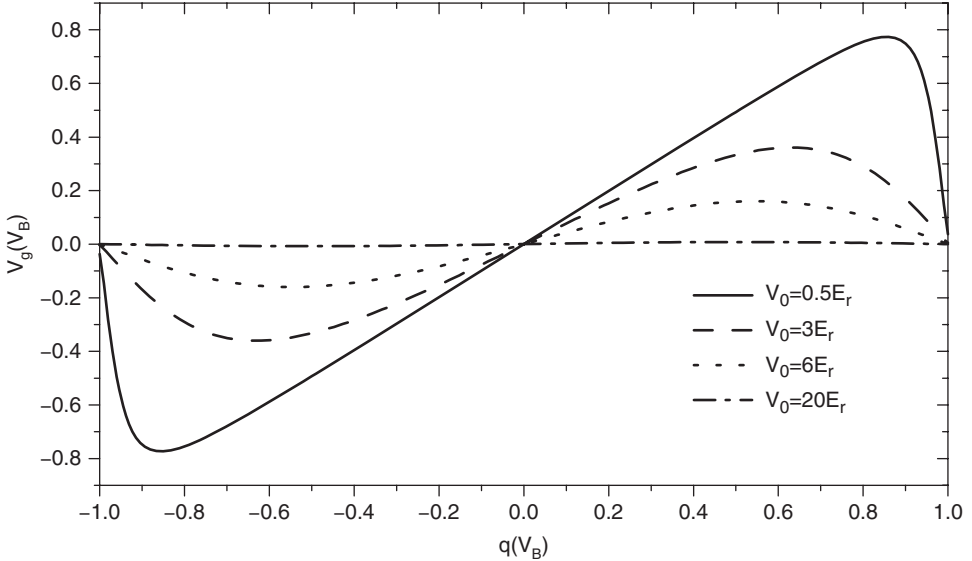


Figure 3.3 Group velocity in a 1D optical lattice for different potential depths as a function of the quasimomentum.

3.4. Bose–Einstein condensates in optical lattices: weak interacting limit

In Section 3.3 we reviewed the physics of a single particle in an external periodic potential. Now we review what happens when a weakly interacting Bose–Einstein condensate, characterized by an extremely narrow momentum distribution, is placed in an optical lattice. The many-body Hamiltonian in second quantization describing a gas of N interacting bosons in an external potential, V_{ext} , reads:

$$\begin{aligned} \hat{H}(t) = & \int d\mathbf{r} \hat{\Psi}^\dagger(\mathbf{r}, t) \left[-\frac{\hbar^2}{2m} \nabla^2 + V_{\text{ext}} \right] \hat{\Psi}(\mathbf{r}, t) \\ & + \frac{1}{2} \int d\mathbf{r} d\mathbf{r}' \hat{\Psi}^\dagger(\mathbf{r}, t) \hat{\Psi}^\dagger(\mathbf{r}', t) V(\mathbf{r} - \mathbf{r}') \hat{\Psi}(\mathbf{r}, t) \hat{\Psi}(\mathbf{r}', t), \end{aligned} \quad (3.19)$$

where $\hat{\Psi}$ and $\hat{\Psi}^\dagger$ are the bosonic annihilation and creation field operators, respectively. Interactions between atoms are given by $V(\mathbf{r} - \mathbf{r}') = (4\pi\hbar^2a/m)\delta(\mathbf{r} - \mathbf{r}') = g\delta(\mathbf{r} - \mathbf{r}')$, with m being the atomic mass, and a being the s -wave scattering length that characterizes the interactions—attractive (repulsive) for negative (positive) a —through elastic binary collisions at low energies between neutral atoms, independently of the actual interparticle two-body potential. This is due to the fact that for ultracold atoms the de Broglie wavelength is much larger than the effective extension of the interaction potential, implying that the interatomic potential can be replaced by a pseudopotential or contact potential. Note that this approximation is valid provided no long-range contributions exist; for more

details about scattering theory see for instance Landau and Lifshitz (1987) and Gribakin and Flambaum (1993).

If the bosonic gas is dilute ($na \ll 1$, where n is the density) the mean-field description applies. The basic idea of the mean-field description was formulated by Bogoliubov (1947) and consists of writing the field operator in the Heisenberg representation as a sum of its expectation value (condensate wave function) plus a fluctuating field operator:

$$\hat{\Psi}(\mathbf{r}, t) = \Psi(\mathbf{r}, t) + \delta\hat{\Psi}(\mathbf{r}, t). \quad (3.20)$$

When classical and quantum fluctuations are neglected, the time evolution of the condensate wave function at $T = 0$ is given by the Gross–Pitaevskii equation (Gross, 1961; Pitaevskii, 1961; Pitaevskii and Stringari, 2003), obtained by using the Heisenberg equation and eqn (3.20) (see Sec. 2.3):

$$i\hbar \frac{d}{dt} \Psi(\mathbf{r}, t) = -\frac{\hbar^2}{2m} \nabla^2 \Psi(\mathbf{r}, t) + [V_{\text{ext}} + g|\Psi(\mathbf{r}, t)|^2] \Psi(\mathbf{r}, t). \quad (3.21)$$

The wave function of the condensate is normalized to the total number of particles N . Here we will consider that the external potential corresponds to an optical lattice and eventually to an harmonic trapping potential.

3.4.1 Shallow optical lattices: Bloch oscillations and Landau–Zener tunneling

At the end of Section 3.3 the phenomenon of Bloch oscillations was introduced. Bloch oscillations, predicted by semiclassical theory, have been successfully reproduced experimentally (Morsch *et al.*, 2001; Cristiani *et al.*, 2002) using very dilute condensates. In such cases, the role of interactions can be largely neglected and one reproduces the linear regime. Also in the linear regime, by accelerating the lattice above some critical value, Landau–Zener tunneling leading to a pulse train of atoms out of the condensate has been reported (Anderson and Kasevich, 1998). For the regime where the non-linear term in the Gross–Pitaevskii equation is relevant and the lattice is shallow, the role of the interactions may be described through an effective potential in a non-interacting gas model. The expression of the effective potential can be obtained perturbatively (Choi and Niu, 1999) and reads:

$$V_{\text{eff}} = \frac{V_0}{1 + 4C}, \quad (3.22)$$

where V_0 is the amplitude of the periodic potential and $C = \pi n a / k^2$, with n being the condensate density, k the laser wave number, and a the scattering length. In this situation, the external potential in eqn (3.21) can be replaced by $V_{\text{eff}} \sin^2(kx)$. The validity of such approach has been experimentally verified (Morsch *et al.*, 2001) by monitoring the Landau–Zener tunneling probability for different values of C . The presence of non-linearity can also lead to asymmetric Landau–Zener tunneling (Jona-Lasinio *et al.*, 2003).

3.4.2 Deep optical lattices: Josephson junctions

If a BEC is placed in an optical lattice whose depth is sufficiently large that the barrier between the neighboring sites is much higher than the chemical potential, and the energy of the system is confined within the lowest band, it can be described in the so-called tight-binding approximation. Such an approximation permits the condensate order parameter $\Psi(\mathbf{r}, t)$ to be written as a sum of wave functions $\Theta(\mathbf{r} - \mathbf{r}_i)$ localized in each well of the periodic potential.

$$\Psi(\mathbf{r}, t) = \sqrt{N} \sum_i \varphi_i \Theta(\mathbf{r} - \mathbf{r}_i), \quad (3.23)$$

where $\varphi_i = \sqrt{n_i(t)} e^{i\phi_i(t)}$ is the amplitude of the i th lattice site with $n_i = N_i/N$ and N_i is the number of particles in the i th site. Introducing the ansatz given by eqn (3.23) into eqn (3.21) (Trombettoni and Smerzi, 2001), one obtains the discrete non-linear Schrödinger equation (DNLSE):

$$i\hbar \frac{\partial \varphi_i}{\partial t} = -K(\varphi_{i-1} - \varphi_{i+1}) + (\epsilon_i + U|\varphi_i|^2)\varphi_i, \quad (3.24)$$

where K denotes the nearest-neighbor tunneling rate:

$$K = - \int d\mathbf{r} \left[\frac{\hbar^2}{2m} \nabla \Theta_i \cdot \nabla \Theta_{i+1} + \Theta_i V_{\text{ext}} \Theta_{i+1} \right]. \quad (3.25)$$

The on-site energies are given by:

$$\epsilon_i = \int d\mathbf{r} \left[\frac{\hbar^2}{2m} (\nabla \Theta_i)^2 + V_{\text{ext}} \Theta_i^2 \right], \quad (3.26)$$

and the non-linear coefficient U by:

$$U = gN \int d\mathbf{r} \Theta_i^4. \quad (3.27)$$

Here we have only reviewed the lowest order DNLSE. Nevertheless, it has been shown (Trombettoni and Smerzi, 2003) that the effective dimensionality of the BECs trapped in each well can modify the degree of non-linearity and the tunneling rate in the DNLSE.

The Josephson effect (Josephson, 1962) essentially consists of the collective coherent tunneling of particles through macroscopic barriers driven by a quantum phase difference between the two sides of the potential barrier. The DNLSE has been applied, for instance, to characterize the first direct observation of a Josephson current in an array of weakly coupled BEC (Cataliotti *et al.*, 2001). Several authors (Trombettoni and Smerzi, 2001; Menotti *et al.*, 2003) used the DNLSE to give full insight into the global dynamics of a BEC in deep periodic potentials, predicting the conditions for the appearance of solitonic structures, breathers, or the self-trapping regime. Although the DNLSE gives good estimates

of the parameters at which all these phenomena appear, as corroborated experimentally in Eiermann *et al.* (2004) and Anker *et al.* (2005), it fails in the quantitative description of the dynamics of both the self-trapping regime (Alexander *et al.*, 2006) and the discrete gap solitons (Ahufinger *et al.*, 2004). In these cases, the description with the full Gross–Pitaevskii equation, including all the bands in the band structure, is needed. The inclusion of an harmonic potential in addition to the optical lattice has also been addressed in the framework of the DNLSE by studying small oscillations of a BEC (Krämer *et al.*, 2002) and the breakdown of those oscillations for large amplitudes (Smerzi *et al.*, 2002; Menotti *et al.*, 2003).

3.5. From weakly interacting to strongly correlated regimes

The mean-field approach used in the previous sections is suitable only for describing a condensate in the weakly interacting regime, i.e. when the interaction energy is small compared to the kinetic energy (Pitaevskii and Stringari, 2003). In the opposite case, when interactions play a fundamental role in the dynamics, one reaches the so-called strongly correlated regime. It is within this regime that lattice gases mimic condensed-matter systems.

In general, ultracold gases are weakly interacting systems. The interaction between atoms is fixed by the scattering length, which can be increased with the help of Feshbach resonances (Chin *et al.*, 2010). Nevertheless, this approach induces three-body losses that strongly reduce the lifetime of the condensate. Another possibility consists of exploiting the properties of ultracold atoms in periodic potentials, where the tunneling energy plays the role of the kinetic energy. By increasing the lattice depth, the tunneling energy exponentially decreases and the strongly correlated regime can be reached, as demonstrated in the seminal experiment of Greiner *et al.* (2002), where the SF–MI quantum phase transition with cold bosons was reported. Very recently a MI state for fermions has also been experimentally observed (Jördens *et al.*, 2008; Schneider *et al.*, 2008).

The seminal theoretical proposal of Jaksch *et al.* (1998) that was followed to reach the strongly correlated regime showed that bosonic atoms with repulsive interactions in a periodic lattice potential are well described by a Bose–Hubbard Hamiltonian (Fisher *et al.*, 1989). The Bose–Hubbard Hamiltonian can be derived from the many-body Hamiltonian in the second quantized form (3.19) by using the single-particle Wannier basis (eqn (3.15)) For sufficiently deep optical potentials and at low temperatures one can safely expand the field operator in the basis of Wannier functions of the lowest band (since typical interaction energies are not strong enough to excite higher vibrational states):

$$\hat{\Psi}(\mathbf{r}) = \sum_i \hat{b}_i w(\mathbf{r} - \mathbf{r}_i), \quad (3.28)$$

where \hat{b}_i , (\hat{b}_i^\dagger) denotes the annihilation (creation) operator of a particle localized to the i th lattice site that obey canonical commutation relations $[\hat{b}_i, \hat{b}_j^\dagger] = \delta_{ij}$. We have omitted the band index here. Introducing the above expansion into the Hamiltonian given in eqn (3.19),

and considering tunneling only between nearest-neighbor lattice sites, one obtains:

$$H = - \sum_{\langle i,j \rangle} t_{ij} (\hat{b}_i^\dagger \hat{b}_j + h.c.) + \frac{U}{2} \sum_i \hat{n}_i (\hat{n}_i - 1), \quad (3.29)$$

where $\langle i,j \rangle$ indicates the sum over nearest neighbors and $\hat{n}_i = \hat{b}_i^\dagger \hat{b}_i$ is the boson number operator at each site. The tunneling matrix element between adjacent sites is given by t (both t and J are used in the literature):

$$t_{ij} = - \int d\mathbf{r} w^*(\mathbf{r} - \mathbf{r}_i) \left[\frac{-\hbar^2 \nabla^2}{2m} + V_{\text{ext}} \right] w(\mathbf{r} - \mathbf{r}_j). \quad (3.30)$$

The subindex (ij) can be omitted in the homogeneous case, when the external optical potential is isotropic and tunneling is the same along any direction. The strength of the two-body on-site interactions U for a contact potential reduces to:

$$U_i = g \int d\mathbf{r} |w(\mathbf{r} - \mathbf{r}_i)|^4. \quad (3.31)$$

If the external potential also accounts for a trapping potential V_T , an extra term in the Bose–Hubbard Hamiltonian appears: $\sum_i \epsilon_i n_i$, where ϵ_i is given by:

$$\epsilon_i = \int d\mathbf{r} V_T |w(\mathbf{r} - \mathbf{r}_i)|^2 \approx V_T(\mathbf{r}_i). \quad (3.32)$$

This term describes an energy offset for each lattice site.

It is possible to obtain analytical expressions for the above integrals to define tunneling (eqn (3.30)), the non-linear energy (eqn (3.31)), and the on-site energy (eqn (3.32)), within the harmonic approximation. Assuming a 3D periodic potential given by:

$$V_{\text{ext}} = \sum_{l=x,y,z} V_{0l} \sin^2(k_l l), \quad (3.33)$$

each potential minimum is replaced, within this approach, by an harmonic potential. Correspondingly, the Wannier functions $w(\mathbf{r} - \mathbf{r}_i)$ (of the lowest band) are replaced by a product of Gaussian wave functions on each direction:

$$w(\mathbf{r} - \mathbf{r}_i) \approx \phi_0(x - x_i) \phi_0(y - y_i) \phi_0(z - z_i), \quad (3.34)$$

where

$$\phi_0(l - l_i) = \frac{e^{-(l - l_i)^2 / 2\sigma_l^2}}{\pi^{1/4} \sqrt{\sigma_l}}, \quad (3.35)$$

with $l = x, y, z$, and σ_l being the harmonic oscillator length in the corresponding direction.

The Bose–Hubbard Hamiltonian, eqn (3.29), exhibits two different quantum phases depending on the ratio between the tunneling energy and the on-site repulsion energy: (i) a superfluid phase when tunneling dominates and (ii) an MI ground state when the on-site interaction term dominates. Next, we briefly summarize the main features of both states. In the superfluid ground state each atom is delocalized over the entire lattice and the many-body wave function corresponds to a product state of identical zero quasi-momentum Bloch waves given by:

$$|\Psi_{SF}\rangle = \frac{1}{\sqrt{N}} \left(\sum_{i=1}^M \hat{b}_i^\dagger \right)^N |0\rangle, \quad (3.36)$$

where M is the number of sites on the lattice and N the number of bosons on the lattice. This superfluid state is characterized by large fluctuations in the on-site number of particles, divergent correlation length, and a vanishing gap. In the limit $U = 0$, the single-site many-body wave function $|\phi_i\rangle$ is equivalent to a coherent state in second quantization, which is an eigenstate of \hat{b}_i . Therefore the many-body state on a lattice site is a superposition of different atom numbers, following a Poissonian atom number distribution.

In the opposite limit, for $U/t \rightarrow \infty$, when the system is dominated by the interactions, the ground state corresponds to an MI state characterized by a well defined number n of atoms per site. The many-body ground state is then a product of local Fock states, with a fixed atom number at each lattice site. For a homogeneous system with commensurate filling of n atoms per site, the many-body wave function reads as follows:

$$|\Psi_{\text{Mott}}\rangle \propto \prod_{i=1}^M (\hat{b}_i^\dagger)^n |0\rangle. \quad (3.37)$$

The MI state has finite correlation length and a gapped spectrum. In this situation, the phase of the coherent matter wave field on a lattice presents maximum uncertainty. The Mott state has zero compressibility $\frac{\partial(N/V)}{\partial\mu} = 0$, i.e. it is incompressible.

4

Quantum simulators of condensed matter

After learning the basics of the interesting phenomena of statistical and condensed-matter physics that we would like to simulate in Chapter 2, and after reviewing the basic concepts on ultracold atoms in optical lattices in Chapter 3, let us now try to be more specific about what ultracold atomic systems can offer. In this chapter, we ask the question: what kind of condensed matter systems one can mimic with ultracold atoms in optical lattices? Here the concept of a *quantum simulator* is important.

4.1. Quantum simulators

The concept of a quantum simulator goes back to Feynman (1986), who pointed out that it might sometimes be possible to find a simpler and experimentally more accessible system to mimic a quantum system of interest. Feynman's argument is based of course on the complexity of the classical simulations of quantum systems. Suppose we want to study a system of N spins $\frac{1}{2}$. The dimension of the Hilbert space is then 2^N , and the number of coefficients we need to describe the system may in principle be as large as the dimension of the Hilbert space. As N grows, this number quickly becomes larger than the number of atoms in the universe; classical simulations are evidently impossible. Of course in practice this number may be very much reduced by using clever representations of the wave function (see Chapters 12 and 13) but in general there are many quantum systems that are very hard to simulate classically. In particular the most powerful quantum Monte Carlo codes fail for many fermionic or frustrated systems, due to the so-called ‘sign problem’. The DMRG and matrix product states (MPS) methods work well in 1D. The novel projected entangled pair states (PEPS) method is, at least in current applications, limited to systems that are not too large. The rule of thumb is that classical simulations are possible for systems with short *entanglement correlations*. These can be expressed in a form of ‘area’ laws: the von Neuman entropy of a block A of a system of size $|A|$ scales as the size of the boundary of the block $|\partial A|$ (see Perez-García *et al.* (2007), Schuch *et al.* (2007), Wolf *et al.* (2008), Verstraete *et al.* (2008), Calabrese and Cardy (2009), Hastings (2009), Latorre and Riera (2009), and Eisert *et al.* (2010)).

The modern concept of quantum simulators is not exactly the same as the one described by Feynman. Since condensed matter systems are typically very complex, theorists make

simplified models of the systems of interest. In this simplification symmetries of the original problem are usually kept intact, and the concept of universality is used: different Hamiltonians with similar symmetry properties belong to the same universality classes, i.e. exhibit the same phase transitions and have the same critical exponents (Cardy, 1996; Amit, 2005). Unfortunately, even these simplified models are often difficult to understand. A paradigmatic example of such a situation concerns high T_c superconductivity of cuprates (Lee *et al.*, 2006; Lee, 2008), where it is believed that the basic physics is captured by the 2D Hubbard model for electrons, i.e. spin- $\frac{1}{2}$ fermions. Even this simple model does not allow for accurate treatment, and there are many controversies concerning, for instance, the phase diagram or the character of the transitions. One prominent theorist told us once: ‘Give me a point in the phase diagram, and I will attach to it any phase you want depending on the approximations’. The role of quantum simulators, as proposed in many quantum information projects, will be to simulate the simple models, such as 2D Hubbard models, and get a better understanding of them, rather than trying to simulate the full complexity of the condensed matter.

A ‘working’ definition of a quantum simulator could be:

- A quantum simulator is an experimental system that mimics a simple model, or a family of simple models of condensed matter (or high energy physics, or quantum chemistry ...).
- The simulated models have to be of some relevance for applications and/or our understanding of challenges in the areas of physics mentioned above.
- The simulated models should be computationally very hard for classical computers. Note that this statement may have two meanings: i) an efficient (scalable to large system size) algorithm to simulate the model might not exist or might not be known; ii) the efficient scalable algorithm is known, but the size of the simulated model is too large to be simulated under reasonable time and memory restrictions. The latter situation in fact starts to occur with the classical simulations of the Bose or Fermi–Hubbard models, in contrast to their experimental quantum simulators (see Troyer’s talk in Fisher *et al.* (2010)). There might also be exceptions to the general rule. For instance, it is desirable to realize quantum simulators to simulate and to *observe* novel phenomena that so far are only theoretically predicted, even though it might be possible to simulate these phenomena efficiently with present computers. Simulating and observing is more than just simulating.
- A quantum simulator should allow for broad control of the parameters of the simulated model, and for control of preparation, manipulation, and detection of states of the system. In particular, it is important to be able to set the parameters in such a way that the model becomes tractable by classical simulations. This then provides a possibility of validating the quantum simulator (Trotzky *et al.*, 2010). Another kind of validation was recently proposed by Hadzibabic. Sometimes it might be impossible to simulate the system classically, but it might still be possible to check the results of the quantum simulation. For instance, the measured ground state energy of the system considered should fulfill all known bounds, such as variational ones etc. Even more sophisticated manners of validation require the checking of the sensitivity of the quantum simulation results with respect to addition of (controlled) noise and/or disorder.

Although there are many proposals for systems that could act as quantum simulators, such as ultracold atoms in optical lattices, atoms in arrays of cavities, atoms in arrays of traps, quantum dots, or superconducting circuits (for a review see Buluta and Nori (2009)), here we mainly focus on ultracold atoms in optical lattices because of their controllability and scalability. It does not mean, however, that these systems are the most suitable for all tasks. In this context it is worth mentioning the proposal for an efficient implementation of a universal quantum simulator for spin models using laser-excited Rydberg atoms in large spacing lattices (Weimer *et al.*, 2010), whose building blocks have already been experimentally implemented (Gaëtan *et al.*, 2009; Urban *et al.*, 2009).

4.2. Hubbard models

Most of the quantum simulators discussed in the recent years correspond to various kinds of Hubbard model. While the original Hubbard model (Hubbard, 1963) was introduced to describe electrons in the solid state, it allows for various generalizations that describe a variety of possible Fermi and Bose systems, and also their mixtures. We are therefore interested in this type of model, the reason being that they are realizable with cold atoms in optical lattices. The simplest optical lattice is a simple 3D cubic lattice, as shown in Figure 3.1(b). It is formed by three pairs of laser beams creating three orthogonal standing waves with orthogonal polarizations. As we discuss below, however, one can create practically arbitrary lattices on demand using optical potentials. Also, as the intensity of one of the standing waves increases, the probability of hopping along this direction decreases rapidly to zero (Jaksch *et al.*, 1998). In effect we obtain a 1D array of 2D square lattices. Consequently, an increase of the laser intensity of another of the standing waves effectively creates a 2D array of 1D lattices (Figure 3.1(a)).

Optical lattices provide an ideal (contain no defects) and rigid (do not support phonon excitations¹) periodic potential in which the atoms move. As is well known from solid-state theory (Ashcroft and Mermin, 1976), the single-particle energy spectrum (in the absence of interactions) consists of bands, and the energy eigenstates of the Hamiltonian are Bloch functions. If the lattice potential is strong enough the band-gaps are large and the bands are well separated energetically. At sufficiently low temperatures it is easy to achieve a situation in which only the lowest band is occupied (the tight-binding approximation). The Bloch functions of the lowest band can be expanded in Wannier functions, which are not the eigenstates of the single-particle Hamiltonian, but are localized at each site. In the tight-binding approximation, we project all the atomic quantum field operators that describe the system onto the lowest band, and then expand into the Wannier basis. Then leaving just the most relevant terms in the Hamiltonian (such as hopping between the nearest-neighboring sites) leads directly to a Hubbard-type Hamiltonian. This procedure was described in more detail in Chapter 3.

Let us write the most general Hubbard model that may be created in this way. Let us assume that we have several bosonic and fermionic species (or bosons/fermions with several internal states), denoted α and β , respectively. The basic objects of the theory will thus be

¹This statement has to be revised when the lattice is created inside an optical cavity. As we discuss later, the presence of atoms may affect the cavity field.

annihilation and creation operators of α -bosons, $\hat{b}_{i\alpha}, \hat{b}_{i\alpha}^\dagger$, at the site i , and analogously annihilation and creation operators of β -fermions, $\hat{f}_{i\beta}, \hat{f}_{i\beta}^\dagger$, at the site i . Of course, bosonic (fermionic) operators fulfill the standard canonical commutation (anticommutation) relations:

$$[\hat{b}_{i\alpha}, \hat{b}_{j\alpha'}] = \{\hat{f}_{i\beta}, \hat{f}_{j\beta'}\} = 0 \quad (4.1)$$

$$[\hat{b}_{i\alpha}, \hat{b}_{j\alpha'}^\dagger] = \delta_{\alpha\alpha'}\delta_{ij}, \quad (4.2)$$

$$\{\hat{f}_{i\beta}, \hat{f}_{j\beta'}^\dagger\} = \delta_{\beta\beta'}\delta_{ij}, \quad (4.3)$$

where $\delta_{(\cdot)}$ denotes the Kronecker delta.

The most general Hubbard-type Hamiltonian that one can realize with cold atoms, assuming lowest band occupation only,² consists of five parts:

$$\hat{H}_{\text{Hubbard}} = \hat{H}_{\text{hop}} + \hat{H}_{\text{int}} + \hat{H}_{\text{int-hop}} + \hat{H}_{\text{pot}} + \hat{H}_{\text{Rabi}}. \quad (4.4)$$

- Hopping part, \hat{H}_{hop} . This describes hopping (tunneling) of atoms from one site to another. Since the hopping probability amplitude decreases exponentially with the distance, hopping is typically assumed to occur between the nearest neighboring sites, denoted $\langle ij \rangle$. On the other hand, hopping might be laser assisted and thus allow for transitions from one internal state to another. Of course, or perhaps unfortunately, it cannot lead to a change of element, or even isotope! Taking these considerations into account, the hopping part of the Hubbard Hamiltonian reads:

$$\hat{H}_{\text{hop}} = - \sum_{\alpha, \alpha', \langle ij \rangle} [t_{ij\alpha\alpha'}^{\text{B}} \hat{b}_{i\alpha}^\dagger \hat{b}_{j\alpha'} + h.c.] - \sum_{\beta, \beta', \langle ij \rangle} [t_{ij\beta\beta'}^{\text{F}} \hat{f}_{i\beta}^\dagger \hat{f}_{j\beta'} + h.c.], \quad (4.5)$$

where $t_{ij\alpha\alpha'}^{\text{B}}$ ($t_{ij\beta\beta'}^{\text{F}}$) accounts for the tunneling rate for bosons (fermions).

- Interactions part, \hat{H}_{int} . Atoms interact in the first place via short-range van der Waals forces, which in the low-energy limit are well described by various kinds of zero-range pseudo-potentials (Huang, 1987; Pitaevskii and Stringari, 2003; Idziaszek and Calarco, 2006). This means that the dominant part of the interactions is of contact type, i.e. occurs on-site. There are, however, situations in which interactions do affect neighboring sites, or even have long-range (such as dipole–dipole) interactions. We thus write the interaction part as:

$$\hat{H}_{\text{int}} = \hat{H}_{\text{on-site}} + \hat{H}_{\text{ext}}, \quad (4.6)$$

²Some authors go beyond this assumption. For some of pioneering papers, see for instance Alon *et al.* (2005). See also the discussion in Chapter 15 of the newly developed trend in ultracold atom physics dealing with orbital lattices.

where

$$\hat{H}_{\text{on-site}} = \frac{1}{2} \sum_{i,\alpha,\beta,\alpha',\beta'} \left[U_{\alpha\beta\alpha'\beta'}^{\text{BB}}(i) \hat{b}_{i\alpha}^\dagger \hat{b}_{i\beta}^\dagger \hat{b}_{i\beta'} \hat{b}_{i\alpha'} + U_{\alpha\beta\alpha'\beta'}^{\text{FF}}(i) \hat{f}_{i\alpha}^\dagger \hat{f}_{i\beta}^\dagger \hat{f}_{i\beta'} \hat{f}_{i\alpha'} \right. \\ \left. + 2U_{\alpha\beta\alpha'\beta'}^{\text{BF}}(i) \hat{b}_{i\alpha}^\dagger \hat{f}_{i\beta}^\dagger \hat{f}_{i\beta'} \hat{b}_{i\alpha'} \right]. \quad (4.7)$$

We now let the indices $\alpha, \alpha', \beta, \beta'$ run over the corresponding species of bosons or fermions, with $U_{\alpha\beta\alpha'\beta'}^{\text{BB}}(i)$, $U_{\alpha\beta\alpha'\beta'}^{\text{FF}}(i)$, and $U_{\alpha\beta\alpha'\beta'}^{\text{BF}}(i)$ denoting the on-site (contact) interactions between bosons, between fermions, and between bosons and fermions at site i , respectively. In the simplest Hubbard models interactions depend only on the on-site atom numbers $\hat{n}_{i\alpha}^{\text{B}} = \hat{b}_{i\alpha}^\dagger \hat{b}_{i\alpha}$ and $\hat{n}_{i\beta}^{\text{F}} = \hat{f}_{i\beta}^\dagger \hat{f}_{i\beta}$. In general, however, they may depend in a non-trivial way on internal states or atomic species. This is, for instance, the standard case for spinor gases (Stamper-Kurn and Ketterle, 2001), see Chapter 7. The models with non-contact interactions are usually termed ‘extended’ Hubbard models and include:

$$\hat{H}_{\text{ext}} = \frac{1}{2} \sum_{i,j,\alpha,\beta,\alpha',\beta'} \left[V_{\alpha\beta\alpha'\beta'}^{\text{BB}}(i,j) \hat{b}_{i\alpha}^\dagger \hat{b}_{j\beta}^\dagger \hat{b}_{j\beta'} \hat{b}_{i\alpha'} + V_{\alpha\beta\alpha'\beta'}^{\text{FF}}(i,j) \hat{f}_{i\alpha}^\dagger \hat{f}_{j\beta}^\dagger \hat{f}_{j\beta'} \hat{f}_{i\alpha'} \right. \\ \left. + 2V_{\alpha\beta\alpha'\beta'}^{\text{BF}}(i,j) \hat{b}_{i\alpha}^\dagger \hat{f}_{j\beta}^\dagger \hat{f}_{j\beta'} \hat{b}_{i\alpha'} \right]. \quad (4.8)$$

with $V_{\alpha\beta\alpha'\beta'}^{\text{BB}}(i,j)$, $V_{\alpha\beta\alpha'\beta'}^{\text{FF}}(i,j)$, and $V_{\alpha\beta\alpha'\beta'}^{\text{BF}}(i,j)$ the interactions between bosons, between fermions, and between bosons and fermions at distant sites i and j . Most typically, the non-contact interactions will depend on the distance between the sites, $|\mathbf{r}_i - \mathbf{r}_j|$, and will be of the density-density form (i.e. they depend only on $\hat{n}_{i\alpha}^{\text{B}}$, and $\hat{n}_{i\beta}^{\text{F}}$), but again, in general, this does not have to be the case. Dipolar interactions, for instance, depend on the angles between the dipole moments and the vector $\mathbf{r}_i - \mathbf{r}_j$.

- Interaction-assisted hopping term in the Hamiltonian $\hat{H}_{\text{int-hop}}$. This is usually omitted. Formally, it appears in the model with contact interactions, when, in the Wannier expansion of the fields in the interaction term, we keep the contributions from, say, the nearest neighboring sites involving one operator from site i and the other three from site j . Again, these kinds of terms may depend on internal degrees of freedom and read:

$$\hat{H}_{\text{int-hop}} = \frac{1}{2} \sum_{i,j,\alpha,\beta,\alpha',\beta'} \left[W_{\alpha\beta\alpha'\beta'}^{\text{BB}}(i,j) \hat{b}_{i\alpha}^\dagger \hat{b}_{j\beta}^\dagger \hat{b}_{j\beta'} \hat{b}_{j\alpha'} + W_{\alpha\beta\alpha'\beta'}^{\text{FF}}(i,j) \hat{f}_{i\alpha}^\dagger \hat{f}_{j\beta}^\dagger \hat{f}_{j\beta'} \hat{f}_{j\alpha'} \right. \\ \left. + 2W_{\alpha\beta\alpha'\beta'}^{\text{BF}}(i,j) \hat{b}_{i\alpha}^\dagger \hat{f}_{j\beta}^\dagger \hat{f}_{j\beta'} \hat{b}_{j\alpha'} + 2W_{\alpha\beta\alpha'\beta'}^{\text{FB}}(i,j) \hat{f}_{i\alpha}^\dagger \hat{b}_{j\beta}^\dagger \hat{b}_{j\beta'} \hat{f}_{j\alpha'} + h.c. \right] \quad (4.9)$$

The importance of these types of terms for electrons and holes has been stressed in a series of papers by Hirsch and collaborators (Guinea 1988a, b; Hirsch 1989a, b;

Micnas *et al.*, 1989; Lin and Hirsch, 1995). Such models, used frequently as models of hole superconductivity, were originally designed to describe high T_c and other types of superconductivity. These models can give rise to superconductivity without introducing explicitly attractive interactions between electrons (Micnas *et al.*, 1990) and far from phase separation instabilities. Recently, there has been a revival of interest in this kind of model or, more generally speaking, in Hubbard models with occupation-dependent parameters (see Dutta *et al.* (2011)) in the context of ultracold atoms.

- On-site single-atom process terms, \hat{H}_{pot} and \hat{H}_{Rabi} . The last two parts of the Hubbard Hamiltonian, \hat{H}_{pot} and \hat{H}_{Rabi} , describe on-site single-atom processes and essentially have the same form as the tunneling part, except that they occur on-site. We distinguish them since they are well defined and controllable in experiments. \hat{H}_{pot} combines the effects of all potentials felt by atoms, such as external trapping potential, possible additional superlattice (i.e. additional lattice) potentials, possible disorder potentials, and last, but not least, chemical potential, which is necessary if one uses the statistical description based on the grand canonical ensemble:

$$\hat{H}_{\text{pot}} = - \sum_{\alpha,i} \left[\mu_{i\alpha}^{\text{B}} \hat{b}_{i\alpha}^\dagger \hat{b}_{i\alpha} + \mu_{i\alpha}^{\text{F}} \hat{f}_{i\alpha}^\dagger \hat{f}_{i\alpha} \right]. \quad (4.10)$$

The last part of the Hamiltonian, \hat{H}_{Rabi} , describes possible coherent on-site transitions between the internal states of atoms; such transitions may be achieved using laser-induced resonant Raman transitions or microwave Rabi-type transitions. We can write this part of the Hamiltonian as time-independent in the interaction picture with respect to the on-site internal-states Hamiltonian:

$$\hat{H}_{\text{Rabi}} = \frac{1}{2} \sum_{\alpha,\beta,i} \left[\Omega_{i\alpha\beta}^{\text{B}} \hat{b}_{i\alpha}^\dagger \hat{b}_{i\beta} + \Omega_{i\alpha\beta}^{\text{F}} \hat{f}_{i\alpha}^\dagger \hat{f}_{i\beta} \right]. \quad (4.11)$$

4.3. Spin models and quantum magnetism

As is well known (see for instance Auerbach (1994)), Hubbard models reduce to spin models in certain limits. Most of these limits, and even others, are accessible with cold atoms. Generally speaking, if bosonic atoms can occupy only $2S + 1$ different states in a lattice site, then one can always map these states onto the states of pseudo-spin S . These states may even correspond to different numbers of bosons, and the dimension of the local on-site Hilbert space might vary in space; in such a case we will be dealing with inhomogeneous models, where at each site there is, in general, a different spin. A similar construction can be done for fermionic atoms, with the caveat that, at a given site, the fermion number differences may only have even values, since otherwise the fermionic character of particles cannot be eliminated.

When constructing specific spin models two aspects play a role: lattice geometry (which we discussed in Chapter 3), and the forms of the interactions, which include Ising, XY , Heisenberg, XXZ , and anisotropic XYZ types, as well as ring-exchange types. Below we

list the most obvious constructions of spin models that have been discussed in the literature on cold atoms. We restrict ourselves here to translationally invariant models.

- *Hard-core bosons and XY models.* Perhaps the simplest way to obtain a non-trivial spin model is to use the simplest Bose–Hubbard Hamiltonian for one component ('spinless') bosons

$$\hat{H} = -t \sum_{\langle ij \rangle} [\hat{b}_i^\dagger \hat{b}_j + h.c.] + \frac{U}{2} \sum_i \hat{n}_i (\hat{n}_i - 1) - \mu \sum_i \hat{n}_i, \quad (4.12)$$

where $\langle ij \rangle$ denotes the sum over nearest neighbors, t is the tunneling rate, U the on-site interactions, and μ the chemical potential. In the hard-boson limit (i.e. when $U \gg t, \mu$), we may have at most one boson per site. We may then encode the spin 1/2 states as the presence (\uparrow) or absence (\downarrow) of the boson at the site. The Hamiltonian then reduces to that of the *XY* model in a transverse magnetic field,

$$\hat{H} = -t \sum_{\langle ij \rangle} [\hat{\sigma}_i^\dagger \hat{\sigma}_j + h.c.] - \frac{\mu}{2} \sum_i (\hat{\sigma}_{z,i} + 1), \quad (4.13)$$

where $\hat{\sigma}_i = (\hat{\sigma}_{x,i} + i\hat{\sigma}_{y,i})/2$, and $\hat{\sigma}_{x,i}$, $\hat{\sigma}_{y,i}$, and $\hat{\sigma}_{z,i}$ denote the standard Pauli matrices at site i . This model has the advantage that in one dimension it is exactly solvable via a Jordan–Wigner transformation (Sachdev, 1999). One interesting application of this approach concerns the 1D disordered chain studied in De Martino *et al.* (2005). The same approach was used recently in Wehr *et al.* (2006) to realize the *XY* model in a random longitudinal 'magnetic' field; along one direction, say x . Last, but perhaps most importantly, is the fact that the spin models obtained in the hard-core boson limit allow us to simulate quantum magnetism at temperatures similar to that of the 'standard' SF–MI transitions, i.e. relatively high.

- *Spatially delocalized qubits.* Considering two neighboring traps or potential wells ('left' and 'right') and assuming one atom per double well it is possible to encode a spin- $\frac{1}{2}$ (qubit) as the presence of the atom in the 'left' or in the 'right' trap (Mompert *et al.*, 2003). A similar idea was used in Dorner *et al.* (2003) and applied to a whole string of neutral atoms yielding improved robustness. This system may be used for generation of maximally entangled many-atom states (Schrödinger cat states) when crossing a quantum phase transition.
- *Multi-component atoms in Mott states.* Whenever we deal with a system of multicomponent atoms, i.e. atoms with say $2S + 1$ internal states, in the MI limit, the system will be well described by the appropriate spin model. The most prominent example is a two-component (or spin- $\frac{1}{2}$) Fermi gas (Auerbach, 1994), which in the Mott state with one atom per site forms a perfect Heisenberg model. Interactions in this system are due the well-known superexchange effect (Anderson, 1963). Several groups are planning experiments with ultracold spin- $\frac{1}{2}$ Fermi atoms tending towards antiferromagnetism in various types of lattices. Prospects for observing antiferromagnetic transitions in such systems are quite good, especially since one expects to be able to employ interaction-induced cooling, an analog of the Pomeranchuk effect in liquid helium

physics (Werner *et al.*, 2005) and disorder-induced increase in T_c (Wehr *et al.*, 2006). One should stress, however, that although the Mott transition typically takes place when $t < U$, the low-temperature physics of the resulting Heisenberg model requires temperatures of order $t^2/U \simeq k_B T$. Such temperatures are often in the nanokelvin range, i.e. they are still hard to achieve experimentally. There are, however, a lot of new proposals for cooling atoms in the Mott states (Rabl *et al.*, 2003; Griessner *et al.*, 2005; Popp *et al.*, 2006*a,b*). Particularly promising are cooling schemes based on entropy control (Bernier *et al.*, 2009; Ho and Zhou, 2009). It is hoped that the ability to achieve sufficiently low temperatures will not set any limitations on experiments with these kinds of spin model in the near future.

The calculations of the superexchange interactions and the resulting effective Hamiltonians in pseudo-spin- $\frac{1}{2}$ Bose–Bose or Bose–Fermi mixtures is quite complicated, and was accomplished for the first time recently (Kuklov and Svistunov, 2003; Lewenstein *et al.*, 2004). The Bose–Bose case can be reduced to an XXZ spin model (for the case of XXZ model in random fields see, for instance, Wehr *et al.* (2006)). The effective Hamiltonian for the Fermi–Bose mixture cannot, in general, be reduced to a spin model, since it involves Fermi operators describing *composite fermions*, consisting of one fermion paired with a number of bosons or bosonic holes (Lewenstein *et al.*, 2004). The Hamiltonian describes a ‘spinless’ interacting Fermi gas of such composites. It can, however, be transformed to an XXZ model in external fields in one dimension via a Jordan–Wigner transformation.

- *Spinor gases in Mott states.* Of course, the above statements are particularly valid for spinor gases. For atoms with spin $F > \frac{1}{2}$ we have effective Hamiltonians containing generalizations (a power series) of Heisenberg interactions. For $F = 1$ and the Mott state with one atom per site, we deal with the so-called bilinear–biquadratic Hamiltonian (Demler and Zhou, 2002; Imambekov *et al.*, 2003; Yip 2003*a*, 2003*b*; García-Ripoll *et al.*, 2004). In the Mott state with two atoms per site, the pair can either compose a singlet state or a state with on-site spin $S = 2$. The resulting Hamiltonian then contains higher powers of the Heisenberg term. The situation is obviously more complicated for higher Mott states and atoms with higher individual spin F . The case $F = 2$ with one atom per site leads to an effective Hamiltonian that is a polynomial of the fourth order in the Heisenberg term (Barnett *et al.*, 2006*b*; Eckert *et al.*, 2007; Zhou and Semenoff, 2006).
- *Spin models in polymerized lattices.* Another interesting way to obtain spin models with cold atoms uses polymerized (dimerized, trimerized, quadrumerized etc.) lattices. These are lattices that can easily be realized with appropriately designed laser configurations or holographic masks (Bakr *et al.*, 2009). They have no direct analog in condensed-matter physics. A simple example of a dimerized lattice in two dimensions is a square lattice of pairs of close sites; a trimerized kagomé lattice (discussed in Chapter 10) is a triangular lattice of trimers of close sites located on a small unilateral triangle; a 2D quadrumerized square lattice is a square lattice of small squares of close sites, etc. When one considers ultracold gases in such lattices, one has to first take into account the lowest-energy state in a dimer, trimer etc. If we deal with polarized ‘spinless’ fermions in a trimerized lattice and we consider two fermions per trimer, fermions have to their disposal a zero-momentum state (which will be necessarily filled at low temperatures) and two states with left and right chirality. The latter are

obviously degenerate and can thus be used to encode the effective spin $\frac{1}{2}$. This is the model discussed in Santos *et al.* (2004), Damski *et al.* (2005a), and Damski *et al.* (2005b). Note that similar encoding is possible in a quadrumerized lattice with two fermions per quadrumer (plaquette). Plaquettes have been also proposed as minimal instances of topological order (Paredes and Bloch, 2008), and have been used to prepare decoherence-free cluster states (Jiang *et al.*, 2009).

- *The celebrated Jordan–Wigner transformation.* Any local fermionic model in one dimension can be transformed exactly into a local spin model, using the Jordan–Wigner transformation (see Chapter 5). The price one has to pay is that the transformation is highly non-local, and so are the relations between the spin–spin and fermion–fermion correlation functions. The Jordan–Wigner transformation cannot be simply generalized to higher dimensions. Recently, interesting 2D versions of the transformation have been proposed (see Verstraete and Cirac (2005) and references therein). The approaches of Verstraete and Cirac transform local Fermi models into local spin models with additional (Ising-like) auxiliary local spin variables. The non-locality is not lifted completely, however, since the auxiliary spin needs to fulfill simple, but non-local, constraints.

5

Bose–Hubbard models: methods of treatment

5.1. Introduction

In the next two chapters we present some of the standard theoretical tools used in condensed-matter theory to treat many-body systems, in particular the Hubbard model and its descendants. The Hubbard model, originally proposed as an idealization or toy model to study magnetic properties of electrons in transition metals, has become a paradigmatic model in condensed matter. It is probably the simplest many-body system that cannot be reduced to a single-particle Hamiltonian. More importantly, it reproduces many experimental situations of interest. The Fermi–Hubbard model is analytically solvable in one dimension only. Although there are theorems that give valuable hints about the physics in two and three dimensions, numerical calculations are needed to find the low-energy physics of the model.

Analytical and numerical methods often rely on the size and dimensionality of the system. Powerful analytical techniques like bosonization (Cazalilla, 2004; Giamarchi, 2004; Gogolin *et al.*, 2004), Bethe ansatz (Korepin and Essler, 1994; Korepin *et al.*, 1997; Essler *et al.*, 2005), or the Jordan–Wigner transformation (Sachdev, 1999; Tsvelik, 2003) are well established as treatments of many-body problems in one dimension, such as the spin- $\frac{1}{2}$ Heisenberg model, XXZ spin chains, or the 1D Hubbard model of strongly interacting electrons. Moreover, numerical methods such as the density matrix renormalization group (DMRG) or matrix product states (MPS) allow us to find the ground state and some low-energy properties of 1D many-body systems, which are not analytically solvable. All the above methods are well-established methods to treat some many-body systems in one dimension, but often fail in higher dimensions. Finite-size effects are also crucial in the study of strongly correlated systems because quantum phase transitions occur only in the thermodynamic limit at zero temperature. It is thus important to assess how finite size affects the statics and dynamics of strongly correlated systems, as well as the signatures of quantum phase transitions.

In this chapter, we focus on the prominent and simpler Bose–Hubbard model, obtained by replacing the spin- $\frac{1}{2}$ particles with spinless bosons, first introduced in the seminal work of Fisher *et al.* (1989). We start in Section 5.2 by considering the Bose–Hubbard model in the weakly interacting limit by means of the Bogoliubov approach and then move to the strongly interacting limit using the so-called strong-coupling expansion in Section 5.3. Section 5.4 is devoted to the mean-field perturbative approach.

We also discuss numerical techniques to solve the Bose–Hubbard model in this chapter. We start with the Gutzwiller mean-field approach (Section 5.5) and move on to exact

diagonalization (Section 5.6), quantum Monte Carlo methods (Section 5.7), and phase-space methods (Section 5.8). In Section 5.9 we move towards explicit analytical 1D methods such as Bethe ansatz, the Jordan–Wigner transformation, and bosonization to illustrate the power of such methods to solve some bosonic and spin models. The last part of the chapter is devoted to more detailed analysis of the novel renormalization group numerical approaches provided by quantum information, the so-called MPS in one dimension (Section 5.10), as well as its recent extensions to two dimensions by means of projected entangled product states (PEPS) and the multiscale entanglement renormalization ansatz (MERA) in Section 5.11. We postpone discussion of the fermionic Hubbard model and its descendants to Chapter 6.

Our starting point is the Bose–Hubbard Hamiltonian in the grand canonical ensemble, where the chemical potential μ (that determines the energy necessary to add (remove) a particle from the system) is fixed, thus determining the average number of bosons

$$\hat{H}_{\text{BH}} = - \sum_{\langle i,j \rangle} t_{ij} (\hat{b}_i^\dagger \hat{b}_j + h.c.) + \frac{U}{2} \sum_i \hat{n}_i (\hat{n}_i - 1) - \mu \sum_i \hat{n}_i. \quad (5.1)$$

We further assume that tunneling, i.e. the kinetic energy necessary for one boson to hop from site to site, is the same for all sites and directions, i.e. $t_{ij} = t$. Creation and annihilation bosonic operators are denoted by the symbols \hat{b}_i^\dagger and \hat{b}_i , respectively, and $[\hat{b}_i, \hat{b}_j^\dagger] = \delta_{ij}$. As discussed in the previous chapter, depending on the ratio between tunneling and interactions, t/U , this Hamiltonian leads to two different quantum phases (at $T = 0$): the superfluid phase and the MI phase. Therefore, it exhibits the SF–MI quantum phase transition. The system is in the MI phase whenever there is an integer number of particles per site and $t/U \ll 1$, so that the kinetic energy is small and it is energetically unfavorable for a particle to move from site to site. The superfluid phase is reached either when the number of particles per site is not integer or when the interactions are small compared to tunneling. The phase diagram in the $\mu/U-t/U$ plane exhibits the celebrated MI lobes, as shown in Figure 5.1(a).

The difficulty in solving the Bose–Hubbard Hamiltonian comes from the tunneling term that couples bosonic operators at different sites. There are, however, several approaches that allow us to describe analytically some of the relevant physics of the Bose–Hubbard model in different t/U regimes. Some of them use a mean-field approach to decouple the non-local term, others consider tunneling as a perturbation, and others move to momentum space to resolve main features of the system. However, some aspects of the zero temperature ($T = 0$) phase diagram can already be grasped from the so-called ‘atomic’ limit, where the kinetic energy vanishes ($t = 0$). Since in the homogenous case all sites are equal, the Bose–Hubbard Hamiltonian simply reduces to the sum of on-site Hamiltonians $\hat{H}_{\text{BH}} = \sum_i [(U/2)\hat{n}_i(\hat{n}_i - 1) - \mu\hat{n}_i]$. The MI regions are easily determined by looking at the energy cost of adding or removing a particle from the system when each site has exactly \bar{n}_0 bosons; $E(\bar{n}_0) < E(\bar{n}_0 + 1)$ and $E(\bar{n}_0) < E(\bar{n}_0 - 1)$. In the $\mu-U$ phase diagram, the above conditions resume into $\bar{n}_0 - 1 < \mu/U < \bar{n}_0$, indicating that there is a finite region of the chemical potential for which the system remains in the insulating state with \bar{n}_0 atoms per site.

The other two limiting cases correspond to the regimes of weak (strong) interactions $t/U \gg 1 (\ll 1)$. In the former, a Bogoliubov mean-field approach in momentum space provides an accurate description of the excitation spectrum for the superfluid phase,

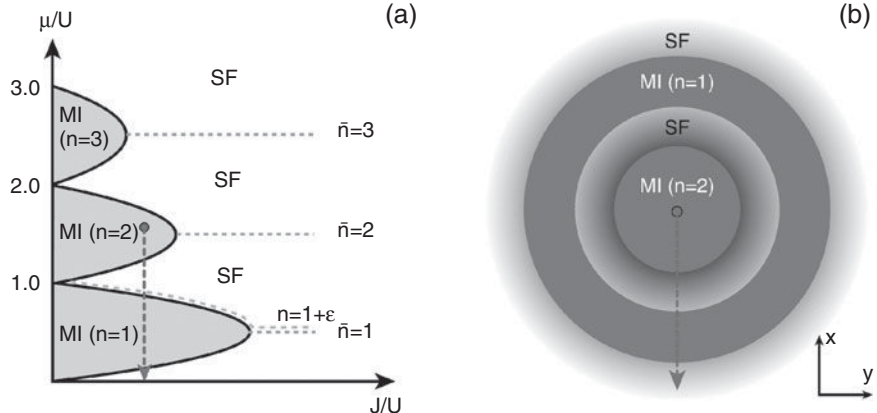


Figure 5.1 (a) Schematic zero-temperature phase diagram of the Bose–Hubbard model displaying the celebrated Mott-insulator (MI) lobes for $n = \bar{n}_0 = 1, 2, 3$. The dashed line corresponds to integer superfluid density $\langle \hat{n} \rangle = 1, 2, 3$. Such a diagram can be obtained using the perturbative mean-field approach of Section 5.4. In the figure J denotes tunneling term (t) in eqn (5.1). (b) MI and superfluid regions in an harmonic trap with MI for $\bar{n} = 2$ in the center. The so-called ‘wedding cake’ structure extends from the center to the edge of the cloud, where the chemical potential vanishes. From Bloch *et al.* (2008). Figure in color online.

but fails to describe the transition boundary to the insulating phase. In the latter, the so-called strong interaction limit, tunneling can be treated as a perturbation and the boundaries of the MI–SF transition can be calculated with high accuracy in any spatial dimension by increasing the order of the expansion. Properties of the Bose–Hubbard model can also be obtained variationally using mean-field approaches in position space. Examples of that are the perturbative mean-field approach, which with little effort provides a reasonable phase diagram in the $\mu – t$ phase space, and the Gutzwiller approach, which assumes that the many-body wave function is simply a product-over-sites and uses a standard numerical procedure to find the ground state variationally. It is conceptually and numerically relatively easy to implement and can be straightforwardly extended to dynamical situations. The Gutzwiller mean-field ansatz works well in the two limiting cases of the Bose–Hubbard Hamiltonian, for $t/U \rightarrow 0(\infty)$, and predicts with some accuracy the critical points separating the Mott phase from the superfluid phase for 3D or even 2D lattices. However, its accuracy decreases dramatically for 1D systems.

5.2. Weak interactions limit: the Bogoliubov approach

Here we illustrate how to solve the Bose–Hubbard model in the limit of small interactions. Our discussion closely follows van Oosten *et al.* (2001), where the Bogoliubov approach was used to study the quantum phases in the bosonic Hubbard model.

Consider a regular d -dimensional lattice consisting of M sites separated by a distance a . In the limit of $t/U \rightarrow \infty$, interactions between atoms are negligible, the system condenses into the zero momentum ground state, and the number of condensed atoms N_0 is equal to

the total number of atoms N . When interactions become non-negligible, atoms gradually start to leave the condensate. To describe this process it is convenient to work in momentum space. The new operators, $(\hat{a}_{\mathbf{k}}, \hat{a}_{\mathbf{k}}^\dagger)$, are given by:

$$\begin{aligned}\hat{b}_j &= \frac{1}{\sqrt{M}} \sum_{\mathbf{k}} \hat{a}_{\mathbf{k}} e^{i\mathbf{k}\mathbf{r}_j}, \\ \hat{b}_j^\dagger &= \frac{1}{\sqrt{M}} \sum_{\mathbf{k}} \hat{a}_{\mathbf{k}}^\dagger e^{-i\mathbf{k}\mathbf{r}_j},\end{aligned}\quad (5.2)$$

where \mathbf{r}_j points into j th lattice site, and \mathbf{k} is discretized over the first Brillouin zone. Using the identity $\sum_j e^{i(\mathbf{k}_1 - \mathbf{k}_2)\mathbf{x}_j} = M\delta_{\mathbf{k}_1, \mathbf{k}_2}$ we obtain $N = \sum_j \hat{b}_j^\dagger \hat{b}_j = \sum_k \hat{a}_{\mathbf{k}}^\dagger \hat{a}_{\mathbf{k}}$, and eqn (5.1) in momentum space reads

$$\hat{H}_{\text{BH}}^k = \sum_{\mathbf{k}} [-\varepsilon(\mathbf{k}) - \mu] \hat{a}_{\mathbf{k}}^\dagger \hat{a}_{\mathbf{k}} + \frac{U}{2M} \sum_{\mathbf{k}_1, \mathbf{k}_2, \mathbf{k}_3, \mathbf{k}_4} \delta_{\mathbf{k}_1 + \mathbf{k}_2, \mathbf{k}_3 + \mathbf{k}_4} \hat{a}_{\mathbf{k}_1}^\dagger \hat{a}_{\mathbf{k}_2}^\dagger \hat{a}_{\mathbf{k}_3} \hat{a}_{\mathbf{k}_4}, \quad (5.3)$$

where $\varepsilon(\mathbf{k}) = 2t \sum_{i=1}^d \cos(k_i a)$. As $t/U \rightarrow \infty$, the ground state converges towards $\sim a_0^{\dagger N} |0\rangle$. The Bogoliubov method is a mean-field approach, where we approximate $\langle \hat{a}_0 \rangle = \langle \hat{a}_0^\dagger \rangle = \sqrt{N_0}$ and express the bosonic operator as a c-number plus fluctuations $\hat{a}_0 = \sqrt{N_0} + \delta \hat{a}_0$. The same replacement is done for the Hermitian conjugated operator. Substituting the above expressions into eqn (5.3), one finds an effective Hamiltonian, up to the quadratic terms:

$$\begin{aligned}\hat{H} &= N_0 \left(-zt - \mu + \frac{U}{2} n_0 \right) + \sqrt{N_0} (Un_0 - tz - \mu) (\hat{a}_0 + \hat{a}_0^\dagger) \\ &\quad + \sum_{\mathbf{k}} (-\varepsilon(\mathbf{k}) - \mu) \hat{a}_{\mathbf{k}}^\dagger \hat{a}_{\mathbf{k}} + \frac{Un_0}{2} \sum_{\mathbf{k}} (4\hat{a}_{\mathbf{k}}^\dagger \hat{a}_{\mathbf{k}} + \hat{a}_{\mathbf{k}} \hat{a}_{-\mathbf{k}} + \hat{a}_{\mathbf{k}}^\dagger \hat{a}_{-\mathbf{k}}),\end{aligned}\quad (5.4)$$

where $n_0 = N_0/M$ is the condensate density and $z = 2d$. We set the chemical potential to $\mu = Un_0 - zt$, or alternatively the density to $n = (\mu + zt)/U$, and in effect remove the linear part in the above Hamiltonian. The quadratic term is diagonalized by the Bogoliubov–de Gennes transformation:

$$\begin{aligned}\hat{c}_{\mathbf{k}} &= u_{\mathbf{k}} \hat{a}_{\mathbf{k}} + v_{\mathbf{k}} \hat{a}_{-\mathbf{k}}^\dagger, \\ \hat{c}_{-\mathbf{k}}^\dagger &= v_{\mathbf{k}}^* \hat{a}_{\mathbf{k}} + u_{\mathbf{k}}^* \hat{a}_{-\mathbf{k}}^\dagger.\end{aligned}\quad (5.5)$$

Notice that $|u_{\mathbf{k}}|^2 - |v_{\mathbf{k}}|^2 = 1$ from the requirement that $[\hat{c}_{\mathbf{k}}, \hat{c}_{\mathbf{k}}^\dagger] = 1$. After some simple algebra, one obtains the result that within the quadratic approximation the Hamiltonian reduces to:

$$\hat{H} = -\frac{Un_0 N_0}{2} + \frac{1}{2} \sum_{\mathbf{k}} (\hbar\omega_{\mathbf{k}} + \varepsilon(\mathbf{k}) - zt - Un_0) + \sum_{\mathbf{k}} \hbar\omega_{\mathbf{k}} \hat{c}_{\mathbf{k}}^\dagger \hat{c}_{\mathbf{k}}, \quad (5.6)$$

if

$$\begin{aligned} (|u_{\mathbf{k}}|^2 + |v_{\mathbf{k}}|^2) [Un_0 - \varepsilon(\mathbf{k}) + zt] - Un_0(v_{\mathbf{k}}u_{\mathbf{k}}^* + v_{\mathbf{k}}^*u_{\mathbf{k}}) &= \hbar\omega_{\mathbf{k}}, \\ (u_{\mathbf{k}}^2 + v_{\mathbf{k}}^2)Un_0 - 2[Un_0 - \varepsilon(\mathbf{k}) + zt]v_{\mathbf{k}}u_{\mathbf{k}} &= 0. \end{aligned} \quad (5.7)$$

Assuming that $u_{\mathbf{k}}$ and $v_{\mathbf{k}}$ are real, one easily obtains from these equations the spectrum of excitations:

$$\hbar\omega_{\mathbf{k}} = \sqrt{[zt - \varepsilon(\mathbf{k})]^2 + 2Un_0[zt - \varepsilon(\mathbf{k})]}, \quad (5.8)$$

$$v_{\mathbf{k}}^2 = u_{\mathbf{k}}^2 - 1 = \frac{1}{2} \left(\frac{zt - \varepsilon(\mathbf{k}) + Un_0}{\hbar\omega_{\mathbf{k}}} - 1 \right). \quad (5.9)$$

These results reveal that the excitation spectrum is gapless in the thermodynamic limit, i.e. $M, N \rightarrow \infty$ with N/M finite. Indeed, for the long wavelength (phonon) modes (i.e. where $|\mathbf{k}|a \ll 1$), we find that $\varepsilon(\mathbf{k}) \simeq 2t(1 - (k^2a^2/2))$ and then

$$\hbar\omega_{\mathbf{k}} \approx |\mathbf{k}|a\sqrt{t}\sqrt{t|\mathbf{k}|^2a^2 + 2Un_0}, \quad (5.10)$$

i.e. the energy of a single excitation can be arbitrarily small. This is an expected result, showing that the Bogoliubov approach correctly describes the phonons' linear dispersion law in the superfluid regime but does not work in the Mott phase.

At zero temperature, there are no excitations in the system, so the ground state is a Bogoliubov vacuum $|\text{vac}\rangle$, such that $\hat{c}_{\mathbf{k}}|\text{vac}\rangle = 0$. At finite temperature, say T , excitations are present and occupations of different modes satisfy

$$\langle \hat{c}_{\mathbf{k}}^\dagger \hat{c}_{\mathbf{k}} \rangle = \left[\exp\left(\frac{\hbar\omega_{\mathbf{k}}}{kT}\right) - 1 \right]^{-1}, \quad (5.11)$$

in accordance with Bose–Einstein statistics. Using these properties and eqns (5.8) and (5.9), one can easily calculate different quantities such as correlation functions, the number of condensed atoms, etc., both at zero and non-zero temperatures. It has to be remembered, however, that reliable predictions can be obtained as long as $N_0(T) \sim N$, which can be self-consistently verified within this approach. It is also worthwhile to stress that the Bogoliubov approach can be applied to *time-dependent* problems without further complications. For instance, it has been recently used to describe the Kibble–Zurek mechanism, i.e. production of defects due to diabatic crossing of the phase boundaries (in this case the SF–MI boundary), where the scaling behavior of the time-dependent correlations at the crossing has been shown (Cucchietti *et al.*, 2007).

5.3. Strong interactions limit: strong coupling expansion

A method to analyze the Bose–Hubbard model in the limit of strong interactions $t/U \ll 1$, i.e. when the system is in the Mott phase, is provided by the strong coupling expansion

(Gelfand *et al.*, 1990; Freericks and Monien, 1994). This is a perturbative expansion in t/U of eqn (5.1). The Hamiltonian is split according to

$$H_{BH} = H_0 + \frac{t}{U} H_1 = \sum_i \left(\frac{1}{2} \hat{n}_i (\hat{n}_i - 1) - \frac{\mu}{U} \hat{n}_i \right) + \frac{t}{U} \sum_{\langle i,j \rangle} (-b_i^\dagger b_j - h.c.) \quad (5.12)$$

and standard Rayleigh–Schrödinger perturbation theory is applied. The bare Hamiltonian, \hat{H}_0 , is exactly solvable since it is local. Its ground state (MI) corresponds to the zero-order ground state in the expansion,

$$|\Psi(n_0)\rangle_{MI}^{(0)} = \prod_{i=1}^M \frac{1}{\sqrt{n_0}} (\hat{b}_i^\dagger)^{n_0} |0\rangle \quad (5.13)$$

where M is the number of lattice sites. The energy reads

$$E_0^{(0)} = Un_0(n_0 - 1)/2 - \mu n_0. \quad (5.14)$$

The tunneling term $\sum_{\langle i,j \rangle} (\hat{b}_i^\dagger \hat{b}_j + h.c.)$ is treated perturbatively. To solve the Schrödinger equation $H|\Psi\rangle_n = E_n |\Psi\rangle_n$, we expand the eigenstates $|\Psi\rangle_n$ and eigenvalues E_n as power series of the perturbation parameter, $|\Psi\rangle_n = \sum_k (t/U)^k |\Psi\rangle_n^{(k)}$, $E_n = \sum_k (t/U)^k E_n^{(k)}$. Corrections to the bare eigenstates and eigenvalues are calculated by solving the Schrödinger equation to the desired order in the expansion coefficient. The method is straightforward but tedious and, as often happens in perturbation theory expansions, high-order corrections are usually very difficult to calculate. In the Bose–Hubbard Hamiltonian, expansions up to 14th order have been calculated, which guarantees, in some cases, impressively high accuracy of the perturbative predictions. An alternative method to calculate the perturbative corrections in a more compact way is by using the diagrammatic Kato expansion (Messiah, 1961; van Oosten *et al.*, 2001; Teichmann *et al.*, 2009) instead of the recursive relations provided by the Rayleigh–Schrödinger expansion. The diagrammatic expansion allows us to easily calculate corrections up to the 12th order in the ground-state energy, atom–atom correlation functions, and occupation number fluctuations for one, two and three dimensions, which agree closely with the high-order symbolic perturbative expansion (Damski and Zakrzewski, 2006).

Let us now explain how to use the strong coupling expansion to determine the phase boundaries on the μ/U – t/U plane, such as those in Figure 5.1(a), for nearest-neighbor hopping on a d -dimensional regular lattice (Freericks and Monien, 1994; Kühner and Monien, 1998). One first calculates to the desired order; (i) the energy of the ground state with exactly n_0 atoms per site, and (ii) the ground state energy of the system with one particle added (subtracted) to (from) the system with filling factor n_0 . Setting the energy difference between cases (i) and (ii) to zero, one obtains the value of the chemical potential at the upper (lower) boundary between insulator and superfluid phases. The ‘defect’ states are generated by adding or removing a particle from the MI ground state. At zero order,

the superfluid degenerate ground state is spanned by:

$$\begin{aligned} |\Psi(n_0 + 1)\rangle_{SF}^{(0)} &= \frac{1}{\sqrt{M(n_0 + 1)}} \sum_{i=1}^M \hat{b}_i^\dagger |\Psi(n_0)\rangle_{MI}^{(0)} \\ |\Psi(n_0 - 1)\rangle_{SF}^{(0)} &= \frac{1}{\sqrt{Mn_0}} \sum_{i=1}^M \hat{b}_i |\Psi(n_0)\rangle_{MI}^{(0)}. \end{aligned} \quad (5.15)$$

Corrections to energy at order (m) are given by $E_n^{(m)} = \langle \psi^{(0)} | H_1 | \psi^{(m-1)} \rangle$. Odd power corrections to the energy in the Mott phase will be zero in bipartite lattices. Corrections to the ground-state wave function are given by $|\psi\rangle_0^{(m)} = \sum_l C_{0,l}^{(m)} |\psi\rangle_l^{(0)}$. The first non-zero correction term is the second-order one:

$$E_0^{(2)} = \sum_l \frac{\langle \psi_0 | H_1 | \psi_l \rangle \langle \psi_l | H_1 | \psi_0 \rangle}{E_0 - E_l}, \quad (5.16)$$

where we have omitted the superscript (0) indicating eigenstates and eigenvalues of the bare Hamiltonian H_0 . Correspondingly the energy of the ground state up to the second order reads

$$E_0(n_0) = E_0^{(0)} + E_0^{(2)} = N(U n_0(n_0 - 1)/2 - \mu n_0 - \frac{t^2}{U} n_0(n_0 + 1)). \quad (5.17)$$

Corrections in the superfluid degenerate subspace are carried out by projecting outside this subspace, i.e. diagonalizing $M = P H_1 \frac{1}{E_{SF} - \Pi H_0 \Pi} H_1 P$ where $\Pi = 1 - P$ and $P = |\psi\rangle_{SF} \langle \psi|$. Parametrizing the chemical potential as $\mu = (n_0 + \delta)U$, one obtains the SF–MI boundaries given in Freericks and Monien (1996). For the upper boundary, resulting from adding an extra particle to the Mott state with n_0 bosons per site ($\delta < 0$), one obtains

$$\begin{aligned} E(n_0)_{(n+1)} - E_0(n_0) &= -\delta U - 2dt(n_0 + 1) + \frac{t^2}{U} [dn_0(5n_0 + 4) - 4d^2 n_0(n_0 + 1)] \\ &\quad + \frac{t^3}{U^2} n_0(n_0 + 1) [-8d^3(2n_0 + 1) + d^2(25n_0 + 14) - 2d(4n_0 + 2)], \end{aligned} \quad (5.18)$$

and for the lower boundary, resulting from taking out a particle from the Mott state with n_0 bosons per site (now $\delta > 0$)

$$\begin{aligned} E(n_0)_{(n-1)} - E_0(n_0) &= \delta U - 2dt n_0 + \frac{t^2}{U} [d(n_0 + 1)(5n_0 + 1) - 4d^2 n_0(n_0 + 1)] \\ &\quad + \frac{t^3}{U^2} n_0(n_0 + 1) [-8d^3(2n_0 + 1) + d^2(25n_0 + 11) - 2d(4n_0 + 2)]. \end{aligned} \quad (5.19)$$

These calculations can be performed for lattices of any dimensionality, and several authors have reached an order of expansion as large as the 13th. For 1D systems (Kühner and Monien, 1998; Kühner *et al.*, 2000), the predicted structure of MI lobes is in very good agreement with the numerical results obtained via DMRG and quantum Monte

Carlo calculations. The perturbative expansions can also be used together with different extrapolation methods, in a process leading to the determination of the critical exponents z and ν (Freericks and Monien, 1996; Elstner and Monien, 1999). The strong coupling expansion has also been used to calculate correlation functions $\langle \hat{b}_i^\dagger \hat{b}_{i+j} \rangle$, density-density correlations $\langle \hat{n}_i \hat{n}_{i+j} \rangle$, and the variance of on-site atom occupation $[(\langle \hat{n}_i^2 \rangle - \langle \hat{n}_i \rangle)^2]^{1/2}$. A typical prediction of the strong coupling expansion reads:

$$\begin{aligned} \langle \hat{b}_i^\dagger \hat{b}_{i+1} \rangle = & 4 \frac{t}{U} - 8 \left(\frac{t}{U} \right)^3 - \frac{272}{3} \left(\frac{t}{U} \right)^5 + \frac{20272}{81} \left(\frac{t}{U} \right)^7 - \frac{441710}{729} \left(\frac{t}{U} \right)^9 \\ & + \frac{39220768}{2187} \left(\frac{t}{U} \right)^{11} + \frac{8020902135607}{94478400} \left(\frac{t}{U} \right)^{13} + \mathcal{O}((t/U)^{15}), \end{aligned}$$

a result that was obtained in a 1D system at unit filling factor in Damski and Zakrzewski (2006). The differences between such an analytical result and the numerical calculation turn out to be hardly visible for $t/U < 0.3$, i.e. in the entire Mott phase.

More recently, this method has been applied to calculate the lobes for a modified 1D Bose–Hubbard model describing atoms in an optical lattice created by pumping a laser beam into the cavity (Larson *et al.*, 2008). The major difference to the standard case is that the intensity of the cavity field depends on the number of atoms present, since the atoms collectively shift the cavity resonance. In effect the coefficients t and U become very complex functions of all of the relevant parameters: cavity detuning, intensity of the pumping laser, N , etc. Moreover, quantum fluctuations of the resonance shift induce long-range interactions between the atoms. The phase diagram is shown in Figure 5.2 as a function of the dimensionless parameters μ/U and κ/η , where κ is the cavity width and η is

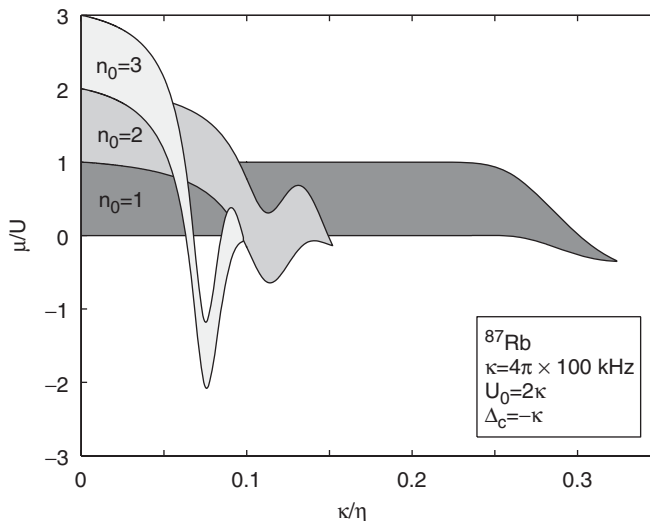


Figure 5.2 Overlapping Mott-insulator phases for a 1D Bose–Hubbard model in an optical cavity. The Mott-insulator lobes have been calculating using a self-consistent strong coupling expansion. By courtesy of J. Larson.

the pumping laser strength, and $1/\sqrt{n_{ph}} = \kappa/\eta$, where n_{ph} is the number of photons in the cavity. The striking effect is the overlap of different Mott phases, which is a consequence of the fact that the expressions for t and U for $n_0 = 1, 2, 3, \dots$ Mott phases are different.

5.4. Perturbative mean-field approach

An straightforward and rather easy way to obtain the phase diagram in the homogeneous case is to use a perturbative mean-field approximation. In this approach one first introduces the superfluid order parameter as the expectation value of the creation operator $\langle \hat{b}_i \rangle = \varphi_i$. Then, by neglecting second-order fluctuations of bosonic annihilation and creation operators, $(\hat{b}_i^\dagger - \langle \hat{b}_i \rangle)(\hat{b}_j - \langle \hat{b}_j \rangle) \simeq 0$, one decouples the hopping terms as $\hat{b}_i^\dagger \hat{b}_j \simeq \varphi(\hat{b}_j + \hat{b}_i^\dagger) - \varphi^2$. Here we assume a homogeneous case and set the superfluid order parameter to be site-independent; without loosing generality it can also be set to be real. Notice that this approximation describes either the Mott phase, where fluctuations in the number of particles per site are small, or the deep superfluid phase. The resulting Hamiltonian now reduces to a sum of local terms

$$\hat{H}_{\text{BH}}^{\text{MF}} = \sum_i \hat{h}_i = \sum_i \left[\frac{U}{2} \hat{n}_i (\hat{n}_i - 1) - \mu \hat{n}_i - 2tz\varphi(\hat{b}_i^\dagger + \hat{b}_i) + 2tz|\varphi|^2 \right], \quad (5.20)$$

where z denotes the number of nearest neighbors. The superfluid order parameter φ has to be determined by minimizing the free energy $F = -1/\beta \log \text{Tr} [\exp(-\beta \hat{h})]$, where $\beta = 1/k_B T$, with k_B being the Boltzmann constant and T the temperature. Here, since we are interested only in the zero-temperature properties, the former condition reduces to the minimization of the ground-state energy $E_0(\psi_0) = \langle \psi_0 | \hat{h} | \psi_0 \rangle$ with the self-consistent condition $\langle \psi_0 | \hat{b} | \psi_0 \rangle = \varphi$. For sufficiently small t we can apply perturbation theory to the Hamiltonian $\hat{h} = \hat{h}_0 + \hat{v}(t)$, with the perturbation term given by

$$\hat{v}(t) = -2tz\varphi(\hat{b}^\dagger + \hat{b}) \quad (5.21)$$

and the unperturbed ground-state energy $E_0(n) = Un(n-1)/2 - \mu n + 2tz\varphi^2$. A trivial calculation of the matrix elements of the perturbation allows us to determine the phase boundaries between the superfluid phase and the MI phase in the $\mu/U-t/U$ plane. Notice that since $v(t) \propto (\hat{b}^\dagger + \hat{b})$, only even terms in the perturbation expansion survive. To second order, the ground state energy is given by:

$$\begin{aligned} E_0 &\simeq E_0^{(0)} + \varphi^2 \sum_k \frac{|\langle k | \hat{v} | 0 \rangle|^2}{E_0^{(0)} - E_k^{(0)}} \\ &= \frac{U}{2} n(n-1) - \mu n + 2tzr\varphi^2, \end{aligned} \quad (5.22)$$

with

$$r = \left(2zt \frac{U+\mu}{U^2 n(n-1) - \mu U(2n-1) + \mu^2} + 1 \right). \quad (5.23)$$

Notice that if $r > 0$, the energy is minimized for $\varphi = 0$, signaling the Mott phase. In contrast, if $r < 0$, the energy is minimized for $\varphi \neq 0$, corresponding to the superfluid phase. The MI–SF boundary is thus given by the condition $r = 0$, which leads to

$$t/U = -\frac{n(n-1) - (\mu/U)(2n-1) + (\mu/U)^2}{2z(1+\mu/U)}. \quad (5.24)$$

5.5. Gutzwiller approach

The Gutzwiller mean-field approach (Rokhsar and Kotliar, 1991; Krauth *et al.*, 1992; Jaksch *et al.*, 1998) is based on approximating the many-body wave function with a product over single-site contributions

$$|\Psi\rangle = \prod_i \sum_{n=0}^{n_{\max}} f_n^{(i)} |n\rangle_i, \quad (5.25)$$

where $|n\rangle_i$ denotes the Fock state of n atoms in the i th lattice site, n_{\max} is a system-size-independent cut-off in the number of atoms per site, and $f_n^{(i)}$ corresponds to the amplitude of having n atoms in the i th lattice site. The probability amplitudes are normalized to $\sum_n |f_n^{(i)}|^2 = 1$. The variational parameters here are the probability amplitudes, which are determined by minimizing the ground-state energy.

5.5.1 Static Gutzwiller approach

To see what the Gutzwiller approach predicts for quantum phase transitions, we focus now on the case of a homogeneous system having an integer number of particles per site n_0 . In this case, one obtains the result that for $t/U < (t/U)_c$, where $(t/U)_c$ denotes a critical value, the Gutzwiller amplitudes are $f_n^{(i)} = \delta_{nn_0}$, so that the wave function becomes a single Fock state. Therefore the Gutzwiller wave function exactly reproduces the system wave function when $t/U \rightarrow 0$. It is also possible to show that the differences between the exact result and eqn (5.25) are negligible in the limit of a lattice of infinite dimensions, and for $t/U \rightarrow \infty$ (Zwerger, 2003). Therefore, the common expectation is that the state described by eqn (5.25) reasonably interpolates between the superfluid and MI limits, which we discuss below, pointing out the advantages and disadvantages of the Gutzwiller method. The critical point for the SF–MI transition, $(t/U)_{cG}$, predicted by the Gutzwiller approach, is located at $\frac{1}{5.8z}$ for $n_0 = 1$ (Zwerger, 2003), where z is the number of nearest neighbors. Comparing this result to the more reliable findings from the strong coupling approach (or numerical DMRG in one dimension) of $(t/U)_c^{1D} \simeq 0.29$, 2D square lattice $(t/U)_c^{2D} \simeq 0.061$, and 3D cubic lattice $(t/U)_c^{3D} \simeq 0.034$, one observes that the agreement improves with the system dimensionality: the Gutzwiller result, as expected, is poor for a 1D system ($z = 2$), and becomes satisfactory in three dimensions ($z = 6$). The reason is that the Gutzwiller method does not take into account correlations between sites. Correlations are stronger in one dimension, where the Gutzwiller approach essentially fails, and are negligible in the limit of large dimensionality, where it becomes essentially exact.

The Gutzwiller method is quite straightforward in numerical implementations. In the static case the amplitudes $f_n^{(i)}$ are real numbers and can be found by minimization of $\langle \Psi | H - \mu \sum_i n_i | \Psi \rangle$, where the chemical potential μ is used to enforce a desired number of atoms in the ground state. The minimization can be done in a standard way, for instance by using the conjugate gradient method (Press *et al.*, 1987), and presents no problems as long as the system is homogeneous or the external potential imposed on it is regular. In particular, the method works well in harmonic traps. Obviously, some problems with minimization may appear for disordered potentials.

In the presence of disorder, or of an external confining potential, different phases can coexist. Let us illustrate this situation by considering a Bose gas in a 2D lattice in the presence of a confining harmonic potential. In the Gutzwiller approach, the superfluid order parameter is given by

$$\varphi_i = \sum_n \sqrt{n+1} f_n^{*(i)} f_{n+1}^{(i)}. \quad (5.26)$$

The order parameter breaks the phase symmetry and picks the phase of the system at site i : it is undefined in the Mott phase, while it assumes a fixed value ($\varphi_i \neq 0$) in the superfluid phase. In Figure 5.1(b) we plot the density of the ground state of the Bose–Hubbard model in a harmonic trap. Note that the MI phase in the center of the trap is surrounded by series of rings of superfluid and MI phases, in a wedding-cake-like structure as discussed first in Jaksch *et al.* (1998). When the number of relevant lattice sites grows the method becomes numerically very tedious. Typically, for experimentally realistic 3D systems one can reach lattice sizes of order 50^3 —in Zakrzewski (2005) 65^3 was actually achieved—without the aid of supercomputers.

5.5.2 Dynamical Gutzwiller approach

The time-dependent version of the Gutzwiller wave function is obtained by allowing the Gutzwiller amplitudes to depend on time $f_n^{(i)}(t)$ (Jaksch *et al.*, 2002). The equations of motion for the amplitudes are then readily obtained by minimizing the action of the system, given by $S = \int dt \mathcal{L}$, with respect to the variational parameters $f_n^{(i)}(t)$ and their complex conjugates $f_n^{*(i)}(t)$. The Lagrangian of the system in the quantum state $|\Psi\rangle$ is given by (Pérez-García *et al.*, 1996; Pérez-García *et al.*, 1997)

$$\mathcal{L} = \frac{\langle \Psi | \dot{\Psi} \rangle - \langle \dot{\Psi} | \Psi \rangle}{2i} - \langle \Psi | \hat{H} | \Psi \rangle, \quad (5.27)$$

where $|\dot{\Psi}\rangle$ is the time derivative of the wave function in eqn (5.25). Setting the variation of the action with respect to $f_n^{*(i)}$ to zero leads to $\langle \Psi | i \frac{d}{dt} - H | \Psi \rangle$. For the Bose–Hubbard Hamiltonian in eqn (5.1), one obtains

$$i \frac{d}{dt} f_n^{(i)} = \frac{U}{2} n(n-1) f_n^{(i)} - \mu n - t \left(\bar{\varphi}_i^* \sqrt{n+1} f_{n+1}^{(i)} + \bar{\varphi}_i \sqrt{n} f_{n-1}^{(i)} \right), \quad (5.28)$$

where $\bar{\varphi}_i = \sum_{i,j} \langle \hat{b}_j \rangle = \sum_{\langle i,j \rangle} \sum_n \sqrt{n} f_{n-1}^{(j)*} f_n^{(j)}$ (the first sum goes over all j being nearest neighbors of i). It is not difficult to verify the commutation relation $[\hat{N}, \hat{H}_{\text{BH}}] = 0$, which

implies that the total number of bosons is a conserved quantity for dynamics in real time (Sachdev, 1999). These equations are of mean-field type because they account for the effect of neighboring sites on the site i and have to be determined self-consistently. Equation (5.28) also constitutes a set of coupled equations, with the coupling arising from the tunneling part. It can be written in matrix form as (Trefzger, 2010):

$$i\hbar \frac{d}{dt} \mathbf{f} = \mathcal{M}[\mathbf{f}, \mu, U, t] \cdot \mathbf{f}, \quad (5.29)$$

where $\mathbf{f} = [f_0^{(1)}, f_1^{(1)}, \dots, f_n^{(i)}, \dots, f_{n_{\max}}^{(M)}]^T$ is the vector of the Gutzwiller amplitudes ordered from site 1 to site M , the latter being the total number of sites. It is worth noticing that the matrix $\mathcal{M}[\mathbf{f}, \mu, U, t]$ is itself a functional of the coefficients \mathbf{f} through the fields $\bar{\varphi}_i$, which have to be calculated in a self-consistent way. Let us clarify this point with an example. Suppose we want to solve eqn (5.29) between an initial time $t_i = 0$ and a final time t_f , with a given initial condition $\mathbf{f}(0)$. We discretize the time interval in N steps of size Δt , with N finite, and define $t_s = s\Delta t$ such that $t_{s=0} \equiv 0$ and $t_{s=N} \equiv t_f$. Therefore, to calculate the solution at a certain point in time $\mathbf{f}(t_{s+1})$, we need to know the solution at the preceding time point $\mathbf{f}(t_s)$. With this we can compute the fields that in turn determine $\mathcal{M}[\mathbf{f}(t_s), \mu, U, t]$. The solution is readily found to be

$$\mathbf{f}(t_{s+1}) = e^{-i\mathcal{M}[\mathbf{f}(t_s), \mu, U, t]\Delta t / \hbar} \mathbf{f}(t_s). \quad (5.30)$$

Starting from $s = 0$, in $N + 1$ steps we determine the solution at the desired time t_f . At the computational level, this is the simplest procedure that one can implement to calculate the dynamics of the system (Trefzger, 2010). However, one needs to be careful in the choice of the time step Δt , especially for fast-oscillating dynamics. In such cases, a Runge–Kutta method with adaptive step-size control has proven to be more efficient. For stiff dynamics, where the solution presents both slowly varying and fast-oscillating regions, the simple procedure described above may be accurate enough, as in the case of imaginary time evolution.

Equation (5.29) can be solved in real time t or in imaginary time $\tau = it$. The imaginary time evolution is a standard technique that has been extensively used because, due to dissipation, its results are supposed to converge to the ground state of the system. Two things are worth noticing. First, because the imaginary time evolution is not unitary it does not conserve the norm of the Gutzwiller wave function, which has to be renormalized after each time step. Second, the total number of particles is no longer a conserved quantity.

One should also appreciate the simplicity of extending the Gutzwiller approach to different systems, e.g. mixtures of bosonic gases (Jaksch *et al.*, 2002; Damski *et al.*, 2003a), Bose–Fermi mixtures (Fehrmann *et al.*, 2004*a,b*; Ahufinger *et al.*, 2005), etc. Particularly interesting are extended Hubbard models, such as those involving dipolar interactions (see Chapter 8). For dipolar Hamiltonians the imaginary time evolution does not always converge to the true ground state; it often gets blocked in configurations that are a local energy minimum. On one hand this makes it difficult to identify the ground state of such systems while on the other hand it is a signature of the existence of metastable states. In general, for dipolar gases one expects the appearance of supersolid and checkerboard-like phases at

low filling factors (Góral *et al.*, 2002; Barnett *et al.*, 2006a; Scarola *et al.*, 2006). Also, for spinor ultracold gases, the Gutzwiller approach provides an easy way to describe the phase diagram (Tsuchiya *et al.*, 2004), even in the presence of disorder (Łacki *et al.*, 2011).

Despite all these nice features, there are obviously problems associated with the Gutzwiller ansatz. The picture obtained—that the MI corresponds to a single Fock state $|n_0\rangle$ for the filling factor n_0 —is obviously only correct in the atomic limit $t = 0$. Another drawback of eqn (5.25) is that the correlation functions between different sites factorize into products of single-site contributions, e.g. $\langle\Psi|b_i^\dagger b_j|\Psi\rangle = \langle\Psi|b_i^\dagger|\Psi\rangle\langle\Psi|b_j|\Psi\rangle$ for $i \neq j$. As a result, the Gutzwiller approach does not account for spatial correlations. Notice also that eqn (5.25) does not correspond to a well-defined number of particles. This problem can be solved by a proper projection of the wave function in eqn (5.25) onto the subspace with a fixed number of atoms (Jaksch *et al.*, 2002; Krauth *et al.*, 1992), but the subsequent calculations become complicated. Finally, the Gutzwiller approach underestimates finite-size effects: it predicts a ‘quantum phase transition’ in systems of any size due to decoupling into the product of single-site contributions (eqn (5.25)). The true quantum phase transition, however, requires a large system, if not an infinite one.

The performance of the Gutzwiller ansatz can, to a limited extent, be perturbatively improved (Schroll *et al.*, 2004). These corrections significantly modify the Gutzwiller wave function for t/U smaller than $(t/U)_g$. As a result, both the variance of an on-site atom occupation and the correlation functions $\langle b_i^\dagger b_{j \neq i} \rangle$ become non-zero for $t/U > 0$, which is an advance on the traditional Gutzwiller approach. A very elegant method of improving the Gutzwiller ansatz has recently been introduced in Trefzger and Sengupta (2011). These authors consider local projector operators onto MI states for nearest-neighbor pairs, and perturbatively calculate corrections to the Bose–Hubbard Hamiltonian of order $(t/U)^2$, so that the resulting effective Hamiltonian contains next-neighbor tunneling processes. The standard Gutzwiller ansatz is then applied to this Hamiltonian; in three dimensions one obtains results that differ by less than 1% from the ‘exact’ quantum Monte Carlo results.

Finally, we should mention that the Gutzwiller approach can be supplemented by other mean-field-like calculations utilizing the properties of Green functions. These predict, in different dimensions, practically the same transition points as the Gutzwiller method, but allow for determination of the excitation spectra and finite temperature calculations (Sheshadri *et al.*, 1993; Menotti and Trivedi, 2008). Alternatively, a dynamical mean-field approach has been formulated (see Amico and Penna (1998, 2000)).

5.6. Exact diagonalization and the Lanczos method

Exact diagonalization of a many-body system can only be performed for small systems because of the enormous dimensions of the supporting Hilbert space, given by

$$\mathcal{HS}(N, M) = \frac{(N + M - 1)!}{N!(M - 1)!}, \quad (5.31)$$

where N and M stand for the number of atoms and the number of lattice sites, respectively. To illustrate the restrictions imposed by eqn (5.31), we consider the size of the Hilbert space for the $M = N$ case. For instance, for $N = 8, 10$, and 12 one obtains $\mathcal{HS}(N, N) = 6435$,

92378, and 1352078, respectively. Moreover, one can easily verify that for $N \gg 1$, $\mathcal{HS}(N+1, N+1) \approx 4\mathcal{HS}(N, N)$, an expression which quantifies the fast increase of the Hilbert space size with system size. This shows that a standard diagonalization where all matrix elements are stored and no symmetries are employed can already face problems for $N = M > 8$. Additionally, from the exponential increase of the size of the Hilbert space with the system size, any significant progress due to improvement of computer resources is unlikely.

To overcome these limitations to some extent one can use numerical routines that store non-zero matrix elements only, e.g. ARPACK (ARPACK, 2010). Diagonalization of a $N = M = 12$ system then presents no problems on a computer with about 1GB of memory, provided one looks for a limited number of eigenstates instead of the full spectrum. It is also possible to cut the Hilbert space by restricting maximal site occupation to K atoms. Such a choice can be justified by a quadratic increase in the interaction energy with the site occupation number, and is routinely used in DMRG and quantum Monte Carlo schemes. The size of the Hilbert space in the system, subject to the restriction that at most K bosons can populate a single lattice site, can be derived as follows. We assume that there are N bosons placed in M lattice sites and therefore $K \leq N$ and $KM \geq N$. By definition

$$\mathcal{HS}(N, M)|_K = \sum_{n_1=0}^K \cdots \sum_{n_M=0}^K \delta_{n_1+\dots+n_M, N}. \quad (5.32)$$

Using the following Kronecker delta representation,

$$\delta_{l,m} = \frac{1}{2\pi} \int_{-\pi}^{\pi} d\varphi e^{i(l-m)\varphi}, \quad (5.33)$$

it reads

$$\mathcal{HS}(N, M)|_K = \frac{1}{2\pi} \int_{-\pi}^{\pi} d\varphi e^{-iN\varphi} \left(\frac{e^{i(K+1)\varphi} - 1}{e^{i\varphi} - 1} \right)^M = \frac{1}{N!} \frac{d^N}{dz^N} \left(\frac{z^{K+1} - 1}{z - 1} \right)^M \Big|_{z=0},$$

where the right-hand side is obtained after integration on a unit circle $z = \exp(i\varphi)$ in the complex plane. With the help of the Leibnitz formula, $\mathcal{HS}(N, M)$ can be further reduced to

$$\mathcal{HS}(N, M)|_K = \sum_{j=0}^{\lfloor \frac{N}{K+1} \rfloor} (-1)^j \binom{M+N-1-j(K+1)}{M-1} \binom{M}{j}, \quad (5.34)$$

where $[x]$ stands for the largest integer number not greater than x . For $K = N$, eqn (5.34) reduces to eqn (5.31). A typical choice, leading to well converged results in a wide range of Bose–Hubbard model parameters, is $K = 4$. This results in Hilbert spaces of 5475, 72403, and 975338 for $N = 8, 10$, and 12, respectively. These numbers suggest that only a rather small improvement can be achieved by cutting the Hilbert space size this way. In Section 5.10 we shall see how to truncate the Hilbert space more appropriately.

The most powerful simplifications are possible when the problem under consideration has some symmetry, i.e. when there exists a set of operators $\{O_i\}$ commuting with the Hamiltonian. One can then split the Hilbert space into subspaces composed of states with well-defined eigenvalues of the O_i operators. In this way the problem of diagonalization of the full Hamiltonian reduces to a few independent diagonalizations of smaller matrices. It allows for reduction of memory requirements and helps in getting a relatively large number of excited eigenstates. A relevant example can be found in Damski *et al.* (2005a), where a system of cold fermions placed in a kagomé lattice is considered. There is a translational symmetry generated by an operator having S different eigenvalues. The Hilbert space splits into S subspaces, and diagonalization of the full Hamiltonian, say an $L \times L$ matrix, reduces to S independent diagonalizations of $\sim L/S \times L/S$ matrices.

The most popular algorithm used to diagonalize symmetric large matrices is the Lanczos method (Bai *et al.*, 2000). The Lanczos algorithm uses a three-term recurrence relation to reduce a large $N \times N$ symmetric matrix H . Given an initial random vector, called the pivot vector \mathbf{v}_1 , and taking $\mathbf{v}_0 = 0$, the algorithm produces in N steps an orthogonal matrix $V = [\mathbf{v}_1, \mathbf{v}_2, \dots, \mathbf{v}_n]$ and a tridiagonal matrix H_N such that $HV = VH_N$. The eigenvalues of H and H_N coincide. In the new basis the matrix is tridiagonal and trivially diagonalized. Indeed, it can be shown that several of the eigenvalues of H_N approximate extremely well with the eigenvalues of H , with only $k \ll N$ steps in the algorithm. The three-step recurrence works as follows

$$\begin{aligned} |w_n\rangle &= H|v_n\rangle - \beta_n|v_{n-1}\rangle, \\ \alpha_n &= \langle v_n w_j \rangle, \\ |w_j\rangle &= |w_j\rangle - \alpha_n|v_n\rangle, \\ \beta_{n+1} &= ||w_j|| = \sqrt{\langle w_j w_j \rangle}, \\ |v_{n+1}\rangle &= |w_j\rangle / \beta_{n+1}, \end{aligned} \tag{5.35}$$

and leads to the following tridiagonal matrix

$$H_N = \begin{pmatrix} \alpha_0 & \beta_1 & 0 & \dots & \dots & \dots & \dots & \dots & \dots & 0 \\ \beta_1 & \alpha_1 & \beta_2 & 0 & \dots & \dots & \dots & \dots & \dots & 0 \\ 0 & \beta_2 & \alpha_2 & \beta_3 & 0 & \dots & \dots & \dots & \dots & 0 \\ & & & & \ddots & & & & & \\ 0 & 0 & 0 & & & 0 & \beta_{N-2} & \alpha_{N-2} & \beta_{N-1} & \\ 0 & 0 & 0 & & & 0 & 0 & \beta_{N-1} & \alpha_{N-1} & \end{pmatrix}.$$

Once the desired eigenvalue has converged one restarts the recursion and obtains the corresponding eigenvector. This is the greatest advantage of the Lanczos algorithm. However, if the matrix is not sparse and there is not a selective search of eigenvalues, the time of convergence can be very long. Recent advances in exact diagonalisation procedures can be found in Laflorencie and Poilblanc (2004), Noack and Manmana (2005), Weisse and Fehske (2008), and Läuchli (2008), and a powerful on-line package is provided with the book *Templates for the Solution of Algebraic Eigenvalue Problems* (Bai *et al.*, 2000).

5.7. Quantum Monte Carlo: path integral and worm algorithms

In this section we discuss quantum Monte Carlo methods. We follow very closely here Trefzger (2010) and Trefzger *et al.* (2011). Monte Carlo (MC) methods are stochastic techniques based on the use of probability statistics, which allow the solving of complex equations for large systems by sampling in a number of random configurations. Quantum Monte Carlo methods give a highly accurate description of bosonic many-body systems using repeated random sampling, but at the cost of statistical uncertainty, although this can be reduced with more simulation time. All stochastic methods must map the quantum state onto a classical one. The mapping is done from the quantum partition function into a probability distribution, i.e. $Z = \text{Tr}e^{-\beta H} = \sum_i e^{E_i/k_B T} = \sum_c p_c$, where p_c are the probabilities of some stochastic events. If some $p_c < 0$, as happens for fermionic and frustrated systems, the so-called sign problem appears, and quantum Monte Carlo fails.

The basic steps of any Monte Carlo algorithm are the following:

1. Define a domain of possible inputs, the so-called *configuration space*.
2. Sample inputs randomly from the configuration space with a certain probability distribution that depends on the specific problem. This step is called the *updating procedure*.
3. Perform a computation based on the randomly generated input.
4. Use the result of the computation to update the final result.

Quantum Monte Carlo methods were first used for studies of the Bose–Hubbard model (Batrouni *et al.*, 1990; Scalettar *et al.*, 1991) shortly after the publication of the seminal paper of Fisher *et al.* (1989). The computer resources and quantum Monte Carlo algorithms available at that time only allowed consideration of systems of the order of a few tens of lattice sites/atoms in 1D and 2D models. Nowadays, systems of 10^3 sites and atoms in any number of dimensions can be studied routinely. This permits consideration of 3D configurations that are quite realistic from an experimental perspective. This progress has obviously been the result of better computer resources and more efficient algorithms (see e.g. Prokof’ev *et al.* (1998*a,b*) and Alet *et al.* (2006)). Interestingly, efficient numerical codes for quantum Monte Carlo simulations are now publicly available (Alet *et al.*, 2005).

The quantum Monte Carlo approach allows us to calculate different properties of a system in equilibrium at non-zero temperatures. In studies of the Bose–Hubbard model these temperatures can be chosen to be so low that the simulation essentially describes the zero-temperature physics of the system. The quantities usually calculated in the quantum Monte Carlo approach are the superfluid fraction, the chemical potential (μ), the density of atoms (ρ), the variance of the on-site occupation, and the compressibility ($\kappa = \partial\rho/\partial\mu$).

There is a large class of quantum Monte Carlo algorithms that can simulate quantum many-body systems, such as the variational Monte Carlo (DuBois and Glyde, 2001; Nilsen *et al.*, 2005), the diffusion Monte Carlo (Giorgini *et al.*, 1999; Astrakharchik *et al.*, 2007), the path integral Monte Carlo (Prokof’ev *et al.*, 1998*a,b*; Pilati *et al.*, 2006), the auxiliary field Monte Carlo (Chang, 2008), etc. Most methods aim to compute the eigenvalue and the properties of the ground-state of the system, with the exception of the path integral Monte Carlo and finite-temperature auxiliary field Monte Carlo methods, which calculate the density matrix. We will explain here in detail the path integral Monte Carlo method.

The famous worm algorithm, which is a particularly efficient version of path integral Monte Carlo, was originally developed by Prokof'ev, Svistunov, and Tupitsyn (Prokofev *et al.*, 1998*a, b*), and is nicely explained in the tutorial of Trefzger *et al.* (2011). These seem to be the most convenient algorithms to solve Bose–Hubbard models, although they are more complex than other quantum Monte Carlo algorithms.

5.7.1 Path integral Monte Carlo

We consider a system described by the Hamiltonian $\hat{H} = \hat{H}_0 + \hat{H}_1$, where \hat{H}_0 is taken to be diagonal in the basis of eigenstates $\{|\alpha\rangle\}$ satisfying the eigenvalue equation

$$\hat{H}_0|\alpha\rangle = E_\alpha|\alpha\rangle, \quad (5.36)$$

and \hat{H}_1 is non-diagonal. The thermodynamic properties of the system at equilibrium can be derived from the partition function $Z = \text{Tr} [e^{-\beta\hat{H}}]$, where $\beta = 1/k_B T$ is the inverse temperature and k_B the Boltzmann constant. In the interaction picture one may write

$$Z = \text{Tr} [e^{-\beta(\hat{H}_0 + \hat{H}_1)}] = \text{Tr} [e^{-\beta\hat{H}_0} \hat{\mathcal{T}}_\tau e^{-\int_0^\beta d\tau \hat{H}_1(\tau)}], \quad (5.37)$$

where $\hat{\mathcal{T}}_\tau$ is the time-ordering operator, $\hat{H}_1(\tau) = e^{\tau\hat{H}_0}\hat{H}_1e^{-\tau\hat{H}_0}$ is the non-diagonal part of the Hamiltonian expressed in the interaction picture, and τ is the imaginary time. The partition function can be conveniently represented using the Feynman path integral formulation—hence the name, path integral Monte Carlo algorithm. Using a Taylor expansion of the second exponent in the right-hand side of eqn (5.37), one gets

$$\begin{aligned} Z = & \sum_\alpha e^{-\beta E_\alpha} \langle \alpha | \hat{1} - \int_0^\beta d\tau \hat{H}_1(\tau) \\ & + \sum_{m=2}^{\infty} (-1)^m \int_0^\beta d\tau_m \dots \int_0^{\tau_2} d\tau_1 \hat{H}_1(\tau_m) \dots \hat{H}_1(\tau_1) | \alpha \rangle, \end{aligned} \quad (5.38)$$

where the integrals are ordered in time and the sum over the states $|\alpha\rangle$ comes from the trace. Inserting $m-1$ identity operators $\hat{1} = \sum_\alpha |\alpha\rangle\langle\alpha|$ between the $\hat{H}_1(\tau_m)$ operator products, we can write

$$\langle \alpha | \hat{H}_1(\tau_m) \dots \hat{H}_1(\tau_1) | \alpha \rangle = \sum_{\alpha_1, \dots, \alpha_{m-1}} H_1^{\alpha\alpha_{m-1}}(\tau_m) \dots H_1^{\alpha_2\alpha_1}(\tau_2) H_1^{\alpha_1\alpha}(\tau_1), \quad (5.39)$$

where the matrix elements

$$H_1^{\alpha'\alpha}(\tau) = e^{\tau E_{\alpha'}} H_1^{\alpha'\alpha} e^{-\tau E_\alpha} = \langle \alpha' | \hat{H}_1 | \alpha \rangle e^{-\tau(E_\alpha - E_{\alpha'})}, \quad (5.40)$$

contain both diagonal (E_α) and off-diagonal ($H_1^{\alpha'\alpha}$) matrix elements. Using eqn (5.40) in eqn (5.38) leads to the final expression for the partition function

$$Z = \sum_{\alpha} e^{-\beta E_{\alpha}} \left\{ 1 - \int_0^{\beta} d\tau H_1^{\alpha\alpha}(\tau) + \sum_{m=2}^{\infty} (-1)^m \int_0^{\beta} d\tau_m \dots \int_0^{\tau_2} d\tau_1 \sum_{\alpha_1, \dots, \alpha_{m-1}} H_1^{\alpha\alpha_{m-1}}(\tau_m) \dots H_1^{\alpha_1\alpha}(\tau_1) \right\}, \quad (5.41)$$

which contains only matrix elements of the operators \hat{H}_0 and \hat{H}_1 . Path integral formalism thus reduces the calculation of the partition function to a classical probability, since only scalars enter into eqn (5.41). This is achieved at the price of an extra dimension τ . In other words, we have shown here that the original d -dimensional quantum system is equivalent to a $(d+1)$ -dimensional classical system.

Note that the partition function is a trace, which implies periodic boundary conditions in imaginary time τ . Therefore, for any given α in the trace, the first matrix element brings α to some α_1 in time $\tau_1 \geq 0$, while the last matrix element brings α_{m-1} back to α in the time $\tau_m \leq \beta$. This is easily understood by looking at the m th order term of Z , which contains the product of m matrix elements $H_1^{\alpha\alpha_{m-1}}(\tau_m) \dots H_1^{\alpha_1\alpha}(\tau_1)$ that are ordered in time from the first at τ_1 to the last at τ_m . Obviously, it describes a path $\alpha \rightarrow \alpha_1$ in time τ_1 , $\alpha_1 \rightarrow \alpha_2$ in time τ_2 , $\alpha_i \rightarrow \alpha_{i+1}$ in time τ_i , and finally α_m back to α in time τ_m . The configuration space spanned by the path integral Monte Carlo algorithm thus corresponds to all possible configurations in eqn (5.41) that are periodic in imaginary time.

5.7.2 Path integral Monte Carlo for a 2D Bose–Hubbard model

So far we have provided a general description of the path integral Monte Carlo method. We now specify it for the 2D Bose–Hubbard model. Let us consider a non-homogenous 2D system of $M \times M$ sites filled with single-component bosons interacting via contact potential. Our procedure is, however, very general and is restricted neither to single component gases nor to contact interactions. We assume spatial periodic boundary conditions and describe the system by the Bose–Hubbard Hamiltonian

$$\hat{H}_{\text{BH}} = -t \sum_{\langle ij \rangle} \left[\hat{b}_i^\dagger \hat{b}_j + \hat{b}_i \hat{b}_j^\dagger \right] + \sum_i \left[\frac{U}{2} \hat{n}_i (\hat{n}_i - 1) - \mu_i \hat{n}_i \right] \quad (5.42)$$

where $\mu_i = \mu - \omega_i^2$ contains the chemical potential μ , which fixes the number of particles, and the curvature ω of an external confining harmonic potential. In the Fock basis $\{|\alpha\rangle = \prod_i^{M^2} |n_i\rangle_i\}$ of localized particles in the $M \times M$ square lattice, where n_i is the occupation number at site i , the diagonal matrix elements (eqn (5.40)) take the form

$$E_{\alpha} = \frac{U}{2} \sum_i n_i (n_i - 1) - \sum_i \mu_i n_i, \quad (5.43)$$

while the off-diagonal ones are given by the expression

$$-H_1^{\alpha'\alpha} = 2t\langle\alpha'|\hat{b}_i^\dagger\hat{b}_j|\alpha\rangle = 2t\sqrt{(n_i^\alpha + 1)n_j^\alpha}, \quad (5.44)$$

that connect only states $|\alpha'\rangle$ and $|\alpha\rangle$ that differ in the occupation number of the two nearest neighboring sites i and j , namely $|\alpha'\rangle \equiv \frac{\hat{b}_i^\dagger\hat{b}_j}{(n_i^\alpha + 1)n_j^\alpha}|\alpha\rangle$, with n_i^α being the number of particles at the i th site of state $|\alpha\rangle$.

To write the partition function for the 2D extended Bose–Hubbard model, we notice that the first-order term vanishes since the matrix elements of eqn (5.44) are off-diagonal, i.e. $H_1^{\alpha\alpha} = 0$, and, due to the geometry of the system (2D square lattice), it is not difficult to see that all the terms with an odd value of m also vanish. Therefore, by rearranging the exponentials and renaming $\alpha \equiv \alpha_0$, we obtain

$$\begin{aligned} Z_{\text{BH}} &= \sum_{\alpha_0} e^{-\beta E_{\alpha_0}} + \sum_{m=2}^{\infty} (-2t)^m A_m \\ &\times \int_0^\beta d\tau_m \dots \int_0^{\tau_2} d\tau_1 \sum_{\alpha_0, \alpha_1, \dots, \alpha_{m-1}} \exp \left\{ -\beta E_{\alpha_0} - \sum_{p=0}^{m-1} E_{\alpha_p}(\tau_{p+1} - \tau_p) \right\}, \end{aligned} \quad (5.45)$$

where A_m is a product of m square root factors coming from eqn (5.44), and we have introduced $\tau_0 = \tau_m$ to compact the notation. We can simplify the notation further by noticing that for $m = 0$ two things happen: (i) the sum in the exponent of eqn (5.45) does not make any sense, since it is the term of order $m \geq 2$ in the Taylor expansion, and we therefore define it to be zero, and (ii) in the sum over the α s only α_0 survives. Keeping these two considerations in mind and defining $A_{m=0} = 1$, we then write the partition function in the compact form

$$\begin{aligned} Z_{\text{eBH}} &= \sum_{m=0}^{\infty} \sum_{\alpha_0, \alpha_1, \dots, \alpha_{m-1}} (-2t)^m A_m \\ &\times \int_0^\beta d\tau_m \dots \int_0^{\tau_2} d\tau_1 \exp \left\{ -\beta E_{\alpha_0} - \sum_{p=0}^{m-1} E_{\alpha_p}(\tau_{p+1} - \tau_p) \right\}. \end{aligned} \quad (5.46)$$

The last expression can be formally written as

$$Z_{\text{eBH}} = \sum_{\nu} W_{\nu}, \quad (5.47)$$

with W_{ν} being the weight of each configuration $\nu \equiv [m, \alpha_0(\tau), \alpha_1(\tau), \dots, \alpha_{m-1}(\tau)]$, where the α s not only define ν but also their distribution in imaginary time. This is better understood from Figure 5.3, where we sketch one such configuration for a 1D lattice.

The imaginary time τ is on the horizontal axis, while on the vertical axis there are all the sites of the lattice. Each line is called a *worldline* and the width of the line is proportional to

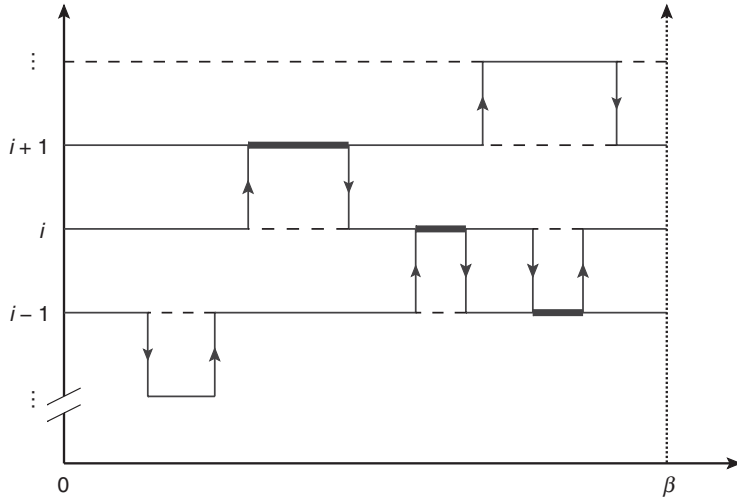


Figure 5.3 Schematic representation of the configurations contributing to the partition function Z_{BH} of the Bose–Hubbard model. The imaginary time τ is on the horizontal axis, while all the sites of the lattice are on the vertical axis. Each line is called a *worldline*. The width of each worldline is proportional to the number of particles; the dashed black line has n particles while the solid and bold lines have occupation numbers equal to $n+1$ and $n+2$. Worldlines have to fulfill periodic boundary conditions in imaginary time τ . The vertical arrows corresponding to changes in the occupation numbers are called kinks. By courtesy of C. Trefzger.

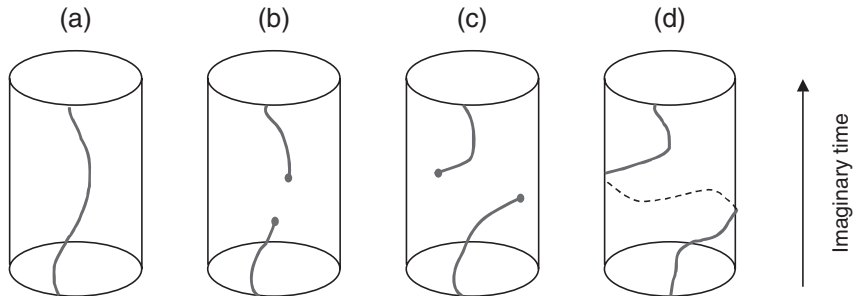


Figure 5.4 1D system with (a) zero and (d) one winding number(s). (b) and (c) show how the worm algorithm is able to go from (a) to (d). By courtesy of C. Trefzger.

the number of particles: the dashed black line is for n particles while the solid and bold blue lines have occupation numbers equal to $n+1$ and $n+2$ respectively. Because the partition function is a trace, worldlines have to close on themselves and since we have also assumed spatial periodic boundary conditions one can imagine the configuration of Figure 5.4 to be wrapped on a torus. The phase space of all possible configurations is called the *closed path configuration space*, which is spanned by the path integral Monte Carlo algorithm.

If we cut one configuration at a certain instant in imaginary time, we get the quantum system in a particular state, and the points in imaginary time where the system changes

state are called *kinks*, which in Figure 5.4 are represented by vertical arrows. A configuration with a number of kinks equal to m contributes to the m th order term of the partition function in eqn (5.46), and it is straightforward to see that there is an infinite number of different configurations with the same number of kinks, the difference being the time at which the kinks take place and/or the different states they connect. The updating procedure of a path integral Monte Carlo algorithm therefore consists of changing the number of kinks and/or their position in imaginary time.

5.7.3 The worm algorithm

A particularly efficient updating procedure generalizes path integral Monte Carlo to the case of a grand canonical ensemble and deals with disconnected worldlines, known as ‘worms’. These worldlines permit us to collect statistics for calculating the Matsubara Green functions, which are defined as

$$G(j, \tau) = \langle \hat{T}_\tau \hat{b}_{i+j}(\tau_0 + \tau) \hat{b}_i^\dagger(\tau_0) \rangle, \quad (5.48)$$

where \hat{T}_τ is the time-ordering operator, τ_0 and τ are two points in imaginary time, i and j are two sites of the lattice, and the symbol $\langle . \rangle$ stands for the statistical average of the expectation value of an operator.

The worm algorithm, originally developed in Prokof’ev *et al.* (1998*a,b*), thus works in an enlarged configuration space and is equivalent to work in the grand canonical ensemble. For a pedagogical tutorial on the worm algorithm see, for example, Trefzger *et al.* (2011).

Here, we should point out that the worm algorithm is also efficient in sampling topologically different configurations and configurations that are separated by an energy barrier, which is a necessary condition in order to maintain ergodicity. An example of two topologically different configurations is shown in Figure 5.4, where a 1D system with one particle (worldline) is considered. Periodic boundary conditions in time and space apply, i.e. the system is a torus where the bottom and top facets of the cylinder are glued together. Figure 5.4(a) represents a configuration with zero winding numbers, i.e. the worldline does not ‘wind’ in imaginary time. Figure 5.4(d), on the other hand, represents a configuration with one winding number, i.e. the worldline winds once in imaginary time. An algorithm based on local updates that only works in the path configuration space would not allow us to sample configurations with different winding numbers unless a global update that introduces a winding number at once is introduced. Instead, the worm algorithm can easily go from the configuration of Figure 5.4(a) to the configuration in Figure 5.4(d) (see Figure 5.4(b) and (c)).

Being able to sample configurations with different winding numbers is crucial in order to simulate superfluid systems. It was shown in Pollock and Ceperley (1987) that the superfluid stiffness can be extracted from the statistics of winding numbers:

$$\rho_s = \frac{T \langle \mathbf{W}^2 \rangle}{dL^{d-2}}, \quad (5.49)$$

where T is the temperature, L the system size, d the dimensionality, and $\mathbf{W}^2 = \sum_{i=1}^d W_i^2$.

5.7.4 Quantum Monte Carlo for trapped Bose gases

Let us lastly comment on the results obtained by quantum Monte Carlo analysis of harmonically trapped systems (Batrouni *et al.*, 2002; Wessel *et al.*, 2004; Batrouni *et al.*, 2005; Sengupta *et al.*, 2005*b*). In a generic situation one finds that there are plateaus characterized by an integer density of atoms and small atom number fluctuations, which are surrounded by regions of space where atom number fluctuations are large and the density is non-integer. The former (latter) are identified as MI (superfluid) domains. Amazingly, images of these domain shells have recently been directly observed experimentally (Campbell *et al.*, 2006; Fölling *et al.*, 2006). It should be stressed, however, that there are significant differences between superfluid and MI ‘phases’ in harmonically trapped and homogeneous models. The harmonically trapped system is gapless, even in the presence of Mott domains (Batrouni *et al.*, 2005). It is also always globally compressible (Batrouni *et al.*, 2002). Both of these properties are in striking contrast to the homogeneous case. Inhomogeneity of a trapped system suggests that the critical behavior might be recovered in local quantities, e.g. the local compressibility $\kappa_i^{\text{local}} = \partial \langle \sum_j n_j \rangle / \partial \mu_i^{\text{local}}$. See Wessel *et al.* (2004) and Gygi *et al.* (2006) for a systematic discussion of both harmonic and quartic trapping potential. This quantity, however, does not show the critical behavior at the border between Mott and superfluid domains. All this leads to conclusion that: (i) in a harmonically trapped system, instead of a true quantum phase transition, there is a crossover and (ii) it will be very interesting to perform the experiments on homogeneous systems in a feasible ‘box’ potential (Meyrath *et al.*, 2005).

Another difference between homogeneous and trapped models is observed in the visibility of interference patterns measured after releasing the atoms from the external potentials (Gerbier *et al.*, 2005). While in a homogeneous system the visibility of interference fringes is a smooth monotonic function of the t/U ratio, in the trapped model one finds both kinks (sudden changes of the slope) and non-monotonic behavior caused by the presence of correlations between disconnected superfluid domains.

5.8. Phase-space methods

Phase-space formulations aim at a description of quantum phenomena closer to the classical one, in order to gain useful physical insights. Phase-space methods are formulated in terms of equations dealing with numbers and not with operators, simplifying the underlying mathematical structure of the formulation. This mathematical advantage arises from the fact that the infinite-dimensional complex Hilbert space structure which is, in principle, a difficult object to work with, can be mapped onto the linear algebra structure of the finite-dimensional real phase space. Phase-space methods were introduced into quantum mechanics relatively early by Wigner (1931, 1932) and Moyal (1949), but their rapid development started in the 1960s with their application to quantum optics by Glauber (1963*b*) and Sudarshan (1963). To a great extent, quantum optical studies of quasi-probability distributions, such as Wigner functions and P - or Q -distributions, contributed enormously to our modern understanding of quantum noise (Gardiner and Zoller, 2004; Walls and Milburn, 2006). Phase-space methods usually map the density matrix of the system being considered onto a function fulfilling a generalized Fokker–Planck-type of equation, and try to replace this equation with systems of Langevin-like equations that

can be simulated using classical Monte Carlo methods. The necessary condition is that the corresponding quasi-probability or phase-space quasi-distribution must be a reasonable probability measure, which is not always the case. The Glauber–Sudarshan P -representation is often a highly singular distribution, and the Wigner function may take negative values. All of these problems can be sometimes overcome and there has been some progress in using phase-space methods to simulate many-body problems, in particular for signatures of strongly correlated ultracold fermions in optical lattices (Steel *et al.*, 1998; Drummond and Corney, 2005; Carusotto and Castin, 2004).

It is worth stressing that stochastic or phase-space methods become very efficient when the fluctuations become classical, i.e. at high, or at least moderately high, temperatures, which for the BEC might mean $T \simeq 0.1 - 0.2T_c$. The truncated Wigner approach, or simulations of the Gross–Pitaevskii equations with random initial conditions that mimic the initial thermal equilibrium are easy to implement and very accurate. Several groups have used such an approach with great success to describe phase fluctuations in a quasi-1D BEC (Dettmer *et al.*, 2001; Petrov *et al.*, 2004), or to study finite temperature dynamics of spinor condensates (Mur-Petit *et al.*, 2006).

5.8.1 Phase fluctuations in quasi-1D condensates

To illustrate these methods in more detail we discuss next the appearance of stripes in the density of the quasi-1D expanding BEC (Dettmer *et al.*, 2001). Such a phenomenon can be understood qualitatively as follows. Within the equilibrium state of an elongated BEC in a magnetic trap the density distribution remains largely unaffected even if the phase fluctuates. The reason is that the mean-field interparticle interaction prevents the transformation of local velocity fields provided by the phase fluctuations into modulations of the density. However, after switching off the trap, the mean-field interaction rapidly decreases and the axial velocity fields are then converted into the density distribution.

In Dettmer *et al.* (2001), numerical simulations of the 3D Gross–Pitaevskii equation are used to understand quantitatively how phase fluctuations lead to the build-up of stripes in the density distribution. It is assumed that the condensate initially had an equilibrium density profile and a random fluctuating phase $\phi(x)$. For elongated BECs, the phase can be represented as $\phi(x) = \sum_{j=1}^{\infty} \phi_j(x)$ (Petrov *et al.*, 2000a), where

$$\phi_j(x) = \left[\frac{(j+2)(2j+3)g}{4\pi R^2 L \epsilon_j(j+1)} \right]^{1/2} P_j^{(1,1)} \left[\frac{x}{L} \right] \frac{(\alpha_j + \alpha_j^*)}{2}. \quad (5.50)$$

Here $\epsilon_j = \hbar\omega_x \sqrt{j(j+3)/4}$ is the spectrum of low-energy axial excitations, $P_j^{(1,1)}$ are Jacobi polynomials, $g = 4\pi\hbar^2 a/m$, with $a > 0$ being the scattering length, and R (L) is the radial (axial) condensate size. In eqn (5.50), quasiparticle creation and annihilation operators have been replaced by complex amplitudes α_j and α_j^* . To reproduce the quantum statistical properties of the phase, α_j and α_j^* are sampled as random variables with a zero mean value and $\langle |\alpha_j|^2 \rangle = N_j$, where $N_j = [\exp(\epsilon_j/k_B T) - 1]^{-1}$ is the occupation number for the quasiparticle mode j .

5.8.2 Classical field methods

The so-called classical field method developed by Burnett (Davis *et al.*, 2001) and, especially, by Rzążewski (Góral *et al.*, 2001) puts some emphasis on the understanding of the concept of temperature in closed systems. The classical fields approximation is a mean-field approximation of the quantum field theory that may be used also for a weakly interacting gas (Sinatra *et al.*, 2002). The typical procedure works as follows: the starting point is the second-quantized Hamiltonian for the atomic system confined in a box with periodic boundary conditions and interacting via pairwise contact potential:

$$\hat{H} = \int d^3r \hat{\Phi}^\dagger \frac{p^2}{2m} \hat{\Phi} + \frac{V\hbar g}{2} \int d^3r \hat{\Phi}^\dagger \hat{\Phi}^\dagger \hat{\Phi} \hat{\Phi}, \quad (5.51)$$

where $\hat{\Phi}$ is an atomic field operator, $V = L^3$ is a volume of the system (L being the size of the box) and $g = \frac{4\pi}{mV} a$ characterizes the atom–atom interactions in the low-energy, s -wave approximation. The field $\hat{\Phi}$ is then expanded in the plane-wave (Fourier) modes:

$$\hat{\Phi}(\mathbf{r}) = \frac{1}{\sqrt{V}} \sum_{\mathbf{k}} \exp(-i\mathbf{k} \cdot \mathbf{r}) \hat{a}_{\mathbf{k}}, \quad (5.52)$$

where $\hat{a}_{\mathbf{k}}$ are bosonic annihilation operators, and $\mathbf{k} = \frac{2\pi}{L} \mathbf{n}$ with $n_i = 0, \pm 1, \pm 2, \dots$ ($i = x, y, z$). With this substitution, the Hamiltonian assumes its final form:

$$\frac{\hat{H}}{\hbar} = \xi \sum_{\mathbf{k}} n^2 \hat{a}_{\mathbf{k}}^\dagger \hat{a}_{\mathbf{k}} + \frac{1}{2} g \sum_{\mathbf{k}, \mathbf{k}', \mathbf{k}''} \hat{a}_{\mathbf{k}+\mathbf{k}'-\mathbf{k}''}^\dagger \hat{a}_{\mathbf{k}''}^\dagger \hat{a}_{\mathbf{k}'} \hat{a}_{\mathbf{k}}, \quad (5.53)$$

where $\xi = \frac{1}{2m} (\frac{2\pi}{L})^2$. In the interaction picture, $\hat{a}_{\mathbf{k}} = \exp(-i\xi n^2 t) \hat{a}_{\mathbf{k}}$ and the Heisenberg equations of motion for the operators $\hat{a}_{\mathbf{k}}$ acquire the following form:

$$\dot{\hat{a}}_{\mathbf{k}} = -ig \sum_{\mathbf{k}', \mathbf{k}''} \exp[2i\xi(\mathbf{n} - \mathbf{n}')(\mathbf{n} - \mathbf{n}'')t] \hat{a}_{\mathbf{k}'+\mathbf{k}''-\mathbf{k}}^\dagger \hat{a}_{\mathbf{k}'} \hat{a}_{\mathbf{k}''}. \quad (5.54)$$

Since solving the non-linear operator (eqn (5.54)) is difficult—if not practically impossible—the semiclassical approximation is then used. This consists of replacing all operators $\hat{a}_{\mathbf{k}}$ by c -number complex amplitudes, called ‘classical fields’. Note that this replacement is reasonable if the corresponding modes are strongly occupied. Of course, at very low temperatures only the lowest-lying states are macroscopically occupied and quantum fluctuations in excited states are important. For these reasons, the use of the semiclassical approximation is not allowed at very low temperatures. In the classical field method one has to solve a set of non-linear differential equations for the ‘classical fields’ $\alpha_{\mathbf{k}}$; these equations, in general, must be solved numerically. Typically, the temperature imposes a cut-off in the number relevant of modes.

5.9. Analytic one-dimensional methods

In this section we give a short guide to some useful analytical 1D methods for treating quantum spin chains. We start by analyzing once again the Bose–Hubbard Hamiltonian in one dimension (eqn (5.1)), i.e. a chain of sites with open ends. We illustrate methods and approximations which reduce the 1D Bose–Hubbard model to an exactly solvable spin model or to a so-called Luttinger liquid theory.

5.9.1 Hard-core bosons

Hard-core bosons refer to the limit in which on-site interactions are infinite ($U \rightarrow \infty$). The Bose–Hubbard model (eqn (5.1)) in this limit has only two possible states with finite energy: the number of bosons per site is either $n_0 = 0$ or $n_0 = 1$. Thus, MI states with filling factor larger than one are excluded. In such a case, the model reduces to an XX model in a transverse field (eqn (4.13)), with at most one boson per site (Sachdev, 1999). We may encode the presence (\uparrow) or absence (\downarrow) of the boson at the site i as a spin- $\frac{1}{2}$ particle:

$$\begin{aligned}\hat{\sigma}^x &= \hat{b} + \hat{b}^\dagger \\ \hat{\sigma}^y &= i(\hat{b} - \hat{b}^\dagger) \\ \hat{\sigma}^z &= 1 - \hat{b}^\dagger \hat{b},\end{aligned}\tag{5.55}$$

where $\hat{\sigma} = (\hat{\sigma}^x, \hat{\sigma}^y, \hat{\sigma}^z)$ are Pauli operators. With such a mapping, the Bose–Hubbard model reduces to the *XX* model in a transverse field (also called the quantum Ising model),

$$H_{XX} = -\frac{t}{2} \sum_{\langle ij \rangle} [\hat{\sigma}_i^x \hat{\sigma}_j^x + \hat{\sigma}_i^y \hat{\sigma}_j^y] + \frac{\mu}{2} \sum_i (\hat{\sigma}_i^z),\tag{5.56}$$

This model describes spin- $\frac{1}{2}$ particles on a lattice site with nearest-neighbor interactions. According to Sachdev (1999), there are two master models required to understand quantum phase transitions: the Bose–Hubbard model and the quantum Ising model. As we have seen, the former cannot be solved analytically. However, the latter can be exactly solved in one dimension using the Jordan–Wigner transformation. This is the simplest quantum lattice system that exhibits a quantum phase transition from a paramagnetic to a ferromagnetic state.

5.9.2 Jordan–Wigner transformation and the 1D quantum Ising model

The Jordan–Wigner transformation is a way to ‘fermionize’ 1D bosonic systems (Sachdev, 1999) mapped to spin- $\frac{1}{2}$ Pauli operators via eqn (5.55). This means that there is a map between the Hilbert space of a system with N spin- $\frac{1}{2}$ particles (\mathbb{C}^{2N}) and the Hilbert space of N spinless fermions such that, while the bosonic operators on different sites commute, the new fermionic operators will anticommute. This map is known as the

Jordan–Wigner transformation. The fermionic operators $(\hat{f}, \hat{f}^\dagger)$ are defined in Sachdev (1999) as:

$$\hat{f}_i = \left(\prod_{j < i} \hat{\sigma}_j^z \right) \hat{\sigma}_i^+, \quad (5.57)$$

$$\hat{f}_i^\dagger = \left(\prod_{j < i} \hat{\sigma}_j^z \right) \hat{\sigma}_i^-. \quad (5.58)$$

where $\hat{\sigma}^\pm = (\hat{\sigma}^x \pm i\hat{\sigma}^y)$. The inverse relations are also simple

$$\hat{\sigma}_i^+ = \prod_{j < i} (1 - 2\hat{f}_j^\dagger \hat{f}_j) \hat{f}_i, \quad (5.59)$$

$$\hat{\sigma}_i^- = \prod_{j < i} (1 - 2\hat{f}_j^\dagger \hat{f}_j) \hat{f}_i^\dagger. \quad (5.60)$$

This map transforms the quantum Ising model in one dimension (eqn (5.56)) into a spinless fermionic model

$$\hat{H}_{XX} = -t \sum_{\langle i \rangle} \left[f_i^\dagger \hat{f}_{i+1} + h.c. \right] - \mu \sum_i f_i^\dagger \hat{f}_i, \quad (5.61)$$

which is exactly solvable since it describes free fermions after diagonalization. To diagonalize it, we go to momentum space (eqn (5.2)), and obtain straightforwardly:

$$\hat{H}_{XX} = \sum_k \epsilon_k \hat{f}_k^\dagger \hat{f}_k \quad (5.62)$$

with the free fermion dispersion $\epsilon_k = -2t \cos(ka) - \mu$. Notice that for $\mu < -2t$, the ground state of the system has no fermions corresponding to the vacuum or MI with $n_0 = 0$. For $\mu > 2t$, every fermion state is occupied, corresponding to $n_0 = 1$.

Had we started from an extended Hubbard model with, say, nearest-neighbor interactions of the form $\propto \hat{V} \sum_i \hat{\sigma}_i^\dagger \hat{\sigma}_{i+1}^\dagger \hat{\sigma}_{i+1} \hat{\sigma}_i$, we would end up with ‘spinless’ interacting fermions with the term $\propto \hat{V} \sum_i \hat{f}_i^\dagger \hat{f}_{i+1}^\dagger \hat{f}_{i+1} \hat{f}_i$.

The Jordan–Wigner transformation is essentially a 1D transformation. There have been many attempts to generalize it to higher dimension (for a review see Tsvelik (2003); for a discussion in the context of applications to atoms see Fehrmann *et al.* (2004a)). Only recently, new ideas related to the concept of projected entangled pair states allowed Verstraete and Cirac to propose an interesting efficient generalization of the Jordan–Wigner transformation to two dimensions (see Verstraete and Cirac (2005), and references therein).

5.9.3 Bosonization and Luttinger liquid theory

Let us now consider the interacting ‘spinless’ Fermi gas and try to formulate the low-energy effective theory for this model. We assume that fermions do not fill the lowest band so that in the absence of interactions the Fermi level is somewhere in the middle of the band. We expect that at low temperatures interesting physics will occur close to the Fermi energy. It is thus reasonable to linearize the fermionic dispersion relation at the Fermi energy, $\epsilon(k) = \epsilon(\pm k_F) \pm c_F(k \pm k_F)$, with the ‘sound velocity’ $c_F = d\epsilon(k)/dk|_{k_F}$. In one dimension there are two values of momenta $\pm k_F$ where the Fermi energy is reached: one corresponds to left- and the other to right-going fermions. Note that all of the interesting low-energy physics happens close to the Fermi surface (points). This implies that states with momenta far from $\pm k_F$ will practically never participate in any relevant physical process and will remain deep in the filled Fermi sea. It is thus reasonable to treat the left- and right-going fermions close to $\pm k_F$ as independent and introduce two fermionic species described in the momentum representation by $\hat{L}(k), \hat{L}^\dagger(k)$, and $\hat{R}(k), \hat{R}^\dagger(k)$, respectively; here k is the momentum relative to $\pm k_F$ and it has values from $-\infty$ to $+\infty$. The Hamiltonian becomes

$$\begin{aligned}\hat{H} = & + \sum_k [-c_F(k)\hat{L}^\dagger(k)\hat{L}(k) + c_F(k)\hat{R}^\dagger(k)\hat{R}(k)] \\ & + \frac{1}{L} \sum_{k_1, k_2, q} V(q)\hat{L}^\dagger(k_1 - q)\hat{R}^\dagger(k_2 + q)\hat{R}(k_2)\hat{L}(k_1).\end{aligned}\quad (5.63)$$

This is the celebrated Luttinger model (Mahan, 1993; Giamarchi, 2004). One now introduces the operators

$$\hat{\rho}_L(q) = \sum_k \hat{L}^\dagger(k + q)\hat{L}(k), \quad (5.64)$$

$$\hat{\rho}_L(-q) = \sum_k \hat{L}^\dagger(k)\hat{L}(k + q) = \hat{\rho}_L^\dagger(q), \quad (5.65)$$

$$\hat{\rho}_R(q) = \sum_k \hat{R}^\dagger(k + q)\hat{R}(k), \quad (5.66)$$

$$\hat{\rho}_R(-q) = \sum_k \hat{R}^\dagger(k)\hat{R}(k + q) = \hat{\rho}_R^\dagger(q), \quad (5.67)$$

and observes that $[\hat{\rho}_R(-q), \hat{\rho}_R(+q')] = \sum_{k_F - q'}^{k_F} \hat{R}^\dagger(k + q - q')\hat{R}(k)$. In the Luttinger–Tomonaga approximation (Mahan, 1993), one now replaces these and similar commutators with their values when averaged over the ideal Fermi sea. The result is

$$[\hat{\rho}_R(-q), \hat{\rho}_R(+q')] = \frac{qL}{2\pi} \delta(q - q'), \quad (5.68)$$

implying that for $q > 0$ we can introduce $\hat{b}_q^\dagger = \hat{\rho}_R(q)\sqrt{2\pi/qL}$ and $\hat{b}_q = \hat{\rho}_R(-q)\sqrt{2\pi/qL}$, which may be regarded as bosonic annihilation and creation operators, respectively, since $\hat{b}_q, \hat{b}_{q'}^\dagger = \delta(q - q')$. A similar construction is made for the operators $\hat{c}_{-q}^\dagger = \hat{\rho}_L(-q)\sqrt{2\pi/qL}$

and $\hat{c}_{-q} = \hat{\rho}_L(q)\sqrt{2\pi/qL}$. These operators can be interpreted as follows: \hat{b}_q^\dagger takes a particle from state k and puts it into state $k + q$. It thus creates fermion–hole pairs when $k < k_F$ and $k + q > k_F$. Analogously, the operator \hat{c}_{-q}^\dagger takes a fermion from an unoccupied state $-k_F < k + p$ to the unoccupied state $k < -k_F$. The whole Hamiltonian becomes

$$\hat{H} = \sum_{q>0} qc_F [\hat{b}_q^\dagger \hat{b}_q + \hat{c}_{-q}^\dagger \hat{c}_{-q}] + \frac{1}{2\pi} \sum_{q>0} [V(q) \hat{c}_{-q}^\dagger \hat{b}_q^\dagger + V(q)^* \hat{b}_q \hat{c}_{-q}]. \quad (5.69)$$

The problem has thus been reduced to an exactly solvable system of interacting harmonic oscillators that describes linear 1D hydrodynamics of the so-called Luttinger liquid. Bosonization theory (Giamarchi, 2004) ensures that such a description can be found for most 1D bosonic and fermionic systems with local interactions. For a very complete description of interacting Bose gases in quasi-1D optical lattices see, for example, Cazalilla *et al.* (2006).

5.9.4 Bethe ansatz

Bethe ansatz is an analytical method for finding exact eigenstates and eigenvalues of some strongly correlated 1D models (although sometimes it has to be complemented with numerical analysis). By appropriately exploiting the symmetries involved in the Hamiltonian it is possible to diagonalize the Hamiltonian exactly. However, the method's power relies on the fact that Bethe ansatz characterizes all eigenstates by a set of quantum numbers that enumerate the states, according to their physical properties. This method was originally developed by Bethe (1931) to solve a 1D array of electrons with uniform next-neighbor interactions, i.e. a spin- $\frac{1}{2}$ Heisenberg model :

$$\hat{H} = -J \sum_{i=1}^N \boldsymbol{\sigma}_i \cdot \boldsymbol{\sigma}_{i+1}, \quad (5.70)$$

where $\boldsymbol{\sigma} = (\sigma_x, \sigma_y, \sigma_z)$ are the standard Pauli matrices and N denotes the number of sites. The parametrization of the eigenvectors, i.e. the Bethe ansatz, has become a fundamental tool with which many other 1D quantum systems have been shown to be solvable. From the eigenvectors one can easily compute the quantities of interest by calculating the expectation values of the desired operators.

In what follows, we summarize the original formulation of Bethe following the pedagogical work of Karbach and Müller (1997) and Karbach *et al.* (1998). Since, the Heisenberg Hamiltonian commutes with the total spin along the z -direction $[\hat{H}, \sigma_T^z] = 0$ with $\sigma_T^z = \sum_i \sigma_i^z$, then:

$$\hat{H} = -J \sum_{i=1}^N \left[\frac{1}{2} (\hat{\sigma}_i^+ \hat{\sigma}_{i+1}^- + \hat{\sigma}_i^- \hat{\sigma}_{i+1}^+) + \hat{\sigma}_i^z \hat{\sigma}_{i+1}^z \right]. \quad (5.71)$$

Thus, eigenstates of $\hat{\sigma}^z$ are also eigenstates of \hat{H} . Bethe ansatz is, as discussed below, a basis transformation.

We denote by $|0\rangle = |\uparrow\rangle$ the eigenstate of $\hat{\sigma}^z$ with value $+\frac{1}{2}$ and by $|1\rangle = |\downarrow\rangle$ the eigenstate with eigenvalue $-\frac{1}{2}$. Sorting the basis according to the quantum number $N/2 - r$, where r is the number of flipped spins, is all that is required to block-diagonalize the Hamiltonian. The block $r = 0$ corresponds to a single state with all spins up, which we call ferromagnetic: $\hat{H}|F\rangle = \hat{H}|\uparrow\ldots\uparrow\rangle = -JN/4$. The case $r = 1$ (one spin down) has N invariant vectors, which are labeled by the position of the flipped spin: $|n\rangle = \hat{\sigma}_n^-|F\rangle$. To diagonalize this block, which has size $N \times N$, we take into account the fact that the Hamiltonian possesses translational symmetry. Therefore a translational invariant basis can be constructed in the subspace with $r = 1$,

$$|\psi\rangle = \frac{1}{\sqrt{N}} \sum_{n=1}^N e^{ikn} |n\rangle, \quad (5.72)$$

with wave numbers $k = 2\pi m/N, m = 0, 1, \dots, N - 1$. The vectors $|\psi\rangle$ correspond to a complete spin alignment of the ferromagnetic ground state $|F\rangle$ that is periodically disturbed by a spin wave with wavelength $\lambda = 2\pi/k$. These states are called magnons or spin waves.

The subspace $r = 2$ cannot be solved by applying any further symmetry, and here is where the full power of the Bethe ansatz appears. Solutions of the type of eqn (5.72), for $r = 1$, can be also obtained starting from the following ansatz

$$|\psi\rangle = \sum_{n=1}^N a(n) |n\rangle \quad (5.73)$$

and finding the values of the coefficients $a(n)$ that satisfy the eigenvalue equation $\hat{H}|\psi\rangle = E|\psi\rangle$ using periodic boundary conditions. If one applies the same procedure to the subspace $r = 2$, i.e. one looks for the coefficients $a(n_1, n_2)$ that determine the eigenstates, one finds:

$$|\psi\rangle = \sum_{1 \leq n_1 < n_2 \leq N}^N a(n_1, n_2) |n_1, n_2\rangle. \quad (5.74)$$

There are $N(N - 1)/2$ eigenstates. These are characterized by pairs of Bethe (integer) quantum numbers λ_1, λ_2 , which define the ‘momenta’ via the relations $Nk_1 = 2\pi\lambda_1 + \theta$, $Nk_2 = 2\pi\lambda_2 - \theta$, such that

$$a(n_1, n_2) = e^{i(k_1 n_1 + k_2 n_2 + \theta_{12}/2)} + e^{i(k_1 n_2 + k_2 n_1 + \theta_{21}/2)}, \quad (5.75)$$

whereas the angles $\theta_{12} = -\theta_{21} = \theta$ fulfill $2 \cot(\theta/2) = \cot(k_1/2) - \cot(k_2/2)$. Depending on the relative values of the pair λ_1, λ_2 , different types of solution exist. In general, the Bethe ansatz for an unrestricted number r of flipped spins reads:

$$|\psi\rangle = \sum_{1 \leq n_1 \leq \dots \leq n_r \leq N}^N a(n_1 \dots n_r) |n_1 \dots n_r\rangle \quad (5.76)$$

and the eigenvectors span a subspace of dimension $N!/(N - r)!r!$. The coefficients $a(n_1 \dots n_r)$ have a form analogous to eqn (5.75), and a generalized solution of the resulting transcendental equations can easily be found numerically.

It is also worthwhile mentioning that the Bethe ansatz can be applied to the 1D Bose–Hubbard model. See Krauth (1991) for a complete discussion. In this case, however, the method faces fundamental problems since one has to assume that the maximal occupation of each lattice site is not larger than 2. As a result, the ansatz is never exact, although it gives some valuable and correct predictions, e.g. the vanishing point of the superfluid fraction in the Mott phase.

5.10. Renormalization approaches in one dimension: DMRG and MPS

We reach the end of this chapter by revisiting the use of renormalization procedures to solve many-body systems. The underlying philosophy of all renormalization-oriented techniques is that many-body systems can be treated almost ‘exactly’ if one is able to truncate the full Hilbert space by removing the degrees of freedom that are involved neither in the ground state nor in the dynamical evolution of the system (Wilson, 1975; White, 1992). The difficulty and glory of the method revolves around how reliably the truncation is performed (see also Chapter 2).

The real-space renormalization group method, which works for classical systems, has been generalized to the quantum domain. It is an iterative method in real space to describe qualitatively the low-energy domain of some 1D many-body systems. The starting point of the technique is to consider a small 1D chain system that can be exactly diagonalized. The size of the chain is then iteratively increased by adding a new lattice site (new spin) at each step. The Hamiltonian that couples a new site n (\mathcal{H}_n) to the chain $\mathcal{H}_{1,\dots,n-1}$ is renormalized by disregarding all physically irrelevant couplings (i.e. making the Hilbert space smaller) and diagonalizing the resulting Hamiltonian. However, the accuracy of the methods is moderately low. The real breakthrough in simulating 1D models came with the DMRG, which was introduced by White (1992). This is a variational method that has been enormously successful in describing ground states of some strongly interacting 1D systems with a rather modest computational effort (Schollwöck, 2005).

The use of DMRG has been, for a long time, rather empirical in the sense that there has not been a clear criterion to assess the convergence of the method and to determine when the truncation should be done. Quantum information has provided a more rigorous framework to understand when and why the DMRG algorithm will succeed. In particular, a new perspective (Vidal 2003a,b; Verstraete *et al.*, 2004a,c; Orus and Lattore, 2004) has been given on the answers to questions such as:

- (i) How should an efficient truncation of the Hilbert space be performed?
- (ii) Which many-body systems can be efficiently simulated?
- (iii) Can dynamical evolution of strongly correlated systems be simulated?
- (iv) How and when should DMRG-oriented methods be implemented to investigate ground states of 2D and 3D systems?
- (v) How should classical concepts such as correlation length, which diverge on the critical points, be linked to entanglement properties?
- (vi) Can frustrated systems be simulated in this way?

The state of the art is that DMRG provides an extraordinary good approximation to the ground state of (finite) 1D spin chains at zero temperature for all gapped Hamiltonians with finite-range interactions. Such ground states fulfill generically a so-called ‘area law’ (see also Chapter 12). The area law indicates that for a given system in D dimensions, the entanglement between a part of the system, say a block of size L_D , and the rest of the system scales as L_{D-1} . In other words it depends on the boundary of the block and not on its volume. Moreover, we know that all states fulfilling an area law can be efficiently approximated by MPSs and that these states are characterized by a number of parameters that scales only polynomially with the number of particles and not exponentially. DMRG generically produces a particular kind of ansatz state: an MPS. Therefore, if the true quantum state of a system is close to an MPS, DMRG algorithms will perform very well.

There are at least three different approaches to performing the truncation in a DMRG algorithm (Schollwöck, 2005):

- By optimizing expectation values (White, 1998). In this approach the value of some bounded operator (energy, magnetization, or density) determines the most relevant states contributing to it. This is the variational approach.
- By optimizing the wave function (White, 1992). The truncation is done in a way such that the renormalized wave function minimizes the Schmidt norm distance to the exact one, i.e. $\| |\Psi\rangle - |\Psi\rangle_{\text{DMRG}} \|^2 \rightarrow 0$.
- By optimizing entanglement properties. It was shown by Vidal (2003a) that the efficiency in simulating many-body systems is directly related to their entanglement behavior. Efficient simulation is possible if the entanglement of a subsystem with respect to the whole is bounded, i.e. follows an area law, or grows at most logarithmically with its size. Thus, if entanglement grows linearly in time and block size, simulation of time evolution may be not efficient even in some non-critical 1D systems (Orus and Lattore, 2004).

A rigorous mathematical background to enable understanding of area laws is discussed in more detail in Chapter 12. In the following we only review briefly the algorithm of Vidal (2003a) to calculate ground states and dynamics using the Schmidt decomposition to truncate the Hilbert space. We shall see that implementing operations on individual sites and on two neighboring sites requires only local updating of the expansion, rendering the calculations of ground states, expectation values, and two-body correlations efficient. We also comment on the issue of how the expansion is linked to the MPS ansatz used in DMRG, and why MPS describes ground states of quantum spin systems so well (Verstraete *et al.*, 2004c).

Consider a general Hamiltonian \hat{H} , in one dimension, with short range interactions, and, to simplify, with translational invariance. We are looking for the ground state $|\Psi\rangle$ of the system. We start by considering the most general description of a state in such a Hilbert space, which is given by

$$|\Psi\rangle = \sum_{i_1=1}^d \dots \sum_{i_M=1}^d C_{i_1 \dots i_M} |i_1\rangle \otimes \dots |i_M\rangle \quad (5.77)$$

where $\{|i\rangle\}$ denotes an orthonormal basis, M is the number of sites, and d is the maximal dimension of the Hilbert space on each site. In the case of the Bose–Hubbard model, with N (spinless) atoms in M lattice sites, d indicates the maximal occupation number of site j (maximal $\langle \hat{b}_j^\dagger \hat{b}_j \rangle$). Note that by taking $d = N$ we can be sure that eqn (5.77) gives an *exact* representation of the state. Let us now split the 1D chain into two blocks: block A, which consists of the first site, and block B, consisting of the remaining $M - 1$ sites. The Schmidt decomposition tell us that for this, or any other bipartite splitting (A, B) , there is always a bi-orthonormal basis, denoted by $|\Phi_\alpha^{[A]}\rangle$ and $|\Phi_\alpha^{[B]}\rangle$, respectively, such that:

$$|\Psi\rangle = \sum_{\alpha}^{\chi_A} \lambda_{\alpha} |\Phi_{\alpha}^{[A]}\rangle |\Phi_{\alpha}^{[B]}\rangle, \quad (5.78)$$

where $\chi_A \leq d$, that is, the number of coefficients of the expansion known as the Schmidt rank is bounded by the dimension of the smallest of the two subspaces of the partition. This simply indicates that the number of degrees of freedom that can be entangled between A and B is at maximum the number of degrees of freedom of the smaller subsystem. If there is only a single coefficient different from zero in the expansion, the two subsystems A and B are in a product state, i.e. they are not entangled. The coefficients of the expansion are unique (up to the degeneracy of the reduced density matrices), real, and $\sum_{\alpha} \lambda_{\alpha}^2 = 1$. Notice also that $\rho_A = Tr_B(|\Psi\rangle\langle\Psi|) = \sum_{\alpha} \lambda_{\alpha}^2 |\Phi_{\alpha}^{[A]}\rangle\langle\Phi_{\alpha}^{[A]}|$ and $\rho_B = Tr_A(|\Psi\rangle\langle\Psi|) = \sum_{\alpha} \lambda_{\alpha}^2 |\Phi_{\alpha}^{[B]}\rangle\langle\Phi_{\alpha}^{[B]}|$.

The Schmidt decomposition is nothing other than the usual singular value decomposition (Horn and Johnson, 1985) of the coefficients matrix C corresponding to the decomposition of $|\Psi\rangle$ in an arbitrary orthogonal basis $|i\rangle_A$ ($|j\rangle_B$):

$$|\Psi\rangle = \sum_{i,j} C_{ij} |i\rangle_A |j\rangle_B. \quad (5.79)$$

If our partition is $1 : (M - 1)$ then C_{ij} is a $d \times d^{M-1}$ matrix. Applying the singular value decomposition to C , one obtains that $C = U D V^T$, where U (V) are unitary matrices of dimensions $d \times d$ ($d^{M-1} \times d^{M-1}$) and D is a diagonal matrix of dimensions $d \times d^{M-1}$. Therefore,

$$|\Psi\rangle = \sum_{i,j} C_{ij} |i\rangle_A |j\rangle_B = \sum_{\alpha} \left[\sum_l U_{l,\alpha} |i\rangle_A \right] D_{l,l} \left[\sum_l V_{\alpha,l} |j\rangle_B \right] = \sum_{\alpha=1}^d \lambda_{\alpha} |\phi_{\alpha}^{[A]}\rangle |\phi_{\alpha}^{[B]}\rangle. \quad (5.80)$$

An iterative treatment of the above procedure, i.e. splitting part B , with $M - 1$ sites, into two new blocks with a partition $1 : M - 2$ and writing its Schmidt decomposition, and then splitting the block of $M - 2$ sites into $1 : M - 3$ and so on, leads to the following expression for the original coefficients:

$$C_{i_1 \dots i_M} = \sum_{\alpha_1 \dots \alpha_{M-1}} \Gamma_{\alpha_1}^{[1]i_1} \lambda_{\alpha_1}^{[1]} \Gamma_{\alpha_1, \alpha_2}^{[2]i_2} \lambda_{\alpha_2}^{[2]} \Gamma_{\alpha_2, \alpha_3}^{[3]i_3} \dots \Gamma_{\alpha_{M-1}}^{[M]i_M}. \quad (5.81)$$

The tensors Γ take into account the correlations arising from the splitting, and are straightforwardly obtained by performing the corresponding singular value decomposition

at each bipartite partition. Notice that, except for the first and the last lattice sites, the corresponding tensor Γ for each site depends on two α indices associated with the two partitions involved. These two indices take into account the correlations of each block with the blocks on its left and right. It can be shown that for translationally invariant 1D systems with short-range interactions, the coefficients of the Schmidt decomposition behave as $\lambda_\alpha^{[l]} \sim \exp(-\alpha)$, and the truncation of the Hilbert space is performed by removing all small coefficients in the corresponding Schmidt decomposition.

For periodic boundary conditions, grouping the Γ tensors with the coefficients λ , the expression of the ansatz takes the more compact form:

$$|\Psi\rangle = \sum_{i_1, \dots, i_M=0}^d \text{Tr}[A^{[1],i_1} \dots A^{[M],i_M}] |i_1, \dots, i_M\rangle, \quad (5.82)$$

where $A^{[k],1} \dots A^{[k],d}$ are $D_k \times \tilde{D}_k$ complex matrices with $D_{k+1} = \tilde{D}_k \leq D$, and d is the dimensionality of the system on site i (for the Bose–Hubbard Hamiltonian, the occupation number on site i). Operations on a single site i involve only updating the value of $A^{[k],i_k}$, which basically implies doing D^2 operations of the type $A'^{[k],i_k} = U A^{[k],i_k}$. In a similar way, operations involving two neighboring sites correspond to updating the matrices of the corresponding sites and the correlations between them and again can be efficiently performed. Thus, the ground state of the Bose–Hubbard Hamiltonian, which includes only next-neighbor interactions plus on-site collisions, can be calculated variationally, whereas time evolutions can be simulated by means of a Trotter expansion (see Chapter 12). The time-dependent version of the algorithm is frequently termed ‘time-evolving block decimation’. For recent work on the dynamical response of the Bose–Hubbard model at the MI–SF transition, see Clark and Jaksch (2006). The method outlined above is not restricted to Bose–Hubbard Hamiltonians but deals with finding ground states of any spin-lattice Hamiltonian in one dimension with short-range interactions fulfilling an area law.

Matrix product states Östlund and Rommer (Östlund and Rommer, 1995; Rommer and Östlund, 1997) realized that DMRG leads to a special type of ansatz known as MPSs, which had first been introduced in the works of Affleck *et al.* (1988a), Fannes *et al.* (1989), and Fannes *et al.* (1992) and schematically shown in Figure 5.5(a). The structure of an MPS system goes as follows: associate a pair of auxiliary systems denoted by i_l and i_r (for left and right respectively) with each site i of the physical lattice. These ‘fictitious’ or auxiliary systems (also called ancillas) live in Hilbert spaces $\mathcal{H}_{i,l}$ and $\mathcal{H}_{i,r}$ respectively. The dimension D of the ancillary Hilbert space at i_r and at $(i+1)_l$ match, while the Hilbert space \mathcal{H}_i of the physical system i is d_i -dimensional. Every pair of nearest ancillary systems on the i and $i+1$ sites are prepared in a maximally entangled state

$$|\phi^+\rangle_{i_r, (i+1)_l} = \frac{1}{\sqrt{D}} \sum_{\alpha=1}^D |\alpha, \alpha\rangle \in \mathcal{H}_{i,r} \otimes \mathcal{H}_{i+1,l}, \quad (5.83)$$

expressed in terms of an orthonormal basis $\{|\alpha\rangle\}$. Thus the ancillas are prepared in the global product state $\otimes_i |\phi\rangle_{i_r, (i+1)_l}^+$. Notice that such a construction immediately guarantees

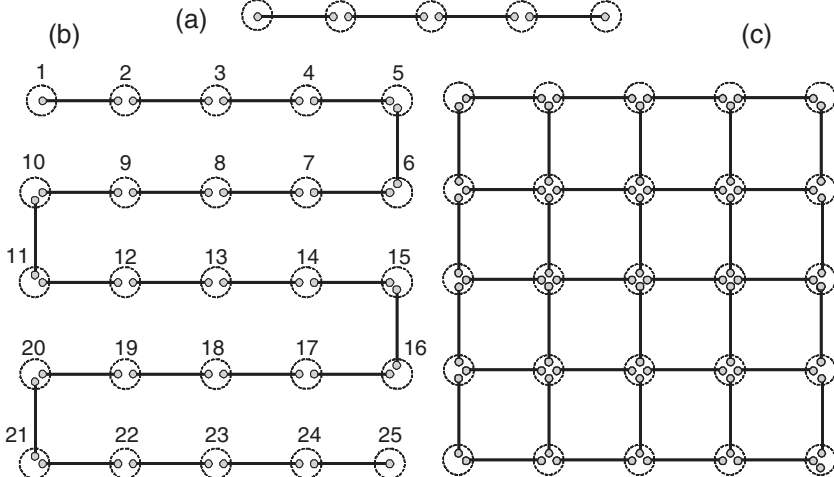


Figure 5.5 Schematic representation of (a) MPS for a 1D system, (b) ‘inefficient’ MPS in 2D, and (c) PEPS for a 2D system. Each pair of nearest-neighbor sites is connected via a maximally entangled state from an auxiliary Hilbert space. In the (a) and (b) matrices, A projects onto the physical space. In (c), matrices have to be replaced by fourth rank tensors in the bulk. From Verstraete and Cirac (2004).

entanglement (quantum correlations) between the physical systems located at two nearest-neighbor sites. To go back to the physical lattice, one projects the ancillary systems onto it as follows,

$$\begin{aligned} \mathcal{P}_i : \mathcal{H}_{i,l} \otimes \mathcal{H}_{i,r} &\rightarrow \mathcal{H}_i, \\ |\alpha \beta\rangle &\rightarrow \sum_I^{d_i} A_{i,\alpha\beta}^k |k\rangle, \end{aligned} \quad (5.84)$$

where $\{|k\rangle\}$ is an orthonormal basis in the 1D chain that spans the d_i -dimensional Hilbert space. The MPS is then given by

$$|MPS\rangle = (\otimes_i P_i) \left(\otimes |\phi^+\rangle_{i_r, (i+1)_l} \right). \quad (5.85)$$

In other words, a chain of N d -dimensional spins can be expressed as the projection of $2N$ ancillary systems of dimension D prepared in maximally entangled states between neighbor lattice sites i and $i + 1$. Due to this maximally entangled link, the structure of the MPS can be written for periodic boundary conditions as

$$|\Psi\rangle = \sum_{i_1, \dots, i_M=1}^d \text{Tr}[A^{[1], i_1} \dots A^{[M], i_M}] |i_1, \dots, i_M\rangle, \quad (5.86)$$

The $A^{[k]i_k}$ are complex matrices with dimension $\leq D \times D$. The reason why this type of state (MPS) can reproduce the ground states of quantum spin systems with nearest-neighbor interactions very well is because the ground states and low-energy excitations are completely determined by their two-body reduced density operators, as shown by Verstraete and Cirac (2006). An intuitive but handwaving argument to understand the reason why MPS parametrize ground states of 1D gapped quantum spin systems comes from Hastings' theorem (Hastings, 2004), which states that for gapped systems all correlations decay exponentially. This means that since $\langle O_A O_B \rangle - \langle O_A \rangle \langle O_B \rangle \simeq \exp(-l_{AB}/\xi_{corr})$, blocks A and B , separated by l_{AB} , can be described by a product state when l_{AB} is much larger than the correlation length ξ_{corr} . MPS have already proven to be an enormously useful tool to characterize 1D gapped systems. In particular, they can be easily extended to calculate time evolution if the entanglement does not increase during the dynamics. They have also been used to characterize quantum phase transitions in spin chains (Verstraete *et al.*, 2004c), simulate infinite systems (Vidal, 2007a), and establish a closer relation between criticality, area law, and block entanglement (Verstraete *et al.*, 2006).

The norm of the MPS's states, as well as mean values of physical observables and correlations, can be easily calculated. The calculations correspond to contracting physical indices of the MPS tensors in an appropriate way.

5.11. Renormalization approaches in two dimensions: PEPS, MERA, and TNS

The firsts attempts to simulate 2D many-body systems by extending DMRG techniques by treating 2D systems as long 1D chains (see Figure 5.5(b)) were not satisfactory. Several extensions of the 1D methods were based on tensors contracted in special ways, as shown in Figure 5.5(b), but until recently no complete algorithm for two or more dimensions had been developed. One promising set of methods that has recently been developed is generically referred to as tensor network states (TNS). There is, however, a strong connection between truncating the Hilbert space (renormalization techniques) and TNS, so that ground states of the short-range local Hamiltonians (in any dimension) are well approximated by some types of tensor product states (for a recent tutorial see Cirac and Verstraete (2009) and Vidal (2010)). This is indeed a surprising result because product tensor states are very rare, forming a set of zero measure in the Hilbert space of the N many-body systems of dimension d , which has a generic dimension of d^M . Below we discuss two examples of what has so far been the most successful TNS.

PEPS Projected entangled pair states (PEPS) are based on a generalization of the MPS structure to higher-dimensional systems. The method was introduced in a seminal preprint by Verstraete and Cirac (2004). The philosophy behind it is exactly the same as for MPS: for each lattice physical system we use as many ancillary systems as the lattice has nearest neighbors (we assume here nearest-neighbor interactions and translational invariance). The pairs of ancillary systems in neighboring sites are in a maximally entangled state of dimension D as in eqn (5.83), and the projection from the whole ancillary system onto the physical one leads to a PEPS. For simplicity, let us assume a 2D square lattice. Each point of the lattice denoted by two indices (i,j) has associated with it four auxiliary systems of

dimension D in a Hilbert space of total dimension $\mathcal{H}_{i_l,j} \otimes \mathcal{H}_{i_r,j} \otimes \mathcal{H}_{i,j_u} \otimes \mathcal{H}_{i,j_d}$, where now the subindices stand for ‘left, right, up, and down’, as schematically shown in Figure 5.5(c). The physical lattice system is recovered by projecting

$$\begin{aligned} \mathcal{P}_{(i,j)} : \mathcal{H}_{i_l,j} \otimes \mathcal{H}_{i_r,j} \otimes \mathcal{H}_{i,j_u} \otimes \mathcal{H}_{i,j_d} &\rightarrow \mathcal{H}_i, \\ |\alpha\beta\gamma\delta\rangle &\rightarrow \sum_I^{d_i} A_{i,\alpha\beta\gamma\delta}^j |j\rangle. \end{aligned} \quad (5.87)$$

Now, instead of matrices, we have tensors resulting from the contraction of one physical index with as many ancilla indices as nearest neighbors. Again, if there is an area law, the ground state can be very well approximated by a PEPS state. However, if the area law is not fulfilled or the entropy increases with time, the PEPS method does not work. What, therefore, are the limitations of PEPS? Below we outline an estimate of the resources needed to approximate the ground state of a many-body system with an MPS state for different lattice dimensionalities. For a many-body system of N particles each of dimension d , and ancillary systems of dimension D , the estimate goes as follows:

$$\begin{aligned} \text{1D lattice} &= \begin{cases} N^2 d^2 D^3 & \text{for OBC} \\ N^2 d^2 D^5 & \text{for PBC} \end{cases} \\ \text{2D lattice} &= \begin{cases} N^2 d^2 D^{10} & \text{for OBC} \\ N^2 d^2 D^{14} & \text{for PBC} \end{cases} \\ \text{3D lattice} &= \begin{cases} N^2 d^2 D^{20} & \text{for OBC} \\ N^2 d^2 D^{??} & \text{for PBC} \end{cases} \end{aligned}$$

where OBC and PBC stand for open and periodic boundary conditions, respectively. For 2D systems with open boundary conditions, reasonable accuracy can be obtained for ancillary systems of $D = 5$, but for 3D systems, even using small auxiliary systems renders any simulation impractical.

MERA A different and very useful way of implementing a renormalization is the multiscale entanglement renormalization ansatz (MERA), which was proposed by Vidal (2007b, 2008). It has been shown that this technique can be used to describe some quantum spin models in one and two dimensions, including symmetry breaking order, topological order as well as characterization of (gapless) quantum critical points in 1D. Entanglement renormalization uses renormalization techniques to consistently remove all short-distance degrees of freedom during coarse-graining. This leads to a significant reduction in computational costs, making scalable calculations feasible even in two dimensions.

In contrast to the PEPS and MPS schemes described earlier, where the renormalization is done by mapping each spin of the quantum system into a ‘super-spin’ (the ancillary systems that have all entanglement properties) and then back to the physical spin, the blocking scheme now maps n spins onto $n' < n$ spins in such a way that locality in the interactions is preserved. The mapping is done by means of isometries. Let us see what this means. The goal is to find the ground state of a many-body quantum lattice system L , form by N d -dimensional particles $|\psi_{GS}\rangle \in \mathbb{V}^{\otimes N}$, where \mathbb{V} is a vector space of

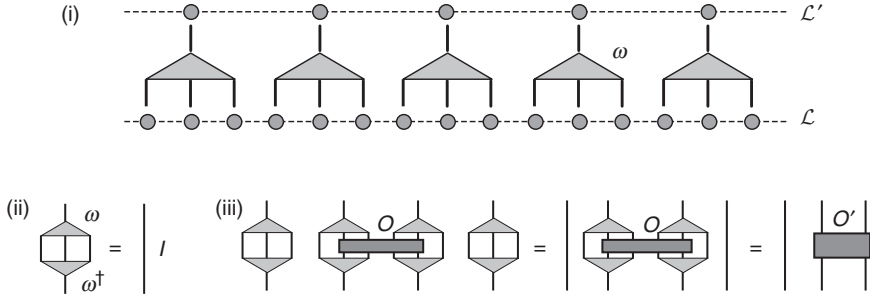


Figure 5.6 (i) Coarse-graining transformations in MERA characterized by an isometry w that maps blocks of three sites of lattice \mathcal{L} into single sites of a coarse-grained lattice \mathcal{L}_0 . (ii) Graphical representation of $w^\dagger w = Id_v$. (iii) An operator O supported on, for example, two blocks of sites of \mathcal{L} becomes a two-site operator. From Vidal, 2010.

dimension d . The particle interactions are given by a Hamiltonian H , which we assume can be decomposed as a sum of local terms, for example if we have nearest-neighbor interactions $H = \sum_{\langle ij \rangle} h_{ij}$. The renormalization procedure consists of finding some isometries w , such that we can map every three spins into a single one, as schematically shown in Figure 5.6,

$$w : \mathbb{V}' \rightarrow \mathbb{V}^{\otimes 3} \quad \text{with} \quad w^\dagger w = \text{id}_v' \quad \text{and} \quad w w^\dagger = P; \quad P^2 = P. \quad (5.88)$$

Now we have an effective lattice L' of $N/3$ sites, with an effective Hamiltonian given by $H' = W^\dagger H W$, with $W = w^{\otimes N/3}$. An operator O acting in r spins of the original lattice L now transforms in the new lattice as

$$O \rightarrow O' = (w^{\dagger \otimes r}) O (w^{\otimes r}) \quad (5.89)$$

Note, that if the original Hamiltonian H had only nearest-neighbor interactions, the transformed Hamiltonian H' would have at most nearest-neighbor interactions. This is a very important observation because it implies that spatial correlations with this mapping can never increase. In order to preserve the properties of the ground state $|\psi_{\text{GS}}\rangle$, the isometry must retain the whole support of the ground-state reduced density matrix of the three-spins $\rho \equiv \text{Tr}_E |\psi_{\text{GS}}\rangle \langle \psi_{\text{GS}}|$, where E denotes the other spins of the chain. In other words, the dimension of \mathbb{V}' has to be the rank R of the Schmidt decomposition of ρ , i.e. the number of non-zero eigenvalues of the ρ . This is the requirement imposed by White (1992) in the DMRG. The problem with this approach is that it fails to remove some of the short-distance degrees of freedom, which remain (and even accumulate) over successive iterations. In one dimension this is not a problem and DMRG works very well, but for two dimensions it is a serious drawback. The reason can be understood by again looking at the area law that makes the entropy of a block of size l scale as $S(l) \sim l^{D-1}$, that is, as the size of the boundary of the block.

To see the link with the entanglement, we approximate the Schmidt rank of the partition by $R \simeq \exp(S)$. Recalling that one site of the renormalized lattice L' accommodates $l = 3^\tau$

sites of L ($l = 3^2$ sites if we had chosen coarse-grain blocks of 3×3 sites in 2D), we end up with the following scaling rule

$$R \sim \begin{cases} e^S & \text{for non-critical 1D} \\ e^\tau & \text{for critical 1D} \\ e^{e^{\sqrt{\tau}}} & \text{for 2D} \end{cases}$$

As this simple scaling indicates, for two dimensions the ‘entanglement’ given by the Schmidt rank scales exponentially with τ . The way to go for a 2D simulation is to look at the way the isometries have been implemented and try to remove the short-distance degrees of freedom. In the MERA approach proposed by Vidal this is done by implementing unitary transformations that act as disentanglers on the boundaries of all the blocks. The algorithm looks for the isometries variationally and the isometries are themselves decomposed into a sequence of so-called disentangling unitaries and isometries. The method has shown to be capable of simulating some 2D systems and even fermionic and anyonic systems (see Vidal (2010) and references therein). Nevertheless it has still some serious limitations on its accuracy for general 2D systems or frustrated systems. A lot of progress in the simulability of such systems using tensor networks is on its way.

6

Fermi and Fermi–Bose Hubbard models: methods of treatment

6.1. Introduction

Most of the methods used to solve Bose–Hubbard models (some of them discussed in the previous chapter) can be carried over to fermionic systems, although typically fermions are much harder to treat due to their non-local character. For example, for weakly interacting trapped fermions the mean-field Bardeen–Cooper–Schrieffer (BCS) method requires much more effort than the bosonic Bogoliubov–de Gennes approach. Quantum Monte Carlo methods notoriously suffer from the so-called ‘sign problem’ (negative probabilities). Naïve Gutzwiller ansatz in dimensions higher than 1 does not take the fermionic anticommutation relations into account properly (see for instance Fehrmann *et al.*, 2004a) due to non-existence of a standard Jordan–Wigner transformation (for generalizations see for instance Verstraete and Cirac (2005)).

In this chapter we therefore discuss in more detail the methods that are specific for fermions and Fermi–Bose mixtures. We focus mostly on the methods for applying the spin- $\frac{1}{2}$ Hubbard model in square or cubic lattices, although many of the physical applications concern trapped Fermi gases. We start by presenting the famous BCS and Hartree–Fock mean-field theories, which are applicable for weakly interacting Fermi gases. These theories give a good although simplified description of the superfluid phase for the case of attractive interactions, and of the normal phase (Fermi liquid) in the case of repulsive interactions. In Section 6.3 we discuss the phenomenon of BCS–BEC crossover and formulate the theory of resonant Fermi superfluidity. We then discuss mean-field solutions for the balanced case of equal spin-up and spin-down populations. The discussion of the imbalanced case is presented in Section 6.4. Section 6.5 is the first one that treats problems that are truly specific for the *lattice*; we discuss various important limits of the Hubbard model, such as the $t - J$ model. This section also covers the so-called slave boson approach and its mean-field solutions.

When we deal with Bose–Bose, Fermi–Fermi, or Fermi–Bose mixtures, it is always useful to study limiting cases that can be realized in experiments. One limit is the weakly interacting regime, where Hartree–Fock, BCS, or Landau’s Fermi liquid theory can be applied. Another one is the strong coupling limit of MI states, where a very useful method involves constructing an effective Hamiltonian describing the low-energy physics. Such a Hamiltonian will often correspond to a spin model if we deal with commensurate filling factors. If the Mott states involve states differing by an odd number of fermions (for instance, the presence or absence of a fermion), then the effective model will necessarily involve

composite fermions. In Section 6.6 we describe in detail how to derive such effective models. We conclude with Section 6.7, where we apply this derivation to obtain an effective low-energy Hamiltonian resulting from the Fermi–Bose Hubbard model. We then also discuss the related physics.

This chapter follows, to a great extent, the recent reviews of Bloch *et al.* (2008), Lee (2008), Giorgini *et al.* (2008), and Radzhovsky and Sheehy (2010).

6.2. Fermi Hubbard model and BCS theory

The starting point for describing a trapped gas of spin- $\frac{1}{2}$ weakly interacting fermions is the quantum field theory model described by the Hamiltonian

$$\hat{H}_F = \int d\mathbf{r} \left[\sum_{\sigma} \hat{\psi}_{\sigma}^{\dagger} \left(-\frac{\hbar^2}{2m} \nabla^2 \right) \hat{\psi}_{\sigma} + \sum_{\sigma} \hat{\psi}_{\sigma}^{\dagger} V(\mathbf{r}) \hat{\psi}_{\sigma} + g \left(\hat{\psi}_{\downarrow}^{\dagger} \hat{\psi}_{\uparrow}^{\dagger} \hat{\psi}_{\uparrow} \hat{\psi}_{\downarrow} \right) \right], \quad (6.1)$$

where $\sigma = \{\uparrow, \downarrow\}$ denotes the spin, the field operators obey fermionic anticommutation relations $\{\hat{\psi}(\mathbf{r})_{\sigma}, \hat{\psi}^{\dagger}(\mathbf{r}')_{\sigma'}\} = \delta_{\sigma\sigma'}\delta(\mathbf{r} - \mathbf{r}')$, V is an external potential that can describe a trap, a lattice, or both, and $g = 4\pi\hbar^2a_s/m$. Applying the standard approach and the tight-binding approximation discussed in Chapters 3 and 5, we obtain perhaps the best-known model of condensed-matter physics: the electronic (or for us atomic spin- $\frac{1}{2}$) Fermi Hubbard model, described by the Hamiltonian,

$$\hat{H}_{FH} = -t \sum_{\langle i,j \rangle, \sigma} (\hat{f}_{i\sigma}^{\dagger} \hat{f}_{j\sigma} + h.c.) + U \sum_i \hat{f}_{i\uparrow}^{\dagger} \hat{f}_{i\downarrow}^{\dagger} \hat{f}_{i\downarrow} \hat{f}_{i\uparrow} - \sum_{i,\sigma} \mu_{i\sigma} \hat{f}_{i\sigma}^{\dagger} \hat{f}_{i\sigma}, \quad (6.2)$$

where $\hat{f}_{i\sigma}^{\dagger}$ ($\hat{f}_{i\sigma}$) is the creation (annihilation) operator of σ fermions at site i .

The BCS theory is essentially a (mean-field) theory of pairing, or a theory of Gaussian fermionic states. When $U \ll t$, one can replace the quartic interaction term in the Hamiltonian, by a ‘Wick-averaged’ bilinear term

$$U \sum_i \hat{f}_{i\uparrow}^{\dagger} \hat{f}_{i\downarrow}^{\dagger} \hat{f}_{i\downarrow} \hat{f}_{i\uparrow} \simeq \left(\Delta_i \hat{f}_{i\uparrow}^{\dagger} \hat{f}_{i\downarrow}^{\dagger} + \Delta_i^* \hat{f}_{i\downarrow} \hat{f}_{i\uparrow} + W_{i\downarrow} \hat{f}_{i\uparrow}^{\dagger} \hat{f}_{i\uparrow} \right. \\ \left. + W_{i\uparrow} \hat{f}_{i\downarrow}^{\dagger} \hat{f}_{i\downarrow} - V_i \hat{f}_{i\uparrow}^{\dagger} \hat{f}_{i\downarrow} - V_i^* \hat{f}_{i\downarrow}^{\dagger} \hat{f}_{i\uparrow} \right), \quad (6.3)$$

where $\Delta_i = U\langle \hat{f}_{i\downarrow} \hat{f}_{i\uparrow} \rangle$, $W_{i\sigma} = U\langle \hat{f}_{i\sigma}^{\dagger} \hat{f}_{i\sigma} \rangle$, and $V_i^* = U\langle \hat{f}_{i\downarrow}^{\dagger} \hat{f}_{i\uparrow} \rangle$. The next steps are straightforward. If we consider the case $T = 0$, we diagonalize the Hamiltonian in eqn (6.2) and find its ground state, which is easy because the Hamiltonian has a bilinear form. We then calculate the ground-state averages of Δ_i , $W_{i\sigma}$, and V_i , and obtain in this way self-consistent, highly non-linear equations for these quantities. Typically, they then have to be treated numerically. The same method can be applied for $T > 0$; in such cases the averages have to be performed with respect to the quantum Boltzmann–Gibbs state, i.e. the thermal canonical state or even better the grand canonical state.

From now on we will neglect the trapping potential and assume translational invariance, i.e. set $\Delta_i = \Delta$, $W_{i\sigma} = W_{\sigma}$, and $V_i = V = 0$. In such cases, the Hartree–Fock terms W_{σ} can

be absorbed into chemical potentials. Assuming in addition a balanced mixture of spin-up and spin-down components, we Fourier transform the operators and obtain in momentum space the well known BCS Hamiltonian

$$\hat{H}_{\text{BCS}} = \sum_{\mathbf{k},\sigma} \left[(\epsilon_{\mathbf{k}} - \mu) \hat{f}_{\mathbf{k}\sigma}^\dagger \hat{f}_{\mathbf{k}\sigma} + \Delta \hat{f}_{\mathbf{k}\uparrow}^\dagger \hat{f}_{-\mathbf{k}\downarrow}^\dagger + \Delta^* \hat{f}_{-\mathbf{k}\downarrow} \hat{f}_{\mathbf{k}\uparrow} \right], \quad (6.4)$$

where in d dimensions $\epsilon_{\mathbf{k}} = t(2d - \sum_{v=1}^d \cos(k_v a))$ and μ has been shifted appropriately. Diagonalization of the above Hamiltonian is simple since it is reduced to a solution of the fermionic Bogoliubov–de Gennes equations. We introduce quasiparticle creation and annihilation operators,

$$\begin{aligned} \hat{g}_{\mathbf{k}\sigma}^\dagger &= u_{\mathbf{k}\sigma}^* \hat{f}_{\mathbf{k}\sigma}^\dagger + v_{\mathbf{k}\sigma}^* \hat{f}_{-\mathbf{k},-\sigma}^\dagger, \\ \hat{g}_{\mathbf{k}\sigma} &= u_{\mathbf{k}\sigma} \hat{f}_{\mathbf{k}\sigma} + v_{\mathbf{k}\sigma} \hat{f}_{-\mathbf{k},-\sigma}^\dagger, \end{aligned} \quad (6.5)$$

so that

$$H_{\text{BCS}} = \sum_{\mathbf{k},\sigma} E_{\mathbf{k}} \hat{g}_{\mathbf{k}\sigma}^\dagger \hat{g}_{\mathbf{k}\sigma} + \text{const.} \quad (6.6)$$

In the balanced case neither $u_{\mathbf{k}}$ nor $v_{\mathbf{k}}$ depend on the spin direction; also $u_{\mathbf{k}} = u_{-\mathbf{k}}$ and $v_{\mathbf{k}} = -v_{-\mathbf{k}}$. The BdG equations then read

$$E_{\mathbf{k}} u_{\mathbf{k}} = (\epsilon_{\mathbf{k}} - \mu) u_{\mathbf{k}} + \Delta^* v_{\mathbf{k}}, \quad (6.7)$$

$$E_{\mathbf{k}} v_{\mathbf{k}} = -(\epsilon_{\mathbf{k}} - \mu) v_{\mathbf{k}} + \Delta u_{\mathbf{k}}, \quad (6.8)$$

implying that the BCS quasiparticle energy is $E_{\mathbf{k}} = \sqrt{(\epsilon_{\mathbf{k}} - \mu)^2 + |\Delta|^2}$. In order to ensure that the quasiparticle operators fulfill the canonical anti-commutation relations, we normalize $|u_{\mathbf{k}}|^2 + |v_{\mathbf{k}}|^2 = 1$.

The ground state is a ‘vacuum’ of the quasiparticles, which corresponds to a ‘condensate’ of Cooper pairs of fermions of zero total momentum. Since working with fixed number of particles is technically difficult, one usually expresses the BCS wave function in the form of a coherent state,

$$|\text{BCS}\rangle \propto \exp\left(\alpha \hat{b}_0^\dagger\right) |0\rangle = \prod_{\mathbf{k}} (u_{\mathbf{k}}^* + v_{\mathbf{k}}^* \hat{f}_{\mathbf{k},\uparrow}^\dagger \hat{f}_{-\mathbf{k},\downarrow}^\dagger) |0\rangle \quad (6.9)$$

where $\hat{b}_0 \propto \sum_{\mathbf{k}} (v_{\mathbf{k}}^*/u_{\mathbf{k}}^*) \hat{f}_{\mathbf{k},\uparrow}^\dagger \hat{f}_{-\mathbf{k},\downarrow}^\dagger$ is the ‘bosonic’ pair creation operator. Notice that pairing is in momentum space. Within the BCS description, the magnitude of Δ is determined by the standard gap equation $\Delta = (U/N) \sum_{\mathbf{k}} \langle \hat{f}_{-\mathbf{k}\downarrow} \hat{f}_{\mathbf{k}\uparrow} \rangle = (U/N) \sum_{\mathbf{k}} u_{\mathbf{k}}^* v_{-\mathbf{k}} = -(U/N) \sum_{\mathbf{k}} u_{\mathbf{k}}^* v_{\mathbf{k}}$, so that we get

$$\Delta = -\frac{U}{2N} \sum_{\mathbf{k}} \frac{\Delta}{\sqrt{(\epsilon_{\mathbf{k}} - \mu)^2 + \Delta^2}}, \quad (6.10)$$

where N is the total number of sites. For repulsive interactions, the only possible solution is $\Delta = 0$ and the system is, for $\mu \leq 0$, in a trivial vacuum state (no particles), for $0 < \mu < 4td$,

in a normal (Fermi liquid) state, and, finally, for $\mu \geq 4td$, in a band-insulator state with all sites doubly occupied. For attractive interactions, no matter how small, there is a non-zero solution for Δ for $0 < \mu < 4td$. The system acquires a gap in the spectrum and becomes superfluid. In the next section we will derive extended BCS equations for the case of balanced BCS–BEC crossover and then perform a continuous limit, in which analytic treatment is possible.

6.3. Balanced BCS–BEC crossover

6.3.1 Feshbach resonances

Trapped ultracold atomic Fermi gases allow us to study one of the most fundamental problems of many-body physics, namely a two-component attractive Fermi gas with extremely strong interactions. This is possible due to the ability to tune the interaction using a Feshbach resonance. One can investigate the crossover from a BCS superfluid, when the attraction is weak and pairing only shows up in momentum space, to a Bose–Einstein condensate of tightly bound pairs in real space.

Feshbach resonance in scattering of fermions occurs when ultracold fermions scatter in an ‘open’ channel, where they are weakly coupled, via the hyperfine interaction, to a ‘closed’ channel (molecular state) that has similar energy. In the open-channel, fermion scattering is characterized by the s -wave scattering amplitude $f_0(k)$. It follows from the unitarity and analyticity of the scattering matrix (Landau and Lifshitz, 1987) that the scattering amplitude must take the form

$$f_0(k) = \frac{1}{-a_s^{-1} + \frac{1}{2}r_0k^2 - ik}, \quad (6.11)$$

where a_s is the s -wave scattering length, and r_0 is the effective range. Note that in the resonant regime r_0 is negative (Gurarie and Radzhovskiy, 2007a). The energy of the bound state in the closed-channel can be tuned through zero by adjusting an external magnetic field B . In effect, the scattering length diverges as

$$a_s(B) = a_{bg} \left(1 - \frac{B_w}{B - B_0} \right), \quad (6.12)$$

where a_{bg} refers to the off-resonant background scattering length, B_0 is the resonance position (in magnetic field units) at which the bound-state energy crosses zero, and B_w is the resonance width.

6.3.2 Theory of resonant Fermi superfluidity

A natural framework to study the BCS–BEC crossover is a two-channel Bose–Fermi resonance model in which fermions in an open channel couple resonantly to a closed-channel bound state (Holland *et al.*, 2001; Timmermans *et al.*, 2001; Ohashi and Griffin, 2002;

Drummond and Kheruntsyan, 2004). It is described by the Hamiltonian

$$\hat{H}_{\text{BF}} = \int d\mathbf{r} \left[\sum_{\sigma} \hat{\psi}_{\sigma}^{\dagger} \left(-\frac{\hbar^2}{2m} \nabla^2 \right) \hat{\psi}_{\sigma} + \hat{\psi}_{\text{B}}^{\dagger} \left(-\frac{\hbar^2}{4m} \nabla^2 + \nu \right) \hat{\psi}_{\text{B}} + \tilde{g} \left(\hat{\psi}_{\text{B}}^{\dagger} \hat{\psi}_{\uparrow} \hat{\psi}_{\downarrow} + \text{h.c.} \right) \right], \quad (6.13)$$

where $\hat{\psi}_{\sigma}(\mathbf{r})$ are fermionic field operators describing atoms in the open channel. The two different hyperfine states are labeled by the spin variable σ . The bound state in the closed channel is denoted by the bosonic field operator $\hat{\psi}_{\text{B}}(\mathbf{r})$. Its energy is detuned by ν with respect to the open channel continuum. Finally, \tilde{g} is the coupling constant for the conversion of two atoms into a closed-channel state and vice versa.

It can be shown (Levinsen and Gurarie, 2006; Gurarie and Radzhivovsky, 2007a), that in the regime of low energies and densities, i.e. when $kr_0 \ll 1$, the two-channel model can be reduced to a simpler one-channel model, described formally by the same Hamiltonian as H_{BCS} , eqn (6.4),

$$\hat{H} = \sum_{\mathbf{k}, \sigma} (\epsilon_{\mathbf{k}} - \mu) \hat{f}_{\mathbf{k}\sigma}^{\dagger} \hat{f}_{\mathbf{k}\sigma} + \frac{\lambda}{V} \sum_{\mathbf{kq}\mathbf{p}} \hat{f}_{\mathbf{k}\uparrow}^{\dagger} \hat{f}_{\mathbf{p}\downarrow}^{\dagger} \hat{f}_{\mathbf{k+q}\downarrow} \hat{f}_{\mathbf{p-q}\uparrow}, \quad (6.14)$$

with single-particle energy $\epsilon_{\mathbf{k}} = \hbar^2 k^2 / 2m$ and volume V . The main difference to the theory discussed in the previous subsection is that now the attractive interactions are parametrized by the parameter $\lambda < 0$ instead of U . In fact, within a relatively straightforward T -matrix approximation and using the relation $-f_0(k) = mT_k / 4\pi\hbar^2$, one can relate the parameter λ to U , or more precisely to the magnetic-field-dependent scattering length (Regal and Jin, 2003; Bartenstein *et al.*, 2004a):

$$\frac{m}{4\pi a_s \hbar^2} = \frac{1}{\lambda} + \frac{1}{V} \sum_{\mathbf{k}} \frac{1}{2\epsilon_{\mathbf{k}}}. \quad (6.15)$$

The second term in eqn (6.15) has to be regularized by a microscopic momentum cut-off scale $\Lambda \sim 1/d$. This scale is determined by the size d of the molecular bound state in the closed channel. This leads (taking $\hbar = 1$) to

$$a_s(\lambda) = \frac{m}{4\pi} \frac{\lambda}{1 - \lambda/\lambda_c} = \frac{m}{4\pi} \lambda_R, \quad (6.16)$$

where λ_R can be called the renormalized coupling (Radzhivovsky and Sheehy, 2010) and $\lambda_c = -\frac{2\pi^2}{\Lambda m}$ is the critical coupling, at which the scattering length diverges.

In the lattice case, the analogous relationship reads:

$$\frac{V}{U} = \frac{V}{\lambda} + \sum_{\mathbf{k}} \frac{1}{2\epsilon_{\mathbf{k}}}, \quad (6.17)$$

where now the volume V is the effective volume of the Wannier function in the lattice site, $V = (\int |w(\mathbf{r})|^4 d\mathbf{r})^{-1}$, and the momentum cut-off is set by the lattice constant, $\Lambda \sim 1/a$.

Apart from the gas parameter (a measure of the resonant interaction strength, $k_{\text{F}}a_s$, with k_{F} being the Fermi momentum), an important dimensionless quantity that characterizes Feshbach resonances is the dimensionless resonance width, which is defined as the ratio between the resonance width (proportional to B_w) and the Fermi energy, ϵ_{F} :

$$\gamma = \frac{8}{\pi} \frac{1}{k_{\text{F}}|r_0|}. \quad (6.18)$$

In the case of narrow Feshbach resonances, with $\gamma \ll 1$, one can use a perturbative approach in γ . Unfortunately, most of the experimentally accessible s -wave resonances are broad, with $\gamma \gg 1$. In such situations, it is difficult to apply any well-controlled approximation (Radzhovskiy and Sheehy, 2010). Nevertheless, it is very useful to look at the mean-field BCS solution of the problem. In fact, another way to systematically treat the BCS–BEC crossover is to replace the spin- $\frac{1}{2}$ fermions by fermions having N_f internal states (known as ‘flavors’, in an analogy with high-energy physics). The mean-field BCS theory then becomes exact in the $N_f \rightarrow \infty$ limit (Nikolić and Sachdev, 2007; Veillette *et al.*, 2007), and one can calculate systematic $1/N_f$ corrections.

6.3.3 Mean-field description of balanced BCS–BEC model

In the standard BCS approach at $T = 0$, one can regard the BCS wave function as a variational trial function that depends on the variational parameters Δ and μ . One can then calculate the mean value of the grand canonical mean ground-state energy by averaging $\hat{H}_{\mu} = \hat{H} - \mu\hat{N}$. The grand canonical ground-state energy density reads

$$E_{\text{G}} = -\frac{\Delta^2}{\lambda} + V^{-1} \sum_k (\xi_k - E_k) = -\frac{m}{4\pi a_s} \Delta^2 + \int \frac{d^3 k}{(2\pi)^3} \left(\xi_k - E_k + \frac{\Delta^2}{2\epsilon_k} \right), \quad (6.19)$$

with $\xi_k \equiv \epsilon_k - \mu$ and $E_k = \sqrt{\xi_k^2 + \Delta^2}$. In the second equality, λ has been reexpressed in terms of the scattering length (eqn (6.15)), thereby regularizing the pairing integral. In order to get the self-consistent mean-field solutions, one now has to minimize the energy $E_{\text{G}}(\Delta, \mu)$ with respect to Δ (to ensure that $\Delta = \lambda \langle \hat{f}_{\downarrow}(\mathbf{r}) \hat{f}_{\uparrow}(\mathbf{r}) \rangle$) and with respect to the chemical potential (to enforce the fixed fermion density $n = -\frac{\partial E_{\text{G}}}{\partial \mu} = V^{-1} \sum_{\mathbf{k}, \sigma} \langle \hat{f}_{\mathbf{k}\sigma}^{\dagger} \hat{f}_{\mathbf{k}\sigma} \rangle$). The results of the BCS calculations, together with the $1/N_f$ corrections and the comparison to quantum Monte Carlo simulations at unitarity ($a_s = \infty$) are presented in Figure 6.1.

In the two limiting cases one can even obtain analytic results. In the BCS regime ($1 < -\frac{1}{k_{\text{F}}a_s}$), $\mu > 0$, and $\Delta \ll \mu$, one finds (Sheehy and Radzhovskiy, 2007a):

$$E_{\text{G}} \approx -\frac{m}{4\pi a_s} \Delta^2 - \frac{8c}{15} \mu^{5/2} - c\sqrt{\mu} \Delta^2 \left(\frac{1}{2} - \ln \frac{\Delta}{8e^{-2}\mu} \right), \quad (6.20)$$

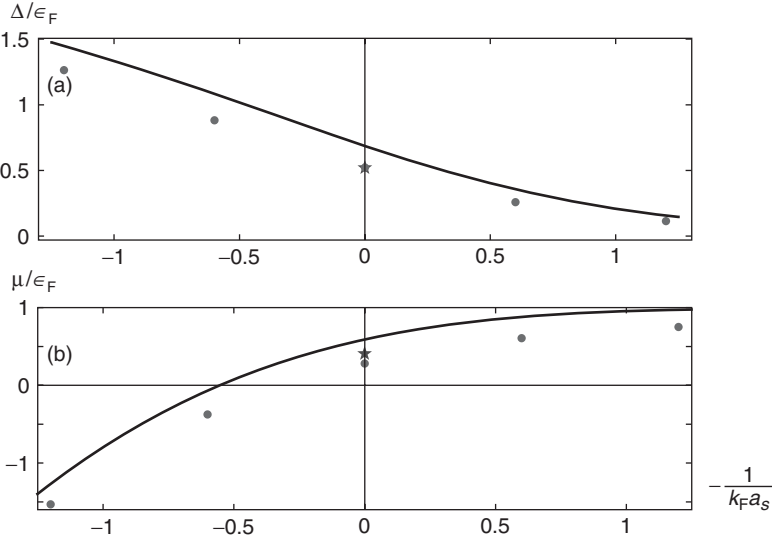


Figure 6.1 (a) Order parameter Δ and (b) chemical potential μ in units of the Fermi energy as a function of $-(k_F a_s)^{-1}$ for the BEC regime (on the left) and the BCS regime (on the right). Solid lines correspond to the mean-field results (Marini *et al.*, 1998). The dots include the $O(1/N_f)$ corrections (Veillette *et al.*, 2007) evaluated at $N_f = 1$. The star symbols at unitarity ($-(k_F a_s)^{-1} = 0$) are the results of the quantum Monte Carlo calculation of Carlson *et al.* (2003). From Radzhivovsky and Sheehy (2010).

where $c = \frac{m^{3/2}}{\sqrt{2}\pi^2}$ and the 3D density of states $N(\epsilon) = c\sqrt{\epsilon}$. Equation (6.20) is non-analytic in Δ , reflecting the well-known fact that an arbitrary weak attraction yields a pairing instability. To leading order in $\Delta \ll \mu$, this gives the standard BCS expressions/equations for the gap ($0 = \frac{\partial E_G}{\partial \Delta}$) and for the density ($n = -\frac{\partial E_G}{\partial \mu}$),

$$\Delta \approx \Delta_{\text{BCS}} \equiv 8e^{-2}\epsilon_F \exp\left(\frac{\pi}{2k_F a_s}\right), \quad (6.21)$$

$$\mu \approx \epsilon_F, \quad (6.22)$$

where the Fermi energy ϵ_F is defined in terms of the particle density via $n = \frac{4}{3}c\epsilon_F^{3/2}$.

In the BEC regime ($-\frac{1}{k_F a_s} < -1$), in which $\mu < 0$ and $|\mu| \gg \Delta$, one instead obtains the analytic Landau form

$$E_G \approx -\frac{m}{4\pi a_s} \Delta^2 + \frac{1}{2}c\sqrt{|\mu|}|\Delta|^2 \left(\pi + \frac{\pi}{32} \frac{\Delta^2}{\mu^2}\right), \quad (6.23)$$

leading to the following gap and number equations:

$$\mu \approx -\frac{1}{2ma_s^2}, \quad (6.24)$$

$$\Delta \approx \epsilon_F \sqrt{\frac{16}{3\pi k_F a_s}}, \quad (6.25)$$

with μ equal to one half of the two-atom binding energy in the BEC limit.

The BCS theory can also be applied to the case of $T > 0$. The rough estimate for the critical temperature is of course $k_B T_c \simeq \Delta$. In the BCS one can obtain a very precise value for T_c by taking into account many-body corrections to the BCS theory, which are known as Melik–Bakhudarov corrections (Gor’kov and Melik-Barkhudarov, 1961). This value is given by

$$T_c = \frac{8 \exp(C)}{(4e)^{1/3} \pi e^2} T_F \exp(-\pi(2k_F|a_s|)), \quad (6.26)$$

where $C = 0.577\dots$ is the Euler constant. In the deep BCS limit, BCS estimation of the critical temperature becomes less accurate (see Figure 6.2). On the other hand, in this limit one can simply use the BEC theory for molecules.

6.3.4 Unitarity limit and universality

In the so-called *unitarity* limit, i.e. $a_s \rightarrow \infty$, the ground-state energy density, gap, and density are well defined: $E_g = 0.5906\frac{3}{5}n\epsilon_F$, $\Delta = 0.6864\epsilon_F$, and $\mu = 0.5906\epsilon_F$. As we see, all these quantities attain a universal form in this limit, and depend on the only available energy scale, ϵ_F . Of course, this universality extends to the whole thermodynamics, as first

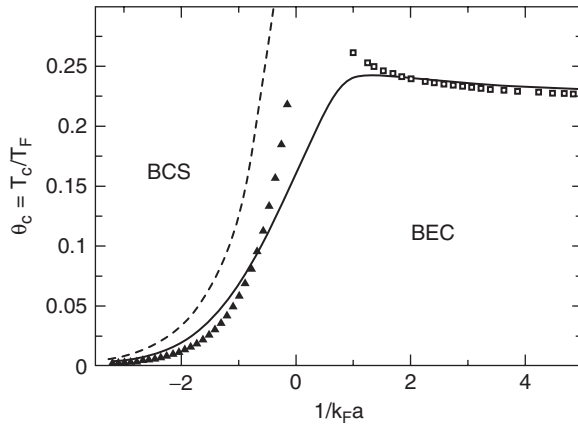


Figure 6.2 Critical temperature of the homogeneous gas as a function of the coupling strength. The exact asymptotic results in the BCS and BEC limits are indicated by triangles and squares, respectively. At unitarity $T_c = 0.16 T_F$. The dashed line schematically denotes the quantum Monte Carlo estimate of the evolution of T^* , i.e. a characteristic temperature below which strong pairing appear. Reprinted from Haussmann *et al.* (2007).

pointed out in the context of nuclear physics (Baker, 1999; Heiselberg, 2001). The free energy per particle F/N , is a universal function of ϵ_F and $\theta = T/T_F$:

$$f(T, n) = \epsilon_F f(\theta).$$

The entropy density is given by $s = -f'(\theta) \geq 0$, which implies that $f(\theta)$ is a decreasing function of θ . One can show that, for small θ , $f(\theta) \simeq f(0) + \alpha\theta^4$, which is very different to the case of the ideal Fermi gas, for which $f(\theta) - f(0) \propto \alpha\theta^2$. The chemical potential is given by $\mu = (5/3)\epsilon_F f(\theta) \equiv \xi(\theta)$ while the pressure is $p = \mu n - n\epsilon_F f(\theta)$. The equation of state is $p = 3u/3$, where u is the internal energy. At $T = 0$, the physics at unitarity is thus governed by a single universal number $\xi(0)$. Recent measurements provide the following values: $\xi(0) \sim 0.32 \pm 0.1$ (Bartenstein *et al.*, 2004a) and $\xi(0) \sim 0.46 \pm 0.05$ (Partridge *et al.*, 2006). These results compare well with fixed-node Green function quantum Monte Carlo results (Carlson *et al.*, 2003; Astrakharchik *et al.*, 2004).

6.4. Mean-field description of imbalanced BCS–BEC crossover

While the balanced BCS–BEC crossover is relatively well understood, this is not the case for *imbalanced* mixtures; that is, when the number of spins up and spins down is not equal. The possibility of exotic pairing in imbalanced fermionic gases is a subject of very intense research. In particular, the mismatch between the Fermi momenta $k_{F\uparrow}$ and $k_{F\downarrow}$ can lead to the appearance of pairs with finite momenta in the so-called FFLO phase, as first proposed in Fulde and Ferrell (1964) and Larkin and Ovchinnikov (1964). To describe such a system one may use the same Hamiltonian as before, except that one has to introduce two distinct chemical potentials for the two species $\mu_\sigma = (\mu_\uparrow, \mu_\downarrow)$ in order to impose separately conserved fermion numbers $N_\sigma = (N_\uparrow, N_\downarrow)$ or, equivalently, total fermion number $N = N_\uparrow + N_\downarrow$ and species imbalance $\Delta N = N_\uparrow - N_\downarrow$. The corresponding grand canonical Hamiltonian $\hat{H}_{\mu_\sigma} = \hat{H} - \mu\hat{N} - h\Delta\hat{N}$ is then

$$\hat{H} = \sum_{\mathbf{k}, \sigma} (\epsilon_k - \mu_\sigma) \hat{f}_{\mathbf{k}\sigma}^\dagger \hat{f}_{\mathbf{k}\sigma} + \frac{\lambda}{V} \sum_{\mathbf{kqp}} \hat{f}_{\mathbf{k}\uparrow}^\dagger \hat{f}_{\mathbf{p}\downarrow}^\dagger \hat{f}_{\mathbf{k+q}\downarrow} \hat{f}_{\mathbf{p-q}\uparrow}, \quad (6.27)$$

with $\mu_\uparrow = \mu + h$ and $\mu_\downarrow = \mu - h$ related to the total-number chemical potential μ and species-imbalance chemical potential h , which is nothing other than an effective Zeeman energy.

The thermodynamics for the imbalanced resonant Fermi gas now depends on $N, \Delta N, T$, and a_s , and the extension of the BCS–BEC crossover has to be numerically treated. Standard techniques include quantum Monte Carlo (Carlson and Reddy, 2005; Pilati *et al.*, 2005), mean-field theory (Pao *et al.*, 2006; Sheehy and Radzhovsky, 2007a,b; Parish *et al.*, 2007), the large- N_f (fermion flavor) (Nikolić and Sachdev, 2007; Veillette *et al.*, 2007, 2008) and the dimensional ϵ expansions (Nihsida and Son, 2007). Standard mean-field theory (Sheehy and Radzhovsky, 2007a) involves minimization of the mean-field ground-state energy E_G with respect to variational parameters for a fixed μ and h . Such an approach

gives results that agree qualitatively with experiments. The derivatives with respect to μ and h

$$\frac{\partial E_G}{\partial \mu} = -\frac{N}{V}, \quad \frac{\partial E_G}{\partial h} = -\frac{\Delta N}{V}, \quad (6.28)$$

determine, respectively, the total atom number, $N = N_\uparrow + N_\downarrow$, and the species imbalance, $\Delta N = N_\uparrow - N_\downarrow$, both of which can be controlled in cold-atom experiments. In Sheehy and Radzhovsky (2007a), the variational ansatz for the gap has the form

$$\Delta(\mathbf{r}) = \Delta_{\mathbf{Q}} e^{i\mathbf{Q}\cdot\mathbf{r}}, \quad (6.29)$$

with $\Delta_{\mathbf{Q}}$ and \mathbf{Q} being variational parameters. Note that this ansatz for $\mathbf{Q} \neq 0$ describes the simplest Fulde–Ferrell–Larkin–Ovchinnikov-type (FFLO) state (Fulde and Ferrell, 1964; Larkin and Ovchinnikov, 1964). Using eqn (6.29), one can derive the ground-state energy density $E_G(\Delta_{\mathbf{Q}}, \mathbf{Q}, \mu, h)$, which, following Sheehy and Radzhovsky (2007a), reads in three dimensions:

$$E_G = -\frac{m}{4\pi a_s} |\Delta_{\mathbf{Q}}|^2 + \int \frac{d^3 k}{(2\pi)^3} \left(\xi_k + \frac{Q^2}{8m} - E_k + \frac{\Delta_{\mathbf{Q}}^2}{2\epsilon_k} \right) + \int \frac{d^3 k}{(2\pi)^3} [E_{\mathbf{k}+} \Theta(-E_{\mathbf{k}+}) + E_{\mathbf{k}-} \Theta(-E_{\mathbf{k}-})]. \quad (6.30)$$

Here $\Theta(x)$ is the Heaviside step function, and

$$E_k \equiv \left[\left(\xi_k + \frac{Q^2}{8m} \right)^2 + \Delta_{\mathbf{Q}}^2 \right]^{1/2}, \quad (6.31)$$

$$E_{\mathbf{k}\pm} \equiv E_k \mp \left(h - \frac{\mathbf{k} \cdot \mathbf{Q}}{2m} \right). \quad (6.32)$$

The minimum of E_G , eqn (6.30), for the stationary $\Delta_{\mathbf{Q}}$ and \mathbf{Q} can be found by supplementing the gap equation with the condition

$$\frac{\partial E_G}{\partial Q} = 0. \quad (6.33)$$

Quoting Radzhovsky and Sheehy (2010):

An important point to keep in mind, for a proper analysis of $E_G(\Delta_{\mathbf{Q}}, \mathbf{Q}, \mu, h)$, is that not every simultaneous solution of the gap and number equations corresponds to a physical ground state of the system; the key additional criterion is that the solution $\Delta_{\mathbf{Q}}$ must also be a *minimum* of E_G at fixed μ, h . The verification that an extremum solution is indeed a minimum is particularly essential when (as is the case for a polarized Fermi gas) there is a possibility of a first-order transition, where E_G exhibits local maxima and saddle points that separate its local minima.

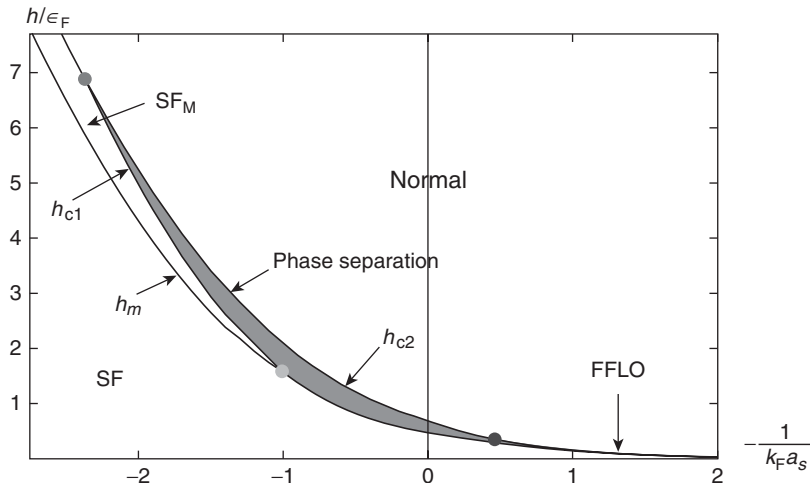


Figure 6.3 Mean-field phase diagram of imbalanced Fermi gases as a function of the coupling strength, $-\frac{1}{k_F a_s}$, and the chemical potential difference, h . Regimes of imbalanced magnetized superfluid (SF_M) are bounded by h_m and h_{c1} , and a strongly-interacting normal Fermi liquid. The region of the balanced BCS–BEC crossover superfluid phase is denoted SF and the central shaded region is a regime of phase separation. The FFLO region is indicated by an arrow and bounded. From Radzhivsky and Sheehy (2010).

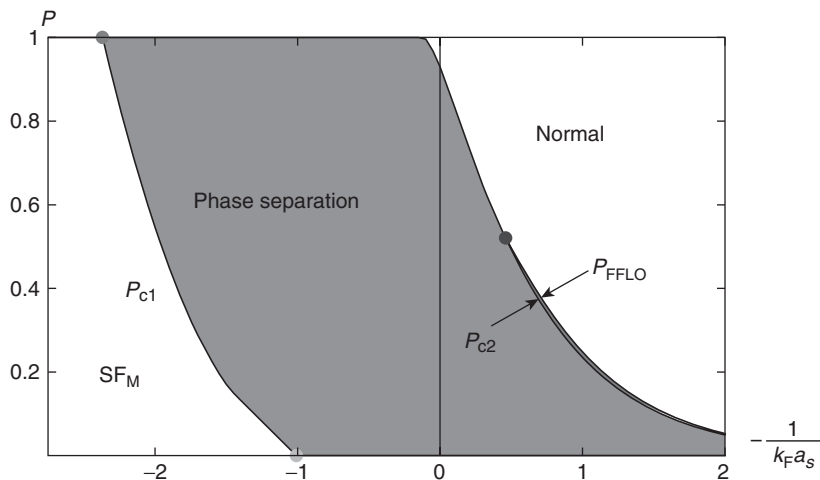


Figure 6.4 Mean-field phase diagram of imbalanced Fermi gases as a function of the coupling strength, $-\frac{1}{k_F a_s}$, and the imbalance, P . SF_M indicates the regime of magnetized (imbalanced) superfluid, and the FFLO region is bounded by P_{FFLO} and P_{c2} . From Radzhivsky and Sheehy (2010).

The mean-field phase diagrams are shown in Figures 6.3 and 6.4 for a fixed density and h , and for a fixed density and imbalance, respectively. Mean field predicts that at small chemical potential imbalance, the fully paired superfluid phase (with $\mathbf{Q} = \mathbf{0}$ and $\Delta_{Q=0} = \Delta = \Delta_{\text{BCS}}$) is stable practically across the whole BCS–BEC crossover. It is separated from the normal phase by a region of phase separation where the gas inhomogeneously coexists between two phases. The FFLO phase appears in three dimensions in a very restricted region of parameters. Amazingly, this is not the case in one dimension, where the theory predicts that FFLO should provide the dominant mechanism of imbalance superfluidity (see Roscilde *et al.* (2009) and references therein). Recent beautiful experiments by the group of Hulet have started to confirm these predictions (Liao *et al.*, 2010).

6.5. Fermi Hubbard model and strongly correlated fermions

Let us concentrate now on the main subject of this chapter, namely the methods that are specific for the lattice models. We will start by discussing perhaps the best-known model describing strongly correlated fermions: the Hubbard model for electrons, or more generally spin- $\frac{1}{2}$ fermions. So far, there is no consensus concerning the mechanisms and nature of high T_c superconductivity. Nevertheless, many researchers believe that the Hubbard model can provide important insights into the high T_c superconductivity of cuprates.

Cuprates were the first known high-temperature superconductors, and all of them have a layered structure, consisting typically of several oxygen–copper planes (see Figure 6.5).

The low-energy physics can thus be described by a simple model of electrons hopping in a 2D square lattice. At low temperatures tight-binding approximations can be used and we end up with a single-band Hubbard model, described by the Hamiltonian,

$$\hat{H} = - \sum_{(i,j),\sigma} t_{ij} (\hat{f}_{i\sigma}^\dagger \hat{f}_{j\sigma} + h.c.) + \frac{U}{2} \sum_i \hat{f}_{i\uparrow}^\dagger \hat{f}_{i\downarrow}^\dagger \hat{f}_{i\downarrow} \hat{f}_{i\uparrow} - \mu \sum_{i,\sigma} \hat{f}_{i\sigma}^\dagger \hat{f}_{i\sigma}, \quad (6.34)$$

where $\hat{f}_{i\sigma}^\dagger$ ($\hat{f}_{i\sigma}$) is the creation (annihilation) operator of an electron with spin σ . The hopping matrix element t_{ij} between sites i and j is not restricted to the nearest neighbors.

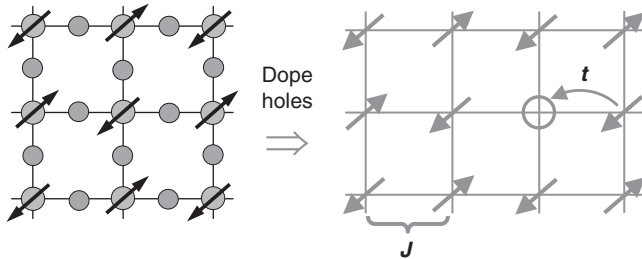


Figure 6.5 Left: schematics of a Cu–O layer (on the left) forming a typical cuprate. Copper atoms sit on a square lattice with oxygen atoms in between. Right: one-band model with electron hopping rate t corresponding to the simplified electronic structure. J denotes the antiferromagnetic super-exchange between spins on neighboring sites. From Lee *et al.* (2006). Figure in color online.

We denote nearest-neighbor hopping by t and further neighbor hopping by t' , t'' etc. U is the repulsive energy of a pair of fermions with opposite spin on the same site and μ denotes the chemical potential.

The fermionic Hubbard model at half-filling (one electron per site) undergoes a metal-to-insulator transition as the ratio U/t is increased. The insulator corresponds to the MI (Mott, 1949) that we already know well from the Bose–Hubbard model. There is exactly one particle per site and the insulating effect is caused solely by strong repulsion. This is in contrast to a band insulator, which has two electrons of opposite spin per site, and cannot have more in the lowest band due to the Pauli exclusion principle. For large enough U/t , fermions remain localized at the lattice sites because any hopping leads to double occupation of some site, *ergo* there is a large energy cost, U . A fermionic MI is also predicted to be antiferromagnetic because antiferromagnetic alignment permits virtual hopping to gain a super-exchange energy $J = 4t^2/U$, whereas hopping is strictly forbidden by Pauli exclusion for parallel spins (see Lee, 2008). Fermionic MI has been realized in beautiful experiments by Jördens *et al.* (2008) and Schneider *et al.* (2008).

Electron vacancies, also called ‘holes’, can be introduced into the copper–oxygen layers in a process called hole doping—this leads to even more complex and interesting physics. In condensed matter, doping is typically realized by introducing a charge reservoir away from the copper–oxygen planes, so that this reservoir removes electrons for the plane. For ultracold atoms the number of ‘spin-up’ and ‘spin-down’ atoms can be controlled independently. Thus in principle one can easily mimic the effect of doping, although in the presence of the confining harmonic potential it is difficult to achieve homogeneous doping in a well-controlled way. One can circumvent this problem in repulsive Fermi–Bose mixtures. In such mixtures, composite fermions consisting of a fermion (spin-up or down) and a bosonic hole may form (as described in Section 6.7), and their number can be controlled by adding bare bosons to the system (Eckardt and Lewenstein, 2010).

The schematic phase diagram that results from hole doping in the plane spanned by temperature T and hole concentration x is shown in Figure 6.6. At low x and low T , the antiferromagnetic order is stable. With increasing x , the antiferromagnetic order is rapidly destroyed by a small percentage of holes. For larger x , a superconducting phase appears. The superconductor is believed to be of d -wave type. The transition temperature reaches a maximum at the optimal doping, of about 15%. The high T_c superfluid region has a characteristic bell shape for all hole-doped cuprates, even though the maximum T_c varies from about 40 K to 93 K and higher. The region below the dashed line in Figure 6.6 in the phase diagram, above T_c in the underdoped region, where x is smaller than optimal, is an exotic metallic state called the pseudogap phase. Below the dotted line there is a region of strong fluctuations of the superconducting phase characterized by the so-called Nernst effect (Lee, 2008).

Related Fermi Hubbard models Apart from the Hubbard model for spin- $\frac{1}{2}$ fermions, there are many related Fermi Hubbard models that are the subject of considerable interest, and may be realized with cold atoms in optical lattices. For example, the asymmetric Hubbard model, describing a mixture of light and heavy fermions, has been studied by Ziegler’s group, who have, in particular, shown quantum phases with self-induced disorder (Ates and Ziegler, 2005; Ziegler, 2006). The models considered by Ziegler in limiting cases involve tunneling of light fermions only, as in the famous Falicov–Kimball model (Falicov and Kimball, 1969). Such Fermi–Fermi mixtures can be realized with ultracold atoms.

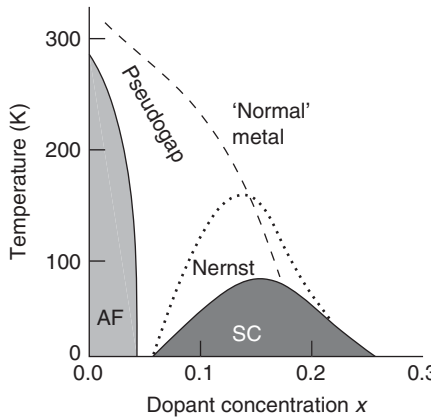


Figure 6.6 Schematic phase diagram of high T_c materials in the T - x plane, where T denotes the temperature and x is the dopant concentration. AF and SC are antiferromagnet and d -wave superconductor, respectively. Fluctuations of the SC appear below the dotted line corresponding to the Nernst effect. The pseudogap region extends below the dashed line. From Lee *et al.* (2006).

There has been thus considerable interest in studying $SU(N)$ symmetric Hubbard models of fermions and bosons (for an early review see Hofstetter (2006)). Recently, there has been a revival of interest in these systems, since it has been shown that they can be realized with ultracold earth alkali atoms (see Cazalilla *et al.* (2009), Hermele *et al.* (2009) and Gorshkov *et al.* (2010)).

Another group of models that can be realized with atoms are Hubbard models for particles with higher spin. In Eckert *et al.* (2007) effective spin Hamiltonians for spin- $\frac{3}{2}$ and spin- $\frac{5}{2}$ ultracold spinor gases, described by the spinor version of the Hamiltonian in eqn (6.34) have been derived and investigated. The same system has been studied in one dimension using the bosonization approach (Lecheminant *et al.*, 2005), and the exact Bethe ansatz method (Controzzi and Tsvelik, 2006). An alternative approach to the spin- $\frac{3}{2}$ and spin- $\frac{5}{2}$ models is presented in Chapter 7 (see Shirmai and Lewenstein (2011)).

Very recently there has been also a lot of interest of realizing 2D exotic metals and in particular non-Fermi-liquid metals (like the ones that are believed to appear in the phase diagram of the spin- $\frac{1}{2}$ Fermi Hubbard model) and Bose metals (see Chapter 15). The latter are believed to appear in Bose Hubbard models with ring (four-boson) exchange in the square lattice (Sheng *et al.*, 2008). Recently it has been conjectured in (Fisher *et al.*, 2010) (see Chapter 15) that an asymmetric Hubbard model, in which attractive Hubbard model, in which spin-up and spin-down particles tunnel differently, exhibits the following phases:

- (i) for small U/t it is a normal metal
- (ii) for large U/t it is a paired superfluid
- (iii) at intermediate U/t it should exhibit a Cooper-pair Bose-metal phase.

6.5.1 $t - J$ model

Returning to the single-band Fermi Hubbard model in eqn (6.34), in the limit of large repulsive interactions, $U \gg t, \mu$, there can be only one, or zero particles at a site. In this

limit the model is termed in the literature the ‘ $t - J$ ’ model (see Spalek and Oleś (1977) and Auerbach (1994)). As we have remarked above, when the system is at full filling with respect to the particles, so that there is one fermion (with spin up or down) at each site, the system is in the MI state. The effective Hamiltonian reduces to that of Heisenberg quantum antiferromagnet with the magnetization fixed by the corresponding numbers of spin-up and spin-down fermions (or external ‘magnetic’ field). In particular, if these numbers are equal (i.e. at half filling with respect to polarized particles), the system then has a zero net magnetization (i.e. it is in a vanishing ‘magnetic’ field).

Let us now analyse how this situation changes in the presence of doping. As we have mentioned before, doped MIs might provide clues to enable us to understand the high T_c superconductivity of cuprates (see Lee *et al.* (2006) and Lee (2008)). It is thus natural that they are widely considered and studied in the atomic context (see Klein and Jaksch (2006), Koponen *et al.* (2006*a,b*) and Eckardt and Lewenstein (2010)). The Hamiltonian of the $t - J$ model reads

$$\hat{H} = P \left[\sum_{(ij),\sigma} t_{ij} f_{i\sigma}^\dagger \hat{f}_{j\sigma} + J \sum_{\langle ij \rangle} \left(\mathbf{S}_i \cdot \mathbf{S}_j - \frac{1}{4} \hat{n}_i \hat{n}_j \right) \right] P. \quad (6.35)$$

The second term in the Hamiltonian is exactly the antiferromagnetic Heisenberg model, describing super-exchange interactions between local spins $\mathbf{S}_i = \frac{1}{2} f_{i\alpha}^\dagger \boldsymbol{\sigma}_{\alpha\beta} \hat{f}_{i\beta}$, with $\boldsymbol{\sigma}$ being the sigma Pauli matrices. Due to the strong repulsion no double occupation is allowed. This truly non-trivial constraint is described by the projection operator P onto the Hilbert space of empty and singly occupied states. Obviously, at half filling, or more generally in the MI state (one particle per site) no tunneling processes are possible and the $t - J$ model reduces to the Heisenberg spin model. Compared with the standard Hubbard model, the Hilbert space is reduced from four states per site to two, namely spin-up and spin-down. Away from half filling, the reduction is from four to three states per site, since the empty sites are allowed.

Although the $t - J$ model is described by quite a simple Hamiltonian, it presumably exhibits the very rich physics of the high T_c phase diagram. Unfortunately, accurate numerical simulations of this model are so far not possible, despite enormous efforts. In particular, all of the systematic methods fail: quantum Monte Carlo due to the ‘celebrated’ fermion sign problem and high- T expansions due to calculational complexity at low temperatures, etc. Meanwhile, methods based on tensor network states encounter difficulties in efficient contraction of the tensors with multiple indices and so on. For this reason, it is important to develop approximate methods that can give at least qualitative insights into the low-temperature phase diagram and properties of the system.

6.5.2 Projective Gutzwiller method

Some analytic insight into the $t - J$ model can be gained using a Gutzwiller variational approach, where one uses an ansatz of the type (see (Lee, 2008))

$$\Psi = P_G \phi, \quad (6.36)$$

where $P_G = \prod_i (1 - n_{i\uparrow} n_{i\downarrow})$ is the Gutzwiller projection and ϕ is any Hartree–Fock or BCS wave function, usually provided by a mean-field theory. The role of the Gutzwiller projection

is to remove all doubly occupied states in ϕ . Equation (6.36) is a suitable variational wave function for the $t - J$ model for two reasons: (i) the constraint is satisfied automatically and (ii) there exist efficient Monte Carlo algorithms that allow us to calculate quantum average values and correlation functions for this ansatz.

It can be shown (see Lee (2008) and references therein) that in the antiferromagnetic region of the phase diagram, the Gutzwiller projection wave function gives excellent results for the ground-state energy and sublattice magnetization. It captures quantum fluctuations of the Néel ordered state. Moreover, it predicts the d -wave pairing ground state (Gros, 1988) and the coexistence of the superconductivity with antiferromagnetic order. This last prediction is in disagreement with experiments. The ground state of the model, with nearest-neighbors hopping only in the superconducting phase, is most probably a d -wave superconductor, although there is some controversy over this issue (Sorella *et al.*, 2002; Shih *et al.*, 1998). Various numerical approaches confirm the d -wave superfluid character of the ground state: DMRG (White and Scalapino, 1999), cluster dynamical mean-field theory (Maier *et al.*, 2006), and variational cluster approximations (Senechal *et al.*, 2005; Tremblay *et al.*, 2006). Moreover, the presence of further next-neighbor tunneling t' considerably stabilizes the d -wave superconducting state (Shih *et al.*, 2004). The Gutzwiller projection method sketched here is related to the slave-boson method, which we discuss in the next subsection.

6.5.3 Slave-boson approach

The so-called slave-boson method was developed originally for the magnetic impurity (Kondo) problem (Barnes, 1976; Coleman, 1984) and for heavy fermion compounds, where an electron's effective mass becomes thousands of times larger than its free mass (Hewson, 1993). We will formulate the method below in order to study the physics of the $t - J$ model. The main idea of the slave-boson method is to introduce an additional auxiliary bosonic and fermionic field so that the single-particle-per-site constraint can be realized automatically. The advantage, as we shall see below, is that the slave-boson approach opens the way towards novel kinds of mean-field theories in which one pairs auxiliary fermions or allows for condensation of auxiliary bosons.

There are many versions of the slave boson approach. Here we follow Lee (2008), and we write the fermion operators as the product of an auxiliary boson \hat{b} and fermion \hat{c} operators, where the latter carry the spin index

$$\hat{f}_{i\sigma}^\dagger = \hat{c}_{i\sigma}^\dagger \hat{b}_i. \quad (6.37)$$

Additionally, one imposes the constraint

$$\hat{c}_{i\uparrow}^\dagger \hat{c}_{i\uparrow} + \hat{c}_{i\downarrow}^\dagger \hat{c}_{i\downarrow} + \hat{b}_i^\dagger \hat{b}_i = 1. \quad (6.38)$$

Note that eqn (6.37) is not an operator identity, instead it should be regarded as a restriction imposed on the available Hilbert space. Both sides of the above equation have to have correct matrix elements in the reduced Hilbert space, with no doubly occupied states. Alternatively, in a weaker sense, one can require that the constraint is fulfilled on average if one introduces the corresponding Lagrange multiplier λ_i .

In the slave-boson formalism, the Heisenberg exchange term is written in terms of $\hat{c}_{\mathbf{i}\sigma}^\dagger$ and $\hat{c}_{\mathbf{i}\sigma}$ only (Baskaran *et al.*, 1987)

$$\begin{aligned} \mathbf{S}_i \cdot \mathbf{S}_j = & -\frac{1}{4} \hat{c}_{\mathbf{i}\sigma}^\dagger \hat{c}_{\mathbf{j}\sigma} \hat{c}_{\mathbf{j}\beta}^\dagger \hat{c}_{\mathbf{i}\beta} \\ & - \frac{1}{4} \left(\hat{c}_{\mathbf{i}\uparrow}^\dagger \hat{c}_{\mathbf{j}\downarrow}^\dagger - \hat{c}_{\mathbf{i}\downarrow}^\dagger \hat{c}_{\mathbf{j}\uparrow}^\dagger \right) \left(\hat{c}_{\mathbf{j}\downarrow} \hat{c}_{\mathbf{i}\uparrow} - \hat{c}_{\mathbf{j}\uparrow} \hat{c}_{\mathbf{i}\downarrow} \right) \\ & + \frac{1}{4} \left(\hat{c}_{\mathbf{i}\alpha}^\dagger \hat{c}_{\mathbf{i}\alpha} \right). \end{aligned} \quad (6.39)$$

One of our aims in this subsection is to formulate novel kinds of mean-field theory with the help of slave-boson methods. In principle this can be done right after rewriting the Hamiltonian in terms of the new operators: one should then apply Bogoliubov–Gross–Pitaevskii theory to bosons and pairing theory to both fermions. This is, in fact, how we treat higher spin fermions in Chapter 7.

Here we describe a more rigorous approach, in which we decouple the quartic exchange terms via the Hubbard–Stratonovich transformation. The Hubbard–Stratonovich transformation is nothing but a mapping of an interacting fermion problem onto a system of non-interacting fermions coupled to an external fluctuating field. We use the identity:

$$e^{\frac{\hat{A}^2}{2}} = 2\sqrt{\pi} \int dx e^{(-\frac{x^2}{2} - x\hat{A})}, \quad (6.40)$$

where \hat{A} is an operator, and we apply it to our Hamiltonian, which has the form $\hat{H}_0 + \hat{H}_i$, where the bare Hamiltonian is quadratic in fermionic operators and the interacting Hamiltonian has a two-body interaction of the form $\hat{H}_i \sim U\hat{n}_\uparrow\hat{n}_\downarrow$. Notice that generically, and in particular in our case, the interaction Hamiltonian \hat{H}_i does not commute with \hat{H}_0 . Therefore one is led to use a functional-integral formulation.

The partition function is written in the form (Lee, 2008)

$$Z = \int Dc Dc^* Db D\lambda D\chi D\Delta \exp \left(- \int_0^\beta d\tau L_1 \right), \quad (6.41)$$

where the Lagrangian reads

$$\begin{aligned} L_1 = & \tilde{J} \sum_{\langle ij \rangle} (|\chi_{ij}|^2 + |\Delta_{ij}|^2) + \sum_{i\sigma} c_{i\sigma}^* (\partial_\tau - i\lambda_i) c_{i\sigma} \\ & - \tilde{J} \left[\sum_{\langle ij \rangle} \chi_{ij}^* \left(\sum_\sigma c_{i\sigma}^* c_{j\sigma} \right) + c.c. \right] \end{aligned} \quad (6.42)$$

$$\begin{aligned}
& + \tilde{J} \left[\sum_{\langle ij \rangle} \Delta_{ij} (c_{i\uparrow}^* c_{j\downarrow}^* - c_{i\downarrow}^* c_{j\uparrow}^*) + c.c. \right] \\
& + \sum_i b_i^* (\partial_\tau - i\lambda_i + \mu_B) b_i - \sum_{ij} t_{ij} b_i b_j^* c_{i\sigma}^* c_{j\sigma}.
\end{aligned}$$

Here χ_{ij} represents fermion hopping and Δ_{ij} represents fermion pairing corresponding to the two ways of representing the exchange interaction in terms of the fermion operators. The coupling $\tilde{J} = 3J/8$ is chosen to reproduce the mean-field self-consistent equation. As we see, the advantage of the Hubbard–Stratonovich transformation is that it reduces the problem to a Gaussian one, with the Lagrangian being a quadratic function of the creation and annihilation fermionic operators: this permits us to calculate the Gaussian integrals exactly.¹

In mean-field theory the functional integral is evaluated using the saddle-point method. The mean-field equations are

$$\chi_{ij} = \sum_\sigma \langle \hat{c}_{i\sigma}^\dagger \hat{c}_{j\sigma} \rangle, \quad (6.43)$$

$$\Delta_{ij} = \langle \hat{c}_{i\uparrow} \hat{c}_{j\downarrow} - \hat{c}_{i\downarrow} \hat{c}_{j\uparrow} \rangle. \quad (6.44)$$

These have to be accompanied by the corresponding equation related to the derivative with respect to λ_i , which is nothing but the constraint in eqn (6.39), and by a ‘dynamical’ equation for b_i ,

$$(\partial_\tau - i\lambda_i + \mu_B) b_i = \sum_j t_{ji} b_j \chi_{ji}. \quad (6.45)$$

In the approach based on Bogoliubov and pairing theory, eqns (6.43) and (6.44) correspond to self-consistency conditions for the mean fields χ_{ij} and Δ_{ij} , whereas eqn (6.45) without the τ derivative is an analog of the Gross–Pitaevskii equation for the bosonic field b_i . To derive it we have replaced $\hat{c}_{i\sigma}^\dagger \hat{c}_{j\sigma}$ by χ_{ij} in the last term in eqn (6.42).

In the further analysis of the mean-field solutions one writes $\chi_{ij} = |\chi_{ij}| e^{ia_{ij}}$ and interprets the matrix elements χ_{ij} as the hoping of bosons and fermions on a lattice. The phases a_{ij} live on the links of the lattice, so that they play the role of the spatial components of a $U(1)$ lattice gauge field. On the other hand, the λ_i fields, responsible for enforcing the constraint in eqn (6.39), appear together with derivatives with respect to τ and become the time (scalar) components of the $U(1)$ gauge potential. In effect, we can view the model as one in which fermions and bosons are coupled to the same gauge field. In addition, the fermions may undergo singlet pairing with an amplitude given by Δ_{ij} . One concludes that the $t - J$ model is equivalent to a lattice gauge theory (LGT) with non-relativistic fermions and bosons coupled with a *compact* $U(1)$ gauge field, where compactness simply means that the gauge field a_{ij} is a phase defined as modulo 2π . At this level of equivalence, however,

¹Strictly speaking, the fermionic Gaussian integral is over Grassman variables (Negele and Orland, 1998).

the gauge fields are not dynamical and can fluctuate freely. By integrating out some of the matter fields, one ends up with an LGT with strong coupling, in which the gauge fields acquire dynamics. We recommend the excellent review by Lee (2008) to readers who wish to learn more about the connection to gauge theory.

6.5.4 Mean-field solutions of the slave-boson model

In the remaining subsection we discuss in more detail the properties of the mean-field solutions of the slave-boson model. In particular, the $U(1)$ gauge field mean-field phase diagram is shown in Figure 6.7 and captures some key features of the high T_c phase diagram shown in Figure 6.6. As we see, there are four different phases characterized by the values of $b = \langle \hat{b} \rangle$, $\chi_{ij} = \chi$, and $\Delta_{ij} = \Delta$:

- (I) a Fermi liquid, for which $\chi \neq 0$, $\Delta = 0$, and $b \neq 0$; in terms of original fermions, it has only non-vanishing correlations $\sum_{\sigma} \langle \hat{f}_{i\sigma}^{\dagger} \hat{f}_{j\sigma} \rangle$;
- (II) a spin-gap phase, for which $\chi \neq 0$, $\Delta \neq 0$, and $b = 0$; in this phase the BCS order parameter vanishes, but the spin gap is non-zero;
- (III) a d -wave superconductor, for which $\chi \neq 0$, $\Delta \neq 0$, and $b \neq 0$; here both the BCS and $\sum_{\sigma} \langle \hat{f}_{i\sigma}^{\dagger} \hat{f}_{j\sigma} \rangle$ are non-zero;
- (IV) a strange metal, for which $\chi \neq 0$, $\Delta = 0$, and $b = 0$.

Following Lee (2008) we detail some of the possible mean-field states:

***d*-wave pairing states** Additionally, in the region (II) and (III) the mean-field states have a d -wave symmetry: $\chi_{ij} = \chi$ is constant in space while $\Delta_{ij} = \Delta$ for (ij) bonds oriented along the x -axis and $\Delta_{ij} = -\Delta$ for (ij) bonds oriented along the y -axis. In the absence of pairing, in region (II), the fermion dispersion relation takes the standard form of that of free fermions hopping in a 2D square lattice, but is proportional to χ ,

$$\varepsilon_{\mathbf{k}} = -2\tilde{J}\chi(\cos k_x a + \cos k_y a). \quad (6.46)$$

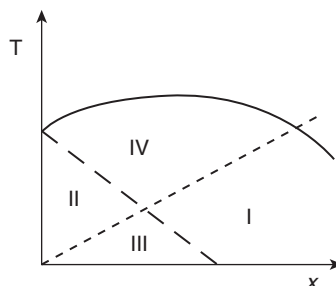


Figure 6.7 Schematic phase diagram of the $U(1)$ mean-field theory in the the T – x plane, where T denotes the temperature and x is the dopant concentration. (I) Fermi-liquid phase, (II) spin-gap phase, (III) d -wave superconductor, and (IV) strange metal. From Lee and Nagaosa (1992).

When pairing is present, in region (III) the d -wave dispersion relation becomes

$$E_{\mathbf{k}} = \sqrt{(\varepsilon_{\mathbf{k}} - \mu_f)^2 + |\Delta_{\mathbf{k}}|^2}, \quad (6.47)$$

where μ_f is the fermion chemical potential and $\Delta_{\mathbf{k}} = 2\Delta(\cos k_x a - \cos k_y a)$. In both regions the bosons condense at the band minimum at low temperatures. In mean-field theory, the Bose condensation temperature is proportional to the boson density, which is directly related to the doping, x . Below this temperature (described by the narrow dashed line in Figure 6.7) $\langle \hat{b} \rangle = b \neq 0$, and the BCS order parameter $\langle \hat{f}_{k\uparrow} \hat{f}_{-k\downarrow} \rangle = b^2 \langle \hat{c}_{k\uparrow} \hat{c}_{-k\downarrow} \rangle \neq 0$. Thus in region (III), the d -wave superconducting state indeed appears at intermediate doping, while the corresponding state in region (II) has a d -wave-like gap for spin excitations, but not for charge (density) excitations.

Staggered flux states Interestingly, d -wave pairing states are not the only possible solutions of the mean-field equations. In the early development of mean-field theory, a variety of mean-field states were discovered that led to the same ground state or free energy. Particularly important is the example of staggered flux states (Affleck *et al.*, 1988*b*), for which χ_{ij} is complex, with $\chi_{ij} = \chi_0 \exp(i(-1)^{i_x+j_y}\Phi_0)$, and the phase is arranged in such a way that it describes free fermion hopping on a lattice with a fictitious alternating ‘magnetic’ flux $\pm 4\Phi_0$ through the plaquettes of the lattice. Remarkably, for $\mu_f = 0$ the dispersion relation for this state is exactly the same as that of the d -wave pairing state, given by eqns (6.46) and (6.47) provided

$$\tan \Phi_0 = \frac{\Delta}{\chi_0}. \quad (6.48)$$

For $\Phi_0 = \frac{\pi}{4}$, called the π -flux phase, is special since it does not break the lattice translation symmetry. In this case the dispersion is as shown in Figure 6.8, from where we see that the energy gap vanishes at the nodal points located at $(\pm\frac{\pi}{2}, \pm\frac{\pi}{2})$. Around the nodal points the dispersion forms a characteristic Dirac cone, mimicking the spectrum of a relativistic massless Dirac particle. For the π -flux state the dispersion around the node is isotropic, while for Φ_0 less than $\frac{\pi}{4}$ the Dirac cone becomes progressively anisotropic, as if ‘light velocities’— v_F in the direction towards (π, π) and v_Δ in the direction towards the maximum gap at $(0, \pi)$ —were different. This behavior is reminiscent of the behavior of the dispersion relation for free fermions subjected to synthetic non-Abelian SU(2) fields (see Chapter 11 and Goldman *et al.* (2009*a*)). For $\mu_f = 0$, i.e. at half filling, and provided eqn (6.48) is satisfied, the d -wave pairing states and π -flux state lead to exactly the same trial function after Gutzwiller projection, up to a trivial overall phase factor. There is a deeper reason for this fact, as explained in Affleck *et al.* (1988*a*) and Dagotto *et al.* (1988), namely that the auxiliary fermion operators within the slave-boson approach exhibit a $SU(2)$ symmetry that corresponds to the following particle-hole transformation

$$\begin{aligned} \hat{c}_{i\uparrow}^\dagger &\rightarrow \alpha_i \hat{c}_{i\uparrow}^\dagger + \beta_i \hat{c}_{i\downarrow} \\ \hat{c}_{i\downarrow} &\rightarrow -\beta_i^* \hat{c}_{i\uparrow}^\dagger + \alpha_i^* \hat{c}_{i\downarrow}. \end{aligned} \quad (6.49)$$

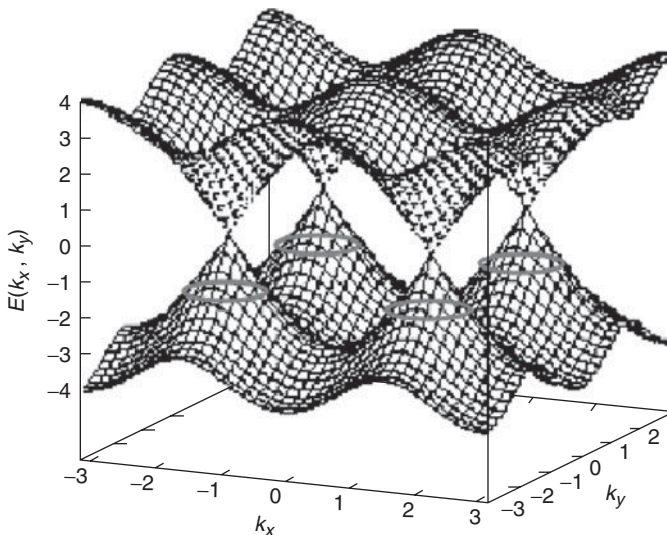


Figure 6.8 Energy dispersion of the staggered flux phase for the special case of the π -flux. Close to the nodal points $(\pm\frac{\pi}{2}, \pm\frac{\pi}{2})$, the spectrum is equal to that of a relativistic massless Dirac fermion. From Lee *et al.* (2006).

The above symmetry conserves the spin quantum number. Physically, it expresses the property that adding a spin-up fermion or removing a spin-down fermion leads to the same state after the projection onto the subspace of singly occupied fermions (for a simple proof see Zhang *et al.* (1988)). The best estimate for the energy of the Néel ordered ground state of the Heisenberg antiferromagnet in the square lattice is $\langle S_i \cdot S_j \rangle = -0.3346$ J (Trivedi and Ceperley, 1989; Runge, 1992). The projected π -flux state (Gros, 1988) gives -0.319 J, which should be regarded as an excellent result, considering that there is no variational parameter in the π -flux state.

In the presence of holes, when the dispersion relation is the same as for $\mu_f = 0$ but the Fermi energy is located at $\mu_f < 0$, the staggered flux state has higher energy than the d -wave superconductor; it has been proposed that this is related to the pseudogap state (Hsu *et al.*, 1991). Additionally, the fluxes in this state alternate the signs between neighboring plaquettes, i.e. they break a kind of Ising-type symmetry. Breaking of the Ising symmetry in two dimensions should, however, occur at non-zero T and unfortunately available numerics do not show such an effect. For this reason many authors have looked intensively for the reasons for ‘rounding’ of the Ising transition. The solution was proposed in Wen and Lee (1996), where the authors formulated another version of the slave-boson theory in which the single auxiliary boson is replaced by a $SU(2)$ doublet of bosons.

6.6. Hubbard models and effective Hamiltonians

Before we turn to more detailed treatment of Fermi–Bose Hubbard model, let us discuss the very general method of deriving an effective low-energy Hamiltonian in the strong

coupling limit. This method is based on systematic degenerate perturbation theory up to the second order in the ratio of tunneling energy and interaction energy.

The Bose Hubbard Hamiltonian or Fermi–Bose Hamiltonian can be split into $\hat{H} = \hat{H}_0 + t\hat{H}_{\text{int}}$, where \hat{H}_0 denotes the on-site Hamiltonian obtained in the limit of zero tunneling and the hopping term (corresponding in this expansion to interactions between the sites) is denoted \hat{H}_{int} . The Hamiltonian \hat{H}_0 can easily be diagonalized and has well-defined (degenerate) eigenstates, which are grouped in blocks (or manifolds). Each manifold is well separated from each other. Typically, different manifolds are separated by terms of the order of U , U being the interaction between two bosons. We denote as \hat{P}_α the projector on each block space, where α is the block index; the i th state in any block is denoted by $|\alpha, i\rangle$. Note that $\hat{P}_\alpha \hat{H}_0 \hat{P}_\beta = 0$ holds for $\alpha \neq \beta$. The \hat{H}_{int} part of the Hamiltonian will introduce couplings between the bare block α and β , i.e. $\hat{P}_\alpha \hat{H}_{\text{int}} \hat{P}_\beta$ can be different from zero for $\alpha \neq \beta$. Following Cohen-Tannoudji *et al.* (1992), one can construct an effective Hamiltonian \hat{H}_{eff} from \hat{H} such that it describes the slow, low-energy perturbation-induced tunneling *strictly within* each manifold of the unperturbed block states and has the same eigenvalues as \hat{H} . Tunneling processes between different manifolds are thus neglected. There are a number of requirements for the effective Hamiltonian \hat{H}_{eff} .

1. It should be, by construction, Hermitian, with the same eigenvalues and the same degeneracies as \hat{H} . To achieve that, one defines $\hat{T} := e^{i\hat{S}}$, with \hat{S} Hermitian, $\hat{S} = \hat{S}^\dagger$, and chosen such that:

$$\hat{H}_{\text{eff}} = \hat{T} \hat{H} \hat{T}^\dagger. \quad (6.50)$$

2. \hat{H}_{eff} does not couple states from different manifolds:

$$\hat{P}_\alpha \hat{H}_{\text{eff}} \hat{P}_\beta = 0, \quad \alpha \neq \beta. \quad (6.51)$$

3. As the first two conditions still allow for an infinite number of unitary transformations (all $\hat{U}\hat{T}$ are still possible, \hat{U} being any unitary transformation acting only *within* the manifolds), the following additional condition is imposed:

$$\hat{P}_\alpha \hat{S} \hat{P}_\alpha = 0 \quad \text{for any } \alpha. \quad (6.52)$$

Expanding the first condition using the Baker–Hausdorff formula, one obtains:

$$\begin{aligned} \hat{H}_{\text{eff}} &= \hat{H} + [i\hat{S}, \hat{H}] + \frac{1}{2!} [i\hat{S}, [i\hat{S}, \hat{H}]] \\ &\quad + \frac{1}{3!} [i\hat{S}, [i\hat{S}, [i\hat{S}, \hat{H}]]] + \dots . \end{aligned} \quad (6.53)$$

Making a power-series ansatz for \hat{S} in the perturbative parameter t ,

$$\hat{S} = t\hat{S}_1 + t^2\hat{S}_2 + t^3\hat{S}_3 + \dots, \quad (6.54)$$

and employing $\hat{H} = \hat{H}_0 + t\hat{H}_{\text{int}}$, one obtains from eqn (6.53) to second order

$$\begin{aligned} \hat{H}_{\text{eff}} &= \hat{H}_0 + t \overbrace{\left([i\hat{S}_1, \hat{H}_0] + \hat{H}_{\text{int}} \right)}^{\hat{H}_{\text{eff}}^1} \\ &\quad + t^2 \overbrace{\left([i\hat{S}_2, \hat{H}_0] + [i\hat{S}_1, \hat{H}_{\text{int}}] + \frac{1}{2} [i\hat{S}_1, [i\hat{S}_1, \hat{H}_0]] \right)}^{\hat{H}_{\text{eff}}^2}. \end{aligned} \quad (6.55)$$

This is a power series for \hat{H}_{eff} , with its moments denoted by $\hat{H}_{\text{eff}}^1, \hat{H}_{\text{eff}}^2 \dots$. In the first order, $\hat{H}_{\text{eff}} = \hat{H}_0 + t\hat{H}_{\text{eff}}^1$ and $\hat{S} = t\hat{S}_1$. Using the second and third conditions, as well as $\hat{P}_\alpha \hat{H}_0 \hat{P}_\beta = 0$ and the expression for \hat{H}_{eff}^1 in eqn (6.55), one finds:

$$\langle \alpha, i | i\hat{S}_1 | \beta, j \rangle (E_{\beta j} - E_{\alpha i}) + \langle \alpha, i | \hat{H}_{\text{int}} | \beta, j \rangle = 0 \quad (6.56)$$

$$\Rightarrow \langle \alpha, i | i\hat{S}_1 | \beta, j \rangle = \begin{cases} \frac{\langle \alpha, i | \hat{H}_{\text{int}} | \beta, j \rangle}{E_{\alpha i} - E_{\beta j}} & \alpha \neq \beta \\ 0 & \alpha = \beta \end{cases}. \quad (6.57)$$

Thus the effective Hamiltonian within the α -manifold depends only on \hat{H}_{int} and not on \hat{S}_1 , i.e. $\langle \alpha, i | \hat{H}_{\text{eff}}^1 | \alpha, j \rangle = \langle \alpha, i | \hat{H}_{\text{int}} | \alpha, j \rangle$. A general result for any n is that $\langle \alpha, i | \hat{H}_{\text{eff}}^n | \alpha, j \rangle$ is independent of \hat{S}_n , based on the third condition and on the observation that \hat{S}_n enters the expression for \hat{H}_{eff}^n only in the commutator with \hat{H}_0 , which is diagonal in the manifold index.

Thus when continuing to second order, the term $[i\hat{S}_2, \hat{H}_0]$ in the expression for \hat{H}_{eff}^2 can be dropped. Of the two remaining terms defining \hat{H}_{eff}^2 in eqn (6.55), the second one can be simplified by observing that, according to eqn (6.56), the operator $[i\hat{S}_1, \hat{H}_0]$ is purely non-diagonal in the manifold index, with values opposite to those of the non-diagonal (nd) part of \hat{H}_{int} . Thus $\frac{1}{2} [i\hat{S}_1, [i\hat{S}_1, \hat{H}_0]] = -\frac{1}{2} [i\hat{S}_1, \hat{H}_{\text{int}}^{\text{nd}}]$. Now inserting the identity between the operators in the still untreated second term in \hat{H}_{eff}^2 , $[i\hat{S}_1, \hat{H}_{\text{int}}]$, one sees that due to \hat{S}_1 being non-diagonal in α , again only the non-diagonal part of \hat{H}_{int} can contribute: $[i\hat{S}_1, \hat{H}_{\text{int}}] = [i\hat{S}_1, \hat{H}_{\text{int}}^{\text{nd}}]$. Therefore one has:

$$\hat{H}_{\text{eff}}^2 = [i\hat{S}_1, \hat{H}_{\text{int}}^{\text{nd}}] + \frac{1}{2} [i\hat{S}_1, \overbrace{[i\hat{S}_1, \hat{H}_0]}^{-\hat{H}_{\text{int}}^{\text{nd}}}] = \frac{1}{2} [i\hat{S}_1, \hat{H}_{\text{int}}^{\text{nd}}]. \quad (6.58)$$

Collecting all terms relevant for $\langle \alpha, i | \hat{H}_{\text{eff}} | \alpha, j \rangle$ to second order in t , and introducing the notation $\hat{Q}_{\alpha i} := \sum_{k, \gamma \neq \alpha} \frac{|\gamma, k\rangle \langle \gamma, k|}{E_{\gamma k} - E_{\alpha i}}$, one finds:

$$\begin{aligned} \langle \alpha, i | \hat{H}_{\text{eff}} | \alpha, j \rangle &= E_{\alpha i} \delta_{ij} + t \langle \alpha, i | \hat{H}_{\text{int}} | \alpha, j \rangle \\ &\quad - \frac{t^2}{2} \left(\langle \alpha, i | \hat{H}_{\text{int}} \left[\hat{Q}_{\alpha i} + \hat{Q}_{\alpha j} \right] \hat{H}_{\text{int}} | \alpha, j \rangle \right), \end{aligned} \quad (6.59)$$

where the identity operator has been inserted in the final expression for \hat{H}_{eff}^2 in eqn (6.58) and then evaluated using eqn (6.57), which naturally leads one to define the operator $\hat{Q}_{\alpha i}$ as above. Note that this construction can be generalized to arbitrary orders in t in a straightforward manner, as detailed in Cohen-Tannoudji *et al.* (1992).

6.7. Fermi–Bose Hubbard models

The spectacular advances in loading atomic samples in optical lattices have allowed for the realization of systems that are well described by a Fermi Hubbard model, as well as mixtures of fermions and bosons (FB) described by Fermi–Bose Hubbard models. In the latter case, and in the limit of strong atom–atom interactions, such systems can be described in terms of composite fermions: a bare fermion, or a fermion paired with one boson (bosonic hole), or two bosons (bosonic holes), etc. This phenomenon, related to the appearance of counterflow superfluidity in Kuklov and Svistunov (2003), may also occur in the absence of the optical lattice (Kagan *et al.*, 2004, 2005). The quantum phase diagram displayed by those systems is amazingly rich and complex. The physics of Fermi–Bose mixtures in this regime has recently been studied by Lewenstein *et al.* (2004), Fehrmann *et al.* (2004*a, b*), using perturbation theory up to second order to derive an effective Hamiltonian (see Section 6.6).

There is a large number of studies of FB mixtures, both of trapped gases in the weakly interacting regime and strongly correlated gases in optical lattices. Extensive lists of references can be found in the review articles by Lewenstein *et al.* (2007) and Bloch *et al.* (2008). The physics of disordered FB mixtures will be discussed in Chapter 9.

In this section we focus on the lattice case and consider the homogeneous situation, where the effects of the weak confining trap potential are neglected. We explain here in detail how to derive the corresponding effective Hamiltonian. We consider a homogeneous mixture of ultracold bosons (\hat{b}) and spinless (or spin-polarized) fermions (\hat{f}), for example ${}^7\text{Li}$ – ${}^{6}\text{Li}$ or ${}^{87}\text{Rb}$ – ${}^{40}\text{K}$, trapped in an optical lattice. As for the bosonic case (described in Chapter 3), in the tight-binding regime, it is convenient to project the wave functions onto the Wannier basis of the fundamental Bloch band (Ashcroft and Mermin, 1976; Kittel, 2004). This leads to the Fermi–Bose Hubbard (FBH) Hamiltonian

$$\hat{H}_{\text{FBH}} = - \sum_{\langle ij \rangle} \left[t_b \hat{b}_i^\dagger \hat{b}_j + t_f \hat{f}_i^\dagger \hat{f}_j + h.c. \right] + \sum_i \left[\frac{U}{2} \hat{n}_i (\hat{n}_i - 1) + V \hat{n}_i \hat{m}_i - \mu^b \hat{n}_i - \mu^f \hat{m}_i \right], \quad (6.60)$$

where \hat{b}_i^\dagger , \hat{b}_i , \hat{f}_i^\dagger , and \hat{f}_i are bosonic and fermionic creation-annihilation operators of a particle in the i th localized Wannier state of the fundamental band, and $\hat{n}_i = \hat{b}_i^\dagger \hat{b}_i$ and

$\hat{m}_i = \hat{f}_i^\dagger \hat{f}_i$ are the corresponding on-site number operators. The FBH model describes: (i) nearest-neighbor boson (fermion) hopping, with an associated negative energy of $-t_b$ ($-t_f$); (ii) on-site boson–boson interactions with an energy U , which we will assume to be repulsive (i.e. positive); (iii) on-site boson–fermion interactions with an energy V , which is positive (negative) for repulsive (attractive) interactions; and finally (iv) on-site energy due to chemical potentials, μ^b and μ^f , in a grand canonical description. Following Lewenstein *et al.* (2004), Ahufinger *et al.* (2005), Fehrmann *et al.* (2004*a, b*), let us review how to derive an effective Hamiltonian to second (or higher) order in $t = t_f = t_b$. For the sake of simplicity we assume here the same tunneling for bosons and fermions. Generalization to the case $t_f \neq t_b$ is straightforward. We will use the notation of Lewenstein *et al.* (2004).

In the limit of vanishing tunneling ($t = 0$), with finite repulsive boson–boson interaction U , and in the absence of interactions between bosons and fermions ($V = 0$), the bosons are in an MI phase, with exactly $\tilde{n} = \lceil \tilde{\mu}^b \rceil + 1$ bosons per site, where $\tilde{\mu}^b = \mu^b/U$ and $\lceil x \rceil$ denotes the integer part of x . In contrast, the fermions can be in any set of Wannier states, since for vanishing tunneling the energy is independent of their configuration. The situation changes when the interparticle interactions between bosons and fermions, V , are turned on. In the following, we define $\alpha = V/U$ and consider the case of a bosonic MI phase with \tilde{n} bosons per site. We also assume that the temperature is small enough ($T < V$) to enable us to neglect the particle–hole excitations. It follows that tunneling of a fermion is necessarily accompanied by the tunneling of $-s$ bosons (if $s < 0$) or opposed tunneling of s bosons (if $s \geq 0$). The dynamics of the Fermi–Bose mixture can thus be regarded as the one of composite fermions made of one fermion plus $-s$ bosons (if $s < 0$) or one fermion plus s bosonic holes (if $s \geq 0$). The annihilation operators describing composite fermions consisting in one fermion and s ($-s$) bosonic holes (bosons) are:

$$\hat{F}_i = \sqrt{\frac{(\tilde{n} - s)!}{\tilde{n}!}} \left(b_i^\dagger \right)^s f_i \quad \text{for } s \text{ bosonic holes} \quad (6.61)$$

$$\hat{F}_i = \sqrt{\frac{\tilde{n}!}{(\tilde{n} - s)!}} (b_i)^{-s} f_i \quad \text{for } -s \text{ bosons.} \quad (6.62)$$

These operators are fermionic in the sub-Hilbert space generated by $|n - ms, m\rangle$ with $m = 0, 1$ in each lattice site. Note that in the picture of fermionic composites the vacuum state corresponds to an MI phase with \tilde{n} bosons per site. At this point different composite fermions appear depending on the values of α , \tilde{n} , and $\tilde{\mu}^b$, as shown in Figure 6.9.

Because all sites are equivalent for the fermions, the ground state is highly degenerate: $([N!/N_f!(N - N_f)!])$, where N denotes the total number of atoms and N_f the number of fermions. Hence the manifold of ground states is strongly coupled by fermion or boson tunneling. We assume now that the tunneling rate t is small but finite. In the homogeneous case, one uses standard second-order perturbation theory to derive an effective Hamiltonian for the fermionic composites (see Auerbach (1994), Cohen-Tannoudji *et al.* (1992), and Ahufinger *et al.* (2005)):

$$\hat{H}_{\text{eff}} = -d_{\text{eff}} \sum_{\langle i,j \rangle} (\hat{F}_i^\dagger \hat{F}_j + h.c.) + K_{\text{eff}} \sum_{\langle i,j \rangle} \hat{M}_i \hat{M}_j - \bar{\mu}_{\text{eff}} \sum_i \hat{M}_i, \quad (6.63)$$

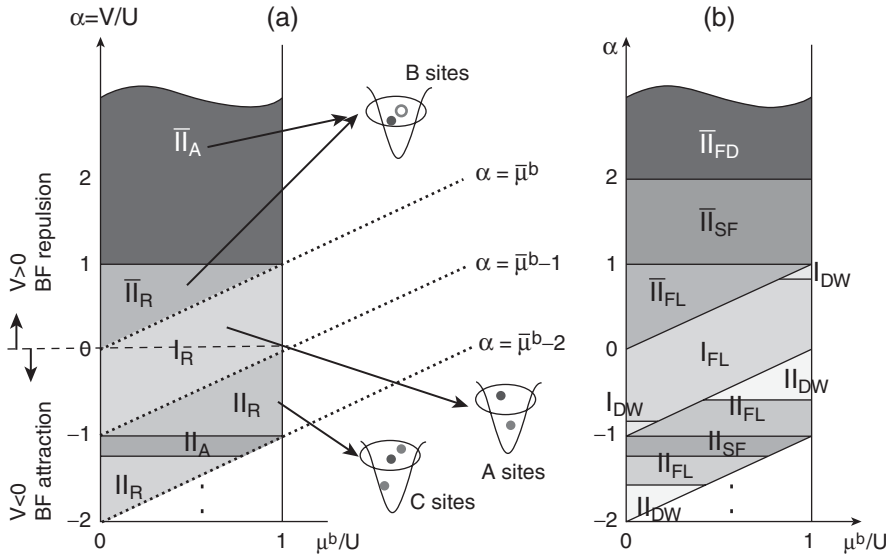


Figure 6.9 Quantum phase diagrams of Fermi–Bose mixtures in an homogeneous optical lattice as functions of $\bar{\mu}^b$ and $\alpha = V/U$ for fermionic filling factor $\rho_f = 0.4$ and $t/U = 0.02$. (a) Diagram of the composite types that arise in the system. Roman numbers denote the total number of particles that form the composite and a bar means that the composite is formed by bosonic holes rather than bosons, as schematically depicted for the case of composites formed by one fermion (A sites), one fermion plus one bosonic hole (B sites), and one fermion plus one boson (C sites). The dark (light) filled small dots symbolize fermions (bosons) and the empty dots, bosonic holes. The subscript A (R) indicates attractive (repulsive) composite interactions. (b) Detailed quantum phase diagram of fermionic composites. The subscripts here denote different phases: DW, density wave; FL, Fermi liquid; SF, superfluid; FD, fermionic domains. The strongly correlated phases for small but finite t are surrounded by characteristic lobes (Fehrmann *et al.*, 2004a), beyond which bosons become superfluid. Therefore there are thin regions of bosonic superfluid between the various composite phases. From Ahufinger *et al.* (2005).

where $\hat{M}_i = \hat{F}_i^\dagger \hat{F}_i$ and $\bar{\mu}_{\text{eff}}$ is the chemical potential whose value is fixed by the total number of composite fermions. The nearest-neighbor hopping for the composites is described by $-d_{\text{eff}}$ and the nearest-neighbor composite–composite interactions are given by K_{eff} , which may be repulsive (> 0) or attractive (< 0). This effective model is equivalent to that of spinless interacting fermions. The interaction coefficient K_{eff} originates from second-order terms in perturbative theory and can be written in the general form (Fehrmann *et al.*, 2004a):

$$K_{\text{eff}} = \frac{-2t^2}{U} \left[(2\tilde{n} - s)(\tilde{n} + 1) - s(\tilde{n} - s) - \frac{(\tilde{n} - s)(\tilde{n} + 1)}{1 + s - \alpha} - \frac{(\tilde{n} - s + 1)\tilde{n}}{1 - s + \alpha} - \frac{1}{s\alpha} \right]. \quad (6.64)$$

This expression is valid in all cases, but when $s = 0$ the last term ($1/s\alpha$) should not be taken into account. d_{eff} originates from $(|s| + 1)$ -th order terms in perturbative theory and

thus presents different forms in different regions of the phase diagram of Figure 6.9. For instance, in region I $d_{\text{eff}} = t$, in region \overline{II} $d_{\text{eff}} = 2t^2/V$, and in region II $d_{\text{eff}} = 4t^2/|V|$.

The physics of the system is determined by the ratio $K_{\text{eff}}/d_{\text{eff}}$ and the sign of K_{eff} . In Figure 6.9(a) the subindex A/R denotes attractive ($K_{\text{eff}} > 0$)/repulsive ($K_{\text{eff}} < 0$) composite interactions. Figure 6.9(b) shows the quantum phase diagram of composites for fermionic filling factor $\rho_f = 0.4$ and tunneling $t/U = 0.02$. For large values of t/U , a transition to the superfluid state takes place for the corresponding 3D lobes over the different regions in Figure 6.9 (see Fehrmann *et al.* (2004a)).

7

Ultracold spinor atomic gases

7.1. Introduction

Spinor ultracold gases are formed by particles with non-zero internal angular momentum or spin whose orientation in space is not externally constrained. The spinor degree of freedom of atoms corresponds to the manifold of degenerate—in the absence of an external magnetic field—Zeeman hyperfine energy levels. The energy levels are described by the total atomic angular momentum $\mathbf{F} = \mathbf{I} + \mathbf{J}$, where \mathbf{I} refers to the nuclear spin and $\mathbf{J} = \mathbf{L} + \mathbf{S}$ describes the total electronic angular momentum, \mathbf{L} being the orbital angular momentum and \mathbf{S} the spin of the outer electron. Since alkaline atoms have a single electron in an ns orbital, $J = S = 1/2$, and thus they have only two possible ground hyperfine levels ($|1/2 - I|$, $|1/2 + I|$). The nuclear spin \mathbf{I} depends on each atomic species. Each ground-state manifold consists of all Zeeman states associated with a given hyperfine level with total angular momentum F , i.e. $\{|F, m_F\rangle\}$, where $m_F = -F, \dots, F$ (see Table 7.1). In this context we identify the spin of an atom with the hyperfine quantum number F .

Notice that if atoms are magnetically trapped the availability of hyperfine states is restricted by the requirement that the trapped atoms remain in low-field-seeking states. Moreover, the degeneracy of each hyperfine level is lost. For example, ^{87}Rb and ^{23}Na have three low-field-seeking states, one in the lower hyperfine manifold $\{|F = 1, m_F = -1\rangle\}$ and two in the upper hyperfine manifold $\{|F = 2, m_F = 1, 2\rangle\}$. The simultaneous confining of different low-field-seeking states is usually unstable against exothermic hyperfine state-changing collisions. This is why magnetic trapping results in a frozen atomic spin F and spin projection m_F (Stamper-Kurn and Ketterle, 2001). In this case, the bosonic quantum field operator $\hat{\Psi}(\mathbf{r})$, which describes the creation of a boson in state $|F, m_F\rangle$ and position \mathbf{r} , is a scalar in the spinor space. In turn, the mean-field description of the ultracold bosonic gas is done via a scalar order parameter, which does not have explicit dependence on the ground-state manifold $|F, m_F\rangle$ in which the atoms are trapped. In some cases, such as in ^{87}Rb , the singlet and the triplet scattering lengths are practically equal, and thus spin-exchange collisions are highly suppressed, allowing simultaneous magnetic trapping of more than one hyperfine component (Myatt *et al.*, 1997). In this situation, one speaks of multi-component ultracold gases or pseudo-spin systems.

In contrast, if atoms are far-off resonance optically trapped, they are simultaneously confined, regardless of their Zeeman level (Stamper-Kurn *et al.*, 1998). The bosonic quantum field operator in such cases is no longer a scalar and has to incorporate this new degree of freedom $\hat{\Psi} = \{\hat{\Psi}_{m_F}\}$. In turn, the corresponding order parameter in the mean-field approach becomes a vector whose components correspond to the different accessible Zeeman levels. As such it transforms under rotations in the spin space as a vector preserving the

Table 7.1 Hyperfine structure of alkaline atoms. Nuclear spin I , (hyperfine) total angular momentum F , and the corresponding Zeeman levels m_F , for the ground state of ^{23}Na , ^{87}Rb , ^{85}Rb , and ^{133}Cs .

Atomic species	Nuclear spin (I)	Hyperfine ground states (F)	Zeeman levels (m_F)
^{23}Na	$\frac{3}{2}$	1	$-1, 0, 1$
		2	$-2, -1, 0, 1, 2$
^{87}Rb	$\frac{3}{2}$	1	$-1, 0, 1$
		2	$-2, -1, 0, 1, 2$
^{85}Rb	$\frac{5}{2}$	2	$-2, -1, 0, 1, 2$
		3	$-3, -2, -1, 0, 1, 2, 3$
^{133}Cs	$\frac{7}{2}$	3	$-3, -2, -1, 0, 1, 2, 3$
		4	$-4, -3, -2, -1, 0, 1, 2, 3, 4$

symmetries present in the corresponding spin space. In such cases one refers to spinor ultracold gases. Apart from the symmetries under rotations, spinor ultracold gases differ from multicomponent ones in the effect of spin relaxation collisions. While spin relaxation collisions provide a limitation of the lifetime of multicomponent gases, they allow for population mixing among different Zeeman states within a hyperfine manifold in spinor gases. The population transfer between the different hyperfine components is subjected to conservation of the total number of atoms and of the total magnetization.

This chapter is organized as follows. In Section 7.2 we describe the role of interactions in bosonic (fermonic) systems with spin degrees of freedom. In clear contrast to the scalar gases where all atoms are in the same internal state, interactions in bosonic systems with spin degrees of freedom lead to different magnetic phases. In Section 7.3 we focus on the weakly interacting regime for spinor gases and we classify, within the mean-field approach, the possible ground states for spin 1 ($F = 1$) and spin 2 ($F = 2$) trapped gases. Section 7.4 describes the explicit spin textures and topological defects of spinor condensates such as vortices, monopoles, skyrmions, and knots. Section 7.5 is devoted to spinor bosonic gases in optical lattices, and we introduce the corresponding Bose–Hubbard Hamiltonians and, as limiting cases of such Hamiltonians, we derive the corresponding spin models. Finally, in Section 7.6 we analyse fermionic spinor gases and we focus on the exotic magnetism present in the $F = \frac{3}{2}$ case. An excellent recent review on spinor condensates can be found in Ueda and Kawaguchi (2010).

7.2. Spinor interactions

As in the scalar case, ultracold atomic spinor interactions can be parametrized by two-body short-range (s -wave) collisions. Due to rotational symmetry, two-body collisions between atoms can only depend on their total spin and not on the orientation. Moreover, symmetry

arguments impose the condition that the collisions between two *identical* bosons in a hyperfine spin level $|F, m_F\rangle$ has to be restricted to even total spins ($S = 0, \dots, 2F - 2, 2F$) while for fermions the total spin must be odd. From now onwards we will denote as S the total spin and *not* the electronic spin). Let us focus for the moment on the bosonic case, where the contact potential can be written as:

$$\hat{V}(\mathbf{r}_1 - \mathbf{r}_2) = \delta(\mathbf{r}_1 - \mathbf{r}_2) \sum_{S=0,2,\dots,2F} g_S \hat{P}_S, \quad (7.1)$$

where \mathbf{r}_i , with $i = 1, 2$, denotes the position of atom i and \hat{P}_S ($S = 0, 2, \dots, 2F$) is the projector onto the subspace with total spin S . The interaction strengths g_S characterizing the contact potential interactions of the different S channels are given by $g_S = 4\pi\hbar^2 a_S/m$, where a_S is the corresponding scattering length and m is the atomic mass. To understand the ground-state properties and the dynamics of spinor gases, it is convenient to express the interaction potential in terms of atomic spin operators. Denoting as $\hat{\mathbf{F}}_i$ the spin of boson $i = 1, 2$ involved in a collision, and using the identity $\hat{\mathbf{S}}^2 = (\hat{\mathbf{F}}_1 + \hat{\mathbf{F}}_2)^2$, one obtains:

$$\hat{\mathbf{F}}_1 \cdot \hat{\mathbf{F}}_2 = \sum_{S=0,2\dots}^{S=2F} \lambda_S \hat{P}_S, \quad (7.2)$$

with $\lambda_S = (1/2)[S(S+1) - 2F(F+1)]$, and where we have further assumed that $F = F_1 = F_2$. For two colliding bosons with spin $F = 1$, the total spin is $S = 2, 0$. Using eqn (7.2) and the normalization condition of the projectors $\hat{I} = \sum_{S=0,2,\dots,2F} \hat{P}_S$, the contact potential can be written as:

$$\hat{V}_{(F=1)}(\mathbf{r}_1 - \mathbf{r}_2) = (c_0 + c_2 \hat{\mathbf{F}}_1 \cdot \hat{\mathbf{F}}_2) \delta(\mathbf{r}_1 - \mathbf{r}_2), \quad (7.3)$$

where $c_0 = (g_0 + 2g_2)/3 = 4\pi\hbar^2(a_0 + 2a_2)/3m$ and $c_2 = (g_2 - g_0)/3 = 4\pi\hbar^2(a_2 - a_0)/3m$ (Ho, 1998; Koashi and Ueda, 2000). Thus the terms with coefficients c_0 and c_2 describe spin-independent and spin-dependent binary elastic collisions in the combined symmetric channels of total spin 0 and 2, respectively. In alkaline atoms, the scattering lengths in the different channels are quite similar, which results in $|c_2| \ll |c_0|$.

It is straightforward to generalize some spin identities to larger spins (Ho, 1998) by noting that $(\hat{\mathbf{F}}_1 \cdot \hat{\mathbf{F}}_2)^n = \sum_S \lambda_S^n \hat{P}_S$. Then the interaction potential can be rewritten as

$$\hat{V}(\mathbf{r}_1 - \mathbf{r}_2) = \left(\sum_{n=0}^F \alpha_n (\hat{\mathbf{F}}_1 \cdot \hat{\mathbf{F}}_2)^n \right) \delta(\mathbf{r}_1 - \mathbf{r}_2), \quad (7.4)$$

where the α_n are linear combinations of the different interaction strengths g_S . In the case of $F = 2$ bosons there are three possible channels with total spin $S = 0, 2$, and 4. Making use of the identities $\hat{I} = \hat{P}_0 + \hat{P}_2 + \hat{P}_4$ and $\hat{\mathbf{F}}_1 \cdot \hat{\mathbf{F}}_2 = -6\hat{P}_0 - 3\hat{P}_2 + 4\hat{P}_4$ in eqn (7.1), the contact potential can be expressed as:

$$\hat{V}_{(F=2)}(\mathbf{r}_1 - \mathbf{r}_2) = (c_0 + c_1 \hat{P}_0 + c_2 \hat{\mathbf{F}}_1 \cdot \hat{\mathbf{F}}_2) \delta(\mathbf{r}_1 - \mathbf{r}_2), \quad (7.5)$$

where the coefficients are given by $c_0 = (3g_4 + 4g_2)/7 = 4\pi\hbar^2(3a_4 + 4a_2)/7m$, $c_1 = (3g_4 - 10g_2 + 7g_0)/7 = 4\pi\hbar^2(3a_4 - 10a_2 + 7a_0)/7m$, and $c_2 = (g_4 - g_2)/7 = 4\pi\hbar^2(a_4 - a_2)/7m$. The projector \hat{P}_0 can be further expressed in terms of a ‘singlet pair operator’, as we shall see in the next section. Finally, note that the contact interaction $\hat{V}(\mathbf{r}_1 - \mathbf{r}_2)$ is invariant under rotations $R(\alpha, \beta, \gamma)$ in spin space, where $\{\alpha, \beta, \gamma\}$ denote the Euler angles defining the rotation. Moreover, the fact that the collisions of alkaline atoms are effectively spin-independent results in the fact that these systems exhibit higher symmetry: in the case of $F = 1$, an $SU(3)$ symmetry.

7.3. Spinor Bose–Einstein condensates: mean-field phases

The first experimental observation of a condensate with spin degree of freedom was optically trapped ^{23}Na (Stamper-Kurn *et al.*, 1998). In the same year, a mean-field approach was developed to describe the $F = 1$ condensate (Ho, 1998; Ohmi and Machida, 1998; Law *et al.*, 1998), its validity experimentally confirmed by Stenger *et al.* (1998). The experimental investigation of $F = 2$ spinor condensates is much more involved (Chang *et al.*, 2004; Schmaljohann *et al.*, 2004; Chang *et al.*, 2005; Kronjäger *et al.*, 2005). The mean-field phase diagram was first calculated by Koashi and Ueda (2000) and Ciobanu, Yip, and Ho (2000). Later, Ueda and Koashi (2002) developed the mean-field theory for $F = 2$ atoms in the presence of an external magnetic field. Success in condensing chromium atoms (Griesmaier *et al.*, 2005) opened the road to the study of mean-field phases for spin $F = 3$ atoms (Diener and Ho, 2006; Santos and Pfau, 2006).

7.3.1 Spin-1 condensates

The Hamiltonian of a trapped cloud of ultracold atoms with spin $F = 1$ in second quantization reads (Ho, 1998; Ohmi and Machida, 1998):

$$\hat{H}_{F_1} = \int d^3r \left\{ \hat{\Psi}_m^\dagger \left(-\frac{\hbar^2}{2m} \nabla^2 + V_{\text{ext}}(\mathbf{r}) \right) \hat{\Psi}_m + \frac{c_0}{2} \hat{\Psi}_m^\dagger \hat{\Psi}_j^\dagger \hat{\Psi}_j \hat{\Psi}_m + \frac{c_2}{2} \hat{\Psi}_m^\dagger (F_\nu)_{mj} \hat{\Psi}_j \cdot \hat{\Psi}_l^\dagger (F_\nu)_{lk} \hat{\Psi}_k \right\}, \quad (7.6)$$

where the repeated indices are summed, $\hat{\Psi}_m(\mathbf{r})$ ($\hat{\Psi}_m^\dagger(\mathbf{r})$) is the field operator that annihilates (creates) a boson in the Zeeman state $|F = 1, m_F = m = -1, 0, 1\rangle$ at point \mathbf{r} , with $\hat{F}_\nu \equiv \sum_{mj} \hat{\Psi}_m^\dagger (F_\nu)_{mj} \hat{\Psi}_j$, and F_ν with $\nu = x, y, z$ denote the spin-1 matrices:

$$F_x = \frac{1}{\sqrt{2}} \begin{pmatrix} 0 & 1 & 0 \\ 1 & 0 & 1 \\ 0 & 1 & 0 \end{pmatrix} \quad F_y = \frac{1}{\sqrt{2}} \begin{pmatrix} 0 & -i & 0 \\ i & 0 & -i \\ 0 & i & 0 \end{pmatrix} \quad F_z = \begin{pmatrix} 1 & 0 & 0 \\ 0 & 0 & 0 \\ 0 & 0 & -1 \end{pmatrix} \quad (7.7)$$

The external trapping potential $V_{\text{ext}}(\mathbf{r})$ is assumed to be spin-independent.

In scalar weakly interacting bosonic systems, where the mean-field approach can be used, the N -particle ground state is found by approximating the bosonic operator in the corresponding Hamiltonian by a c -number order parameter and minimizing the energy

functional under the constraint that the number of particles is fixed: $\delta E = \delta\langle H - \mu N \rangle = 0$, where μ is the chemical potential. For spinor gases, one follows the same approach (Ho, 1998; Ohmi and Machida, 1998; Huang and Gou, 1999), and replaces the field operators $\hat{\Psi}_m$ in eqn (7.6) by their expectation values: $\langle \hat{\Psi}_m \rangle = \phi_m$, being the components of the vector order parameter ϕ . The energy functional $E[\phi] = \langle \hat{H} - \mu N \rangle$ then reads:

$$E_{F_1} = \int d^3r \left\{ \frac{\hbar^2}{2m} (\nabla \sqrt{n})^2 + \frac{\hbar^2}{2m} (\nabla \xi)^2 n + (V_{\text{ext}} - \mu)n + \frac{n^2}{2} (c_0 + c_2 \langle \hat{\mathbf{F}} \rangle^2) \right\}, \quad (7.8)$$

where a normalized spinor ξ has been defined such that $\phi = \sqrt{n}\xi$, where n is the atomic density, and $|\xi|^2 = 1$ and now $\langle \hat{\mathbf{F}} \rangle = \sum_{kl} \xi_k^* \mathbf{F}_{kl} \xi_l$. The coefficient c_0 must be positive to avoid collapse. Minimization of the spin-dependent interaction energy in eqn (7.8) leads to different spinor ground states depending on the values of the spin-spin coupling. There are two distinct ground-state mean-field phases for spin $F = 1$ (Ho, 1998; Ohmi and Machida, 1998) (see Table 7.2):

- **Ferromagnetic phase.** The system exhibits ferromagnetic order if $c_2 < 0$ (i.e. $g_0 > g_2$), since the energy is minimized for $\langle \hat{\mathbf{F}} \rangle^2 = 1$. In this case, the ground state corresponds to all possible rotations of the state $|F = 1, m_F = 1\rangle$:

$$\xi_F = e^{i\varphi} U \begin{pmatrix} 1 \\ 0 \\ 0 \end{pmatrix} = e^{i(\varphi-\gamma)} \begin{pmatrix} e^{-i\alpha} \cos^2(\beta/2) \\ \sqrt{2} \cos(\beta/2) \sin(\beta/2) \\ e^{i\alpha} \sin^2(\beta/2) \end{pmatrix}, \quad (7.9)$$

where $U = e^{-i\alpha F_z} e^{-i\beta F_y} e^{-i\gamma F_z}$ and $\{\alpha, \beta, \gamma\}$ are the Euler angles. Note that the symmetry group $U(1) \times SO(3)$ reduces to $SO(3)$ since the rotation in spin space through the Euler angle γ is equivalent to the gauge transformation $e^{-i\gamma}$, the so-called spin-gauge symmetry (Ho and Shenoy, 1996). ^{87}Rb in the $F = 1$ manifold exhibits ferromagnetic ordering.

- **Polar phase.** The $F = 1$ condensate exhibits polar (sometimes called antiferromagnetic) ordering if $c_2 > 0$. Minimal energy is achieved by demanding that the expectation values of the spin component are zero along any direction, i.e. $\langle \hat{\mathbf{F}} \rangle = 0$. The degenerate ground state spinors then correspond to all possible rotations of the state $|F = 1, m_F = 0\rangle$. The general expression for the spinor in this case reads:

$$\xi_P = e^{i\varphi} U \begin{pmatrix} 0 \\ 1 \\ 0 \end{pmatrix} = e^{i\varphi} \begin{pmatrix} -\frac{1}{\sqrt{2}} e^{-i\alpha} \sin(\beta) \\ \cos(\beta) \\ \frac{1}{\sqrt{2}} e^{i\alpha} \sin(\beta) \end{pmatrix}. \quad (7.10)$$

Due to the fact that eqn (7.10) is independent of the Euler angle γ , the symmetry group of the polar state is $U(1) \times S^2$ where $U(1)$ denotes a global phase φ and S^2 is a surface of a unit sphere denoting all orientations $\{\alpha, \beta\}$ of the spin-quantization angle. Notice that this ‘antiferromagnetic’ ordering does not refer to antiparallel orientation of neighboring spins, i.e. Neél order, as happens classically. ^{23}Na and ^{85}Rb in the manifold $F = 1$ exhibit the polar phase.

Table 7.2 Classification of the ground-state spinors for $F = 1$ and $F = 2$.

Phase	Conditions	Ground-state spinor	$\langle \hat{\mathbf{F}} \rangle$	$\langle \hat{S}_+ \rangle$	Atomic species	
$F = 1$	Ferromagnetic	$c_2 < 0$	(1, 0, 0)	$\neq 0$	—	^{87}Rb
	Polar	$c_2 > 0$	(0, 1, 0)	0	—	^{23}Na
$F = 2$	Ferromagnetic	$c_2 < 0$	(1, 0, 0, 0, 0)	$\neq 0$	0	^{83}Rb
		$c_2 - c_1/20 < 0$	(0, 0, 0, 0, 1)			
		$c_1 < 0$	(0, 0, 1, 0, 0)	0	$\neq 0$	
	Polar	$c_2 - c_1/20 > 0$	$(0, 1, 0, 1, 0)/\sqrt{2}$ $(1, 0, 0, 0, 1)/\sqrt{2}$			$^{23}\text{Na}, ^{87}\text{Rb}$
	Cyclic	$c_1 > 0$ $c_2 > 0$	$(1, 0, \sqrt{2}, 0, 1)/2$	0	0	

7.3.2 Spin-2 condensates

For $F = 2$ bosons, collisions can occur in three channels corresponding to the total spin of $S = 0, 2$, and 4 . As a result, there is one more possible magnetic ground state apart from the ferromagnetic and the polar: the so-called cyclic ground state. The order parameters defining the phases are the magnetization $\langle \hat{\mathbf{F}} \rangle$ and the so-called ‘spin-singlet pair creation’ $\langle \hat{S}_+ \rangle = \langle \hat{b}_0^\dagger \hat{b}_0^\dagger / 2 - \hat{b}_1^\dagger \hat{b}_{-1}^\dagger + \hat{b}_2^\dagger \hat{b}_{-2}^\dagger \rangle$, where $\hat{b}_{m_F}^\dagger$ creates a particle with spin projection m_F (Koashi and Ueda, 2000; Ciobanu *et al.*, 2000).

The operator \hat{S}_+ applied on the vacuum creates, up to normalization, two bosons in a spin-singlet state. Defining $\hat{S}_- \equiv \hat{S}_+^\dagger$, we have $[\hat{S}_+, \hat{S}_-] = -2\hat{S}_z$ and $[\hat{S}_z, \hat{S}_\pm] = \pm \hat{S}_\pm$, where $\hat{S}_z \equiv (2\hat{N} + 5)/4$ and \hat{N} is the number operator.

The term proportional to \hat{P}_0 in the contact potential for the $F = 2$ case (see eqn (7.5)) can be rewritten using $\hat{P}_0 = (2/5)\hat{S}_+ \hat{S}_-$. Introducing such an expression into the second quantized form of the Hamiltonian and following the same procedure as the one described for the $F = 1$ case, the energy functional within the mean-field theory reads:

$$E_{F_2} = \int d^3r \left\{ \frac{\hbar^2}{2m} (\nabla \sqrt{n})^2 + \frac{\hbar^2}{2m} (\nabla \boldsymbol{\xi})^2 n + (V_{\text{ext}} - \mu) n + \frac{n^2}{2} (c_0 + c_2 \langle \hat{\mathbf{F}} \rangle^2 + \frac{4c_1}{5} |\langle \hat{S}_+ \rangle|^2) \right\}, \quad (7.11)$$

where $\langle \hat{\mathbf{F}} \rangle \equiv \sum_{kl} \xi_k^* \mathbf{F}_{kl} \xi_l$, with \mathbf{F} being the vector formed by the spin-2 matrices, and $\langle \hat{S}_+ \rangle \equiv \frac{1}{2} \sum_k (-1)^k \xi_k \xi_{-k}$ being the spin-singlet pair amplitude.

The ground states of the $F = 2$ spinor BEC can be classified (Ciobanu *et al.*, 2000; Koashi and Ueda, 2000; Martikainen and Suominen, 2001; Ueda and Kawaguchi, 2010) (see Figure 7.1 and Table 7.2) as follows.

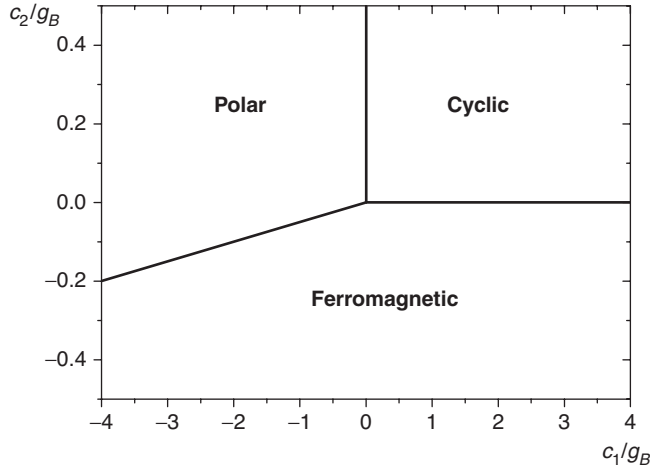


Figure 7.1 Mean-field phase diagram for $F = 2$ bosons in the $c_1 - c_2$ plane ($g_B = \frac{4\pi\hbar^2 a_B}{m}$, with a_B the Bohr radius).

- **Ferromagnetic phase.** This corresponds to $\langle \hat{\mathbf{F}} \rangle \neq 0$ and $\langle \hat{S}_+ \rangle = 0$. The conditions required to exhibit ferromagnetic order are $c_2 < 0$ and $c_2 - (c_1/20) < 0$ or, equivalently, $a_2 - a_4 > 0$ and $(1/5)(a_0 - a_4) + (2/7)(a_2 - a_4) > 0$. The ferromagnetic ground state is characterized by $\langle \hat{\mathbf{F}} \rangle = \pm 2$ (states with $\langle \hat{\mathbf{F}} \rangle = \pm 1$ have higher energy) and corresponds to the state:

$$\xi_F = e^{i\varphi} U \begin{pmatrix} 1 \\ 0 \\ 0 \\ 0 \\ 0 \end{pmatrix}, \quad (7.12)$$

where φ is an arbitrary global phase and U a generic spin rotation. Since the ground state is degenerate with respect to the global phase, it exhibits gauge invariance corresponding to conservation of the number of particles and, therefore, of the spin angular momentum (Ueda and Koashi, 2002).

- **Polar condensate** Polar or antiferromagnetic ordering for $F = 2$ is described by zero magnetisation, $\langle \hat{\mathbf{F}} \rangle = 0$, and a non-zero spin-singlet pair amplitude, $\langle \hat{S}_+ \rangle \neq 0$. In the c_1, c_2 plane, the polar phase occupies the regions $c_1 < 0$ and $c_2 - (c_1/20) > 0$ or, equivalently, $a_0 - a_4 < 0$ and $(1/5)|a_0 - a_4| - (2/7)|a_2 - a_4| < 0$. There are, up to rotations, two different degenerate (at the mean energy level) polar ground states,

sometimes denoted uniaxial (UN) and biaxial (BI):

$$\boldsymbol{\xi}_{\text{UN}} = e^{i\varphi} U \begin{pmatrix} 0 \\ 0 \\ 1 \\ 0 \\ 0 \end{pmatrix}, \quad \boldsymbol{\xi}_{\text{BI}} = e^{i\varphi} U \begin{pmatrix} 1/\sqrt{2} \\ 0 \\ 0 \\ 0 \\ 1/\sqrt{2} \end{pmatrix} \quad (7.13)$$

where φ is an arbitrary phase and U a generic spin rotation. Notice that the state $\boldsymbol{\xi} \propto (0, 1, 0, 1, 0)^T$ can be obtained, up to normalization, as $\boldsymbol{\xi} = ie^{-iF_y\pi/2}e^{-iF_z\pi/4}\boldsymbol{\xi}_{\text{BI}}$ (here F_ν are the spin-2 matrices) while it is not possible to obtain $\boldsymbol{\xi}_{\text{UN}}$ as a rotation of $\boldsymbol{\xi}_{\text{BI}}$.

- **Cyclic phase** Cyclic ordering for $F = 2$ is characterized by $\langle \hat{\mathbf{F}} \rangle = 0$ and $\langle \hat{S}_+ \rangle = 0$, and appears for $c_1, c_2 > 0$ or, equivalently, for $a_2 - a_4 < 0$ and $(1/5)(a_0 - a_4) - (2/7)(a_2 - a_4) > 0$. In this case neither the ferromagnetic nor the polar phase are favored and the ground state of this phase can be written as:

$$\boldsymbol{\xi}_{\text{C}} = \frac{1}{2}e^{i\varphi} U \begin{pmatrix} 1 \\ 0 \\ \sqrt{2} \\ 0 \\ -1 \end{pmatrix}. \quad (7.14)$$

Note that the spinor in eqn (7.14) is a superposition of $\boldsymbol{\xi}_{\text{UN}}$ and $\boldsymbol{\xi}_{\text{BI}}$ states of the polar phase.

It is worth noticing that the states of a particle with integer spin F can be expressed in terms of the $2F$ states of spin- $\frac{1}{2}$ particles (Majorana, 1932; Bloch and Rabi, 1945; Bacry, 1974). This representation allows for a beautiful and complete classification of the mean-field phases for arbitrary F (Barnett *et al.*, 2006b), making explicit the symmetries of the states and therefore giving the number of Goldstone modes and allowing to classify topological excitations. To illustrate the method we follow Barnett *et al.* (2006b). Consider a particle with spin F in a state:

$$|\Psi\rangle = \sum_{\alpha=-F}^F A_\alpha |\alpha\rangle, \quad (7.15)$$

where $\hat{F}_z |\alpha\rangle = \alpha |\alpha\rangle$ and A_α are a set of normalized complex coefficients. The idea is to find the ‘maximally polarized’ states orthogonal to $|\Psi\rangle$ considering that the maximally polarized state $|\zeta\rangle$ pointing in the \mathbf{n} direction, determined by $\hat{\mathbf{F}}\mathbf{n}|\zeta\rangle = F|\zeta\rangle$, can be represented as:

$$|\zeta\rangle = \sum_{\alpha=0}^{2F} \sqrt{\binom{2F}{\alpha}} \zeta^\alpha |F-\alpha\rangle, \quad (7.16)$$

where $\zeta = e^{i\phi} \tan \theta/2$. The values of the $2F$ complex roots of the characteristic polynomial $\langle \Psi | \zeta \rangle$, which are in a one-to-one correspondence with a set of points on the unit sphere

(θ, ϕ) , determine $|\Psi\rangle$, the symmetries of which correspond to the operations under which the points on the unit sphere are invariant. This method gives a complete description of the spinor state.

Moreover, using the representation of pure states of a particle with spin F in terms of $2F$ points on the surface of a sphere (Majorana, 1932; Bloch and Rabi, 1945), a geometrical method for determining inert states—those that are stationary points of the energy regardless of the exact form of the energy—of arbitrary spin F systems can be found (Mäkelä and Suominen, 2007).

7.4. Spin textures and topological defects

Topological defects in scalar condensates correspond to singularities of the order parameter that cannot be adiabatically or smoothly eliminated. The first topological defect observed in scalar Bose–Einstein condensates was a quantized vortex created by using the phase-imprinting method (Matthews *et al.* (1999); see also Dobrek *et al.* (1999) for a theoretical description), by rotating the trap potential (Madison *et al.*, 2000), or by means of adiabatic spin rotation accompanied by a topological Berry phase (Leanhardt *et al.*, 2002). The vectorial nature of the order parameter of spinor condensates in general allows for more complex topological defects than in scalar condensates—for a review see Ueda and Kawaguchi (2010). These physical defects are described by homotopy groups of the order-parameter space (Mermin, 1979; Mäkelä *et al.*, 2003; Ueda and Kawaguchi, 2010). Let us focus here on the possible topological excitations of a spin-1 Bose–Einstein condensate.

7.4.1 Singular and non-singular line defects: vortices

In scalar condensates, a single quantized vortex in a symmetrically cylindrical trap has, in the rotating frame $\hat{H} = H_{\text{Lab}} - \Omega \hat{L}_z$, an angular momentum equal to $N\hbar$, with N being the number of particles. The order parameter exhibits a node at the center of the trap. In spinor condensates, vortices may exhibit a much richer internal structure (Ho, 1998; Ohmi and Machida, 1998; Yip, 1999). The difference in symmetry between polar and ferromagnetic ground states leads to fundamental differences in their vortices (Ho, 1998), which can be studied with their superfluid velocity, $\mathbf{v}_s = (\hbar/m)\boldsymbol{\xi}^\dagger \nabla \boldsymbol{\xi}$. Using eqns (7.9) and (7.10) for the ferromagnetic (F) and polar (P) case, respectively, one obtains:

$$(\mathbf{v}_s)_P = \frac{\hbar}{m} \nabla \varphi, \quad (7.17)$$

$$(\mathbf{v}_s)_F = \frac{\hbar}{m} [\nabla(\varphi - \gamma) - \cos \beta \nabla \alpha], \quad (7.18)$$

where the Euler angles (α, β, γ) and φ are space-dependent. In the ferromagnetic case the superfluid velocity depends on spin rotations while in the polar case it does not, i.e. it is irrotational ($\nabla \times (\mathbf{v}_s)_P = 0$). Singular vortices have been shown to be unstable (Ho, 1998) in ferromagnetic $F = 1$ spinor condensates, while the non-singular Mermin–Ho (MH) (Mermin and Ho, 1976) and Anderson–Toulouse (AT) (Anderson and Toulouse, 1977) coreless vortices, which are shown in Figure 7.2, have been predicted to be thermodynamically stable under rotation (Mizushima *et al.*, 2002). For the MH vortex, the bending angle β_r

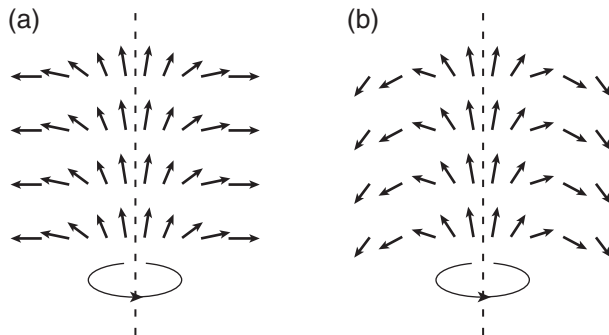


Figure 7.2 A schematic representation of the spin moment of non-singular coreless vortices known as (a) the Mermin–Ho (MH) and (b) the Anderson–Toulouse (AT) vortices. From Pietilä (2010).

varies from $\beta_0 = 0$ at the center to $\beta_R = \pi/2$ at the boundary, while in the AT vortex the bending angle at the boundary equals $\beta_R = \pi$. Thus the spin moment rotates in the radial direction from vertical at the center to horizontal (MH) or downwards (AT) at the boundary. The combination of winding numbers in these two types of vortex is $\langle w_1, w_0, w_{-1} \rangle = \langle 0, 1, 2 \rangle$ for components $(1, 0, -1)$, each integer denoting the phase change by $2\pi w_i$ around the singularity of the i th component (Mizushima *et al.*, 2002). The central region of the condensate is the filled by the $m_F = 1$ component, while the $m_F = 0$ is pushed outwards due to the winding number 1 and the $m_F = -1$ occupies the outermost region with winding number 2. The angular momentum per particle in a ferromagnetic condensate with a coreless vortex can be anything between 0 and 2. Moreover, a coreless vortex can be transformed continuously into a state with vanishing angular momentum. Ferromagnetic $F = 1$ spinor condensates can also exhibit polar core vortices. In this case the vortex core is filled by the component $m_F = 0$ in such a way that only the spin density vanishes at the core while the number density remains finite (Mizushima *et al.*, 2004). Coreless vortices have been experimentally created in ^{23}Na (Leanhardt *et al.*, 2002), polar core vortices in ^{87}Rb (Sadler *et al.*, 2006). In the antiferromagnetic case the circulation is quantized but the unit of quantization is half of the scalar case, i.e. $\frac{1}{2m}$ (Martikainen *et al.*, 2002a; Mukerjee *et al.*, 2006; Ji *et al.*, 2008). For this reason, these vortices are sometimes called half vortices.

7.4.2 Singular point defects: monopoles

Monopoles are topological excitations that are predicted for $F = 1$ spinor condensates in the case of antiferromagnetic interactions (Stoof *et al.*, 2001; Ruostekoski and Anglin, 2003). These singular point defects are analogous to the 't Hooft–Polyakov monopole ('t Hooft, 1974; Polyakov, 1974) (see Fig. 7.3(a)). Monopoles consist of a stable core rather like a spherical symmetric hedgehog and have vanishing density (Stoof *et al.*, 2001). In the weakly interacting regime, the defect core undergoes an instability, extending its size and deforming to a circle: a half-quantum vortex ring called an Alice ring (Ruostekoski and Anglin, 2003). Other instabilities have been studied by Busch and Anglin (1999) (see Fig. 7.3(b)) and proposals on how to create monopoles in spinor condensates can be found in the work of Martikainen *et al.* (2002b). For polar condensates described by eqn (7.10), the overall phase,

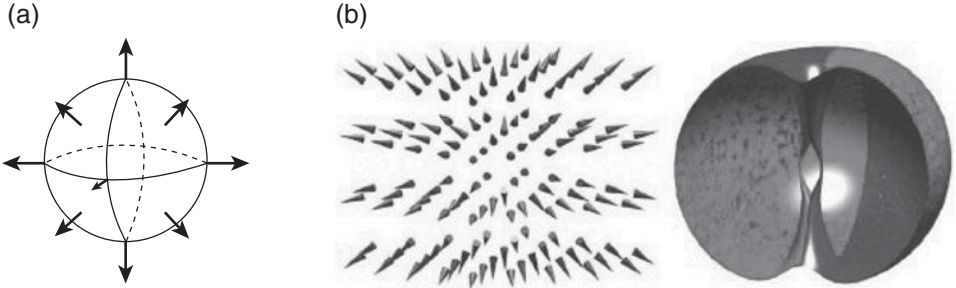


Figure 7.3 (a) Schematic representation of the spin texture of a 't Hooft–Polyakov monopole (from Stoof *et al.* (2001)). (b) Stable half-quantum vortex ring (Alice ring) obtained when the energy of an initially spherically symmetric monopole is minimized by continuously deforming the field configuration. The constant surface density plots for the $m_F = -1$ (light grey) and the $m_F = 1$ (dark grey) components are also shown (from Ruostekoski and Anglin (2003)).

the superfluid phase, can have spatial dependence $\varphi(\mathbf{r})$ and can be rewritten as:

$$\xi_F = \frac{1}{\sqrt{2}} e^{i\varphi(\mathbf{r})} \begin{pmatrix} -d_x + id_y \\ \sqrt{2}d_z \\ d_x + id_y \end{pmatrix}. \quad (7.19)$$

Using eqn (7.19), and assuming an isotropic 3D harmonic trapping potential $V_{\text{ext}}(\mathbf{r})$, one can rewrite the mean-field energy in eqn (7.8) in terms of unit vector field $\mathbf{d}(\mathbf{r})$ and the density profile $n(\mathbf{r})$ of the monopole. Since the gradient term of $\mathbf{d}(\mathbf{r})$, the so-called spin texture (Stoof *et al.*, 2001), is not coupled with the superfluid phase, the presence of a monopole does not induce any superfluid flow in the condensate. Minimization of the gradient energy term of the energy functional (eqn (7.8)):

$$E_{\text{grad}} = \int d\mathbf{r} \frac{n(\mathbf{r})\hbar^2}{2m} [\nabla \mathbf{d}(\mathbf{r})]^2, \quad (7.20)$$

with the condition of the topological winding number W being equal to one:

$$W = \frac{1}{8\pi} \int d\mathbf{r} \epsilon_{ijk} \epsilon_{\alpha\beta\gamma} \partial_i d_\alpha \partial_j d_\beta \partial_k d_\gamma = 1, \quad (7.21)$$

imposes that $\mathbf{d} = \mathbf{r}/r$ for the spin texture of the monopole at the center of the trap (Stoof *et al.*, 2001). Substituting this hedgehog solution for the spin texture in the energy functional, one determines the density profile. The core of the monopole is typically of the order of the correlation length and the density in this core is strongly reduced.

7.4.3 Non-singular point defects: skyrmions

Skyrmions are non-singular but topologically non-trivial point-like spin textures consisting of reversing of the average spin in a finite region of space; they are known from nuclear

physics (Skyrme, 1961, 1962) and the quantum Hall effect (Sondhi *et al.*, 1993). In ferromagnetic spinor condensates (eqn (7.9)) skyrmion excitations have been predicted (Al Khawaja and Stoof, 2001*a*, 2001*b*) to exist. The skyrmion excitation is a space-dependent spin deformation of the ground state that can be expressed as:

$$\boldsymbol{\xi}(\mathbf{r}) = \exp\left(-\frac{i}{F}\boldsymbol{\Omega}(\mathbf{r}) \times \mathbf{F}\right) \boldsymbol{\xi}_F, \quad (7.22)$$

where $\boldsymbol{\xi}_F = (1, 0, 0)^T$ is the constant spinor associated with the ferromagnetic ground state as indicated in eqn (7.9). This means that at point \mathbf{r} , the spinor $\boldsymbol{\xi}_F$ is rotated by an angle that equals $|\boldsymbol{\Omega}(\mathbf{r})|/F$ around the direction of $\boldsymbol{\Omega}(\mathbf{r})$. Assuming the maximum symmetry of the skyrmion, one can take $\boldsymbol{\Omega}(\mathbf{r}) = \omega(r)\mathbf{r}/r$, where $\omega(r)$ should satisfy the boundary conditions: (i) $\omega(0) = 2\pi$ to ensure the absence of singularity at the origin and (ii) $\lim_{r \rightarrow \infty} \omega(r) = 0$ to ensure that the spin deformations have finite range. Moreover, $\omega(r)$ should decrease monotonically as the radius increases to minimize the gradient energy for spin deformations (Al Khawaja and Stoof, 2001*a*). On the z -axis and far away from the center of the skyrmion the spins are directed as in the ground state. Close to the center of the skyrmion the spins should complete an integer number of cycles equal to $1/F$ in order to have a non-zero topological winding number (see Fig. 7.4(a)–(d)). By minimizing the energy functional with the expression for the spinor given in eqn (7.22), $n(r)$ and $w(r)$ can be calculated explicitly. It has been shown (Al Khawaja and Stoof, 2001*a*, 2001*b*) that skyrmions are thermodynamically unstable without rotation; nevertheless there have been some proposals of how to create and detect them in spinor condensates (Marzlin *et al.*, 2000; Tsuchiya and Kurihara, 2001).

7.4.4 Knots

Knots are unique topological objects characterized by a topological charge Q , also known as Hopf invariant. This is in contrast to vortices, monopoles, and skyrmions, which are characterized by a winding number. Knots are described by means of mappings from a 3D sphere S^3 to S^2 . Knots, which can be created in polar spinor condensates as shown by Kawaguchi *et al.* (2008), belong to the third homotopy group, $\pi_3(M) \cong \pi_3(S^2) = \mathbb{Z}$, because neither $U(1)$ nor Z_2 symmetry contributes to homotopy groups in spaces of higher dimensions than 1. The topological charge Q is defined as:

$$Q = \frac{1}{4\pi^2} \int d\mathbf{r} \epsilon_{ijk} F_{ij} A_k, \quad (7.23)$$

where $F_{ij} = \partial_i A_j - \partial_j A_i = \mathbf{d} \cdot (\partial_i \mathbf{d} \times \partial_j \mathbf{d})$ (Faddeev and Niemi, 1997), and \mathbf{d} is the vector unit in spin space related to the order parameter through eqn (7.19) (Kawaguchi *et al.*, 2008) A \mathbf{d} field is depicted in Fig. 7.4(e) for a knot with Hopf charge $Q = 1$.

Aside from all the spin textures and topological defects above, various kinds of defect are generated according to the Kibble–Żurek mechanism (Kibble, 1976; Żurek, 1985) during the spontaneous symmetry-breaking in $F = 1$ spinor condensates, which are rapidly quenched across a quantum phase transition. The first experiments in the presence of a magnetic field in ^{87}Rb $F = 1$ spinor condensate have been reported in Sadler *et al.* (2006). After the

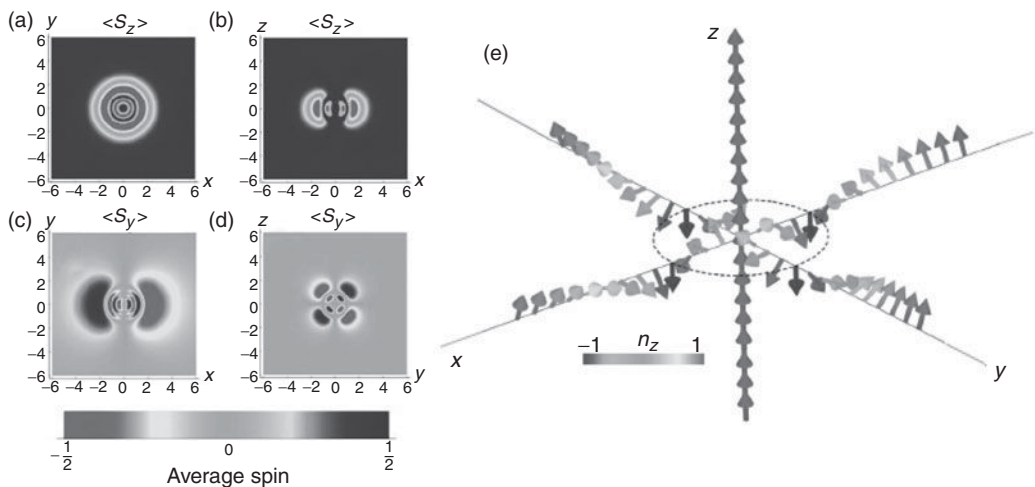


Figure 7.4 (a)–(d) The average spin texture of a skyrmion numerically generated in a spin- $\frac{1}{2}$ condensate of ^{87}Rb atoms, reprinted after Al Khawaja and Stoof (2001b) by courtesy of the authors. (e) 3D configuration of the \mathbf{d} field of a knot with Hopf charge $Q = 1$, redrawn after Kawaguchi *et al.* (2008) by courtesy of the authors.

quenching, transverse ferromagnetic domains of variable size were formed throughout the condensate, divided by narrow non-magnetized domain walls. The dynamics of the quantum phase transition have also been addressed theoretically (Saito *et al.*, 2007). Breaking of chiral symmetry originated from an interplay between ferromagnetic interactions and spin conservation was also predicted (Saito *et al.*, 2006).

7.5. Bosonic spinor gases in optical lattices

Spinor gases in optical lattices offer the possibility of studying magnetic quantum systems with unprecedented control of the parameters. The confinement of the particles in the lattice enhances the effects of the interactions, leading to the strongly correlated regimes. As already mentioned in Chapters 3 and 4, when the physics in the optical lattice is restricted to the lowest band, the corresponding Hamiltonian is of the Hubbard type. In the scalar case, the ratio between tunneling and on-site interactions is the control parameter that determines the quantum phase transition between superfluid and MI states (Greiner *et al.*, 2002). If the atoms exhibit spin degrees of freedom, the phase diagram on the MI side becomes much richer. Hence lattice spinor systems provide a new tool to simulate quantum magnetism by implementing spin Hamiltonians that are often extremely difficult to study in condensed-matter physics (García-Ripoll *et al.*, 2004). Moreover, they provide key ingredients for the study of artificial non-Abelian gauge theories (Wilczek and Zee, 1984), as explained in detail in Chapter 11. Another interesting application of spinor gases in optical lattices is the engineering of strongly correlated states for quantum information processing (Widera *et al.*, 2005), as discussed in Chapter 13.

7.5.1 Bose–Hubbard model for spin-1 particles

The derivation of the Bose–Hubbard Hamiltonian for lattice spinor gases is analogous to the scalar case (see Chapter 3), but with the addition of the spin-dependent part of the interaction in the Hamiltonian in second quantization, see eqn (7.6). The Bose–Hubbard Hamiltonian for spin-1 particles reads (Imambekov *et al.*, 2003):

$$\hat{H} = -t \sum_{\langle i,j \rangle, \sigma} (\hat{b}_{\sigma i}^\dagger \hat{b}_{\sigma j} + h.c.) + \frac{U_0}{2} \sum_i \hat{n}_i (\hat{n}_i - 1) + \frac{U_2}{2} \sum_i (\hat{\mathbf{S}}_i^2 - 2\hat{n}_i) - \mu \sum_i \hat{n}_i, \quad (7.24)$$

where, as usual, $\langle i, j \rangle$ indicates nearest neighbors, $\hat{b}_{\sigma i}^\dagger$ ($\hat{b}_{\sigma i}$) denotes the creation (annihilation) operator of a boson in the lowest Bloch band localized at site i and in the $\sigma (= m_F)$ -th Zeeman state $|F = 1, m_F = -1, 0, 1\rangle$. Notice that F refers to the atom hyperfine state, while

$$\hat{\mathbf{S}}_i = \sum_{\sigma\sigma'} \hat{b}_{\sigma i}^\dagger \mathbf{F}_{\sigma\sigma'} \hat{b}_{\sigma' i} \quad (7.25)$$

is the total spin operator at site i , with $\mathbf{F} = (F_x, F_y, F_z)$ denoting the usual spin-1 matrices (eqn (7.7)). The boson number operator at site i is given by $\hat{n}_i = \sum_{\sigma} \hat{b}_{\sigma i}^\dagger \hat{b}_{\sigma i} = \sum_{\sigma} \hat{n}_{\sigma i}$, and the spin operator $\hat{\mathbf{S}}_i$ has the following components:

$$\hat{S}_{ix} = \frac{1}{\sqrt{2}} \left(\hat{b}_{1i}^\dagger \hat{b}_{0i} + \hat{b}_{0i}^\dagger \hat{b}_{1i} + \hat{b}_{0i}^\dagger \hat{b}_{-1i} + \hat{b}_{-1i}^\dagger \hat{b}_{0i} \right), \quad (7.26)$$

$$\hat{S}_{iy} = \frac{i}{\sqrt{2}} \left(-\hat{b}_{1i}^\dagger \hat{b}_{0i} + \hat{b}_{0i}^\dagger \hat{b}_{1i} - \hat{b}_{0i}^\dagger \hat{b}_{-1i} + \hat{b}_{-1i}^\dagger \hat{b}_{0i} \right), \quad (7.27)$$

$$\hat{S}_{iz} = \hat{n}_{1i} - \hat{n}_{-1i}, \quad (7.28)$$

and obeys the usual angular momentum commutation relations: $[\hat{S}_{i\mu}, \hat{S}_{i\nu}] = i\epsilon_{\mu\nu\lambda} \hat{S}_{i\lambda}$ with $\{\mu, \nu, \lambda\} = \{x, y, z\}$.

The first term in eqn (7.24) represents spin-symmetric tunneling between nearest-neighbor sites, where the tunneling rate t is assumed to be spin- and site-independent. The second and third terms account for spin-independent and spin-dependent on-site interactions respectively, with energies at site i $U_{0,2} = c_{0,2} \int d\mathbf{r} w^4(\mathbf{r} - \mathbf{r}_i)$, with $w(\mathbf{r} - \mathbf{r}_i)$ being the single-particle Wannier function at site i and $c_{0,2}$ being as defined in eqn (7.3). Note that the third term penalizes nonzero spin configurations in individual lattice sites for antiferromagnetic interactions (Law *et al.*, 1998; Imambekov *et al.*, 2003). The last term in eqn (7.24) corresponds to the chemical potential. Some constraints apply here. First, since the orbital part of the wave function in one lattice site is the product of Wannier functions for all the atoms, it is symmetric under permutation for identical bosons and therefore the spin part of the wave function should also be symmetric due to Bose statistics. This imposes that $S_i + n_i$ has to be even, i.e. S_i is even (odd) if n_i is even (odd) (Wu, 1996) being S_i and n_i the quantum numbers labeling the eigenvalues of $\hat{\mathbf{S}}_i$ and \hat{n}_i , respectively. Also $S_i \leq n_i$, since the total spin of a system with N spin-1 particles cannot exceed N .

As in the scalar case, the spinor Bose–Hubbard Hamiltonian with $U_0 > 0$ is expected to describe a quantum phase transition between superfluid and insulating states (Imambekov

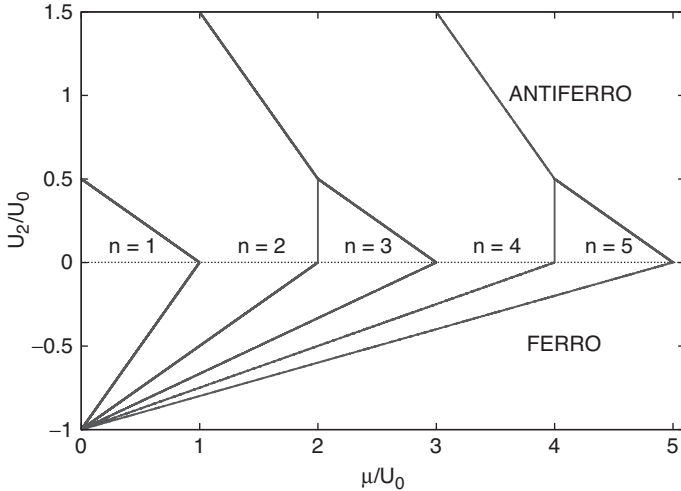


Figure 7.5 The phase diagram in the (U_2, μ) plane of the spinor $F = 1$ Bose–Hubbard model in the atomic limit $t = 0$. Each region (lobe) corresponds to a MI phase with a different occupation number n . From Łącki *et al.* (2011).

et al., 2003; Tsuchiya *et al.*, 2004). In fact, the spin degree of freedom in the Bose–Hubbard Hamiltonian provides a rich phase diagram with different insulating phases differing in their spin correlations.

It is instructive to explore the predictions of the spinor Bose Hubbard model in the so-called atomic limit, i.e. for $t = 0$. In this case, the Hamiltonian becomes trivially a sum of independent single-site Hamiltonians

$$\hat{H}(t = 0) = \sum_i \hat{H}_0^i = \sum_i \frac{U_0}{2} \hat{n}_i(\hat{n}_i - 1) + \frac{U_2}{2} (\hat{\mathbf{S}}_i^2 - 2\hat{n}_i) - \mu \hat{n}_i. \quad (7.29)$$

The eigenstates of the single-site Hamiltonian \hat{H}_0^i are also eigenstates of $\hat{\mathbf{S}}_i$, \hat{S}_{iz} , and \hat{n}_i and hence trivially labeled by the quantum numbers as $|S_i, m_i; n_i\rangle$, such that:

$$\hat{H}_0^i |S_i, m_i; n_i\rangle = E_0(S_i, n_i) |S_i, m_i; n_i\rangle \quad (7.30)$$

From the above equation, one can derive the $(U_2/U_0, \mu/U_0)$ phase diagram of the MI phases in the limit $t = 0$, shown in Figure 7.5. The widths of the MI lobes are obtained as follows:

- The ferromagnetic side of the diagram ($U_2 < 0$) is trivially obtained by imposing an integer number of particles per site and realizing that minimization of the energy implies maximum spin value, i.e. $S_i = n_i$.
- The antiferromagnetic side ($U_2 > 0$), on the other hand, minimizes the energy when S_i is minimum. Its specific value depends of the number of atoms per site. For an even filling factor the minimum spin is zero and the ground state is described by $|0_i, 0_i; n_i\rangle$,

with n_i even. This state is known as the spin-singlet insulator (Demler and Zhou, 2002). MI lobes with spin 0 on each site then appear for $(n_i - 1)U_0 - 2U_2 < \mu < n_i U_0$ for $U_2/U_0 \leq 0.5$. For higher values, odd lobes do not exist and the stability conditions read $E_0(0, n_i) < E_0(0, n_i - 2)$ and $E_0(0, n_i) < E_0(0, n_i + 2)$. The last two conditions set an n_i -dependent upper bound on the maximum value of $U_2/U_0 \leq (n_i + \frac{1}{2})$. For an odd filling factor, the ground state reads $|1_i, m_i; n_i\rangle$. Mott lobes appear for spin-1 in each site for $(n_i - 1)U_0 < \mu < n_i U_0 - 2U_2$. These conditions set an upper bound on the spin coupling $U_2/U_0 \leq 0.5$ above which there are no odd lobes.

It is interesting to note that the right boundary of even lobes in the range $0 < U_2/U_0 < 0.5$ does not change with U_2 . In the antiferromagnetic region, for U_2 large enough, odd lobes disappear while even lobes broaden. In the ferromagnetic case the lobes shrink as $|U_2|$ increases and disappear for $U_2/U_0 = -1$.

7.5.2 Effective Hamiltonian for spin-1 particles

For small but non-zero tunneling $t/U_0 \ll 1$ and $|U_2| \ll U_0$ (which is normally the case in alkaline atoms), it is possible to perform perturbation theory and derive an effective Hamiltonian in the second order in t/U_0 . To this end one splits, as usual, the full Hamiltonian into $\hat{H} = \hat{H}_0 + \hat{H}_t$, where $\hat{H}_0 = \sum_i \hat{H}_0^i$ is a sum of independent single-site Hamiltonians and \hat{H}_t is the perturbation term that preserves the total spin S and the projection of the total spin m_S . If the system is homogeneous, the on-site Hamiltonian becomes site-independent and one can restrict the analysis to two sites, calculating the shift of the energy of the two-site ground state at zero tunneling $|S_g; n_g\rangle$ as:

$$\epsilon_S = - \sum_{\nu} \frac{|\langle \nu | \hat{H}_t | S_g; n_g \rangle|^2}{E_{\nu} - E_g}, \quad (7.31)$$

where ν labels all the (virtual) intermediate states and E_{ν} , E_g denote the unperturbed energies of the two-site states $|\nu\rangle$, $|S_g; n_g\rangle$, respectively. Tunneling processes induce effective nearest-neighbor spin–spin interactions in the lattice.

When the number of bosons per site is odd, the effective Hamiltonian can then be written as:

$$\hat{H}_{eff} = \sum_{S=0,1,2} \epsilon_S \sum_{\langle i,j \rangle} \hat{P}_{ij}(S), \quad (7.32)$$

where $\hat{P}_{ij}(S)$ is the projector for a pair of spins on near-neighbor sites i and j onto a state with total spin $S = S_i + S_j = 1 \oplus 1 = 0, 1, 2$. The unperturbed two-site state (for odd occupancy) should be $|S_g = 1 + 1; n_g\rangle$, and therefore:

$$\epsilon_S = - \sum_{\nu} \frac{|\langle \nu | \hat{H}_t | S_g = 1 + 1; n_g \rangle|^2}{E_{\nu} - E_g} \quad (7.33)$$

For $S = 1 \oplus 1 = 0$, there are two possible intermediate states corresponding to

$$|S_i = 0, S_j = 0; n_i = 2n + 2, n_j = 2n\rangle,$$

and the corresponding state interchanging i and j . For $S = 1 \oplus 1 = 1$, there are also two intermediate states satisfying:

$$|S_i = 2, S_j = 2; n_i = 2n + 2, n_j = 2n\rangle,$$

and $i \leftrightarrow j$. Finally, for $S = 1 \oplus 1 = 2$, there are four intermediate states given by:

$$|S_i = 2, S_j = 0; n_i = 2n + 2, n_j = 2n\rangle \quad \text{and} \quad |S_i = 0, S_j = 2; n_i = 2n + 2, n_j = 2n\rangle$$

plus the corresponding ones interchanging i and j . Applying eqn (7.33) and taking into account the allowed intermediate states, one obtains (Imambekov *et al.*, 2003):

$$\epsilon_0 = -\frac{4t^2(n+1)(2n+3)}{3(U_0 - 2U_2)} - \frac{16t^2n(5+2n)}{15(U_0 + 4U_2)} \quad (7.34)$$

$$\epsilon_1 = -\frac{4t^2n(2n+5)}{5(U_0 + 4U_2)} \quad (7.35)$$

$$\epsilon_2 = -\frac{28t^2n(2n+5)}{75(U_0 + 4U_2)} - \frac{4t^2(15+20n+8n^2)}{15(U_0 + U_2)} \quad (7.36)$$

Using the operator identities of Section 7.2 for spin-1 particles, the effective Hamiltonian, eqn (7.32), can be written as a generalized quadratic Heisenberg Hamiltonian (Imambekov *et al.*, 2003):

$$\hat{H}_{\text{eff}} = -J_0 - J_1 \sum_{\langle i,j \rangle} \hat{\mathbf{S}}_i \hat{\mathbf{S}}_j - J_2 \sum_{\langle i,j \rangle} (\hat{\mathbf{S}}_i \cdot \hat{\mathbf{S}}_j)^2, \quad (7.37)$$

which can be rewritten as the bilinear biquadratic Hamiltonian (Demler and Zhou, 2002; Yip, 2003a):

$$\hat{H}_{\text{BBH}} = \sqrt{J_1^2 + J_2^2} \sum_{\langle i,j \rangle} [\cos \theta (\hat{\mathbf{S}}_i \cdot \hat{\mathbf{S}}_j) + \sin \theta (\hat{\mathbf{S}}_i \cdot \hat{\mathbf{S}}_j)^2], \quad (7.38)$$

where the explicit expressions for J_0 , J_1 , and J_2 of eqn (7.37) and (7.38) can be straightforwardly derived (Imambekov *et al.*, 2003). The explicit expressions for the J s change when higher orders in t are considered. Nevertheless, in the limit $t \ll U_0$, the contribution of higher orders in t can be neglected (Yip, 2003a). Thus the spinor Bose–Hubbard model for odd filling in the limit of small tunneling leads to the bilinear biquadratic Heisenberg Hamiltonian, eqn (7.38), a paradigmatic model in condensed matter; its phase diagrams are schematically shown in Figures 7.6 and 7.8 for 1D spin chains and higher-dimensional spin models, respectively.

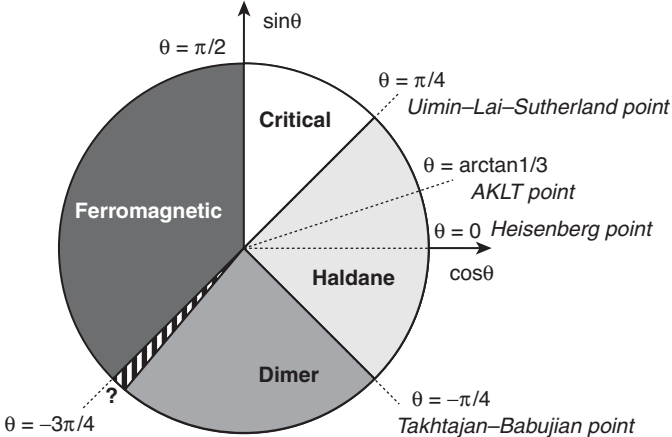


Figure 7.6 Ground state phase diagram of the bilinear biquadratic Hamiltonian for $F = 1$ bosons in a 1D lattice.

One-dimensional systems In one dimension and with an odd filling factor, the phase diagram is well understood. In this case, some exact solutions and high-precision numerical calculations have established the nature and the transition points of most of the phases, although there is still some controversy, as we will discuss below. The diagram sketched in Figure 7.6 as function of $\theta \in [-\pi, \pi]$ has the following phases.

- **Ferromagnetic phase.** For $\theta \in (\pi/2, \pi] \cup [-\pi, -3\pi/4)$ the ground state is ferromagnetic, with spontaneous magnetization that breaks the $SU(2)$ symmetry. It is characterized by:

$$|F\rangle = \prod_i |S_i = 1, m_i = 1, -1\rangle. \quad (7.39)$$

For all the other values of θ , i.e. $-3\pi/4 < \theta < \pi/2$, the ground state has zero magnetization.

- **Dimerized phase.** For the region $-3\pi/4 < \theta < -\pi/4$ the ground state is characterized by dimerization and has a non-vanishing dimer order parameter $\mathbb{D} = |\langle \hat{H}_i - \hat{H}_{i+1} \rangle|$, where

$$\hat{H}_i = \left[\cos \theta (\hat{S}_i \cdot \hat{S}_{i+1}) + \sin \theta (\hat{S}_i \cdot \hat{S}_{i+1})^2 \right],$$

i.e. the local part of the Hamiltonian (eqn (7.38)). A dimerized state is created when the translational symmetry is broken, favoring singlets on each second bond. The most simple variational ansatz for this state is (Affleck, 1989; Chubukov, 1991; Yip, 2003a):

$$|D\rangle = \prod_{i,\text{odd}} |S_i = 1, S_{i+1} = 1, S_i + S_{i+1} = 0\rangle \quad (7.40)$$

A state with all dimer pairs shifted by one lattice period is degenerate with (7.40). This state fulfills $\langle \hat{S}_{iz} \rangle = 0$ and $\langle (\hat{S}_{iz})^2 \rangle = \frac{2}{3}$.

- **Nematic phase.** A nematic phase has been conjectured (Chubukov, 1991). This would separate the ferromagnetic phase from the dimerized ones. Its existence is, however, still debated. A variational ansatz for the nematic state mixes states with total spin $S = 0$ and $S = 2$ (and $m_F = 0$) in each bond and can be written as the following product state:

$$|N\rangle = \prod_i |S_i = 1, m_i = 0\rangle. \quad (7.41)$$

This nematic state has zero expectation value of all spin components: $\langle \hat{S}_{ix} \rangle = \langle \hat{S}_{iy} \rangle = \langle \hat{S}_{iz} \rangle = 0$. However, spin symmetry is broken since $\langle (\hat{S}_{ix})^2 \rangle = \langle (\hat{S}_{iy})^2 \rangle = \frac{1}{2}$ and $\langle (\hat{S}_{iz})^2 \rangle = 0$. Thus nematic states are in direct analogy with the polar phase in the bulk (see Section 7.3.1). The existence of this region has been actively discussed and the question is still open.

- **Critical phase.** The critical phase (Fáth and Sólyom, 1991) extends in the interval $\frac{\pi}{4} < \theta < \frac{\pi}{2}$ and it is a gapless phase with algebraic decay of correlations. This phase exhibits, however, a ‘trimer’ order, i.e. it can be roughly approximated locally by the trimer state:

$$|T\rangle = \prod_{i,\text{odd}} |S_i = 1, S_{i+1} = 1, S_{i+2} = 1, S_i + S_{i+1} + S_{i+2} = 0\rangle. \quad (7.42)$$

- **Haldane phase.** The Haldane phase (Haldane, 1983a, 1983b) extends in the region $[-\frac{\pi}{4}, \frac{\pi}{4}]$ and its main features are first that the excitation spectrum above the ground state displays a finite energy gap and second that it exhibits a hidden topological order. For $\tan \theta = \frac{1}{3}$, the bilinear biquadratic Hamiltonian in eqn (7.38) takes the form of the Affleck, Kennedy, Lieb and Tasaki (AKLT) Hamiltonian (Affleck *et al.*, 1987, 1988a). This value of θ is therefore known as the AKLT point. The AKLT Hamiltonian is the parent Hamiltonian for the specific valence bond crystal (VBC) state, that is, the exact ground state:

$$|\text{VBC}\rangle = \prod_{\langle i,j \rangle} \left(\hat{a}_i^\dagger \hat{b}_j^\dagger - \hat{b}_i^\dagger \hat{a}_j^\dagger \right)^M |0\rangle, \quad (7.43)$$

where $\langle i, j \rangle$ are all the nearest-neighbor bonds of the lattice and $M = 2S/z$, with z the lattice coordination number and \hat{a}_i , \hat{b}_i being Schwinger bosons (Auerbach, 1994), i.e. spin representations in which the rotational invariance of the Hamiltonian is manifested:

$$\begin{aligned} \hat{S}_x + i\hat{S}_y &= \hat{a}^\dagger \hat{b}, \\ \hat{S}_x - i\hat{S}_y &= \hat{b}^\dagger \hat{a}, \\ \hat{S}_z &= \frac{1}{2} \left(\hat{a}^\dagger \hat{a} - \hat{b}^\dagger \hat{b} \right). \end{aligned} \quad (7.44)$$

The $|VBC\rangle$ state can also be viewed as an MPS, as discussed in Chapter 12. Another special point is $\theta = 0$, which corresponds to the Heisenberg point. The bilinear biquadratic Hamiltonian at this point reduces to the Heisenberg Hamiltonian (see Chapter 4). The limits of the Haldane phase are critical points—solvable by Bethe ansatz—in which the correlation length diverges: (i) $\theta = -\frac{\pi}{4}$ corresponds to the Takhtajan–Babujian point (Takhtajan, 1982; Babujian, 1982), displaying a second-order phase transition towards the dimerized phase, while (ii) $\theta = \frac{\pi}{4}$ is known as the Uimin–Lai–Sutherland point (Uimin, 1970; Lai, 1974; Sutherland, 1975), where a phase transition to the critical phase occurs.

Very recently considerable interest has been devoted to the generalization of the bilinear biquadratic Hamiltonian that includes the effects of magnetic fields, which are always present in experiments (Rodriguez *et al.*, 2011; De Chiara *et al.*, 2011). Since the bilinear biquadratic Hamiltonian conserves the magnetization, at fixed magnetization the linear Zeeman effect does not change the physics. Moreover, in experimental situations very often the magnetic fields oscillate very rapidly in time and their effects average to zero. The case of the quadratic Zeeman effect (corresponding in condensed matter to *single-ion anisotropy*) is more complex. The modified bilinear biquadratic Hamiltonian takes the form

$$\hat{H}_{BBH} = J \sum_{\langle i,j \rangle} \left[\cos \theta (\hat{\mathbf{S}}_i \cdot \hat{\mathbf{S}}_j) + \sin \theta (\hat{\mathbf{S}}_i \cdot \hat{\mathbf{S}}_j)^2 \right] + D \sum_i (\hat{S}_{iz})^2. \quad (7.45)$$

In Figure 7.7 we show the complete diagram of this model in the $D/J - \theta/\pi$ plane, as obtained numerically by using DMRG method (De Chiara *et al.*, 2011). Analytic results for part of the diagram (in excellent agreement with the numerics) have been reported in (Rodriguez *et al.*, 2011).

Two- and three-dimensional systems In the case of dimensions higher than one, knowledge of the ground-state phase diagram at zero temperature of the bilinear biquadratic Hamiltonian largely relies on mean-field and semiclassical approaches (Papanicolaou, 1986, 1988; Fáth and Sólyom, 1995) (see Figure 7.8), although Monte Carlo methods are available for specific regions of the phase diagram (Harada and Kawashima, 2001, 2002). This diagram contains four phases, in which the $SU(2)$ symmetry of the model is spontaneously broken: (i) ferromagnetic ($\frac{\pi}{2} < \theta < \frac{5\pi}{4}$), (ii) antiferromagnetic ($-\frac{\pi}{2} < \theta < \frac{\pi}{4}$), (iii) collinear nematic ($\frac{5\pi}{4} < \theta < -\frac{\pi}{2}$), and (iv) orthogonal nematic ($\frac{\pi}{4} < \theta < \frac{\pi}{2}$). In the so-called nematic phases the expectation value of the spin operators vanishes $\langle \hat{S}_{ix} \rangle = \langle \hat{S}_{iy} \rangle = \langle \hat{S}_{iz} \rangle = 0$, while $\langle \hat{S}_{ix}^2 \rangle = \langle \hat{S}_{iy}^2 \rangle \neq \langle \hat{S}_{iz}^2 \rangle$.

Spin-1 bosonic lattice gases with antiferromagnetic interactions were first studied by Demler and Zhou (2002), who pointed out the different phases appearing when the SF–MI transition is studied. A more extensive analysis was presented in Imambekov *et al.* (2003) and later in Tsuchiya *et al.* (2004). Variational analysis showed that, for ^{23}Na and one particle per site, the ground state is the dimer phase in all dimensions (Yip, 2003a). The case of a general pairwise interaction and larger occupation was also studied by Yip (2003b). While two and three dimensions still mostly rely on mean-field methods, 1D systems have been numerically explored using DMRG. Rizzi *et al.* (2005) confirmed

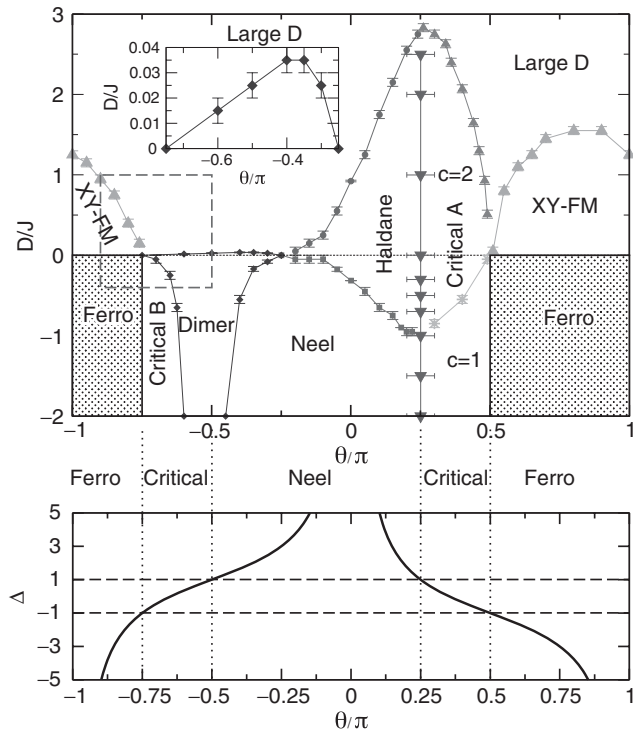


Figure 7.7 The phase diagram for the 1D modified BBH model with quadratic Zeeman effect in the $D/J - \theta/\pi$ plane. This was obtained using the DMRG method. In the limit of large negative D the modified BBH model reduces to the spin- $\frac{1}{2}$ XXZ , with anisotropy Δ that can be calculated perturbatively. The lower panel shows a plot of Δ as a function of θ . The ground state of the XXZ model is critical for $|\Delta| < 1$ and ferro- (antiferro-) magnetic for $\Delta < -1$ ($\Delta > 1$), respectively. From De Chiara *et al.* (2011).

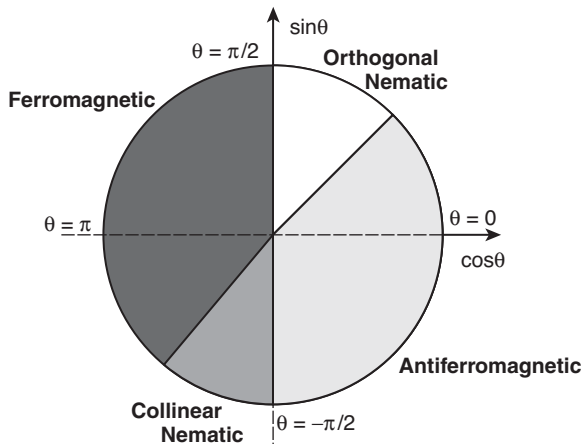


Figure 7.8 Ground state phase diagram of the bilinear biquadratic Hamiltonian for $F = 1$ bosons in an optical lattice for dimensionality higher than one.

the dimerized ground state for ^{23}Na in the low-tunneling regime of the first MI lobe of the SF–MI transition. Porras *et al.* (2006) addressed the actively discussed existence of the conjectured spin nematic region (Chubukov, 1991). Nematic order seems strictly speaking to be absent in one dimension in the thermodynamic limit. However, close to the border of the ferromagnetic phases susceptibility to nematic ordering grows, indicating that it may persist in finite systems. A completely new insight can be gained by looking at entanglement transport properties of $F = 1$ chains (Romero-Isart *et al.*, 2007), which seem to confirm the existence of nematic and trimer regions for finite systems.

7.5.3 Superfluid–Mott insulator transition for spin-1 particles

One-dimensional systems In one dimension, the SF–MI transition has been studied numerically using finite-size DMRG with open boundary conditions (see Section 5.10), solving the spinor Bose–Hubbard model for spin-1 particles (eqn (7.24)) for different values of the U_2 parameter. To determine the boundaries between the insulating and superfluid phases, one takes into account that in the insulating phase the first excited state is always separated from the ground state by an energy gap. In the limit of zero hopping, the gap is determined by the extra energy needed to place or remove a boson at a given site. The gap vanishes at the critical value (quantum phase transition) and the system enters into the superfluid regime. In Rizzi *et al.* (2005), chains were considered of up to 128 sites for the first lobe and up to 48 for the second lobe. An extrapolation procedure was then applied to extract asymptotic values. The phase diagram in the $\mu - t$ plane for different values of the spin-coupling U_2 is shown in Figure 7.9. The first lobe tends to reduce its size on increasing the spin coupling U_2 , while the second lobe shows the opposite tendency. The analysis presented in Rizzi *et al.* (2005) showed no evidence of the conjectured nematic phase predicted in the bilinear biquadratic Heisenberg model.

Two- and three-dimensional systems: mean-field perturbative approach For higher dimensions, the MI–SF transition for spin-1 has been studied using a standard mean-field perturbative approach (Tsuchiya *et al.*, 2004). As explained in detail in Section 5.4, the mean field perturbative approach is obtained by neglecting second-order fluctuations of the bosonic annihilation and creation operators. Introducing the superfluid order parameter $\psi_{j\sigma} = \langle \hat{b}_{j\sigma} \rangle$, which in a homogeneous lattice is site-independent, into the Bose-Hubbard Hamiltonian for spin-1 particles (eqn (7.24)), the Hamiltonian reduces to a sum of local terms $\hat{H}_{\text{MF}} = \sum_i \hat{h}_i$, with

$$\hat{h} = -tz \sum_{\sigma} \left[\left(\psi_{\sigma} \hat{b}_{\sigma}^{\dagger} + \psi_{\sigma}^* \hat{b}_{\sigma} \right) - |\psi_{\sigma}|^2 \right] - \mu \hat{n} + \frac{U_0}{2} \hat{n}(\hat{n} - 1) + \frac{U_2}{2} \left(\hat{\mathbf{S}}^2 - 2\hat{n} \right), \quad (7.46)$$

where the site index i has been dropped since we are considering a homogeneous system, and z denotes the number of nearest neighbors. The superfluid phase is associated with a finite value of the superfluid order parameter, while the MI phase corresponds to a zero value of the superfluid order parameter.

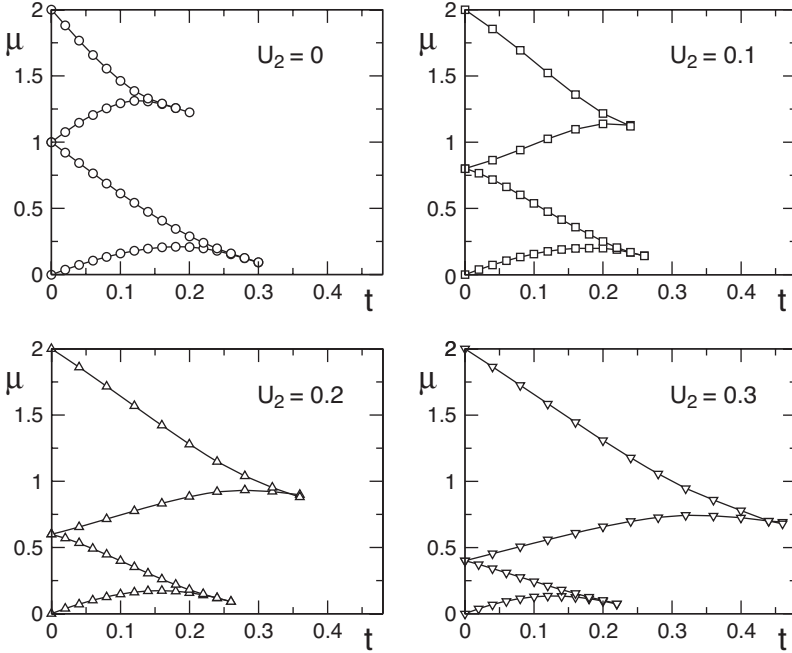


Figure 7.9 Phase diagram for the first two lobes of the 1D Bose–Hubbard spin-1 model with nearest-neighbor interactions, solved numerically by DMRG. The different panels correspond to different values of U_2 with U_0 being the energy scale unit. From Rizzi *et al.* (2005).

For sufficiently small tunneling t , we apply perturbation theory, $\hat{h} = \hat{H}_0 + \hat{H}_t$, and use as a basis the eigenstates of \hat{H}_0 (eqn (7.30)). The perturbation term is given by

$$\hat{H}_t = -tz \sum_{\sigma} \left[\left(\psi_{\sigma} \hat{b}_{\sigma}^{\dagger} + \psi_{\sigma}^* \hat{b}_{\sigma} \right) - |\psi_{\sigma}|^2 \right]. \quad (7.47)$$

Let us focus first on the antiferromagnetic case $U_2 > 0$. A tedious but straightforward calculation of the matrix elements of the perturbation leads to the phase boundaries between the superfluid phase and the MI phase in the $(\mu/U_0, t/U_0)$ plane for a given value of the U_2/U_0 coupling. Notice again that with $\hat{H}_t \propto (\hat{b}_{\sigma}^{\dagger} + \hat{b}_{\sigma})$ only even terms on the perturbation expansion survive. As derived in Tsuchiya *et al.* (2004), for odd occupation number, the ground-state energy up to second order is given by:

$$E^{(2)}(S=1, n, t, U_0, U_2, \mu, \psi_{\sigma}) = zt \left[1 - zt \sum_{j=1,4} \alpha_j(n, U_0, U_2, \mu) \right] \sum_{\sigma} |\psi_{\sigma}|^2, \quad (7.48)$$

and for even occupation by

$$E^{(2)}(S = 0, n, t, U_0, U_2, \mu, \psi_\sigma) = zt \left[1 - \frac{zt}{3} \sum_{j=1,2} \gamma_j(n, U_0, U_2, \mu) \right] \sum_\sigma |\psi_\sigma|^2, \quad (7.49)$$

with

$$\begin{aligned} \alpha_1(n, U_0, U_2, \mu) &= \frac{n+2}{3\delta_{n-1,0;n,1}(U_0, U_2, \mu)}, \\ \alpha_2(n, U_0, U_2, \mu) &= \frac{4(n-1)}{15\delta_{n-1,2;n,1}(U_0, U_2, \mu)}, \\ \alpha_3(n, U_0, U_2, \mu) &= \frac{n+1}{3\delta_{n+1,0;n,1}(U_0, U_2, \mu)}, \\ \alpha_4(n, U_0, U_2, \mu) &= \frac{4(n+4)}{15\delta_{n+1,2;n,1}(U_0, U_2, \mu)}, \end{aligned} \quad (7.50)$$

and

$$\begin{aligned} \gamma_1(n, U_0, U_2, \mu) &= \frac{n+3}{\delta_{n+1,1;n,0}(U_0, U_2, \mu)}, \\ \gamma_2(n, U_0, U_2, \mu) &= \frac{n}{\delta_{n-1,1;n,0}(U_0, U_2, \mu)}, \end{aligned} \quad (7.51)$$

and $\delta_{l,r;n,s}(U_0, U_2, \mu) = E_0(l, r, U_0, U_2, \mu) - E_0(s, n, U_0, U_2, \mu)$.

Minimization of the energy for a finite order parameter (corresponding to superfluid) is achieved when the expressions in parentheses in eqn (7.48) and (7.49) are negative. On the other hand, the MI phase, corresponding to a zero-order parameter is associated with a positive value of such expressions. Therefore the phase boundaries between the superfluid and the MI in the $(\mu/U_0, t/U_0)$ plane for a given value of the spin interaction U_2 are given by (Łacki *et al.*, 2011):

$$t_{\text{odd}} = \frac{1}{z \sum_{j=1,4} \alpha_j(n, U_0, U_2, \mu)} \quad (7.52)$$

$$t_{\text{even}} = \frac{3}{z \sum_{j=1,2} \gamma_j(n, U_0, U_2, \mu)} \quad (7.53)$$

Notice also that the dimensionality of the lattice is included here through the parameter z , which indicates the number of nearest neighbors.

The analysis of the ferromagnetic regime ($U_2 < 0$) can be done in the same way, imposing the condition $S = n$. Since in this case all the spins are aligned, we can consider only one

of the components $m_S = \pm S$ in the perturbative expansion. A straightforward calculation leads to the following explicit expression for the MI to superfluid boundary:

$$t_{\text{ferro}} = -\frac{(n + nU_2 - \mu) [(-1 + n)(1 + U_2) - \mu]}{z(1 + U_2 + \mu)}. \quad (7.54)$$

Variational Gutzwiller approach It is possible to use as a mean field a variational Gutzwiller approximation too, as explained in detail in Chapter 5. Being a generalization of the standard mean-field approximation, the Gutzwiller ansatz is expected to be exact in the limit of infinite dimensions. Moreover, the Gutzwiller approach does not demand site-invariance and thus permits calculation of mean-field quantities in non-homogeneous systems, when, for example, a trapping potential is included or disorder is considered. For the spinor case, the variational wave function ansatz takes the form of a product over all M sites of the lattice

$$|\psi\rangle = \prod_{i=1}^M \sum_{n=0}^{n_{\max}} g_i(n) \sum_{S=0}^n f_i(S, n) \sum_{m=-S}^S h_i(S, m, n) |S, m, n\rangle_i \quad (7.55)$$

where g_i , h_i , and f_i are the variational coefficients to be determined by minimizing the Bose–Hubbard Hamiltonian for spin-1 particles (eqn (7.24)) with the above ansatz. This implies decoupling in the tunneling term: $\langle \hat{b}_{i\sigma}^\dagger \hat{b}_{j\sigma} \rangle = \hat{n}_{i\sigma} \delta_{ij} + \langle \hat{b}_{i\sigma}^\dagger \rangle \langle \hat{b}_{j\sigma} \rangle (1 - \delta_{ij})$. Observe that for consistency of notation we should use $\psi_{i\sigma}$ instead of $\langle \hat{b}_{j\sigma} \rangle$.

To mark the limits between the superfluid and MI phases in the Gutzwiller approach, we recall that the MI phase prevails for small hopping amplitude and that it is characterized by a finite gap in the spectrum and zero compressibility, defined as $\kappa = \frac{\partial \rho}{\partial \mu}$, with

$$\rho = \frac{1}{N} \left\langle \sum_j \hat{n}_j \right\rangle, \quad (7.56)$$

and N the total number of bosons. On the other hand, in the superfluid phase, bosons are delocalized and a current flow is possible. This phase is characterized by a finite compressibility, gapless excitations, and off-diagonal long-range order accompanied by a non-vanishing order parameter. Since the order parameter is not directly measurable, it is important to define experimental observable quantities marking the superfluid phase. These are typically the superfluid fraction ρ_S and the condensate fraction ρ_C (Roth and Burnett, 2003a), although direct measurement of the compressibility has recently been proposed by Delande and Zakrzewski (2009). The superfluid fraction can be evaluated by imposing a phase gradient in the tunneling corresponding to a current flow, while the condensate fraction is defined as the highest eigenvalue of the one-particle density matrix (Roth and Burnett, 2003a; Damski *et al.*, 2003b).

The left-hand column of Figure 7.10 displays the MI–SF transition calculated with both the Gutzwiller ansatz (where the filled lobes correspond to vanishing ρ_C), and the perturbation mean-field approach, (solid lines given by eqn (7.53) and (7.54)), for different values of the parameter U_2/U_0 . As expected from the discussions in previous sections, with increasing values of U_2 , the even lobes start to dominate while the odd lobes shrink.

For small U_2/U_0 ratios, there is a discrepancy between the perturbative mean-field and Gutzwiller predictions for the boundaries of the even lobes, as already reported by Kimura *et al.* (2005). This discrepancy is correlated with the character of MI–SF transition as visualized in the right-hand column of Figure 7.10, where the condensate fraction is shown for selected $\mu = \text{const}$ lines corresponding to the tips of the lobes in the corresponding phase diagram. For $U_2/U_0 \leq 0.1$ (Figure 7.10 first and second row) the condensate fraction is continuous across the phase transition for odd lobes (corresponding to second-order phase transition), while it reveals a discontinuous jump characteristic of the first-order phase

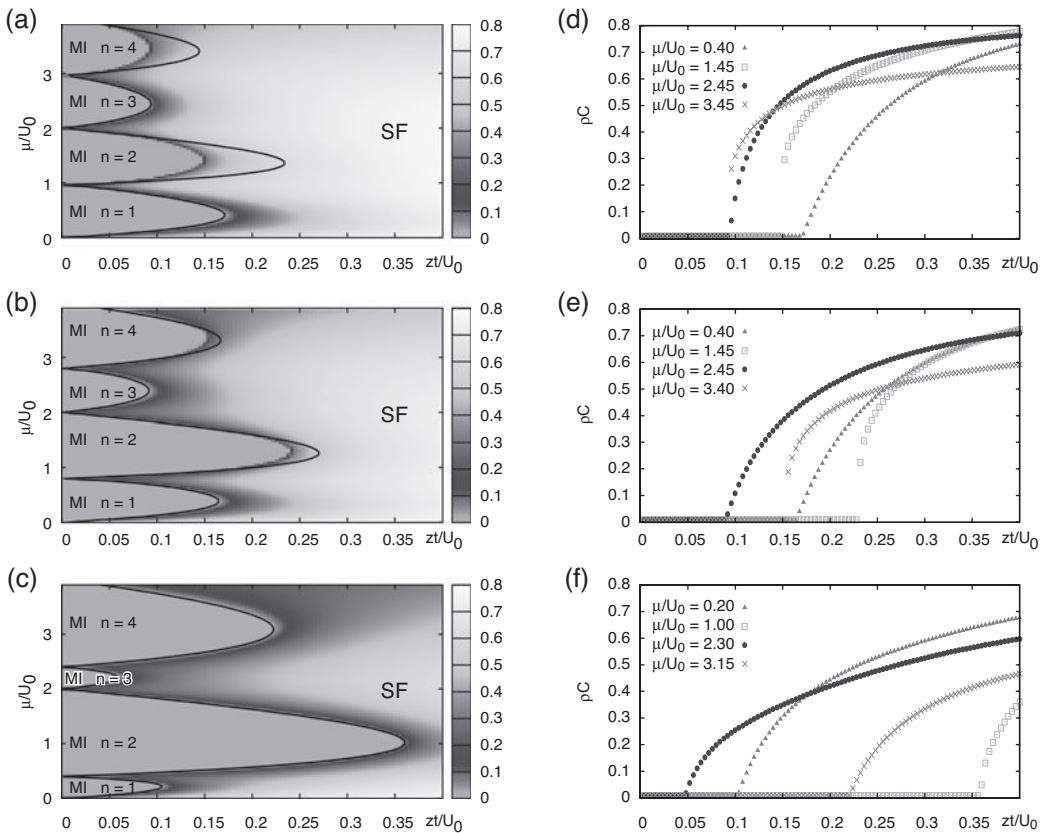


Figure 7.10 Left-hand panels depict the condensate fraction ρ_C obtained numerically by the Gutzwiller ansatz for (a) $U_2/U_0 = 0.02$, (b) $U_2/U_0 = 0.1$, and (c) $U_2/U_0 = 0.3$, where Mott insulator (MI) lobes correspond to vanishing ρ_C (filled areas). The lobes are compared with the boundaries obtained with the mean-field perturbation approach (solid lines). In the right-hand panels ρ_C is depicted as a function of zt/U_0 for values of μ/U_0 corresponding to the lobes' tips. In the transition between the MI and superfluid (SF) on the tip one can observe a first-order transition for the even occupation lobes in panels (d) and (e) (abrupt jump on the condensate fraction), while for lobes corresponding to odd occupation the transition is always of second order. From Łącki *et al.* (2011).

transition for even lobes. For $U_2/U_0 \geq 0.3$ (Figure 7.10 bottom row) only second-order SF–MI transitions from both odd and even lobes are observed. In between these values it is not easy to characterize the order of the phase transition. An exhaustive numerical analysis shows that the value where the transition passes from first to second order is approximately $U_2/U_0 = u_c \simeq 0.2$.

The observation of a first-order phase transition in the even lobes—where MI is formed by singlets on each site—has been also pointed out in the mean-field analysis of Tsuchiya *et al.* (2004) and Kimura *et al.* (2005) in two dimensions, as well as in quantum Monte Carlo calculations in one dimension (Batrouri *et al.*, 2009). Looking at the state provided by the Gutzwiller ansatz near the even lobes' tips, it has been observed (Łacki *et al.*, 2011) that in the MI only the $S = 0$ component is relevant, while in the superfluid phase the state becomes a linear combination of $f(S = 2, n)|S = 2, m = 0, n\rangle + f(S = 0, n)|S = 0, m = 0, n\rangle$ with $|f(S = 2, n)|^2 + |f(S = 0, n)|^2$ close to 1. This is the origin of the discrepancy with the mean field perturbation result, where only states with $S = 0$ are taken into account in the energy corrections. Even if we find that in the MI the state is singlet, the second-order phase transition indicates a metastability inside the lobe of a nematic phase. In contrast, for $U_2/U_0 > u_c$, Gutzwiller and mean-field perturbation approaches coincide and effectively the contribution of the state $S = 2$ is irrelevant close to the tip of the lobe and the transition is of second order.

7.5.4 Bose–Hubbard model for spin-2 particles

The corresponding Bose–Hubbard Hamiltonian for spin $F = 2$ can be conveniently expressed (Ueda and Koashi, 2002) as:

$$\hat{H} = -t \sum_{\langle ij \rangle, \sigma} (\hat{b}_{\sigma i}^\dagger \hat{b}_{\sigma j} + h.c.) + \frac{U_0}{2} \sum_i \hat{n}_i (\hat{n}_i - 1) + \frac{U_2}{2} \sum_i : \hat{\mathbf{S}}_i \cdot \hat{\mathbf{S}}_i : + \frac{2U_1}{5} \sum_i \hat{S}_{+i} \hat{S}_{-i}, \quad (7.57)$$

where $\hat{\mathbf{S}}_i = \sum_{\sigma\sigma'} \hat{b}_{\sigma j}^\dagger \mathbf{F}_{\sigma\sigma'} \hat{b}_{\sigma j}$ is the spin operator at site i , with \mathbf{F} the spin-2 matrices, $: \dots :$ denotes normal ordering and $U_n = c_n \int d\mathbf{r} w(\mathbf{r} - \mathbf{r}_i)$, with $w(\mathbf{r} - \mathbf{r}_i)$ being the single particle Wannier function at site i , and c_n defined after eqn (7.5). \hat{S}_+ is defined in Section 7.3.2.

7.5.5 Effective Hamiltonian for spin-2 particles

Analogous to the case of spin-1 bosons (Imambekov *et al.*, 2003), it is possible to derive an effective Hamiltonian for spin-2 particles using second-order perturbation theory with $t/U_0 \ll 1$ (Eckert *et al.*, 2007). At zeroth order, the Hamiltonian is a sum of independent single-site Hamiltonians, which, if the system is homogeneous, are site-independent:

$$\hat{H}_0 = \frac{U_0}{2} \hat{n}(\hat{n} - 1) + \frac{U_2}{2} : \hat{\mathbf{S}} \cdot \hat{\mathbf{S}} : + \frac{2U_1}{5} \hat{S}_+ \hat{S}_-. \quad (7.58)$$

Exact eigenstates of this Hamiltonian have been obtained by Ueda and Koashi (2002). Since \hat{S}_+ and \hat{S} commute with the total spin operator, the energy eigenstates can be labeled with four quantum numbers as $|n, n_s, S, m_S\rangle$, where n is the number of particles per site,

n_s is the number of spin-singlet pairs, S is the total on-site spin, and m_S is the z -component of the total spin. The states have a $(2S + 1)$ -fold degeneracy associated with the quantum number m_S and their energies are given by:

$$E_0(n, n_s, S) = \frac{U_0}{2}n(n-1) + \frac{U_2}{2}(S(S+1) - 6n) + \frac{U_1}{5}n_s(2n - 2n_s + 3). \quad (7.59)$$

Assuming the two-site problem and following the lines of the $F = 1$ case, one can derive an effective Hamiltonian for the Bose-Hubbard model for spin-2 particles (eqn (7.57)) in the second order in t . To this end, we calculate the shift in energy of the two-site ground state at zero tunneling with total spin S using eqn (7.31). As in the $F = 1$ case, these energy shifts introduce nearest-neighbor spin–spin interactions. As tunneling cannot mix states with different m_S and the overlaps $|\langle \nu | \hat{H}_t | S_g, n_g \rangle|$ are rotational invariant, it is enough to calculate the energy shifts for one value of m_S .

Considering one atom per site, six intermediate states are possible and the effective Hamiltonian to second order in the perturbation parameter t/c_0 has the following form (Barnett *et al.*, 2006b; Eckert *et al.*, 2007):

$$\hat{H}_{\text{eff}} = \sum_{\langle ij \rangle} \hat{H}_{ij} = \sum_{\langle ij \rangle} \left[\epsilon_0 \hat{P}_{ij}(0) + \epsilon_2 \hat{P}_{ij}(2) + \epsilon_4 \hat{P}_{ij}(4) \right], \quad (7.60)$$

with:

$$\epsilon_0 = -\frac{4t^2}{U_0 + U_1 - 6U_2}, \quad (7.61)$$

$$\epsilon_2 = -\frac{4t^2}{U_0 - 3U_2}, \quad (7.62)$$

$$\epsilon_4 = -\frac{4t^2}{U_0 + 4U_2}. \quad (7.63)$$

It is worth noticing that the mean-field states we found in Section 7.3.2 are also valid for MI states with one atom per lattice site, provided all atoms are described by the same single-particle wave function attached to a given site. Note that the effective Hamiltonian, eqn (7.60), can be transformed into a polynomial of fourth order in the Heisenberg interaction $\hat{\mathbf{S}}_i \cdot \hat{\mathbf{S}}_j$:

$$\begin{aligned} \hat{H}_{\text{eff}} = & \sum_i \hat{H}_{0,i} + \sum_{\langle ij \rangle} \frac{39\epsilon_0 - 80\epsilon_2}{51} (\hat{\mathbf{S}}_i \cdot \hat{\mathbf{S}}_j) + \frac{9\epsilon_0 - 8\epsilon_2}{102} (\hat{\mathbf{S}}_i \cdot \hat{\mathbf{S}}_j)^2 \\ & + \left(-\frac{7\epsilon_0}{204} + \frac{10\epsilon_2}{204} + \frac{\epsilon_4}{72} \right) (\hat{\mathbf{S}}_i \cdot \hat{\mathbf{S}}_j)^3 + \frac{7\epsilon_0 + 10\epsilon_4}{1020} (\hat{\mathbf{S}}_i \cdot \hat{\mathbf{S}}_j)^4. \end{aligned} \quad (7.64)$$

In the special case in which all the scattering lengths are equal, $\epsilon_0 = \epsilon_2 = \epsilon_4$, the effective Hamiltonian, eqn (7.64), exhibits $SU(5)$ symmetry. In this situation, the state $|\Psi\rangle = \prod_i A_e |e\rangle_i$, with A_e being complex coefficients, will be an exact eigenstate of eqn (7.60) and, being a product state of each site, has a correspondence to the mean-field phase.

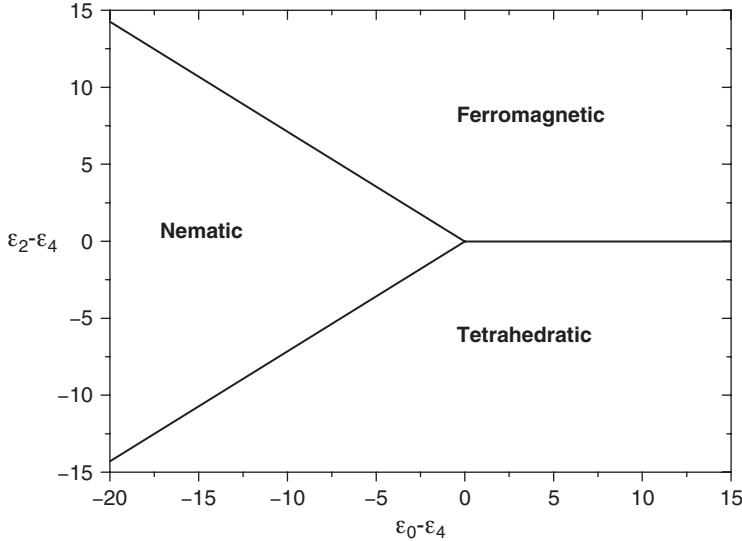


Figure 7.11 Phase diagram of the effective Hamiltonian, eqn (7.60), for $F = 2$ bosons in a Mott insulator state with one boson per site.

Since the ground-state energy will not depend on A_e , the state will be highly degenerate. For the more general case of different scattering lengths, the phase diagram can be calculated within the mean field by minimizing $\langle \Psi | \hat{H}_{\text{eff}} | \Psi \rangle$ over the five complex coefficients A_e . Figure 7.11 shows the phase diagram with phases corresponding to $(A_{-2}, A_{-1}, A_0, A_1, A_2)$ (Barnett *et al.*, 2006b):

- **ferromagnetic state**, $|e\rangle = (1, 0, 0, 0, 0)$
- **nematic state** has the η -degeneracy, $|e\rangle = (\sin(\eta)/\sqrt{2}, 0, \cos(\eta), 0, \sin(\eta)/\sqrt{2})$; an MI version of the polar phase
- **tetrahedratic (cyclic) state**, $|e\rangle = (1/\sqrt{3}, 0, 0, \sqrt{2/3}, 0)$; an MI version of the cyclic state.

The ground-state phase diagram of a 1D $F = 2$ spinor gas has been explored (Eckert *et al.*, 2007) using MPS methods. MPSs represent the ground state of a translationally invariant short-range Hamiltonian exactly (Verstraete and Cirac, 2006), or nearly exactly—see Chapters 5 and 12. A straightforward way to look for ground states is to add to the two-site bond Hamiltonian, \hat{H}_{ij} in eqn (7.60), $c (> 0)$ times the identity operator $\hat{I}_{ij} = \sum_S \hat{P}_{ij}(S)$ on the bond, so that the new Hamiltonian $\hat{H}'_{ij} = \hat{H}_{ij} + c\hat{I}$ becomes positive definite (Wolf *et al.*, 2006),

$$\hat{H}'_{ij} = \sum_{S=0}^4 \lambda_S \hat{P}_{ij}(S), \quad (7.65)$$

i.e. all λ_S are non-negative. In particular, for $\lambda_1 = \lambda_3 = c$ and $\lambda_0 = c - 4t^2/g_0$, $\lambda_2 = c - 4t^2/g_2$, and $\lambda_4 = c - 4t^2/g_4$. Since, by definition, $\lambda_1 = \lambda_3$ are the largest parameters,

the ground state will obviously belong to the symmetric subspace. In one dimension, since the Hamiltonian is a sum of nearest-neighbor bond Hamiltonians, we have

$$\sum_{k,k'} \langle e_k, e_k \dots | \hat{H}'_{ij} | e_{k'}, e_{k'} \dots \rangle \propto \langle e_k | e_{k'} \rangle^{N-2}, \quad (7.66)$$

and thus in the limit of an infinite chain the ground states are equally well described by product states (which will typically break the rotational symmetry). This means that in this case we expect mean-field product states to provide a very good approximation of the ground states with translational symmetry. A schematic classification of the possible ground states for the specific λ_i values is (Eckert *et al.*, 2007):

- $\lambda_4 = \lambda_2 = \lambda_0 = 0$

All symmetric states are ground states, and in particular all product states $|e, e \dots\rangle$ with arbitrary $|e\rangle$.

- $\lambda_4 = \lambda_2 = 0, \lambda_0 > 0$

The ground states $|e, e \dots\rangle$ recall the cyclic states of Demler and Zhou (2002), i.e. they correspond to translationally, but not rotationally invariant product states, which now mix $S = 2$ and $S = 4$ contributions on each bond, and they have to fulfill the condition $\langle \text{singlet} | e, e \rangle = 0$. Denoting $|e\rangle = (e_2, e_1, e_0, e_{-1}, e_{-2})$, this implies that $e_0^2 - 2e_1e_{-1} + 2e_2e_{-2} = 0$. These states form a much greater class than the cyclic ones, since they may have non-vanishing (and even maximal) components of the spin. Interestingly, the transition between the cyclic phase for $\lambda_2 = 0$, and the ferromagnetic phase for $\lambda_4 = 0$, occurs via such states, i.e. at the transition point the degeneracy of the ground-states manifold explodes.

- $\lambda_4 = 0$ and $\lambda_2, \lambda_0 > 0$

The ground states are ferromagnetic, corresponding to a maximal projection of the local spin onto a given direction $\mathbf{n} = (\sin \theta \cos \phi, \sin \theta \sin \phi, \cos \theta)$, that is:

$$|\text{Ferro}\rangle = |2\rangle_{\mathbf{n}} |2\rangle_{\mathbf{n}} \cdots |2\rangle_{\mathbf{n}}.$$

Such vectors for $F = 2$ may be parametrized in the basis of $\hat{\mathbf{S}}_{\mathbf{n}}$ with descending m_F as $\propto (z^{-2}, 2z^{-1}, \sqrt{6}, 2z, z^2)$, with $z = |z|e^{i\phi}$, $|z| \in (-\infty, \infty)$. It should be stressed that ferromagnetic states are the exact ground states for $\lambda_4 = 0$.

- $\lambda_0 = 0$ and $\lambda_4, \lambda_2 > 0$

The ground states apparently favor antiferromagnetic order. This, however, can be misleading if $\lambda_4 \ll \lambda_2$. In that case, as the mean-field diagram suggests, ferromagnetic order might prevail. In one dimension a more general variational approach, going beyond mean field has been applied (Eckert *et al.*, 2007) to mean-field (product) states $|e, e \dots\rangle$, Néel-type states $|e, f, e, f \dots\rangle$, and valence-bond solid states with singlet states for distinct pairs (dimers) of neighboring atoms and translational dimer symmetry. For the mean-field case, as discussed earlier, the energy is either minimized by the ferromagnetic state $|e\rangle = |2\rangle_{\mathbf{n}}$ (for $\lambda_2 \geq 17\lambda_4/10$), by a nematic state $|e\rangle = |0\rangle_{\mathbf{n}}$ (for $3\lambda_4/10 \leq \lambda_2 \leq 17\lambda_4/10$; in this case the state is a combination of total spin 0, 2, and 4), or, for $\lambda_2 \leq 3\lambda_4/10$, by a cyclic state, $|e\rangle = (e_2, e_1, e_0, e_{-1}, e_{-2})$, with $e_0 = 1/\sqrt{2}$, $e_2 = -e_{-2} = 1/2$, $e_1 = e_{-1} = 0$. Imposing Néel order with $\langle e|f\rangle \neq 1$ always

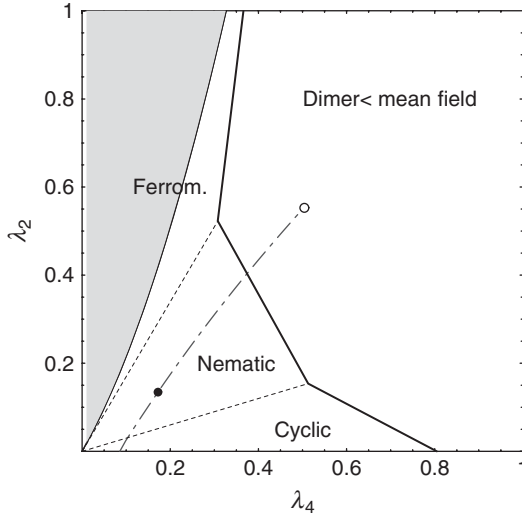


Figure 7.12 Sketch of the phase diagram, for the 1D case, obtained by applying the variational principle in the $\lambda_2 > 0$, $\lambda_4 > 0$ phase space (for $\lambda_0 = 0$) to mean field, Néel, and dimer states with one atom per site. The scale is set by letting $\lambda_1 = \lambda_3 = 1$. Néel-type states are never favorable over nematic states. The *ferromagnetic* region (gray) was obtained numerically by imaginary time evolution of MPS (and comparing the results from runs with $d = 1$ and $d = 5$) in a chain of 50 sites with open boundary conditions (Verstraete *et al.*, 2004c). Note that here d is the dimension of the ancillary system that is used in the MPS method (see Chapter 5). Of course, on the line ($\lambda_4 = 0, \lambda_2$) ferromagnetic states always give ground states. Dashed lines indicate the regions where the type of mean-field state with lowest energy changes qualitatively. The dashed-dotted line gives the values of (λ_2, λ_4) which can be obtained by changing the spin-independent scattering length $c_0 = (3g_4 + 4g_2)/7$ through optical Feshbach resonances (Fedichev *et al.*, 1996; Theis *et al.*, 2004). Black and white circles indicate changes of c_0 of 10% and 100%, respectively. From Eckert *et al.* (2007).

results in a larger energy, as $\lambda_{1,3} > \lambda_{2,4}$, and the overlap with the singlet may already be maximized by restricting to product states. On the other hand, for the dimer state the energy per bond is given by $\frac{1}{2}\text{Tr}(\hat{H}'_{ij} \frac{1}{25} \mathbf{1} \otimes \mathbf{1})$. One can apply MPS codes to search numerically for the exact ground states in one dimension using the method of Verstraete and Cirac (2006) to confirm the existence and phase borders of the ferromagnetic ground state, nematic, and dimer regions. This particular phase diagram in the λ_2, λ_4 phase space is displayed in Figure 7.12 (Eckert *et al.*, 2007).

- $\lambda_2 = 0$ and $\lambda_4, \lambda_0 > 0$

As in the previous case, mean field cyclic states are favorable over Néel states. One can compare them variationally to the analogs of the dimer states in the present case, i.e. configurations that have a state with total spin $S = 2$ on distinct bonds. We call this state *para-dimers*. Now, contrary to the dimerized states in the previous case, where the states on the bond are unique, here states with different $m_{S=2}$ can form

superpositions. It is easy to see, however, that the best superposition should have maximal possible entanglement in order to minimize interaction on the bonds that are not covered by the para-dimers (Eckert *et al.*, 2007).

7.6. Spinor Fermi gases

Spinor Fermi gases open the possibility of exploring new states of matter with no equivalent in condensed matter. While typical electronic systems are constrained to spin rotational symmetry $SU(2)$, atomic fermionic systems can have total angular momentum larger than $\frac{1}{2}$. For instance, ${}^6\text{Li}$ has hyperfine manifolds with $F = \frac{1}{2}$ and $F = \frac{3}{2}$ and ${}^{40}\text{K}$ has manifolds $F = \frac{7}{2}$ and $F = \frac{9}{2}$. Optical trapping of the states $|F = \frac{9}{2}, m_F = -\frac{5}{2}, -\frac{7}{2}, -\frac{9}{2}\rangle$ of ${}^{40}\text{K}$ has been reported (Regal and Jin, 2003).

Pairing of fermions with two spin components may lead to s -wave superfluidity. In an equal mixture of two states of fermions, pairing can be complete and the entire system will become superfluid. Experiments to demonstrate pairing were initiated some years ago (Regal *et al.*, 2004; Zwierlein *et al.*, 2004; Bartenstein *et al.*, 2004b; Kinast *et al.*, 2004). When the two populations of fermions are unequal more exotic phases have been predicted as paired states with broken translational symmetry (LOFF states) consisting of pairs with a non-zero center-of-mass momentum (Fulde and Ferrell, 1964; Larkin and Ovchinnikov, 1964; Larkin and Ovchinnikov, 1965) or gapless excitations phases like Sarma (Sarma, 1963) and breached pair (Liu and Wilczek, 2003) phases. A mixed phase in which superfluid regions are surrounded by an unpaired normal phase has also been proposed (Bedaque *et al.*, 2003; Caldas, 2004; Carlson and Reddy, 2005). Experiments on fermionic superfluidity with imbalanced spin populations have been also performed for some years (Zwierlein *et al.*, 2006; Partridge *et al.*, 2006; Liao *et al.*, 2010). A more detailed description of the Fermi superfluidity in such systems and a description of relevant recent literature can be found in Chapter 6.

The $F = \frac{1}{2}$ fermionic Hubbard model is perhaps the most paradigmatic and the most studied model in condensed-matter physics because of its apparent relevance for high T_c superconductivity. We have discussed some of the theoretical methods for its treatment in Chapter 6. Here, we only note the studies directly related to cold-atoms implementations. A quantum simulator of the $F = \frac{1}{2}$ Hubbard model was studied in Hofstetter *et al.* (2002). For attractive interactions, a phase transition to a superfluid state at a highly increased transition temperature is expected. For strong repulsive interactions, an antiferromagnetic phase in which adjacent sites are occupied by atoms with alternating spin is predicted in the case of a filling fraction close to 1. For filling fractions smaller than 1, anisotropic d -wave pairs have been conjectured (Scalapino, 1995). Here the phase diagram of the system in two dimensions was calculated within the fluctuation-exchange approximation (Bickers *et al.*, 1989). These d -wave pairs can result in a d -wave superfluid phase for high tunneling rates, opening up possibilities of studying the properties of high- T_c superconducting cuprates. Exotic kinds of superfluidity, such as states supporting superfluid and normal components even at zero temperature, have been predicted for $F = \frac{1}{2}$ fermions in spin-dependent optical lattices (Liu *et al.*, 2004).

Fermionic atoms with N different spin states in a 2D optical lattice are described by the fermionic $SU(N)$ Hubbard model. This model was studied in the large- N limit in

the context of high- T_c superconductivity (Affleck and Marston, 1988; Marston and Affleck, 1989). For $N = 3$ with small interactions, a color superfluid state was predicted (Honerkamp and Hofstetter, 2004a, 2004b), while for low filling factors and strong interactions, it has been shown that a quantum phase transition from the superfluid phase to a Fermi-liquid phase is expected, in which groups of three fermions bind together to form trions. At low densities, baryon formation is expected (Rapp *et al.*, 2007, 2008). These studies set out the link between spinor fermions and quantum chromodynamics.

Properties of $F = \frac{3}{2}$ Fermi gases have been theoretically addressed both in the continuum and in the presence of a lattice. An overview of hidden symmetries and competing orders in spin- $\frac{3}{2}$ gases can be found in the excellent paper of Wu (2006) and references therein. Wu and coworkers realized that the spin- $\frac{3}{2}$ fermion models with contact interactions have a generic $SO(5)$ symmetry at arbitrary filling and $SO(7)$ at half filling, and employed this fact to form a quantum Monte Carlo algorithm that was free of the sign problem. Novel competing orders in 1D optical traps and lattices have also been studied (Wu, 2005). In particular, the quarteting phase, a four-fermion counterpart of Cooper pairing, is seen in a large portion of the phase diagram. It was also realized that in the low-energy limit, the total symmetry of the spin- $\frac{3}{2}$ fermion systems was greater, being $U(1) \times O(5) \times Z_2$ and $SO(7) \times Z_2$ for arbitrary and half filling, respectively (Wu, 2005; Lecheminant *et al.*, 2005). In this context, an exact solution of a model describing the low-energy behavior of cold isospin $\frac{3}{2}$ fermionic atoms on a 1D optical lattice has been proposed (Controzzi and Tsvelik, 2006). Ground-state properties of $F = \frac{3}{2}$ and $F = \frac{5}{2}$ Fermi spinor gases in optical lattices were addressed in Eckert *et al.*, 2007.

In the next subsection, we present in some detail how the fermionic Hubbard model with $F > \frac{1}{2}$ can be treated using a type of mean-field theory in two or three dimensions. We follow the approach given in Szirmai and Lewenstein (2011), which is somewhat similar to the approach employing slave bosons, which was discussed in Chapter 6.

7.6.1 Effective Hamiltonian for $F = \frac{3}{2}$ fermions at quarter filling

The approach in this subsection is in principle similar to that of previous sections. However, our aim is not to obtain the effective spin model in terms of the spin representation; instead we obtain an effective low-energy Hamiltonian with nearest-neighbor interactions, which is still expressed in terms of fermionic operators, but is subjected to a particle-conservation constraint. This Hamiltonian will turn out to be suitable for formulation of a novel and non-trivial mean-field approach.

We consider a fermionic system described by a Hamiltonian with nearest-neighbor hopping:

$$\hat{H}_{\text{kin}} = -t \sum_{\langle i,j \rangle} \sum_{\alpha} \hat{f}_{i,\alpha}^{\dagger} \hat{f}_{j,\alpha}, \quad (7.67)$$

and strong on-site repulsive interactions:

$$\hat{H}_{\text{int}} = \sum_i \sum_{\alpha,\beta,\gamma,\delta} V_{\gamma,\delta}^{\alpha,\beta} \hat{f}_{i,\alpha}^{\dagger} \hat{f}_{i,\beta}^{\dagger} \hat{f}_{i,\delta} \hat{f}_{i,\gamma}. \quad (7.68)$$

Here, $\hat{f}_{i,\alpha}^\dagger$ ($\hat{f}_{i,\alpha}$) are the usual creation (annihilation) operators of fermions in the spin state α at site i . The interactions can be expressed as:

$$V_{\gamma,\delta}^{\alpha,\beta} = \sum_{S=0}^{2F} g_S [P_S]_{\gamma,\delta}^{\alpha,\beta}. \quad (7.69)$$

where P_S projects to the total spin- S subspace and g_S is the coupling constant in the corresponding scattering channel. For spin- $\frac{3}{2}$ fermions the interaction has to be antisymmetric. Therefore, the only contributing terms are the total spin-0 (singlet) and the spin-2 (quintet) scatterings:

$$V_{\gamma,\delta}^{\alpha,\beta} = \sum_{S=0}^3 g_S [P_S^{(as)}]_{\gamma,\delta}^{\alpha,\beta} = g_0 [P_0]_{\gamma,\delta}^{\alpha,\beta} + g_2 [P_2]_{\gamma,\delta}^{\alpha,\beta}. \quad (7.70)$$

As usual, the spin projector operators \hat{P}_S can be expressed as a polynomial of the $\hat{\mathbf{F}}_1 \cdot \hat{\mathbf{F}}_2$ product with $(\hat{\mathbf{F}}_1 \cdot \hat{\mathbf{F}}_2)^0 \equiv \hat{\mathbf{E}}$:

$$\hat{P}_S = \sum_{l=0}^{2F} a_{S,l} (\hat{\mathbf{F}}_1 \cdot \hat{\mathbf{F}}_2)^l \quad (7.71)$$

for all $S = 0, 1, \dots, 2F$. $a_{S,l}$ are the coefficients of the expansion and vector $\hat{\mathbf{F}}$ denotes the three generators of the $SU(2)$ Lie algebra in the appropriate representation.

If we are aiming at a fermionic rather than a spin representation of the low-energy effective Hamiltonian, it is useful to consider the symmetric (s) or antisymmetric (as) part of the total spin space. One can thus use the following decomposition:

$$(\hat{\mathbf{F}}_1 \cdot \hat{\mathbf{F}}_2)^l = \left((\hat{\mathbf{F}}_1 \cdot \hat{\mathbf{F}}_2)^l \right)^{(as)} + \left((\hat{\mathbf{F}}_1 \cdot \hat{\mathbf{F}}_2)^l \right)^{(s)}, \quad (7.72)$$

and now the symmetric and antisymmetric projectors can be expressed as follows:

$$\hat{P}_S^{(as)} = \sum_{l=0}^{\#_{(as)}-1} b_{S,l} \left((\hat{\mathbf{F}}_1 \cdot \hat{\mathbf{F}}_2)^l \right)^{(as)}, \quad (7.73)$$

$$\hat{P}_S^{(s)} = \sum_{l=0}^{\#_{(s)}-1} c_{S,l} \left((\hat{\mathbf{F}}_1 \cdot \hat{\mathbf{F}}_2)^l \right)^{(s)}, \quad (7.74)$$

where $\#_{(as)}$ and $\#_{(s)}$ denote the number of antisymmetric and symmetric subspaces of the total spin space, respectively. Notice that the antisymmetric and the symmetric parts of an

operator \hat{A} can be constructed by the exchange of two spin indices:

$$\left[\hat{A}^{(as)} \right]_{\gamma,\delta}^{\alpha,\beta} = \hat{A}_{\gamma,\delta}^{\alpha,\beta} - \hat{A}_{\delta,\gamma}^{\alpha,\beta}, \quad (7.75)$$

$$\left[\hat{A}^{(s)} \right]_{\gamma,\delta}^{\alpha,\beta} = \hat{A}_{\gamma,\delta}^{\alpha,\beta} + \hat{A}_{\delta,\gamma}^{\alpha,\beta}, \quad (7.76)$$

for example, the antisymmetric part:

$$\left[\hat{\mathbf{E}}^{(as)} \right]_{\gamma,\delta}^{\alpha,\beta} = \delta_{\alpha,\gamma} \delta_{\beta,\delta} - \delta_{\alpha,\delta} \delta_{\beta,\gamma}, \quad (7.77)$$

$$\left[(\hat{\mathbf{F}}_1 \cdot \hat{\mathbf{F}}_2)^{(as)} \right]_{\gamma,\delta}^{\alpha,\beta} = \left[\hat{\mathbf{F}}_1 \right]_{\alpha,\gamma} \left[\hat{\mathbf{F}}_2 \right]_{\beta,\delta} - \left[\hat{\mathbf{F}}_1 \right]_{\alpha,\delta} \left[\hat{\mathbf{F}}_2 \right]_{\beta,\gamma}. \quad (7.78)$$

Let us apply the above formalism to a 2D spin- $\frac{3}{2}$ fermion system. The components of $\hat{\mathbf{F}}$ are now 4×4 matrices. At quarter filling and for strong repulsion, the system can be described by an effective Hamiltonian with nearest-neighbor interactions. The effective model based on perturbation theory up to second (leading) order in the hopping t is the following:

$$\hat{H}_{\text{eff}} = \sum_{\langle i,j \rangle} \sum_{\alpha,\beta,\gamma,\delta} \tilde{V}_{\gamma,\delta}^{\alpha,\beta} \hat{f}_{i,\alpha}^\dagger \hat{f}_{j,\beta}^\dagger \hat{f}_{j,\delta} \hat{f}_{i,\gamma}, \quad (7.79)$$

where $\tilde{V}_{\gamma,\delta}^{\alpha,\beta} = \sum_{S=0,2} G_S \left[P_S^{(as,s)} \right]_{\gamma,\delta}^{\alpha,\beta}$ with $G_S = -4t^2/g_S$ gives the energy shift due to the weak nearest-neighbor hopping. The effective model preserves the symmetry of the on-site interaction, so it remains antisymmetric for the exchange of two spin indices. From eqn (7.73) one obtains the following form: $\hat{\mathbf{E}}^{(as)} = P_0 + P_2$ and $(\hat{\mathbf{F}}_1 \cdot \hat{\mathbf{F}}_2)^{(as)} = -15P_0/4 - 3P_2/4$. Using these expressions the effective Hamiltonian becomes

$$\hat{H}_{\text{eff}} = a_n \sum_{\langle i,j \rangle} \hat{\mathbf{E}}_{i,j}^{(as)} + a_s \sum_{\langle i,j \rangle} \left(\hat{\mathbf{F}}_1 \cdot \hat{\mathbf{F}}_2 \right)_{i,j}^{(as)}, \quad (7.80)$$

where $a_n = (5G_2 - G_0)/4$, $a_s = (G_2 - G_0)/3$, and

$$\hat{\mathbf{E}}_{i,j}^{(as)} = \sum_{\alpha,\beta,\gamma,\delta} \hat{f}_{i,\alpha}^\dagger \hat{f}_{j,\beta}^\dagger \hat{f}_{j,\delta} \hat{f}_{i,\gamma} \left[\hat{\mathbf{E}}^{(as)} \right]_{\gamma,\delta}^{\alpha,\beta}, \quad (7.81)$$

$$\left(\hat{\mathbf{F}}_1 \cdot \hat{\mathbf{F}}_2 \right)^{(as)} = \sum_{\alpha,\beta,\gamma,\delta} \hat{f}_{i,\alpha}^\dagger \hat{f}_{j,\beta}^\dagger \hat{f}_{j,\delta} \hat{f}_{i,\gamma} \left[\left(\hat{\mathbf{F}}_1 \cdot \hat{\mathbf{F}}_2 \right)^{(as)} \right]_{\gamma,\delta}^{\alpha,\beta}, \quad (7.82)$$

with the definitions of eqns (7.77) and (7.78). After straightforward calculations one arrives at the following form of the effective Hamiltonian:

$$\hat{H}_{\text{eff}} = V^{(0)} + \sum_{\langle i,j \rangle} \left[a_n \left(\hat{n}_i \hat{n}_j + \hat{\chi}_{i,j}^\dagger \hat{\chi}_{i,j} - \hat{n}_i \right) + a_s \left(\hat{\mathbf{S}}_i \hat{\mathbf{S}}_j + \hat{\mathbf{J}}_{i,j}^\dagger \hat{\mathbf{J}}_{i,j} - \frac{15}{4} \hat{n}_i \right) \right], \quad (7.83)$$

where as usual $\hat{n}_i = \sum_\alpha \hat{f}_{i,\alpha}^\dagger \hat{f}_{i,\alpha}$ and $\hat{\mathbf{S}}_i = \sum_{\alpha,\beta} \hat{f}_{i,\alpha}^\dagger \hat{\mathbf{F}}_{\alpha,\beta} \hat{f}_{i,\beta}$ are the particle number and spin operators on site i , and

$$\hat{\chi}_{i,j} = \sum_\alpha \hat{f}_{i,\alpha}^\dagger \hat{f}_{j,\alpha}, \quad (7.84)$$

$$\hat{\mathbf{J}}_{i,j} = \sum_{\alpha,\beta} \hat{f}_{i,\alpha}^\dagger \hat{\mathbf{F}}_{\alpha,\beta} \hat{f}_{j,\beta}, \quad (7.85)$$

are introduced to denote the nearest-neighbor link operators, which we term $U(1)$ and $SU(2)$ links, respectively. Note, that in general the $SU(2)$ link operators do not satisfy the spin commutation relations although they clearly relate to bond-centered spin. Using Feshbach resonances, one can, in principle, tune a_n and a_s on demand and in this way control the competition between the spin and particle fluctuations. The effective Hamiltonian in eqn (7.83) can be applied for fillings less than $\frac{1}{4}$ too, provided the kinetic term is added. $V^{(0)}$ only shifts the ground-state energy and is neglected in the section below.

7.6.2 Exotic magnetic phases of $F = \frac{3}{2}$ fermions

Following Szirmai and Lewenstein (2011), we will next study the possible phases of the quarter-filled system with the constraint $\sum_\alpha \hat{f}_{i,\alpha}^\dagger \hat{f}_{i,\alpha} = 1$: only single-occupied sites are allowed due to the strong on-site interaction. Due to this local constraint the Hamiltonian is invariant under the rotation of the phase of the fermions at each site. This means that the Lagrangian of the system $\mathcal{L} = \sum_i \hat{f}_{i,\sigma}^\dagger \partial_\tau \hat{f}_{i,\sigma} + \hat{H}$ is invariant under the $U(1)$ gauge transformation $\hat{f}_{i,\sigma} \rightarrow \hat{f}_{i,\sigma} e^{i\phi_i}$, reflecting the local constraint for the particle number. Considering the Hamiltonian in eqn (7.83), the terms containing single n_i do not make a contribution at quarter filling and the four-fermion terms can be decoupled via a mean-field treatment by introducing the expectation values of the link operators $\hat{\chi}_{i,j}$ and $\hat{\mathbf{J}}_{i,j}$, and the spin operator $\hat{\mathbf{S}}_i$. Now the mean-field Hamiltonian is $\hat{H}^{\text{MF}} = \sum_{\langle i,j \rangle} \hat{H}_{i,j}$:

$$\begin{aligned} \hat{H}_{i,j} = & a_n \sum_\alpha \left(\langle \hat{\chi}_{j,i} \rangle \hat{f}_{i,\alpha}^\dagger \hat{f}_{j,\alpha} + \langle \hat{\chi}_{i,j} \rangle \hat{f}_{j,\alpha}^\dagger \hat{f}_{i,\alpha} - |\langle \hat{\chi}_{i,j} \rangle|^2 \right) \\ & + a_s \sum_{\alpha,\beta} \left(\langle \hat{\mathbf{J}}_{j,i} \rangle \hat{f}_{i,\alpha}^\dagger \hat{\mathbf{F}}_{\alpha,\beta} \hat{f}_{j,\beta} + \langle \hat{\mathbf{J}}_{i,j} \rangle \hat{f}_{j,\alpha}^\dagger \hat{\mathbf{F}}_{\alpha,\beta} \hat{f}_{i,\beta} \right. \\ & \left. - |\langle \hat{\mathbf{J}}_{i,j} \rangle|^2 + \langle \hat{\mathbf{S}}_i \rangle \hat{\mathbf{S}}_j + \langle \hat{\mathbf{S}}_j \rangle \hat{\mathbf{S}}_i - \langle \hat{\mathbf{S}}_i \rangle \langle \hat{\mathbf{S}}_j \rangle \right). \end{aligned} \quad (7.86)$$

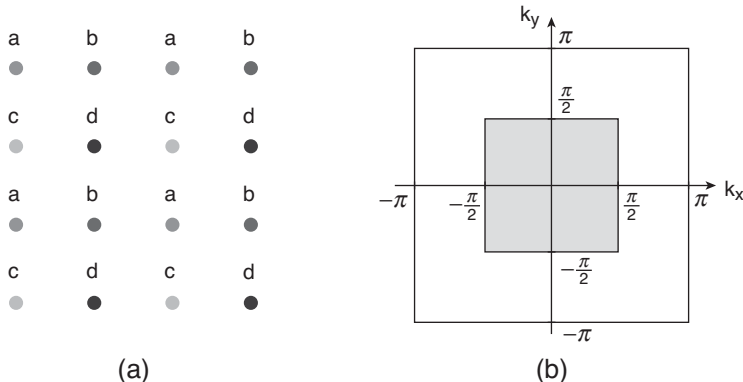


Figure 7.13 (a) Lattice splitting into four sublattices, leading to shrinking of the Brillouin zone. (b) The shadow area depicts the reduced Brillouin zone. By courtesy of E. Szirmai.

Obviously, the Hamiltonian has to remain invariant under the gauge transformation mentioned above. To this end, the link variables must transform as $\langle \hat{A}_{i,j} \rangle \rightarrow \langle \hat{A}_{i,j} \rangle e^{i(\phi_j - \phi_i)}$. The expectation values of the spin and link operators have to be determined self-consistently. Anticipating the appearance of a plaquette phase similar to the one that is the ground state of the system for $G_0 = G_2$, it is reasonable to split the lattice into four sublattices (see Figure 7.13), leading to the shrinking of the area of the Brillouin zone to a quarter of its original value. The only space-dependence that we admit is that the values of the order parameters for the different sublattices and for the alternating links may be different. The following gauge non-equivalent states are found: Néel order, $U(1)$ plaquette orders, $SU(2)$ plaquette or flux states, and $SU(2)$ dimer order. The phase diagram of the system can be seen in Figure 7.14. If the effective interaction of the singlet channel is significantly stronger than that of the quintet channel, the dominant order is purely antiferromagnetic without any bond order. For $a_n \geq 0$, stable $U(1)$ link order can also not be expected because it would lead to an increasing in the energy but the $SU(2)$ bond-order parameter remains zero in this regime. For $a_n < 0$ and $a_s > 0$, the spin and particle order compete with each other. Note that in Wu (2006), a magnetically ordered dimer phase was suggested to appear in this regime; such a state is not found, however, using the approach outlined here. When the antiferromagnetically ordered Néel phase (Fig. 7.15(a)) becomes unstable, plaquette order appears. The phase border is at around $G_0 \approx 1.9G_2$ or equivalently at $-a_n \approx 2.6a_s$. In the plaquette phase the non-zero $U(1)$ links form ‘boxes’, as shown in Figure 7.15(b). In this phase one can define the $U(1)$ plaquette as $\Pi = \hat{\chi}_{i,j}\hat{\chi}_{j,k}\hat{\chi}_{k,l}\hat{\chi}_{l,i}$, where i, j, k , and l denote the sites of an elementary plaquette of the square lattice and $\hat{\chi}$ is defined for nearest neighbors only. The $U(1)$ flux Φ is the phase of the plaquette. The plaquette and therefore the flux are invariant under the $U(1)$ gauge transformation. Two different gauge-non-equivalent states with the same energy are found in the plaquette phase. These are denoted $\Phi = 0$ and $\Phi = \pi$, respectively. For $|G_0| < 1.9|G_2|$ any order controlled by the a_s coupling is reported. This can be due to the fact that for repulsive on-site interaction in this part of the parameter space, the coupling constant a_n is always dominant compared to a_s — independently of the sign of a_s .

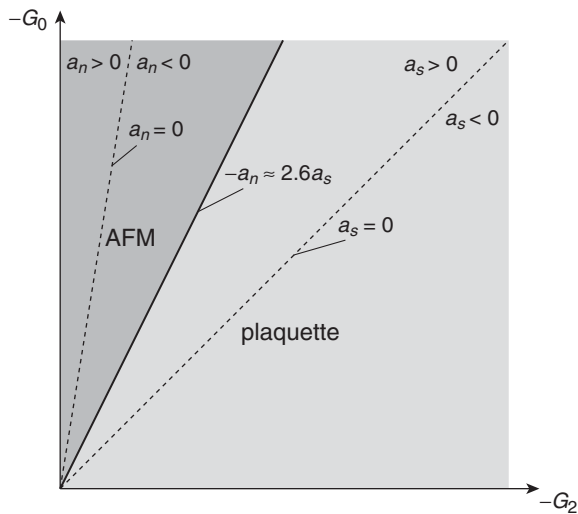


Figure 7.14 The phase diagram of a $\frac{3}{2}$ fermion system with strong on-site repulsion on a 2D square lattice at quarter filling. The Néel order (AFM) suppresses any other order for dominant antiferromagnetic spin coupling ($a_s < 0$ and $|a_s| > 1.9a_n$). In the plaquette phase the a_n coupling is dominant. Here the zero flux and the π -flux state have the same energy. From Szirmai and Lewenstein (2011).

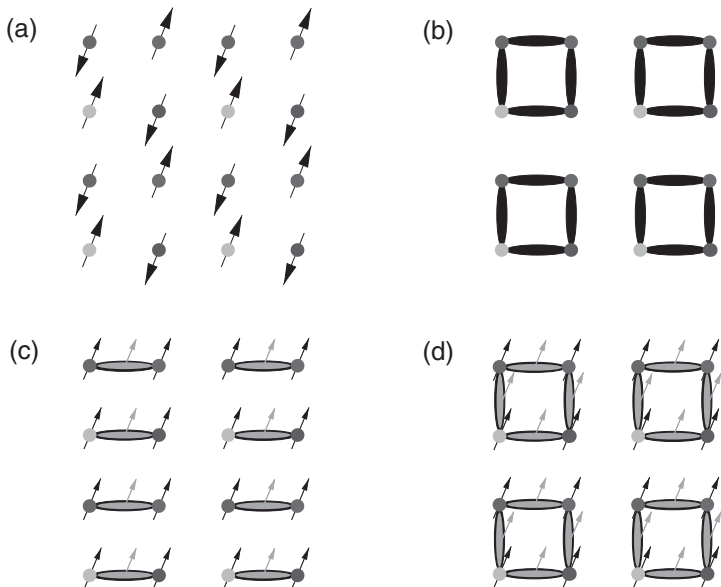


Figure 7.15 Different configurations that can be stable in the presence or absence of a magnetic field. (a) In the Néel order, the only non-zero expectation values are of the spin operators \hat{S}_i and they alternate on the neighboring sites. (b) In the plaquette order, bond-centered density waves form disconnected boxes. In the ground state the flux passing through the plaquettes can be 0 or π . In both the $SU(2)$ dimer (c) and plaquette (d) phases, the site-centered ferromagnetic order coexists with bond-centered density waves that also carry spin — both $\langle \hat{\chi}_{i,j} \rangle$ and $\langle \hat{\mathbf{J}}_{i,j} \rangle$ are non-zero. From Szirmai and Lewenstein (2011).

While the plaquette order is the ground state of the system for $|G_0| < 1.9|G_2|$, two other phases having 10–15% higher energy than the ground state are found: the $SU(2)$ dimer phase and the $SU(2)$ flux phase (see Figure 7.15(c) and (d)), which correspond to two different states but have the same energy. Both the dimer and the flux phase have the same energy. In the $SU(2)$ dimer state, in addition to weak ferromagnetic order, both types of link operator $\hat{\chi}$ and $\hat{\mathbf{J}}$ have non-zero expectation values on every second link in one direction. In the $SU(2)$ flux phase the link operators with non-zero expectation values constitute plaquettes. Both states violate the spin-rotation invariance of the plaquette phase, and the $SU(2)$ dimer state—in contrast to the plaquette and flux phases—preserves the translational invariance by one lattice site in one spatial dimension.

At this point let us explain the names of these states. Obviously, $\hat{\mathbf{J}}$ is not a member of the $SU(2)$ group, but let us define the link parameter in the following way:

$$U_{i,j} = \langle \hat{\mathbf{J}}_{i,j} \rangle \hat{\mathbf{F}}, \quad (7.87)$$

with the usual inner product of the vectors in the 3D space of the generators $\hat{\mathbf{F}}$. Now $\hat{U}_{i,j}$ is a member of $SU(2)$ and a 4×4 matrix and the same holds for the plaquette $\Pi^{SU(2)} = \hat{U}_{i,j} \hat{U}_{j,k} \hat{U}_{k,l} \hat{U}_{l,i}$. The mean-field Hamiltonian remains invariant under the same $U(1)$ gauge transformation:

$$\begin{aligned} \hat{f}_{i,\sigma} &\rightarrow \hat{f}_{i,\sigma} e^{i\phi_i}, \\ \langle \hat{\chi}_{i,j} \rangle &\rightarrow \langle \hat{\chi}_{i,j} \rangle e^{i(\phi_j - \phi_i)}, \\ \hat{U}_{i,j} &\rightarrow \hat{U}_{i,j} e^{i(\phi_j - \phi_i)}. \end{aligned}$$

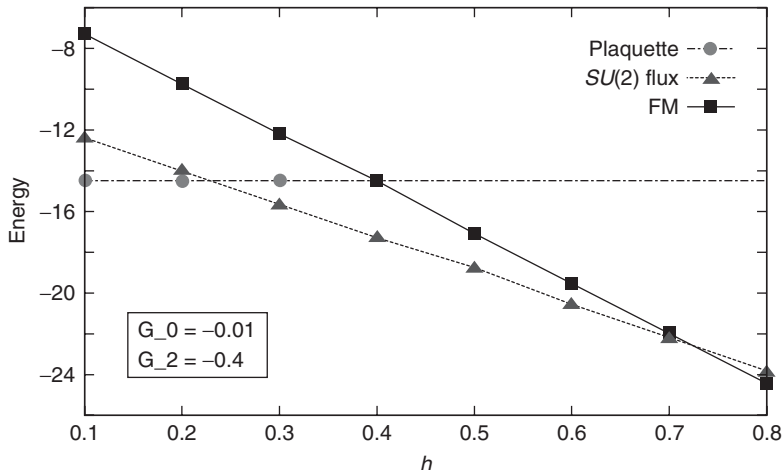


Figure 7.16 The magnetic field dependence of the energy of the different states with $t = 1$. Above a critical value of the magnetic field the $U(1)$ plaquette phase becomes unstable and is completely suppressed by the $SU(2)$ flux phase. For strong magnetic fields the ferromagnetic order is the only stable order. The lines are only guides for the eyes. From Szirmai and Lewenstein (2011).

Note that the $SU(2)$ plaquette $\Pi^{SU(2)}$ is also $U(1)$ gauge-invariant. The flux Φ passing through the plaquette is defined by the form: $\Pi^{SU(2)} = e^{i\Phi\hat{F}}$. The $SU(2)$ phases are of great interest, but they are suppressed by the $U(1)$ plaquette state. Moreover, since the $SU(2)$ flux as well as the dimer order coexist with ferromagnetic order, it can be expected that a weak magnetic field will not destroy the $SU(2)$ order, but it should stabilize it. To check this, let us investigate the changes in these states in the presence of an external magnetic field h taken into account as a Zeeman term in the Hamiltonian:

$$\hat{H}^h = \hat{H}^{\text{MF}} + h \sum_i \hat{\mathbf{S}}_i. \quad (7.88)$$

The magnetic field dependence of the energy of the $SU(2)$ flux state compared to the $U(1)$ plaquette state and the ferromagnetic order is shown in Figure 7.16, for typical values of the couplings in units of the nearest-neighbor hopping. The $U(1)$ plaquette phase is stable only for a weak magnetic field. As the applied magnetic field h is increased, the $SU(2)$ flux and dimer order become the ground state of the system. Although both the dimer and flux states have the same energy, if we prepare the system in the $U(1)$ plaquette state and start increasing the applied magnetic field, the evolving state will always be the $SU(2)$ flux, with the flux passing through the plaquette determined by the initial $U(1)$ flux. Further increasing the magnetic field, as expected stabilizes the strong ferromagnetic order and destroys the $SU(2)$ plaquettes and any other order in the system.

8

Ultracold dipolar gases

8.1. Introduction

In this chapter we discuss a novel class of systems, namely ultracold dipolar gases, which due to the specific properties of their interactions exhibit a whole variety of fascinating effects and phenomena. Although quantum gases are very dilute systems (with densities typically ranging from 10^{14} to 10^{15} cm $^{-3}$), most of their properties are governed by the interaction between particles. As we pointed out above, for temperatures in the nanokelvin range, essentially only *s*-wave scattering between particles can take place. This permits us to replace the real interatomic potential (i.e. the usual Van der Waals interaction $V(\mathbf{r}) \propto -C_6/r^6$) with a short-range and isotropic pseudo-potential,

$$\frac{4\pi\hbar^2a}{m}\delta(\mathbf{r}-\mathbf{r}')\frac{\partial}{\partial|\mathbf{r}-\mathbf{r}'|}|\mathbf{r}-\mathbf{r}'|, \quad (8.1)$$

where a is the *s*-wave scattering length, m is the atomic mass, and a regularization operator is added to remove the singularity of the delta potential in three dimensions. This result was first demonstrated in the seminal paper by Huang and Yang (1957) for a gas of hard spheres. It has, however, a wider applicability and holds for arbitrary short-range potentials. In the language of many-body theory it is the result of the T-matrix, or ladder approximation, applied to many-body systems (Mahan, 1993). It amounts to the summation of diagrams corresponding to multiple two-body scattering processes. Note that, when acting on a non-singular function, the pseudo-potential is not different from the simple contact (Fermi) potential $4\pi\hbar^2a\delta(\mathbf{r}-\mathbf{r}')/m$:

$$U_{\text{contact}}(\mathbf{r}) = \frac{4\pi\hbar^2a}{m}\delta(\mathbf{r}) \equiv g\delta(\mathbf{r}). \quad (8.2)$$

We remind the reader that the magnitude and even the sign of the scattering length a can be tuned, for example by means of an external magnetic field. This phenomenon, called a Feshbach resonance (Köhler *et al.*, 2006), has found multiple applications since its first experimental observation in cold gases (Inouye *et al.*, 1998; Courteille *et al.*, 1998).

In recent years, there has been a quest to produce quantum gases with different, richer interactions. It has been pointed out that the dipole-dipole interaction, acting between particles having a permanent electric or magnetic dipole moment, should lead to a novel

kind of degenerate quantum gas already in the weakly interacting limit. Its effects should be even more pronounced in the strongly correlated regime. The dipole–dipole interaction has attracted a huge interest in this context, for two reasons.

- The properties of the dipole–dipole interaction are radically different from the contact interaction. The interaction energy between two dipoles polarized along the same direction is *long-range* (it decays like $1/r^3$, where r is the distance between the particles) and *anisotropic* (the strength and sign of the interaction depend on the angle θ between the polarization direction and the relative position of the particles). Long-range and/or anisotropic interactions are already known to lead to completely new physical phenomena in classical fluids. Similarly, anisotropy of interactions lies behind the fascinating physics of liquid crystals (de Gennes and Prost, 1995). As we will see, dipole interactions in quantum gases also lead to a variety of novel, fascinating, and sometimes completely unexpected effects (for recent reviews see Baranov *et al.* (2002), Baranov (2008) and Lahaye *et al.* (2009)).
- In recent years it has become possible to cool and trap polar molecules (Krems *et al.*, 2009) and atomic species having a large magnetic moment. For the case of polar molecules, a very promising technique is to associate ultracold atoms using Feshbach resonances and then use photoassociation to bring the weakly bound Feshbach molecules to their ground state (Ospelkaus *et al.*, 2008, 2009). In 2008, the groups of Jin and Ye at JILA were able to create a gas of ultracold rubidium–potassium molecules in their ground rotovibrational states (Ni *et al.*, 2008). For the case of magnetic dipoles, BEC of ^{52}Cr , a species with a large magnetic moment of $6\mu_{\text{B}}$ (μ_{B} being the Bohr magneton), was achieved in 2004 (Griesmaier *et al.*, 2005). This has since then allowed for numerous experimental investigations of the unique properties of dipolar quantum gases (Lahaye *et al.*, 2009).

This chapter is organized as follows. In Section 8.2 we review the basic properties of dipole–dipole interactions. In Section 8.3 we analyse the properties that atoms and molecules must possess in order to show strong dipolar interactions, looking in particular at Rydberg atoms and polar molecules. Section 8.4 deals with trapped dipolar gases, their ground states, stability of the excitations, and the physics of roton–maxon. At the end of the section, we briefly review trapped dipolar fermions, whose complexity goes beyond the scope of this book. The main topic of the chapter—dipoles in optical lattices—is treated in Section 8.5, where extended Bose–Hubbard models are introduced, and in Section 8.6, where dipolar bosonic lattice gases in two dimensions are studied in detail. Since the dipolar interactions are non-local, standard methods of numerical resolution such as the Gutzwiller ansatz or a perturbative mean-field approach often fail. In Section 8.7 we review the results obtained with quantum Monte Carlo methods for dipolar gases. We conclude this chapter with a brief overview of the different and rich physics displayed by dipolar gases. Throughout this chapter we have used, with the permission of the authors, some parts of the reviews by Lahaye *et al.* (2009), Menotti *et al.* (2008), and Menotti and Lewenstein (2008), which were co-written by one of us, as well as Trefzger (2010).

8.2. Properties of dipole-dipole interaction

For two particles 1 and 2 with dipole moments along the unit vectors \mathbf{e}_1 and \mathbf{e}_2 , and whose relative position is \mathbf{r} (see Figure 8.1(a)), the dipole-dipole interaction energy is

$$U_{dd}(\mathbf{r}) = \frac{C_{dd}}{4\pi} \frac{(\mathbf{e}_1 \cdot \mathbf{e}_2) r^2 - 3(\mathbf{e}_1 \cdot \mathbf{r})(\mathbf{e}_2 \cdot \mathbf{r})}{r^5}. \quad (8.3)$$

The coupling constant $C_{dd} = \mu_0 \mu_m^2$ for particles having a permanent magnetic dipole moment μ_m (μ_0 is the permeability of vacuum) and $C_{dd} = \mu_e^2 / \varepsilon_0$ for particles having a permanent electric dipole moment μ_e , ε_0 being the permittivity of vacuum. For a polarized sample where all dipoles point in the same direction z (Figure 8.1(b)), this expression simplifies to

$$U_{dd}(\mathbf{r}) = \frac{C_{dd}}{4\pi} \frac{1 - 3 \cos^2 \theta}{r^3}, \quad (8.4)$$

where θ is the angle between the direction of polarization and the relative position of the particles. Two main properties of the dipole-dipole interaction, namely its long-range ($\sim 1/r^3$) and anisotropic characters, are obvious from eqns (8.3) and (8.4), and contrast strongly with the short-range, isotropic contact interaction of eqn (8.2).

8.2.1 Long-range character

For particles interacting via short-range interactions, the energy is extensive in the thermodynamic limit. In contrast, in systems with long-range interactions, the energy per particle might depend explicitly on the total number of particles. In order to see this, we consider

$$\int_{r_0}^{\infty} U(\mathbf{r}) d^D r, \quad (8.5)$$

where D is the dimensionality of the system and r_0 some short-distance cut-off. For interactions decaying at large distances as $1/r^n$, this integral converges for $D < n$, implying that the interaction is short-range. Therefore, strictly speaking the dipole-dipole interaction ($n = 3$) is long range in three dimensions and short range in one and two dimensions. Nevertheless, even in one and two dimensions, the dipole-dipole forces lead to qualitatively new phenomena, such as the appearance of stable supersolids or dilute MIs with ‘crystal’ order.

8.2.2 Anisotropy

The dipole-dipole interaction has the angular symmetry of the Legendre polynomial of second order $P_2(\cos \theta)$, i.e. d -wave. As θ varies between 0 and $\pi/2$, the factor $1 - 3 \cos^2 \theta$ varies between -2 and 1 , and thus the dipole-dipole interaction is repulsive for particles sitting side by side, but attractive for dipoles in a ‘head-to-tail’ configuration (see Figure 8.1(c) and (d)). For the special ‘magic angle’ $\theta_m = \arccos(1/\sqrt{3}) \simeq 54.7^\circ$, the dipole-dipole interaction vanishes.

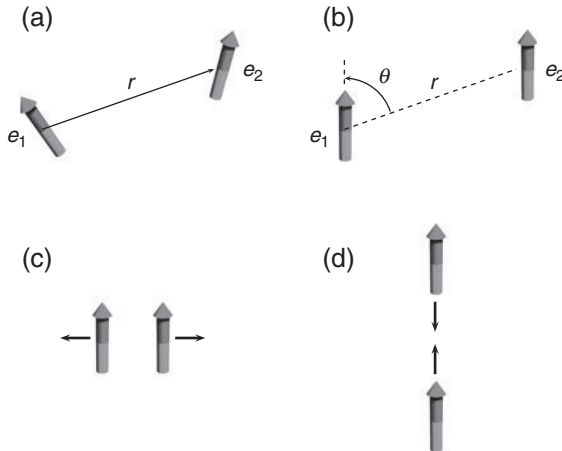


Figure 8.1 Two particles interacting via the dipole–dipole interaction: (a) non-polarized case, (b) polarized case, (c) two polarized dipoles side by side repel each other (black arrows), (d) two polarized dipoles in a ‘head-to-tail’ configuration attract each other. From Lahaye *et al.* (2009).

8.2.3 Scattering properties

The van der Waals potential between two atoms separated by a distance r behaves as $-C_6/r^6$ at large distances. For such a potential, only the s -wave scattering plays a role in cold collisions. This comes from the general result that for a central potential falling off at large distances like $1/r^n$, the scattering phase shifts $\delta_\ell(k)$ scale, for $k \rightarrow 0$, as $k^{2\ell+1}$ if $\ell < (n-3)/2$ and like k^{n-2} otherwise (Landau and Lifshitz, 1987). In the ultracold regime, the scattering is thus fully characterized by the scattering length a .

In the case of the dipole–dipole interaction, the slow decay as $1/r^3$ at large distances implies that, for all ℓ , $\delta_\ell \sim k$ at low momentum and all partial waves contribute to the scattering amplitude. Moreover, due to the anisotropy of the dipole–dipole interaction, partial waves with different angular momenta couple with each other. Therefore one cannot replace the true potential by a short-range, isotropic contact interaction. This property of the dipolar interactions allows, in particular, their use for evaporative cooling of polarized Fermi gases, for which s –wave scattering is not possible due to the Pauli exclusion principle.

8.2.4 Fourier transform

In studies of ultracold dipolar gases, it is often useful to use the Fourier transform of the dipole–dipole interaction U_{dd} :

$$\tilde{U}_{dd}(\mathbf{k}) = \int U_{dd}(\mathbf{r}) e^{-i\mathbf{k}\cdot\mathbf{r}} d^3r = C_{dd} (\cos^2 \gamma - 1/3), \quad (8.6)$$

where γ is the angle between \mathbf{k} and the polarization direction.

8.3. Ultracold dipolar systems

In principle, to realize a quantum gas with significant dipole–dipole interactions, particles having either an electric dipole moment μ_e or a magnetic dipole moment μ_m are required. Usually the dipolar coupling is stronger in the electric case. Indeed, the typical order of magnitude of μ_e for an atomic or molecular system is $\mu_e \sim q_e a_0$, where q_e is the electron charge and $a_0 = 0.53$ Å—the Bohr radius. The magnetic moments, meanwhile, are of the order of the Bohr magneton $\mu_B = 927.40 \times 10^{-26}$ J · T⁻¹. Using the definitions of a_0 and μ_B in terms of fundamental constants, one sees that the ratio of magnetic to electric dipolar coupling constants, C_{dd} , is

$$\frac{\mu_0 \mu_m^2}{\mu_e^2 / \epsilon_0} \sim \alpha^2 \sim 10^{-4}, \quad (8.7)$$

where $\alpha \simeq 1/137$ is the fine structure constant.

For a given species, it is convenient to define various measures to quantify the strength of the dipolar interaction. From the dipolar coupling constant C_{dd} and the mass m of the particle one can define the following ‘dipolar length’:

$$a_{dd} \equiv \frac{C_{dd} m}{12\pi\hbar^2}, \quad (8.8)$$

which is a measure of the absolute strength of the dipole–dipole interaction. However, to observe dipolar effects it is the ratio of the dipolar length to the *s*-wave scattering length, comparing the relative strength of the dipolar interaction and the contact interaction which needs to be non-negligible:

$$\varepsilon_{dd} \equiv \frac{a_{dd}}{a} = \frac{C_{dd}}{3g}. \quad (8.9)$$

The numerical factors in eqn (8.8) are chosen in such a way that for $\varepsilon_{dd} \geq 1$, a *homogeneous* BEC is unstable against collapse (as explained in Section 8.4.2). Table 8.1 summarizes the typical numerical values of the dipolar constants for various atomic and molecular species.

Below we describe various systems that can be used experimentally to study ultracold dipolar gases.

Table 8.1 Dipolar constants for various atomic and molecular species, where μ_B is the Bohr magneton, a_0 the Bohr radius, and D denotes a Debye (1 D $\simeq 3.335 \times 10^{-30}$ C · m). For the molecular species, the (unknown until now) scattering length is assumed to be $100a_0$.

Species	Dipole moment	a_{dd}	ε_{dd}
⁸⁷ Rb	$1.0 \mu_B$	$0.7 a_0$	0.007
⁵² Cr	$6.0 \mu_B$	$16 a_0$	0.16
KRb	0.6 D	$2.0 \times 10^3 a_0$	20
ND ₃	1.5 D	$3.6 \times 10^3 a_0$	36
HCN	3.0 D	$2.4 \times 10^4 a_0$	240

8.3.1 Polar molecules

Due to their strong electric dipole moment, polar molecules are ideal candidates to exhibit dipolar effects. Three requirements need to be fulfilled for a molecule in order to have a significant dipole moment:

- (i) The molecule has to be *heteronuclear* to have a permanent dipole moment.
- (ii) The molecule must be in a low rotovibrational state in order to have a significant dipole moment and to be stable against collisional relaxation.
- (iii) An external electric field (with typical values of the order of 10^4 V/cm) must be applied to *orient* the molecule in the laboratory frame and approach the asymptotic value of the permanent electric dipole moment along the internuclear axis. Indeed, the ground state $J = 0$ is rotationally symmetric and therefore the dipole moment averages to zero; only by a mixing with higher rotational levels induced by the electric field can the average dipole become non-zero.

Under these three requirements, the dipole moment is of the order of few Debyes ($1\text{ D} \simeq 3.335 \times 10^{-30}\text{ C}\cdot\text{m}$). Assuming that the scattering length of the molecule is similar to that of the atoms commonly used in BEC experiments (typically around $100a_0$), the corresponding value of ε_{dd} is of the order of 100 (see Table 8.1), implying that the properties of a quantum gas of such molecules will be dominated by the dipole–dipole interaction.

8.3.2 Rydberg atoms

Extraordinarily high electric dipole moments can be obtained for highly excited Rydberg atoms. As the Kepler radius scales with n^2 , where n is the main quantum number, the dipolar interaction energy can in principle scale as n^4 . Individual Rydberg atoms experience lifetimes that scale as n^{-3} . However, due to the weak binding of the valence electrons and the strong and partially attractive forces between Rydberg atoms, the lifetime of a dense gas is limited to timescales much shorter than the lifetime of a free Rydberg atom. Therefore Rydberg atoms in a BEC (Heidemann *et al.*, 2008) are currently investigated as a frozen gas. Collective behavior in the excitation dynamics has been observed, as well as excitation blockade due to dipolar interactions (Vogt *et al.*, 2006). On the other hand, hydrodynamic collective phenomena due to moving dipoles have not been observed to date.

8.3.3 Light-induced dipoles

Atoms in their ground state, which is a parity eigenstate, do not possess an electric dipole moment. Their electric polarizability is usually very small, so that extreme electric field strengths would be necessary to induce a sizeable dipolar interaction (Marinescu and You, 1998; Yi and You, 2000, 2001). However, one might consider using resonant excitation of a dipole optical-allowed transition to induce an AC dipole moment of the order of one atomic unit $q_e a_0$. Since this dipole moment also couples to the vacuum modes of the radiation field, the spontaneous light forces scale just like the light-induced dipolar interactions, which makes their observation very difficult. Nevertheless, the anisotropic nature of the interaction might be used for a proof-of-principle experiment, which would allow discrimination of the spontaneous light forces from the dipolar forces (Löw *et al.*, 2005). Due to retardation effects, the AC dipolar interaction also contains terms that fall off like $1/r$, which may, in

theory, be used to simulate an effective isotropic, gravity-like $1/r$ potential (O'Dell *et al.*, 2000, 2003; Giovanazzi *et al.*, 2002).

8.3.4 Magnetic dipoles

Some atoms, such as chromium, erbium, europium, dysprosium, and others, have a large magnetic moment of several Bohr magnetons (μ_B) in their ground state, and thus experience significant magnetic dipole–dipole interaction. Of these, only ^{52}Cr has been Bose-condensed to date (Griesmaier *et al.*, 2005; Beauflis *et al.*, 2008), but there has also been a lot of progress in trapping and cooling other species (see for instance Lu *et al.* (2011) for results with dysprosium). Chromium has a magnetic dipole moment of $6\mu_B$, and a scattering length of about $100a_0$. This gives $\varepsilon_{dd} \simeq 0.16$ (Griesmaier *et al.*, 2006), which allows observation of a perturbative effect of the dipolar interaction on the expansion dynamics of the cloud (Stuhler *et al.*, 2005). The main steps leading to the creation of a ^{52}Cr BEC, with a special emphasis on the role of the dipole–dipole interaction, are reviewed in Lahaye *et al.* (2009).

8.4. Ultracold trapped dipolar gases

Before we turn to the discussion of strongly correlated dipolar gases in optical lattices, let us briefly review the properties of trapped dipolar gases. Dipolar interactions are expected to change many of the properties of the gas, even in the non-degenerate case where thermodynamical quantities can be affected. For instance, dipolar effects change the critical temperature of condensation if the system is strongly dipolar. However, the most dramatic effects of the dipolar interactions arise for pure condensates. Below, unless otherwise stated, we thus consider the case of a bosonic gas at zero temperature.

8.4.1 Trapped dipolar Bose gases

We start by the description of a BEC of polarized dipoles, pointing, for example, along the z -axis. For polarized dipolar BECs, due to the anisotropy of the dipolar interactions the geometry of the trapping potential plays a fundamental role, first in determining the spatial distribution of the density and second in the stability of the gas.

Qualitatively, there are two extreme scenarios depending on the aspect ratio $\lambda = \omega_z/\omega_\rho$ between the axial ω_z and radial frequencies $\omega_\rho = \omega_x = \omega_y$, as shown in Figure 8.2:

- (i) For a cigar-shaped trap elongated along the z -axis, i.e. $\lambda \ll 1$, the density is mainly distributed along the polarization axis and the effect of dipole–dipole interactions is mostly attractive, which might lead to an instability of the gas even in the presence of a weak repulsive contact interaction, see Figure 8.2(a).
- (ii) For a pancake-shaped trap, which is strongly confining along the z -axis, i.e. $\lambda \gg 1$, the dipolar interaction is mostly repulsive and the BEC is stable for repulsive contact interactions, and might even be stable for attractive contact interactions, see Figure 8.2(b).

In an intermediate situation in which the confining potential is perfectly spherical ($\lambda = 1$), the density distribution is isotropic and the dipole–dipole interaction averages out to zero

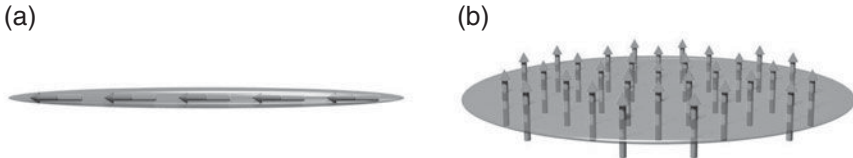


Figure 8.2 Polarized dipoles in anisotropic harmonic potentials. (a) In a cigar-shaped trap elongated in the direction of polarization, the resulting dipolar interaction is attractive. (b) In a pancake trap with a strong confinement in the direction of polarization, the dipolar interactions are repulsive. From Lahaye *et al.* (2009).

(see Section 8.4.2), which leads to a stable BEC for repulsive contact interactions. One can switch between the above scenarios simply by adjusting the frequency of the confining potential along the z -axis with respect to the radial x and y . It is, therefore, natural to expect that for any given aspect ratio λ there is a critical value of scattering length $a = a_{\text{crit}}$ below which the BEC is unstable and that, reciprocally, for a given a there is a λ_{crit} marking the stability regime (Santos *et al.*, 2000; Góral *et al.*, 2001).

The Hamiltonian of the system in the presence of the dipole–dipole interaction U_{dd} given by eqn (8.4) reads

$$\hat{H} = \int d^3r \hat{\psi}^\dagger(\mathbf{r}) \left[-\frac{\hbar^2 \nabla^2}{2m} + V_{\text{ext}}(\mathbf{r}) + \frac{g}{2} \hat{\psi}^\dagger(\mathbf{r}) \hat{\psi}(\mathbf{r}) - \mu \right] \hat{\psi}(\mathbf{r}) + \frac{1}{2} \int d^3r d^3r' \hat{\psi}^\dagger(\mathbf{r}) \hat{\psi}^\dagger(\mathbf{r}') U_{\text{dd}}(\mathbf{r} - \mathbf{r}') \hat{\psi}(\mathbf{r}) \hat{\psi}(\mathbf{r}'), \quad (8.10)$$

where $\hat{\psi}(\mathbf{r})$ and $\hat{\psi}^\dagger(\mathbf{r})$ are the bosonic annihilation and creation field operators, respectively, g is defined in eqn (8.2), and μ is the chemical potential. With the same approximations used to derive the Gross–Pitaevskii equation (see Section 3.4) one can write the bosonic field operator $\hat{\psi}(\mathbf{r}) = \psi(\mathbf{r}) + \delta\hat{\psi}(\mathbf{r})$ as a sum of a classical field $\psi(\mathbf{r})$, the condensate wave function, plus the non-condensate component $\delta\hat{\psi}(\mathbf{r})$. By neglecting the fluctuations $\delta\hat{\psi}(\mathbf{r})$ one can calculate the energy of the system given by

$$E[\psi] = \int \left[-\frac{\hbar^2}{2m} |\nabla \psi(\mathbf{r})|^2 + V_{\text{ext}}(\mathbf{r}) |\psi(\mathbf{r})|^2 + \frac{g}{2} |\psi(\mathbf{r})|^4 + \frac{1}{2} |\psi(\mathbf{r})|^2 \int U_{\text{dd}}(\mathbf{r} - \mathbf{r}') |\psi(\mathbf{r}')|^2 d^3r' \right] d^3r. \quad (8.11)$$

Variation of $E[\psi]$ with respect to ψ at fixed norm leads to the Gross–Pitaevskii equation that includes the non-contact dipole term,

$$i\hbar \frac{\partial \psi}{\partial t} = -\frac{\hbar^2}{2m} \Delta \psi + (V_{\text{ext}} + g|\psi|^2 + \Phi_{\text{dd}}) \psi, \quad (8.12)$$

where Φ_{dd} is the dipolar contribution to the mean-field interaction

$$\Phi_{\text{dd}}(\mathbf{r}, t) = \int |\psi(\mathbf{r}', t)|^2 U_{\text{dd}}(\mathbf{r} - \mathbf{r}') d^3 r'. \quad (8.13)$$

This term is *non-local* (due to the long-range character of the dipolar interaction) and makes it much more complicated to solve the Gross–Pitaevskii equation, even numerically, as one now faces an integro-differential equation. In the time-independent case, the left-hand side of eqn (8.12) has to be replaced by $\mu\psi$, with μ being the chemical potential. The Gross–Pitaevskii equation then becomes:

$$\mu\psi = -\frac{\hbar^2}{2m}\Delta\psi + (V_{\text{ext}} + g|\psi|^2 + \Phi_{\text{dd}})\psi. \quad (8.14)$$

8.4.2 Ground-state properties and excitations of dipolar Bose gases

Homogeneous gas: phonon instability Because of the partially attractive character of the dipole–dipole interaction, the stability of a dipolar BEC is a problem that needs to be addressed. Indeed it is well known that a homogeneous condensate with attractive contact interactions ($a < 0$) is unstable, as the Bogoliubov excitations have imaginary frequencies at low momentum (Pitaevskii and Stringari, 2003).

In order to study the stability of a homogeneous dipolar condensate one can use the hydrodynamic equations derived from the Gross–Pitaevskii equation, eqn (8.12), by writing $\psi = \sqrt{n} \exp(i\phi)$, with n the atomic density and ϕ the phase of the order parameter (the latter being related to the superfluid velocity field $\mathbf{v} = \hbar/m\nabla\phi$), and separating the real and imaginary parts. They read:

$$\frac{\partial n}{\partial t} + \nabla \cdot (n\mathbf{v}) = 0, \quad (8.15)$$

$$m \frac{\partial \mathbf{v}}{\partial t} = -\nabla \left(\frac{mv^2}{2} + gn + V_{\text{ext}} + \Phi_{\text{dd}} - \frac{\hbar^2}{2m} \frac{\Delta\sqrt{n}}{\sqrt{n}} \right). \quad (8.16)$$

Considering a homogeneous dipolar condensate with an equilibrium density n_0 and small perturbations with frequency ω and wavevector \mathbf{k} , and linearizing the hydrodynamics equations (eqn (8.15) and (8.16)) around equilibrium, one can show that the excitation spectrum is given by

$$\omega = k \sqrt{\frac{n_0}{m} \left[g + \frac{C_{\text{dd}}}{3} (3 \cos^2 \gamma - 1) \right] + \frac{\hbar^2 k^2}{4m^2}}, \quad (8.17)$$

which corresponds to the usual Bogoliubov spectrum $\omega = k\sqrt{gn_0/m + \hbar^2 k^2/(4m^2)}$, with the Fourier transform of the contact interaction of eqn (8.2) complemented by the one of the dipole–dipole interaction eqn (8.6). With the definition in eqn (8.9) for ε_{dd} , eqn (8.17) implies that a dipolar uniform condensate is unstable for $\varepsilon_{\text{dd}} > 1$ because phonons ($k \rightarrow 0$) acquire imaginary frequencies, the most unstable situation being the case of a wavevector perpendicular to the orientation of the dipoles ($\gamma = \pi/2$).

Trapped gas: geometrical stabilization We discussed in Section 8.4.1 that the aspect ratio of the trap λ affects the nature of the dipolar interactions and thus the stability of the gas. To obtain an estimate for the critical value of the scattering length $a_{\text{crit}}(\lambda)$ below which the BEC is unstable, one can use a variational method. For this purpose, we assume that the condensate wave function ψ is Gaussian, with an axial size σ_z and a radial size σ_ρ , which we take as variational parameters:

$$\psi(r, z) = \sqrt{\frac{N}{\pi^{3/2} \sigma_\rho^2 \sigma_z l_{\text{ho}}^3}} \exp \left[-\frac{1}{2l_{\text{ho}}^2} \left(\frac{r^2}{\sigma_\rho^2} + \frac{z^2}{\sigma_z^2} \right) \right]. \quad (8.18)$$

Here, $l_{\text{ho}} = \sqrt{\hbar/(m\bar{\omega})}$ is the harmonic oscillator length corresponding to the average trap frequency $\bar{\omega} = (\omega_\rho^2 \omega_z)^{1/3}$. Inserting the ansatz (eqn (8.18)) into the energy functional (eqn (8.11)) leads to the following expression for the energy:

$$E(\sigma_\rho, \sigma_z) = E_{\text{kin}} + E_{\text{trap}} + E_{\text{int}}, \quad (8.19)$$

with the kinetic energy

$$E_{\text{kin}} = \frac{N\hbar\bar{\omega}}{4} \left(\frac{2}{\sigma_\rho^2} + \frac{1}{\sigma_z^2} \right), \quad (8.20)$$

the potential energy due to the trap

$$E_{\text{trap}} = \frac{N\hbar\bar{\omega}}{4\lambda^{2/3}} (2\sigma_\rho^2 + \lambda^2\sigma_z^2), \quad (8.21)$$

and the interaction, including contact and dipolar, energy

$$E_{\text{int}} = \frac{N^2\hbar\bar{\omega}a_{\text{dd}}}{\sqrt{2\pi}l_{\text{ho}}} \frac{1}{\sigma_\rho^2\sigma_z} \left(\frac{a}{a_{\text{dd}}} - f(\kappa) \right), \quad (8.22)$$

where $\kappa = \sigma_\rho/\sigma_z$ is the aspect ratio *of the cloud*, which differs from that of the trap due to the elongation induced by the dipole–dipole interaction (see for instance Lahaye *et al.* (2009)), and $f(k)$ is given by

$$f(\kappa) = \frac{1+2\kappa^2}{1-\kappa^2} - \frac{3\kappa^2 \operatorname{artanh} \sqrt{1-\kappa^2}}{(1-\kappa^2)^{3/2}}. \quad (8.23)$$

The calculation of the function $f(\kappa)$ is tedious but elementary. The general result, shown in Figure 8.3, shows that $f(\kappa)$ is monotonically decreasing, has asymptotic values $f(0) = 1$ and $f(\infty) = -2$, and vanishes for $\kappa = 1$, implying that for an isotropic density distribution the dipole–dipole mean-field potential averages to zero.

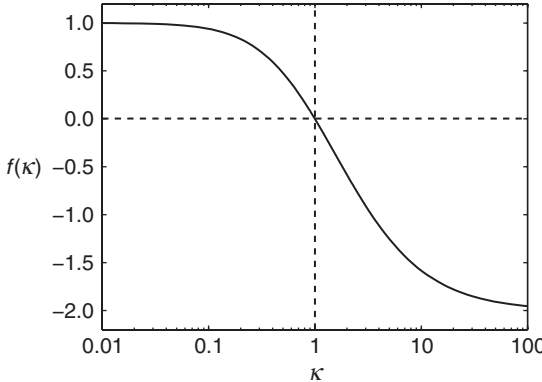


Figure 8.3 κ -dependence of the $f(\kappa)$ function that appears in the mean-field dipolar interaction. From Lahaye *et al.* (2009).

Let us illustrate how to calculate the mean-field dipolar interaction energy for a Gaussian ansatz in a spherical trap. The dipolar interaction energy of eqn (8.11) is given by

$$E_{\text{dd}} = \frac{1}{2} \int d^3r d^3r' \rho(\mathbf{r}) \rho(\mathbf{r}') U_{\text{dd}}(\mathbf{r} - \mathbf{r}') \quad (8.24)$$

with $\rho(\mathbf{r}) = |\psi(\mathbf{r})|^2$ being the condensate density at \mathbf{r} . The above expression can be simplified by means of the convolution theorem (Góral *et al.*, 2001; Santos *et al.*, 2000), which states

$$\int d^3r' U_{\text{dd}}(\mathbf{r} - \mathbf{r}') \rho(\mathbf{r}') = \mathcal{F}^{-1} \left\{ \tilde{U}_{\text{dd}}(\mathbf{k}) \tilde{\rho}(\mathbf{k}) \right\}, \quad (8.25)$$

where $\tilde{U}_{\text{dd}}(\mathbf{k})$ and $\tilde{\rho}(\mathbf{k})$ are the Fourier transform of the dipole-dipole potential and the density, respectively. \mathcal{F}^{-1} indicates the inverse Fourier transform, and using its definition we can write

$$E_{\text{dd}} = \frac{1}{2} \int d^3r \rho(\mathbf{r}) \frac{1}{(2\pi)^3} \int d^3k \tilde{U}_{\text{dd}}(\mathbf{k}) \tilde{\rho}(\mathbf{k}) e^{i\mathbf{k}\cdot\mathbf{r}} = \frac{1}{16\pi^3} \int d^3k \tilde{U}_{\text{dd}}(\mathbf{k}) \tilde{\rho}^2(\mathbf{k}), \quad (8.26)$$

where we have used the relation $\tilde{\rho}(\mathbf{k}) = \tilde{\rho}(-\mathbf{k})$.

Using eqn (8.6) and considering that for the simple case of an isotropic potential ($\sigma_z = \sigma_\rho$) $\rho(\mathbf{r})$ becomes a product of three Gaussian distributions with equal widths σ , and then

$$\tilde{\rho}(\mathbf{k}) = \frac{N}{(\sqrt{\pi}\sigma l_{\text{ho}})^3} \int d^3r e^{-i\mathbf{k}\cdot\mathbf{r}} e^{-\frac{r^2}{\sigma^2 l_{\text{ho}}^2}} = \exp \left[-\frac{\sigma^2 l_{\text{ho}}^2}{4} \mathbf{k}^2 \right], \quad (8.27)$$

the integral in eqn (8.26) can now easily be evaluated in polar (r, γ, φ) coordinates giving, as expected for an isotropic trap, a zero value for the dipolar interactions

$$\begin{aligned} E_{\text{dd}} &= \frac{NC_{\text{dd}}}{2} \int \sin \gamma d\gamma d\varphi k^2 dk (\cos^2 \gamma - 1/3) \exp \left[-\frac{\sigma^2 l_{\text{ho}}^2}{4} \mathbf{k}^2 \right] \\ &= NC_{\text{dd}} 2\pi \int dk k^2 \exp \left[-\frac{\sigma^2 l_{\text{ho}}^2}{2} \mathbf{k}^2 \right] \int_{-1}^{+1} dx (x^2 - 1/3) = 0, \end{aligned} \quad (8.28)$$

where we have performed the change of variable $x = \cos \gamma$. The generalization to anisotropic density distributions is mathematically more demanding, but in principle straightforward, and leads to eqn (8.22).

Trapped gas: stability threshold To determine the stability threshold $a_{\text{crit}}(\lambda)$, one needs to minimize the energy (eqn (8.19)) with respect to σ_ρ and σ_z and for fixed values of N , λ and $\bar{\omega}$. For $a > a_{\text{crit}}$, one has a minimum of energy—at least a local one—for finite values of σ_ρ and σ_z , while as soon as $a < a_{\text{crit}}$, no such minimum exists. Figure 8.4 shows contour plots of the energy $E(\sigma_\rho, \sigma_z)$ for $N = 2 \times 10^4$, $\lambda = 10$, and different values of a , clearly showing that $a_{\text{crit}}(10) \simeq -8.5a_0$ for the chosen parameters. In the right-hand panel of Figure 8.5, the critical scattering length $a_{\text{crit}}(\lambda)$ is obtained in this way for different values of the trap aspect ratio λ (shown as a thick line) while keeping the number of atoms fixed. In the limit $N \rightarrow \infty$, the asymptotic behavior of this curve, $a_{\text{crit}}^\infty(0) = a_{\text{dd}}$ and $a_{\text{crit}}^\infty(\infty) = -2a_{\text{dd}}$, can easily be understood as only the sign of the interaction term (eqn (8.22)), which scales as N^2 and not as N like the kinetic and potential energy, determines the stability. For an extremely pancake-shaped trap $\lambda \rightarrow \infty$, the cloud has an aspect ratio $\kappa \rightarrow \infty$, and, as $\lim_{\kappa \rightarrow \infty} f(\kappa) = -2$, the condensate is stable (or metastable) only if $a > -2a_{\text{dd}}$. In the same way, one readily understands that for $\lambda \rightarrow 0$ the critical scattering length is a_{dd} . The minimum value of λ for which a purely dipolar condensate ($a = 0$) is stable is the one for which $\kappa = 1$. It is found numerically to be close to $\lambda \simeq 5.2$ (Santos *et al.*, 2000; Góral *et al.*, 2002; Yi and You, 2001; Eberlein *et al.*, 2005; Koch *et al.*, 2008).

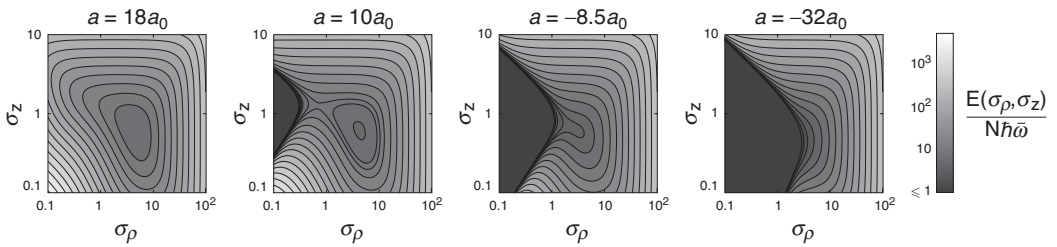


Figure 8.4 The energy landscape $E(\sigma_\rho, \sigma_z)$ as a function of the variational parameters σ_ρ and σ_z of the Gaussian ansatz, eqn (8.18), for a trap of aspect ratio $\lambda = 10$ and various values of the scattering length a . When a decreases, one goes from a *global* minimum (at $a = 18a_0$) to a *local* minimum corresponding to a metastable condensate (at $a = 10a_0$). This local minimum vanishes at $a = a_{\text{crit}}$ (here $-8.5a_0$). Below a_{crit} the energy can be lowered without bound by forming an infinitely thin cigar-shaped cloud. From Lahaye *et al.* (2009).

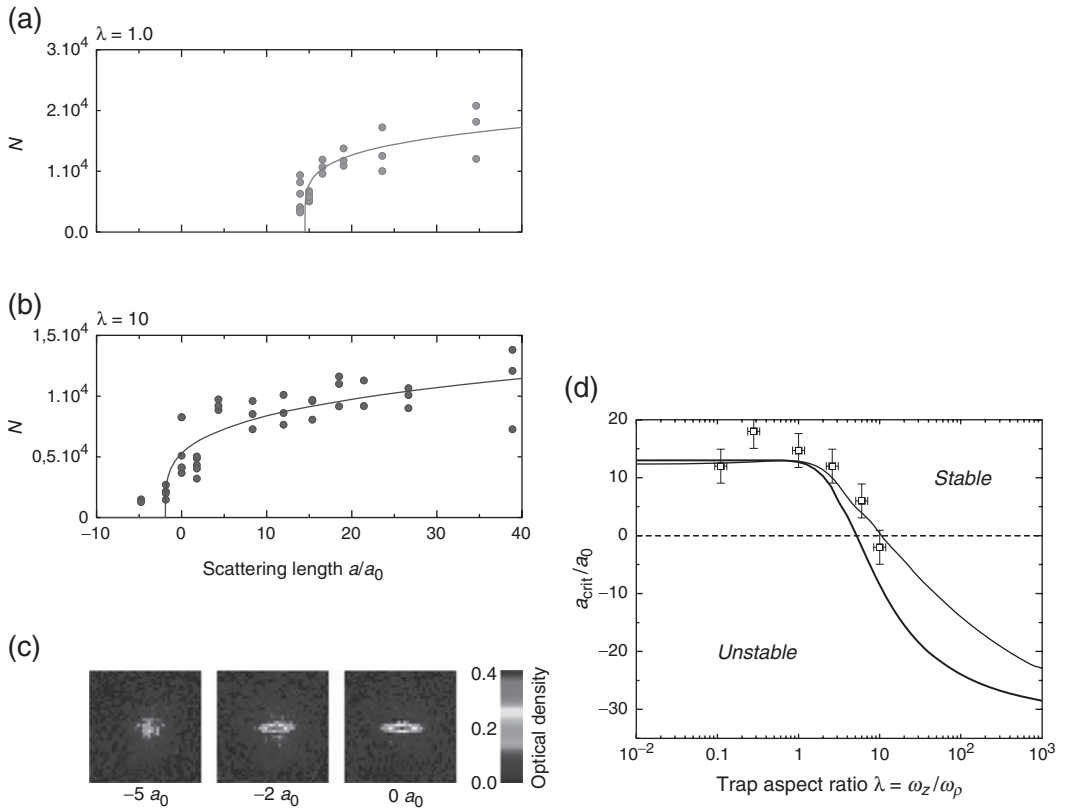


Figure 8.5 (a), (b) and (c) Experimental observation of the geometry-dependent stability of a dipolar BEC—redrawn after Koch *et al.*, 2008 by courtesy of the authors. (a) BEC atom number N as a function of the scattering length, a , for a spherical trap; N vanishes for a smaller than $a_{\text{crit}} \simeq 15a_0$. (b) For an oblate trap ($\lambda = 10$), one has $a_{\text{crit}} \simeq -2a_0$; such a trap can thus stabilize a purely dipolar BEC. In (a) and (b) the solid lines are fits to the empirical threshold law $(a - a_{\text{crit}})^\beta$. (c) Sample images of the atomic cloud as a function of a for $\lambda = 10$. Right panel (d)—from Bohn *et al.*, 2009—shows the stability diagram of a dipolar condensate: the thick line is the solution for $a_{\text{crit}}(\lambda)/a_0$ calculated with the Gaussian ansatz (8.18), the thin line is the numerical solution of the GP equation and the dots with error bars are experimental data of Koch *et al.*, 2008.

The influence of the trapping geometry in the stability analysis has been demonstrated experimentally for a BEC of ^{52}Cr by Koch *et al.* (2008). The aspect ratio variation is achieved by superimposing on the optical trapping potential a 1D optical lattice along the z -direction with a very long period ($7\ \mu\text{m}$), so that only one site of the optical lattice is loaded with the condensate. By varying the powers of the beams the aspect ratio λ can

be changed over two orders of magnitude: from $\lambda \simeq 0.1$ —a prolate trap—to $\lambda \simeq 10$ —an oblate trap—while keeping the average trap frequency $\bar{\omega} = (\omega_\rho^2 \omega_z)^{1/3}$ almost constant (with a value of $2\pi \times 800$ Hz). Using the Feshbach resonance at 589 G, the scattering length was ramped adiabatically to a final value of a and the atom number in the BEC was measured. A typical measurement is shown in the left-hand panel of Figure 8.5. When a is reduced, the atom number decreases, first slowly and then very abruptly when a approaches a critical value a_{crit} , below which no condensate can be observed. The right-hand panel of Figure 8.5 shows the measured value of a_{crit} (dots with error bars) as a function of λ . One clearly observes that for prolate traps a_{crit} is close to a_{dd} , as expected from the discussion above. For the most pancake-shaped trap, meanwhile, the critical scattering length is close to zero, evidencing that for such a geometry a *purely dipolar* condensate is stable. As mentioned above, the solid line is the stability threshold $a_{\text{crit}}(\lambda)$ obtained by the Gaussian ansatz for a number of atoms $N = 2 \times 10^4$, which is in good agreement with the measurements. Note that for the parameters used in the experiment, the critical scattering length for pure contact interaction would be $-0.3a_0$ for $\lambda = 1$, which clearly shows that the instability is driven here by the dipole–dipole interaction (Koch *et al.*, 2008).

To calculate the exact stability threshold, one needs, however, to solve numerically the Gross–Pitaevskii equation (8.12); the result of such a calculation (Bohn *et al.*, 2009) is displayed as a thin line in the right panel of Figure 8.5 and shows a very good agreement with the experimental data. The numerical solution reveals, for some values of the parameters (λ, a) close to the instability region, the appearance of ‘biconcave’ condensates, where the density has a local minimum in the center of the trap (Ronen *et al.*, 2007).

Trapped gas: excitations and roton–maxon spectrum The study of the excitations of a dipolar BEC should be in principle realized using the non-local Bogoliubov–de Gennes equations (Yi and Tou, 2000, 2001; Góral *et al.*, 2002). A dipolar gas exhibits two kinds of instability. In cigar-like traps, when the dipoles are oriented along the trap axis, the dipolar interactions have an attractive character and the gas collapses. The collapse is similar to the case of the contact interactions with negative scattering length, but has a different geometrical nature, and different critical scaling behavior. There is, however, another instability mechanism that occurs even in quasi-2D pancake traps for dipoles polarized perpendicularly to the trap plane (along the z -axis). In this case, when the dipolar interactions are sufficiently strong, the gas, despite the quasi-2D trap geometry, feels the 3D nature of the dipolar interactions, i.e. their partially attractive character. This so-called ‘roton–maxon’ instability was discovered by Santos *et al.* (2003), and has been discussed by many authors since then.

In Santos *et al.* (2003), the authors considered an infinite pancake trap (with slab geometry) with dipoles oriented along the z -direction perpendicular to the trap plane. The roton–maxon physics occurs in the Thomas–Fermi limit, i.e. when the quantum pressure effects are neglected, in the z -direction. The condensate was hence assumed to have a Thomas–Fermi shape along the z -axis and a constant amplitude with respect to x - and y coordinates. The 3D Bogoliubov–de Gennes equations were then solved. Here we follow a somewhat simplified effective 2D approach (Dutta and Lewenstein, 2010), which nevertheless captures the main physics. The bosons are also polarized along the z direction, so that the dipolar interaction in momentum space reads $\tilde{U}_{dd} = C_{\text{dd}}(k_z^2/k^2 - 1/3)$. As we

shall see below, the cases of repulsive (attractive) contact interactions with $g > 0$ ($g < 0$) lead to qualitatively different physics. We first consider the case of positive g .

In the standard (simple) quasi-2D approach, one assumes that the condensate has a Gaussian shape along the z direction, with the width determined by the harmonic potential. The problem is then projected onto two dimensions by integrating over the condensate profile. Such an approach is valid when the chemical potential $\mu \ll \hbar\omega_z$. The roton–maxon instability occurs outside this regime and hence the simple quasi-2D approach cannot be employed to understand it. However, we can still use an effective quasi-2D approach, where we assume that the bosonic wave function in the z direction is given by the Thomas–Fermi profile. In this way we may obtain an effectively 2D model with the dipole interactions ‘averaged’ along the z direction. This approach corresponds approximately to the approach made in Santos *et al.*, 2003, with the only difference being that for the lowest-energy branch of excitations we neglect their ‘kinetic’ energy, i.e. the terms in the Bogoliubov–de Gennes equation involving derivatives with respect to z . The quantitative differences between the exact results presented in Santos *et al.* (2003) and the present effective quasi-2D approach amount typically to 10–20% in the entire regime relevant for rotonization. Qualitatively, both approaches describe the same physics and the same mechanism of appearance of the instability, namely the momentum-dependence of the dipole–dipole interactions.

For simplicity, we have made the approximation of using a Gaussian profile in the z direction with a variationally determined width ℓ_z , which turns out to be of the order of the Thomas–Fermi (TF) radius $\ell_z \simeq \ell_{\text{TF}}/\sqrt{5}$. The dipolar interaction in two dimensions, after integrating out the z direction, takes the simple form

$$\tilde{U}_{\text{eff}} = \frac{C_{\text{dd}}}{4\pi\ell_z} \mathcal{V}(k_{\perp}), \quad (8.29)$$

with

$$\mathcal{V}(k_{\perp}) = 1 - \frac{3}{2} \sqrt{\frac{\pi}{2}} k_{\perp} \ell_z \operatorname{erfc} \left[k_{\perp} \ell_z / \sqrt{2} \right] \exp \left[k_{\perp}^2 \ell_z^2 / 2 \right]. \quad (8.30)$$

Here $k_{\perp}^2 = k_x^2 + k_y^2$ and erfc refers to the complementary error function, which is defined as $\operatorname{erfc}(x) = 2/\sqrt{\pi} \int_x^{\infty} e^{-t^2} dt$. The interaction $\mathcal{V}(k_{\perp})$ is repulsive for small momenta and can be attractive for large momenta. Now we can write the Hamiltonian of the condensed (non-interacting) dipolar bosons as

$$\hat{H} = \sum_{\mathbf{k}_{\perp}} \Omega(k_{\perp}) \hat{b}_{\mathbf{k}_{\perp}}^{\dagger} \hat{b}_{\mathbf{k}_{\perp}}, \quad (8.31)$$

where $\hat{b}_{\mathbf{k}_{\perp}}^{\dagger}$ and $\hat{b}_{\mathbf{k}_{\perp}}$ are Bogoliubov quasi-particle operators. The spectrum of the above Hamiltonian is given, in units of the trap frequency, by

$$\Omega^2(\tilde{k}_{\perp}) = \frac{\tilde{k}^4}{4} + g_{3\text{d}} \mathcal{V}(\tilde{k}_{\perp}) \tilde{k}^2, \quad (8.32)$$

where $\tilde{k}_{\perp} = k_{\perp} \ell_z$ and $g_{3\text{d}} = m C_{\text{dd}} n \ell_z / (4\pi\hbar^2)$ is the dimensionless interaction strength. Since the interaction in eqn (8.30) is repulsive for small momenta and attractive in the

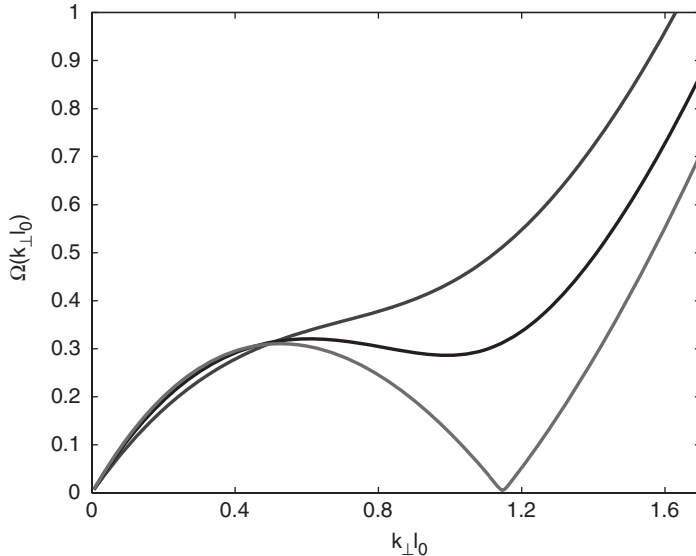


Figure 8.6 The excitation spectrum $\Omega(\tilde{k}_\perp)$ in units of the trap frequency as a function of \tilde{k}_\perp (l_0 corresponds to l_z). The upper, middle and lower curves correspond to $g_{3d} = 0.4, 0.6$ and 0.72 , respectively. By courtesy of O. Dutta.

high-momentum limit (with a zero-crossing at $k_\perp \ell_z \simeq 1$), the properties of the excitation spectrum in eqn (8.32) are very different from those of bosons with contact interactions. For any bosonic density, $\Omega(k_\perp)$ exhibits two regimes: (i) a phonon spectrum for small momenta and (ii) a free-particle spectrum for higher momenta. For g_{3d} greater than a certain critical value, $\Omega(k_\perp)$ has a minimum at the intermediate momentum regime (see Figure 8.6). Following Landau, the excitations around the minimum are called ‘rotons’ and $\Omega(\tilde{k}_0)$ is known as the ‘roton gap’. With increasing g_{3d} the ‘roton’ gap decreases and eventually vanishes for a critical particle density. When the critical density is exceeded, $\Omega(\tilde{k}_0)$ becomes imaginary and the condensate becomes unstable. Once more we stress that in the presence of repulsive contact interactions the roton instability occurs in pancake traps in the regime in which the standard quasi-2D approximation does not hold. The condensate attains the Thomas–Fermi profile in the z direction and the system starts to experience the 3D (partially attractive) nature of the dipolar forces (Fischer, 2006). The situation is, however, different if the contact interactions are attractive ($g < 0$). In that case the roton instability already appears in the standard quasi-2D regime, when the chemical potential $\mu \ll \hbar\omega_z$ and the condensate profile is Gaussian with the bare harmonic oscillator width. While in the previous case it was the attractive part of the dipolar interactions that led to the roton instability. In this quasi-2D situation, the dipolar interactions, which are on average repulsive, stabilize the phonon instability for $\mu = (g + 8\pi g_{dd}/3)n > 0$. In the absence of dipole–dipole interaction this leads to the well-known collapse for gases with $a < 0$. For details we refer the reader to Lahaye *et al.* (2009).

The presence of a roton minimum in the spectrum of elementary excitations may be revealed in various ways. For instance, using the Landau superfluidity criterion (Landau

and Lifshitz, 1987) it is clear that the superfluid critical velocity is reduced in the presence of a roton minimum (Santos *et al.*, 2003).

The question of whether ‘there is a life after the roton instability’ has been studied by many researchers in the hope of finding novel types of stable Bose superfluids with supersolid character, i.e. self-assembled density modulations. This possibility is suggested by the fact that the instability occurs at a specific value of the momentum, indicating instability towards a non-uniform ground state (Pomeau and Rica, 1994; Josserand *et al.*, 2007). The ultimate answer to the question is negative: the condensate undergoes a sequence of local collapses (Dutta and Meystre, 2007; Komineas and Cooper, 2007). In Komineas and Cooper (2007) it is shown numerically that in the mean-field theory supersolid states of dipolar BEC are unstable. In Dutta *et al.* (2007) a variational ansatz with density wave modulations along the z direction in a cylindrically symmetric trap is used, showing that it is not stable for a dipolar gas due to roton instability. It can, however, be stabilized by allowing for admixture of a single-component polarized Fermi gas. Along the same lines, the stability of a mixture of dipolar bosons and fermions in a pancake cylindrically symmetric trap was investigated at $T = 0$ using a variational approach (Dutta *et al.*, 2008). Fermion-induced interactions stabilize the system in such traps and allow for quantum phase transition from the Gaussian-shaped BEC to a supersolid state characterized by a hexagonal density wave. Interestingly, while fermions stabilize dipolar bosons leading to novel types of states, the opposite is also true: boson-mediated interactions between polarized fermions may lead to the appearance of ‘exotic’ Fermi superfluids with p -wave, f -wave, or even h -wave pairing (Dutta and Lewenstein, 2010).

8.4.3 Trapped dipolar Fermi gases

The dependence of the physics of trapped dipolar gases on the geometry leads also to a novel quantum phase transition in the case of Fermi gases (Baranov *et al.*, 2004). Let us consider again for simplicity a dipolar gas of N Fermi particles trapped in a harmonic trap, with all the dipoles d oriented in the same direction, the interaction being predominantly of a dipole–dipole kind. The question is whether at sufficiently low temperatures such a gas will undergo a transition to a superfluid state (i.e. BCS state) and whether its behavior is well described by the BCS equations. This latter fact is by no means obvious. Pioneering papers on this subject were written by the groups of You and Stoof, who looked at the possibility of p -wave pairing, and also the group of Rzążewski, who studied the Thomas–Fermi theory. The BCS theory in a homogeneous dipolar gas was investigated in detail by Baranov and Shlyapnikov (we refer the reader to the review in Baranov (2008) for more details).

The analysis of the BCS transition in the trap indeed shows the existence of a critical aspect ratio, similar to the case of a Bose gas (Baranov *et al.*, 2004). The phase diagram is presented in Figure 8.7 as a function of λ^{-1} and dipole interactions in units of the Fermi energy Γ . This figure can be interpreted in two ways: for a given λ the system undergoes a transition from the normal to the superfluid state as the dipole interactions grow. Conversely, for fixed dipole interactions the system undergoes the normal–superfluid transition as λ decreases. For very small dipole interactions this transition occurs in a region of the parameters that goes beyond the applicability of the theory used.

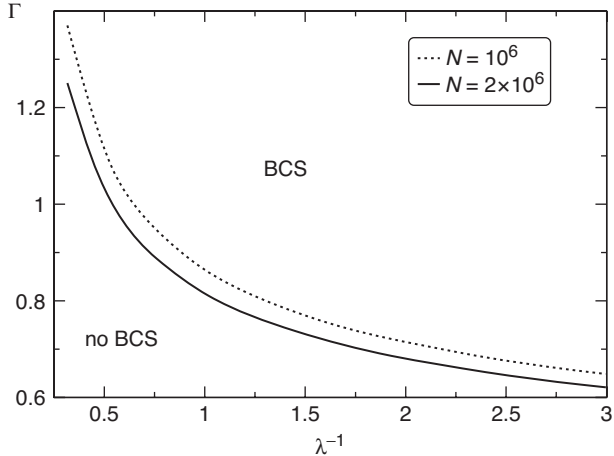


Figure 8.7 Phase diagram for a trapped dipolar Fermi gas as a function of the inverse of the aspect ratio, λ^{-1} , showing the critical dipole interactions in units of the Fermi energy Γ , above which BCS takes place. The upper (lower) curve corresponds to $N = 10^6$ ($N = 2 \times 10^6$). From Baranov et al. (2004).

8.5. Dipolar gas in a lattice: extended Hubbard models

In this section we turn to the main subject of this chapter, namely ultracold dipolar gases in optical lattices, where the strongly correlated regime is achieved. We begin the discussion by deriving the corresponding generalized Hubbard models, which are termed *extended* Hubbard models in the literature.

8.5.1 Hubbard model: extended derivation

As in Chapter 3, we will use here the expansion of the field operators in the basis of Wannier functions. We will also restrict ourselves to the first Bloch band. Within this approximation, the Hamiltonian in eqn (8.10) leads to the standard Bose–Hubbard Hamiltonian plus the dipolar term which, in the basis of Wannier, gives rise to the contribution

$$\hat{H}_{dd} = \sum_{ijkl} \frac{V_{ijkl}}{2} \hat{b}_i^\dagger \hat{b}_j^\dagger \hat{b}_k \hat{b}_l, \quad (8.33)$$

where the matrix elements V_{ijkl} are given by the integral

$$V_{ijkl} = \int d^3r d^3r' w^*(\mathbf{r} - \mathbf{R}_i) w^*(\mathbf{r}' - \mathbf{R}_j) U_{dd}(\mathbf{r} - \mathbf{r}') w(\mathbf{r} - \mathbf{R}_k) w(\mathbf{r}' - \mathbf{R}_l). \quad (8.34)$$

The Wannier functions are centred at the bottom of the optical lattice wells with a spatial localization that we assume to be σ . For sufficiently deep optical potentials we can assume σ to be much smaller than the optical lattice spacing d , i.e. $\sigma \ll d$. In this limit, each function

$w(\mathbf{r} - \mathbf{R}_i)$ is significantly non-vanishing for $\mathbf{r} \sim \mathbf{R}$, and thus the integral in eqn (8.34) is significantly non-zero for the indices $i = k$ and $j = l$. Therefore, there are two main contributions to V_{ijkl} : the *off-site* term V_{ijij} , corresponding to $k = i \neq j = l$, and the *on-site* term V_{iiii} , when all the indices are equal. Below we will explain the physical meaning of these two contributions.

Off-site contribution The dipolar potential $U_{dd}(\mathbf{r} - \mathbf{r}')$ changes slowly on the scale of σ , and therefore one may approximate it with the constant $U_{dd}(\mathbf{R}_i - \mathbf{R}_j)$ and take it out of the integration. The integral then reduces to

$$V_{ijij} \simeq U_{dd}(\mathbf{R}_i - \mathbf{R}_j) \int d^3r |w(\mathbf{r} - \mathbf{R}_i)|^2 \int d^3r' |w(\mathbf{r}' - \mathbf{R}_j)|^2, \quad (8.35)$$

which leads to the off-site Hamiltonian

$$\hat{H}_{dd}^{\text{off-site}} = \sum_{i \neq j} \frac{V_{ij}}{2} \hat{n}_i \hat{n}_j. \quad (8.36)$$

In the last expression $V_{ij} = U_{dd}(\mathbf{R}_i - \mathbf{R}_j)$, $\hat{n}_i = \hat{b}_i^\dagger \hat{b}_i$ is the bosonic number operator at site i , and the sum runs over all different sites of the lattice.

On-site contribution At the same lattice site i , where $|\mathbf{r} - \mathbf{r}'| \sim \sigma$, the dipolar potential changes very rapidly and diverges for $|\mathbf{r} - \mathbf{r}'| \rightarrow 0$. Therefore the above approximation is no longer valid and the integral

$$V_{iiii} = \int d^3r d^3r' \rho(\mathbf{r}) U_{dd}(\mathbf{r} - \mathbf{r}') \rho(\mathbf{r}'), \quad (8.37)$$

with $\rho(\mathbf{r}) = |w(\mathbf{r})|^2$ being the single particle density, has to be calculated taking into account the atomic spatial distribution at the lattice site, similarly to what was described in Section 8.4.1¹. As discussed in Section 8.4.1, apart from a factor of 2, the solution can be found by Fourier transforming, i.e.

$$V_{iiii} = \frac{1}{(2\pi)^3} \int d^3k \tilde{U}_{dd}(\mathbf{k}) \tilde{\rho}^2(\mathbf{k}), \quad (8.38)$$

which leads to an on-site dipolar contribution to the Hamiltonian of the type

$$\hat{H}_{dd}^{\text{on-site}} = \sum_i \frac{V_{iiii}}{2} \hat{n}_i (\hat{n}_i - 1). \quad (8.39)$$

The extended Bose–Hubbard Hamiltonian is given by the sum of the standard Bose–Hubbard Hamiltonian and the dipolar Hamiltonian calculated above. This leads to the

¹Since \mathbf{R}_i is a constant, we have renamed the variables as $\mathbf{r} - \mathbf{R}_i = \mathbf{r}$ and $\mathbf{r}' - \mathbf{R}_i = \mathbf{r}'$.

expression

$$\hat{H}_{\text{eBH}} = -t \sum_{\langle ij \rangle} \hat{b}_i^\dagger \hat{b}_j + \frac{U}{2} \sum_i \hat{n}_i (\hat{n}_i - 1) - \sum_i \mu_i \hat{n}_i + \sum_{i \neq j} \frac{V_{ij}}{2} \hat{n}_i \hat{n}_j, \quad (8.40)$$

where U is now taken into account as an effective on-site interaction

$$U = g \int d^3r |w(\mathbf{r})|^4 + \frac{1}{(2\pi)^3} \int d^3k \tilde{U}_{\text{dd}}(\mathbf{k}) \tilde{\rho}^2(\mathbf{k}), \quad (8.41)$$

which contains the contribution of the contact potential and the dipolar contribution coming from eqn (8.39). Approximating each lattice site with a tiny harmonic trap and approximating the atomic density distribution with Gaussians, one can clearly see that the resulting on-site interaction U can be increased or decreased by changing the anisotropy and strength of the lattice confinement. To find the phase diagram of the extended dipolar Bose–Hubbard Hamiltonian as a function of t , U , and V_{ij} the approaches discussed in the following sections are used.

8.5.2 Extended Hubbard model: theoretical methods

Gutzwiller mean-field approach As discussed extensively in Chapter 5, the Gutzwiller mean-field approach is an approximation of the many-body wave function of Hubbard-type Hamiltonians and is given by

$$|\Psi\rangle = \prod_i \sum_{n=0}^{n_{\max}} f_n^{(i)} |n\rangle_i, \quad (8.42)$$

where $|n\rangle_i$ represents the Fock state of n atoms occupying the site i , n_{\max} is a cut-off in the maximum number of atoms per site, and $f_n^{(i)}$ is the probability amplitude of having the site i occupied by n atoms. The probability amplitudes are normalized to unity: $\sum_n |f_n^{(i)}|^2 = 1$.

In the presence of dipolar interactions, as we shall see later on, it is also necessary to account for non-uniform quantum phases, because even in the uniform system the presence of dipolar interactions may lead to spontaneous symmetry breaking of translational invariance on a scale larger than the lattice constant. The equations of motion for the amplitudes in the presence of dipolar interactions read (see Section 5.5 for the case of contact interactions):

$$\begin{aligned} i\hbar \frac{d}{dt} f_n^{(i)} &= -t \left[\bar{\varphi}_i \sqrt{n} f_{n-1}^{(i)} + \bar{\varphi}_i^* \sqrt{n+1} f_{n+1}^{(i)} \right] \\ &\quad + \left[\frac{U}{2} n(n-1) + n \sum_{j \neq i} V_{ij} \langle \hat{n}_j \rangle - \mu_i n \right] f_n^{(i)}, \end{aligned} \quad (8.43)$$

where $\bar{\varphi}_i = \sum_{\langle j \rangle_i} \varphi_j$, the sum runs over all nearest neighbors j of site i and $\varphi_j = \langle \Psi | \hat{b}_j | \Psi \rangle$, $\langle \hat{n} \rangle$ is the average particle number at site j , and V_{ij} and U are defined in eqns (8.36) and (8.41), respectively.

For dipolar Hamiltonians, the imaginary time evolution does not always converge to the true ground state since it often gets blocked in configurations that are a local minimum of the energy. On one hand, this fact makes it an arduous task to identify the ground state of such systems. However, on the other hand it is a signature of the existence of metastable states, as we will discuss in detail in the next sections.

Perturbative mean-field approach A more convenient method to determine the insulating phases of a dipolar Hamiltonian is to use a mean-field approach perturbative in $\varphi_i = \langle \hat{b}_i \rangle$ (described in Section 5.4 for the homogeneous case in the presence of contact interactions). Considering that the expectation value of the annihilation operator at the i th site is given by the trace

$$\varphi_i = \langle \hat{b}_i \rangle = \text{Tr}(\hat{b}_i \hat{\rho}), \quad (8.44)$$

where $\hat{\rho} = Z^{-1} e^{-\beta \hat{H}}$ is the density matrix operator, $Z = \text{Tr}(e^{-\beta \hat{H}})$ is its normalization, and $\beta = 1/k_B T$ is the inverse temperature of the system, with k_B the Boltzmann constant. We write the Hamiltonian of eqn (8.40) in the form $\hat{H} = \hat{H}_0 + \hat{H}_1$ where

$$\hat{H}_0 = \frac{U}{2} \sum_i \hat{n}_i (\hat{n}_i - 1) - \mu \sum_i \hat{n}_i + \sum_{i \neq j} \frac{V_{ij}}{2} \hat{n}_i \hat{n}_j, \quad (8.45)$$

$$\hat{H}_1 = -t \sum_{\langle ij \rangle} \hat{b}_i^\dagger \hat{b}_j, \quad (8.46)$$

and we assume a uniform chemical potential μ (the generalization to a site-dependent chemical potential is straightforward). Furthermore, we assume low temperatures $\beta \rightarrow \infty$ and also that the tunneling coefficient is the smallest energy in the system, i.e. $t \ll U, \mu, V_{ij}$ such that we can treat \hat{H}_1 as a small perturbation on \hat{H}_0 and use the Dyson expansion up to the first order in \hat{H}_1 for all the exponential operators,

$$e^{-\beta(\hat{H}_0 + \hat{H}_1)} \simeq e^{-\beta \hat{H}_0} \left[\hat{\mathbf{1}} - \int_0^\beta e^{\tau \hat{H}_0} \hat{H}_1 e^{-\tau \hat{H}_0} d\tau \right]. \quad (8.47)$$

The mean-field decoupling, which involves writing the annihilation operator as $\hat{b}_i = \hat{A}_i + \varphi_i$, leads to the following expression for the tunneling term

$$\hat{b}_i^\dagger \hat{b}_j = \hat{A}_i^\dagger \varphi_j + \hat{A}_j^\dagger \varphi_i + \varphi_i \varphi_j + \hat{A}_i^\dagger \hat{A}_j \simeq \hat{b}_i^\dagger \varphi_j + \hat{b}_j^\dagger \varphi_i - \varphi_i \varphi_j, \quad (8.48)$$

where in the last step we have assumed small fluctuations, linearized the equations, and replaced $\hat{A}_i^\dagger \hat{A}_j \simeq 0$. Replacing $\hat{b}_i^\dagger \hat{b}_j$ in eqn (8.46) with eqn (8.48) and neglecting terms of the order of φ^2 , we find the mean-field tunneling Hamiltonian

$$\hat{H}_1^{\text{MF}} = -t \sum_i \left(\hat{b}_i^\dagger \bar{\varphi}_i + \bar{\varphi}_i^* \hat{b}_i \right). \quad (8.49)$$

Now given a classical distribution of atoms in a lattice such as

$$|\Phi\rangle = \prod_i |n_i\rangle_i, \quad (8.50)$$

satisfying $\hat{H}_0|\Phi\rangle = E_\Phi|\Phi\rangle$, let us suppose that this configuration is a local minimum of the energy. In the basis of the eigenfunctions of \hat{H}_0 , satisfying the relation $\hat{H}_0|\Upsilon\rangle = E_\Upsilon|\Upsilon\rangle$, the partition function then takes the simple form

$$Z \simeq \text{Tr}(e^{-\beta\hat{H}_0}) = \sum_{|\Upsilon\rangle} \langle \Upsilon | e^{-\beta\hat{H}_0} | \Upsilon \rangle \xrightarrow{\beta \rightarrow \infty} e^{-\beta E_\Phi}, \quad (8.51)$$

where the last limit holds because we do not trace over all the states of the basis, but only around the state $|\Phi\rangle$, which is assumed to be a local minimum of the energy. Again using a Dyson expansion of the exponential of the density operator, we obtain the order parameter as

$$\begin{aligned} \varphi_i &\simeq -e^{\beta E_\Phi} \int_0^\beta \text{Tr} \left[\hat{b}_i e^{-(\beta-\tau)\hat{H}_0} \hat{H}_1^{\text{MF}} e^{-\tau\hat{H}_0} \right] d\tau \\ &= t\bar{\varphi}_i e^{\beta E_\Phi} \int_0^\beta \sum_{|\Upsilon\rangle} \langle \Upsilon | \hat{b}_i e^{-(\beta-\tau)\hat{H}_0} \hat{b}_i^\dagger e^{-\tau\hat{H}_0} | \Upsilon \rangle. \end{aligned} \quad (8.52)$$

The trace is then non-trivial only for $|\Upsilon\rangle = |\Phi\rangle$ and $|\Upsilon\rangle = \frac{\hat{b}_i}{\sqrt{n_i}}|\Phi\rangle$, where n_i is integer on $|\Phi\rangle$. After the integration in the $\beta \rightarrow \infty$ limit we are left with the result

$$\varphi_i = t\bar{\varphi}_i \left[\frac{n_i + 1}{E_P^i} + \frac{n_i}{E_H^i} \right], \quad (8.53)$$

where the quantities E_P^i , E_H^i are defined as

$$\begin{aligned} E_P^i &= -\mu + Un_i + V_{\text{dip}}^{1,i} \\ E_H^i &= \mu - U(n_i - 1) - V_{\text{dip}}^{1,i}, \end{aligned} \quad (8.54)$$

and are the energy cost for a particle (P) and hole (H) excitation on top of the $|\Phi\rangle$ configuration, respectively; $V_{\text{dip}}^{1,i} = \sum_{j \neq i} V_{ij} n_j$ is the dipole-dipole interaction felt by one atom placed at site i due to the rest of the atoms in the lattice. The integral in eqn (8.52) is performed in the limit of $\beta \rightarrow \infty$, and one finds that the integral converges only for positive values of the particle and hole excitation energies, namely

$$U(n_i - 1) + V_{\text{dip}}^{1,i} < \mu < Un_i + V_{\text{dip}}^{1,i}. \quad (8.55)$$

These requirements have to be fulfilled at every site i of the lattice and they simply state that the configuration $|\Phi\rangle$ is a local minimum with respect to adding and removing particles

at any site. According to this statement, the restriction on the trace of eqn (8.51) is now rigorous. Notice that if $|\Phi\rangle$ is not a local minimum, one finds that the conditions of eqn (8.55) are never satisfied and the integral of eqn (8.52) indeed diverges. This treatment is of course also valid for $|\Phi\rangle$ as the ground state of the system.

The convergence conditions (eqn (8.55)) are simple and among them one has to choose the most stringent to find the boundary of the lobe at $t = 0$. The equations for the order parameters are coupled due to the $\bar{\varphi}_i$ term and they can be written in a matrix form $\mathcal{M}(\mu, U, t) \cdot \boldsymbol{\varphi} = 0$, with $\boldsymbol{\varphi} \equiv (\cdots \varphi_i \cdots)$. For every μ , the smallest t for which $\det[\mathcal{M}(\mu, U, t)] = 0$ gives the lobe of the $|\Phi\rangle$ configuration in the $t - \mu$ plane.

Perturbative mean-field vs dynamical Gutzwiller approach The predictions of the perturbative mean-field treatment are in perfect agreement with the results of the dynamical Gutzwiller approach, since they both rely on the same mean-field approximations. The former concerns the stability of a given density distribution $|\Phi\rangle = \prod_i |n_i\rangle_i$ of integer n_i atoms per site with respect to particle and hole excitations, while the latter minimizes the energy of a random initial configuration with respect to particle and hole excitations leading to the distribution $|\Phi\rangle$ if the initial condition is sufficiently close. However, the first method can only identify the phase boundaries of the insulating lobes without providing any further information on the superfluid phases outside the lobes. The latter can instead be explored with imaginary time evolution. Nevertheless, for dipolar Hamiltonians, due to the presence of many local minima of the energy (Menotti *et al.*, 2007; Trefzger *et al.*, 2008), it is very difficult to identify the ground state with the dynamical Gutzwiller approach. This can be achieved more efficiently through the perturbative mean-field approach. Therefore the two methods complement each other.

8.6. Dipolar bosons in a 2D optical lattice

8.6.1 The model

We focus now on a concrete realization of the extended Bose–Hubbard model for dipole bosons in a 2D lattice. We will follow Menotti *et al.* (2007) and Trefzger *et al.* (2008) to study the phase diagram and the properties of dipolar bosons in an infinite 2D optical lattice. To this end, consider an elementary cell of finite dimensions $L \times L$ ($N_S = L^2$ sites) satisfying periodic boundary conditions. The dipoles are aligned and point perpendicularly out of the plane so that the dipole–dipole interaction between two particles at relative distance \mathbf{r} becomes $U_{dd}(\mathbf{r}) = C_{dd}/(4\pi r^3)$: repulsive and isotropic in the 2D plane of the lattice. Furthermore for computational simplicity, the range of the off-site interactions is truncated at a finite number of nearest neighbors (NN), as shown in Figure 8.8 for the case of fourth nearest neighbors.

The system is described by the Hamiltonian

$$\hat{H} = -t \sum_{\langle ij \rangle} \hat{b}_i^\dagger \hat{b}_j - \sum_i \mu \hat{n}_i + \sum_i \frac{U}{2} \hat{n}_i (\hat{n}_i - 1) + \frac{U_{NN}}{2} \sum_{\ell} \sum_{\langle\langle ij \rangle\rangle_{\ell}} \frac{1}{|\ell|^3} \hat{n}_i \hat{n}_j, \quad (8.56)$$

where $U_{NN} = C_{dd}/(4\pi d_{2D}^3)$ is the dipole–dipole interaction between nearest-neighboring sites, d_{2D} is the lattice period, and $\langle\langle ij \rangle\rangle_{\ell}$ represents neighbors at relative distance ℓ , measured in units of d_{2D} (Menotti *et al.*, 2007; Trefzger *et al.*, 2008).

8.6.2 Metastability

Let us start the discussion by introducing our definition of the stability of a given classical distribution of atoms in the lattice, i.e. a product over single-site Fock states

$$|\Phi\rangle = \prod_i |n_i\rangle_i. \quad (8.57)$$

At $t = 0$, we define the state in eqn (8.57) to be stable if (i) there exists a finite interval $\Delta\mu = \mu_{\max} - \mu_{\min} > 0$ in the μ domain in which the particle (P) and hole (H) excitations at each site i of the lattice are positive and (ii) the system is gapped. Using the dipolar Hamiltonian (eqn (8.56)), the particle and hole excitation energies of $|\Phi\rangle$ are given in eqn (8.54). From there it is straightforward to find that $\Delta\mu$, if it exists, is given by the set of inequalities

$$U(n_i - 1) + V_{\text{dip}}^{1,i} < \mu < Un_i + V_{\text{dip}}^{1,i}. \quad (8.58)$$

This is consistent with the stability conditions discussed in the seminal paper of Fisher *et al.* (1989). Indeed, in the absence of dipolar interactions one recovers the well-known conditions $U(n_i - 1) < \mu < Un_i$ for the stability of the MI with n_i particles per site, MI(n_i). One can also extend the stability analysis for small values of t and, for a given stable state, calculate its insulating lobe with the perturbative mean-field approach developed in Section 8.5.2. In this context we define a state, such as the one given in eqn (8.57), to be *metastable* if it satisfies two conditions: (i) the state must have an insulating lobe, inside which it is gapped and (ii) the energy of the state must be higher than the ground-state energy.

In the absence of dipolar interactions, no metastable states are found. In the low-tunneling region the ground state of the system consists of MI lobes with integer filling factors $\nu = N_a/N_S$ (number of atoms/number of sites), while for large values of t the system is superfluid. In this treatment, metastable states appear as soon as one introduces at least one nearest neighbor of the dipolar interaction. In fact, the imaginary time evolution, which for Bose–Hubbard Hamiltonians with only on-site interactions converges unambiguously to the ground state, for the dipolar Hamiltonian (eqn (8.56)) often converges to different metastable configurations depending on the specific initial condition. Moreover, in real-time

		4	3	4	
4	2	1	2	4	
3	1	0	1	3	
4	2	1	2	4	
	4	3	4		

Figure 8.8 Representation of the first four nearest neighbors of the site labeled 0, for which the dipole interaction is considered in a 2D lattice. From Trefzger (2010).

evolution, their stability manifests itself as characteristic small oscillations of frequency ω_0 around the local minimum of the energy.

The phase diagram of a 2D dipolar gas in an optical lattice for an $L = 4$ elementary cell satisfying periodic boundary conditions is summarized in Figure 8.9, with a cut-off on the dipolar interactions range at (a) one, (b) two, and (c) four nearest neighbors. The on-site interaction is given by $U/U_{\text{NN}} = 20$ (Menotti *et al.*, 2007; Trefzger *et al.*, 2008). Thick lines correspond to the ground state while thin lines correspond to metastable insulating states.

In clear contrast to the standard Bose Hubbard phase diagram, where only integer fillings are possible in the insulating lobes, now considering just nearest-neighbor dipolar interactions, fractional fillings appear (see Fig. 8.9 (a)). In fact, the MI(1) lobe undergoes a global shift of zU_{NN} ($z = 4$ in the figure) towards higher values of μ , and the new fractional filling factor $\nu = \frac{1}{2}$ appears with a ground-state density distribution modulated in a checkerboard pattern (marked as GS in Figure 8.9), with white sites empty and grey

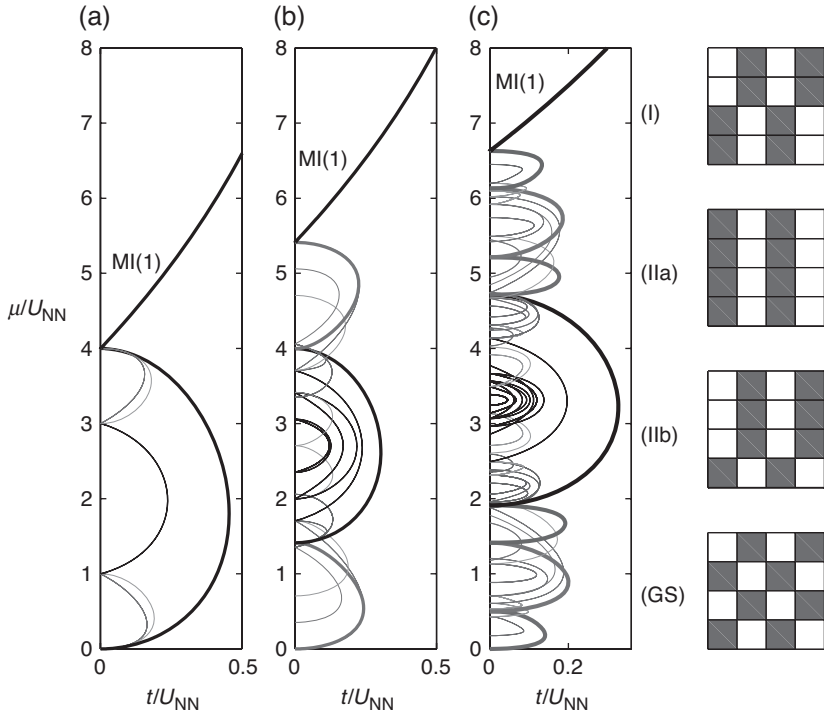


Figure 8.9 (a), (b) and (c) Phase diagrams for $U/U_{\text{NN}} = 20$ with the range of dipole-dipole interactions cut at the first, second, and fourth-nearest neighbors, respectively. The thick line is the ground state and the other lobes correspond to the metastable states. The ground-state filling factors are multiples of $\frac{1}{2}$, $\frac{1}{4}$, and $\frac{1}{8}$, respectively, while the metastable-state filling factors are $\frac{m}{4}$, $\frac{m}{8}$, and $\frac{m}{16}$ ($\forall m \neq 1$), respectively. In the right-hand column we show metastable configurations for $\nu = \frac{1}{2}$ appearing at the first- (I) and second-nearest neighbors (IIa, IIb), and the corresponding ground state (GS); those metastable states remain stable for all larger ranges of the dipole-dipole interaction. From Trefzger *et al.* (2008).

sites occupied by one atom. Instead, the density distribution shown in Figure 8.9 (I) is metastable, with $\nu = \frac{1}{2}$, and its insulating lobe given by the thin line extending from $1 < \mu/U_{\text{NN}} < 3$. Remarkably, in Figure 8.9(a) the two lobes extending from $0 < \mu/U_{\text{NN}} < 1$ correspond to metastable configurations at filling factors $\nu = \frac{1}{4}, \frac{5}{16}$, while the two lobes between $3 < \mu/U_{\text{NN}} < 4$ correspond to metastable states at filling factors $\nu = \frac{3}{4}, \frac{11}{16}$, but no ground state is found for these fillings. In the region immediately outside the ground-state lobes, evidence of supersolid (SS) phases are found. In these the order parameters φ_i are non-zero and are spatially modulated, e.g. in a checkerboard (CB) structure. Earlier studies of Bose–Hubbard models with extended interactions pointed to the existence of novel quantum phases, such as the SS and CB phases, but not the existence of metastable states.

Further increasing the range of the dipolar interactions (Fig. 8.9 (b) and (c)) leads to the appearance of more metastable states, as shown in Figure 8.9 (IIa) and (IIb). In addition the MI(1) undergoes a larger shift, which is accompanied by the emergence of other insulating fractional filling factors. The number of metastable states varies depending on the parameters of the Hamiltonian and the filling factor; it is found to be up to 400 for $U/U_{\text{NN}} = 20$ at filling $\nu = \frac{1}{2}$ and up to 1500 for $U/U_{\text{NN}} = 2$ at unit filling. With this picture in mind, it is now clear why the imaginary time evolution, which often converges to different metastable configurations, is very inefficient both for finding the ground state of the system and for computing the lobe boundaries of a given metastable state. Instead, the mean-field perturbative approach of Section 8.5.2 has proven to be satisfactory for this purpose, but it also has some limitations. In fact, all possible values of ν and the corresponding configurations that are detectable with this method are limited by the size of the elementary cell. Evidently the possible filling factors of an elementary cell of size L are given by multiples of $\nu = 1/L^2$. There is usually a gap between the ground state and the lowest metastable state, which might allow us to reach the ground state by ramping up the optical lattice under some adiabaticity condition. However, this feature is strongly reduced in the case of larger elementary cells because the number of metastable configurations and the variety of their patterns increase very rapidly with the size of the elementary cell L . Indeed, there are many metastable configurations that differ from the ground state only in having small localized defects, the energy of which reduces the size of the gap.

8.6.3 Harmonic confinement

In real experiments atoms are first trapped in a harmonic trap and then the optical lattice is raised. It is therefore important to understand the behavior of these systems in the presence of a confining potential. As an example, the ground state for a finite 20×20 square lattice is calculated (Trefzger *et al.*, 2008) and presented in Figure 8.10. A trapping potential mimicked by local chemical potentials is superimposed (Jaksch *et al.*, 1998) without periodic boundary conditions. The range of the dipole–dipole interactions is cut at the fourth-nearest neighbor and the external potential for the system in Figure 8.10 is given by

$$V(x, y) = \frac{K}{U_{\text{NN}}} \left[(x - x_0)^2 + (y - y_0)^2 \right], \quad (8.59)$$

where (x_0, y_0) is the center of the 2D isotropic trap. On the two outermost sites of the lattice the potential is sufficient to force the density to zero. In Figure 8.10(a) there is clearly a

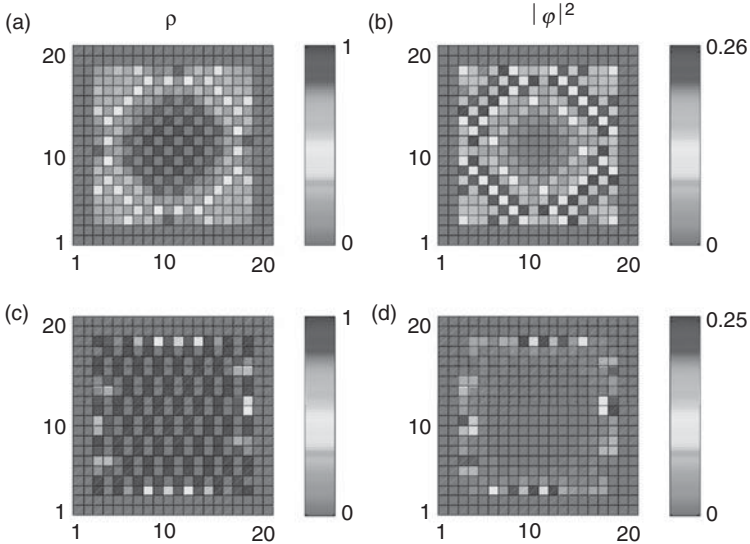


Figure 8.10 Density $\rho(x, y)$, and superfluid parameter $|\varphi(x, y)|^2$ in the harmonic potential of eqn (8.59). The parameters of the system are given in units of $\hbar = 1$ by $\mu/U_{\text{NN}} = 2.8$, $t/U_{\text{NN}} = 0.26$, and $K = 107 \times 10^{-3} \text{ s}^{-1}$ for panels (a) and (b), and $\mu/U_{\text{NN}} = 3.3$, $t/U_{\text{NN}} = 0.16$, and $K = 3.1 \times 10^{-3} \text{ s}^{-1}$ for panels (c) and (d). From Trefzger *et al.* (2008).

region around the center of the trap where the density $\rho(x, y)$ follows a CB pattern, and where the superfluid parameter $|\varphi(x, y)|^2$ is zero, as shown in Figure 8.10(b). Notice the SS–SF area that surrounds the MI phase. Instead, in Figure 8.10(c) and (d) the density in the center of the trap follows the metastable state atomic distribution of Figure 8.9 (I), with a zero superfluid parameter, while in the outer region of the trap a superfluid state is present.

8.6.4 The lifetime of the metastable states

For any given initial metastable configuration $|\Phi\rangle_{\text{initial}}$, one could estimate the time T in which $|\Phi\rangle_{\text{initial}}$ has tunneled completely into a different metastable state $|\Phi\rangle_{\text{final}}$, in analogy to the case of a classical particle tunneling through a potential barrier as shown in Figure 8.11(a). The difference is that now one does not have *a priori* any information regarding the potential barrier separating initial and final states. The stability of the metastable states with a path integral formulation in imaginary time and a generalization of the instanton theory (Wen, 2004) was addressed in Trefzger *et al.* (2008). There it was shown that one can estimate the barrier and the time T in three steps. First, one constructs the imaginary time Lagrangian of the system described by a quantum state $|\Phi\rangle$. Second, one makes use of a variational method on $|\Phi\rangle$ with only one variational parameter q and its conjugate momenta P , which interpolate continuously between $|\Phi\rangle_{\text{initial}}$ and $|\Phi\rangle_{\text{final}}$. Finally, through the variation of q one calculates the minimal action S_0 with the imaginary time Lagrangian along the stationary path starting at $|\Phi\rangle_{\text{initial}}$; this path is called an *instanton*

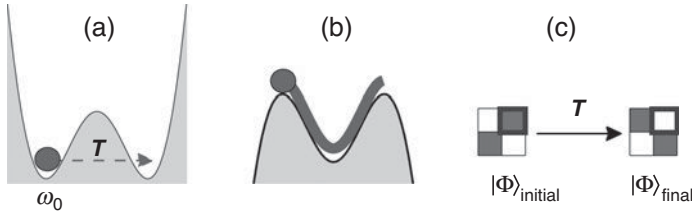


Figure 8.11 (a) Particle in a minimum of a potential barrier: the particle oscillates with frequency ω_0 around the local minimum and tunnels into the right-hand well in a time T . (b) The instanton and (c) the process for which a checkerboard state tunnels into the anti-checkerboard that shows complete exchange of particle with holes and vice versa. The process happens in a time T analogously to (a). From Trefzger (2010).

path, or instanton in short. It connects $|\Phi\rangle_{\text{initial}}$ and $|\Phi\rangle_{\text{final}}$ only if the two states are degenerate; otherwise the stationary path connects $|\Phi\rangle_{\text{initial}}$ with an intermediate state called the *bouncing point* $|\Phi\rangle_{\text{bounce}}$. One gets an estimate of the energy barrier separating the two states by evaluating the Lagrangian from $|\Phi\rangle_{\text{initial}}$ to $|\Phi\rangle_{\text{final}}$ and imposing zero ‘momentum’ $P = 0$, i.e. as one would do in the Lagrangian of a classical particle in a potential.

Once the minimal action S_0 is known the tunneling time T is readily calculated (Wen, 2004) as

$$\omega_0 T = \frac{\pi}{2} e^{S_0}, \quad (8.60)$$

where ω_0 is of the order of the frequency of the characteristic small oscillations of $|\Phi\rangle_{\text{initial}}$ around the local minimum of the energy. Analogously to a classical particle tunneling through a barrier, the instanton has the nice interpretation of a stationary path connecting the two local minima in the inverted potential, as schematically represented in Figure 8.11(b).

The imaginary time Lagrangian of a system described by a quantum state $|\Phi\rangle$ in units of \hbar is given by (Pérez-García *et al.*, 1997):

$$\mathcal{L} = -\frac{\langle \dot{\Phi} | \Phi \rangle - \langle \Phi | \dot{\Phi} \rangle}{2} + \langle \Phi | \hat{H} | \Phi \rangle, \quad (8.61)$$

with $|\dot{\Phi}\rangle$ indicating the time-derivative and \hat{H} being the Hamiltonian of the system. In the approximation where $|\Phi\rangle$ is the Gutzwiller wave function of a given metastable state, we write the amplitudes as

$$f_n^{(i)} = \frac{1}{\sqrt{2}} \left(x_n^{(i)} + i p_n^{(i)} \right), \quad (8.62)$$

where $x_n^{(i)}$ and $p_n^{(i)}$ are real numbers, the former related to the variational parameters and the latter to the conjugate momenta. For simplicity, we consider states with a maximum

occupation number of $n_{\max} = 1$ (i.e. $n = 0, 1$), and therefore we have a total of $4N_S$ parameters, with N_S being the total number of sites. The Lagrangian (eqn (8.61)) becomes a functional of the $4N_S$ parameters, namely

$$\mathcal{L}[x_n^{(i)}, p_n^{(i)}] = -i \sum_{i,n=0}^1 p_n^{(i)} \dot{x}_n^{(i)} + \langle \Phi | \hat{H} | \Phi \rangle, \quad (8.63)$$

as well as the expectation value of the Hamiltonian $\langle \Phi | \hat{H} | \Phi \rangle$. In order to put the Lagrangian (eqn (8.63)) in its canonical form we must introduce the new coordinates $q_n^{(i)} = x_n^{(i)}$ and their conjugate momenta $P_n^{(i)} = \partial \mathcal{L} / \partial \dot{q}_n^{(i)} = -ip_n^{(i)}$. One can then rewrite it as

$$\mathcal{L}[q_n^{(i)}, P_n^{(i)}] = \sum_{i,n=0}^1 P_n^{(i)} \dot{q}_n^{(i)} - \mathcal{H}[q_n^{(i)}, P_n^{(i)}], \quad (8.64)$$

where $\mathcal{H}[q_n^{(i)}, P_n^{(i)}] = -\langle \Phi | \hat{H} | \Phi \rangle$ is a constant of the motion.² The goal is now to reduce the dynamics described by the Lagrangian (eqn (8.64)) to a 1D problem, described only by one variable q and its conjugate momentum P . Through the variation of (q, P) we want to describe the interchange between the states $|\Phi\rangle_{\text{initial}}$ and $|\Phi\rangle_{\text{final}}$, like, for example, the interchange represented in Figure 8.11(c). At the end of this section, examples of how to reduce the number of variational parameters to one— q —and its conjugate momentum P are presented. The reduction of the number of variational parameters is done by making use of a variational ansatz, as well as the normalization of the coefficients (eqn (8.62)), and the conservation of the total number of particles. These conditions enter into the expression of the Lagrangian (eqn (8.64)) through Lagrange multipliers λ_c . Consequently the equations of motion given by $\dot{q} = \partial H / \partial P$ and $\dot{P} = -\partial H / \partial q$ are governed by a Hamiltonian that also includes the constraints as follows

$$H = \mathcal{H}[q, P] + \sum_c \lambda_c \mathcal{C}_c, \quad (8.65)$$

where an explicit expression for the conditions \mathcal{C}_c will be given below. The action is then readily calculated along the stationary path of eqn (8.65) as follows

$$S_0 = \int \mathcal{L}[q, P] d\tau = \int_{\text{path}} \mathcal{L}[q, P] \frac{dq}{\dot{q}}, \quad (8.66)$$

with $\dot{q} = \partial H / \partial P$ from eqn (8.65).

²Note that in the analogy with a classical particle in a potential $V(x)$, the conserved quantity in the imaginary time would be $\mathcal{H} = \frac{P^2}{2m} - V(x)$, which describes the particle's motion in the inverted potential.

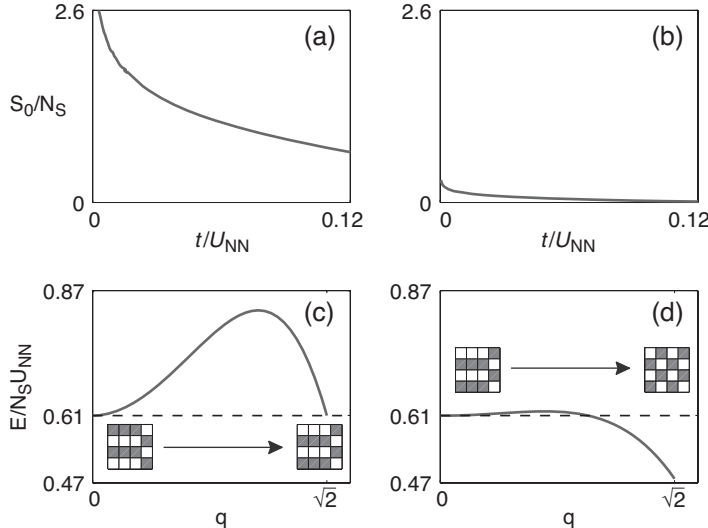


Figure 8.12 Action per site (a) ((b)) and energy barrier (c) ((d)) for the process sketched in the inset of (c) ((d)). In the two processes, the initial state is the configuration (IIb) of Figure 8.9 and the value $t = 0.12U_{NN}$ corresponds to the tip of its insulating lobe. The first set, (a) and (c), corresponds to degenerate initial and final configurations while for the second set, (b) and (d), the final configuration is energetically deeper. The difference in the two processes manifests also in the height of the barrier which is smaller for the second case leading to a smaller action and, consequently, to a smaller lifetime. From Trefzger (2010).

Parametrization Through the variation of (q, P) , one aims to describe the interchange between states $|\Phi\rangle_{\text{initial}}$ and $|\Phi\rangle_{\text{final}}$, like, for example, the interchange schematically represented in Figure 8.11(c). During this process there are initially occupied sites that empty, such as the framed site of Figure 8.11(c), which we call the (B)-site. There are also sites that are initially empty but are occupied at the end, for example the site on the left of B. We call this the (A)-site. When the initial and final states are non-degenerate, for example in the case sketched in Figure 8.12(d), there are also sites that do not change and remain either full (F) or empty (E).

During this process, the Gutzwiller amplitudes (eqn (8.62)) have to be normalized at each site and the total number of particles has to be conserved, namely

$$|f_0^{(i)}|^2 + |f_1^{(i)}|^2 = 1, \forall i \quad (8.67)$$

$$\sum_{i=1}^{N_S} |f_1^{(i)}|^2 = N, \quad (8.68)$$

where N_S is the total number of sites. We choose $(q, P) \equiv (q_0^B, P_0^B)$ to be the variational parameters of the framed site, and the normalization condition (eqn (8.67)) together with

the conservation of the number of particles between A and B (eqn (8.68)) give us three coupled equations

$$\begin{aligned} q^2 - P^2 + (q_1^B)^2 - (P_1^B)^2 &= 2, \\ (q_0^A)^2 - (P_0^A)^2 + (q_1^A)^2 - (P_1^A)^2 &= 2, \\ (q_1^B)^2 - (P_1^B)^2 + (q_1^A)^2 - (P_1^A)^2 &= 2. \end{aligned} \quad (8.69)$$

One can make use of the following ansatz (Trefzger *et al.*, 2008)

$$\begin{aligned} q_1^A &= q, \\ P_1^A &= P, \\ P_0^A = P_1^B &= -P, \\ q_0^A = q_1^B &, \end{aligned} \quad (8.70)$$

from which it is clear that $(q, P) = (0, 0)$ corresponds to a situation in which site A is empty and site B is full, while for $(q, P) = (\sqrt{2}, 0)$ the opposite is true. For degenerate initial and final states as in the case of Figure 8.11(c), the remaining sites either behave like A or B, which implies another set of conditions that can be summarized as follows

$$\begin{aligned} q_0^{(i)} &= q_0^{A(B)}, \\ P_0^{(i)} &= P_0^{A(B)}, \\ q_1^{(i)} &= q_1^{A(B)}, \\ P_1^{(i)} &= P_1^{A(B)}, \end{aligned} \quad (8.71)$$

depending on whether the site i is initially empty (A) or occupied (B). Instead, when the initial and the final states are non-degenerate, as is the case in Figure 8.12(d), there are also sites that remain either full (F) or empty (E). For these sites the constraints are respectively given by

$$\begin{aligned} q_0^F &= 0 \\ q_1^F &= 2 \\ P_0^F = P_1^F &= 0, \end{aligned} \quad (8.72)$$

and

$$\begin{aligned} q_0^E &= 2 \\ q_1^E &= 0 \\ P_0^E = P_1^E &= 0. \end{aligned} \quad (8.73)$$

All the conditions (8.69)–(8.73), which we collectively denote \mathcal{C}_c , enter explicitly into the calculation of the Hamiltonian (eqn (8.65)).

8.6.5 Action and tunneling time

Figure 8.12(a) and (b) show the minimal action divided by the total number of sites N_S of the cell as a function of the tunneling coefficient t for two different processes. Meanwhile in Figure 8.12(c) and (d), the corresponding potential barrier between initial and final states ($-H(q, P = 0)$) is plotted. In the first process, shown in Figure 8.12(a) and (c), in which initial and final state are degenerate, the exchange of particles with holes occurs in the whole lattice as sketched in the lower part of Figure 8.12(c). On the other hand, in the second process, shown in Figure 8.12(b) and (d), the final state is the ground state, i.e. deeper in energy with respect to the initial state. Few sites of the lattice exchange particles with holes during the process, as sketched in the upper part of Figure 8.12(d). The point where the thick line of the barrier encounters the dashed line is the *bouncing point* $|\Phi\rangle_{\text{bounce}}$.

The action in general diverges for $t \rightarrow 0$, indicating a divergent tunneling time T , and then decreases monotonically up to a minimum value corresponding to the tip of the lobe, $t = 0.12U_{\text{NN}}$, signaling a minimum lifetime at the tip of the lobe, as expected. In between these two extreme behaviors the action increases monotonically with the number of sites involved in the exchange of particles with holes: the more sites involved, as in the case of Figure 8.12(a) and (c), the bigger the action is. In summary, small energy differences between the initial $|\Phi\rangle_{\text{initial}}$ and the final state $|\Phi\rangle_{\text{final}}$ and large regions of the lattice undergoing particle-hole exchange in the tunneling process contribute to large barriers, i.e. long lifetimes T . On the other hand, for big energy differences and small regions of the lattice undergoing particle-hole exchange, the barrier is small. Hence, in general, it is more likely for a given state to tunnel into a state deeper in energy, e.g. the ground state, than into its complementary, which implies the exchange of particles with holes in the whole lattice. Still, the estimated lifetime is generally quite long, so that the metastable states should be accessible for experimental observations. As we shall see in the next section, they are indeed clearly present in ‘exact’ quantum Monte Carlo calculations.

8.7. Quantum Monte Carlo studies of dipolar gases

Quantum Monte Carlo is one of the most powerful methods we have to study equilibrium properties of strongly interacting many-body quantum systems. In the literature, there is a large number of studies devoted to the application of quantum Monte Carlo techniques to dipolar gases. The physics of such systems is indeed very rich, and examples, to name just a few, range from self-assembled dipolar lattices (Büchler *et al.*, 2007*b*; Astrakharchik *et al.*, 2007), to floating lattices provided by trapped polar molecules (Pupillo *et al.*, 2008), to the possibility of tuning and shaping the long-range interaction potential of polar molecules (Pupillo *et al.*, 2009), to self-organized mesoscopic structures of matter waves in zigzag chains (Astrakharchik *et al.*, 2008*b*), and to the emergence of an emulsion phase in triangular lattices (Pollet *et al.*, 2009).

The results presented in this section (Capogrosso-Sansone *et al.*, 2010) are based on the path integral Monte Carlo method and the worm algorithm, both of which, as discussed in Section 5.7, turn out to be very efficient in simulating systems with superfluid phases. Due to its efficiency in collecting statistics for the Green function, the worm algorithm has proven to be a very powerful tool to investigate the ground-state properties of such systems, particularly for Hubbard models. In fact, as we will explain below, from the behavior of the

Green function in imaginary time, one can extract information about the insulating phases of the ground state of the system, which are typical of Hubbard models.

8.7.1 Zero momentum Green function and the particle–hole excitations

For what follows, it is instructive to introduce a rather technical but useful quantity: the zero-momentum Green function, defined as

$$G(\mathbf{p} = 0, \tau) = \sum_j G(j, \tau), \quad (8.74)$$

where the sum extends over all sites j of the lattice. This quantity is particularly useful to determine the ground-state phase diagram of various types of Bose–Hubbard Hamiltonians (Capogrosso-Sansone *et al.*, 2010). In particular, for the dipolar Hamiltonian the phase boundaries of the MI lobes are readily found from the exponential decay of the Green function (eqn (8.74)) with the imaginary time (see Trefzger (2010) and references therein). In fact, for any values of the tunneling coefficient t and of the chemical potential μ inside a given insulating lobe, it is straightforward to determine the dispersion relation for the single-particle and single-hole excitations by using a Lehman expansion and extrapolation in the $\tau \rightarrow \infty$ limit. In this limit one finds that the zero-momentum Green function in the momentum space behaves as follows:

$$G(\mathbf{p} = 0, \tau) \longrightarrow \begin{cases} e^{-\tau E_P(\mu, t)}, & \tau \rightarrow +\infty \\ e^{+\tau E_H(\mu, t)}, & \tau \rightarrow -\infty, \end{cases} \quad (8.75)$$

where $E_P(\mu, t)$ and $E_H(\mu, t)$ are the single-particle and single-hole excitation energies at a given μ and t inside the lobe. At the lobe boundaries $\mu = \mu_b$, one of the two excitations, either $E_P(\mu_b, t)$ or $E_H(\mu_b, t)$, vanishes and only at the critical point given by the tip of the insulating lobe at (μ_c, t_c) are both of the excitations zero. Therefore the phase boundaries are easily found by searching the values of (μ, t) for which one or both the energies of the elementary excitations vanish.

8.7.2 Incompressible and supersolid phases

We describe here the ground-state properties of dipolar hard-core bosons confined in a 2D square lattice of linear size L , satisfying periodic boundary conditions (Capogrosso-Sansone *et al.*, 2010). The system is described by the extended Bose–Hubbard Hamiltonian (eqn (8.56)), where no cut-off in the dipolar interaction potential is used. In the hard-core limit, the Hamiltonian can be written as:

$$\hat{H} = -t \sum_{\langle ij \rangle} \hat{b}_i^\dagger \hat{b}_j + V \sum_{i < j} \frac{\hat{n}_i \hat{n}_j}{r_{ij}^3} - \sum_i (\mu - \Omega i^2) \hat{n}_i, \quad (8.76)$$

where $V = \mu_e^2/d^3$, with μ_e being the electric dipole moment and d the lattice spacing, $r_{ij} = |i - j|$ is the distance between sites i and j , and $\Omega = m\omega^2 d^2/2$. The incompressible and

supersolid phases are both characterized by a finite value of the structure factor, defined as

$$S(\mathbf{k}) = \sum_{\mathbf{r}, \mathbf{r}'} \frac{\langle n_{\mathbf{r}} n_{\mathbf{r}'} \rangle}{N} e^{i\mathbf{k}(\mathbf{r}-\mathbf{r}')}, \quad (8.77)$$

with \mathbf{k} the reciprocal lattice vector, $\hat{n}_{\mathbf{r}}$ the density at position \mathbf{r} , and N the total number of particles. While for the incompressible phases the superfluid fraction vanishes, i.e. $\rho_s = 0$, the supersolid phase is characterized by a finite value of ρ_s , indicating the presence of superfluid.

Homogeneous case For the case $\Omega = 0$, Figure 8.13 shows the zero-temperature phase diagram of the system in the $t-\mu$ plane, and in the range $t/V > 0.02$ (indicated by the unshaded area) and $1 < \mu/V < 6$.

For finite t , three main solid Mott lobes emerge, with filling factors $\nu = \frac{1}{2}, \frac{1}{3}$, and $\frac{1}{4}$, and named checkerboard (CB), stripe (ST), and star (SR) solids, respectively. The corresponding ground-state configurations are sketched in panels (b)–(d) of Figure 8.13. The boundaries of the Mott lobes have been calculated from the zero-momentum Green function (eqn (8.74)) for linear system sizes up to $L = 20$ (CB and SR lobes), and from μ -curves with sizes up to $L = 24$ (ST lobe). The CB solid is found to be the most robust against hopping and doping, and thus it extends furthest in the $\mu-t$ plane.

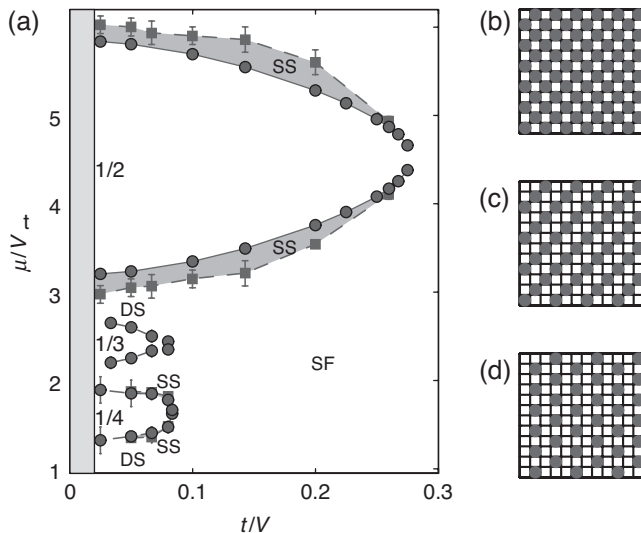


Figure 8.13 Phase diagram corresponding to the Hamiltonian (eqn (8.76)) as a function of μ and t at zero temperature and $\Omega = 0$. (a) Lobes corresponding to Mott solids (densities indicated); supersolid phase (SS), superfluid phase (SF), and parameter region corresponding to devil's staircase (DS). Panels (b), (c), and (d) sketch the ground-state configuration for the Mott solids in panel (a), with $\nu = \frac{1}{2}$ (checkerboard phase), $\frac{1}{3}$ (stripe solid phase) and $\frac{1}{4}$ (star solid phase), respectively. From Capogrosso-Sansone *et al.* (2010).

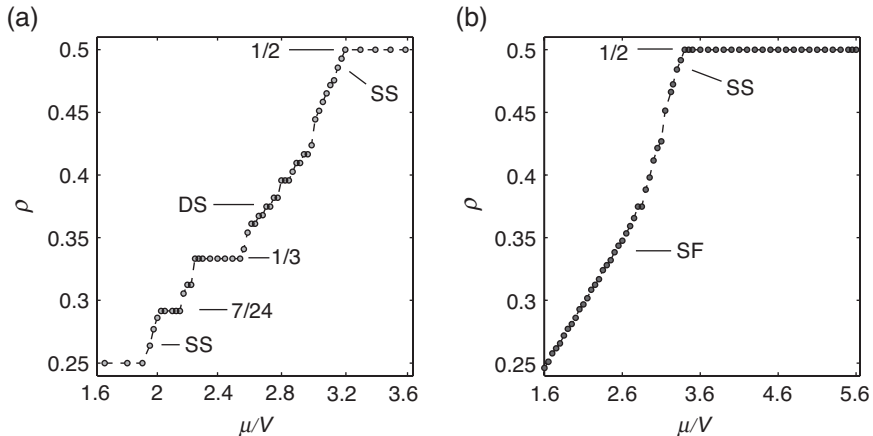


Figure 8.14 Particle density ρ vs chemical potential μ . (a) Solids and supersolids (SS) for a system with linear size $L = 12$ and $t/V = 0.05$. Some values of ρ are indicated. (b) Superfluid (SF) and vacancy-SS for $L = 16$ and $t/V = 0.1$. From Capogrosso-Sansone *et al.* (2010).

For large enough t/V , the low-energy phase is superfluid for all μ . At intermediate values of t/V , however, it is found that by doping the Mott solids either with vacancies (removing particles) or interstitials (adding extra particles) a supersolid phase (SS) can be stabilized, with coexisting superfluid and crystalline orders. On the other hand no evidence of SS in the absence of doping is found. The shaded areas above and below the CB lobe boundaries in Figure 8.13 correspond to SSs obtained by doping the CB crystal with interstitials and vacancies respectively. Remarkably, the long-range interactions stabilize the supersolid in a wide range of parameters, in fact for 1NN or 2NN in the range of the dipolar interaction no stable CB SS was found for particle densities $\rho < \frac{1}{2}$ (Sengupta *et al.*, 2005a).

Interestingly, evidence for incompressible phases in addition to those corresponding to the lobes in Figure 8.13 has been found. This is shown in Figure 8.14, where the particle density ρ is plotted as a function of the chemical potential μ , a continuous increase of ρ as a function of μ signals a compressible phase, while a solid phase is characterized by a constant ρ for increasing μ . Panel (a), corresponding to $t/V = 0.05$, shows a series of large constant-density plateaus connected by a progression of smaller steps and regions of continuous increase of ρ . Here the main plateaus correspond to the Mott lobes of Figure 8.13, while the other steps correspond to incompressible phases, with a fixed, integer number of particles. This progression of steps is an indication of a devil's-like staircase in the density, which was discussed in Burnell *et al.* (2009) for a 1D system. Instead, for $t/V = 0.1$ in panel (b), no evidence of such a phase is found.

Non-zero temperature The worm algorithm can also be applied for temperatures strictly $T > 0$. Within this approach, the melting of the supersolid into a normal phase as a function of T has been studied for the case of vacancy supersolidity below the CB solid. Figure 8.15 shows the superfluid fraction ρ_s and the structure factor $S(\pi, \pi)$ for the CB solid as a function of T (Capogrosso-Sansone *et al.*, 2010). It is found that the melting

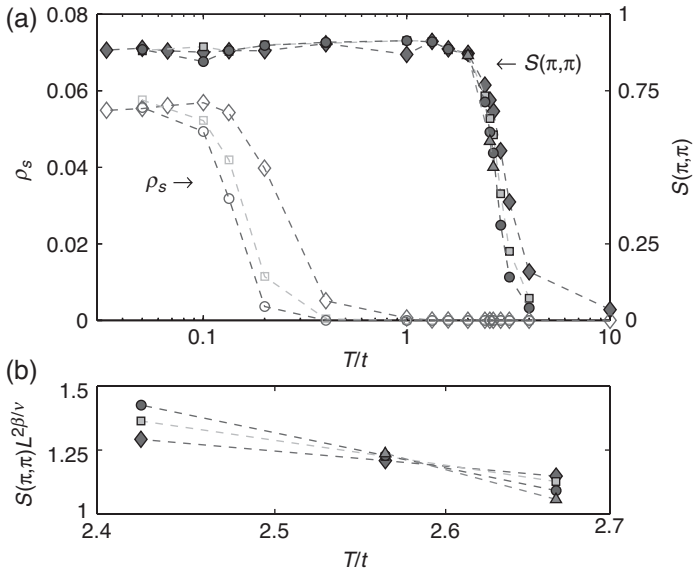


Figure 8.15 Non-zero- T melting of SS at $t/V = 0.1$. Top, superfluid fraction ρ_s (empty symbols) and structure factor, $S(\pi, \pi)$ (full symbols), versus temperature T for linear systems of size $L = 8, 12, 16$, and 20 (diamonds, squares, dots, and triangles, respectively); bottom, $S(\mathbf{k})L^{2\beta/\nu}$ vs T with $2\beta/\nu = \frac{1}{4}$. From Capogrosso-Sansone *et al.* (2010).

of the supersolid proceeds through two successive transitions. First, the supersolid melts into a liquid-like phase reminiscent of a liquid crystal, with zero ρ_s and finite $S(\pi, \pi)$. The drop of ρ_s for $T \simeq 0.1t$ in Figure 8.15 signals a transition of the Kosterlitz–Thouless–Berezinskii (KTB) type, with critical melting temperature $T_{\text{KT}} = \pi\rho_s\hbar^2\rho/2m$, where ρ is the filling factor and $m = 1/2td^2$, d being the lattice spacing. Upon further increasing the temperature, the second transition is signaled by a drop in the static structure factor for $T \simeq 2.6t$. Panel (b) of Figure 8.15 shows that this is consistent with an Ising-type transition: the expected scaling for $S(\pi, \pi)$ in two dimensions is plotted, with the ratio between critical exponents being $2\beta/\nu = \frac{1}{4}$ (for an Ising-type transition the critical exponent $\nu = 1$, showing the divergence of the correlation length, while $\beta = \frac{1}{8}$).

Harmonic confinement The recent experimental achievement of single-site addressability in optical lattices using electron and optical microscopy allows for a direct, in-situ observation of particle positions and particle-particle correlations in experiments (Bakr *et al.*, 2009, 2010; Heine *et al.*, 2010; Sherson *et al.*, 2010). Thus the key observables for present and future experiments are the in-situ density distribution and particle correlations, from which the phases above can be detected. The question is how the phases described in Figure 8.13 will be seen in an experiment. The spatial density distribution in the lattice for realistic experimental situations— $N \sim 10^3$ particles trapped with harmonic confinement and small finite T —have been calculated and are displayed in Figure 8.16 for a single quadrant. Each circle corresponds to a different site and its radius is proportional to the

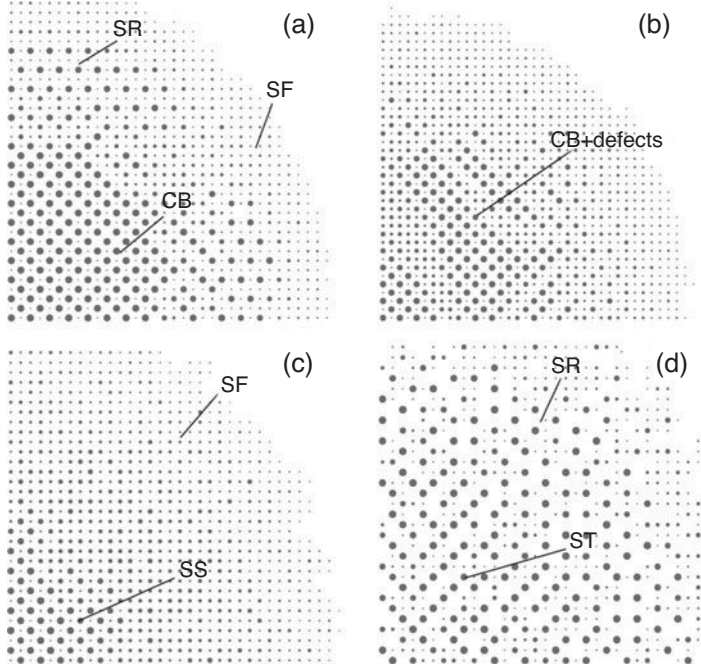


Figure 8.16 Spatial density profile in two dimensions for $N \simeq 1000$ particles in a harmonic potential. Phases are indicated as follows SF, superfluid; CB, checkerboard; SR, star; ST, stripe; SS, supersolid. (a)–(b) $V/t = 15$, $\mu/t = 55$, $\Omega/t = 0.05$, and $T/t = 0.0377$. (c) $V/t = 5$, $\mu/t = 19$, $\Omega/t = 0.01$, and $T/t = 0.1$. (d) $V/t = 20$, $\mu/t = 51$, $\Omega/t = 0.04$, and $T/t = 0.25$. From Capogrosso-Sansone *et al.* (2010).

local density (Capogrosso-Sansone *et al.*, 2010). In panels (a) and (b), μ has been chosen such that particles at the trap center are in the CB phase, with very small T . The density profile shows a wedding-cake structure, with concentric Mott lobes with filling factors of $\rho = \frac{1}{2}$ and $\frac{1}{4}$. However, while the system parameters are the same in both figures, panel (a) shows regular CB and SR patterns while in panel (b) extended defects are present in the CB phase and the SR is barely visible. This is due to the different preparation of the states in panels (a) and (b). In fact, in panel (a) temperature annealing of the system prior to taking the snapshot is performed, while this is not done in panel (b). It is found that the defects in (b) reflect the existence of a large number of low-energy metastable states, which are a direct consequence of the long-range nature of the interactions and will be of relevance for experiments. Supersolid (SS) and stripe (ST) phases are shown in panels (c) and (d), respectively. In panel (c), μ has been chosen to realize an extended vacancy-SS region surrounded by a superfluid. Note that here finite $T = 0.1t$ has been chosen, compatible with the existence of the SS phase. The density distribution in the vacancy-SS looks similar to the ordered CB phase, even without annealing. Self-annealing is in fact enabled here by the (small) superfluid component of the SS phase. Small coherence peaks will be present in time-of-flight experiments, allowing for a clear determination of this phase. Panel (d) shows

a disordered ST phase at the center, surrounded by an extended Mott shell with $\rho = \frac{1}{4}$. The disorder in this case is a result of both finite $T/t = 0.25$ and the fact that the ST solid is less robust towards quantum and classical fluctuations than the CB and SR ones.

These exact results for $\Omega \neq 0$ confirm that the phase diagram in Figure 8.13 is the key to predict and interpret experimental observables, assuming a local density approximation.

8.8. Further dipole effects

There are several fascinating topics related to dipole interactions that have not been addressed in this chapter. We list few of them as a concluding remark of the broadness of the physics that can be attained with dipoles.

8.8.1 Tailoring interactions with polar molecules

Thanks to their promisingly large dipole moments (typically of the order of a few Debye), polar molecules have been the subject of extensive theoretical investigations centred on the possibility of tailoring the shape of their interaction (Pupillo *et al.*, 2008).

Polar molecules prepared in a mixture of rotational states interact through long-range dipole–dipole interactions even in the absence of an external electric field. The possible Mott phases exhibit different ordering depending on the preparation of the initial superposition. When the Mott state is melted the superfluid state can interpolate between homogeneous and antiferromagnetic ordering, or phase separate depending on the Hamiltonian parameters (Barnett *et al.*, 2006b).

On the other hand, appropriate static and/or microwave fields can be applied to design effective potentials between two molecules (Micheli *et al.*, 2006; Büchler *et al.*, 2007b). Such manipulation leads to long-range interaction potentials, in contrast to the typical van der Waals interaction in the absence of external fields.

The mechanism to induce tailored interactions relies on the simple rigid rotor Hamiltonian that provides the low energy rotational states of the molecules. Such rotational states can be coupled by static or microwave fields to design long-range interaction potentials. In two dimensions, a static electric field induces a typical repulsive dipolar potential, which scales as $1/r^3$, and leads to crystallization (Büchler *et al.*, 2007b).

8.8.2 Three-body interactions

Further investigation has shown that the static electric field and the microwave field dressing the molecular rotational levels can be chosen in such a way as to obtain dominant three-body interactions (Büchler *et al.*, 2007b). Hamiltonians with many-body interactions have been studied in the context of non-Abelian topological phases (like the Pfaffian wave function accounting for the quantum Hall effect, or systems with a low-energy degeneracy characterized by string nets), multiple species in frustrated lattice topologies, ring-exchange models (like the one responsible for the nuclear magnetism in helium-3), etc. In typical condensed matter systems many-body interactions are rarely dominant, but polar molecules provide a setting where these can be controlled and designed independently from two-body interactions.

8.8.3 Exotic spin models

As we have already seen, by tuning the optical potential parameters and by means of external electric and magnetic fields, one can induce and control the interaction between spin states of neutral atoms in an optical lattice and engineer quantum spin Hamiltonians (Duan *et al.*, 2003; García-Ripoll *et al.*, 2004; Lewenstein *et al.*, 2007). Such proposals are aimed at studying a variety of quantum phases, among them the Haldane phase, critical phases, quantum dimers, and models with complex topological order supporting exotic anyonic excitations. By including a spin degree of freedom in addition to the rotational degrees of freedom of polar molecules, spin models for half-integer and integer spins with larger coupling constants can be obtained (Micheli *et al.*, 2006; Brennen *et al.*, 2007). The main ingredient of these proposals is the dipole–dipole interaction: it strongly couples the rotational motion of the molecules, it can be controlled by means of microwave fields (as explained above), and it can be made spin-dependent, exploiting the spin–rotation splitting of the molecular rotational levels. The final goal is to reproduce models with emergent topological order that are robust to arbitrary perturbations of the underlying Hamiltonian, and hence are suitable for error-resistant qubit encoding and for quantum memories.

8.8.4 Self-assembled structures

The long-range character of the dipole–dipole interaction allows the formation of self-assembled structures. Examples include the formation of chains of polar molecules in 1D optical lattices driven by the attractive part of the dipole potential and the appearance of crystal ordering in 1D or 2D systems driven instead by the repulsive character of the interaction.

In the 2D homogeneous system for dipoles pointing perpendicular to the plane, the repulsive interaction is responsible for the formation of hexagonal crystal ordering (Büchler *et al.*, 2007*b*; Astrakharchik *et al.*, 2007; Mora *et al.*, 2007), similar to the formation of Wigner crystals for electrons or ions interacting via the Coulomb repulsion (see Mahan (1993)). However, two important differences are found, namely that the transition to the crystal phase in dipolar systems happens at high density (instead of at low density for Coulomb systems) and the spectrum shows two phononic linear branches with different slopes (rather than the dispersion $\omega \sim q^{1/2}$ typical of Coulomb crystals). The formation of crystal ordering has been identified as a first-order phase transition (Büchler *et al.*, 2007*b*).

8.8.5 Dipolar gases and trapped ions

A promising and fascinating idea allowing investigation of many-body quantum systems and bearing a very close similarity to ultracold atomic gases, comes from trapped ions. Mintert and Wunderlich (2001) and Wunderlich and Balzer (2003) used inhomogeneous magnetic fields and long-wavelength radiation to solve the problem of individual-ion addressing in ion traps. Mintert and Wunderlich discovered that the internal degrees of freedom of ions behave as coupled pseudo-spins where the coupling is mediated by the phonons in the trap. Independently, this idea was fully put forward by Porras and Cirac (2004*b*) (see also Deng *et al.* (2005)), who argued that trapped ions can be systems that are as useful for quantum simulations as ultracold atoms or molecules in optical lattices. The most interesting aspect of this work in the present context is that the interactions mediated by phonons are of

long-range character and in fact typically decay with distance as $1/r^3$. The typical spin Hamiltonian one can simulate with ions has the form

$$\hat{H} = \frac{1}{2} \sum_{i,j} \hat{S}_i^z \hat{S}_j^z - \frac{1}{2} \sum_{i,j} t_{ij}^x \hat{S}_i^x \hat{S}_j^x - \frac{1}{2} \sum_{i,j} t_{ij}^y \hat{S}_i^y \hat{S}_j^y - \sum_i \left(B_i^x \hat{S}_i^x + B_i^y \hat{S}_i^y + B_i^z \hat{S}_i^z \right), \quad (8.78)$$

where the overall sign and magnitude of $t_{ij}^{x,y,z}$ can be controlled. The spatial dependence is $t_{ij}^{x,y,z} \propto 1/|\mathbf{r}_i - \mathbf{r}_j|^3$. When $t^x = t^y$ these models correspond nearly exactly to hard-core Bose gases, with dipole–dipole interactions in transverse and longitudinal ‘magnetic’ fields. The only differences are that the tunneling now has a non-local character and its amplitude also decays as slowly as $1/r^3$ since the phonons allow for such long-range interactions.

All these observations are not inventions of theoreticians. Many of the leading experimental ion trapper groups are working on quantum simulations with ions and the first spectacular experimental results have been already obtained (Friedenauer *et al.*, 2008).

9

Disordered ultracold atomic gases

Impurities, defects, and dislocations are common in Nature, but understanding disorder effects is a complex task that poses some of the most challenging questions in condensed-matter and many-body systems. In ultracold gases, disorder can be created in a controlled and repeatable way, thus opening a new route for its study, which is the scope of this chapter. We start, after a general introduction in Section 9.1, by reviewing some of the key effects driven by disorder in condensed-matter systems in Section 9.2. In particular, we examine in some detail the transition from metal to insulator due to disorder in non-interacting systems, the so-called Anderson localization transition. Disorder in strongly correlated bosonic systems, which gives rise for instance to the Bose glass phase, is also discussed. In Section 9.3 we focus on ultracold atoms, explaining first the possible realizations of disorder and stressing the advantages such systems offer for its study. The interplay between disorder and interactions also remains a challenging problem in atomic systems. Advances in this area are reported in Section 9.4 for interacting bosonic systems, in Section 9.5 for fermionic systems, and in Section 9.6 for Bose–Fermi mixtures. We move then to a discussion of spin glasses in ultracold lattice gases in Section 9.7, and we close this chapter with the presentation of the phenomena of disorder-induced order in Section 9.8.

9.1. Introduction

Since the discovery of the quantum localization phenomenon due to disorder by Anderson (1958), the field of quantum disordered systems has been a very active research field in condensed-matter physics. In particular, quenched disorder—disorder that is frozen on the typical timescales of the systems considered—determines the physics of a large variety of phenomena such as, to mention just a few:

- transport, conductivity, localization effects, and metal–insulator transitions; for reviews see for instance Nagaoka and Fukuyama (1982), Lee and Ramakrishnan (1985), Ando and Fukuyama (1988), and Kramer and MacKinnon (1993)
- spin glasses; see Mézard *et al.* (1987), Newman and Stein (2003), and Sachdev (1999)
- neural networks; see Amit (1989)
- percolation; see Aharony and Stauffer (1994), Grimmett (1999), and Barbosa *et al.* (2003)
- high T_c superconductivity; see Auerbach (1994)
- quantum chaos; see Haake (2010).

Disorder effects also appear in open questions of condensed matter such as glassy transitions, breakdown of ergodicity in random systems, superconductor–insulator transition, metal–insulator transition in two dimensions, or low-temperature decoherence in disordered conductors. See for instance Cusack (1987), Balian *et al.* (1979), Chowdhury (1986), and Ong and Bhatt (2001).

Theoretical studies of disordered systems imply severe difficulties. One is that the characterization of these systems independently of the particular disorder realization entails averaging over the disorder. Such a quenched average of physical quantities, for example the free energy, usually requires the use of special methods such as the replica trick (Mézard *et al.*, 1987) or the supersymmetry method (Efetov, 1997). Interestingly, a quantum information approach might help to calculate averages by using quantum superpositions (Paredes *et al.*, 2005*b*). Regarding numerical approaches, the characterization of the system demands either simulations of very large samples to achieve ‘self-averaging’ or numerous repetitions of simulations of small samples with different configurations of the disorder. Obviously, this difficulty is particularly important for quantum disordered systems. Another difficulty that emerges is the possible existence of a large number of low-energy excitations. Similar difficulties arise in frustrated non-disordered systems (Misguich and Lhuillier, 2003). Also, the interplay between disorder and interactions has been, and still is, a challenging problem.

Disorder effects are present in many condensed-matter systems, in particular in electronic systems. Nevertheless, these systems do not provide the best scenario to test theoretical predictions, mainly because of two factors: (i) the disorder is not controllable, but is fixed by the specific realization of the sample and (ii) the electrons interact via the long-range Coulomb interaction, which is fixed by Nature. The advantages of disordered ultracold atomic systems are clear: (i) extreme control over the generation of random potentials that induce disorder in the system (see Section 9.3), (ii) control of the atomic interactions by means of e.g. Feshbach resonances, (iii) selection of the type of quantum statistics, which can be chosen to be bosonic, fermionic, or a mixture, and (iv) full control of the trapping potentials and therefore of the effective dimensionality of the system. Obviously, standard control parameters, such as the temperature of the system, can also be controlled, but in these aspects atomic systems do not differ much from condensed-matter ones. Of course, there are also disadvantages: atomic systems are ‘small’. Typical experiments with ultracold lattice gases involve lattices of sizes up to $100 \times 100 \times 100$ and a number of atoms of up to a few times 10^6 .

9.2. Disorder in condensed matter

9.2.1 Metal–insulator transition driven by disorder: Anderson localization

In condensed matter, insulators can be classified as (Gebhard, 1997): (i) insulators due to electron–electron interactions appearing in interacting many-body systems such as MIs or (ii) insulators due to the electron–ion interactions described by single-electron theory. The latter type includes: (ii.a) band insulators, due to the interaction of electrons with the periodic potential of the atoms, (ii.b) Peierls insulators, due to the interaction of electrons with static deformations of the lattice, and (ii.c) Anderson insulators, due to the interaction of electrons with impurities or lattice imperfections.

Non-interacting perfectly periodic electronic systems exhibit universal features such as the existence of energy bands separated by energy gaps, the presence of extended wave functions (Bloch waves), and the appearance of quasimomentum as a good quantum number (see Section 3.3). Nevertheless, in Nature this long-range translational order is most often broken by random impurities. In 1958, Anderson reported for first time that in the presence of a critical amount of random impurities the diffusive motion of an electron will come to a halt. This constitutes the idea of electron localization, which takes place at the single-particle level through coherent back-scattering.

Adding a weak disorder to a crystal mainly affects the phase of the extended wave functions of the electrons (Bloch waves). Thus for weak disorder the wave function still looks like a plane wave on a sufficiently short length scale. However, above a certain length scale, the mean-free path l , the phase of the wave function deviates appreciably from a plane wave. The mean free path, corresponding to the average distance between two successive scattering events, is of the order of the coherence length, the distance at which the memory of the value of the phase of a given point is lost. If the disorder is strong enough it will affect not only the phase but also the amplitude of the wave function, which may become localized with an exponentially decaying envelope (see Figure 9.1)

$$|\psi| \sim \exp(-|\mathbf{r} - \mathbf{r}_i|/\xi), \quad (9.1)$$

where ξ is the localization length. Therefore, in localization theory three length scales play an important role: lattice spacing, mean-free path, and localization length, as schematically shown in Figure 9.2. Anderson localization can be defined formally as the phenomenon in which static disorder in a single-particle Hamiltonian for an infinite system causes all the eigenstates to localize in space. The spectrum of the Hamiltonian is no longer continuous, but rather becomes dense point-like; the eigenvalues are infinitely close to each other and the eigenfunctions are exponentially localized. In an infinite system, bound states with infinitely close energies are possible because they correspond to localized eigenstates that are infinitely far apart and hardly overlap. One consequence of the dense point-like spectrum is that the localized regime has a finite number of eigenstates per unit volume and energy interval. Nevertheless, since unbounded media do not exist, one should analyse what happens for finite systems. This issue was first raised by Thouless (1974).

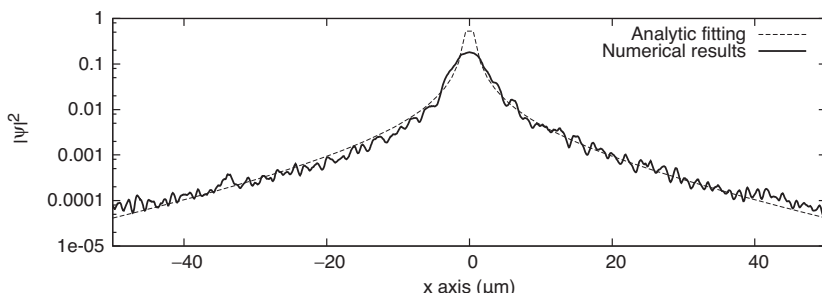


Figure 9.1 Exponential decay of a localized wave function in an speckle-disordered potential in one dimension. The analytical fit corresponds to $|\psi(x)| \propto |x|^{3/2} \exp(-|x|/\xi)$. By courtesy of V. Caprara.

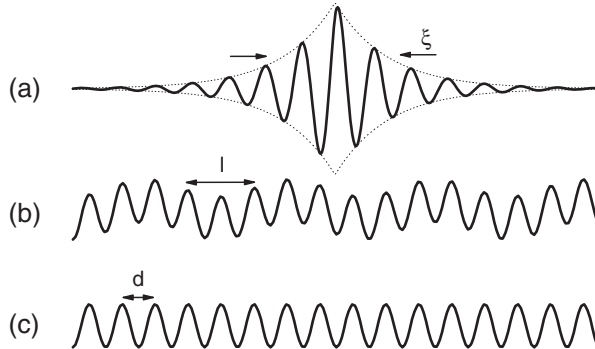


Figure 9.2 Schematic representation of the three length scales that appear in lattice-disorder problems: (a) localization length ξ , (b) mean-free path l , and (c) periodicity of the lattice d .

In a finite open medium, eigenvalues are discretized by the quantization conditions and they achieve a finite width due to leakage through the boundaries. Thouless showed that Anderson localization occurs when the level width is smaller than the level separation. The dimensionless ratio of both energies g is known as the dimensionless Thouless conductance, and (i) sets the link between spectrum and transport properties and (ii) settles the basis of the scaling theory, being the single parameter that controls the behavior of the system as it doubles in size (Edwards and Thouless, 1972, 1974; Licciardello and Thouless, 1975; Wegner, 1976; Abrahams *et al.*, 1979; Gork'ov *et al.*, 1979).

From scaling arguments, the scaling function constructed through the Thouless conductance

$$\beta(g) = d(\log(g))/d(\log(L)) \quad (9.2)$$

where L is the size of the system, evidences the important role of the dimensionality of the system for the behavior of the insulating transition. We shall discuss this consideration later, but first we analyse dimensionality effects further.

- In one dimension it has been rigorously proven that infinitesimally small disorder leads to exponential localization of all the eigenfunctions by repeated back-scattering (Mott and Twose, 1961; Borland, 1963). It is also known that the localization length ξ is of the order of the mean-free path l . Also in one dimension, the localization length is a function of the ratio between the energy (potential and kinetic (or tunneling)) of the eigenstate and the disorder strength. For discrete systems with constant tunneling rates and a local disorder distributed according to a Lorentzian distribution—Lloyd's model; see Haake (2010)—the exact expression for the localization length is known. In general, an exact relation between the density of states and the range of localization in one dimension has been provided by Thouless (1974).
- In two dimensions, following the scaling theory (Abrahams *et al.*, 1979), it is believed that localization also occurs for arbitrarily small disorder, but its character interpolates smoothly between algebraic for weak disorder and exponential for strong disorder.

- In three dimensions, scaling theory predicts completely different behavior. The scaling function for $D > 2$ vanishes at some critical value, $\beta(g_c) = 0$, with $g_c \approx 1$, defining the Thouless criterion for localization, i.e. a critical value of the disorder above which localization takes place. This critical point, $g_c \approx 1$, signals the mobility edge, a concept introduced for first time by Mott (1968b), which corresponds to the energy at which a continuous $T = 0$ transition between localized and extended states occurs. Therefore, low energy states with $E < E_c$, where E_c is the mobility edge, are exponentially localized while those with $E > E_c$ are extended. So, if the Fermi energy, E_F , lies below the mobility edge, the system is localized. Also, the Ioffe and Regel criterion (Ioffe and Regel, 1960) states that the description of the electrons as waves that scatter off random impurities requires the wavelength of the electron to be larger than the mean-free path. This determines a minimum value for the mean-free path for extended states, $l \approx \lambda_F \approx 2\pi/k_F$, where $k_F = \sqrt{2mE_F}/\hbar$.

The original model of disorder by Anderson (1958) considers a single electron in a regular 3D lattice, hopping from one site to one of the near neighboring sites with constant amplitude t . The on-site energies μ_i vary randomly and independently for each site over a given range. The probability that the electron starting at a given site returns to it is non-zero above a certain value of the disorder strength, i.e. for a given amplitude of the on-site energy range. The Anderson model can be written as:

$$\hat{H} = -t \sum_{\langle i,j \rangle} \hat{f}_i^\dagger \hat{f}_j - \sum_i \mu_i \hat{f}_i^\dagger \hat{f}_i, \quad (9.3)$$

where \hat{f}_i^\dagger (\hat{f}_i) are the creation (annihilation) operators of an electron at site i ; since these are non-interacting electrons, spin provides only a trivial factor of two and can be omitted. The uncorrelated on site energies are characterized by their probability distributions $P(\mu_i)$, which can be considered, for instance, as constant within some interval of width W , that is to say:

$$P(\mu_i) = \begin{cases} 1/W & |\mu_i| < W/2, \\ 0 & \text{elsewhere,} \end{cases} \quad (9.4)$$

or Gaussian:

$$P(\mu_i) = \frac{1}{\sqrt{2\pi}W} \exp(-\mu_i^2/2W^2). \quad (9.5)$$

A more physical approach in the context of disorder induced by lattice defects involves considering the on-site energies correlated over a given length scale. Binary disorder, often called Bernoulli potential, $P(\mu_i) = p\delta(\mu_i - \mu_A) + (1-p)\delta(\mu_i - \mu_B)$, in which on-site energy μ_A occurs with probability p , and μ_B with probability $1-p$, is an example of substitutional disorder, and it is strongly related to the site percolation problem. Moreover, disorder can also be induced with all the on-site energies identical but with the position of the sites being random variables; in this case the system is said to be topologically disordered. Amorphous solids and liquids belong to this class of system. This implies disorder for the tunneling rates t_{ij} , which depend on the distances between sites.

9.2.2 Anderson localization in one dimension

As already mentioned, in one and two dimensions even infinitesimal uncorrelated disorder on the lattice leads to Anderson localization for non-interacting particles: all eigenstates of the single-particle Hamiltonian are localized in space. In three dimensions or in the presence of correlated disorder the typical situation is that for small values of disorder, low-energy states are localized but high-energy states are extended and can conduct currents or flows. Anderson transition to the situation in which all eigenstates localize and the system becomes insulating occurs at sufficiently large, critical values of disorder.

Here we analyse Anderson localization in one dimension following the approach given in Haake (2010). To this end, we write the explicit form of the single-particle Schrödinger equation for the Anderson model (eqn (9.3)). Denoting the wave function in one dimension by ψ_m , with $m = \dots, -1, 0, 1, 2, \dots$, we get

$$E\psi_m = -t(\psi_{m+1} + \psi_{m-1}) - \mu_m \psi_m. \quad (9.6)$$

It is useful to rewrite this equation in the form of recurrence

$$\begin{pmatrix} \psi_{m+1} \\ \psi_m \end{pmatrix} = M_m \begin{pmatrix} \psi_m \\ \psi_{m-1} \end{pmatrix} = \begin{pmatrix} -(E + \mu_m)/t & -1 \\ 1 & 0 \end{pmatrix} \begin{pmatrix} \psi_m \\ \psi_{m-1} \end{pmatrix}. \quad (9.7)$$

Note that the 2×2 matrices M_m are unimodular, i.e. they have determinants equal to one. Starting with $m = 1$ and applying the recurrence to the left, we obtain

$$\begin{pmatrix} \psi_{m+1} \\ \psi_m \end{pmatrix} = M_m M_{m-1} \dots M_2 M_1 \begin{pmatrix} \psi_1 \\ \psi_0 \end{pmatrix}. \quad (9.8)$$

Now we are in a position to use one of the theorems of mathematical physics, here in the version proven by Furstenberg:

Theorem 9.1: Furstenberg theorem (Furstenberg, 1963; Crisanti *et al.*, 1993) *Let M_m be random, unimodular matrices. Then, under quite general conditions,*

$$\lim_{m \rightarrow \infty} \frac{1}{m} \log \text{Tr}[M_m M_{m-1} \dots M_2 M_1] \equiv \gamma > 0. \quad (9.9)$$

The proof of the existence of the limit is, more or less, a consequence of the standard central limit theorem. The proof that γ is strictly positive is highly non-trivial, however. In our case, the Furstenberg theorem implies that the matrix $M_m M_{m-1} \dots M_2 M_1$ has, for $m \rightarrow \infty$, two eigenvalues, $\exp(\pm \gamma m)$. This means that for almost all (ψ_1, ψ_0) the solution of (eqn (9.8)) will grow exponentially to the right. That is why the parameter γ is called the Lyapunov exponent of the random transformation (eqn (9.7)). To get a physically acceptable eigenvector, we have to fix (ψ_1, ψ_0) in such a way that the wave function decays exponentially to the right. At the same time, the same argument must be applied for the behavior of the wave function to the left, i.e. for negative m . This cannot happen generically unless the energy E takes a definite discrete value E_ν , where ν denotes the position at which

the eigenvector is centered. We see that the spectrum cannot be continuous, but rather it has to be point-like, and that the wave functions behave as

$$\psi_m^\nu \sim \exp(-\gamma|\nu - m|) = \exp(-|\nu - m|/\xi), \quad (9.10)$$

for $|\nu - m| \rightarrow \infty$, where we have introduced the localization length $\xi = 1/\gamma$. Typically, ξ is an increasing function of the energy E . For the special case of the so-called Lloyd's model, for which the distribution of μ_m is Lorentzian, $\xi(E)$ can be calculated analytically (for a pedagogical derivation see Haake (2010)).

Unfortunately, the Furstenberg theorem cannot be simply extended to higher dimensions, so that essentially no rigorous results concerning Anderson localization are known in two or three dimensions. In the next subsections we will derive non-rigorous arguments based on the so-called Imry–Ma argument and the renormalization group approach. In contrast, much more is known rigorously about properties of the states belonging to the low-energy tail, due the seminal work of Lifshits *et al.* (1988), which we will discuss in Section 9.4.2.

9.2.3 Imry–Ma argument

Before turning to the scaling approach to Anderson localization pioneered by Thouless and the ‘gang of four’, we will first remind the readers of a very beautiful and simple argument by Imry and Ma (1975), which determines when a random magnetic field destroys the long-range order in classical spin systems. The argument is based on the same sensitivity to boundary conditions as in the case of the Thouless approach to localization.

We focus here on the case of ferromagnetic interactions with nearest-neighbor couplings J only, and consider Ising models with \mathbb{Z}^2 symmetry as well as various models with continuous symmetry (XY , Heisenberg, etc.). The spins are located in a hypercubic lattice of dimension d , and we consider a block of linear size L and hypervolume L^d . We apply antisymmetric boundary conditions in one direction and ask their energy cost. The argument can be extended to temperatures $T > 0$ by asking for free-energy costs.

In the absence of disorder the results are:

- *Ising models.* The spins have to flip and form a domain wall. The energy cost is proportional to the area of the wall: $E_{DW} \sim JL^{d-1}$. We immediately conclude that in the absence of disorder, Ising models do order for $d > 1$, and in particular in two dimensions. The case $d = 1$ is marginal: the Ising models order at $T = 0$, but infinitesimally small T destroys the order. This can be seen easily by observing that the domain wall can be located anywhere in L places, i.e. its contribution to the entropy, $\sim \log L$, easily wins the L independent energy cost.
- *Models with continuous symmetry.* This time, the spins may turn instead of flipping, so it costs much less energy to form a so-called Bloch wall. The spin turns by an angle π/L from layer to layer. The energy cost is proportional to the volume times the energy cost of the misalignments of the neighboring spins $\sim 1 - \cos(\pi/L) \sim \pi^2/2L^2$, i.e. $E_{BW} \sim J\pi^2 L^{d-2}/2$. We immediately conclude that in the absence of disorder Heisenberg and XY models do order for $d > 2$, and in particular in three dimensions. In this case $d = 2$ is marginal: the models order at $T = 0$ but infinitesimally small T again destroys the order.

Let us now consider the same models in the presence of a random magnetic field h_j in the z direction with mean $\langle h_j \rangle = 0$ and variance $\langle h_j^2 \rangle = h^2$. The random-field energy cost in a fixed-spin configuration, such as the one corresponding to a domain or Bloch wall, is on average zero, but its typical fluctuations scale as $E_{RF} \sim hL^{d/2}$. Comparison with the previously obtained scalings gives:

- *Random-field Ising models.* Comparing $E_{RF} \sim hL^{d/2}$ to $E_{DW} \sim JL^{d-1}$, we immediately conclude that an infinitesimal disorder destroys order in Ising models for $d < 2$, and in two dimensions for any $T > 0$ due to entropy.
- *Models with continuous symmetry.* This time, we compare $E_{RF} \sim hL^{d/2}$ to $E_{BW} \sim J\pi^2 L^{d-2}/2$ and conclude that infinitesimal disorder destroys order in Heisenberg and XY models for $d < 4$, and in particular in three dimensions. The 4D case is marginal, but the order is definitely destroyed for any $T > 0$, due to entropy again.

Although the Imry–Ma argument also applies to quantum systems it is, strictly speaking, classical. Thus it does not concern subtle interference phenomena such as Anderson localization. The essence of the argument, however, is the idea of sensitivity with respect to boundary conditions, and this idea can be directly carried over to the Anderson problem, as shown by Thouless and his collaborators (Edwards and Thouless, 1972, 1974).

9.2.4 Thouless formalism

The intuition behind the Thouless idea is clear: the energy of an exponentially localized state centered far from the boundaries can only exponentially weakly depend on the boundary conditions. It suffices for the calculation and comparison of the energy levels for periodic and antiperiodic boundary conditions in a finite system of length L . This is done by ordering the levels with growing energy and calculating the respective energy differences. If the states are strongly localized this difference should be exponentially small. For the extended states, the change in boundary should correspond to a change of quasimomentum of π/L , which causes a much larger change in energy. A good measure of the degree of localization is the ratio of the energy differences to the level spacing.

Let us develop this idea further. Consider a system of size L with boundary conditions fixed by a general phase factor $\exp(iKL)$. For $K = 2\pi n/L$ and n integer, this corresponds exactly to the periodic boundary conditions. Similarly, for K being an odd multiple of π/L we obtain antiperiodic boundary conditions. Following Edwards and Thouless (1972), we use the continuous limit instead of the lattice description, and insert the ansatz $\psi(\mathbf{r}) = \exp(iKx)\phi(\mathbf{r})$ into the Schrödinger equation obtaining:

$$E(K)\psi(\mathbf{r}) = \left(\frac{(p_x + \hbar K)^2}{2m} + \frac{p_y^2}{2m} + \frac{p_z^2}{2m} - \mu(\mathbf{r}) \right) \psi(\mathbf{r}), \quad (9.11)$$

where $\mu(\mathbf{r})$ is the random potential. The energy difference (energy shift of the i th level) can be calculated using second-order perturbation theory in K . The result reads:

$$\Delta E_i = \frac{\hbar^2 K^2}{m^2} \sum_{j \neq i} \frac{|\langle i | p_x | j \rangle|^2}{E_i - E_j} + \frac{\hbar^2 K^2}{2m}. \quad (9.12)$$

If the states are localized and the spectrum is discrete, using sum rules we obtain the result that $|\langle i|p_x|j\rangle|^2 = m^2|\langle i|x|j\rangle|^2(E_i - E_j)^2$. By inserting this expression into eqn (9.12), we immediately see that $\Delta E_i = 0$. For finite systems the result is not exactly zero, but has exponentially small correction due to the fact the operator x is not properly defined with periodic boundary conditions.

Equation 9.12 has to be used with more care if the spectrum is continuous or if there are quasi-degenerate levels. In fact, Edwards and Thouless pointed out the similarity of eqn (9.12) to the famous Kubo–Greenwood formula for the electronic conductivity σ of a cube of side L :

$$\sigma = \frac{2\pi e^2 \hbar L^3}{m^2} |\langle i|p_x|j\rangle|_{\text{av}}^2 N(E)^2, \quad (9.13)$$

where $N(E)$ is the electron density of states per unit volume at the Fermi surface, and the average is over i, j . The validity of the formula requires us to assume that the matrix elements $|\langle i|p_x|j\rangle|^2$ depend weakly on the energy difference $E_i - E_j$ (this assumption will bring us to a final result, but is not really necessary, see Abrahams *et al.* (1979)). If this assumption is correct then we can use it to evaluate $(\Delta E_i)_{\text{av}}$. The sum over j in eqn (9.12) is dominated by the smallest denominator, which is of the order of the level spacing between the energy levels $\eta = 1/L^3 N(E)$. If we further assume that the energy levels are uncorrelated, the sum has a width, which is $\sim \pi\eta$. One then obtains

$$(\Delta E_i)_{\text{av}} = \frac{\pi \hbar^2 K^2 L^3 N(E)}{m^2} |\langle i|p_x|j\rangle|_{\text{av}}^2 = \frac{\sigma \hbar K^2 L^3}{2e^2} \eta. \quad (9.14)$$

Finally, employing the relation between the conductivity and the mean-free path l , we can express the conductivity as $\sigma = e^2 k^2 l / 3\pi^2 \hbar$, where k is the wavevector. Now we are in a position to obtain the final estimates for the shifts in the energy of the i th level when there are antiperiodic boundary conditions $KL \simeq \pi$. However, this value overestimates the shift since the shift is a periodic function of KL , with period 2π . A better fit is obtained by approximating $KL \simeq 2$ (Edwards and Thouless, 1972). Thus, the Thouless relation between the conductivity and the response to perturbation of boundary conditions, in a finite sampling, and in three dimensions reads:

$$\frac{(\Delta E_i)_{\text{av}}}{\eta} \approx \frac{2k^2 L l}{3\pi^2}, \quad (9.15)$$

and in two dimensions, where $\eta = 1/L^2 N(E)$

$$\frac{(\Delta E_i)_{\text{av}}}{\eta} \approx \frac{k l}{\pi}. \quad (9.16)$$

Note that these expressions have indeed a lot of similarities with the Imry–Ma formulas: sensitivity (defined through $(\Delta E_i)_{\text{av}}/\eta$) scales as L^{d-2} for non-localized states and vanishes exponentially for localized ones. This quantity allows us thus to distinguish the insulating phase from the conducting one. The numerical results of Edwards and Thouless (1972) show that in two dimensions the mean-free path is of the order of the interatomic spacing at the mobility edge.

9.2.5 Scaling theory of localization

Thouless's ideas were developed further in the seminal contribution of Abrahams *et al.* (1979). Their starting point was the Thouless relation, eqns (9.15) and (9.16) for a hypercube of size L^d :

$$\frac{\Delta E}{\eta} = \frac{\Delta E}{dE/dN} = \frac{2\hbar}{e^2} \sigma L^{d-2} = \frac{2\hbar}{e^2} G, \quad (9.17)$$

where $N(E) = \int^E dE' L^d n(E')$ is the cumulative density of states, σ is the conductivity, G is the conductance of the hypercube, $dE/dN = \eta$ is the mean spacing of its energy levels, and again ΔE is the geometric mean of the fluctuation in energy levels caused by replacing periodic boundary conditions with antiperiodic ones.

The scaling theory is based on the following ideas and assumptions.

- A generalized dimensionless conductance (called Thouless number) is defined as

$$g(L) = \frac{\Delta E(L)}{dE(L)/dN} = \frac{2\hbar}{e^2} G(L). \quad (9.18)$$

- The quantity $g(L)$ is the only relevant dimensionless ratio when two cubes of size L^d are fitted together.
- When b^d cubes are combined to form a hypercube of lateral size bL , the new conductance scales as

$$g(bL) = f(b, g(L)). \quad (9.19)$$

Setting $b = 1 + \epsilon$ for infinitesimal ϵ and differentiating we obtain

$$d \log g(L) / d \log L = \beta(g(L)), \quad (9.20)$$

with $\beta(g(L)) = df(b, g(L))/db|_{b=1}$.

- At large and small g one uses the expected asymptotic behavior. For large g , using macroscopic transport theory one obtains, as above,

$$G(L) = \sigma L^{d-2}, \quad (9.21)$$

and then

$$\lim_{g \rightarrow \infty} \beta(g) = d - 2. \quad (9.22)$$

In contrast, for small g exponential localization is probably valid, so that

$$g = g_\alpha \exp(-\alpha L), \quad (9.23)$$

i.e. the asymptotic behavior as $g \rightarrow 0$ or $\log(g) \rightarrow -\infty$ is

$$\beta(g) \sim -\alpha L = \log(g/g_\alpha). \quad (9.24)$$

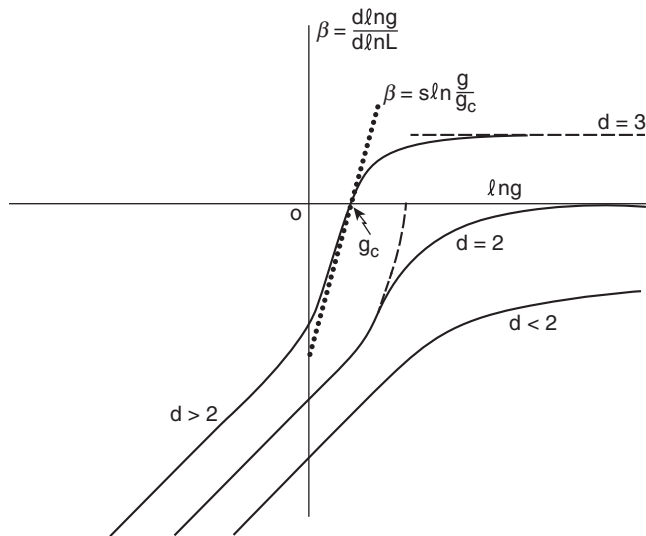


Figure 9.3 Plot of $\beta(g)$ as a function of $\log(g)$ for $d < 2$, $d = 2$, and $d > 2$, where $g(L)$ is the normalized ‘local conductance’. From Abrahams *et al.* (1979).

The sketch of the universal curve $\beta(g)$ is presented in Figure 9.3 for $d = 1, 2, 3$. One can use the perturbation theory in g (i.e. inverse of the strength of disorder) to show that in fact for small g ,

$$\beta(g) = \log(g/g_\alpha)(1 + \alpha g + \dots). \quad (9.25)$$

Steepening of the slope for small g combined with the asymptotic behavior for large g is evidently responsible for the Anderson transition in three dimensions. Perturbation theory in g^{-1} (i.e. in the disorder strength) leads, on the other hand, to

$$\beta(g) = d - 2 - a/g + \dots, \quad (9.26)$$

for $d \neq 2$. This calculation is rather complex in two dimensions. Nevertheless, Abrahams *et al.* (1979) argue that $\beta(g) \sim 1/g$, in accordance with eqn (9.26). The consequences of their analysis can be summarized as follows.

- For $d > 2$, $\beta(g)$ is zero at $g_c \sim 1$, signaling the mobility edge, where the Anderson transition occurs. In the vicinity of g_c we can approximate $\beta(g) = s \log(g/g_c)$ with $s > 1$, and since $\alpha > 0$ we can integrate β from a microscopic $g_0 > g_c$ and L_0 to obtain

$$\sigma \sim A \frac{e^2}{\hbar} \frac{g_c}{L_0^{d-2}} \left(\log \frac{g_0}{g_c} \right)^{(d-2)/s}, \quad (9.27)$$

Denoting $\epsilon = \log(g_0/g_c) \simeq (g_0 - g_c)/g_c$, one obtains in the localized regime

$$g \simeq g_c \exp(-A|\epsilon|^{1/s} L/L_0),$$

which implies that the critical exponent describing the critical divergence of the localization length is $\nu = 1/s < 1$.

- For $d = 2$, no critical behavior is expected. Instead, we expect a crossover from the regime of exponential behavior for small g to logarithmic at large g . Translated into properties of wave functions, this means that infinitesimally small disorder in two dimensions causes localization, which, however, is algebraic at small disorder strength, crossing over to exponential at large disorder. It should be stressed that so far there is no rigorous mathematical proof of these statements.

Note that the scaling approach presented above is quite general and should remain valid for interacting, or at least weakly interacting, Fermi systems, which we discuss in the next section.

9.2.6 Metal–insulator transition: interplay between disorder and interactions

Generally speaking, a metal–insulator transition is characterized by the localization of the charge carriers thus preventing electronic transport. In the previous section we saw how disorder can induce such a transition via Anderson localization (Anderson, 1958). But in the absence of disorder, strong repulsive interactions between electrons can also lead to localization in the form of a MI phase (Mott, 1968a). The question of the simultaneous presence of disorder and interactions constitutes an important and complex many-body problem that is still far from being understood (Byczuk *et al.*, 2010). Electronic phenomena in the intermediate- and strong-coupling regimes in disordered media are described by the disordered Anderson–Hubbard Hamiltonian:

$$\hat{H} = \sum_{\langle i,j \rangle, \sigma} t_{ij} \hat{f}_{i,\sigma}^\dagger \hat{f}_{j,\sigma} + \sum_{i,\sigma} \mu_i \hat{n}_{i,\sigma} + U \sum_i \hat{n}_{i,\uparrow} \hat{n}_{i,\downarrow} \quad (9.28)$$

where the t_{ij} is the hopping matrix element between neighboring sites, $\hat{f}_{i,\sigma}^\dagger$ is the fermionic creation operator for an electron with spin $\sigma = \{\uparrow, \downarrow\}$ in the Wannier state i , U is the local Coulomb interaction, and $\hat{n}_{i,\sigma}$ is the particle number operator.

For weakly correlated electrons, however, most of the physics can be explained using Landau–Fermi liquid theory (Landau 1957a, 1957b, 1959), in which the elementary particles are not the individual electrons, but electrons dressed by the density fluctuations around them. Initially, it was believed that weak disorder would not modify the essentials of this picture, and a Fermi liquid theory for electrons in disordered solids was formulated and termed the Fermi glass theory (Anderson, 1970; Freedman and Hertz, 1977). According to this approach, Landau’s quasiparticle description is still valid in the presence of disorder but the quasiparticle wave functions are not extended as in the translationally invariant case; they have no long-range coherence and may be even localized. Each quasiparticle is viewed as a single entity moving in the self-consistent field of all the other quasiparticles, and the resulting theory has the form of a mean-field theory for the quasiparticles.

More recently, it was proved, by applying perturbation theory to the lowest order in the interaction strength, that even weak disorder leads to surprisingly singular corrections to the electronic density of states near the Fermi surface and to transport properties (Altshuler and Aronov, 1979a, 1979b; Altshuler *et al.*, 1980; Fukuyama, 1980). Further discussion about the role of interactions was stimulated by Shepelyansky (1994), who considered two interacting particles in a random potential, arguing that there is an interaction-induced enhancement of the two-particle localization length as compared to the non-interacting case. The lines of this work have been developed further (Imry, 1995; Frahm *et al.*, 1995; Weinmann *et al.*, 1995; von Oppen *et al.*, 1996; Martin *et al.*, 1996; Jacquod and Shepelyansky, 1997). A Fermi liquid approach for finite densities was suggested by Imry (1995), and later developed by von Oppen *et al.* (1996) and Jacquod and Shepelyansky (1997). This reduced the problem to the study of the delocalization of few quasiparticles above the Fermi sea.

Several groups have studied in more detail the interplay between disorder and repulsive interactions in the regime where the Fermi liquid becomes unstable as the MI state is approached by increasing the interactions. In other words, investigation has taken place of the crossover between a Fermi glass, which involves Anderson localized states populated with the restriction of the Pauli principle, and an MI, involving states for which repulsion dominates over kinetic energy and disorder.

For example, in one dimension DMRG studies were performed for spinless fermions with nearest-neighbor (NN) interactions in a disordered mesoscopic ring (i.e. with periodic boundary conditions) (Schmitteckert *et al.*, 1998), and for spin- $\frac{1}{2}$ electrons in a ring described by the half-filled Hubbard–Anderson model (Gambetti-Césare *et al.*, 2002). Spinless fermions with Coulomb repulsion (reduced to NN repulsion) in two dimensions (Benenti *et al.*, 1999; Waintal *et al.*, 2000) were also studied. This collection of studies shows that as interactions become comparable with disorder, delocalization does takes place. In a 1D ring it leads to the appearance of persistent currents. In two dimensions, the delocalized state also exhibits an ordered flow of persistent currents. This is believed to constitute a novel quantum phase corresponding to the metallic phase observed for a similar range of parameters in experiments with, for instance, a gas of holes in GaAs heterostructures (Abrahams *et al.*, 2001).

Another subject of intense investigation concerns metal (Fermi liquid)–insulator transitions driven by disorder in three dimensions. A theoretical description of this phenomenon goes back to the seminal works of Efros and Shklovskii (1975, 1976, 1981) and MacMillan (1981). In this context, results of experiments on disordered alloys (Lee *et al.*, 1998; Lee *et al.*, 2000) allowed determination of the critical exponents that govern the conductivity dynamics on both sides of a quantum phase transition in a disordered electronic system. Weakly doped semiconductors provide a good model of a disordered solid, and their critical behavior at the metal–insulator transition has been closely studied (see Paalanen *et al.* (1983) and Bogdanovich *et al.* (1999)). Results for various forms of electronic glass—from Fermi glass (with negligible effects of Coulomb repulsion) to Coulomb glass (dominated by the electronic correlations) (Davies *et al.*, 1982; Davies and P. A. Lee, 1984; Pollak and Ortúñ, 1985)—were obtained in the group of Dressel (Hering *et al.*, 2005; Scheffler *et al.*, 2005).

Dynamical mean-field theory (DMFT) has become a good method to study electronic phenomena in the intermediate- and strong-coupling regimes (Byczuk *et al.*, 2010). With this method, the paramagnetic ground-state phase diagram of eqn (9.28), at half filling and

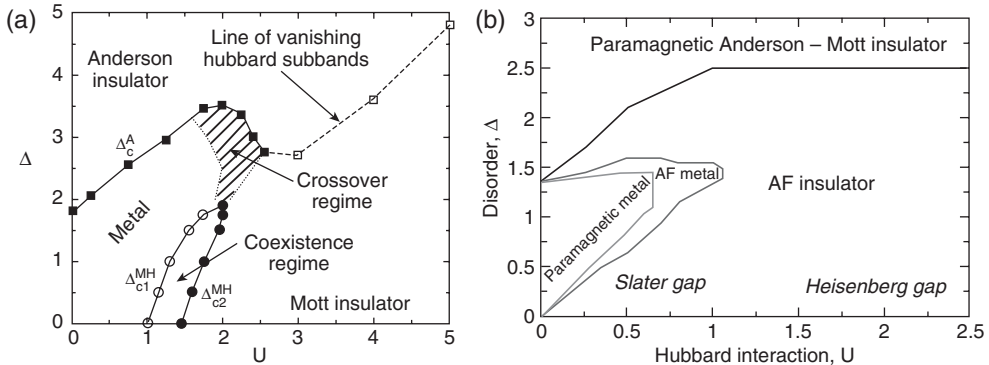


Figure 9.4 (a) Paramagnetic and (b) magnetic phase diagram of the Anderson–Hubbard model, eqn (9.28), at half filling using DMFT and local density of states. From Byczuk *et al.* (2005) and Byczuk *et al.* (2009), respectively.

for arbitrary interaction and disorder strength, has been calculated (Byczuk *et al.*, 2005), with a geometric average over the disorder of the local density of states (see Figure 9.4(a)). Competition between Anderson insulator and MI appears in this analysis. In Byczuk *et al.* (2009), the antiferromagnetic ordering was considered and the magnetic ground-state phase diagram of eqn (9.28) was found (see Figure 9.4(b)).

9.2.7 Disordered interacting Bose systems: dirty bosons problem

The subject of localization in disordered strongly interacting bosonic systems was analysed in the seminal paper of Fisher *et al.* (1989). The model under consideration was the disordered Bose–Hubbard Hamiltonian at zero temperature

$$\hat{H} = \sum_{\langle i,j \rangle} t_{ij} \hat{b}_i^\dagger \hat{b}_j + h.c. + \sum_i \mu_i \hat{n}_i + \frac{U}{2} \sum_i \hat{n}_i (\hat{n}_i - 1). \quad (9.29)$$

The chemical potential $\mu_i = \mu + \delta\mu_i$ included an average chemical potential to fix the total number of bosons and a disordered potential $\delta\mu_i$ which was taken either to be uniformly distributed between $-\Delta$ and Δ or with a Gaussian distribution. For diagonal disorder $t_{ij} = t$, Fisher *et al.* (1989) treated tunneling as a perturbation and derived the phase diagram of the system in the $\mu/U-t/U$ plane for any dimension. In the presence of disorder, three possible ground states were predicted: (i) an incompressible MI for integer filling factor with a gap for particle–hole excitations, (ii) a superfluid phase with the usual off-diagonal long-range order, and (iii) a gapless Bose glass (BG) insulator with finite compressibility, exponentially decaying superfluid correlations in space, and infinite superfluid susceptibility. This phase bears some similarity to the Fermi glass phase that appears for interacting fermions in the presence of disorder.

Fisher *et al.* also predicted that the BG phase would most likely always appear between the Mott and the superfluid phases, as depicted schematically in Figure 9.5. Furthermore, using scaling theory the relation between critical exponents and dimensionality was

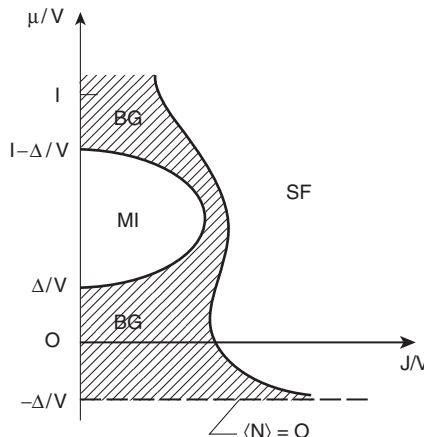


Figure 9.5 Predicted zero-temperature phase diagram for the disordered boson lattice model for weak-bounded disorder, $\Delta/V < 1/2$, where V accounts for the non-linear contact interactions and J is the tunneling rate (which we denote U and t , respectively). BG, MI and SF account for Bose glass, Mott insulator and superfluid, respectively. From Fisher *et al.* (1989).

worked out. Previously, the onset of superfluidity in a random potential was also studied in one dimension by Giamarchi and Schulz (1988), using the renormalization group approach and treating disorder as a perturbation. The existence of a localized–superfluid transition was shown and universal power laws for correlation functions on the transition line were found.

After these seminal studies the question of whether a direct transition between the MI phase and the superfluid phase is possible in the presence of disorder has been intensively studied for more than 20 years. Several papers treating the problem of disordered bosonic systems for both weak and strong disorder, have appeared without reaching a converging result. Finally, however, this question appears to have been solved by Pollet *et al.* (2009), who confirmed the original prediction of the absence of a direct SF–MI transition.

Before sketching the proof, we briefly report some of the extensive work that has dealt with this problem. Singh and Rokhsar (1992), using a real-space renormalization group in one and two dimensions, showed that when weak disorder is introduced a direct transition from the MI to the superfluid occurs, so that infinitesimally weak disorder does not stabilize a Bose glass at commensurate filling. The Bose glass was found beyond a threshold disorder, in contradiction with the arguments of Fisher *et al.* (1989). By mapping the disordered bosonic system in the limit of hard bosons onto a quantum spin- $\frac{1}{2}$ XY model with transverse random field and using real-space renormalization group methods (Zhang and Ma, 1992; Zhang and Wang, 1993; Zhang, 1993), it was concluded that randomness is always relevant in 1D systems, while in two and three dimensions there is a critical amount of disorder below which the superfluid phase is stable. It was also stated that there is only one universality class for the SF–BG transition. Other methods leading to the existence of a direct transition included (i) a 2D path-integral quantum Monte Carlo approach in Krauth *et al.* (1991), contradicting the original picture of disorder of Fisher *et al.* (1989) and Giamarchi and Schulz (1988), but in agreement with the results obtained using a real-space renormalization

group approach by Singh and Rokhsar (1992); (ii) DMRG in one dimension in Pai *et al.* (1996); (iii) quantum Monte Carlo simulations in two dimensions by Kisker and Rieger (1997); (iv) a mean-field theory approach (Pázmándi *et al.*, 1995).

Using Monte Carlo techniques—the world-line algorithm—in Scalettar *et al.* (1991), the first convincing evidence of a second insulating phase in one dimension: the Anderson glass phase was presented. The Anderson-glass phase appears at weak couplings where the interactions compete with the disorder and tend to delocalize the bosons, contrary to what happens in the Bose glass phase, which appears at strong couplings where disorder and interactions cooperate. Moreover, these two phases differ substantially in the nature of the boson-density distribution: in the Bose glass phase, the density is reasonably uniform while in the Anderson-glass phase, boson-density correlations are expected to decay exponentially. The existence of two such separate insulating phases was conjectured previously (Giamarchi and Schulz, 1988); for a detailed review of the different models see for example Lewenstein *et al.* (2007) and references therein.

In contrast, a transition via the Bose glass phase was indicated, for instance, in Wallin *et al.* (1994) and Prokof'ev and Svistunov (2004) using continuous Monte Carlo simulations, in Kim and Wen (1994) using renormalization group methods, in Freericks and Monien (1996) using a strong-coupling expansion for the phase boundary of the MI, and in Rapsch *et al.* (1999) with an improved application of the DMRG with respect to Pai *et al.* (1996). It is worth noticing that in the results of Rapsch *et al.* (1999) there is no indication of a qualitative difference between the glass phase at small or large values of the repulsion, i.e. between Anderson and Bose glass phases.

Thus, from these collections of contradicting results for the problem of dirty bosons, one can grasp the difficulties entailed in disordered systems. The controversy seems to have been solved, however, by Pollet *et al.* (2009) where, using the theorem of inclusions, the authors showed in a simple and beautiful way that for any system (bosons or fermions) with generic bounded disorder, a direct transition between a gapless (superfluid) phase and a fully gapped (MI) phase is not possible, a finding that is consistent with recent numerical quantum Monte Carlo simulations.

The theorem of inclusions is in fact, more general; it refers to arbitrary phase transitions between two given phases A and B in the presence of *generic bounded* disorder, i.e. $P(\mu_i) \neq 0$ for $\mu_i \in [-\Delta, \Delta]$. If the position of the boundary between the two phases, denoted Δ_c , changes as a function of the model of disorder, then the next theorem applies (see Pollet *et al.* (2009) and also Fisher *et al.* (1989) and Freericks and Monien (1996) for an early account):

Theorem 9.2. Theorem of inclusions *For a given phase transition between the phases A and B in a system with generic bounded disorder, there exist rare but arbitrarily large inclusions of the phase $A(B)$ inside $B(A)$ across the transition line.*

An immediate consequence of the above theorem is that there must be an intermediate phase between the superfluid and the MI phases. If that was not the case, and a direct transition was possible, the theorem of inclusions would apply, implying that there were arbitrarily large, although very unusual, gapped regions inside the superfluid phase as well as arbitrarily large, but rare, gapless regions inside the Mott phase. Since the fully gapped Mott is gapped with respect to ground state and any excitation, that simply cannot occur.

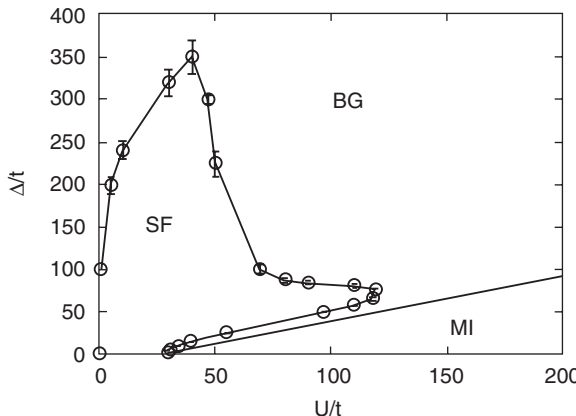


Figure 9.6 Predicted phase diagram of the disordered 3D Bose–Hubbard model at unity filling where BG, SF and MI refer to Bose glass, superfluid and Mott insulator, respectively. From Gurarie *et al.* (2009).

Conversely, if Theorem 9.2 does not apply and the transition is direct, the critical point Δ_c between Mott and superfluid, cannot depend on the model of disorder. Again, this is not the case, since we know that for sufficiently large disorder amplitude, the MI phase becomes unstable, so the transition line has a dependence on the probability distribution of the disordered model. Therefore, a Bose glass should always intervene in the MI–SF transition.

We could ask which are the consequences of Theorem 9.2 for the transition between the gapless Bose glass phase and the MI phase. In this case, the transition must be of the so-called Griffiths type; that is, it is entirely driven by statistically rare fluctuations, where the transition point Δ_c does not depend on the model of disorder, and the theorem of inclusions does not therefore apply (Gurarie *et al.*, 2009). This implies that in the vicinity of the critical point, the gapless phase must be ‘glassy’, containing well separated gapless islands embedded in a gapped state, while the disorder bound protect the gapped phase. Griffiths transitions are the only possibility for gapped-to-gapless transitions.

Assuming these results, the phase diagram of the disordered 3D Bose–Hubbard Hamiltonian at unit filling has been calculated numerically using QMC techniques in Gurarie *et al.* (2009); it is shown in Figure 9.6.

9.2.8 Disordered gas of hard-core bosons in 1D

De Martino *et al.* (2005) took a different approach to the dirty bosons problem in one dimension. By mapping a disordered (hard-core) bosonic system to a *non-interacting* disordered fermionic system, one can take advantage of the known results on Anderson localization in electronic systems to characterize the disorder effects. To this end, it is necessary to first perform a Jordan–Wigner transformation and then a Bose–Fermi mapping (these procedures are discussed in Chapters 5 and 6).

The starting point is the lattice description of bosons via the disordered Bose–Hubbard model, eqn (9.29), with a confining harmonic potential included in the chemical potential

$\mu_l = \delta\mu_l + bl^2$, which applies immediately to optical-lattice experiments with atoms. Since in ultracold atoms in optical lattices, hopping disorder is suppressed when compared to the on-site disorder, one can assume, as in the previous subsection, that $t_{ij} = t$. The on-site disorder is assumed to be distributed according to a Gaussian ensemble, such that

$$\overline{\delta\mu_l} = 0, \quad \overline{\delta\mu_l \delta\mu_{l'}} = \Delta \delta_{ll'}, \quad (9.30)$$

where the bar denotes the average over the disorder, and Δ the disorder strength. For most of the disorder mechanisms used for ultracold atoms, precise estimates of Δ are available (see Section 9.3).

Following De Martino *et al.* (2005), in the hard-core boson limit, i.e. $U \rightarrow \infty$, the model of eqn (9.29) becomes equivalent to a 1D XY spin chain. This, in turn, can be mapped to a non-interacting lattice fermion model by means of the Jordan–Wigner transformation (see Chapter 5):

$$\hat{b}_l = e^{i\pi \sum_{j < l} \hat{f}_j^\dagger \hat{f}_j} \hat{f}_l, \quad (9.31)$$

where \hat{f}_l are lattice fermion operators. The resulting non-interacting fermionic Hamiltonian reads

$$\hat{H} = \sum_l \left(-t_l [\hat{f}_{l+1}^\dagger \hat{f}_l + \hat{f}_l^\dagger \hat{f}_{l+1}] + \mu_l \hat{f}_l^\dagger \hat{f}_l \right). \quad (9.32)$$

As pointed out by Girardeau (1960), there is a one-to-one mapping between the many-body bosonic and fermionic wave functions

$$\Phi_\nu^B(l_1, \dots, l_N) = |\Phi_\nu^F(l_1, \dots, l_N)|. \quad (9.33)$$

The mapping thus allows us to compute the eigenenergies E_ν for an N -boson eigenstate Φ_ν^B in terms of the non-interacting fermionic Hamiltonian (eqn (9.32)). It is enough to calculate the single-particle energies $\mu_i^{(j)}$ for the j^{th} fermion in the single-particle solutions Ψ_i to eqn (9.32), and from the Pauli exclusion principle we reach $E_\nu = \sum_{j=1}^N \mu_i^{(j)}$. The many-body fermionic wave function $\Phi_\nu^F(l_1, \dots, l_N)$, and hence also the bosonic one up to a sign difference, is then a Slater determinant, $\det[\Psi_i(l_j)]/\sqrt{N!}$. In fact, the correlation functions of the particle density and the local density of states of the interacting bosonic case coincide with the non-interacting fermionic ones, because they only depend on the modulus square $|\Phi_\nu^B|^2$ of the wave function. The local density of states read:

$$\rho(\mu, l) = \sum_\nu \sum_{l_2, \dots, l_N} \delta(\mu - E_\nu) |\Phi_\nu^B(l, l_2, \dots, l_N)|^2.$$

Moreover, the density of states per site for bosons and fermions also coincide and in a lattice with L sites this equals to $\rho(\mu) = \sum_{l=1}^L \rho(\mu, l)/L$. The momentum distribution is not equal for bosons and fermions but the mapping allows for a simple calculation of the disorder-averaged boson momentum distribution.

The momentum distribution averaged over the disorder,

$$\hat{n}(p) = \frac{1}{N} \sum_{ll'} e^{-ip(l-l')d} \langle \hat{b}_l^\dagger \hat{b}_{l'} \rangle. \quad (9.34)$$

where d is the lattice spacing, can be calculated in a simple and exact way via the Bose–Fermi mapping (De Martino *et al.*, 2005). Using the Jordan–Wigner transformation and Wick’s theorem, eqn (9.34) can be written as the so-called Töplitz determinant for a given disorder realization. For $l > l'$, one finds $\langle \hat{b}_l^\dagger \hat{b}_{l'} \rangle = 2^{l-l'-1} \det[G^{(l,l')}]$, where the $(l-l') \times (l-l')$ matrix has the entries $G_{i,j}^{(l,l')} = \langle \hat{f}_{l'+i}^\dagger \hat{f}_{l'+j-1} \rangle - \delta_{i,j-1}/2$. De Martino *et al.* (2005) computed eqn (9.34) numerically for fixed disorder $\{\delta\mu_l\}$ and arbitrary trap potential, and then averaged it over different disorder realizations. Notice that in this case one deals with a single (fermionic) particle problem instead of the one of interacting dirty bosons. The results for $N = 50$ ^{87}Rb atoms in a harmonic axial trap with $b = 0.01t$ are presented in Figure 9.7. It is clearly seen that disorder has a significant effect on the momentum distribution: one observes significant transfer to large momenta and a decrease of the zero-momentum peak; see inset in Figure 9.7.

In the homogeneous case, where $b = 0$ and there is no disorder, the momentum distribution is known to possess a singularity $\hat{n}(p \rightarrow 0) \propto |p|^{-1/2}$ due to the one-particle density matrix $\rho(x - x') \propto |x - x'|^{-1/2}$ for $|x - x'| \rightarrow \infty$ (Lenard, 1964; Vaidya and Tracy, 1979; Gangardt, 2004), but in the presence of disorder, $\hat{n}(0)$ remains finite. By calculating

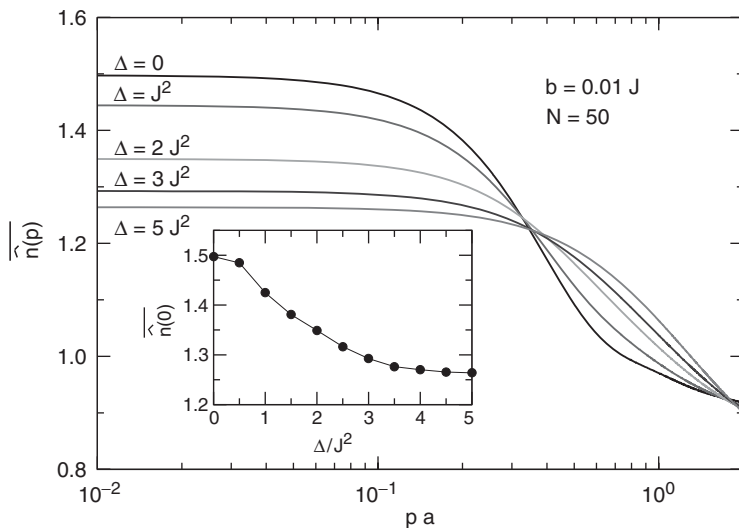


Figure 9.7 Momentum distribution (eqn (9.34)) for several values of the disorder strength Δ (here $J \equiv t$ and $a \equiv d$) for $N = 50$ ^{87}Rb atoms in a harmonic axial trap. For the disorder average, at most 300 disorder realizations were sufficient for convergence, and L was chosen to be large enough to ensure L -independence. Note the linear–logarithmic scale. Inset: zero-momentum peak as a function of disorder strength. From De Martino *et al.* (2005).

numerically the full momentum distribution for a ring (De Martino *et al.*, 2005) it has been shown the complete destruction of quasi-long-range order by disorder and the flattening of the momentum distribution for sufficient strong disorder.

9.3. Realization of disorder in ultracold atomic gases

As discussed in Chapter 3, the possibility to engineer, among other parameters, the external potential offers unprecedented possibilities for the study of disorder-related phenomena in ultracold gases. Although most of the methods presented here can be extrapolated for fermions and mixtures, for simplicity we focus here on bosonic systems. The experimental implementation of such types of disorder in the weakly interacting ultracold gases is reviewed in Section 9.4 and Section 9.5 deals with the strongly interacting case.

The different methods to create disorder in ultracold atoms can be summarized as follows:

9.3.1 Superlattices and quasicrystals

By superimposing laser beams from different directions and with different frequencies, it is possible to generate a huge variety of lattice geometries in a very controlled way. For instance, the use of two-color superlattices has been proposed (Diener *et al.*, 2001; Damski *et al.*, 2003b; Roth and Burnett, 2003b; Roth and Burnett, 2003a), i.e. the superposition of two standing-wave lattices with incommensurate wavelengths as a form of quasi-disorder. In one dimension, the bichromatic potential reads:

$$V(x) = V_1 \sin^2(k_1 x) + V_2 \sin^2(k_2 x + \phi), \quad (9.35)$$

where $k_i = 2\pi/\lambda_i$ ($i = 1, 2$) are the lattice wavenumbers, with λ_i the wavelength of the lasers forming the corresponding optical lattice, V_i is the depth of each of the lattices, and ϕ an arbitrary phase. In general, it is assumed that $V_1 \gg V_2$, i.e. the potential at wavelength λ_1 corresponds to the main lattice, which is perturbed by a weak optical lattice with an incommensurate wavelength λ_2 . The ratio between the wavenumbers of the main and secondary lattice, $q = k_2/k_1$, determines the (quenched) pseudorandomness of the system. In the ideal case, the wavelengths of both lattices should be incommensurate, leading to an irrational value for q . Nevertheless, in experiments the wavelengths can only be measured with a finite number of digits, leading to rational q and, moreover, real systems have finite size. The system will therefore be effectively incommensurate if the size of the system does not exceed the periodicity of the bichromatic lattice and if it extends over several lattice sites (Modugno, 2009). Experimental implementations of pseudodisorder using bichromatic lattices in ultracold atomic setups have been performed in a series of experiments (Fallani *et al.*, 2007; Roati *et al.*, 2008; Deissler *et al.*, 2010).

Ultracold atoms in bichromatic lattices can be mapped, in the tight-binding limit, onto the Harper (Harper, 1955) or the Aubry–André model (Aubry and André, 1980; Thouless, 1983) as shown in Drese and Holthaus (1997) and very recently in Roati *et al.* (2008) and Modugno (2009). The Aubry–André Hamiltonian reads (Ingold *et al.*, 2002; Roati *et al.*,

2008; Modugno, 2009):

$$\hat{H} = -t \sum_j (|w_j\rangle\langle w_{j+1}| + |w_{j+1}\rangle\langle w_j|) + \Delta \sum_j \cos(2\pi q j + \phi) |w_j\rangle\langle w_j|, \quad (9.36)$$

where $|w_j\rangle$ is the Wannier state localized at site j , t is the tunneling energy, Δ is the amplitude of the disorder, $q = k_2/k_1$, and ϕ an arbitrary phase.

More complex topologies in two and three dimensions, the so-called quasicrystal optical lattices, have also been explored in two and three dimensions (Guidoni *et al.*, 1997, 1999; Guidoni and Verkerk, 1998; Sanchez-Palencia and Santos, 2005). These systems exhibit long-range order but not translational invariance. An example of a laser configuration (Sanchez-Palencia and Santos, 2005) that gives rise to a quasicrystal lattice consists of N_b laser beams arranged on the xy plane with N_b -fold symmetry rotation. The polarization ϵ_j of laser j with wavevector \mathbf{k}_j is linear and makes an angle α_j with the xy plane. The optical potential in this case is:

$$V(\mathbf{r}) = \frac{V_0}{|\sum_j \epsilon_j|^2} \left| \sum_{j=0}^{N_b-1} \epsilon_j \exp^{-i(\mathbf{k}_j \cdot \mathbf{r} + \varphi_j)} \right|^2, \quad (9.37)$$

where $\mathbf{r} = [x, y]$, $0 \leq \epsilon_j \leq 1$ stand for different laser intensities and φ_j are the corresponding phases.

9.3.2 Speckle patterns

Truly random potentials for ultracold atoms can be achieved using speckle light patterns. Speckle potentials are formed as follows (Goodman, 2007): a coherent laser beam is diffracted through a ground-glass plate and focused by a converging lens. The ground-glass plate transmits the laser light without altering the intensity, but imprinting a random phase profile on the emerging light. The complex electric field $\mathcal{E}(\mathbf{r})$ on the focal plane results from the coherent superposition of partial waves, with random phases—uncorrelated and uniformly distributed between 0 and 2π —generated at different points of the diffusor. This superposition leads to constructive or destructive interferences (see Figure 9.8(a)–(d)). The field is thus a Gaussian random process. In such a light field, atoms with a resonance slightly detuned with respect to the laser light experience a disordered potential $V(\mathbf{r})$. This potential, up to a shift introduced to ensure that its statistical average $\langle V \rangle$ vanishes, is proportional to the light intensity, $V(\mathbf{r}) = \pm(|\mathcal{E}(\mathbf{r})|^2 - \langle |\mathcal{E}|^2 \rangle)$.

Although the electric field $\mathcal{E}(\mathbf{r})$ is a complex Gaussian random variable, the disordered potential $V(\mathbf{r})$ is not Gaussian itself, and its single-point probability distribution is a truncated, exponentially decaying function,

$$P(V(\mathbf{r})) = \frac{1}{eV_R} e^{(-V(\mathbf{r})/V_R)} \Theta(V(\mathbf{r})/V_R + 1), \quad (9.38)$$

where $|V_R| = \sqrt{\langle V^2 \rangle}$ is the disorder amplitude and Θ is the Heaviside function. Both the modulus and sign of the potential induced on atoms by V_R can be controlled experimentally.

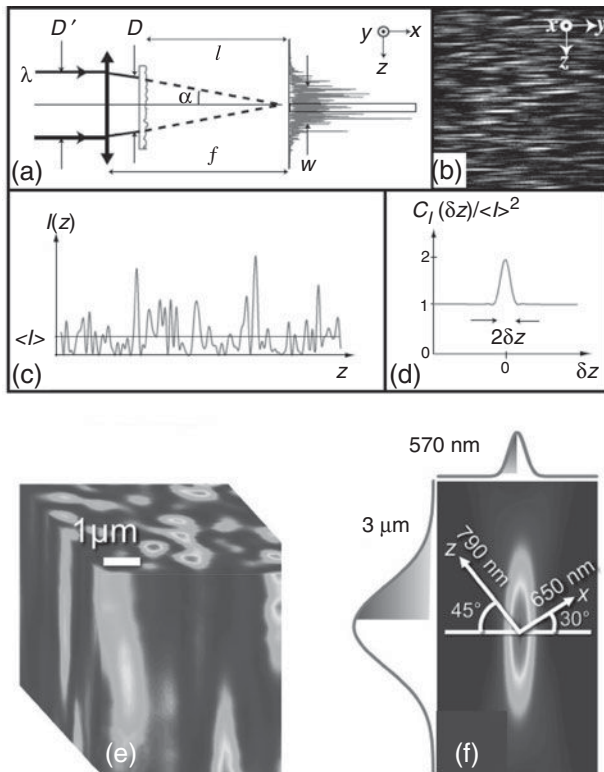


Figure 9.8 (a) Experimental realization of the speckle pattern, (b) image of an anisotropic speckle pattern to induce a 1D random potential along z , (c) zoom of the speckle pattern in the boxed region of (a), and (d) intensity autocorrelation function of the speckle potential, from Clément *et al.* (2006). (e) Sample of the volume of the 3D speckle intensity distribution, and (f) radii of the autocorrelation distribution along transverse and speckle propagation directions in the 3D speckle, from White *et al.* (2009).

The modulus is proportional to the incident laser intensity while the sign is determined by the detuning of the laser relative to the atomic resonance. V_R is positive for ‘blue-detuned’ laser light and negative for ‘red-detuned’ light.

The two-point autocorrelation function of the disordered potential $C_2(\mathbf{r}) = \langle V(\mathbf{r})V(\mathbf{r}') \rangle$ is determined by the overall shape of the ground-glass plate but not by the details of its asperities. It is thus also controllable experimentally. The intensity correlation length or disorder length is given by the half-width of C_2 and the average is taken over the disorder. There is, however, a fundamental constraint: since speckle potentials result from interference between light waves of wavelength λ coming from a finite-size aperture of angular width 2α , as indicated in Figure 9.8(a), they do not contain Fourier components beyond a value $2k_c$, where $k_c = (2\pi/\lambda) \sin(\alpha)$. To take into account the finite size of the diffusor, the electric field at the observation plane, $\mathcal{E}_P(\mathbf{r})$, should be transformed by Fourier transform to the electric field at the diffusor, $\mathcal{E}_D(\mathbf{r})$, and the latter should be multiplied by a window function $W(\mathbf{r})$

that takes a value different from 0 only in the region of the diffusor. The result, Fourier transformed back into the final field distribution at the observation plane, gives the random speckle intensity:

$$V_P^{\text{final}}(\mathbf{r}) = \left| F^{-1} [W(\mathbf{r}) F [\mathcal{E}_P(\mathbf{r})]] \right|^2. \quad (9.39)$$

The speckle size in each direction can be derived by applying Fresnel–Kirchoff theory of diffraction (Goodman, 2007), assuming that the diffusor is illuminated by an uniform rectangular light beam of dimensions D_x and D_y :

$$\begin{aligned} \Delta_{x(y)} &= \lambda \frac{l}{D_{x(y)}} \\ \Delta_z &\approx 7.6\lambda \frac{l^2}{D_x D_y}, \end{aligned} \quad (9.40)$$

where l is the distance from the diffusor to the sample and λ the wavelength of the incident light. Therefore, by adjusting the geometry of the set-up, Δ_y, Δ_x could be fixed larger than the transverse dimensions of the sample and, simultaneously, Δ_z could be much smaller than the longitudinal dimensions of the sample. In this way, an effective 1D speckle potential can be generated, as explained in detail in Clément *et al.* (2006). 3D speckle potentials have also been experimentally implemented (White *et al.*, 2009) as shown in Figure 9.8(e)–(f). In recent experiments (Billy *et al.*, 2008; White *et al.*, 2009), speckle sizes smaller than 1 μm are possible.

9.3.3 Random impurities and Bernoulli potentials

One can also create a disordered potential by using atoms of a second species or internal state quenched randomly at the nodes of an optical lattice (Gavish and Castin, 2005; Zoller *et al.*, 2005*b*; Massignan and Castin, 2006). These randomly distributed atoms act as point-like scatterers for the atoms of the first species that are not trapped by the optical lattice. One possibility to randomly trap the atoms of the second species is by rapidly quenching them from the superfluid to the MI phase. Experimental candidates to explore this possibility are Bose–Fermi mixtures in optical lattices.

In this approach to generate disorder, the probability distribution becomes bimodal, i.e. the on-site energies can take two values, $\mu_i = \mu_A$ or $\mu_i = \mu_B$, in the presence or absence of the impurity, respectively. The correlation length is of the order of the Wannier function, which can be smaller than the lattice spacing—of the order of 0.5 μm —if the lattice that quenches the motion of the disorder species is deep enough. Bimodal disorder, often termed the ‘Bernoulli potential’, is particularly interesting for the study of the spin-glass transition in the 2D Ising model (Kawashima and Rieger, 2004). The impurity potential can be written in one dimension as (Lifshits *et al.*, 1988; Sanchez-Palencia *et al.*, 2008):

$$V(x) = V_0 \sum_j g(x - x_j) \quad (9.41)$$

where $g(X)$ is a peaked function centered at $X = 0$, positive and bounded from above, $0 \leq g(X) \leq 1$, and the locations of the impurities are denoted by x_j .

9.3.4 Random interatomic interactions

The generation of disorder in ultracold atoms can also be induced by generating bounded disorder in the strength of the on-site interparticle interactions U_i in eqn (9.29) (Kantian, 2004; Gimperlein *et al.*, 2005). The idea is to exploit the significant modifications of the scattering properties of two atoms that can be induced close to Feshbach resonances by slight modifications of the magnetic field—for a review see Chin *et al.* (2010). In this scenario, a spatially random magnetic field will induce random local interatomic interactions. Experimentally, this can be achieved by placing the system at the verge of a Feshbach resonance by means of an offset magnetic field in the presence of a spatially random magnetic field, which appears, for instance, in magnetic microtraps and atom chips as a result of the roughness of the underlying surface (see, for example, Lewenstein *et al.* (2007) and references therein). Controllable disorder on the level of next-neighbor interactions can be generated by means of tunneling-induced interactions in systems with local disorder (Sanpera *et al.*, 2004); details can be found in Section 9.6, which is devoted to disordered Bose–Fermi mixtures.

9.4. Disordered Bose–Einstein condensates

9.4.1 Weakly interacting regime: disorder-induced trapping and Anderson localization

In the weakly interacting regime the dynamics of Bose–Einstein condensates can be described by the Gross–Pitaevskii equation:

$$i\hbar \frac{d}{dt} \Psi(\mathbf{r}, t) = -\frac{\hbar^2}{2m} \nabla^2 \Psi(\mathbf{r}, t) + [V_t(\mathbf{r}) + V_d(\mathbf{r}) + g|\Psi(\mathbf{r}, t)|^2] \Psi(\mathbf{r}, t), \quad (9.42)$$

where Ψ is the condensate wave function and $g = 4\pi\hbar^2a/m$, with m the atomic mass and a the s -wave scattering length. The potential V_t refers to the trap potential, while V_d is the disordered random or quasirandom potential.

The first experiments on Bose–Einstein condensates in random potentials used speckles with a correlation length of several microns and were performed in the regime of relatively strong interactions and strong disorder, leading to suppression of transport due to classical reflections. Considerable effort was later invested to reduce the correlation length of the disorder and the effect of the interactions in order to reach the regime of Anderson localization.

In Lye *et al.* (2005), Schulte *et al.* (2005), Chen *et al.* (2008), and Clément *et al.* (2008), an elongated trapped condensate with repulsive interactions in the presence of a speckle potential was suddenly released, and time of flight (TOF) images were recorded for different values of the speckle height, V_R —in Schulte *et al.* (2005), the effect of a speckle pattern was superimposed on a regular 1D optical lattice. The results of these experiments reveal different regimes:

- (i) For strengths of the disorder much smaller than the chemical potential of the condensate, $V_R \ll \mu$, practically no change with respect to the standard Thomas–Fermi profile is observed.

- (ii) For intermediate values of V_R , stripes appear in the expanded density profile. The fringes are neither due to disorder-induced phase fluctuations in the trapped BEC nor to interference between a few BECs separated by potential barriers, since they are reproducible in repeated measurements when using the same realization of disorder. Instead they occur during the TOF due to the generation of phase modulations from the initial density modulations (Clément *et al.*, 2008).
- (iii) When V_R is larger than the chemical potential of the harmonically trapped condensate, the tunneling between the different minima of the random potential is strongly suppressed and the condensate breaks into ‘independent’ fragments. This array of randomly distributed condensates does not produce visible interference in TOF measurements (Hadzibabic *et al.*, 2004).

The effects of disorder in collective excitations has also been intensively studied. For instance, Lye *et al.* (2005) and Chen *et al.* (2008) excited the dipolar mode by abruptly displacing the magnetic trap in the axial direction in the presence of a disorder potential. Different behaviors were then observed:

- (i) in the absence of the speckle potential, the condensate oscillated, without damping, at the frequency of the trap
- (ii) for $V_R \ll \mu$, slightly damped oscillations were obtained with the same frequency as in the undamped case
- (iii) for intermediate V_R , strong damping of the oscillations was observed
- (iv) for high values of V_R , the atomic cloud did not oscillate and remained pinned to the side of the magnetic trap, behavior related with the fragmentation of the BEC.

In the quadrupolar mode, the anharmonicities of the random potential result in frequency shifts that increase with increasing V_R ; the sign and the amplitude of the shift depend on the exact realization of the speckle potential (Lye *et al.*, 2005). In Drenkelforth *et al.* (2008), the damping of Bloch oscillations induced by the broadening of the quasimomentum spectrum due to the spatially varying phase evolution of the condensate was studied both experimentally and theoretically.

Concerning transport properties, the experimental results (Fort *et al.*, 2005; Clément *et al.*, 2005) show that, while without the speckles the condensate freely expands, in the presence of a random potential with sufficiently high amplitude the growth of the root of its mean-squared size is strongly suppressed. The expansion dynamics change completely, and both the axial expansion and the center-of-mass motion are inhibited. Although this strong suppression of expansion is due to disorder-induced trapping of the BEC, it corresponds to localization due to classical reflections from large peaks of the disordered potential and not to Anderson-like localization (Clément *et al.*, 2005; Clément *et al.*, 2006; Modugno, 2006).

The absence of Anderson localization in these experiments of free expansion of a condensate in the presence of a disordered potential, has been explained (Modugno, 2006; Sanchez-Palencia, 2006; Sanchez-Palencia *et al.*, 2007; Shapiro, 2007; Sanchez-Palencia *et al.*, 2008; Akkermans *et al.*, 2008) as being mainly due to three factors:

- (i) the smoothing of the disordered potential due to the interactions
- (ii) the large value of the correlation length of the disorder L_{dis} compared with the healing length, l_{heal}
- (iii) the large strength of the disorder.

The healing length provides the typical distance over which the order parameter of the condensate recovers its bulk value when it is forced to vanish at a given point by, for instance, an impurity. It is therefore a measure of the importance of the interactions. When $l_{\text{heal}} \ll L_{\text{dis}}$ the density profile tends to follow the spatial modulations of the disordered potential and the condensate cannot localize. This means that the opposite condition, $l_{\text{heal}} \gg L_{\text{dis}}$, is necessary in order to observe Anderson localization. Nevertheless, it has been shown (Sanchez-Palencia, 2006) that this condition is not sufficient. The healing length also has to be large compared with the size of the system L , meaning that the interactions have to be negligible at the center of the condensate. Moreover, the disorder has to be sufficiently weak so as to avoid classical reflections at the edges of the condensate during expansion (Sanchez-Palencia *et al.*, 2008).

All the requirements to achieve Anderson localization of matter waves were fulfilled in Billy *et al.* (2008), where an initially trapped BEC was released to a 1D guide in the presence of a speckle potential, weak enough to assure that localization was due to many quantum reflections of small amplitude. After expansion, the atomic density of the condensate was low enough to allow interactions to be neglected, and the system was formed by a distribution of free matter waves with the momenta determined by the healing length of the initially trapped condensate. Therefore, in the presence of a disordered potential each matter wave localized, leading to a density profile with exponentially decaying tails and a localization length corresponding to that of a non-interacting particle with momentum $1/l_{\text{heal}}$. The localization length as a function of the strength of the disorder in this experiment can be seen in Figure 9.9(b). Moreover, data reported in this experiment are consistent with the existence of a crossover from exponential to algebraic localization, and therefore with the theoretical prediction of Sanchez-Palencia *et al.* (2007, 2008) of the existence of an effective mobility edge at $k = 1/L_{\text{dis}}$, k being the atomic wavevector.

A completely different approach to achieve exponential localization of matter waves was used in Roati *et al.* (2008), where a non-interacting condensate in which the scattering length was fixed to zero by means of Feshbach resonances, and which was in a quasiperiodic lattice, was employed to implement the non-interacting Harper or Aubry–André model of eqn (9.36). This model shows a sharp metal–insulator phase transition at a finite value of the quasidisorder of $\Delta/t = 2$, for maximally incommensurate ratio q (Aubry and André, 1980). Figure 9.9(a) shows that in the experiments, the transition is broadened and shifted towards higher Δ/t . Modugno (2009) performed a detailed analysis of the effect of the commensurability of the two lattices forming the quasiperiodic potential and the magnetic trap. It is also worth noticing that the quasiperiodic kicked rotor model (Casati *et al.*, 1979; Grempel *et al.*, 1984; Moore *et al.*, 1995) leads to Anderson localization for ultracold atoms in momentum space (Chabé *et al.*, 2008).

The interplay between disorder and weak interactions has also been addressed (Schulte *et al.*, 2005; Lye *et al.*, 2007; Deissler *et al.*, 2010). Schulte *et al.* (2005) reported the screening effect of repulsive non-linear interactions, while Lye *et al.* (2007) observed a blockage of the center-of-mass motion of a BEC in a 1D incommensurate optical lattice in the limit of low number of atoms, and a return into motion when the interactions increased. In Deissler *et al.* (2010) a systematic study of the role of weak interactions in a degenerate Bose gas with tunable repulsive interactions in a quasiperiodic lattice potential was performed.

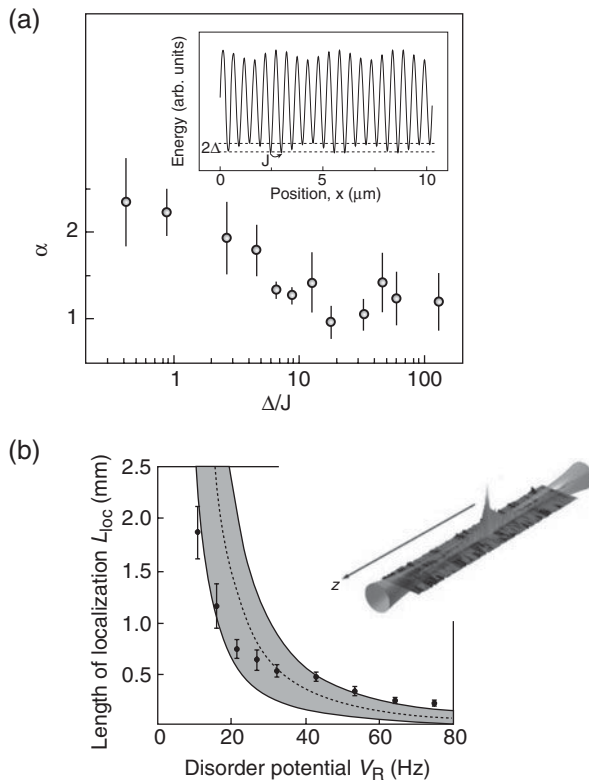


Figure 9.9 (a) Sketch of the quasiperiodic potential used in experiments on Anderson localization and the fitting parameter α of a function $\exp(-|(x - x_0)/l|^\alpha)$ to the tails of the condensate in equilibrium as a function of Δ/J (in our notation $J \equiv t$). Redrawn after Roati *et al.* (2008) by courtesy of the authors. (b) Localization length as a function of the amplitude of the disordered potential and pictorial representation of the experimental set-up. Redrawn after Billy *et al.* (2008) by courtesy of the authors.

Perhaps the simplest way to understand the properties of disordered BECs in the weakly interacting regime employs the concept of the Lifshits tail of non-interacting single-particle low-energy states, and the so-called Lifshits glass regime (Lugan *et al.*, 2007).

9.4.2 Lifshits tails and Lifshits glass regime

There is a fundamental difference between the Anderson localization for Fermi and Bose systems, even in the non-interacting case. For fermions, we are essentially interested in the conductor-insulator transition, for which the relevant states are those close to the Fermi surface. Obviously, if all single-particle states are localized, there cannot be any transport. For bosons, in contrast, we are only interested in single-particle low-energy states. For the latter at $T = 0$, we expect only occupation of the ground state, which almost certainly will be localized. Also for $T > 0$, but still below the condensation temperature, only the ground

state will be occupied macroscopically. This latter statement is not exactly true for finite systems with disorder. In such systems there can exist many localized states of energies E_ν , very close to the ground-state energy E_0 . Moreover, the difference $(E_\nu - E_0)$ typically tends to zero with the size of the system. Note that while the properties of the low-energy states are relevant for BECs, the localization of high-energy states it is not.

The problem of localization of low-energy states was rigorously treated in the seminal works of Lifshits (Lifshits *et al.*, 1988), who in particular investigated the properties of the density of states for the random Schrödinger operators

$$\hat{H} = \frac{\hat{p}^2}{2m} - \mu(\hat{x}), \quad (9.43)$$

or their corresponding lattice versions. Under quite general assumptions, the density of states exhibits a universal, dimension-independent, low-energy tail

$$n(E) \propto \exp(-A/\sqrt{(E - E_0)}). \quad (9.44)$$

The states in the tail with energies very close to E_0 are all localized, but centered at very different locations. The universal Lifshits picture thus suggests that:

- for non-interacting Bose systems at small temperatures $T > 0$, condensation will occur into the states of the Lifshits tail, with relative occupations determined by Boltzmann factors.
- for weakly interacting Bose systems at $T = 0$, a similar scenario takes place: the condensation occurs into the states of the Lifshits tail, with relative occupations determined, for instance, by a generalized Hartree–Fock theory (Lugan *et al.*, 2007).

In both cases, the corresponding quantum state consists of several co-existing, localized micro-BECs. Such a state is termed a Lifshits glass (Lugan *et al.*, 2007). Of course, a Lifshits glass is just a regime of behavior of the Bose glass phase. It differs from the Bose Anderson regime in the appearance of multiple BECs instead of a single localized one. The above scenario in one dimension has been suggested by analysis of the solutions of the Gross–Pitaevskii equation (Schulte *et al.*, 2005), where the ground state of a condensate in a disordered lattice was investigated. The Lifshits-glass scenario has been analysed more rigorously in Lugan *et al.* (2007). We closely follow this analysis below.

The starting point is a d -dimensional Bose gas at zero temperature with repulsive interactions, placed in a 1D random potential with arbitrary amplitude and correlation length. The Bose gas is trapped axially in a box of length $2L$ and radially by a 2D harmonic trap with frequency ω_\perp . The random potential $V(z)$ is taken to be a 1D speckle potential $V(z) = V_R v(z/L_{\text{dis}})$, where L_{dis} is the correlation length of the disorder and $v(u)$ is random, with a probability distribution $\mathcal{P}(v) = \Theta(v + 1) \exp[-(v + 1)]$, where Θ is the Heaviside function. Thus, v is bounded from below by $v_{\min} = -1$ and we have $\langle v \rangle = 0$ and $\langle v^2 \rangle = 1$. In addition, for a square aperture the correlation function reads

$$\langle v(u)v(u') \rangle = \text{sinc}^2 \left[\sqrt{3/2} (u - u') \right].$$

The different quantum regimes of the disordered gas are determined by the interplay between interactions and disorder.

BEC regime For strong repulsive interactions, the Bose gas is delocalized and forms a BEC. The density profile is then governed by the Gross-Pitaevskii equation (Pitaevskii and Stringari, 2003),

$$\mu = -\frac{\hbar^2}{2m\sqrt{n}} \nabla^2(\sqrt{n}) + m\omega_{\perp}^2\rho^2/2 + V(z) + gn(\mathbf{r}), \quad (9.45)$$

where $\rho(z)$ is the radial (axial) coordinate, g the coupling constant, and μ the chemical potential. In the case of a shallow radial trap ($\hbar\omega_{\perp} \ll \mu$), the radial profile is a Thomas-Fermi inverted parabola (Pitaevskii and Stringari, 2003). One finds that the BEC density has a generalized Thomas-Fermi profile:

$$n(\rho, z) \simeq \frac{\mu(\rho)}{g} \left[1 - \frac{\tilde{V}(\rho, z)}{2\mu(\rho)} \right]^2, \quad (9.46)$$

where $\mu(\rho) = \mu[1 - (\rho/R_{\perp})^2]$ is the local chemical potential, $R_{\perp} = \sqrt{2\mu/m\omega_{\perp}^2}$ is the radial Thomas-Fermi half-size and there is a *smoothed potential* $\tilde{V}(\rho, z) = \int dz' G(\rho, z') V(z - z')$ with

$$G(\rho, z) = \frac{1}{\sqrt{2}l_{\text{heal}}(\rho)} \exp\left(-\frac{\sqrt{2}|z|}{l_{\text{heal}}(\rho)}\right), \quad (9.47)$$

and

$$l_{\text{heal}}(\rho) = \hbar/\sqrt{2m\mu(\rho)} \quad (9.48)$$

being the local healing length. Different behavior occurs depending on the ratio between l_{heal} and L_{dis} :

- (i) For $l_{\text{heal}}(\rho) \ll L_{\text{dis}}$, i.e. for

$$\mu(\rho) \gg \hbar^2/2mL_{\text{dis}}^2, \quad (9.49)$$

the smoothed potential is just the random potential $\tilde{V}(\rho, z) \simeq V(z)$, and the BEC density follows the modulations of the random potential in the Thomas-Fermi regime.

- (ii) For $l_{\text{heal}}(\rho) \gtrsim L_{\text{dis}}$, the kinetic energy cannot be neglected and competes with the disorder and the interactions. The random potential is therefore smoothed, that is $\Delta\tilde{V}(\rho) < \Delta V$ where ΔV ($\Delta\tilde{V}(\rho)$) is the standard deviation of the (smoothed) random potential. The solution (eqn (9.46)) corresponds to a delocalized *disordered BEC*.

The perturbative approach is valid when $\mu(\rho) \gg \Delta\tilde{V}(\rho)$. From the expression for \tilde{V} , we write $\Delta\tilde{V}(\rho) = V_R \sqrt{\Sigma^0(L_{\text{dis}}/l_{\text{heal}}(\rho))}$. For the speckle potential, one can approximate the correlation function to $V_R^2 \exp(-z^2/2L_{\text{dis}}^2)$, and one finds (Sanchez-Palencia, 2006):

$$\Sigma^0(\tilde{\sigma}_R) = \tilde{\sigma}_R^2 + (1 - 2\tilde{\sigma}_R^2)\tilde{\sigma}_R e^{\sigma_R^2} \int_{\sigma_R}^{\infty} d\theta e^{-\theta^2}, \quad (9.50)$$

with $\tilde{\sigma}_R = L_{\text{dis}}/l_{\text{heal}}(\rho)$. In the center, at $\rho = 0$ or in one dimension, the validity condition of the BEC regime thus reduces to

$$\mu \gg V_R \sqrt{\Sigma^0(L_{\text{dis}}/l_{\text{heal}})} \quad \text{with} \quad l_{\text{heal}} = l_{\text{heal}}(0). \quad (9.51)$$

If the condition (eqn (9.51)) is not fulfilled, the Bose gas will form a *fragmented BEC*. The latter is a compressible insulator and thus corresponds to the *Bose glass* phase (Fisher *et al.*, 1989).

Non-interacting regime In the opposite situation, for vanishing interactions, the problem is separable and the radial wave function is the ground state of the radial harmonic oscillator. We are therefore left with the eigenproblem of the single-particle 1D Hamiltonian $\hat{h} = -\hbar^2 \partial_z^2 / 2m + V(z)$. In the presence of disorder, the eigenstates χ_ν are all localized, and are characterized according Lifshits *et al.* (1988) by:

- (i) a finite localization length
- (ii) a dense pure-point density of states \mathcal{D}_{2L}
- (iii) a small participation length $P_\nu = 1 / \int dz |\chi_\nu(z)|^4$.

The participation length scales as the width of the wave function and thus decreases for stronger localization. If $V(z)$ is bounded below, so is the spectrum, and the low-energy states belong to the Lifshits tail, which is characterized by a stretched exponential cumulative density of states (CDOS),

$$\mathcal{N}_{2L}(\epsilon) = \int^\epsilon d\epsilon' \mathcal{D}_{2L}(\epsilon') \sim \exp\left(-c \sqrt{\frac{V_R}{\epsilon - V_{\min}}}\right),$$

in one dimension, where $V_{\min} = \min(V)$. Figure 9.10 shows how the CDOS exhibits a stretched exponential form, the lowest Lifshits states (LS) are spatially localized, and $P(\epsilon)$ increases with energy, indicating a weaker localization, although $P(\epsilon)$ is almost constant at low energy. Note also that the LSs hardly overlap if their extension is much smaller than the system size.

Lifshits regime We turn now to the regime of non-zero but weak interactions, where the chemical potential μ lies in the Lifshits tail of the spectrum. Owing to the fact that the lowest single-particle LSs hardly overlap, it is convenient to work in the basis of the LSs, $\{\chi_\nu, \nu \in \mathbb{N}\}$. These can be regarded as trapping microsites populated with N_ν bosons in the quantum state $\phi_\nu(\rho)\chi_\nu(z)$, where the longitudinal motion is frozen to χ_ν , and ϕ_ν is the

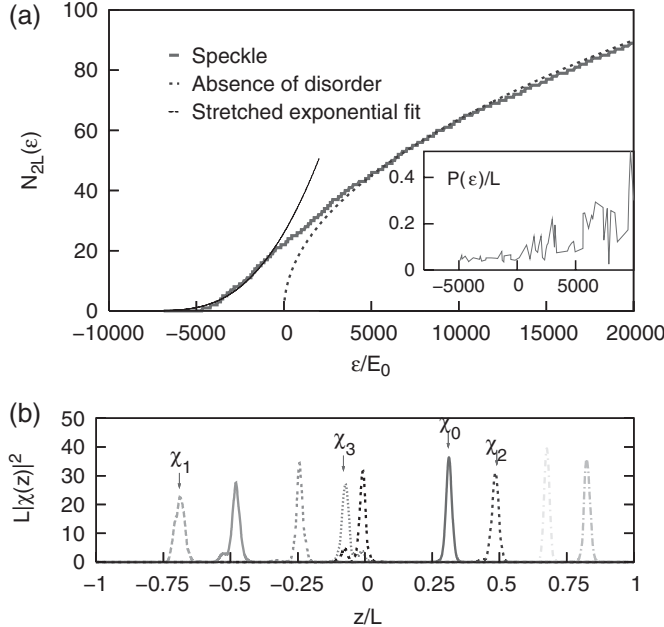


Figure 9.10 (a) Cumulative density of states of single particles in a speckle potential with $L_{\text{dis}} = 2 \times 10^{-3}L$ and $V_R = 10^4 E_0$, where $E_0 = \hbar^2/2mL^2$ ($V_{\min} = -V_R$). Inset: participation length. (b) Low-energy Lifshits eigenstates. For the realization of disorder considered, $\epsilon_0 \simeq -5 \times 10^3 E_0$. From Lugan *et al.* (2007).

radial extension in the microsite ν . Therefore, the many-body wave function is the Fock state

$$|\Psi\rangle = \prod_{\nu \geq 0} (N_\nu!)^{-1/2} (\hat{b}_\nu^\dagger)^{N_\nu} |\text{vac}\rangle, \quad (9.52)$$

where \hat{b}_ν^\dagger is the creation operator in the state $\phi_\nu(\rho)\chi_\nu(z)$. Each ϕ_ν can be a transverse 2D BEC for $N_\nu \gg 1$. However, the quantum state (eqn (9.52)) does not correspond generally to a single 3D BEC since it does not reduce to $(N!)^{-1/2} (\hat{b}_0^\dagger)^N |\text{vac}\rangle$. Rather, the Bose gas splits into several fragments whose longitudinal shapes are those of the LSs, χ_ν , and are hardly affected by the interactions.

The mean-field energy associated with the state in eqn (9.52) reads

$$\begin{aligned} E[\Psi] &= \sum_\nu N_\nu \int d\rho \phi_\nu^* \left(\frac{-\hbar^2 \nabla_\perp^2}{2m} + \frac{m\omega_\perp^2 \rho^2}{2} + \epsilon_\nu \right) \phi_\nu \\ &\quad + \sum_\nu \frac{N_\nu^2}{2} \int d\rho U_\nu |\phi_\nu|^4, \end{aligned} \quad (9.53)$$

where $U_\nu = g \int dz |\chi_\nu(z)|^4 = g P_\nu^{-1}$ is the local interaction energy in the LS, χ_ν . Minimizing $E[\Psi]$ for a fixed number of atoms ($E[\Psi] - \mu \sum_\nu N_\nu \rightarrow \min$), we find the equation

$$(\mu - \epsilon_\nu) \phi_\nu = [-\hbar^2 \nabla_\perp^2 / 2m + m\omega_\perp^2 \rho^2 / 2 + N_\nu U_\nu |\phi_\nu|^2] \phi_\nu. \quad (9.54)$$

Solving the 2D Gross–Pitaevskii equation (eqn (9.54)) for each microsite ν , one finds the atom numbers N_ν and the wave functions ϕ_ν . As μ increases, $|\phi_\nu|^2$ will turn continuously from a Gaussian (for $\hbar\omega_\perp \gg \mu$) into an inverted parabola (for $\hbar\omega_\perp \ll \mu$).

Denoting ν^{\max} as the index of the highest LS such that all lower LSs hardly overlap, the Lifshits description requires the chemical potential μ to be sufficiently small for the number of populated LSs to be smaller than ν^{\max} , i.e.

$$\mathcal{N}_{2L}(\mu) \leq \nu^{\max}. \quad (9.55)$$

If this condition is not fulfilled, several populated LSs will overlap and the Bose gas will start to form a fragmented BEC. Each fragment will be a superposition of LSs and its shape will be modified by the interactions.

Although both \mathcal{N}_{2L} and ν^{\max} may have complex dependencies versus V_R , L_{dis} , and the model of disorder, general properties can be obtained using scaling arguments. We rewrite the single-particle problem as

$$(\epsilon_\nu / V_R) \varphi_\nu(u) = -\alpha_R \partial_u^2 \varphi_\nu(u) + v(u) \varphi_\nu(u), \quad (9.56)$$

where $u = z/L_{\text{dis}}$, $\varphi_\nu(u) = \sqrt{L_{\text{dis}}} \chi_\nu(z)$ and $\alpha_R = \hbar^2 / 2m L_{\text{dis}}^2 V_R$. Thus all characteristics of the spectrum depend only on the parameter α_R after renormalization of energies and lengths. Scaling arguments show that in the Lifshits tail

$$\mathcal{N}_{2L}(\epsilon) = (L/L_{\text{dis}}) \zeta(\alpha_R, \epsilon/V_R) \quad \text{and} \quad \nu^{\max} = (L/L_{\text{dis}}) \eta(\alpha_R), \quad (9.57)$$

where ζ and η are v -dependent functions. Finally, inserting these expressions into eqn (9.55) and solving formally, we obtain the validity condition of the Lifshits regime:

$$\mu \leq V_R F(\alpha_R), \quad (9.58)$$

where F is the solution of $\zeta(\alpha_R, F(\alpha_R)) = \eta(\alpha_R)$, which can be computed numerically.

After all these considerations, one may draw the schematic quantum-state diagram of the zero-temperature Bose gas as a function of μ and V_R (see Figure 9.11) (Lugan *et al.*, 2007). From the discussion above, it is clearly fruitful to fix the parameter α_R while varying V_R . The boundaries between the various regimes (Lifshits glass, fragmented BEC, BEC and smoothed BEC) result from the competition between the interactions and the disorder, and are given by eqns (9.49), (9.51), and (9.58). We stress that they are crossovers rather than phase transitions. Interestingly, all these boundaries are straight lines with slopes depending on the parameter α_R . This is clear from eqn (9.58) for the boundary between the Lifshits and the fragmented regimes. In addition, since $V_R = (\hbar^2 / 2m L_{\text{dis}}^2) / \alpha_R$, the non-smoothing condition (eqn (9.49)) reduces to $\mu \gg \alpha_R V_R$. Finally, since $\mu = \hbar^2 / 2m l_{\text{heal}}^2$ and thus $L_{\text{dis}} / l_{\text{heal}} = \frac{1}{\sqrt{\alpha_R}} \sqrt{\mu / V_R}$, the non-fragmented BEC condition (eqn (9.51)) also

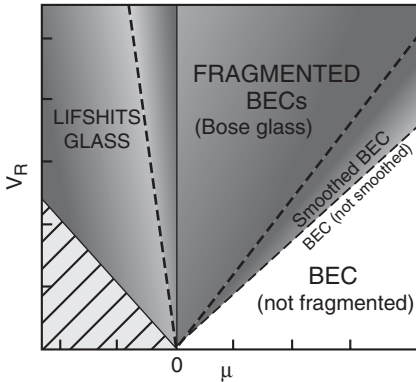


Figure 9.11 Schematic quantum-state diagram of an interacting ultracold Bose gas in 1D disorder. The dashed lines represent the boundaries (corresponding to crossovers). The hatched part corresponds to a forbidden zone ($\mu < V_{\min}$). From Lugan *et al.* (2007). Figure in color online.

corresponds to a straight line with a slope depending on α_R in Figure 9.11. The Lifshits glass idea extends to higher dimensions. Below we discuss it for Bernoulli potentials (see Section 9.3.3) in one and two dimensions.

9.4.3 Lifshits glasses in Bernoulli potentials

The aim of this subsection is to illustrate the idea of Lifshits glass for Bernoulli potentials. We report novel and rigorous results concerning Bernoulli potentials in one dimension and extend them numerically to 2D systems. The results come from Bishop and Wehr (2011) and Stasińska *et al.* (2011).

Consider the (discrete) Schrödinger equation in one dimension

$$E\psi_m = t(2\psi_m - \psi_{m+1} - \psi_{m-1}) + \mu_m\psi_m, \quad (9.59)$$

with the index m running from 0 to $L + 1$, and a Bernoulli potential μ_m , being random independent identically distributed entries, given by

$$\mu_m = \begin{cases} 0 & \text{with probability } p, \\ b & \text{with probability } q = 1 - p. \end{cases} \quad (9.60)$$

The main result (Bishop and Wehr, 2011) concerns the full characteristics of the ground state of the system considered. The ground state energy, E_0^L is approximately the energy of the sinusoidal function (vanishing at the boundaries) supported by the largest island of zero potential which has length l_L . More specifically:

Theorem 9.3 (Bishop and Wehr, 2011) *In every realization of disorder with l_L sufficiently large, the ground state energy E_0^L is bounded by:*

$$\frac{\pi^2}{(l_L + 1)^2} \geq E_0^L \geq \left(1 - \frac{3\pi^2}{b l_L^\gamma}\right) \left(1 - \frac{1}{l_L^{1/2-\gamma/2}}\right)^2 \frac{\pi^2}{(l_L + 1)^2}, \quad (9.61)$$

where $0 < \gamma < 1$. Thus, with probability 1, E_0^L is asymptotically equal to $\frac{\pi^2}{(l_L + 1)^2}$.

The upper bound is obtained simply by using the Ritz variational principle. The proof of the lower bound is highly involved. Note that, the length of the largest island l_L itself is a random variable, and so is E_0 . Their exact limiting distributions are known.

Theorem 9.4 (Bishop and Wehr, 2011) *The exact limiting distribution of l_L is:*

$$P[l_L \leq \log_p \tau - \log_p pqL] \rightarrow \exp[-\tau p^{\text{Int}(u_{pqL}(\tau)) - u_{pqL}(\tau)}], \quad (9.62)$$

where $u_M(\tau) = \log_p \tau - \log_p M$, and $\text{Int}(\cdot)$ denotes the integer part.

Note that the distribution does not converge: it varies with the factor $p^{\text{Int}(u_{pqL}(\tau)) - u_{pqL}(\tau)}$, which is the lattice effect. Here $\log_p(\cdot)$ denotes the logarithm of base p . Note that l_L is of order of $\log_p L$, which can be expected from the following simple argument. Let k_{ch} be the characteristic size of an island (of zeros in the potential) and $p^{k_{\text{ch}}}$ an estimate of the probability of its occurrence. The number of such islands is expected to be of order $M \propto L$, so that the product $M p^{k_{\text{ch}}} \rightarrow \text{const} > 0$ when L tends to infinity. This implies immediately that k_{ch} scales as $\log L$.

Similarly, the limiting distribution of the ground-state energy fulfills:

Theorem 9.5 (Bishop and Wehr, 2011) *The exact limiting distribution of E_0^L reads:*

$$P \left[\left(\frac{\log_p(pqL)}{2} \right) \left(\frac{\log_p^2(pqL)}{\pi^2} E_0^L - 1 \right) \geq \log_p \tau \right] \simeq \exp(p^{-\tau + \text{Int}(u_{pqL}(\tau)) - u_{pqL}(\tau)}). \quad (9.63)$$

We stress also that both limiting distributions are highly non-trivial. Numerical results performed for L of the order of several hundreds agree nearly perfectly with the limiting rigorous results (Stasińska *et al.*, 2011).

Amazingly, numerical analysis shows that a very similar situation holds in two dimensions. The results of Stasińska *et al.* (2011) in this area can be summarized as follows:

- In principle, very many islands of zero potential, which can have regular, i.e. quasi-circular, or irregular shapes with ‘fractal’ boundaries, are encountered. Generically, however, the ground state occupies the largest island of regular shape. Sometimes, this island is connected with another via a narrow path; quantum interference effects keep the ground-state wave function within the regular shape; spreading over the two islands via the narrow path costs energy.

- The sizes of the islands of regular shapes scale as $\sqrt{\log(L)}$. This can be understood in a similar manner to the explanation in one dimension. Let k_{ch} be the characteristic linear size and k_{ch}^2 the area of a regular island. $p^{2k_{\text{ch}}}$ then estimates the probability of its occurrence. The number of such islands is expected to be of order $M \propto L^2$, so that the product $M p^{2k_{\text{ch}}} \rightarrow \text{const} > 0$, when L tends to infinity. This implies immediately that k_{ch} scales as $\sqrt{\log L}$.
- Correspondingly, the ground state energy scales as $E_0 \sim 1/k_{\text{ch}}^2 \sim 1/\log(L)$.

Having understood the ground-state properties one can check the validity of the Lifshits scaling for the low-energy states and study the effects of finite temperature, ($T > 0$) as well as the effects of interactions.

A simple way to simulate the effect of temperature in the absence of interactions is to randomize the system's wave function at $T > 0$ as

$$\psi(\mathbf{r}, t) = \sum_{\nu=0}^{L^2} \alpha_{\nu} \psi_{\nu}(\mathbf{r}) \exp(-i E_{\nu} t / \hbar), \quad (9.64)$$

where the α are complex independent Gaussian random variables of mean value zero and mean squares $\propto n(E_{\nu}/k_B T)$, where $n(E_{\nu}/k_B T)$ are the occupations of the corresponding energy levels, with k_B the Boltzmann constant. For distinguishable particles (or at high T) $n(E_{\nu}/k_B T) \propto \exp(-E_{\nu}/k_B T)$, whereas for bosons, $n(E_{\nu}/k_B T)$ are given by Bose–Einstein distribution. Here ψ_{ν} and E_{ν} denote the ground and excited eigenstates and the corresponding energies obtained by solving the Schrödinger equation. A similar procedure can be used for weakly interacting systems, if the Gross–Pitaevskii equation is used; in such a case ψ_{ν} and E_{ν} denote the ground-state condensate wave function, the Bogoliubov–de Gennes quasiparticle modes, and the corresponding quasi-energies, respectively.

The presence of interactions can also be included in a multi-orbital Hartree–Fock method. In this treatment, the energy is written as the sum of all independently occupied orbitals

$$E = \sum_k n_k E_k + \sum_{k,l} \frac{g}{2} \left[n_k (n_k - 1) P_{kk} + \sum_{k \neq l} 2 n_k n_l P_{kl} \right], \quad (9.65)$$

where E_k are the eigenvalues of the single-particle problem, n_k the occupation number of each eigenstate, g is the interaction constant, and $P_{kl} = \int d\mathbf{r} |\psi_k(\mathbf{r})|^2 |\psi_l(\mathbf{r})|^2$ is the inverse of the participation length.

The results considering the thermal states for the non-interacting particles (eqn (9.64)) and interacting particles in the multi-orbital Hartree–Fock approach (eqn (9.65)) are presented in Figure 9.12. They provide an explicit illustration of the nature and properties of BECs in the Lifshits-glass regime (Stasińska *et al.*, 2011). Distinguishable Boltzmann particles tend to occupy many fragmented mini-condensates already at very low T (first row). This effect is very significantly suppressed for bosons (second row) due to their quantum statistics and the ‘boson-enhancement effect’, i.e. the fact that bosons tend to occupy already occupied states. At $T = 0$ the multi-orbital Hartree–Fock approach

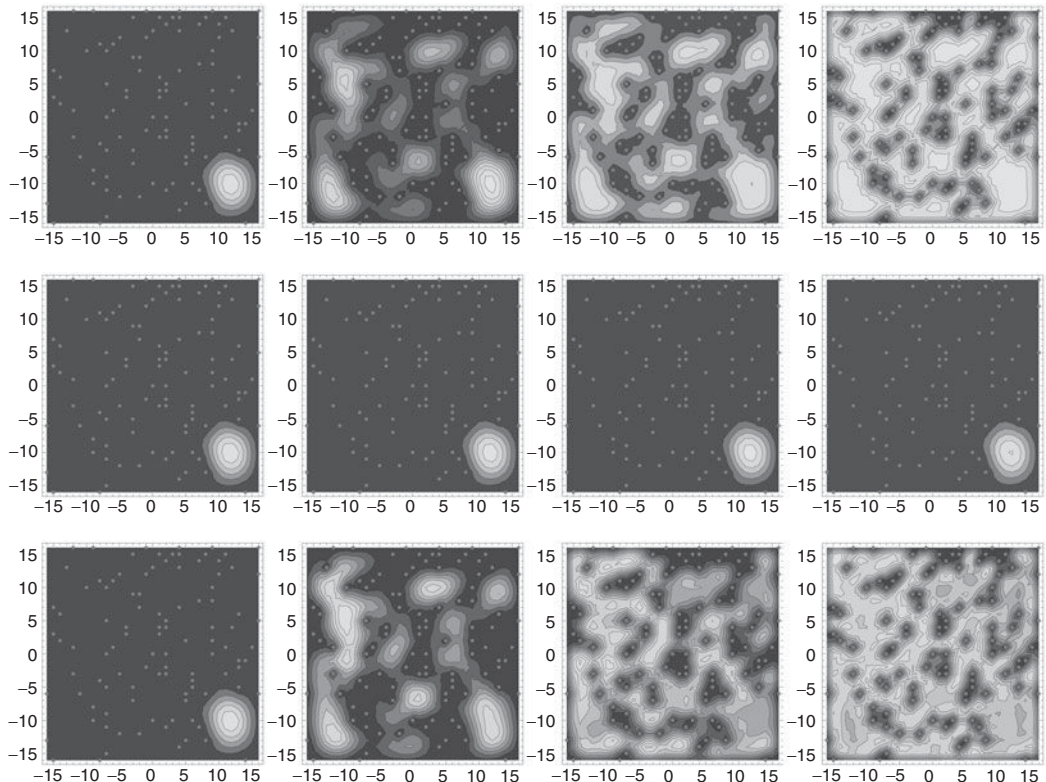


Figure 9.12 Comparison of temperature and interaction effects. First two rows: thermally averaged single particle density with respectively Boltzmann (top) and Bose (centre) statistics; from left to right, $T/t = 0, 0.1, 0.2, 0.5$. Bottom row: single particle density of an interacting gas; from left to right, $g\rho/t = 0, 0.1, 2, 10$. Dots indicate the sites occupied by the disordered scatterers. The average density is $\rho = 0.9$ particles/site — Stasińska *et al.*, 2011.

provides a very accurate description of the ground state of a bosonic cloud with repulsive interactions, for which the density profile is strikingly similar to the finite-temperature profile for Boltzmann particles. One can say that the effects of interactions at $T = 0$ are equivalent to the effect of finite T , along with the suppression of the Bose statistics. This qualitative statement is, however, only partially true; it holds for the density profiles but not for the distributions of the single particle state occupations.

9.4.4 The strongly interacting regime: towards the Bose glass

In the previous section we discussed the role of disorder in non- or weakly interacting degenerate Bose gases. Here we turn to the strongly interacting regime, reachable in the

presence of deep optical lattices—due to the increase of the local density and large effective mass—and well described by the Bose-Hubbard Hamiltonian:

$$\hat{H} = - \sum_{\langle ij \rangle} \left[t_{ij} \hat{b}_i^\dagger \hat{b}_j + h.c. \right] + \sum_i \frac{U_i}{2} \hat{n}_i (\hat{n}_i - 1) + \sum_i \mu_i \hat{n}_i. \quad (9.66)$$

This model exhibits the possibility of diagonal disorder through site-dependent on-site energy μ_i and on-site non-linear interactions U_i and of off-diagonal disorder through site-dependent tunneling rates t_{ij} . Notice that in the presence of a speckle or a superlattice potential, the tunneling coefficients t_{ij} should be site-dependent due to the changes in the potential barriers between sites. Also, the on-site non-linear interactions U can become site-dependent due to the change in the curvature of the lattice site. Nevertheless, normally the most important contribution of on-site disorder comes from the term μ_i , which accounts for the external harmonic trapping potential, if present, plus the potential energy shifts produced by the disordered potential (White *et al.*, 2009). Eventually, μ_i also contains the chemical potential in the grand canonical description as we have seen in the previous sections.

The pseudorandom on-site energies are calculated (Damski *et al.*, 2003b) by using:

$$\mu_i = \int d^3r w^*(\mathbf{r} - \mathbf{r}_i) V(\mathbf{r}) w(\mathbf{r} - \mathbf{r}_i), \quad (9.67)$$

where $w(\mathbf{r} - \mathbf{r}_i)$ are the Wannier functions in the lowest Bloch band and $V(\mathbf{r})$ is the superlattice potential or the potential induced by the speckle pattern. In White *et al.* (2009) it has been experimentally shown, using a BEC in a deep cubic 3D optical lattice in the presence of a fine-grained disorder with speckle size comparable to the lattice spacing that t_{ij} is directly correlated with $|\mu_i - \mu_j|$.

As discussed at length in Section 9.2, seminal studies of the disordered Bose Hamiltonian (Fisher *et al.*, 1989; Giamarchi and Schulz, 1988) predicted the existence of a novel compressible insulating phase called a Bose glass phase, which is characterized by a gapless excitation spectrum.

The possibility of generating a Bose glass using ultracold atoms was discussed for first time in Damski *et al.* (2003b) and Roth and Burnett (2003b, 2003a). In Damski *et al.* (2003b), the dynamical generation of the Bose glass in a ultracold bosonic gas in a 2D disordered lattice was calculated using the time-dependent Gutzwiller ansatz method, which is described in Chapter 5. In Roth and Burnett (2003b, 2003a), meanwhile, the ground state of the system was determined by solving the eigenvalue problem of the 1D Bose-Hubbard Hamiltonian numerically. An elegant method to describe (at least qualitatively) the properties of the disordered Bose-Hubbard model was developed by Hoffstetter and his collaborators (Bissbort and Hoffstetter, 2009). This method is particularly well suited to ultracold atoms in optical lattices since it allows us to include the trapping potential in a straightforward manner. We sketch the method in the next subsection.

Experimentally, the first attempt to reach the Bose glass phase was performed by Fallani *et al.* (2007). The authors used a collection of 1D interacting BECs in a bichromatic

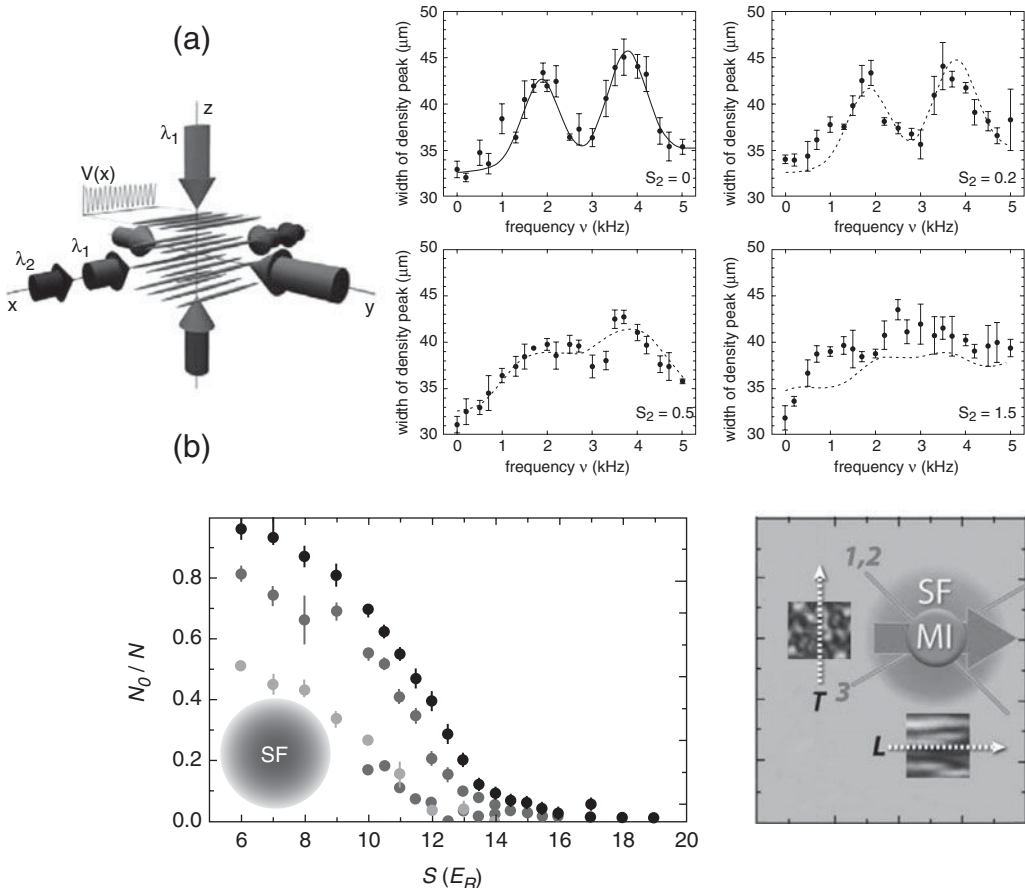


Figure 9.13 (a) Experimental set-up and data on broadening of the excitation spectrum as disorder grows with the amplitude of the second incommensurate lattice s_2 . Redrawn from Fallani *et al.* (2007) by courtesy of the authors. (b) Condensed fraction as a function of the lattice depth in the presence of different disorder strength, given in this case by the intensity of the speckles: $\Delta = 0$ (black), $\Delta = 0.75E_R$ (dark grey), and $\Delta = 3E_R$ (light grey), where E_R is the recoil energy of the lattice. Redrawn after Pasienski *et al.* (2010) by courtesy of the authors.

lattice with incommensurate wavelengths along the tubes (see Figure 9.13(a)). The authors measured:

- the excitation spectrum, by time-modulating the lattice potential (Stöferle *et al.*, 2004a), observing a smearing of the resonance peaks for increasing disorder strength, as shown in Figure 9.13(a)
- a decrease of the long-range phase coherence in TOF experiments by increasing the disorder.

Although these two observations are consistent with the existence of the Bose glass phase, more conclusive measurements are desirable. From the theoretical point of view, a detailed study of the phase diagram of the Bose–Hubbard Hamiltonian with a quasiperiodic potential has been carried out by using quantum Monte Carlo methods (Roscilde, 2008) and the DMRG technique (Roux *et al.*, 2008), the aim being to understand the experimental results. A different approach was followed in the experiments reported in White *et al.* (2009), where a BEC was loaded into a 3D optical lattice in the presence of a 3D speckle potential with speckle size of the order of the lattice spacing, as shown in Figure 9.8(e) and (f). In this study it was shown, by independently varying the disorder strength and the ratio between the tunneling and the non-linear energy, that disorder suppresses the condensate fraction, measured using TOF imaging, for superfluid or coexisting superfluid and MI phases. In the experiment of Pasienski *et al.* (2010), a experimental set-up similar to the one used in White *et al.* (2009) was used, but with unit filling factor. These authors measured the quasimomentum distribution using TOF imaging and transport properties by looking at the motion of the center of mass of the atomic gas after applying an impulse kick (McKay *et al.*, 2008). While a disorder-induced superfluid–insulator transition was clearly observed, there was no evidence for a transition from a disorder-dominated insulator to a superfluid (see Figure 9.13(b)). This absence of a transition is in apparent contradiction with the theoretical phase diagram (Gurarie *et al.*, 2009; Bissbort and Hofstetter, 2009; Wu and Phillips, 2008; Krüger *et al.*, 2009); the most probable reason for this discrepancy is the non-zero temperatures inevitably present in the experiments (Pasienski *et al.*, 2010; Gurarie *et al.*, 2009). At the moment, due to the lack of a direct measure of the gap and of the compressibility, experiments with ultracold atoms cannot distinguish between Bose glass and MI, and can only distinguish between superfluid and insulating phases. An unambiguous experimental observation of the Bose glass phase is therefore still missing. In fact, new methods of producing more conclusive measurements are being investigated (Delande and Zakrzewski, 2009).

Recently, there have also been several theoretical proposals dealing with mixtures in a lattice, and these show the possibility of inducing binary disorder for one of the species in the strongly-correlated regime (Mering and Fleischhauer, 2008; Krutitsky *et al.*, 2008; Buonsante *et al.*, 2009).

9.4.5 Stochastic mean-field theory for the disordered Bose–Hubbard model

In this section we describe and apply to the disordered Bose–Hubbard model a useful mean-field method: stochastic mean-field theory (SMFT), which follows closely the work of Bissbort and Hofstetter (2009). The starting point is the single-band disordered Bose–Hubbard Hamiltonian

$$\hat{H}_{\text{BH}} = -t \sum_{\langle i,j \rangle} (\hat{b}_i^\dagger \hat{b}_j + \hat{b}_j^\dagger \hat{b}_i) + \sum_i (\epsilon_i - \mu) \hat{b}_i^\dagger \hat{b}_i + \frac{U}{2} \sum_i \hat{b}_i^\dagger \hat{b}_i^\dagger \hat{b}_i \hat{b}_i, \quad (9.68)$$

where the disorder is considered diagonal and parametrized by on-site energies ϵ_i which are independently and identically distributed according to a box distribution $p(\epsilon) = \Theta(\Delta/2 - |\epsilon|)/\Delta$, where Δ is the disorder strength.

The mean field Gutzwiller ansatz is then applied (see Chapter 5):

$$|\text{GW}\rangle = \prod_i \left[\sum_{n=0}^{\infty} \frac{f_n^{(i)}}{\sqrt{n!}} (\hat{b}_i^\dagger)^n \right] |\text{vac}\rangle, \quad (9.69)$$

and the mean-field ground state is determined by minimizing the energy expectation value $\langle \text{GW} | \hat{H}_{\text{BH}} | \text{GW} \rangle$ with respect to the amplitudes $\{f_n^{(i)}\}$ under the constraint $\langle \text{GW} | \text{GW} \rangle = 1$. For a non-disordered system ($\Delta = 0$) at $T = 0$, this leads to the ground state of the mean-field (site-decoupled) Hamiltonian

$$\hat{H}_{\text{MF}} = \sum_i \left[-t \sum_{\langle ij \rangle} (\psi_j^* \hat{b}_i + \psi_j \hat{b}_i^\dagger - \psi_j^* \psi_i) + (\epsilon_i - \mu) \hat{b}_i^\dagger \hat{b}_i + \frac{U}{2} \hat{b}_i^\dagger \hat{b}_i^\dagger \hat{b}_i \hat{b}_i \right], \quad (9.70)$$

where the mean-field parameters (MFPs) $\psi_i = \langle \hat{b}_i \rangle$, are determined self-consistently.

For disordered bosons, SMFT extends the self-consistent Gutzwiller approach to the thermodynamic limit, and is free of finite-size effects. As Bissbort and Hofstetter (2009) state:

its numerical efficiency, and absence of finite size effects make this method a good candidate for future analysis of more complex systems, such as multicomponent gases in disordered lattices. This is achieved by a probabilistic description of an infinite system, by using a probability density function (PDF) $P(\psi)$ to allow disorder-induced fluctuations of the MFPs.

The idea behind SMFT is displayed in Figure 9.14. Technically, it works as follows. One considers an arbitrary site i with energy ϵ_i , and the scaled sum of MFPs from

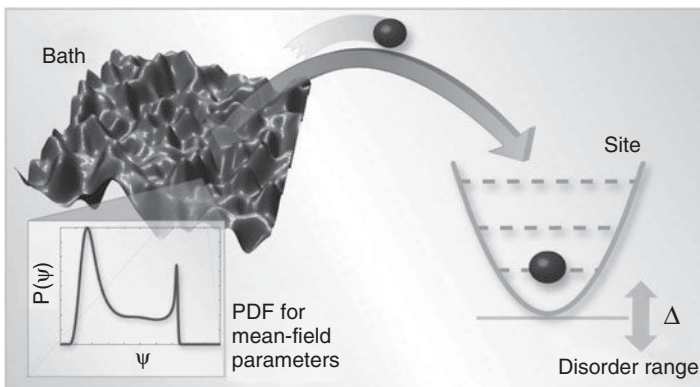


Figure 9.14 Schematic representation of the stochastic mean-field theory. The many-body system is approximated by an effective single-site theory, where the single site is coupled to a bath of mean-field parameters. Disorder-induced fluctuations of the mean-field parameters are accounted for by a probability distribution function, $P(\psi)$. From Bissbort and Hofstetter (2009).

the neighboring sites $\eta = t \sum_{\text{NN } j}^z \psi_j$ distributed according to the probability density distribution

$$Q(\eta) = \int_0^\infty d\psi_1 P(\psi_1) \dots \int_0^\infty d\psi_z P(\psi_z) \delta\left(\eta - t \sum_{m=1}^z \psi_m\right). \quad (9.71)$$

One immediately observes that once the self-consistent solution $P(\psi)$ is known, any disorder-averaged expectation value of a single-site operator can be calculated as:

$$\overline{\langle \hat{A} \rangle} = \int d\epsilon p(\epsilon) \int d\eta Q(\eta) \langle \text{gs}(\epsilon, \eta) | \hat{A} | \text{gs}(\epsilon, \eta) \rangle, \quad (9.72)$$

where $|\text{gs}(\epsilon, \eta)\rangle$ is the ground state of

$$\hat{H} = \eta(\hat{b}^\dagger + \hat{b}) + (\epsilon - \mu)\hat{b}^\dagger \hat{b} + \frac{1}{2}\hat{b}^\dagger \hat{b}^\dagger \hat{b} \hat{b}. \quad (9.73)$$

The self-consistency of SMFT is formulated in the following manner: from a randomly chosen energy ϵ from $p(\epsilon)$, one obtains the z MFPs from $P(\psi)$ or, equivalently, one draw η from $Q(\eta)$. Then the calculated expectation values $\langle \hat{b} \rangle$ have to be distributed according to the initially assumed probability density distribution $P(\psi)$ (illustrated in Figure 9.14). The self-consistency equation thus reads

$$P(\psi) = \int_0^\infty d\eta Q(\eta) \tilde{P}_\eta(\psi)$$

where $\tilde{P}_\eta(\psi) := \frac{d}{d\psi} \int d\epsilon p(\epsilon) \Theta\left(\psi - \langle \text{gs}(\epsilon, \eta) | \hat{b} | \text{gs}(\epsilon, \eta) \rangle\right).$ (9.74)

Here $\tilde{P}_\eta(\psi)$ denotes the conditional probability density for a site having the MFP ψ if the external coupling η is given and the disorder energy is distributed according to $p(\epsilon)$. Typical results for distributions $P(\psi)$ are shown in Figure 9.15 (Bissbort and Hofstetter, 2009) for a variety of increasing disorder-strength values Δ . At $\Delta = 0$ the distribution $P(\psi)$ is a δ -function at the value of ψ corresponding to the solution of the usual Gutzwiller bosonic MFT in the absence of disorder. In the presence of disorder ($\Delta > 0$), $P(\psi)$ acquires a finite width in the superfluid phase. This can be understood to have two origins:

- (i) fluctuations of the on-site energy ϵ necessarily lead to a variation in the calculated MFP $\langle \hat{b} \rangle$ (for non-zero MFPs from the neighboring sites)
- (ii) subsequent additional fluctuations in the MFPs further enhance the fluctuations of $\langle \hat{b} \rangle$.

By decreasing the hopping strength for fixed disorder, it is found that the system is always driven into an insulating state with $\bar{\psi} = 0$.

Typical phase diagrams obtained from SMFT for a 3D lattice show that with increasing disorder the MI regions ($\bar{\psi} = 0, \kappa = 0$) shrink, and are completely replaced by the Bose glass ($\bar{\psi} = 0, \kappa > 0$) and superfluid ($\bar{\psi} > 0, \kappa > 0$) phases at $\Delta = 1$. The transitions between the MI, BG, and superfluid phases are of second order, since the density $\langle n(\mu) \rangle$ varies

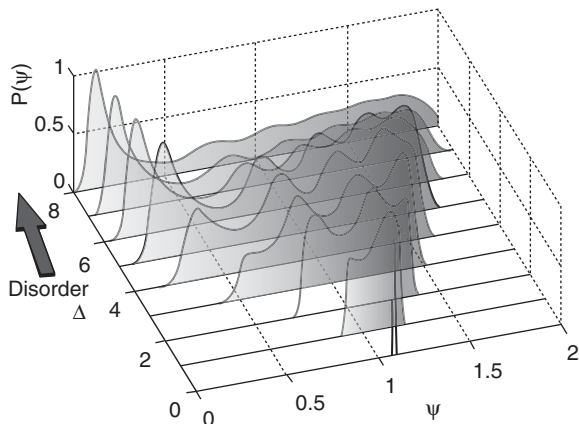


Figure 9.15 Mean-field parameter probability density distributions determined self-consistently at fixed $\mu = 1.0$, $t = 0.05$, $z = 6$, and increasing disorder strength Δ . From Bissbort and Hofstetter (2009).

continuously, but the compressibility, κ , is discontinuous at the transition points (Bissbort and Hofstetter, 2009).

A similar approach has been used in Łącki *et al.*, 2011 to study the transition to the Bose glass for a spinor condensate. Using a mean-field Gutzwiller ansatz and a probabilistic mean-field perturbation theory, the zero-temperature phase diagram of the disordered spin-1 Bose–Hubbard model in a 2D square lattice was determined. As explained in detail in Chapter 7, for spin-1 the spin interaction induces two different regimes corresponding to ferromagnetic and antiferromagnetic order. In the ferromagnetic case, the introduction of disorder reproduces features analogous to the ones found in the disordered scalar Bose–Hubbard model, involving the formation of a Bose glass phase between MI lobes. In the antiferromagnetic regime, the phase diagram differs substantially from the scalar case. Disorder in the chemical potential can lead to the disappearance of MI lobes with odd integer filling factor and, for sufficiently strong spin coupling, to a Bose glass of local singlets between even filling MI lobes. Disorder in the spinor coupling parameter results in the appearance of a Bose glass phase only between the n and $n + 1$ lobes for n odd. Disorder in the scalar Hubbard interaction inhibits MI regions for occupation larger than a critical value.

9.5. Disordered ultracold fermionic systems

Interacting fermions in periodic potentials are well modeled by the Fermi–Hubbard Hamiltonian (Hubbard, 1963; Lee *et al.*, 2006). They exhibit physics that is very rich and not well understood, such as high T_c superconductivity, and are very challenging. In condensed matter systems, experimental studies are limited, however, by the lack of control over most of the parameters. This limitation can be overcome in the context of ultracold atoms in optical lattices, where disorder and interactions can be tuned independently. In fact,

ultracold fermionic atoms have been loaded into a 3D optical lattice (Köhl *et al.*, 2005), and the formation of an MI of a repulsively interacting two-component Fermi gas in an optical lattice has also been reported (Jördens *et al.*, 2008; Schneider *et al.*, 2008). In these experiments, the suppression of double occupancy, the incompressibility of the Mott phase, and the existence of a gap in the excitation spectrum have been measured. It is important to note that, in order to achieve the fermionic MI phase, the external trapping potential is crucial, since it allows the average entropy per particle at its center to be reduced substantially because most of the entropy is carried by the metallic shells (Schneider *et al.*, 2008). In this context, experiments in the presence of disorder should lead to the observation of the Fermi glass phase.

Even more interesting would be to be able to achieve the magnetically ordered quantum phase in a repulsively interacting two-component Fermi gas in an optical lattice. However, the low-temperature requirements (De Leo *et al.*, 2008), which demand more advanced cooling mechanisms, and the lack of a quantitative determination of temperature and entropy (Jördens *et al.*, 2010), mean that this regime is still unachievable in current experiments. In this context, thermodynamics of a spin mixture of attractively interacting fermionic atoms in an optical lattice in the strongly interacting regime has also been explored (Hackermüller *et al.*, 2010).

Regarding theoretical approaches, several studies of the influence of disorder in the phase diagram of the Fermi–Hubbard Hamiltonian (eqn (9.28)) at half filling have been published using different numerical techniques (Tusch and Logan, 1993; Ulmke *et al.*, 1995; Denteneer *et al.*, 1998; Singh *et al.*, 1998; Heidarian and Trivedi, 2004; Byczuk *et al.*, 2005; Andersen *et al.*, 2007; Pezzoli *et al.*, 2009; Byczuk *et al.*, 2009); it would be very interesting to test the predicted phases experimentally.

Two spin-component fermionic atoms in an optical superlattice potential have also been studied in Paredes *et al.* (2005a), where it was shown that the system realizes an Anderson-lattice Hamiltonian (Anderson, 1961):

$$\begin{aligned} \hat{H} = & -t \sum_{\langle l, l' \rangle, \sigma} \hat{c}_{l\sigma}^\dagger \hat{c}_{l'\sigma} + U \sum_l \hat{n}_{l\uparrow} \hat{n}_{l\downarrow} + U_f \sum_s \hat{n}_{s\uparrow} \hat{n}_{s\downarrow} - \Delta\epsilon \sum_{s,\sigma} \hat{n}_{s\sigma} \\ & + V \sum_{\langle l, s \rangle, \sigma} (\hat{f}_{s\sigma}^\dagger \hat{c}_{l\sigma} + h.c.), \end{aligned} \quad (9.75)$$

where $\hat{c}_{l\sigma}$ and $\hat{f}_{s\sigma}$ are fermionic operators that annihilate an atom with spin σ on normal sites l and supersites s , respectively (a supersite is defined as the deepest type of site), $\hat{n}_{l\sigma} = \hat{c}_{l\sigma}^\dagger \hat{c}_{l\sigma}$ and $\hat{n}_{s\sigma} = \hat{f}_{s\sigma}^\dagger \hat{f}_{s\sigma}$. The tunneling rate between normal sites (normal–supersite) is denoted by t (V), while U and U_f are the corresponding on-site energies. In the limit $U_f, \Delta\epsilon \gg t$ and $V \gg U$, the system enters the Kondo regime (Tsunetsugu *et al.*, 1997), where an array of impurities located at the supersites is connected through small conducting islands with a discretized set of levels formed by the normal sites. It has been shown (Paredes *et al.*, 2005a) that in this situation finite size effects gives rise to strongly correlated effects, and that by tuning the superlattice parameters two phases can be observed:

- (i) a Kondo-singlet phase, in which each impurity forms a singlet with the Fermi level of its neighboring conducting islands

- (ii) a magnetic phase, in which long-range magnetic order is established between the impurities, mediated by the intermediate islands.

9.6. Disordered ultracold Bose–Fermi and Bose–Bose mixtures

Amazingly, mixtures of bosons and fermions in optical lattices broaden the studies of disorder to a regime in which the competition between different quantum statistics also plays a role. Bose–Fermi (B–F) mixtures (Ospelkaus *et al.*, 2006; Günter *et al.*, 2006; Catani *et al.*, 2008), and Bose–Bose (B–B) mixtures (Catani *et al.*, 2008) have been experimentally loaded into 3D optical lattices. In the Bose–Fermi case, a shift of the visibility loss of the bosonic interference pattern in the SF–MI transition towards shallower lattices was reported. Many mechanisms were theoretically proposed as being the origin of this shift, but presently it is commonly accepted that the attractive interspecies interactions lead to a self-trapping of the bosons, imposing modifications of the parameters of the effective Bose–Hubbard Hamiltonian (Lühmann *et al.*, 2008; Best *et al.*, 2009). These modifications are then responsible for the experimentally observed shift in the SF–MI transition.

In the absence of disorder and in the limit of strong atom–atom interactions, lattice B–F systems can be described in terms of composite fermions (Lewenstein *et al.*, 2004) (for B–B mixtures see Kuklov and Svistunov (2003)), consisting of one fermion plus $-s$ bosons (if $s < 0$), or one fermion plus s bosonic holes (if $s \geq 0$) (see Section 6.7). The physics of mixtures in this regime has been studied in several papers; an extensive list of references can be found in the review articles by Lewenstein *et al.* (2007) and Bloch *et al.* (2008). It has been shown that the low-temperature dynamics of the fermionic composites is described by an effective Hamiltonian corresponding to a spinless interacting Fermi gas. The validity of the effective Hamiltonian for fermionic composites in one dimension was studied using exact diagonalization and the DMRG method (Mehring *et al.*, 2005).

The effects of inhomogeneous trapping potentials on lattice Bose–Fermi mixtures were reported in Cramer *et al.* (2004), while the disordered case in the strong coupling limit was studied by Sanpera *et al.* (2004) and Ahufinger *et al.* (2005). In the presence of disorder, degenerate second-order perturbation theory cannot be applied to derive the effective Hamiltonian, as was done in Kuklov and Svistunov (2003) and Lewenstein *et al.* (2004), since even for zero hopping rates there is a well-defined single ground state determined by the values of the local chemical potentials. Nevertheless, in general, there will be a manifold of many states with similar energies. The differences of energy inside a manifold are of the order of the difference of the chemical potential at different sites, whose random distribution is bounded. Moreover, the lower-energy manifold is separated from the excited states by a gap given by the boson–boson interaction. Therefore, one can apply a form of quasidegenerate perturbation theory by projecting onto the manifold of near-ground states (Cohen-Tannoudji *et al.*, 1992; Ahufinger *et al.*, 2005). As in the homogeneous case (Lewenstein *et al.*, 2004) described in Section 6.7, composite fermions behave as a spinless interacting Fermi gas, but in the presence of local disorder they interact via random couplings and feel effective random local potentials. The effective Hamiltonian that describes their physics can be written as follows (Sanpera *et al.*, 2004):

$$\hat{H}_{\text{eff}} = \sum_{\langle i,j \rangle} \left[-d_{ij} \hat{F}_i^\dagger \hat{F}_j + h.c. \right] + \sum_{\langle i,j \rangle} K_{ij} \hat{M}_i \hat{M}_j + \sum_i \bar{\mu}_i \hat{M}_i, \quad (9.76)$$

where \hat{F}_i are the annihilation operators of the composite fermions—their expression in terms of the fermionic and bosonic operators is given in eqns (6.61) and (6.62)—and $\hat{M}_i = \hat{F}_i^\dagger \hat{F}_i$. The nearest-neighbor hopping for the composites is described by $-d_{ij}$ and the nearest-neighbor composite–composite interactions is given by K_{ij} , which may be repulsive (> 0) or attractive (< 0). $\bar{\mu}_i$ are the on-site energies.

The explicit calculation of the coefficients d_{ij} , K_{ij} , and $\bar{\mu}_i$ depends on the particular type of composite fermion (Sanpera *et al.*, 2004; Ahufinger *et al.*, 2005). For a fermion–bosonic-hole composite and for a fermion–boson composite, it has been shown that the hopping amplitudes d_{ij} are always positive. Depending on the ratio $\alpha = V/U$ between the boson–fermion and the boson–boson interactions, the effective interactions between composites K_{ij} may be either repulsive or attractive for all values of the disorder or, for certain values of α , the qualitative character of the interactions may be controlled by the inhomogeneity. These two types of composite have been studied in two limits:

- (i) the small-disorder limit, where the contributions of the disorder to the interactions and hopping are neglected, $K_{ij} = K$ and $d_{ij} = d$, and only the leading contributions in the on-site energies are kept;
- (ii) the large-disorder or spin-glass limit, where the tunneling becomes non-resonant and can be neglected in eqn (9.76), while the couplings K_{ij} fluctuate strongly; this situation corresponds to the (fermionic) Ising spin-glass model (see Section 9.7).

For the case of disorder applied only to the bosonic component of the mixture and in the small disorder limit, when disorder does not affect the composite formation, the following quantum phases can be achieved depending on the type of composite:

- *Fermion–bosonic-hole composites.* In this case, each site contains either one boson or one fermion and one bosonic hole. When $K/d \ll 1$, i.e. when the interactions are negligible, the system is in the Fermi glass phase, i.e. Anderson localized and many-body corrected single-particle states are occupied according to the Fermi–Dirac rules. For large repulsive interactions, $K/d \gg 1$ and $K > 0$, the ground state will be a MI and the composite fermions will be pinned for large filling factors. We can use eqn (6.64) of Section 6.7 for $\tilde{n} = 1$ and $s = 1$ to get the value of $K/d = 2(1 - \alpha)$, which is, however, clearly bounded from above by 2; this seems to be insufficient to achieve a MI state. For intermediate values of K/d , with $K > 0$, delocalized metallic phases with enhanced persistent currents are possible. For attractive interactions ($K < 0$) and $|K|/d < 1$ one expects competition between pairing of fermions and disorder, i.e. a ‘dirty’ superfluid phase; for $|K|/d \gg 1$, the fermions will form a domain insulator: a state in which fermionic composites stick together to form a rigid immobile cluster. In Ahufinger *et al.* (2005) the crossover from Fermi-gas to Fermi glass phase and from fermionic domain insulator to a disordered insulating phase has been studied numerically by means of the dynamical Gutzwiller ansatz method. The summary of these possible phases is shown in Figure 9.16(a).
- *Fermion–boson composites.* The regimes where $K \ll d$ lead to a weakly-interacting Fermi glass, while the regimes of strong effective repulsive interactions, where $K \gg d$ and $K > 0$, correspond to an MI or, if the filling factor is $\frac{1}{2}$, to a checkerboard phase. In this case, no strong attractive interaction regime occurs, since from eqn (6.64) with $\tilde{n} = 1$, and $s = -1$ we obtain that $K/d = -4\alpha - 5/2 + 3\alpha/(4 + 2\alpha)$, and this

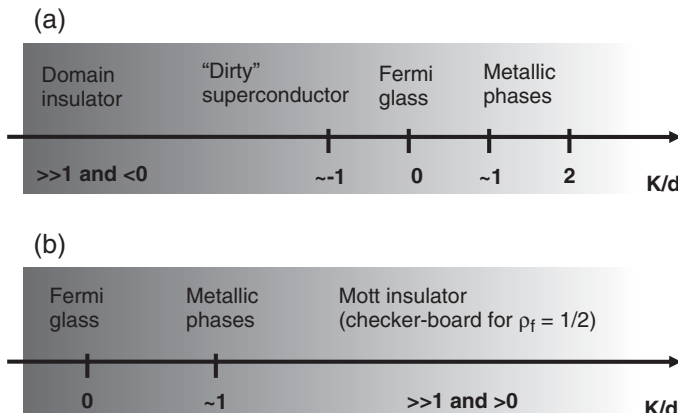


Figure 9.16 Schematic mean-field phase diagram of a disordered Bose–Fermi mixture following eqn (9.76) in the small disorder limit as a function of the ratio between the nearest-neighbor composite–composite interactions K and nearest-neighbor tunneling d . (a) Composite formed by a fermion plus a bosonic hole, (b) composite formed by a fermion plus a boson. From Lewenstein *et al.* (2007).

expression reaches a minimum of $\simeq -0.07$. Therefore, the domain insulator phase does not appear, and even the ‘dirty’ superfluid phase may be washed out. Figure 9.16(b) shows a schematic diagram of these phases.

- *Bare fermion composites.* In the case of bare fermions flowing on top of an MI with one boson per site, it has been shown that for finite boson–fermion interactions, the fluctuations of the effective composite interactions may be large, and the dynamics of this type of composite resembles *quantum bond percolation* (Ahufinger *et al.*, 2005). One can assume, in a somewhat simplified view, that the interaction parameter K_{ij} takes either very large or zero values. The lattice then decomposes into two sublattices: a ‘weak’ bond sublattice (corresponding to $K_{ij} \ll d_{ij}$), in which fermions flow as in an almost ideal Fermi liquid, and a ‘strong’ sublattice (corresponding to $K_{ij} \gg d_{ij}$), where only one fermion per bond is allowed. Additionally, for the case of lattices with different types of site, i.e. sites in which disorder affects the formation and character of composites, it has been predicted that the physics of quantum site percolation will become relevant.

Bose–Bose strongly repulsive lattice mixtures have been predicted to exhibit self-generated randomness leading to the existence of metastable quantum emulsion states with glassy features—using Monte Carlo simulations for the homogeneous case (Roscilde and Cirac, 2007) and the Gutzwiller approach in the presence of a trapping potential (Buonsante *et al.*, 2008).

A completely different situation, in which disorder plays an important role in mixtures, was reported in Niederberger *et al.* (2008), where an analog of the disorder (random-field) induced order (Aharony, 1978; Minchau and Pelcovits, 1985; Feldman, 1998; Wehr *et al.*, 2006) was proposed. The authors considered two component Bose–Einstein condensates trapped in harmonic potentials and coupled via a real-valued random Raman field.

9.7. Spin glasses

Spin glass is a phase that appears in spin systems interacting via random couplings that can be positive (antiferromagnetic), or negative (ferromagnetic). Such variations of the couplings lead typically to frustration, i.e. it is impossible to find a spin configuration that fulfills the constraints imposed by the random interactions in the Hamiltonian (see Chapter 10). Spin-glass behavior thus requires two essential ingredients: quenched disorder and frustration.

In a somewhat oversimplified picture, these kinds of system are characterized by two order parameters:

- (i) the magnetization $M := \sum_i \langle \overline{\mathbf{S}_i} \rangle$, characterizing the magnetic order of the system
- (ii) the Edwards–Anderson order parameter for spin-glass ordering, $Q_{\text{EA}} := \sum_i \overline{\langle \mathbf{S}_i \rangle^2}$, where $\overline{(\cdot)}$ denotes the average over disorder and $\langle (\cdot) \rangle$ the thermal average.

Experimental studies have identified three distinct phases in the phase diagram of the spin glasses (Sherrington, 1998):

- (i) At high temperature and small average spin exchange \overline{K} , the system exhibits a paramagnetic phase with $M = 0$ and $Q_{\text{EA}} = 0$.
- (ii) For $\overline{K} < 0$ and large, the system exhibits a ferromagnetic phase with $M \neq 0$ and $Q_{\text{EA}} \neq 0$.
- (iii) For weak \overline{K} and small temperatures, a spin-glass phase appears with $M = 0$ and $Q_{\text{EA}} \neq 0$.

$Q_{\text{EA}} \neq 0$ thus signals that the local magnetization is frozen, but may vary from site to site so that the disorder prevents long-range magnetic order. A spin-glass phase is an example of ‘order in the presence of disorder’ (Sherrington, 1998).

The physics of spin glasses is not well understood and remains as one of the challenges of statistical physics. In particular, the question of the nature of the spin-glass order is still open. There exist two competing theories: the *Parisi-Mézard* (PM) model and the *droplet* model. The PM picture is a mean-field theory based on the replica method (Mézard *et al.*, 1987) and predicts that the spin-glass phase consists of a large number of low-energy states with very similar energies. The applicability of the PM picture for short-range spin glasses, like the Edwards–Anderson model (Edwards and Anderson, 1975), is questionable. The rival theory, the *droplet* model (Fisher and Huse, 1986; Bray and Moore, 1987; Fisher and Huse, 1988a; Fisher and Huse, 1988b; Newman and Stein, 2003), is a phenomenological theory based on scaling arguments and numerical results. The *droplet* model predicts that there are two ground states related by spin-flip symmetry, and that excitations over the ground state correspond to regions with fractal boundary—the droplets—in which the spins are inverse with respect to the ground state.

One remarkable result of Sanpera *et al.* (2004) and (Ahufinger *et al.*, 2005) is the possibility of realizing a fermionic Ising spin glass model by using a disordered Bose–Fermi mixture. The spin-glass limit is obtained from the composite fermionic model (eqn (9.76)) when the interactions between fermions and bosons are of the same order but slightly smaller than the interactions between bosons, and in the limit of large disorder. In this situation, the hopping vanishes due to strong site-to-site energy fluctuations and the nearest-neighbor interactions K_{ij} fluctuate around mean zero with random positive

and negative values. Replacing the composite number operators with a classical Ising spin variable $\sigma_i := 2M_i - 1 = \pm 1$, one ends up with the Hamiltonian:

$$H_{\text{EA}} = \frac{1}{4} \sum_{\langle ij \rangle} K_{ij} \sigma_i \sigma_j + \frac{1}{2} \sum_i \bar{\mu}_i \sigma_i. \quad (9.77)$$

Equation (9.77) describes a fermionic Ising spin glass (Oppermann and Rosenow, 1999; Oppermann and Sherrington, 2003), which differs from the standard Edwards–Anderson model (Binder and Young, 1986; Mézard *et al.*, 1987), since it includes an additional random magnetic field $\bar{\mu}_i$ and moreover has to satisfy the constraint of a fixed magnetization value, $m = 2N_F/N - 1$, as the number of fermions N_F in the underlying FBH model is conserved; here N is the number of sites. It shares, however, the same basic characteristic of the Edwards–Anderson model of being a spin Hamiltonian with random spin-exchange terms K_{ij} . In particular, this provides bond frustration, which in this model is essential for the appearance of a spin-glassy phase. Due to the differences mentioned, it is necessary to slightly reformulate the Mézard–Parisi mean-field description of the system by adapting the Sherrington–Kirkpatrick–Parisi calculations (Sherrington and Kirkpatrick, 1975; Mézard *et al.*, 1987) to this specific case (Ahufinger *et al.*, 2005). We sketch this calculation in the next subsection.

The experimental study of this limit in ultra-cold Bose–Fermi mixtures may represent a way to address various open questions of spin-glass physics concerning the nature and the ordering of its ground and possibly metastable states, broken symmetry and dynamics in classical spin glasses (in the absence of hopping) and quantum spin glasses (with small, but nevertheless present hopping) (Sachdev, 1999; Georges *et al.*, 2001). Particularly interesting are the prospects for studying questions that have been addressed only recently:

- (i) the existence of the celebrated *de Almeida–Thouless line*—the line separating the replica symmetry-broken spin-glass phase from the replica symmetric phase in the magnetic field in the Parisi picture—in short-range spin glasses (Young and Katzgraber, 2004; Katzgraber and Young, 2005)
- (ii) disorder chaos in spin glasses: ground state sensitivity to small changes of disorder (Krzakala and Bouchaud, 2005)
- (iii) spin-glass transition in two dimensions and its dependence on the bond distribution (Katzgraber *et al.*, 2007)
- (iv) universality classes (Katzgraber *et al.*, 2006) and so on; for a review see Kawashima and Rieger (2004).

A fascinating approach towards the study of spin glasses using ultracold atoms involves the analysis of the correlations between different replicas, i.e. systems with identical disorder landscape (Morrison *et al.*, 2008), and which gives information about the Edwards–Anderson order parameter. The replicas can be created, as suggested in Morrison *et al.* (2008), in a 3D optical lattice with tunneling suppressed in one direction—direction z for instance—in such a way that an array of 2D lattice potentials in the $x - y$ plane is formed. Adding a superlattice of half of the original period in direction z , each plane can be split in two, forming the replicas, which should have the same realization of disorder. In this way one can obtain an array of replicated pairs of 2D random landscapes. This is obviously an ideal

tool to study the questions concerning the existence of finite- T spin-glass transitions in an Ising model with bimodal bond distribution (Kawashima and Rieger, 2004).

An algorithm allowing us to simulate classical randomness in quantum many-body systems by encoding quantum mechanically all possible realizations of the random parameters in a superposition state of an auxiliary system has also been proposed (Paredes *et al.*, 2005*b*). In this way, by appropriately choosing the interaction with the ancilla, all possible quantum evolutions can be simulated in parallel, opening the way towards more accessible methods of simulating quantum random systems.

9.7.1 Parisi–Mézard picture

The *Parisi–Mézard* (PM) picture is fundamentally guided by the results of the mean-field theory. On the level of statistical physics, the Gibbs equilibrium distribution of the spin system in the PM picture at temperature T and for a particular disorder configuration K can be written as a unique convex combination of infinitely many pure equilibrium state distributions (Newman and Stein, 2003; van Enter and van Hemmen, 1983; van Enter and van Hemmen, 1984),

$$\rho_{T,K} = \sum_{\alpha} w_{T,K}^{\alpha} \rho_{T,K}^{\alpha}, \quad \text{with} \quad \sum_{\alpha} w_{T,K}^{\alpha} = 1, \quad (9.78)$$

and all $w_{T,K}^{\alpha} > 0$, where the overlap between two pure states, α and β is defined as

$$Q_{\alpha\beta} \equiv \Omega^{-1} \sum_i \langle s_i \rangle_{T,K}^{\alpha} \langle s_i \rangle_{T,K}^{\beta}, \quad (9.79)$$

where Ω denotes the size of the system and $\langle (\cdot) \rangle$ is the thermal average. The mean-field version of $Q_{\alpha\beta}$ emerges naturally from the calculation shown in the Section 9.7.4 and motivates definition (eqn (9.79)).

In the PM picture, the spin-glass transition is interpreted as being akin to the transition from an Ising paramagnet to a ferromagnet. There, the Gibbs distribution is written as a sum of only two pure states, corresponding to the two possible fully spin-polarized ferromagnetic ground states. As the temperature of the system decreases, the \mathbb{Z}_2 symmetry of the system is broken and a phase transition to a ferromagnetic phase occurs, whose equilibrium properties are not described by the Gibbs state but by the relevant pure-state distribution alone (Mézard *et al.*, 1987). Analogously, the spin-glass transition is characterized by the breaking of the infinite index symmetry, called replica symmetry-breaking in the mean-field case, by which one pure-state distribution $\rho_{T,K}^{\alpha}$ is chosen and alone describes the low-temperature properties of the system (Mézard *et al.*, 1987). However, unlike the Ising ferromagnet, the pure states of the spin glass are not related to each other by a symmetry of the Hamiltonian, but rather by an accidental, infinite degeneracy of the ground state caused by the randomness of the bonds and the frustration effects. This picture can be interpreted as the system getting frozen into one particular state out of infinitely many different ground or metastable states of the system. These states are all taken to be separated by free-energy barriers, whose height either diverges with the system size or are finite but still so large that the decay into a

‘true’ ground state does not occur on observable timescales. Thus, fluctuations around one of these ground states can only sample excited states within one particular free-energy valley. Consequently, Q_{EA} in the spin-glass phase must be redefined as $Q_{EA} := Q_{\alpha\alpha}$, the self-overlap of the state, whereas it remains unchanged for the paramagnetic phase.

9.7.2 de Almeida–Thouless plane

Based on the results of mean-field theory, one of the predictions of the PM picture concerns the order of the infinitely many spin-glass ground states, which is ultrametric (Mézard *et al.*, 1987), as can be seen from the joint probability distribution of three different ground state overlaps, $P_K(Q_{12}, Q_{13}, Q_{23})$. Upon choosing independently three pure states 1, 2, and 3 from the decomposition (eqn (9.78)), one should find that with probability $\frac{1}{4}$, $Q_{12} = Q_{13} = Q_{23}$ and with probability $\frac{3}{4}$ two of the overlaps are equal and smaller than the third. Ultrametricity then follows from the canonical distance function $D_{\alpha\beta} = Q_{EA} - Q_{\alpha\beta}$. The mean-field theory, both with and without a magnetic field, predicts the existence of a plane in the space of the Hamiltonian parameters, called the de Almeida–Thouless (dAT) plane (de Almeida and Thouless, 1978), below which the naïve ansatz for the spin-glass phase becomes invalid and the system is characterized by the transition to this ultrametrically ordered infinite manifold of ground states. It should be pointed out that the clear occurrence of such a dAT plane in the finite-range Edwards–Anderson model would be an important indicator for the validity of the PM picture in these systems. As we discuss in Section 9.7.3, this conclusion has to be drawn with great care.

9.7.3 ‘Droplet’ model

The very applicability of the PM model for finite-range systems is, however, still unproven. It is both challenged by a rival theory, the so-called *droplet* model (Fisher and Huse, 1986), as well as by mathematical analysis (see Newman and Stein (2003) and references therein) that questions the validity of transferring a picture developed for the infinite-range mean-field case to the short-range model. Being a phenomenological theory based on scaling arguments and numerical results, the droplet model describes the ordered spin-glass phase below the transition as one of just two possible pure states, connected by spin-flip symmetry, analogous to the ferromagnet mentioned above. Consequently there can be no infinite hierarchy of any kind, and thereby no ultrametricity. Excitations over the ground state are regions with a fractal boundary—the droplets—in which the spins are in the configuration of the opposite ground state. The free energy of droplets of diameter L is taken to scale as $\sim L^\theta$, with $\theta < 0$ at and below the critical dimension, which is generally taken to be two. So three is the only physical dimension where the spin-glass transition is stable with non-zero transition temperature, with $\theta \sim 0.2$ in this case. The free energy barriers for the creation and annihilation of a droplet scales in 3D as $\sim L^\psi$, with $\theta \leq \psi \leq 2$.

Although there can be no dAT plane in the strict sense in the droplet model, for an external magnetic field the system can be kept from equilibration on experimental timescales for parameters below a line that scales just like the dAT line. This phenomenon might mimic the effects of the replica symmetry-breaking in the PM picture.

9.7.4 Replica-symmetric solution for fixed magnetization

This subsection serves to show that the mean-field version of the effective Hamiltonian (eqn (9.77)) with random magnetic field and magnetization constraint exhibits replica symmetry-breaking just as for the pure Edwards–Anderson model, and would therefore be a candidate to examine the validity of the PM or droplet-picture in a realistic short-ranged spin-glass model. Following Sherrington and Kirkpatrick (SK), the mean-field model is given by:

$$H_{\text{SK}} = \frac{1}{4} \sum_{(i,j)} K_{ij} s_i s_j + \frac{1}{2} \sum_i \bar{\mu}_i s_i, \quad (9.80)$$

where the round brackets (\cdot, \cdot) are used to denote sums over all pairs of different indices. This model differs from eqn (9.77) by the long-range spin exchange. As the mean of $\bar{\mu}_i$, H is generally non-zero this model will not exhibit a phase transition, which, however, is not a concern as the number of (quasi-)ground states will be the quantity of interest. Following the analysis of SK, we aim to find the free energy, ground-state overlap, and magnetization constraint. Then we will use the de Almeida and Thouless approach to show that the solution obtained is unstable in a certain parameter region that lies below the so-called dAT plane of stability. The type of instability that emerges is known to require the replica symmetry-breaking solution of Parisi (Mézard *et al.*, 1987).

As the disorder is quenched (static on experimental timescales), one cannot average directly over disorder in the partition function as would be done for annealed disorder. One must instead average the free-energy density $\bar{f} = -\beta \ln \bar{Z}$ using the 'replica trick': we form n identical copies of the system (the replicas) and the average is calculated for an integer n and a finite number of spins N . Then, using the general formula $\ln x = \lim_{n \rightarrow 0} (x^n - 1)/n$, $\bar{\ln Z}$ is obtained from the analytic continuation of \bar{Z}^n for $n \rightarrow 0$. Finally, we take the thermodynamic limit $N \rightarrow \infty$. Explicitly, \bar{Z}^n is given by:

$$\bar{Z}^n = \sum_{\{s_i^\alpha = \pm 1\}} \exp \left[-\beta \overline{H_{\text{SK}}[s_i^\alpha, n]} \right], \quad (9.81)$$

where $\overline{H_{\text{SK}}[s_i^\alpha, n]}$ is the sum of n independent and identical spin Hamiltonians (eqn (9.80)), averaged over the Gaussian disorder, with Greek indices now numbering the n replicas.

Executing the average over the Gaussian distributions for K_{ij} and $\bar{\mu}_i$ leads to coupling between spin–spin interactions of different replicas. As the mean-field approach means that the double sum over the site indices in eqn (9.80) can be simplified into a square using $(s_i^\alpha)^2 = 1$, one finds:

$$\begin{aligned} \overline{f_N^n} &= -(Nn\beta)^{-1} \left\{ e^{Nn(\beta K)^2/4} e^{-n^2(\beta K)^2/2+n(\beta h)^2/2} \times \right. \\ &\quad \left. \sum_{\{s_i^\alpha = \pm 1\}} \exp \left[\frac{N(\beta K)^2}{2} \sum_{\alpha < \beta} \left(\sum_i \frac{s_i^\alpha s_i^\beta}{N} \right)^2 + (\beta h)^2 \sum_{\alpha < \beta, i} s_i^\alpha s_i^\beta - \beta H \sum_{\alpha, i} s_i^\alpha \right] - 1 \right\}, \end{aligned} \quad (9.82)$$

where the prefactor $e^{-n^2(\beta K)^2/2+n(\beta h)^2/2}$ becomes irrelevant in the limit $n \rightarrow 0$ and is subsequently dropped. As in the standard procedure, the square of the operator sum

$\sum_i s_i^\alpha s_i^\beta$ is decoupled by introducing auxiliary operators $q_{\alpha\beta}$ via a Hubbard–Stratonovich transformation:

$$\begin{aligned} \overline{f_N^n} = & -(Nn\beta)^{-1} \left\{ e^{Nn(\beta K)^2/4} \int_{-\infty}^{\infty} \left[\prod_{\alpha<\beta} dq_{\alpha\beta} \left(\frac{N}{2\pi} \right)^{\frac{1}{2}} \beta K \right] \right. \\ & \times \exp \left. \left[-\frac{N(\beta K)^2}{2} \sum_{\alpha<\beta} q_{\alpha\beta}^2 + N \ln \left(\sum_{\{s^\alpha=\pm 1\}} \exp [L(q_{\alpha\beta})] \right) \right] - 1 \right\}, \end{aligned} \quad (9.83)$$

where the functional $L(q_{\alpha\beta})$ is:

$$L(q_{\alpha\beta}) = \beta^2 \sum_{\alpha<\beta} (K^2 q_{\alpha\beta} + h^2) s^\alpha s^\beta - \beta H \sum_\alpha s^\alpha, \quad (9.84)$$

and the configuration sum of $\exp [L(q_{\alpha\beta})]$ now only goes over the n spins s^α in $L(q_{\alpha\beta})$, the Hubbard–Stratonovich transformation having made it possible to decouple the configuration sum over Nn spins in eqn (9.82) into a N -fold product of n -spin sums. Assuming that the thermodynamic limit ($N \rightarrow \infty$) can be taken before $n \rightarrow 0$, i.e. that the usual limiting process can be inverted, eqn (9.83) can be evaluated by the method of steepest descent, as the exponent is proportional to N . According to this method, the free energy per spin in the thermodynamic limit is the maximum of the $q_{\alpha\beta}$ -dependent function in the exponent:

$$-\beta \overline{f} = \lim_{n \rightarrow 0} \max \left\{ \frac{(\beta K)^2}{4} \left(1 - \frac{1}{n} \sum_{(\alpha,\beta)} q_{\alpha\beta}^2 \right) + \frac{1}{n} \ln \left(\sum_{\{s^\alpha=\pm 1\}} \exp [L(q_{\alpha\beta})] \right) \right\} \quad (9.85)$$

(with $\overline{f} := \lim_{n \rightarrow 0} \overline{f^n}$) with the self-consistency condition:

$$\frac{\partial \overline{f}}{\partial q_{\alpha\beta}} = 0 \quad \Leftrightarrow \quad q_{\alpha\beta} = \langle s^\alpha s^\beta \rangle_L, \quad (9.86)$$

and the magnetization:

$$m = -\frac{1}{\beta} \frac{\partial \overline{f}}{\partial H} = \langle s^\alpha \rangle_L = 2N_F/N - 1, \quad (9.87)$$

where the average $\langle (\cdot) \rangle_L$ is defined as:

$$\langle (\cdot) \rangle_L = \lim_{n \rightarrow 0} \frac{\sum_{\{s^\alpha=\pm 1\}} (\cdot) \exp [L(q_{\alpha\beta})]}{\sum_{\{s^\alpha=\pm 1\}} \exp [L(q_{\alpha\beta})]}. \quad (9.88)$$

The mean-field approach has allowed a decoupling of the spins and the reduction of the problem to a single-site model with ‘Hamiltonian’ $L[q_{\alpha\beta}]$. For this new problem the overlap parameter emerges naturally, albeit in a self-consistent manner. To push the calculation

further some assumption for $q_{\alpha\beta}$ has to be made. Naïvely, from the requirement that the result should be independent of the replica indices, the most natural choice for q is to consider all identical overlaps between the replicas, $q_{\alpha\beta} = q$, which is the SK ansatz. Thus the double sum over the replicas $\sum_{(\alpha,\beta)} s^\alpha s^\beta$ in eqn (9.84) can be written as a square, keeping $(s^\alpha)^2 = 1$ in mind. Another Hubbard–Stratonovitch transformation with auxiliary variable z then decouples the square and yields an expression for the free-energy density, which has to be evaluated self-consistently and in which the limit $n \rightarrow 0$ can easily be calculated:

$$\begin{aligned} -\beta \bar{f}_{\text{SK}} &= \lim_{n \rightarrow 0} \left\{ \frac{(\beta K)^2}{4} (1 - (n-1)q^2) + \frac{1}{n} \ln \left(\frac{1}{\sqrt{2\pi}} \int_{-\infty}^{\infty} dz \exp \left[-\frac{z^2}{2} \right] \right. \right. \\ &\quad \times \left. \left. \left(\exp \left[-\frac{\beta^2(K^2q + h^2)}{2} \right] \sum_{s=\pm 1} \exp \left[\beta \sqrt{K^2q + h^2}s - \beta Hs \right] \right)^n \right) \right\} \\ \Rightarrow \beta \bar{f}_{\text{SK}} &= \frac{(\beta K)^2}{4} (1 - q)^2 - \frac{(\beta h)^2}{2} + \left(\frac{1}{2\pi} \right)^{\frac{1}{2}} \int_{-\infty}^{\infty} dz e^{-\frac{z^2}{2}} \ln(2 \cosh(A(z))), \end{aligned} \quad (9.89)$$

with $A(z) := \beta \sqrt{K^2q + h^2} - \beta H$. The overlap (eqn (9.86)) and the magnetization constraint (eqn (9.87)) can also be evaluated in the same way:

$$q = \frac{1}{\sqrt{2\pi}} \int_{-\infty}^{\infty} dz e^{-\frac{z^2}{2}} \tanh^2(A(z)) \quad (9.90)$$

$$m = \frac{1}{\sqrt{2\pi}} \int_{-\infty}^{\infty} dz e^{-\frac{z^2}{2}} \tanh(A(z)) = 2N_F/N - 1. \quad (9.91)$$

A well-known problem with the SK ansatz for $q_{\alpha\beta}$ is that it yields negative entropy for low temperatures and thus becomes unphysical. This is due to a fundamental technical problem with the replica trick: for the method of steepest descent to be valid the SK solution must be a maximum of the exponent in eqn (9.83) and must *stay* a maximum as the replica limit $n \rightarrow 0$ is reached. But there is *no* unique way of choosing the zero-dimensional limit of the matrix $q_{\alpha\beta}$. The SK solution just corresponds to one possible choice for this limit. Thus, the question arises of whether the SK solution for the free energy is still a good, i.e. maximal, choice in the replica limit.

To answer this question, one proceeds, in a manner analogous to the de Almeida and Thouless procedure, to analyse the fluctuations around the SK solution, while taking the magnetization constraint into account. Developing eqns (9.85) and (9.87) to second and first order respectively around $q_{\alpha\beta} = q$, one finds that in the replica limit $n \rightarrow 0$ there is an eigenvalue λ_2 of the matrix $\partial^2 \bar{f} / \partial q_{\alpha\beta} \partial q_{\gamma\delta}$ that can have negative values while still respecting the constraint, yielding the condition:

$$\lambda_2 = \frac{1}{(\beta K)^2} - \frac{1}{\sqrt{2\pi}} \int_{-\infty}^{\infty} dz e^{-\frac{z^2}{2}} \operatorname{sech}^4(A(z)) > 0, \quad (9.92)$$

which is violated for sufficiently low T/K , H/K , and h/K . The plane in parameter space below which this happens is the so-called dAT surface. This instability is rectified by a

much more involved ansatz for $q_{\alpha\beta}$, which breaks the symmetry of the replicas and leads to the phenomena described in subsection above.

9.8. Disorder-induced order

In this last section, we discuss the general effect and mechanism of *disorder-induced order*, also called *random-field-induced order*. The paradigmatic example of this effect is the classical ferromagnetic *XY* model in a 2D lattice. Random-field-induced order has, however, its quantum analogs that can be particularly well realized with ultracold atoms (see Aharony (1978), Dotsenko and Feigelman (1981), Minchau and Pelcovits (1985), Feldman (1998), Wehr *et al.* (2006), and Niederberger *et al.*, (2008, 2009, 2010), and references therein). The mechanism occurs in systems with continuous symmetry in which the disordered field (coupled to the order parameter) breaks this symmetry. In the *XY* model, breaking of the symmetry acts against the Mermin–Wagner–Hohenberg no-go rule in two dimensions (see Chapter 2). In Wehr *et al.* (2006) it was proven rigorously that the classical *XY* spin model on a 2D lattice in a uniaxial random field magnetizes spontaneously at $T = 0$ in the direction *perpendicular* to the magnetic field axis. Moreover, strong evidence was provided that this is also the case at small positive temperatures.

Consider a classical spin system on the 2D square lattice \mathbb{Z}^2 in a random magnetic field, \mathbf{h} . Our 2D spin variable $\boldsymbol{\sigma}_i = (\cos \theta_i, \sin \theta_i)$ at a site $i \in \mathbb{Z}^2$ is a unit vector in the *XY* plane; our system is therefore described by

$$H = -J \sum_{|i-j|=1} \boldsymbol{\sigma}_i \cdot \boldsymbol{\sigma}_j - \epsilon \sum_i \mathbf{h}_i \cdot \boldsymbol{\sigma}_i. \quad (9.93)$$

Here the first term is the standard nearest-neighbor interaction of the *XY* model, and the second term represents a small random field perturbation. The \mathbf{h}_i are assumed to be independent, identically distributed random planar vectors.

For $\epsilon = 0$ the model has no spontaneous magnetization m at any positive T . In higher dimensions the system does magnetize at low temperatures. The impact of a random field term on the behavior of the model was first addressed in Imry and Ma (1975), where it was argued that if the distribution of the random variables \mathbf{h}_i is invariant under rotations, there is no spontaneous magnetization at any positive T in any dimension $d \leq 4$. A rigorous proof of this statement was given in Aizenman and Wehr (1989, 1990). Both works crucially use the rotational invariance of the distribution of the random field variables.

In Wehr *et al.* (2006) the authors consider the case where \mathbf{h}_i is directed along the *y*-axis: $\mathbf{h}_i = \eta_i \mathbf{e}_y$, where \mathbf{e}_y is the unit vector in the *y* direction, and η_i is a random real number. Such a random field obviously breaks the continuous symmetry of the interaction, and a question arises over whether the model still has no spontaneous magnetization in two dimensions.

Below we sketch the proof that the system indeed magnetizes at $T = 0$, and argue that the ground-state magnetization is stable under inclusion of small thermal fluctuations. For this, we use a version of the Peierls contour argument (Peierls, 1936), eliminating first the possibility that Bloch walls or vortex configurations destroy the transition.

Let us start by a rigorous analysis of the ground state. Consider the system in a square Λ with the ‘right’ boundary conditions, $\boldsymbol{\sigma}_i = (1, 0)$, for the sites i on the outer boundary

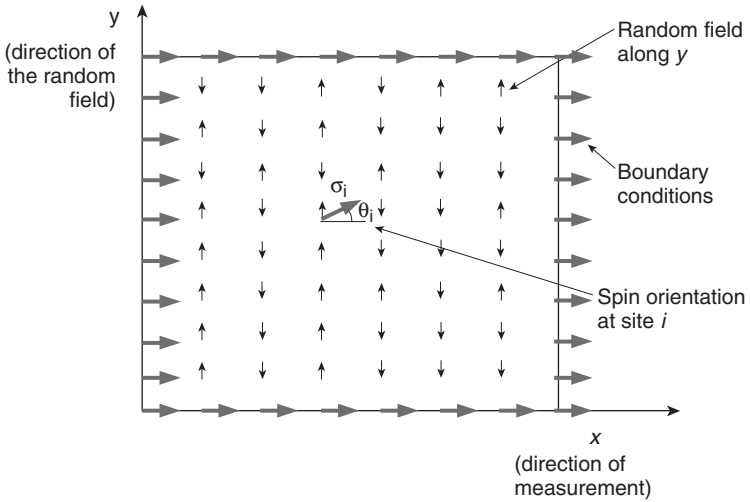


Figure 9.17 XY model on a 2D square lattice in a random magnetic field. The magnetic field is oriented along the y -axis, $\mathbf{h}_i = \eta_i \mathbf{e}_y$, where η_i is a real random number. Right boundary conditions are assumed on the outer square, possibly placed at infinity. From Wehr *et al.* (2006).

of Λ (see Figure 9.17). The energy of any spin configuration decreases if we replace the x components of the spins by their absolute values and leave the y components unchanged. It follows that in the ground state x components of all the spins are non-negative. As the size of the system increases, we expect the x component of the ground-state spins to decrease, since they feel less influence from the boundary conditions and the ground-state value of each spin will converge. We thus obtain a well-defined infinite-volume ground state with the ‘right’ boundary conditions at infinity.

The above convergence statement is physically quite natural. Mathematically, however, it is non-trivial and requires a proof. *A priori* the infinite-volume ground state could coincide with the ground state of the random field Ising model, in which all spins have zero x component. The following argument shows that this is *not* the case. Suppose that the spin σ_i at a given site i is aligned along the y -axis, i.e. $\cos \theta_i = 0$. Since the derivative of the energy function with respect to θ_i vanishes at the minimum, we obtain

$$\sum_{j:|i-j|=1} \sin(\theta_i - \theta_j) = 0. \quad (9.94)$$

Since $\cos \theta_i = 0$, this implies $\sum_{j:|i-j|=1} \cos \theta_j = 0$. Because in the ‘right’ ground state all spins lie in the (closed) right half-plane $x \geq 0$, all terms in the above expression are non-negative and hence have to vanish. This means that at all the nearest neighbors j of the site i , the ground-state spins are directed along the y -axis as well. Repeating this argument, we conclude that the same holds for all spins of the infinite lattice, i.e. the ground state is the (unique) random field Ising model ground state. This conclusion, however, leads to a contradiction, since assuming it to be the case, one can construct a field configuration,

occurring with a positive probability, that forces the ground state spins to have non-zero x components. To achieve this we put strong positive ($\eta_i > 0$) fields on the boundary of a square and strong negative fields on the boundary of a concentric smaller square. If the fields are very weak in the area between the two boundaries, the spins will form a Bloch wall, rotating gradually from $\theta = \frac{\pi}{2}$ to $\theta = -\frac{\pi}{2}$. Since such a local field configuration occurs with a positive probability, the ground state *cannot* have zero x components everywhere, contrary to our assumption.

To study the system at low positive T , we need to ask what are the typical low-energy excitations from the ground state. For $\epsilon = 0$, continuous symmetry allows Bloch walls, i.e. configurations in which the spins rotate gradually over a large region, for example from left to right. The total excitation energy of a Bloch wall in two dimensions is of order one, and it is the presence of such walls that underlies the absence of continuous symmetry-breaking. However, for $\epsilon > 0$ a Bloch wall carries additional energy, coming from the change of the direction of the y component of the spin, which is proportional to the area of the wall—of order L^2 for a wall of linear size L in two dimensions—since the ground-state spins are adapted to the field configuration and hence overturning them will increase the energy per site. Similarly, vortex configurations, which are important low-energy excitations in the non-random XY model are no longer energetically favored in the presence of a uniaxial random field.

We are thus left, as possible excitations, with sharp domain walls, where the x component of the spin changes sign rapidly. To a first approximation we consider excited configurations, in which spins take either their ground-state values, or the reflections of these values in the y -axis. As in the standard Peierls argument (Peierls, 1936), in the presence of the right boundary conditions, such configurations can be described in terms of contours γ (domain walls), separating spins with positive and negative x components. If m_i is the value of the x component of the spin σ_i in the ground state with the right boundary conditions, the energy of a domain wall is the sum of $m_i m_j$ over the bonds (ij) crossing the boundary of the contour. Since changing the signs of the x components of the spins does not change the magnetic field contribution to the energy, the Peierls estimate shows that the probability of such a contour is bounded above by $\exp(-2\beta \sum_{(ij)} m_i m_j)$, with $\beta = J/k_B T$.

We want to show that for a typical realization of the field \mathbf{h} (i.e. with probability 1), these probabilities are summable, i.e. their sum over all contours containing the origin in their interior is finite. It then follows that at a still-lower T this sum is small, and the Peierls argument proves that the system magnetizes (in fact, a simple additional argument shows that summability of the contour probabilities already implies the existence of spontaneous m). To show that a series of random variables is summable with probability 1, it suffices to prove the summability of the series of the expected values. We present two arguments for the last statement to hold.

If the random variables m_i are bounded away from zero, i.e. $m_i > \sqrt{c}$, for some $c > 0$, the moment-generating function of the random variable $\sum_{(ij)} m_i m_j$ satisfies

$$\mathbf{E} \left[\exp \left(-\beta \sum_{(ij)} m_i m_j \right) \right] \leq \exp[-c\beta L(\gamma)], \quad (9.95)$$

with $L(\gamma)$ denoting the length of the contour γ . The sum of the probabilities of the contours enclosing the origin is thus bounded by $\sum_{\gamma} \exp[-c\beta L(\gamma)]$. The standard Peierls–Griffiths bound proves the desired summability.

The above argument does not apply if the distribution of the ground state m contains zero in its support. For unbounded distribution of the random field this may very well be the case, and then another argument is needed. If we assume that the terms in the sum $\sum_{(ij)} m_i m_j$ are independent and identically distributed, then

$$\mathbf{E}[\exp(-2\beta \sum_{(ij)} m_i m_j)] = \mathbf{E}[\exp(-2\beta m_i m_j)]^{L(\gamma)} = \exp\{L(\gamma) \log \mathbf{E}[\exp(-2\beta m_i m_j)]\}, \quad (9.96)$$

and we just need to observe that $\mathbf{E}[\exp(-2\beta m_i m_j)] \rightarrow 0$ as $\beta \rightarrow \infty$ (since the expression under the expectation sign goes pointwise to zero and lies between 0 and 1) to conclude that

$$\mathbf{E}[\exp(-2\beta \sum_{(ij)} m_i m_j)] \sim \exp[-g(\beta)L(\gamma)] \quad (9.97)$$

for a positive function $g(\beta)$ with $g(\beta) \rightarrow \infty$ as $\beta \rightarrow \infty$. While $m_i m_j$ are not, strictly speaking, independent, it is natural to assume that their dependence is weak, so that their correlation decays fast with the distance of the corresponding bonds (ij) . The behavior of the moment-generating function of their sum is then qualitatively the same, with a renormalized rate function $g(\beta)$ still diverging as $\beta \rightarrow \infty$. As before, this is enough to carry out the Peierls–Griffiths estimate, which implies spontaneous magnetization in the x direction. We note that our assumption about the fast decay of correlations implies that the sums of $m_i m_j$ over subsets of \mathbb{Z}^2 satisfy a large-deviation principle analogous to that for sums of independent random variables, and that the above argument can be restated using this fact. Disorder-induced order, discussed here for the classical XY model, is by its very nature a general phenomenon, and can occur also in quantum systems. In recent years it has been studied in particular in relation to ultracold atoms:

- Disorder-induced order occurs in a two-component BEC with random inter-component Raman coupling of fixed phase, say ϕ_0 . Such coupling, even when very small, controls in an amazingly efficient way the relative phase between the BEC components, and sets it to be $\phi_0 \pm \frac{\pi}{2}$ (Niederberger *et al.*, 2008).
- A similar effect occurs at the BCS–BEC crossover when we consider a coupling of the Fermi superfluid to a molecular BEC via random photo-associative coupling of fixed phase. Such coupling, even when very small, efficiently controls the relative phase between the Fermi superfluid and the molecular condensate (Niederberger *et al.*, 2009).
- Last, but not least, disorder-induced order has been demonstrated in a 1D XY spin chain with an external, site-dependent uni-axial random field within the XY plane, and there are also possible realizations in ultracold atoms (Niederberger *et al.*, 2010). Using numerical matrix product states (MPS) and time evolving block decimation (TEBD) algorithms (see Chapters 5 and 6) one can investigate numerically the signature of

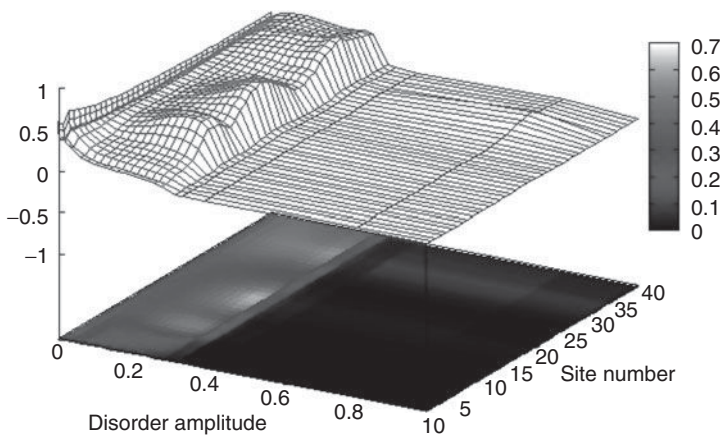


Figure 9.18 The orthogonal magnetization is non-zero up to a threshold, even for a given pseudorandom external field. The sudden drop to zero at a certain amplitude (0.3 in this realization) indicates the phase transition between the disorder-induced order state and the state primarily following the external magnetic field. From Niederberger *et al.* (2010).

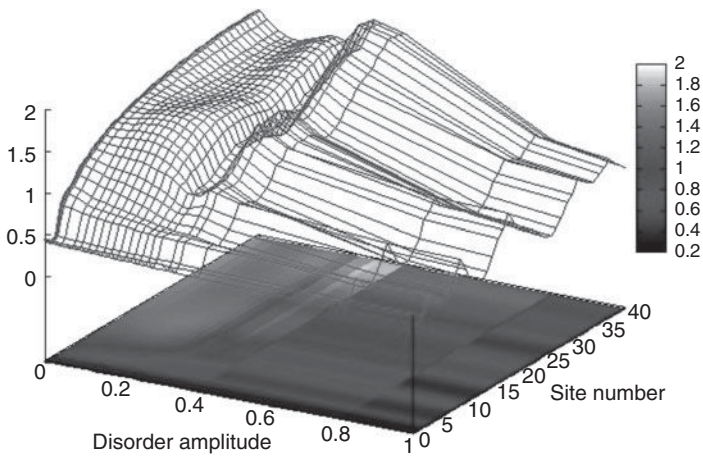


Figure 9.19 Block-entropy in a 1D XY chain in a random magnetic field directed along the x -axis. It is plotted as a function of the size of the block (i.e. site number, corresponding to the site at which partition of the system was done) and of the strength of disorder. It exhibits an apparent discontinuity at the disorder amplitude at which the orthogonal magnetization disappears (0.3 in this realization of the disorder). From Niederberger *et al.* (2010).

a quantum phase transition at $T = 0$, which exhibits an arousal of magnetization in the direction orthogonal to the external magnetic field, and the logarithmic scaling of the block-entropy with the block size as the amplitude of the external field crosses the criticality. Typical results are illustrated in Figures 9.18 and 9.19.

Disorder-induced order has not yet been observed with disordered ultracold atoms, and thus remains one of the challenging novel phenomena to be realized in the future.

10

Frustrated ultracold atom systems

10.1. Introduction

Frustration reflects the impossibility of fulfilling simultaneously all constraints posed by some Hamiltonians. It is an inherent property of some strongly correlated classical models, such as various Ising or spin ice models, but also of some quantum spin models. The incompatibility between the different constraints can arise due to the lattice geometry, the nature of the interactions or the presence of some type of disorder, to mention but a few. Such incompatibility often translates into a severe problem of energy minimization when finding the ground state of the system. However, frustrated systems are not just disordered systems; many of them order (in the standard definition) at zero or low temperatures but also those that do not order and lay beyond the Landau theory of phase transitions present a fascinating underlying structure. Particularly interesting effects appear when a system is both disordered and frustrated (see, for example, Mézard *et al.* (1987) and Sachdev (1999)).

Here we focus on several frustrated models in *regular* lattices, and discuss their possible realizations using ultracold atoms in optical lattices. The chapter is organized as follows. We start in this section by reviewing the classical Ising antiferromagnetic model, which is the archetypal example of geometrical frustration. In Section 10.2 we move to frustrated quantum antiferromagnets and classify the ground states of such frustrated systems according to the spontaneous breaking or not breaking of symmetries and the absence of local order parameters. Section 10.3 deals with the physical properties of frustrated quantum antiferromagnets, illustrated with some well known examples of such systems. Finally Section 10.4 focuses on the realization of frustrated models with ultracold gases. There are already several theoretical proposals for experimental realization of quantum magnets in cold atom/ion systems. We expect that these experiments will help to verify existing theoretical predictions, and point out new directions in theoretical investigations for quantum magnetism and high T_c superconductivity.

10.1.1 Classical antiferromagnetic Ising model

Consider a physical system described by the classical Ising Hamiltonian

$$H_I = J \sum_{\langle ij \rangle} \sigma_i^z \sigma_j^z, \quad (10.1)$$

where $\langle ij \rangle$ denotes the summation over nearest neighbors, and on each lattice site i , the spin is $\sigma_i^z = \pm 1$. The constant coupling J determines the character of the ground state, either

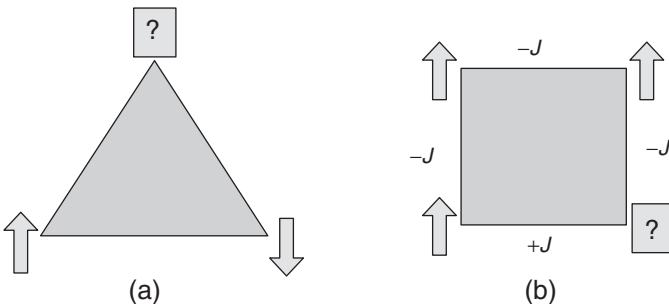


Figure 10.1 (a) Antiferromagnetic ($J > 0$) Ising model on a triangular lattice; it is not possible to determine the orientation of the spins by requiring all couplings to be simultaneously fulfilled, and so the system becomes frustrated. (b) Example of a square lattice with an odd (odd) number of antiferromagnetic (ferromagnetic) Ising couplings. The model is again frustrated.

ferromagnetic (F) for $J < 0$, or antiferromagnetic (AF) if $J > 0$. This model, for $J > 0$ and when considered on a 2D triangular lattice, is a paradigmatic example of a frustrated system (Moessner and Sondhi, 2001a). It is clear from Figure 10.1(a) that it is not possible to minimize the energy on such a triangular lattice, satisfying all the bonds simultaneously. In this case, the ground state is highly degenerate due to the frustration, and not just to the invariance of the Hamiltonian under global spin flip, which is the case for the ferromagnetic Ising model ($J < 0$) on the same lattice.

Frustration can be met even in a lattice that has a relatively simple structure (e.g. a 2D square lattice) if some interactions are ferromagnetic while others are antiferromagnetic. For instance, in the 2D ferromagnetic Ising model, if one replaces an odd number of F bonds by antiferromagnetic ones, one obtains a frustrated model from a non-frustrated one. The model of a square lattice in Figure 10.1(b) is an example of such a case. In general, we say that the model is frustrated when the orientations of spins cannot be obtained by satisfying all the couplings simultaneously while minimizing the energy of the model (Mézard *et al.*, 1987). Many antiferromagnetic spin models in regular lattices are easily frustrated by the geometry of the lattice, with prominent examples being the triangular and kagomé lattices.

Detailed studies of quantum antiferromagnets can be found in the books of Auerbach (1994) and Sachdev (1999) as well as in the recent reviews by Misguich and Lhuillier (2003), Lhuillier (2005), and Alet *et al.* (2006). Frustrated models have been also discussed in the context of spin glasses (see Binder and Young (1986)). The concept of frustration has also been studied from the perspective of high-temperature superconductors (e.g. see the reviews by Rasolt and Tesanović (1992) and Sigrist and Rice (1995)).

10.2. Quantum antiferromagnets

The interest in quantum antiferromagnets is motivated by several factors. First, a ‘rule of thumb’ says that close to a high-temperature superconducting phase, there is always an antiferromagnetic phase; understanding the latter should thus help to understand the former. Second, quantum antiferromagnets are almost always frustrated according

to the definition given in the introduction. Third, frustrated quantum antiferromagnets are expected to exhibit novel quantum phases, such as a spin-liquid phase. These phases seem to break the standard Landau–Ginzburg symmetry-breaking picture of phases and phase transitions, in which ordered phases are related to order parameters. Spin liquids do not have any local order parameter, yet some of them may exhibit a hidden topological order—in this sense they are somewhat similar to quantum liquids appearing in fractional quantum Hall effects (Kalmeyer and Laughlin, 1987; Wen *et al.*, 1989). Because of these properties they are related to the most challenging open questions of condensed-matter physics (see Chen *et al.* (2010)). Let us recall first some basic properties of quantum antiferromagnets.

According to several authors (Misguich and Lhuillier, 2003; Lhuillier, 2005; Alet *et al.*, 2006; Sachdev, 2008), at zero and low temperatures quantum antiferromagnets exhibit one of five generic (non-critical) behaviors.

- **Néel order.** This is a standard up-down-up-down type of ordering that often occurs in regular *bipartite* lattices—lattices that can be split into two sublattices A and B in such a way that all spins on A interact only with spins on B and vice versa. Examples include square lattices in two dimensions or cubic in three dimensions. Generalized (planar, or non-planar) Néel order might, however, also occur in frustrated (classical $O(3)$) antiferromagnets, for instance in the ideal triangular lattice (Bernu *et al.*, 1992, 1994). Néel order breaks rotational and translational symmetry, exhibits long-range order, but connected correlation functions (cumulants) decay; excitations are gapless, and have a form of spin waves (see Figure 10.2).
- **Valence-bond solids** (VBSs). This order breaks the lattice translational symmetry and consists of an ordered covering of the lattice by singlets (zero-spin states). For singlets formed by two spins in different lattice sites—often called dimers—the order is termed Peierls’ order (see Figure 10.3). VBSs can consist of singlets formed on bigger elementary cells or plaquettes in the lattice (see Figure 10.4). There is a long-range order in dimer correlations, but the system is gapped and correlation functions decay exponentially. Excitations in 2D VBSs are gapped (confined spinons) (Alet *et al.*, 2006; Sachdev, 2008).
- **Valence-bond crystals** (VBCs). A famous example of a VBC is the Affleck–Kennedy–Lieb–Tasaki (AKLT) state (Affleck *et al.*, 1987). These states do not exhibit any long-range order of local observables, they do not break the lattice translational symmetry, the system is gapped, and correlation functions decay exponentially (Auerbach, 1994).¹
- **Spin liquid of type I.** This order has no $SU(2)$ symmetry-breaking, gapped excitations, and decaying correlations. The concept of spin liquids has been introduced by theorists in attempts to understand high T_c superconductivity. In particular, Anderson (1987) introduced in this context a resonating valence-bond spin liquid. When a valence-bond solid starts melting due to quantum fluctuations introduced in the system, the situation gives rise to a new phase called a resonating valence-bond

¹It is worth noticing, as pointed out to us by Claire Lhuillier, that different authors use the names VBS and VBC in different senses, and sometimes do not even make any distinction between VBSs and VBCs.

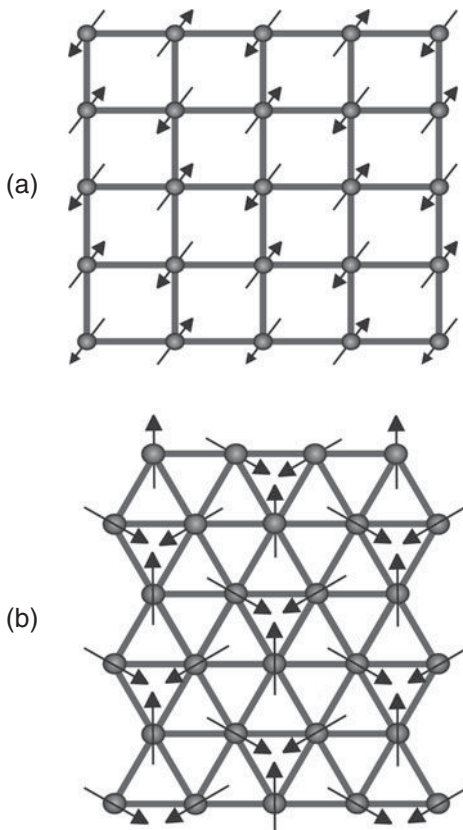


Figure 10.2 Néel ground state of the $S = \frac{1}{2}$ antiferromagnet H_H (eqn (10.2)) with all $J_{ij} = J$ on (a) a square lattice and (b) a triangular lattice. The spin polarization is (a) collinear and (b) coplanar. Redrawn after Sachdev (2008) by courtesy of the author.

liquid (see Figure 10.5). The Heisenberg antiferromagnet in a trimerized kagomé lattice, discussed later, provides an example of such behavior, representing a resonating valence-bond state (RVB). Numerical Monte Carlo simulations suggest that this liquid does not show any long-range correlations (Liang *et al.*, 1988), and is a superposition of products of singlets (Alet *et al.*, 2006). Particularly interesting are topological spin liquids (Alet *et al.*, 2006; Wen, 2004), for which degeneracy of the ground state depends on the topology of the underlying lattice. Among them, one can distinguish *chiral spin liquids*, which break discrete symmetries: time reversal and parity (for a very recent review and classification in terms of local unitary transformations and tensor network states, see Chen *et al.* (2010), or for PEPS states see Schuch *et al.* (2010)). Chiral spin liquids are somewhat analogous to various states known from the theory of the fractional quantum Hall effect (Laughlin state, Pfaffian state, Moore–Read states (Kalmeyer and Laughlin, 1987; Cooper, 2008).

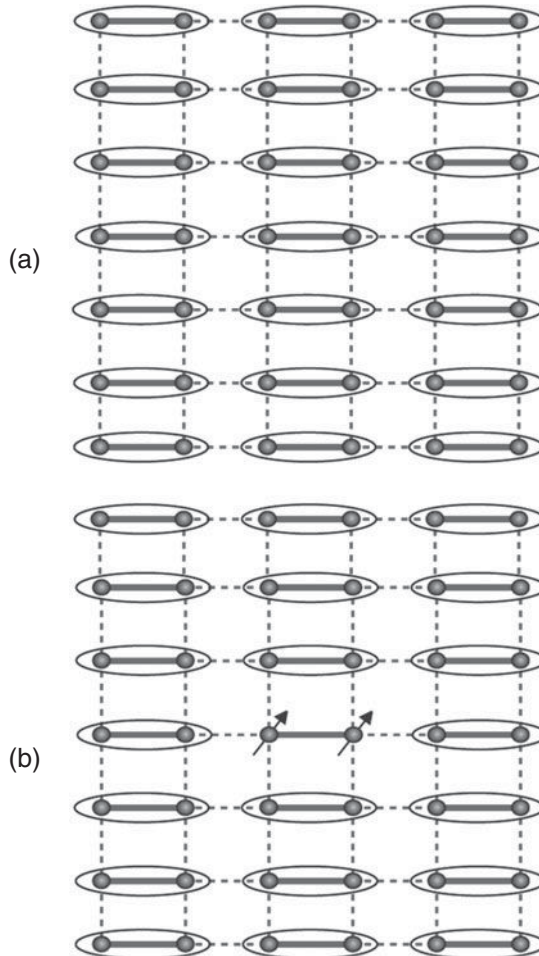


Figure 10.3 The coupled dimer antiferromagnet, described by the Hamiltonian H_H (eqn (10.2)), with $J_{ij} = J$ on the full lines and $J_{ij} = J/g$ on the dashed lines. (a) ground state (for a large value of g) with each ellipse representing a singlet valence bond $(|\uparrow\downarrow\rangle - |\downarrow\uparrow\rangle)/\sqrt{2}$. (b) The $S = 1$ spin triplon excitation. The pair of parallel spins on the broken valence bond hops between dimers using the J/g couplings. Redrawn after Sachdev (2008) by courtesy of the author.

- **Spin liquids of type II.** This order has no $SU(2)$ symmetry breaking, is gapless, and has large density of states of low-energy excitations. Such spin liquids, similar to high- T_c superconductors, break neither time reversal nor parity symmetry, and thus are often termed *symmetric spin liquids*. Symmetric spin liquids might be of type I and might exhibit topological order (implying a gapped spectrum). Wen proposed classifying the gapless symmetric spin liquids using a so-called *projective symmetry group* (Chen *et al.*, 2010; Wen, 2004).

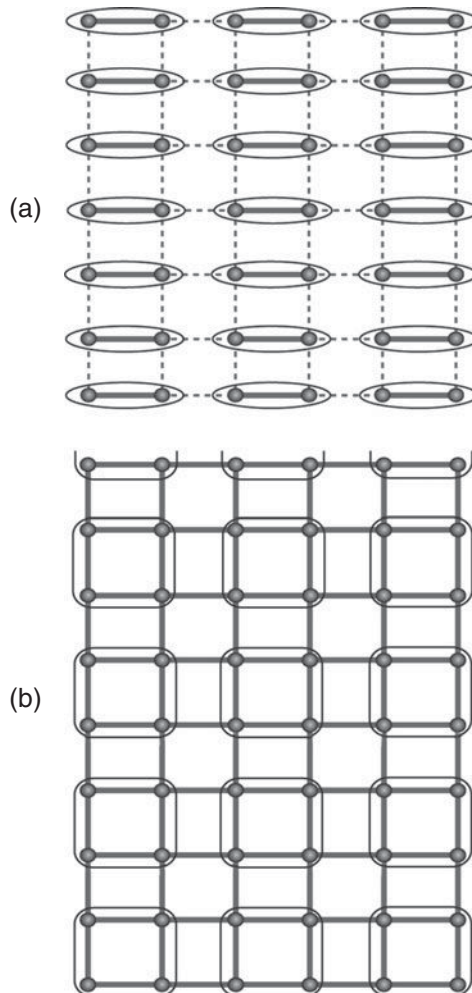


Figure 10.4 (a) Columnar valence-bond solid of $H_H + H_1$ with H_H (eqn (10.2)), with $J_{ij} = J$ on all bonds and H_1 a perturbation that involve four spins interacting on a plaquette. This state is the same as in Figure 10.3(a), but the square lattice symmetry has been broken spontaneously. Rotations by multiples of $\frac{\pi}{2}$ about a lattice site yield the four degenerate states. (b) Four-fold degenerate plaquette valence-bond solid state with the rounded squares representing the $S = 0$ combination of four spins. Redrawn after Sachdev (2008) by courtesy of the author.

We somewhat speculatively add to this list a sixth possibility (Damski *et al.*, 2005a; Damski *et al.*, 2005b).

- **Quantum spin-liquid crystals.** This order combines planar Néel order with spin liquid type II behavior. We speculate about the possibility of such order, based on numerical studies of one particular spin model (Damski *et al.*, 2005a, 2005b; Honecker

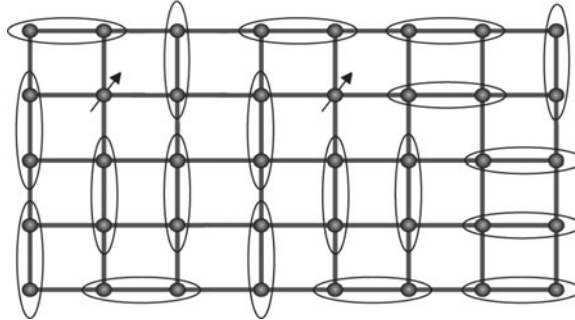


Figure 10.5 Caricature of a spin-liquid state. The valence bonds are entangled between different pairings of the spins, only one of which is shown. Also shown are two unpaired $S = \frac{1}{2}$ spinons, which can move independently in the spin-liquid background. Redrawn after Sachdev (2008) by courtesy of the author.

et al., 2007), which revealed that it had a large number of low-energy excitations as in spin-liquids of type II, and presumably no gap. The explanation of this behavior is that in the thermodynamical limit there are infinitely many classical degenerate ground states, which are on the one hand relevant quantum mechanically, and, on the other, have correlations that exhibit planar Néel order.

Note that when a (continuous second-order) quantum phase transition occurs at $T = 0$, the gap in the excitation spectrum at criticality closes. The states at criticality typically have similar properties to the generic non-critical ones, except that they exhibit algebraically decaying order parameters and correlations. A standard example would be the ground state of the Heisenberg model for spin- $\frac{1}{2}$ in one dimension. It indeed exhibits Néel-like correlations which decay algebraically.

10.3. Physics of frustrated quantum antiferromagnets

To gain a deeper understanding of the physics appearing in frustrated quantum systems, we discuss in this section several examples of antiferromagnetic spin models that exhibit frustration. For the sake of completeness, we start with the simple example of the non-frustrated Heisenberg model on a square lattice.

10.3.1 Heisenberg model on a square lattice

Let us consider the Heisenberg model

$$H_H = \sum_{\langle ij \rangle} J_{ij} \boldsymbol{\sigma}_i \cdot \boldsymbol{\sigma}_j, \quad (10.2)$$

where $\boldsymbol{\sigma}$ is the vector of spin- $\frac{1}{2}$ Pauli operators.

The ferromagnetic case For the 2D Heisenberg ferromagnetic model $J_{ij} = J < 0$ the exact ground state is given by the state (Ashcroft and Mermin, 1976)

$$|\psi_G^F\rangle = \prod_i |0\rangle_i, \quad (10.3)$$

where $|0\rangle_i$ and $|1\rangle_i$ represent respectively the up and down eigenstates of σ^z at the i th site.

The antiferromagnetic case For the Heisenberg antiferromagnetic model $J_{ij} = J > 0$ on the square lattice, the exact ground state is hard to find, although the system is not frustrated. Nonetheless, the classical ground states, obtained after replacement of the σ operators by vectors, can be explicitly written down. To this end the lattice is divided into two sublattices A and B in such a way that all nearest neighbors of sublattice A belong to the sublattice B, and vice versa. Such a split lattice is called a bipartite lattice. The classical ground state can be obtained by taking some orientation (e.g. in the z -direction) of all spins in one sublattice and the opposite orientation of all spins in the other sublattice. In this way, one can find the classical ground state of a square lattice (Sachdev, 1999; Manousakis, 1991):

$$|\psi_{\text{clG}}^{\text{AF}}\rangle = \prod_{i \in A, j \in B} |0\rangle_i |1\rangle_j. \quad (10.4)$$

This classical ground state is known as the Néel state. Note here that any pair of spins in this classical ground state is either parallel or antiparallel, which means that the ordering is collinear. The ordering of classical ground states in frustrated systems, however, is non-collinear, even in bipartite lattices (Sachdev, 1999; Messio *et al.*, 2011).

For the 1D Heisenberg antiferromagnetic model, the exact ground state of the spin- $\frac{1}{2}$ antiferromagnet in the thermodynamic limit is known (see discussion of the Bethe solution, Chapter 5) (Bethe, 1931; Yang and Yang, 1966a, 1966b; Hulthén, 1938; Auerbach, 1994). As mentioned before, it is gapless and exhibits algebraically decaying Néel order and correlations. According to the famous Haldane conjecture, the systems with integer and half-integer spin behave completely differently in one dimension (Haldane, 1983a, 1983b; Bonner, 1987). While half-integer spins behave similarly to spin- $\frac{1}{2}$ (gapless, algebraic decay), the integer spin typically leads to gapped VBC states. Interestingly, properties of such systems can be tested with ultracold atoms in many ways. One way is to look for low-temperature states of systems interacting antiferromagnetically. As discussed in Chapter 6, the Fermi–Hubbard model describing spin- $\frac{1}{2}$ fermions reduces exactly to what we need, i.e. the antiferromagnetic Heisenberg model. The same approach will, however, not work for bosons of spin-1 since the range of possible scattering lengths reduces the corresponding spinor Bose–Hubbard to a ferromagnetic spin-1 model. One can, however, use the approach of García-Ripoll *et al.* (2004), and instead of looking at the low-energy states of the system of interest, look at the high-energy states that correspond to low-energy states of the Hamiltonian with inverted signs for the couplings, i.e. the antiferromagnetic model.

In higher dimensions and for bipartite lattices, generally speaking Néel theory works well for both integer and non-integer spins. For instance, in quantum antiferromagnets made up

of spin- $\frac{1}{2}$ particles and placed in the infinite square lattice, the ground state energy can be well approximated by that of the Néel state (eqn (10.4)) despite the fact that it is not an eigenstate of the quantum Hamiltonian (eqn (10.2)).

10.3.2 The $J_1 - J_2$ model

Let us now move on to the $J_1 - J_2$ model, which can be frustrated for some values of interaction couplings. Its ground state is a paradigmatic example of a VBS. The Hamiltonian of this model can be written as

$$H_{J_1 J_2} = J_1 \sum_{\langle ij \rangle} \boldsymbol{\sigma}_i \cdot \boldsymbol{\sigma}_j + J_2 \sum_{\langle\langle ij \rangle\rangle} \boldsymbol{\sigma}_i \cdot \boldsymbol{\sigma}_j, \quad (10.5)$$

where $\langle\langle ij \rangle\rangle$ denotes the next-nearest neighbors. This is a frustrated model (even in the case of a linear chain) when both $J_{1,2} \neq 0$ and at least one of them is positive. As will be discussed in Section 10.4, this Hamiltonian can be obtained using ultracold ions in microtraps. Its importance comes from its usefulness in explaining the magnetic properties of $\text{Li}_2\text{VOSiO}_4$ and $\text{Li}_2\text{VOGeO}_4$ compounds (Melzi *et al.*, 2000). Below, we discuss the different phases of this model.

One-dimensional model The Hamiltonian (eqn (10.5)) for the case of the 1D lattice with an even number of sites, periodic boundary conditions, and $J_1 = 2J_2 > 0$ is known as the Majumdar–Ghosh model (Majumdar and Ghosh, 1969). The ground-state space of the model is spanned by the two possible coverings by the dimers,

$$|\psi_G^{\text{MG}}\rangle_{\pm} = \prod_{i=1}^{N/2} (|0\rangle_{2i}|1\rangle_{2i\pm1} - |1\rangle_{2i}|0\rangle_{2i\pm1}) / \sqrt{2}, \quad (10.6)$$

where N is the number of sites in the lattice. We also call these singlet states ‘valence-bond states’. Note that, unlike the AKLT state, this model breaks translational symmetry. A ‘valence-bond solid’ is formed from these valence-bond states after they order between themselves.

Two-dimensional model The 2D case is far more complicated. The quantum phase diagram of this model is not known even for the square lattice, while the classical phase diagram is quite well understood (Misguich and Lhuillier, 2003). In the latter case, it is known that when J_2/J_1 is very small the system is Néel ordered, and at the opposite extreme (i.e. $J_2 \gg J_1$) it has collinear ordering (different from Néel) characterized by

$$|\Psi_{\text{cl}, J_2 \gg J_1}^G\rangle = \prod_i \prod_{\text{odd } j} |1\rangle_{ij} \prod_{\text{even } j} |0\rangle_{ij}, \quad (10.7)$$

where i and j are the indices of rows and columns of the 2D lattice, respectively. However, when $0.4 < J_2/J_1 < 0.6$ (the strongly frustrated regime), no such orderings exist.

These classical predictions are in qualitative agreement with semi-classical and fully quantum calculations based on: series expansion (Dagotto and Moreo, 1989; Ceccatto

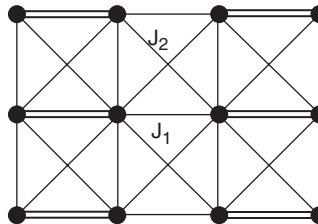


Figure 10.6 The $J_1 - J_2$ model with dimer configurations in a square lattice. The double lines indicate singlets between the two corresponding spins. The interaction strengths corresponding to the diagonals of the squares are J_2 , while those of the sides are J_1 .

(*et al.*, 1992; Richter, 1993; Oitmaa and Weihong, 1996) (see Singh and Narayanan (1990) and Gelfand (1990) for an introduction to this method), spin-wave theory (Shender and Holdsworth, 1994; Henley, 1989) (first introduced by Anderson (1951) and then extended to higher order by Kubo (1952) and Oguchi (1960)), exact diagonalizations (Poilblanc *et al.*, 1991; Schulz and Ziman, 1992; Einarsson and Schulz, 1995), and quantum Monte Carlo (Sandvik, 1997).

In the semi-classical limit, spin-wave theory predicts a first-order phase transition from the Néel ordered phase to the collinear ordered phase (in the highly frustrated region at $J_2/J_1 = 0.5$). However, when quantum fluctuations are introduced in this region, a new phase will appear to separate these two phases. From the exact diagonalization (Dagotto and Moreo, 1989; Figueirido *et al.*, 1990; Schulz *et al.*, 1996) one discovers that there are two phase transitions: one at $J_2/J_1 \approx 0.38$ and another one at $J_2/J_1 \approx 0.6$. The first one is a second-order phase transition from the Néel state to a spin-liquid (type II) valence-bond state. The second transition is a first-order phase transition from the spin-liquid state to a collinear state. In the regime $0.38 < J_2/J_1 < 0.6$, many calculations (Read and Sachdev, 1989; Read and Sachdev, 1991; Murthy and Sachdev, 1990; Kotov *et al.*, 1999; Gelfand *et al.*, 1989; Gelfand, 1990; Singh *et al.*, 1999) suggest that the ground state may have the VBS dimer configuration with long-range ordering, as shown in Figure 10.6.

Despite all these efforts, the phase diagram of this model is still not completely understood. In particular, many candidates for the ground states have been proposed for this highly frustrated regime. For example, the variational approach suggests (Capriotti *et al.*, 2001) that a ground state is a spin-liquid resonating valence-bond state for a spin- $\frac{1}{2}$ system. Sushkov *et al.* (2001) (see also Poilblanc *et al.* (1991)) found two new second-order phase transitions using series-expansion method; one of them around $J_2/J_1 = 0.34 \pm 0.04$, the other in the strongly frustrated regime at $J_2/J_1 = 0.50 \pm 0.02$.

10.3.3 Quantum antiferromagnets in kagomé lattices

In the preceding subsection, we discussed quantum magnets either in a linear chain or in a square lattice. In this section, we move to a more complicated lattice: the kagomé lattice. The Heisenberg antiferromagnet in this lattice is frustrated. A schematic diagram of the kagomé lattice is depicted in Figure 10.7. Over the last 15 years, extensive work has been done on this model—with Ising-type nearest-neighbor interactions (Moessner *et al.*, 2000;

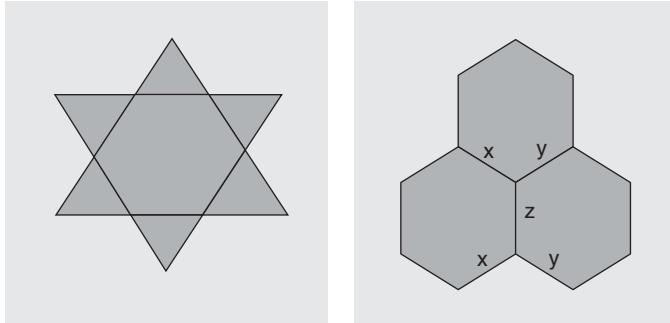


Figure 10.7 (a) The kagomé lattice. Two parent triangles superimposed on each other. Each of the parent triangles (one of which is inverted) contains three triangles at its three corners. The triangles in one of the parent triangles (say, in the non-inverted one) have interaction couplings J between all their vertices, while those in the other have J' . The kagomé lattice consists of a 2D array of such superimposed parent triangles. (b) The honeycomb lattice for a spin- $\frac{1}{2}$ system, whose Hamiltonian is given in eqn (10.23). The three types of link are depicted in the figure.

Moessner and Sondhi, 2001a) or with Heisenberg-type nearest and next-nearest neighbor interactions (Waldtmann *et al.*, 1998; Zeng and Elser, 1990; Singh and Huse, 1992; Leung and Elser, 1993; Zeng and Elser, 1995; Sindzingre *et al.*, 1994; Nakamura and Miyashita, 1995; Lecheminant *et al.*, 1997; Mila, 1998; Mambrini and Mila, 2000; Budnik and Auerbach, 2004). All these have given us a lot of information about the ground and excited states of these models. There are still, however, many questions to be answered.

The Heisenberg model in a trimerized kagomé lattice The Hamiltonian in this case is given by

$$H_{\text{kag}} = J \sum_{\langle ij \rangle} \boldsymbol{\sigma}_i \cdot \boldsymbol{\sigma}_j + J' \sum_{\langle ij \rangle} \boldsymbol{\sigma}_i \cdot \boldsymbol{\sigma}_j, \quad (10.8)$$

where J and J' are the couplings and the geometry of the model is explained in detail in the caption of Figure 10.7. Both J and J' are positive.

Numerical simulations of the spin- $\frac{1}{2}$ system on the kagomé lattice for $J = J'$ suggest that the energy gap between the ground state and the lowest triplet state, if any, is very small (of order $J/20$). This gap is filled with low-lying singlets, whose number scales with the number of spins N as 1.15^N (Waldtmann *et al.*, 1998). All these results suggest that this model may be well described by a resonating valence-bond state. There is an ongoing discussion concerning the nature of ground state. While many studies support the gapped spin liquid idea (see Jiang *et al.* (2008a)), several authors have supported the hypothesis that the ground state is VBS, with a large 36-site unit cell, called the honeycomb valence-bond solid (HVBS) (for a recent study using MERA, see Evenly and Vidal (2010)). The very recent and very careful DMRG study by Yan *et al.* (2011) seems to have brought the final answer: the ground state is a gapped spin liquid.

Using a mean-field approximation, Mila and Mambrini (Mila, 1998; Mambrini and Mila, 2000) have found the number, the form, and the spectrum of singlets in the trimerized limit, i.e. when the ratio J'/J is very small. The ground state corresponds to a short-range resonating valence-bond state. This method also predicts a gap of $2J'/3$ between singlet and triplets, and the gap remains in the thermodynamic limit. In the fully trimerized limit (i.e. $J'/J = 0$), the ground state in the subspace of short-range resonating valence-bond states is one singlet in each of the triangles. Although there are many theoretical predictions about this model there are no clear experimental confirmations. In the next section we will consider possible ways of verifying these theoretical results by using ultracold atoms (Santos *et al.*, 2004).

The spinless interacting Fermi gas in a trimerized kagomé lattice Let us now show that an interacting Fermi gas placed in a trimerized kagomé lattice behaves as a very special quantum magnet, a *quantum spin-liquid crystal*, possessing both antiferromagnetic order and an exceptionally large number of low-energy excitations (Damski *et al.*, 2005a, 2005b). Such a lattice consists of trimers (i.e. sets of three closely packed potential minima) arranged in a perfect triangular pattern (see Figure 10.8(a)). The ultracold fermions that are loaded into the lattice stay localized around potential minima, and the Fermi–Hubbard model can be shown to capture all essential properties of this system. The density of fermions is assumed to be such that there are two fermions per trimer. It is also assumed that there is a long-range interaction between fermions at nearest-neighboring sites in nearest-neighbor trimers. This long-range interaction can be achieved, for example, in a gas of polarized dipolar fermions.

In fact, the spinless interacting Fermi gas in the trimerized kagomé lattice is described by the following extended Fermi–Hubbard Hamiltonian

$$\hat{H}_{\text{FH}} = - \sum_{\langle a,b \rangle} (t_{ab} \hat{f}_a^\dagger \hat{f}_b + h.c.) + \sum_{\langle a,b \rangle} U_{ab} \hat{n}_a \hat{n}_b, \quad (10.9)$$

where $\langle a,b \rangle$ denotes nearest neighbors, $a = \{\alpha, i\}$ with α referring to intratrimer indices, and i numbering the trimers. The t_{ab} and U_{ab} take the values t and U for intratrimer and t'

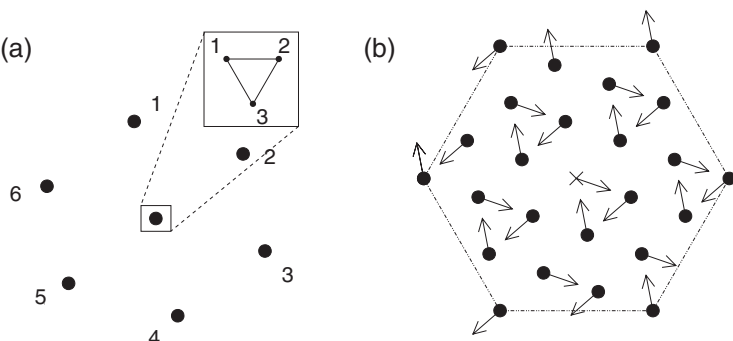


Figure 10.8 (a) Enumeration of intertrimmer (intratrimer) nearest neighbors. (b) Classical 120° Néel state with *left* chirality.

and U' for intertrimer couplings, $\hat{n}_a = \hat{f}_a^\dagger \hat{f}_a$, and \hat{f}_a is the fermionic annihilation operator. The sites in each trimer are enumerated as in Figure 10.8(a). We denote the three different intratrimer modes by

$$\hat{f}^{(i)} = (\hat{f}_{1,i} + \hat{f}_{2,i} + \hat{f}_{3,i})/\sqrt{3}, \quad (10.10)$$

for the zero-momentum mode, and

$$\hat{f}_\pm^{(i)} = (\hat{f}_{1,i} + z_\pm \hat{f}_{2,i} + z_\pm^2 \hat{f}_{3,i})/\sqrt{3}, \quad (10.11)$$

for the left and the right chirality modes, with $z_\pm = \exp(\pm 2\pi i/3)$.

The quantum magnet Hamiltonian In the limit of weak coupling between trimers, the extended Hubbard Hamiltonian for the problem of two fermions per trimer becomes equivalent to a quantum magnet on a triangular lattice with couplings that depend on the bond directions

$$\hat{H}_{\text{magnet}} = \frac{J}{2} \sum_{i=1}^N \sum_{j=1}^6 \hat{\sigma}_i(\phi_{i \rightarrow j}) \hat{\sigma}_j(\tilde{\phi}_{j \rightarrow i}), \quad (10.12)$$

where N denotes number of trimers, $J = 4U'/9$, and the nearest neighbors are enumerated as in Figure 10.8(a) (Santos *et al.*, 2004; Damski *et al.*, 2005a; Damski *et al.*, 2005b). In eqn (10.12) we have $\hat{\sigma}_i(\phi) = \cos(\phi)\hat{\sigma}_x^{(i)} + \sin(\phi)\hat{\sigma}_y^{(i)}$, where the spin- $\frac{1}{2}$ operators are expressed by the fermionic operators as:

$$\begin{aligned} \hat{\sigma}_x^{(i)} &= (\hat{f}_+^{(i)\dagger} \hat{f}_-^{(i)} + \hat{f}_-^{(i)\dagger} \hat{f}_+^{(i)})/2, \\ \hat{\sigma}_y^{(i)} &= -i(\hat{f}_+^{(i)\dagger} \hat{f}_-^{(i)} - \hat{f}_-^{(i)\dagger} \hat{f}_+^{(i)})/2. \end{aligned}$$

The angles ϕ are given by

$$\begin{aligned} \phi_{i \rightarrow 1} &= \phi_{i \rightarrow 6} = 0, \\ \phi_{i \rightarrow 2} &= \phi_{i \rightarrow 3} = 2\pi/3, \\ \phi_{i \rightarrow 4} &= \phi_{i \rightarrow 5} = -2\pi/3, \\ \tilde{\phi}_{1 \rightarrow i} &= \tilde{\phi}_{2 \rightarrow i} = -2\pi/3, \\ \tilde{\phi}_{3 \rightarrow i} &= \tilde{\phi}_{4 \rightarrow i} = 0, \\ \tilde{\phi}_{5 \rightarrow i} &= \tilde{\phi}_{6 \rightarrow i} = 2\pi/3. \end{aligned} \quad (10.13)$$

The physical picture behind mapping the Fermi–Hubbard Hamiltonian onto a spin model is the following: there are two fermions on each trimer and in the ground state configuration one of them occupies the zero-momentum mode while the second one has to choose between either right or left chirality modes, so it stays in the superposition of these two modes, which can then be identified as spin- $\frac{1}{2}$ states.

Classical analysis A lot of insight into the physics of this model can be obtained by looking at its classical version, i.e. the large- S (spin) limit, which allows us to replace quantum mechanical spin operators by classical spins in eqn (10.12). This problem turns out also to be highly non-trivial, as pointed out by Honecker *et al.* (2007), who analysed the classical counterpart of an effective Hamiltonian in the regime of a strongly trimerized kagomé lattice.

Note that the model displayed in eqn (10.12) is invariant with respect to lattice translations and under the point group $Z_6 = Z_3 \cdot Z_2$. The generator of Z_3 here is the combined rotation of the lattice by an angle of $4\pi/3$, and of the spins by an angle of $2\pi/3$, while the generator of Z_2 is the spin inversion in the lattice plane. There are three ordered classical states with small unit cells that are compatible with this point-group symmetry: a ferromagnetic state and two 120° Néel-type structures with left (Figure 10.8(b)) and right (Figure 10.9(a)) chiralities (Damski *et al.*, 2005a, 2005b). Although the Hamiltonian only has discrete symmetry, the classical ground-state manifold turns out to have a continuous global rotational symmetry. Again, two cases are distinguished by the sign of the exchange constant.

- For $J < 0$, there is a one-parameter family of ordered ground states with left-handed chirality, $\mathbf{S}_i = (\cos(\phi_i), \sin(\phi_i), 0)$, with $\phi_a = \theta$, $\phi_b = \theta + 2\pi/3$, and $\phi_c = \theta - 2\pi/3$ for the three intratrimer vertices, respectively (120° Néel order, see Figure 10.8). The energy of these states, $E^{J<0} = 6 J N$, is independent of θ . Computing the free energy $\mathcal{F}^{J<0}(\theta)$ by including the effect of Gaussian fluctuations, one finds that $\mathcal{F}^{J<0}(\theta)$ has minima at $\theta = (2n+1)\pi/6$, $n = 0, 1, \dots, 5$. This implies that the 120° Néel structures above lock in at these angles at low temperatures, and the transition temperature can

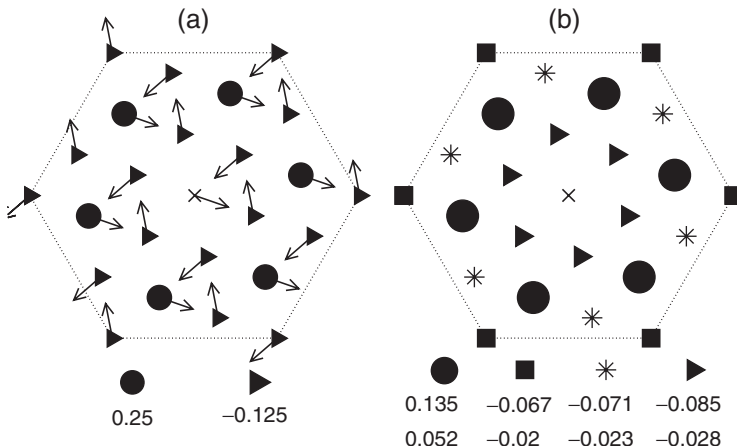


Figure 10.9 (a) Classical 120° Néel state with *right* chirality. Dots and triangles show $\sigma_x^{(i)} \sigma_x^{(10)} + \sigma_y^{(i)} \sigma_y^{(10)}$, where $|\sigma| = \frac{1}{2}$, and the central spin defines the x -axis. (b) Spin–spin correlations: $\langle \hat{\sigma}_x^{(i)} \hat{\sigma}_x^{(10)} + \hat{\sigma}_y^{(i)} \hat{\sigma}_y^{(10)} \rangle$. The upper (lower) set of values correspond to $kT = 0$ ($kT = 10^{-2} J/2$). In both plots $N = 21$ and $i = 10$ at the central site.

be determined by performing Monte Carlo simulations and measuring, for instance, specific heat and the order parameter (Honecker *et al.*, 2007).

- For $J > 0$, as for $J < 0$, there is a one-parameter family of 120° Néel-ordered ground states with energy $-3JN$. They have right chirality and differ from the states found for $J < 0$ by an interchange of the spin directions on, say, the b and c sublattices. The contribution of Gaussian fluctuations around these states yields a free energy $\mathcal{F}^{J>0}(\theta)$, which has minima at $\theta = \pi n/3$, $n = 0, 1, \dots, 5$. Hence the Néel structure should lock in at these angles for $J > 0$.

Surprisingly, an inspection of all states of finite cells of the lattice in which the mutual angles between pairs of spins are multiples of $2\pi/3$ reveals that there is a macroscopic number of ground states in addition to the 120° Néel states, i.e. the number of ground states grows exponentially with N . In Damski *et al.* (2005b), a simplified numerical study of the 12-spin cell was done by fixing the direction of every spin to $n\pi/3$ ($n = 0, \dots, 5$), and checking the energies of the resulting 6^{12} configurations. This analysis revealed that for $J < 0$ there are indeed *six* ground states (Z_6 symmetry of eqn (10.12)), each exhibiting left-chirality Néel order. For $J > 0$, however, the results were dramatically different: there were 240 degenerate classical ground states in this case. A more detailed analysis implies that 120° Néel state has $N/3$ soft modes, whereas all other ground states have fewer soft modes (Honecker *et al.*, 2007). At low temperatures the 120° Néel state should therefore be selected by the so-called thermal order-by-disorder mechanism (Villain *et al.*, 1980). Indeed, a non-zero but very small transition temperature was detected by Monte Carlo simulations.

As will be seen below, the large number of degenerate *classical* ground states for $J > 0$ finds its analog in a large density of low-lying excitations of the *quantum* version of the model (eqn (10.12)).

Quantum mechanical results Insight into the quantum mechanical properties of the system can be obtained through exact diagonalization of the Hamiltonian (eqn (10.12)). Unfortunately, this can be done only for systems of limited size. Numerical findings are presented in Figure 10.8(b) and Tables 10.1 and 10.2. For $J > 0$, the ground state exhibits the 120° Néel order with right chirality. This is illustrated in Figure 10.9(b), where the planar spin-spin correlations are presented. Direct comparison with the correlations of the classical state, Figure 10.9(a), shows that the exact quantum correlations, although smaller, have the same order of magnitude and sign as the classical ones. In particular, the relative values of correlations compare nicely to the classical result. Interestingly, the 120° Néel

Table 10.1 Spin–spin correlations, $\langle \hat{\sigma}_x^{(i)} \hat{\sigma}_x^{(j)} + \hat{\sigma}_y^{(i)} \hat{\sigma}_y^{(j)} \rangle$, for $J > 0$ as a function of distance (expressed in lattice units) between sites i and j . The first row presents classical predictions for the 120° Néel state (compare to Figure 10.9).

	1	$\sqrt{3}$	2	$\sqrt{7}$	3
120°	−0.125	0.250	−0.125	−0.125	0.250
$N = 24$	−0.096	0.162	−0.083	−0.080	0.156
$N = 21$	−0.085	0.135	−0.071	−0.067	

Table 10.2 Spin–spin correlations as for Table 10.1, but for $J < 0$.

	1	$\sqrt{3}$	2	$\sqrt{7}$
120°	−0.125	0.250	−0.125	−0.125
$N = 21$	−0.134	0.237	−0.117	−0.116
$N = 12$	−0.137	0.251	−0.125	

order survives at finite temperatures, as indicated by the results obtained for $kT = 10^{-2} J/2$ (Figure 10.9(b)). At such temperatures, about 800 low-energy eigenstates contribute to the correlations. To quantify how exceptionally dense the excitation spectrum is, we note that for $N = 21$ there are about 2000 (800) excited states with energies less than $0.09 J$ ($0.05 J$) above the ground state. Most of them support the spin order of the ground state so that antiferromagnetic order persists at finite temperatures. Moreover, numerical simulations show that the spectrum becomes more dense as N increases.

The exact diagonalizations do not give a definite answer as to whether the gap to the triplet states vanishes in the limit of an infinite lattice. What can be found out from exact diagonalizations is that the gap, if any, should be smaller than about $10^{-2} J/2$. The appearance of this very small energy scale is surprising, but can be related to the classical results. The smallness of the gap and the large density of low-energy states very much resemble the behavior of a quantum spin liquid of type II. Spin liquids of type II, however, possess extremely short-range correlations, which is in striking contrast to the behavior of the quantum magnet we are considering. For this reason it was proposed to name this system a *quantum spin-liquid crystal*.

The above results for $J > 0$ are in a strong contrast to those for $J < 0$. In the latter case, the ground state (in agreement with the classical theory) is the standard quantum antiferromagnet with 120° Néel order and left chirality. The spectrum is gapped and the classical spin–spin correlations approximate the quantum ones well (Table 10.2). In fact, the semiclassical spin-wave theory works here remarkably well even for system sizes as small as $N = 12$ (Damski *et al.*, 2005b; Damski *et al.*, 2007). The gap is of the order of $|J|/2$ in this case, so that there are at most few (strictly speaking, six) states with energies substantially below $|J|/2$ for $J < 0$, as opposed to the huge number for $J > 0$.

As is clear from the above discussion, theoretical studies of quantum spin-liquid crystals are, so far, limited to relatively small systems. We hope that future experiments will verify these predictions (note that the first experimental realization of a kagomé lattice has just been reported (Jo *et al.*, 2011)).

10.3.4 Frustrated antiferromagnetism with bosons in a triangular lattice

Another lattice that can support frustrated antiferromagnetism bosons is the 2D triangular lattice. This has been realized experimentally (Becker *et al.*, 2010). Frustration may be achieved directly for spin- $\frac{1}{2}$ fermions, as in the kagomé lattice. Interestingly, it can be also achieved for bosons by introducing, dynamically, a change in the sign of tunneling (hopping) matrix elements (Eckardt *et al.*, 2010; Eckardt *et al.*, 2005; Lignier *et al.*, 2007).

The consequences of the dynamical approach proposed in Eckardt *et al.* (2010), Eckardt *et al.* (2005), and Lignier *et al.* (2007) can be grasped in what follows. Consider a sample of ultracold bosonic atoms in a deep triangular optical lattice that is forced inertially by moving the lattice rapidly along an elliptical orbit. As we will see in the next section, the time evolution of such a system has a simple description. Integrating out the fast oscillatory motion on the short timescale $T = 2\pi/\omega$ of the elliptical forcing, one finds that the system's evolution on longer timescales is governed by the time-independent effective Bose–Hubbard Hamiltonian

$$\hat{H}_{\text{eff}} = \sum_{\langle ij \rangle} J_{ij}^{\text{eff}} \hat{b}_i^\dagger \hat{b}_j + \sum_i \left[\frac{U}{2} \hat{n}_i (\hat{n}_i - 1) - \mu_i \hat{n}_i \right]. \quad (10.14)$$

Here \hat{b}_i and \hat{n}_i are the bosonic annihilation and number operators for Wannier states localized at the minima \mathbf{r}_i of the triangular lattice potential. The first term comprises the tunneling between adjacent sites i and j with—and this is the crucial point—matrix elements J_{ij}^{eff} that are smoothly tunable from negative to positive values by varying the forcing strength.² The second term refers to on-site terms characterized by a positive interaction U , and a local chemical potential $\mu_i \equiv \mu - V_i$, which incorporates the trapping potential V_i . We consider the anisotropic lattice shown in Figure 10.10(a), where $J_{ij}^{\text{eff}} = J$ or $J_{ij}^{\text{eff}} = J' \equiv \alpha J$, with $\alpha \geq 0$.

Let us analyse this model in more detail. The homogeneous model ($\mu_i = \mu$) interpolates between a classical-rotor and a quantum-spin model. For weak interactions $U \ll n|J|$ the superfluid ground state can (locally) be approximated by $\prod_i \exp(\psi_i \hat{b}_i^\dagger) |\text{vacuum}\rangle$ with discrete order parameter $\psi_i = \sqrt{n_i} \exp(i\varphi_i)$ and with a mean filling of n particles per site. A homogeneous density $n_i = n$ is favored and the local phases φ_i play the role of classical rotors, adopting a configuration $\varphi_i \equiv \mathbf{q} \cdot \mathbf{r}_i$ described by the ordering vector \mathbf{q} . Antiferromagnetic coupling, $J > 0$, implies Néel-ordered phases φ_i as depicted in Figure 10.10(b)–(e). We call such a superfluid state a Néel superfluid. When α exceeds a value α_0 , the spiral order continuously transforms into staggered Néel order. In the absence of interactions $\alpha_0 = 2$, while the value slightly decreases with increasing interaction ($U > 0$).

In the limit of strong interaction $U \gg n|J|$ there are only two energetically favored site occupations: $n_i = [n] \equiv g$ (the largest integer smaller than n) and $n_i = g + 1$. Associating these with ‘spin-up’ and ‘spin-down’, respectively, gives the Bloch-sphere representation $|\vartheta_i, \varphi_i\rangle \equiv \cos(\vartheta_i/2)|g\rangle_i + \sin(\vartheta_i/2)\exp(i\varphi_i)|g+1\rangle_i$ at each site. Replacing $(g+1)^{-1}\hat{b}_i$ by the spin-lowering operator $(\hat{\sigma}_i^x - i\hat{\sigma}_i^y)/2$, one arrives at the XY model

$$\hat{H}_{XY} = \sum_{\langle ij \rangle} J_{ij}^{XY} (\hat{\sigma}_i^x \hat{\sigma}_j^x + \hat{\sigma}_i^y \hat{\sigma}_j^y) + \sum_i h_i \hat{\sigma}_i^z, \quad (10.15)$$

with $h_i \equiv \frac{1}{2}(\mu_i - Ug)$, $J_{ij}^{XY} \equiv \frac{g+1}{4} J_{ij}^{\text{eff}}$, and $\hat{\sigma}_i^x, \hat{\sigma}_i^y, \hat{\sigma}_i^z$ being spin- $\frac{1}{2}$ Pauli operators at site i . The ground state of \hat{H}_{XY} cannot be a product state like $\prod_i |\vartheta_i, \varphi_i\rangle$ with definite local phases φ_i any longer, since $|\vartheta_i, \varphi_i\rangle$ cannot be an eigenstate of both $\hat{\sigma}_i^x$ and $\hat{\sigma}_i^y$. Viewed from the

²We use the convention that $\langle ij \rangle$ denotes an oriented pair of neighboring sites, $\langle ij \rangle \neq \langle ji \rangle$.

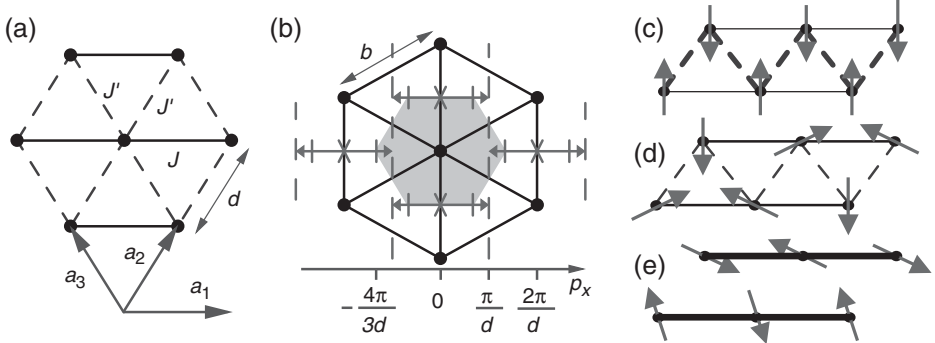


Figure 10.10 (a) The anisotropic triangular lattice considered, with primitive vectors $\mathbf{a}_1 \equiv d\mathbf{e}_x$, $\mathbf{a}_2 \equiv d[(1/2)\mathbf{e}_x + (\sqrt{3}/2)\mathbf{e}_y]$, and $\mathbf{a}_3 \equiv -\mathbf{a}_1 + \mathbf{a}_2$. The tunneling matrix elements J_{ij}^{eff} take values J and $J' \equiv \alpha J$ (with $\alpha \geq 0$) along the solid and dashed bonds, respectively. (b) Reciprocal lattice with $b = (4\pi/\sqrt{3})d^{-1}$. The first Brillouin-zone, centered at $\mathbf{p} = \mathbf{0}$, is shaded. Considering antiferromagnetic coupling $J > 0$, we have marked the ordering vector \mathbf{q} describing a Néel superfluid in the limit of weak interaction; for $\alpha \geq \alpha_0$ \mathbf{q} lies on one of the x-shaped crosses (being equivalent to modulo reciprocal lattice vectors). This corresponds to a staggered configuration of the local phase angles φ_i on the rhombic lattice of J' -bonds, shown in (c) with the φ_i visualized by pointers. Lowering α , at $\alpha = \alpha_0$ the position of \mathbf{q} splits in a continuous way into two non-equivalent possible positions that separate symmetrically along the arrows drawn in (b). The phases φ_i assume a spiral pattern with two possible chiralities; subfigure (d) corresponds to the isotropic lattice ($\alpha = 1 < \alpha_0$), with \mathbf{q} lying on one of the corners of the first Brillouin zone. Finally, in the 1D limit ($\alpha = 0$) only q_x has a defined value, which is marked by the dashed lines in (b). The phase pattern is staggered along the 1D chains of J -bonds, as sketched in (e). From Eckardt *et al.* (2010).

Bose–Hubbard perspective, increasing interparticle repulsion increases the fluctuations of the local phases φ_i . Notice that while for ferromagnetic couplings, $J < 0$, the classical phase configuration is supposed to survive the presence of quantum fluctuations, in the limit of strong interactions ($U \gg n|J|$), for antiferromagnetic coupling $J > 0$ recent simulations suggest that (for $\sum_i \langle \hat{\sigma}_i^z \rangle = 0$) classical Néel order is not necessarily preserved (Schmied *et al.*, 2008). Along the α -axis different Néel phases are separated by gapped spin-liquid phases with exponentially decaying spin correlations. The results of Schmied *et al.* (2008) are displayed along the upper edge of the phase diagram shown in Figure 10.11. Further insight into the physics of the frustrated positive-hopping Bose–Hubbard model, eqn (10.14), can be obtained in the limit of weak interaction $U \ll n|J|$ and assuming a homogeneous system, by analysing quantum fluctuations using the Bogoliubov approach (Eckardt *et al.*, 2010; Mora and Castin, 2003).

The basic idea is as follows (Mora and Castin, 2003): for fillings (moderately) larger than 1, one can replace

$$\hat{b}_i \simeq \exp[i(\varphi_i + \delta\hat{\varphi}_i)] \sqrt{n_i + \delta\hat{n}_i},$$

where $\delta\hat{n}_i = \delta\hat{n}_i^\dagger$ and $\delta\hat{\varphi}_i \simeq \delta\hat{\varphi}_i^\dagger$ describe quantum fluctuations of the local particle numbers n_i and phases φ_i , respectively, with $[\delta\hat{n}_i, \delta\hat{\varphi}_i] \simeq i\delta_{i,j}$. While $\langle(\delta\hat{n}_i)^2\rangle_i/n^2 \ll 1$ can be

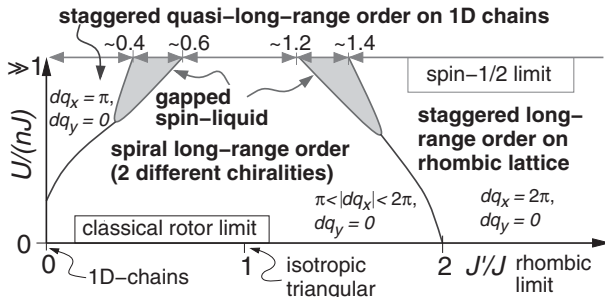


Figure 10.11 Sketch of the phase diagram of the anisotropic positive-hopping Bose–Hubbard model on a triangular lattice for half-odd-integer filling. The parameter plane is spanned by the interaction strength $U/(nJ)$ and the anisotropy ratio $\alpha = J'/J$. The data (in gray) signaling the borders of the gapped spin-liquid phase for the spin- $\frac{1}{2}$ limit ($U/(nJ) \gg 1$) are taken from Schmied *et al.* (2008). We assume the spin-liquid phases to survive at small finite values of J/U , since they are protected by a gap. The behavior at small $U/(nJ)$ corresponds to results obtained within a generalized Bogoliubov theory. From Eckardt *et al.* (2010).

assumed, the phase fluctuations $\langle (\delta\hat{\varphi}_i)^2 \rangle$ diverge in the 1D limit ($\alpha = 0$) (as well as at finite temperatures) where only quasi-long-range order is possible. However, one can still expect the fluctuation of the *relative* phases $\langle (\delta\hat{\varphi}_i - \delta\hat{\varphi}_j)^2 \rangle$ between neighboring sites i and j to be small. Expanding the Hamiltonian (eqn (10.14)) up to second order in $\delta\hat{n}_i/n_i$ and $(\delta\hat{\varphi}_i - \delta\hat{\varphi}_j)$, it will be quadratic in terms of new bosonic operators $\hat{d}_i \equiv \sqrt{n_i}[\delta\hat{n}_i/(2n_i) + i\delta\hat{\varphi}_i]$ and \hat{d}_i^\dagger , and can be diagonalized by a Bogoliubov transform (keeping $\langle \delta\hat{n}_i \rangle = 0$). However, when computing correlations, such as $\langle \hat{b}_i^\dagger \hat{b}_j \rangle$, between distant sites i and j , $(\delta\hat{\varphi}_i - \delta\hat{\varphi}_j)$ cannot be treated as a small quantity and Wick's theorem has to be used instead to evaluate the expectation values of all powers of $\delta\hat{\varphi}_i$.

This analysis has been extended further by also taking into account the (Wick-decomposed) quartic corrections to the Hamiltonian when minimizing the ground-state energy with respect to both the Bogoliubov coefficients and the wave vector \mathbf{q} at which the order occurs (Eckardt *et al.*, 2010). In fact, in the case of spiral order ($\pi < d|q_x| < 2\pi$ with $q_y = 0$), one finds two solutions, \mathbf{q} and $\mathbf{q}' = -\mathbf{q}$, and has to choose one of them. Such a self-consistent correction to the standard Bogoliubov approach allows us to explain the lower part of the phase diagram in Figure 10.11, and in particular the lack of staggered 1D quasi-long-range order as well as the shift of the phase boundary between the spiral and staggered long-range orders with increasing interaction. Note that the spiral long-range order is an example of a *chiral* superfluid, i.e. a superfluid with the time-reversal symmetry broken. Such an exotic superfluid phase has been observed by Struck *et al.* (2011).

10.4. Realization of frustrated models with ultracold atoms

Here we discuss several concrete proposals for realizing frustrated models with ultracold atoms. Such realizations require either the creation of a lattice with the appropriate geometry or the control of the effective atomic interactions, or both.

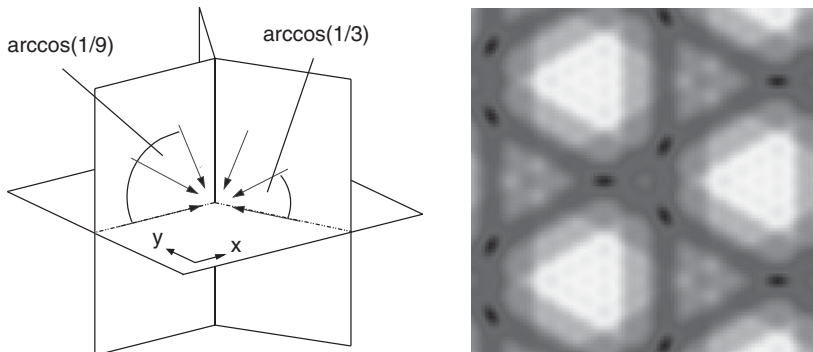


Figure 10.12 Scheme of the proposed experimental set-up. Each arrow depicts a wave vector of a standing wave laser. The three vertical planes intersect at an angle of 120° . Dark (dark blue in the online version) spots in the right kagomé figure indicate the potential lattice minima. From Damski *et al.* (2005b). Figure in color online.

10.4.1 Engineering the geometry of the lattice

The geometry of the lattice, as we have already mentioned, can be engineered using superlattice techniques (see Figure 10.12). In particular, the trimerized kagomé lattice can be created by a proper superposition of standing laser beams (Santos *et al.*, 2004; Damski *et al.*, 2005b) where the atoms are considered to be in a 2D optical lattice in the xy plane, being strongly confined (magnetically or optically) in the z direction. In order to form a kagomé lattice one can use blue detuned lasers, so that the potential minima coincide with the laser-intensity maxima. A perfect triangular lattice can easily be created by two standing waves in the xy plane $\cos^2(\mathbf{k}_{1,2}\mathbf{r})$, with $\mathbf{k}_{1,2} = k\{\frac{1}{2}, \pm \frac{\sqrt{3}}{2}\}$, and an additional standing wave $\cos^2(\mathbf{k}_3\mathbf{r} + \phi)$, with $\mathbf{k}_3 = k\{0, 1\}$. The resulting triangles have a side of length $2\pi/\sqrt{3}k$. By varying ϕ the third standing wave is shifted along the y axis, and, in principle, a kagomé pattern can be realized.

However, such a direct procedure presents two problems. First, three lasers in a plane cannot have a mutually orthogonal polarization, and consequently undesired interference between different standing waves occurs. This can be avoided by randomizing the relative orientation of the polarization between different standing waves, or by introducing small frequency mismatches, which, however, have to be larger than any other relevant frequencies. Second, due to the diffraction limit, the ratio ξ between the separation of the maxima and the half-width at half maximum (HWHM) is 4. Because of that, for any ϕ , the three potential minima forming the kagomé triangles cannot be resolved. This can be avoided by using superlattices. For instance, one may substitute each standing wave ($i = 1, 2, 3$) by a laser potential $(\cos(\mathbf{k}_i\mathbf{r}) + 2\cos(\mathbf{k}_i\mathbf{r}/3))^2$. For this potential $\xi = 7.6$, and the generation of a perfect kagomé lattice for $\phi = \frac{\pi}{2}$, and a modestly TKL for $\frac{5\pi}{12} \leq \phi \leq \frac{\pi}{2}$ is possible. Using another superlattice, $(\cos(\mathbf{k}_i\mathbf{r}) + 2\cos(\mathbf{k}_i\mathbf{r}/3) + 4\cos(\mathbf{k}_i\mathbf{r}/9))^2$, one can reach $\xi \sim 14$, and generate for $\phi = \frac{\pi}{4}$ a strongly trimerized kagomé lattice. The necessary laser configuration is sketched in Figure 10.12.

Heisenberg model in a kagomé lattice using Fermi–Fermi mixtures Having achieved the trimerized kagomé lattice, one can then realize various frustrated spin models in such a lattice. Consider, for this purpose, a Fermi–Fermi mixture at half filling for each species. The Hamiltonian in this case is the spin- $\frac{1}{2}$ Hubbard model, given by

$$\hat{H}_{\text{FF}} = - \sum_{\langle ij \rangle} t_{ij} (\hat{f}_i^\dagger \hat{f}_j + \hat{\tilde{f}}_i^\dagger \hat{\tilde{f}}_j + \text{h.c.}) + \sum_i V \hat{n}_i \hat{\tilde{n}}_i, \quad (10.16)$$

where $\hat{n}_i = \hat{f}_i^\dagger \hat{f}_i$ ($\hat{\tilde{n}}_i = \hat{\tilde{f}}_i^\dagger \hat{\tilde{f}}_i$), and the operators \hat{f}_i and \hat{f}_i^\dagger ($\hat{\tilde{f}}_i$ and $\hat{\tilde{f}}_i^\dagger$) are the annihilation and creation operators for the two species. Here t_{ij} takes the value t_0 for intratrimer and t'_0 for intertrimer hopping. In the strong-coupling limit $t_0, t'_0 \ll V$ ($t-J$ model) (Auerbach, 1994), \hat{H}_{FF} reduces to the Heisenberg antiferromagnet Hamiltonian H_{kag} (eqn (10.8)), where the couplings due to superexchange interactions are $J = 4t_0^2/V$ and $J' = 4t'_0^2/V$, and $\sigma = (\hat{\sigma}^x, \hat{\sigma}^y, \hat{\sigma}^z)$, with

$$\hat{n} - \hat{\tilde{n}} = 2\hat{\sigma}^z, \quad \hat{f}^\dagger \hat{\tilde{f}} = \hat{\sigma}^x + i\hat{\sigma}^y, \quad \hat{\tilde{f}}^\dagger \hat{f} = \hat{\sigma}^x - i\hat{\sigma}^y. \quad (10.17)$$

The total spin in the trimer takes the minimal value $\frac{1}{2}$, and there are four degenerate states having $\sigma^z = \pm \frac{1}{2}$ and left or right chirality. The spectrum of the system in the singlet sector consists of a narrow band of low-energy states of a width of order J' and separated from the higher singlet (triplet) bands by a gap of order $3J/4$ ($2J'/3$).

10.4.2 Quantum antiferromagnets using super-exchange interactions

The idea proposed by Duan *et al.* (2003) to realize quantum antiferromagnets involves exploiting superexchange interactions between atoms with internal states (or atomic mixtures) loaded in optical lattices in the strongly correlated regime (MI). The lattices formed by a standing wave are, however, state-dependent: $V_{\mu\sigma} \sin^2(\mathbf{k}_\mu \cdot \mathbf{r})$ in the direction μ (\mathbf{k} is the beam wave vector). Let us illustrate the simpler case in which the lattice is filled with one boson per site. Each boson has two different internal states (pseudo-spin- $\frac{1}{2}$ bosons), enumerated by the index $\sigma = \{\uparrow, \downarrow\}$. The system is described by the following Hubbard Hamiltonian,

$$\hat{H}_{\text{at}} = - \sum_{\langle ij \rangle \sigma} (t_{\mu\sigma} \hat{b}_{i\sigma}^\dagger \hat{b}_{j\sigma} + \text{h.c.}) + \frac{1}{2} \sum_{i\sigma} U_\sigma \hat{n}_{i\sigma} (\hat{n}_{i\sigma} - 1) + U_{\uparrow\downarrow} \sum_i \hat{n}_{i\uparrow} \hat{n}_{i\downarrow}, \quad (10.18)$$

where $\langle ij \rangle$ denotes nearest neighbors and $\hat{b}_{i\sigma}$ ($\hat{b}_{i\sigma}^\dagger$) is the annihilation (creation) operator of bosons in the i th lattice site. The above Hamiltonian (eqn (10.18)), describes tunneling of bosons in different internal states between neighboring lattice sites, and their on-site interactions.

Using the same approach as the one discussed for Fermi–Bose mixtures in Chapter 6, the Hamiltonian in eqn (10.18) can be cast into the quantum-magnet form, if the following conditions are satisfied:

- $t_{\mu\sigma} \ll U_\sigma, U_{\uparrow\downarrow}$, which typically requires large enough $V_{\mu\sigma}$
- $\langle \hat{n}_{i\uparrow} \rangle + \langle \hat{n}_{i\downarrow} \rangle \simeq 1$.

Then, to the lowest non-trivial order approximation in $t_{\mu\sigma}/U_{\uparrow\downarrow}$, one obtains the effective Hamiltonian

$$\hat{H}_{\text{at}} \approx \sum_{\langle i,j \rangle} [\lambda_{\mu z} \hat{\sigma}_i^z \hat{\sigma}_j^z - \lambda_{\mu\perp} (\hat{\sigma}_i^x \hat{\sigma}_j^x + \hat{\sigma}_i^y \hat{\sigma}_j^y)], \quad (10.19)$$

where $\hat{\sigma}_i^z = \hat{n}_{i\uparrow} - \hat{n}_{i\downarrow}$, $\hat{\sigma}_i^x = \hat{b}_{i\uparrow}^\dagger \hat{b}_{i\downarrow} + \hat{b}_{i\downarrow}^\dagger \hat{b}_{i\uparrow}$, and $\hat{\sigma}_i^y = -i(\hat{b}_{i\uparrow}^\dagger \hat{b}_{i\downarrow} - \hat{b}_{i\downarrow}^\dagger \hat{b}_{i\uparrow})$, and

$$\lambda_{\mu z} = \frac{t_{\mu\uparrow}^2 + t_{\mu\downarrow}^2}{2U_{\uparrow\downarrow}} - \frac{t_{\mu\uparrow}^2}{U_\uparrow} - \frac{t_{\mu\downarrow}^2}{U_\downarrow}, \quad \lambda_{\mu\perp} = \frac{t_{\mu\uparrow} t_{\mu\downarrow}}{U_{\uparrow\downarrow}}. \quad (10.20)$$

The Hamiltonian \hat{H}_{at} corresponds to the anisotropic Heisenberg spin- $\frac{1}{2}$ model. The anisotropy of the model can be investigated by adjusting the $t_{\mu\sigma}$, U_σ , and $U_{\uparrow\downarrow}$ couplings via, for example, manipulation of the lattice potentials imposed on atoms or by the use of Feshbach resonances.

To further illustrate the possibilities offered by cold atomic systems, we consider the limit of $t_{\mu\downarrow}/t_{\mu\uparrow} \rightarrow 0$, i.e. $V_{\mu\uparrow} \ll V_{\mu\downarrow}$. In this case \hat{H}_{at} approximates to the nearest-neighbor Ising model of eqn (10.1). Depending on $V_{\mu\uparrow}$ the couplings $\lambda_{\mu z}$ can be either isotropic or anisotropic. Moreover, they can all be either positive or negative depending on the $U_{\uparrow\downarrow}/U_\uparrow$ ratio. Therefore, as discussed in Section 10.1, both the ferromagnetic and antiferromagnetic Ising model can be simulated with cold bosons in a lattice. Additionally, as considered in Duan *et al.* (2003), the successful experimental realization of the Ising model in a system of cold atoms can be very useful in the experimental implementation of the one-way quantum computer, introduced by Raussendorf and Briegel (Briegel and Raussendorf, 2001; Raussendorf and Briegel, 2001a) and explained in Chapter 13.

Moreover, pursuing this idea further, an unusual quantum magnet corresponding to the anisotropic 2D spin- $\frac{1}{2}$ model on a hexagonal lattice can be realized. The hexagonal lattice can be created in a carefully designed setup of laser beams (Duan *et al.*, 2003). In such a hexagonal lattice, one wishes to engineer anisotropic Heisenberg exchange for each tunneling direction (denoted by D_x , D_y , and D_z , respectively). To this end, one can apply an additional superlattice consisting of three blue-detuned standing-wave laser beams in the $X - Y$ plane along these tunneling directions:

$$V_{\nu\sigma}(x, y) = V_{\nu\sigma} \sin^2 [k(x \cos \theta'_\nu + y \sin \theta'_\nu)], \quad (10.21)$$

where $\nu = x, y, z$, and $\theta'_x = -\frac{\pi}{3}$, $\theta'_y = \pi$, $\theta'_z = \frac{\pi}{3}$. The most important assumption is that the potential depth $V_{\nu\sigma}$ depends on the atomic spin state as

$$V_{\nu\sigma} = V_{\nu+} |+\rangle_\nu \langle +| + V_{\nu-} |-\rangle_\nu \langle -|, \quad (\nu = x, y, z), \quad (10.22)$$

where $|+\rangle_\nu$ ($|-\rangle_\nu$) is the eigenstate of the corresponding Pauli operator σ^ν with the eigenvalue +1 (-1).

The spin-dependent potentials in the form of eqns (10.21) and (10.22) can be and have been realized in experiments (see Soltan-Panahi *et al.* (2011)). The basic idea of Duan, Demler, and Lukin is to couple the two hyperfine levels of the atom with different energies to

the common excited level $|e\rangle$ with a blue detuning Δ , respectively, through the laser beams L_1 and L_2 with frequencies matching the corresponding transitions. The quantization axis is chosen to be perpendicular to the X-Y plane, and the phase-locked laser beams L_1 and L_2 are both polarized along this direction. In the tunneling direction D_z one applies only the L_1 laser beam, which induces a potential $V_{z\sigma}(x, y)$ with the desired form of its depth $V_{z\sigma}$. In the tunneling directions D_x or D_y we apply both lasers L_1 and L_2 , but with different relative phases. Such configuration realizes then the desired potential depth $V_{x\sigma}$ or $V_{y\sigma}$ of the form of eqn (10.22) in the corresponding direction.

The spin-dependent potentials do not have influence on the equilibrium positions of the atoms, but they do change the potential barrier between the neighboring atoms in the D_ν direction from $V_0/4$ to $V'_{\nu\sigma} = V_0/4 + V_{\nu\sigma}$. The parameters $V_{\nu+}$ and $V_{\nu-}$ in eqn (10.22) can be tuned by varying the laser intensity of L_1 and L_2 in the D_ν direction, and one can easily find the appropriate values so that the atom can virtually tunnel in the D_ν direction with a rate $t_{+\nu}$ only when it is in eigenstate $|+\rangle_\nu$. Hence it follows that the effective Hamiltonian for the system is given by

$$\hat{H}_{\text{at}} \approx \lambda_x \sum_{x\text{-links}} \hat{\sigma}_i^x \hat{\sigma}_j^x + \lambda_y \sum_{y\text{-links}} \hat{\sigma}_i^y \hat{\sigma}_j^y + \lambda_z \sum_{z\text{-links}} \hat{\sigma}_i^z \hat{\sigma}_j^z, \quad (10.23)$$

where the summation goes over nearest neighbors i and j placed on the x, y, z links (see Figure 10.7). The couplings are given by $\lambda_\nu \approx -t_{+\nu}^2/(2U)$ provided $U_{\uparrow\downarrow} \approx U_\uparrow \approx U_\downarrow \approx U$. In the above expression effective magnetic fields have been compensated.

The Hamiltonian above corresponds to the famous Kitaev model. This model is exactly solvable (Kitaev, 1997; Kitaev, 2003; Kitaev, 2006), exhibits *topological order*, and its excitations include both Abelian and non-Abelian anyons (Wilczek, 1982a; Wilczek, 1982b) with exotic fractional statistics. Its realization should provide an exceptional possibility for experimental observation of such exotic quasi-particles. Such anyons could be used in quantum information applications as protected qubits. Various Kitaev models, their properties, and their application in quantum computing are discussed in more detail in Chapter 13.

10.4.3 Frustrated models with polar molecules

A different scheme to realize spin Hamiltonians using polar molecules has been proposed in Micheli *et al.* (2006). For developments in trapping and cooling polar molecules see for example the special issue of the *European Physical Journal D* on ultracold polar molecules (Vol. 31(2), November 2004) and Rieger *et al.* (2005). The proposal assumes initially two polar molecules trapped in an optical lattice. The outermost shell of an electron of a heteronuclear molecule represents the spin- $\frac{1}{2}$ system. The total Hamiltonian of a pair of heteronuclear molecules trapped in an optical lattice is given by

$$\hat{H} = \underbrace{\left(\hat{H}_{\text{dd}} + \sum_{i=1}^2 \hat{H}_m^i \right)}_{H_{\text{int}}} + \underbrace{\left(\sum_{i=1}^2 \frac{\hat{P}_i^2}{2m} + \hat{V}_i(x - \bar{x}_i) \right)}_{H_{\text{ext}}}, \quad (10.24)$$

Table 10.3 Spin Hamiltonians achievable for different frequencies, chosen to be near-resonant to the indicated excited-state potential, and polarizations of the microwave field applied to induce strong dipole–dipole interactions between a pair of heteronuclear molecules trapped in an optical lattice. From Micheli *et al.* (2006).

Polarization	Resonance	Spin pattern
\hat{x}	2_g	$\sigma_z \sigma_z$
\hat{z}	0_u^+	$\sigma \sigma$
\hat{z}	0_u^-	$\sigma_x \sigma_x + \sigma_y \sigma_y - \sigma_z \sigma_z$
\hat{y}	0_u^-	$\sigma_x \sigma_x - \sigma_y \sigma_y + \sigma_z \sigma_z$
\hat{y}	0_u^+	$-\sigma_x \sigma_x + \sigma_y \sigma_y + \sigma_z \sigma_z$
$(\hat{y} - \hat{x})/\sqrt{2}$	0_u^+	$-\sigma_x \sigma_x - \sigma_y \sigma_y + \sigma_z \sigma_z$
$\cos \xi \hat{x} + \sin \xi \hat{y}$	1_g	$\lambda_1(\sigma_x \sigma_z + \sigma_z \sigma_x) + \lambda_2 \sigma_z \sigma_z$ + $\lambda_3(\sigma_x \sigma_x + \sigma_y \sigma_y)$
$\cos \xi \hat{y} + \sin \xi \hat{x}$	1_g	$\lambda_1(\sigma_y \sigma_z + \sigma_z \sigma_y) + \lambda_2 \sigma_z \sigma_z$ + $\lambda_3(\sigma_x \sigma_x + \sigma_y \sigma_y)$

where H_{int} and H_{ext} represent the internal and external dynamics of molecules, respectively. H_{dd} is the Hamiltonian for dipole–dipole interactions between two molecules (see Chapter 8). The rotational excitation of each molecule is described by the Hamiltonian

$$\hat{H}_m = B \hat{N}^2 + \gamma \hat{N} \cdot \hat{S}, \quad (10.25)$$

where \hat{N} is the dimensionless orbital angular momentum of the nuclei, \hat{S} is the electronic spin, B is the rotational constant, and γ is the spin–rotation coupling constant. The rotational motion of molecules is coupled by the dipole–dipole interactions that are already present in the heteronuclear molecule. To obtain strong dipole–dipole interactions, a microwave field is introduced. If the field polarization is set to the z -axis of the two molecules and the frequency is fixed as near-resonant with the excited-state potential, it leads to one of several possible spin patterns of ground states. By changing the frequency and field polarization, it is possible to obtain various spin models like the Ising, Heisenberg, or Kitaev models (see Table 10.3). The advantage of using polar molecules is that they exhibit strong couplings relative to decoherence rates due to their inherent strong dipole–dipole interactions. Also, the use of microwave fields is advantageous, since it avoids problems related to spontaneous emission processes, always present when laser fields are used.

10.4.4 Ion-based quantum simulators of spin systems

Cold ions are also another system suitable for simulating quantum spin models (Porras and Cirac, 2004a; Deng *et al.*, 2005). In fact, it seems that ions are perfectly suitable for such experimental studies since:

- (i) they can be trapped and cooled very efficiently
- (ii) the position and internal state of every single ion can be measured and manipulated almost at will

- (iii) the external parameters of that system can be well controlled and changed in real time.

Let us present the original proposal introduced in Porras and Cirac (2004a). The spin- $\frac{1}{2}$ states are encoded in two internal hyperfine states of each ion. The local dynamics of these internal states is governed by the Hamiltonian

$$H_m = \sum_{j=1\dots N}^{\alpha=x,y,z} B^\alpha \hat{\sigma}_j^\alpha, \quad (10.26)$$

where N is the number of ions, B^x and B^y are ‘analogs’ of the magnetic field induced by lasers resonant with the internal transition, and B^z is the energy gap between the two internal states.

The ions are affected by both an external harmonic trapping potential with frequencies $(\Omega_x, \Omega_y, \Omega_z)$ and Coulomb interactions. The corresponding potential is:

$$V = \frac{m}{2} \sum_{j=1\dots N} (\Omega_x^2 x_j^2 + \Omega_y^2 y_j^2 + \Omega_z^2 z_j^2) + \sum_{j>i} \frac{e^2}{\sqrt{(x_i - x_j)^2 + (y_i - y_j)^2 + (z_i - z_j)^2}}, \quad (10.27)$$

where m is the mass of the ion and e is the electron charge. It is further assumed that the trap has a cigar-shaped geometry, with an axial z direction and radial x and y ones: $\Omega_z \ll \Omega_x, \Omega_y$. The competition between harmonic squeezing and Coulomb repulsion results in oscillations of ions around their equilibrium positions. Dynamics of these oscillations is governed by the vibrational Hamiltonian: $\hat{H}_v = \sum_{j=1\dots N}^{\alpha=x,y,z} \frac{(\hat{p}_j^\alpha)^2}{2m} + \hat{V}$, where \hat{p}_j^α is the momentum operator of the j th ion. After expanding \hat{V} up to quadratic order in the ions’ displacement from their equilibrium positions, the vibrational Hamiltonian can be diagonalized in a standard way in terms of collective modes (phonons):

$$\hat{H}_v = \sum_n^{\alpha=x,y,z} \hbar \omega_{\alpha,n} \hat{a}_{\alpha,n}^\dagger \hat{a}_{\alpha,n}, \quad (10.28)$$

where $\hat{a}_{\alpha,n}$ ($\hat{a}_{\alpha,n}^\dagger$) represents the phonon annihilation (creation) operators and $\omega_{\alpha,n}$ are the collective mode frequencies.

Finally, one needs a coupling between internal and external degrees of freedom, i.e. between ‘effective’ spins and phonons \hat{H}_m and \hat{H}_v . This is achieved by placing the ions in off-resonant standing-wave beams. For instance, by imposing standing light waves on ions one can realize the following Hamiltonian (Deng *et al.*, 2005):

$$\hat{H}_f = -F_x \sum_j x_j |\uparrow\rangle\langle\uparrow|_{z,j} - F_y \sum_j y_j |\uparrow\rangle\langle\uparrow|_{y,j}, \quad (10.29)$$

where $\sigma^\alpha |\uparrow\rangle_\alpha = |\uparrow\rangle_\alpha$. This Hamiltonian assumes that the laser beams push the ions only if they are in the the upper state, which can be achieved by a proper adjustment of the relative phases of the beams.

The total Hamiltonian of the system then becomes $\hat{H} = \hat{H}_m + \hat{H}_v + \hat{H}_f$. The final step to get the clear picture of the phonon-mediated interactions between ‘effective’ spins relies on the unitary transformation $\hat{H} \rightarrow \hat{U}\hat{H}\hat{U}^\dagger$, as specified in Mintert and Wunderlich (2001), Porras and Cirac (2004a), and Deng *et al.* (2005). As a result of this canonical transformation the spin–spin interaction arises naturally. Let us examine some particular examples.

- For $F_x \neq 0$ and $F_y = 0$ one gets, to the lowest order in $\eta_\alpha = F_\alpha \sqrt{\hbar/2m\Omega_\alpha}/\hbar\Omega_\alpha$, the following Hamiltonian

$$\hat{H} \approx \frac{1}{2} \sum_{i,j} J_{i,j}^{[x]} \hat{\sigma}_i^z \hat{\sigma}_j^z + \sum_i B^x \hat{\sigma}_i^x + \hat{H}_v + \hat{H}_E, \quad (10.30)$$

where

$$J_{i,j}^{[\alpha]} \sim \frac{1}{|\langle z_i \rangle - \langle z_j \rangle|^3}, \quad (10.31)$$

with $\langle z_i \rangle$ being the equilibrium position of the i th ion. The first two terms in eqn (10.30) act in the ‘spin’ space and exhibit the quantum Ising-model type of spin–spin and spin–field interactions. Since the interactions are long-range one can study quantum properties of the Ising model for long range but also restrict to short range if the corrections coming from the perturbation \hat{H}_E are negligible. As shown in detail in Deng *et al.* (2005) the influence of the perturbation \hat{H}_E on spin dynamics can indeed be neglected, or in the worst case included in the theory as a source of very limited errors.

- Another possibility emerges for $F_x, F_y \neq 0$. Then one obtains the result that the transformed Hamiltonian is

$$\hat{H} \approx \frac{1}{2} \sum_{i,j} (J_{i,j}^{[x]} \hat{\sigma}_i^z \hat{\sigma}_j^z + J_{i,j}^{[y]} \hat{\sigma}_i^y \hat{\sigma}_j^y) + \sum_i B^x \hat{\sigma}_i^x + \hat{H}_v + \hat{H}_E, \quad (10.32)$$

where $J_{i,j}^{[\alpha]}$ are given by eqn (10.31). This time, the first two terms correspond to the XY model with long-range interactions. The perturbation affecting spin dynamics, \hat{H}_E , is now a little different to the one above, but as long as $\omega_x \neq \omega_y$ the errors induced by leaving the \hat{H}_E out are of the same order. Obviously, employing two radial forces in radial directions x and y ($F_x, F_y \neq 0$) and one longitudinal (F_z), one can get an asymmetric XYZ model with long-range interactions.

As shown above, ion chains can be used for simulating various important spin models. These possibilities include dipolar hard-core Bose gases, various versions of the $J_1 - J_2$ model, or, interesting by itself, a long range ionic model (for a recent study see Hauke *et al.* (2010)). Although the discussion above focused on the 1D geometry of the ion trap, a similar approach can be used for studies of ions in 2D geometries, where they form Coulomb crystals (Itano *et al.*, 1998; Mitchell *et al.*, 1998). Even more promising is the use of strong

microtraps to trap the ions (see developments by T. Schätz and Ch. Monroe). One can then trap ions in a 2D lattice (i.e. in an desired array of microtraps). In such a case, 2D ‘effective’ spin models could be realized.

Finally, we note that the scheme discussed in this section offers access to measurements and manipulations of arbitrarily selected ion(s): an exciting opportunity unavailable in traditional condensed-matter systems. Interestingly, since the ‘spin’ configuration is encoded in ions’ internal states, the fluorescence signal of the sample can contain enough information for detection of different phases. The first experimental results using cold ions for simulations of quantum magnetism have now been published (Friedenauer *et al.*, 2008; Islam *et al.*, 2011).

10.4.5 Quantum antiferromagnetism via lattice acceleration

In this last subsection we develop in more detail the realization of frustrated quantum systems with dynamical manipulations of ultracold gases, that—in contrast to the approaches discussed above—can be pursued in currently available experimental setups and at temperatures that have already been reached. As shown in Section 10.3.4, such a proposal leads in the hard-core boson limit of strong-repulsive interaction to the physics of the antiferromagnetic spin- $\frac{1}{2}$ XY model on the triangular lattice.

The sign change of the tunneling matrix element, from negative to positive values, can be induced by dressing the system with a fast time-periodic lattice acceleration. For hypercubic lattices such a dynamical modification of tunneling has been predicted theoretically and it has been experimentally demonstrated not only for single particles (Dunlap and Kenkre, 1986; Grossmann *et al.*, 1991; Lignier *et al.*, 2007) but also for many-particle systems (Eckardt *et al.*, 2005; Zenesini *et al.*, 2009), where it has been used to induce the quantum phase transition from a superfluid to an MI and back. The driving scheme necessary to create a suitable triangular lattice geometry has been considered in Eckardt *et al.* (2010), and we follow their approach here. The scheme involves moving the lattice along an elliptical orbit $\mathbf{x}(t) = \Delta x_c \cos(\omega t)\mathbf{e}_c + \Delta x_s \sin(\omega t)\mathbf{e}_s$ in space, with angular frequency ω , orthogonal unit vectors \mathbf{e}_c and \mathbf{e}_s , and amplitudes Δx_c and Δx_s . The resulting inertial force in the lattice frame of reference reads $\mathbf{F}(t) = -m\ddot{\mathbf{x}} = F_c \cos(\omega t)\mathbf{e}_c + F_s \sin(\omega t)\mathbf{e}_s$, where m is the boson mass and $F_{c/s} = m\omega^2 \Delta x_{c/s}$. Choosing ω and $F_{c/s}$ small enough to exclude transitions from the lowest to higher Bloch bands, one can describe the system in the lattice frame of reference by the driven Bose–Hubbard model

$$\hat{H}(t) = \sum_{\langle ij \rangle} J_{ij} \hat{b}_i^\dagger \hat{b}_j + \frac{U}{2} \sum_i \hat{n}_i (\hat{n}_i - 1) + \sum_i [v_i(t) - \mu_i] \hat{n}_i. \quad (10.33)$$

Here $J_{ij} < 0$ are the bare tunneling matrix elements and $v_i(t) \equiv -\mathbf{r}_i \cdot \mathbf{F}(t)$ the oscillating on-site energies.

If $\hbar\omega$ is taken to be large compared to the energy scales given by interaction U , tunneling $|n|J_{ij}|$, and trapping ($|\mu_i - \mu_j|$ with neighbors i and j), it corresponds to a force that is fast with respect to the timescales governing the undriven model. Under these conditions the time evolution of the driven system’s state $|\psi(t)\rangle$ can be approximated by

$$|\psi(t)\rangle \approx \hat{U}(t)|\psi_{\text{eff}}(t)\rangle, \quad (10.34)$$

where the unitary operator

$$\hat{U}(t) \equiv \exp \left(-\frac{i}{\hbar} \sum_i \hat{n}_i W_i(t) \right), \quad (10.35)$$

and where

$$W_i(t) \equiv \int_0^t d\tau v_i(\tau) - \frac{1}{T} \int_0^T dt' \int_0^{t'} d\tau v_i(\tau), \quad (10.36)$$

simply describes a periodically time-dependent shift of $-m\dot{\mathbf{x}}$ in the quasimomentum of the whole system, $W_i = \mathbf{r}_i \cdot m\dot{\mathbf{x}}$. On top of this simple oscillatory motion on the short timescale $T = 2\pi/\omega$, the time evolution on longer timescales is governed by the effective time-independent Hamiltonian \hat{H}_{eff} shown in eqn (10.14), namely

$$|\psi_{\text{eff}}(t)\rangle = \exp \left(-\frac{i}{\hbar} \hat{H}_{\text{eff}} t \right) |\psi_{\text{eff}}(0)\rangle. \quad (10.37)$$

The dressed tunneling matrix elements are given by

$$J_{ij}^{\text{eff}} = J_{ij} J_0 \left(\frac{K_{ij}}{\hbar\omega} \right). \quad (10.38)$$

Here J_0 is the zero-order Bessel function and $K_{ij} \equiv \sqrt{(F_c \mathbf{e}_c \cdot \mathbf{r}_{ij})^2 + (F_s \mathbf{e}_s \cdot \mathbf{r}_{ij})^2}$ is the amplitude of the potential modulation between sites i and j , where $\mathbf{r}_{ij} \equiv \mathbf{r}_i - \mathbf{r}_j$. Thus in the lattice frame, apart from the superimposed fast oscillation in quasimomentum, the system behaves as the one described by \hat{H}_{eff} . When measuring the momentum distribution of the system in the laboratory frame by taking time-of-flight absorption images, one will see the periodic quasimomentum distribution of $|\psi_{\text{eff}}\rangle$ at rest being enveloped by the momentum distribution of the Wannier wave function oscillating like $m\dot{\mathbf{x}}$. The result presented in the preceding paragraph relies on the separation of timescales as well as on time averaging.

The above derivation is based on stationary degenerate-state perturbation theory on the level of an extended Hilbert space including time as a coordinate. Let us give a simple argument making the \hat{H}_{eff} description plausible: transforming $|\psi'\rangle = \hat{U}^\dagger |\psi\rangle$ leads to the new Hamiltonian $\hat{H}' = \hat{U}^\dagger \hat{H} \hat{U} - i\hbar \hat{U}^\dagger (d_t \hat{U})$. Accordingly, \hat{H}' is obtained from \hat{H} by subtracting the oscillating potential terms $\propto v_i(t)$ and replacing $J_{ij} \rightarrow J_{ij} \exp(i[W_i - W_j]/\hbar)$. Now the rapidly oscillating phase factors in the tunneling terms of \hat{H}' can approximately be taken into account on a time average, $\hat{H}'(t) \rightarrow \frac{1}{T} \int_0^T dt \hat{H}'(t) = \hat{H}_{\text{eff}}$, giving $|\psi'\rangle \approx |\psi_{\text{eff}}\rangle$.

The scheme proposed here has been realized in several experiments (Becker *et al.*, 2010; Struck *et al.*, 2011). As explained before, a 2D triangular optical lattice can be realized by superimposing three laser beams, all polarized in the z direction, at an angle of $2\pi/3$ in the xy -plane, while a standing light wave in the z direction can be used to create a stack of effectively 2D systems. A further beam in the z direction allows modification of the trapping potential in the xy -plane. The lattice motion can be realized by varying the relative frequencies of the beams by means of acousto-optical modulators. For the purposes

described above, an orbit $\mathbf{x}(t) = \Delta x_c \cos(\omega t)\mathbf{e}_c + \Delta x_s \sin(\omega t)\mathbf{e}_s$ is required, with $\Delta x_{s/c}$ of the order of a lattice constant and $\omega/(2\pi)$ being a few kilohertz. Starting from an isotropic static lattice with bare tunneling matrix elements $J_{ij} = \bar{J} < 0$ and choosing $\mathbf{e}_{c/s} = \mathbf{e}_{x/y}$, one obtains effective tunneling matrix elements (eqn (10.38)) distributed as depicted in Figure 10.10(a). That is to say, K_{ij} reads $K \equiv d|F_c|$ and $K' \equiv d\sqrt{F_c^2 + 3F_s^2}/2$ along the solid and dashed bonds, respectively, giving $J = \bar{J}J_0(K/(\hbar\omega))$ and $J' = \bar{J}J_0(K'/(\hbar\omega))$ according to eqn (10.38). This allows for any value of the anisotropy parameter $\alpha = J'/J$. In experiments in this area, a triangular optical lattice has been implemented and loaded with ultracold ^{87}Rb atoms, and the transition from a superfluid to an MI has been observed (Becker *et al.*, 2010). Moreover, a controlled elliptical motion of the lattice has been achieved. Also in the weakly interacting limit a superfluid with broken time-reversal symmetry has been observed (Struck *et al.*, 2011). The strongly correlated regime, when achieved, should allow study of frustrated antiferromagnetism in the range of temperatures of order 50 nK, i.e. orders of magnitude higher than those typical for systems with superexchange interactions.

11

Ultracold atomic gases in ‘artificial’ gauge fields

11.1. Introduction

Quantum systems in external magnetic fields exhibit intriguing behavior. Among them, the integer and fractional quantum Hall effects are the paradigmatic examples of topological order (Prange and Girvin, 1987). The integer quantum Hall effect (IQHE) is a single-particle effect of 2D systems and is related to Hall conductivity, i.e. the transverse transport induced by an external magnetic field at low temperatures. The dependence of Hall conductivity on the external magnetic field shows several plateaus, each of them corresponding to an integer multiple of e^2/h , e and h being the electron charge and Planck’s constant, respectively (Klitzing *et al.*, 1980). At larger applied magnetic fields, plateaus also appear for fractional values of e^2/h . This phenomenon is known as the fractional quantum Hall effect (FQHE). It cannot, however, be explained at single-particle level since it is a strongly correlated phenomenon corresponding to a novel quantum liquid and described by a many-body state known as the Laughlin state (Laughlin, 1983).

The most appealing effects related to magnetic fields are due to the Lorenz force acting on charged particles. However, since atoms are neutral they can, at most, exhibit magnetic dipolar effects as discussed in Chapter 8. Thus if we seek to simulate in neutral atoms effects analogous to those realized by ‘normal’ magnetic fields in charged particles, we are naturally brought to the idea of ‘artificial’ or ‘synthetic’ magnetic fields. Presently, there are various ways to achieve such ‘artificial’ magnetic fields, depending on whether one desires to synthesize Abelian or non-Abelian gauge fields. Some of the ideas put forward to reach such goals can be grouped as follows.

- (I) **Proposals employing rapidly rotating trapped ultracold gases.** These methods concern the creation of artificial Abelian gauge fields—analogous to standard magnetic fields—in rotating traps. Trap rotation has become a routine method to generate vortices in Bose or Fermi superfluids. For macroscopic trapped atomic clouds, however, it is difficult to reach the strongly correlated regime by using rotations.
- (II) **Proposals employing rapidly rotating atoms in microtraps.** These methods also consider Abelian gauge fields in microtraps, and allow the strongly correlated regime to be reached. They are limited with respect to the size of the systems, which are microscopic or, in the best case, mesoscopic, containing a few to a few hundred atoms.

- (III) **Proposals employing laser-imprinted (Berry’s) phases.** These methods are typically designed for trapped atomic clouds, although in principle can also be applied to atoms in optical lattices. They may serve to create Abelian and non-Abelian gauge fields both in the weak and in the strongly correlated regime.
- (IV) **Proposals employing laser-induced gauge fields in optical lattices.** These approaches are quite similar to type III, but they exploit implicit properties of optical lattices: laser-assisted tunneling, superlattices, lattice tilting or acceleration, etc. There are also complex or more exotic proposals such as optical lattice rotation, immersion of a lattice into a rotating superfluid, or elliptical lattice shaking, as we shall see later.

This chapter is organized as follows. In Section 11.2 we discuss ultracold atoms in rapidly rotating microtraps (type II proposals). We demonstrate how the physics of the FQHE arises in such systems for high rotation frequencies. We also review the low- or moderate-rotation regime leading to quantum vortex nucleation effects. Section 11.3 deals with the basic notions of lattice gauge theory (LGT), i.e. the meaning of gauge symmetries in a lattice. Sections 11.4–11.6 are devoted to laser-induced Abelian and non-Abelian gauge fields (class IV proposals) and we discuss the first phenomena and effects that have been predicted and could be observed with ultracold atoms: the famous energy spectrum given by the Hofstadter ‘Butterfly’ (Section 11.4) and its generalization, the ‘Moth’ spectrum (Section 11.5). The spectra for atoms in Abelian $U(1)$ and non-Abelian $SU(2)$ gauge fields, together with the IQHE and the emergence of Dirac fermions in $SU(2)$ gauge fields, are discussed in Section 11.6. In Section 11.7 the FQHE in $SU(2)$ gauge fields is analysed. All previous sections deal with *external, non-dynamical* gauge fields. In Section 11.8 we shortly report recent proposals for the realization of true LGT with ultracold atoms, i.e. gauge fields that are dynamical variables and that evolve in accordance with the corresponding LGT. Finally, Section 11.9 focuses on the state of the art in generating artificial magnetic fields using approaches I–IV. An excellent and exhaustive review on artificial magnetic field generation in ultracold gases can be found in Dalibard *et al.* (2010). A universal ‘toolbox’ for synthetic $SU(N)$ fields in three dimensions using superlattices and assisted tunneling (type IV) is described in Mazza *et al.* (2011).

11.2. Ultracold atoms in rapidly rotating microtraps

Rotation of ultracold trapped BEC systems is usually discussed in the context of vortex formation, which can be described by the Gross–Pitaevskii mean-field equations and has been widely confirmed in experiments in atomic systems of large size (Madison *et al.*, 2000; Abo-Shaeer *et al.*, 2001). However, for trapped systems formed by few atoms, rotation leads to a strongly correlated regime that cannot be described by the mean-field approach. The nature of these strongly correlated systems can be probed by analysing two-point correlation functions describing the probability of finding one atom at one position conditioned to the presence of a second atom in another position. The differences between large and small atomic samples manifest not only for trap rotations close to the trap frequency, but even for moderate or small rotational frequencies, as we will see in this section.

The rotation of an atom of mass m in a trap is formally equivalent to an electron placed in a magnetic field. This observation leads straightforwardly to the realisation of ‘artificial’ magnetic fields. In what follows we discuss in some detail the physics of rotating microtraps with small or moderate atomic-size samples. To be specific, we consider a system of N bosons rotating in an axially symmetric harmonic-trap potential with a strong confinement along the rotation axis, e.g. the z -axis. Assuming that the temperature T and the chemical potential μ , are much smaller than the axial confinement ($T, \mu \ll \omega_z$) the gas is effectively 2D and the Hamiltonian of the system in the rotating reference frame reads

$$H = \sum_{j=1}^N \left[\frac{\mathbf{p}_j^2}{2m} + \frac{1}{2}m\omega_{\perp}^2 \mathbf{r}_j^2 - \Omega L_{jz} \right] + V_{\text{int}}. \quad (11.1)$$

Here $\omega_{\perp} \ll \omega_z$ is the radial trap frequency, Ω is the rotation frequency, L_{jz} is the projection onto the z -axis of the angular momentum of the j th particle located at $\mathbf{r}_j = x_j \mathbf{e}_x + y_j \mathbf{e}_y$, and V_{int} refers to the particle-particle interaction. For the moment, we take $V_{\text{int}} = 0$. The above Hamiltonian can be conveniently rewritten in the form

$$H = \sum_{j=1}^N \underbrace{\left[\frac{1}{2m} (\mathbf{p}_j - m\omega_{\perp} \mathbf{e}_z \times \mathbf{r}_j)^2 \right]}_{H_{\text{Landau}}} + \underbrace{(\omega_{\perp} - \Omega)L_{jz}}_{H_{\Delta}}, \quad (11.2)$$

where H_{Landau} is formally equivalent to the Landau Hamiltonian of particles with mass m and charge e moving in a constant perpendicular magnetic field with vector potential $\mathbf{A} = (cm\omega_{\perp}/e)\mathbf{e}_z \times \mathbf{r}$, H_{Δ} describes the shift of single-particle energy levels as a function of their angular momentum, and the difference between the radial trap and the rotating frequencies equals $\Delta\omega = \omega_{\perp} - \Omega$. Since $[H, L] = 0$, a common eigenbasis of H and L is given by the unnormalized Hermite functions $\varphi_{l,n} = e^{r^2/a_{\perp}^2} (\partial_x + i\partial_y)^l (\partial_x - i\partial_y)^n e^{-r^2/a_{\perp}^2}$ with $a_{\perp} = \sqrt{\hbar/m\omega_{\perp}}$, where l and n are non-negative integers. The eigenvalues of the L_z are $\hbar(l-n)$ and the eigenvalues of the energy are $E_{l,n} = \hbar\omega_{\perp} + l\hbar\Delta\omega + n\hbar(\omega_{\perp} + \Omega)$.

In the limit of critical rotation, $\Omega = \omega_{\perp}$, the Hamiltonian reduces to H_{Landau} . In this case, the spectrum becomes $E_n = 2\hbar\omega_{\perp}(1/2+n) = \hbar\omega_c(1/2+n)$, with $\omega_c = 2\omega_{\perp}$ being the cyclotron frequency and $n \geq 0$. Each energy level is infinitely degenerated (for any value of l). Those are the well-known Landau levels, which are equidistantly spaced by $\hbar\omega_c$. In the vicinity of the critical rotation, $\Omega \rightarrow \omega_{\perp}$ so that Ω approaches the critical rotation from below, the above description is still valid if Ω is sufficiently large that $\omega_{\perp} - \Omega \ll \omega_{\perp} + \Omega$. The distance between two consecutive states $(l, l+1)$ inside a given Landau level is $\hbar\Delta\omega \ll \hbar\omega_{\perp}$. Thus, to all effects, the Landau levels remain highly degenerate and contain $N_{\text{LL}} = 1/2\pi l_0^2$ states per unit area, where $l_0 = \sqrt{\hbar/m\omega_c}$ is the magnetic length. For a given surface filled with bosons at density \bar{n} , one can introduce the filling factor $\nu = 2\pi l_0^2 \bar{n}$, which denotes the fraction of occupied Landau levels. Note that under the condition of critical rotation the density of the trapped gas is uniform except at the boundary provided by an external confining potential. If the interaction potential is sufficiently small, there is no mixing between different Landau levels.

If we now consider N atoms in the trap rotating at a frequency $\Omega \rightarrow \omega_{\perp}$, for filling fractions $\nu \leq 1$, particles solely occupy the lowest Landau level (LLL) with $n = 0$. In this

case, the many-body system can be described in terms of $n = 0$ single particle eigenstates with no nodes in the radial direction, also known as Fock–Darwin states. These states are taken as a basis to represent wave functions and operators in the second quantized formalism. We denote them as

$$|\varphi_{l,n=0}\rangle = |l\rangle = \frac{1}{\lambda\sqrt{\pi l!}} \left(\frac{z}{\lambda}\right)^l e^{-|z|^2/2a_\perp^2} \quad (11.3)$$

with generalized complex coordinates $z = x + iy$.

The corresponding many-body eigenfunction in the LLL manifold is a linear superposition of single-particle solutions with $n = 0$, and in the $x - y$ plane takes the form

$$\Psi(z_1, z_2, \dots, z_N) = \mathcal{N}P[z_1, \dots, z_N] \exp\left(-\sum_{j=1}^N |z_j|^2/4l_0^2\right), \quad (11.4)$$

where $P[\{z_j\}]$ is a totally antisymmetric polynomial in the coordinates $z_j = x_j + iy_j$ of the particles and \mathcal{N} is the normalization factor. The corresponding eigenenergy is independent of the specific choice of $P[\{z_j\}]$ and equals $N\hbar\omega_c/2$, where N is the total number of particles. This degeneracy is removed if an interaction is considered. From now on we will assume that interactions are contact type, $V_{\text{int}} = g \sum_{i < j} \delta(\mathbf{r}_i - \mathbf{r}_j)$, where g is the coefficient that models the potential of the Van der Waals forces between the atoms in the very dilute limit. In this case the axial symmetry is preserved.

The Hamiltonian (eqn (11.1)) in the LLL can be written in second quantization as

$$\hat{H}_{\text{LLL}} = \hbar\omega_\perp \hat{N} + \hbar(\omega_\perp - \Omega)\hat{L} + \hat{V}_{\text{int}} = \hat{H}_0 + \hat{V}_{\text{int}}, \quad (11.5)$$

where $\hat{L} = \sum_j L_{zj}$ is the total z component angular momentum and \hat{N} the particle number operator. The kinetic energy is given by \hat{H}_0 . The interaction reads

$$\hat{V}_{\text{int}} = \frac{1}{2} \sum_{l_1 l_2 l_3 l_4} V_{1234} \hat{a}_1^\dagger \hat{a}_2^\dagger \hat{a}_4 \hat{a}_3, \quad (11.6)$$

where the matrix elements of the interaction term are given by

$$V_{1234} = \langle l_1, l_2 | \hat{V} | l_3, l_4 \rangle = \frac{g}{\lambda^2 \pi} \frac{\delta_{l_1+l_2, l_3+l_4}}{\sqrt{l_1! l_2! l_3! l_4!}} \frac{(l_1 + l_2)!}{2^{l_1+l_2+1}}. \quad (11.7)$$

The operators \hat{a}_i^\dagger and \hat{a}_i create and annihilate a boson in a single-particle eigenstate of \hat{H}_0 with angular momentum l_i , respectively (Fock–Darwin basis). The cylindrical symmetry of the Hamiltonian allows the diagonalization to be performed in different subspaces of a well-defined total z component of angular momentum L . Thus, for a given rotation frequency Ω , we denote the ground state (i.e. the lowest eigenstate of the Hamiltonian) of the system in the L -subspace by Ψ_L . In Figure 11.1 we plot, for a system of $N = 5$ particles, the total angular momentum of the ground state of the Hamiltonian of eqn (11.5)

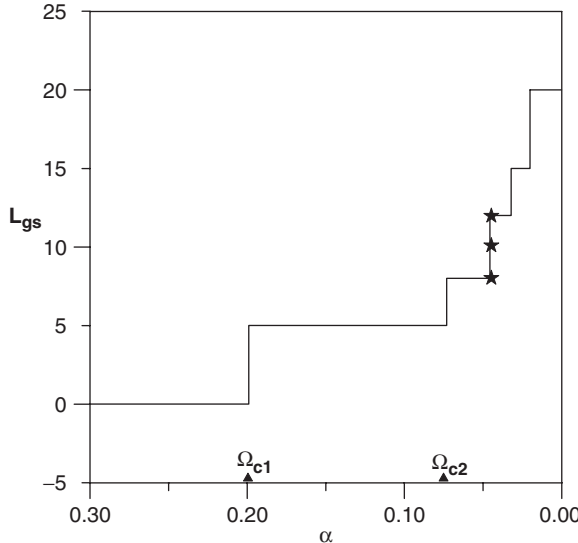


Figure 11.1 Change of the ground-state angular momentum L_{gs} for $N = 5$ as the rotation frequency increases; transitions take place at critical values of the rotational frequency labeled by Ω_{cn} ($\alpha = \hbar(\omega_\perp - \Omega)$). From Barberán *et al.* (2006).

as a function of Ω as it grows from zero to ω_\perp , the maximum possible value before the system becomes centrifugally unstable. We observe that the ground-state angular momentum remains constant for a finite range of Ω until transitions to new angular momenta take place at critical values labeled as Ω_{cn} . Not all L -values can be associated with the ground states. However, within the steps, different L -states may be degenerate in energy as is the case of the ground states with $L = 8, 10$, and 12 on the third step (indicated by stars in Figure 11.1). The last possible ground state at $L = N(N - 1)$ ($L = 20$ for $N = 5$ in the figure) is the Laughlin state for which the interaction energy is zero due to the fact that the wave function of each atom has zeros of order two at the positions of the other $N - 1$ atoms; this can be easily deduced from the analytical expression of the many-body wave function given by (where for brevity we denote $\lambda = a_\perp$)

$$\Psi_{\text{Laughlin}} = N \prod_{i < j} (z_i - z_j)^2 e^{-|z_i|^2/2\lambda^2}. \quad (11.8)$$

11.2.1 Ordered structures in the ground state

Notice that when the cylindrical symmetry is broken, the one-particle density already shows mixing of degenerate ground states with different total angular momenta (Barberán *et al.*, 2006). It is important to realize, however, that the density operator $\rho(\mathbf{r}) = \sum_i \delta(\mathbf{r} - \mathbf{r}_i)$ does not exhibit any interference pattern when calculated for a definite Ψ_L , as can be inferred

from its analytical expression in second quantized form

$$\hat{\rho}(\mathbf{r}) = \sum_{ij} \langle \varphi_i(\mathbf{r}') | \delta(\mathbf{r} - \mathbf{r}') | \varphi_j(\mathbf{r}') \rangle \hat{a}_i^\dagger \hat{a}_j, \quad (11.9)$$

where $|\varphi_i(\mathbf{r})\rangle = |l_i\rangle$ as in eqn (11.3). Due to angular momentum conservation, the operator $\hat{a}_i^\dagger \hat{a}_j$ selects only one single-particle state and, as a consequence, it loses all information contained in products of different amplitudes, thus losing the interference pattern. It only preserves the information of individual densities:

$$\rho(\mathbf{r}) = \langle \Psi_L | \hat{\rho}(\mathbf{r}) | \Psi_L \rangle = \sum_i^N |\varphi_i(\mathbf{r})|^2 O c_i, \quad (11.10)$$

where $O c_i$ is the total occupation of the sp-state $|l_i\rangle$ in the ground state. In fact, $\rho(\mathbf{r})$ can only represent cylindrically symmetric distributions. However, this cylindrical symmetry is a direct consequence of the definition of the operator $\hat{\rho}(\mathbf{r})$ and is not necessarily a manifestation of the symmetric nature of the ground state. Therefore, one has to look not only at the mean density, but also at the pair correlation functions for states with fixed L . In view of the recent detection methods at the single-atom level (Bakr *et al.*, 2009; Bakr *et al.*, 2010; Sherson *et al.*, 2010), both of the considered quantities can be directly measured.

The pair correlation operator (in the first quantization) is defined as

$$\rho(\mathbf{r}, \mathbf{r}_0) = \sum_{i < j}^N \delta(\mathbf{r}_i - \mathbf{r}_0) \delta(\mathbf{r}_j - \mathbf{r}), \quad (11.11)$$

and yields the joint probability of finding an atom at \mathbf{r} , when another is simultaneously found at \mathbf{r}_0 . This operator contains information that originates from the amplitudes of sp-wave functions and not only from their density, as is the case for the single-particle density operator. Its expected value with respect to Ψ_L reads

$$\begin{aligned} \rho(\mathbf{r}, \mathbf{r}_0) &= \langle \Psi_L | \hat{\rho}(\mathbf{r}, \mathbf{r}_0) | \Psi_L \rangle \\ &= \sum_{i j k s} \sum_{p p'} \alpha_p^* \alpha_{p'} \varphi_i^*(\mathbf{r}) \varphi_j^*(\mathbf{r}_0) \varphi_k(\mathbf{r}) \varphi_s(\mathbf{r}_0) \langle \Phi_p | \hat{a}_i^\dagger \hat{a}_j^\dagger \hat{a}_s \hat{a}_k | \Phi_{p'} \rangle, \end{aligned} \quad (11.12)$$

where

$$\Psi_L = \sum_{p=1}^{n_d} \alpha_p \Phi_p, \quad (11.13)$$

and Φ_p are the bosonic Fock N -body states of the basis in the L -subspace of dimension n_d . The condition $i + j = k + s$ must be fulfilled for angular momentum conservation. It should

be stressed that $\rho(\mathbf{r}, \mathbf{r}_0)$ in eqn (11.11) obviously differs from the single-particle density matrix (SPDM)

$$n^{(1)}(\mathbf{r}, \mathbf{r}_0) = \langle \Psi_L | \hat{\Psi}^\dagger(\mathbf{r}) \hat{\Psi}(\mathbf{r}_0) | \Psi_L \rangle, \quad (11.14)$$

where $\hat{\Psi}^\dagger(\mathbf{r})$ is the creation operator that creates a boson at position \mathbf{r} . The SPDM can be used to define the off-diagonal long-range order that characterizes Bose condensation (Pitaevskii and Stringari, 2003). The operator $\hat{\rho}(\mathbf{r}, \mathbf{r}_0)$ is a two-particle operator, whereas $\hat{n}^{(1)}(\mathbf{r}, \mathbf{r}_0)$ is a single-particle operator. As a rule of thumb, if $\hat{n}^{(1)}(\mathbf{r}, \mathbf{r}_0)$ reveals symmetry breaking, so does $\hat{\rho}(\mathbf{r}, \mathbf{r}_0)$, whereas the opposite is not necessarily true.

Equation (11.12) can be interpreted as the sum of products of amplitudes at \mathbf{r} weighted by a factor that depends on \mathbf{r}_0 and on the ground state via the α_p coefficients. In the particular case $\mathbf{r}_0 = \mathbf{0}$, cylindrical symmetry is recovered, since in this case $s = j = 0$ is the unique non-zero contribution. This implies $i = k$ and yields

$$\rho(\mathbf{r}, \mathbf{0}) = |\varphi_0(\mathbf{0})|^2 \sum_i |\varphi_i(\mathbf{r})|^2 \sum_{pp'} \alpha_p^* \alpha_{p'} \langle \dots \rangle, \quad (11.15)$$

In order to understand the role of the parameter \mathbf{r}_0 in $\langle \Psi_L | \hat{\rho}(\mathbf{r}, \mathbf{r}_0) | \Psi_L \rangle$ as a function of \mathbf{r} , we consider

$$\varphi_i^*(\mathbf{r}) \varphi_j^*(\mathbf{r}_0) \varphi_k(\mathbf{r}) \varphi_s(\mathbf{r}_0) = \frac{1}{\pi^2} \frac{r^{l_i}}{\sqrt{l_i!}} \frac{r_0^{l_j}}{\sqrt{l_j!}} \frac{r^{l_k}}{\sqrt{l_k!}} \frac{r_0^{l_s}}{\sqrt{l_s!}} e^{i(l_k - l_i)\theta} e^{i(l_s - l_j)\theta_0} e^{-r^2} e^{-r_0^2}, \quad (11.16)$$

in units of λ (see eqn (11.3)). As $s - j = i - k$ follows from angular momentum conservation, the angular dependence reads

$$e^{i(l_k - l_i)\theta} e^{i(l_s - l_j)\theta_0} = e^{i(l_k - l_i)(\theta - \theta_0)}. \quad (11.17)$$

Evidently, if \mathbf{r}_0 is fixed, the change of θ_0 is nothing but a rigid rotation of the function. In other words, any arbitrary choice of θ_0 fixes the origin of angles and breaks cylindrical symmetry, in a way analogous to what happens in experiments that perform a single shot measurement. From this point of view, the experimental measurement and the choice of θ_0 are equivalent processes (see for instance Altman *et al.* (2004) and Fölling *et al.* (2005)).

The expected values of the pair-correlation function for $\mathbf{r}_0 \neq 0$ are much more complex and can reveal very different situations (see Barberán *et al.* (2006) for details): from circular symmetric structures showing no spatial correlation to ordered structures that reveal intrinsic Wigner molecules or crystals while passing through all possible intermediate states. Contours of pair-correlation functions for Laughlin states of $N = 6, 7, 8$ bosonic atoms interacting solely via Van der Waals forces are shown in Figure 11.2. Note that precursors of such states have very recently been experimentally realized and observed (Gemelke *et al.*, 2010).

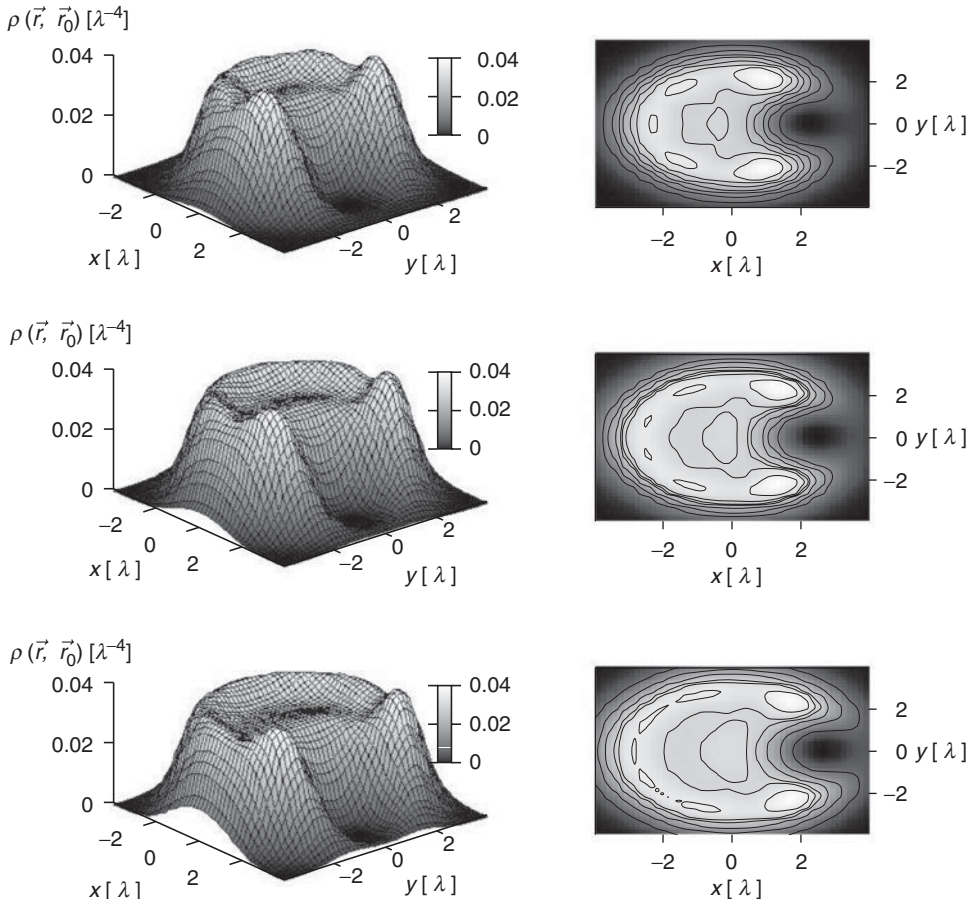


Figure 11.2 3D (left) and contour (right) plots of the pair correlation function $\rho(\mathbf{r}, \mathbf{r}_0)$ for the Laughlin states of $N = 6, 7$, and 8 atoms of mass m in a lattice site; $r_0 = \sqrt{N}$ in harmonic oscillator units and $\lambda = \sqrt{\hbar/2m\omega_\perp}$. From Barberán *et al.* (2006).

11.2.2 Quantum vortex nucleation

Interestingly enough, strongly correlated states do not only appear in the fast-rotation case, but also in the regime where one expects the Gross–Pitaevskii mean-field approach to be accurate. The response to rotation provides one of the most striking properties of superfluids and condensates. The way to acquire angular momentum is by vortex generation, i.e. topological singularities of zero density with condensed atoms revolving around them. A slow sweep of the rotation frequency changes the state of the system from being at rest to one containing one vortex. Within the mean-field framework, the jump in symmetry occurs through a turbulent phase around a certain critical frequency. A generic but difficult question concerns the relation between the symmetry properties of the true many-body state and its mean-field approximation. In Dagnino *et al.* (2009*b*, 2009*a*), the authors addressed

this question by a theoretical consideration of vortex nucleation in a rotating Bose–Einstein condensate, showing that the exact many-body ground state at the critical frequency at which the vortex appears exhibits strong correlations and entanglement. This study provides a paradigm example of symmetry-breaking or the change of the order parameter in quantum many-body systems in the course of adiabatic evolution. Below we analyse the mean-field approach in an anisotropic potential.

Mean-field analysis The Hamiltonian of a 2D gas confined by an anisotropic quadratic potential in the XY plane rotating at angular frequency ω_\perp reads in the rotating frame:

$$H = \sum_{j=1}^N \left[\frac{\mathbf{p}_j^2}{2m} + \frac{1}{2}m\omega_\perp^2 \mathbf{r}_j^2 + 2Am\omega_\perp^2(x^2 - y^2) - \Omega L_{jz} \right] + V_{\text{int}}. \quad (11.18)$$

The coefficient $A \ll 1$ measures the strength of the anisotropy in the stirring potential, and we assume again the contact potential for the interactions. The role of the anisotropy is to lift the axial symmetry, which in turn lifts the degeneracy of the ground state at the critical rotation Ω_{cr} where the angular momentum changes.

For $A \ll 1$ and $\Omega \rightarrow \omega_\perp$, one arrives again at the results of the previous section, namely that the single-particle energy levels in the rotation frame are grouped in Landau levels, and if the rotating frequency is large enough one can restrict the physics to the LLL. The mean-field approach provides a good description below and above the critical frequency, but fails to describe the many-body wave function at the criticality where strong correlations and entanglement appear. We analyse the physics in the vicinity of the first jump, $\Omega \rightarrow \Omega_1$, when the first vortex is nucleated, for a small anisotropy $A = 0.03$, $N = 12$, and $g = 0.5$. From the ground state of the Hamiltonian in eqn (11.18), one can extract the single-particle density matrix $n^{(1)}(\mathbf{r}, \mathbf{r}')$, and its eigenstates ψ_k and eigenvalues n_k . Far from the critical rotation, the contribution of a single eigenstate ψ is relevant, while in the vicinity of the critical rotation Ω_1 it is enough to consider two eigenstates ψ_1 and ψ_2 . The expansion of these two eigenstates in the Fock–Darwin basis φ_l indicates that only the first three LLL single-particle states with angular momentum $l = 0, 1, 2$ are relevant.

The mean-field approach in the vicinity of the Ω_1 assumes that all atoms in the same state $f(\vec{r}, t) = \sum_{l=0}^2 a_l(t) \varphi_l(\mathbf{r})$ with $\sum |a_l|^2 = 1$. The average angular momentum per particle is $L = |a_1|^2 + 2|a_2|^2$ and the average energy per particle $E(\psi) = \frac{1}{N} \langle f^{\otimes N} | H | f^{\otimes N} \rangle$ reads (up to an additive constant):

$$\begin{aligned} E(\psi) = & (1 - \Omega)(|a_1|^2 + 2|a_2|^2) + \sqrt{2}A(a_0a_2^* + a_0^*a_2) + \frac{Ng}{4\pi} \left[|a_0|^4 + \frac{1}{2}|a_1|^4 + \frac{3}{8}|a_2|^4 \right. \\ & \left. + 2|a_0|^2|a_1|^2 + |a_0|^2|a_2|^2 + \frac{3}{2}|a_1|^2|a_2|^2 + \frac{1}{\sqrt{2}}(a_0a_2(a_1^*)^2 + a_0^*a_2^*a_1^2) \right]. \end{aligned} \quad (11.19)$$

The Lagrange equations associated with this energy are given by $i\dot{a}_j = \partial E / \partial a_j^*$, leading to

$$i\dot{a}_0 = \sqrt{2}Aa_2 + \frac{Ng}{2\pi} \left[a_0 \left(|a_0|^2 + |a_1|^2 + \frac{1}{2}|a_2|^2 \right) + \frac{1}{2\sqrt{2}}a_1^2a_2^* \right], \quad (11.20)$$

plus two similar equations for \dot{a}_1 and \dot{a}_2 . The 2D contact interaction strength g appears only in the Ng factor and in particular whether N is odd or even has no relevance here. The stationary solutions are found by inserting $a_l(t) = e^{-i\mu t}a_l(0)$ into the three Lagrange equations. A detailed analysis of the resulting 3×3 non-linear system shows that two classes of solution exist. The first class (f_a) corresponds to $a_1 = 0$. Depending on the value of the parameters Ng , A , and Ω , there may exist two, three, or four solutions of this kind. After some tedious but straightforward calculation, one can obtain for this first class of solution an analytical relation between Ω and the angular momentum per particle $L = 2|a_2|^2$:

$$\Omega = 1 - \frac{Ng}{8\pi} \left(1 - \frac{3}{8}L \right) \pm \sqrt{2}A \frac{1-L}{\sqrt{L(2-L)}} .$$

The second class of solution corresponds to a non-zero value for a_1 . A numerical analysis permits us to find the local minima of the energy. One solution of this kind exists if and only if $\Omega > 0.766$. Comparing the energy of this solution with the lowest energy of the solutions in the first class we obtain that for $\Omega < \tilde{\Omega} = 0.773$, the ground state is obtained with a solution belonging to the first class. For $\Omega > \tilde{\Omega} = 0.773$ the ground state is obtained with a solution belonging to the second class.

The dynamical stability of the solutions of the first class ($a_1 = 0$) can be studied by adding a small perturbation $b_1(t) = a_1 e^{i\mu t}$. Since the stationary solution corresponds to $b_1 = 0$, it is stable if $b_1(t)$ stays around 0, when starting from a small non-zero initial value. In contrast, one obtains the result that b_1 undergoes an exponential divergence from any initial noise, signaling a dynamical instability of the solution. Using dynamical perturbation theory, one can calculate critical parameters such as Ω_c analytically. The dynamical instability of the mean-field theory signals the appearance of the strongly correlated states.

We show in Figure 11.3, the variation of n_1/N and n_2/N as a function of Ω , for $N = 12$, $g = 0.5$, and $A = 0.03$. These two populations are equal for $\Omega_c = 0.775$. We see that $n_1 + n_2 \simeq N$ over the whole range of frequencies of this figure, indicating that most of the population of the SPDM is concentrated in the first two modes ψ_1 and ψ_2 . As intuitively expected, below Ω_c , ψ_1 is approximately a coherent superposition of φ_0 and φ_2 , corresponding to two off-centered vortices (even parity). ψ_2 meanwhile is very close to a well-centered single-vortex state φ_1 (odd parity). Above Ω_c , ψ_1 and ψ_2 abruptly exchange their form. The situation described above concerns the breakdown of the mean-field analysis, when the ground state undergoes a symmetry change or breaking as some parameter of the system, say η , crosses a critical value η_c . Far from the critical value, the system is well described by the mean-field theory with order parameters reflecting the appropriate symmetry. At the critical value, a dynamical mean-field description shows that the system exhibits dynamical instability, signaling the breakdown of the mean-field approach and the presence of strongly correlated correlated states.

Many other quantum systems follow similar but not identical scenarios, but of course the rigorous generality of the above statements remains an open question.

Exact analysis: quantum correlations for $\Omega \sim \Omega_c$ By fixing N to be even, the many-body ground state $|\Psi_0\rangle$ of eqn (11.18) remains non-degenerate at $\Omega = \Omega_c$, and is even over the whole range $[\Omega_i, \Omega_f]$. At the critical frequency Ω_c , the two largest eigenvalues

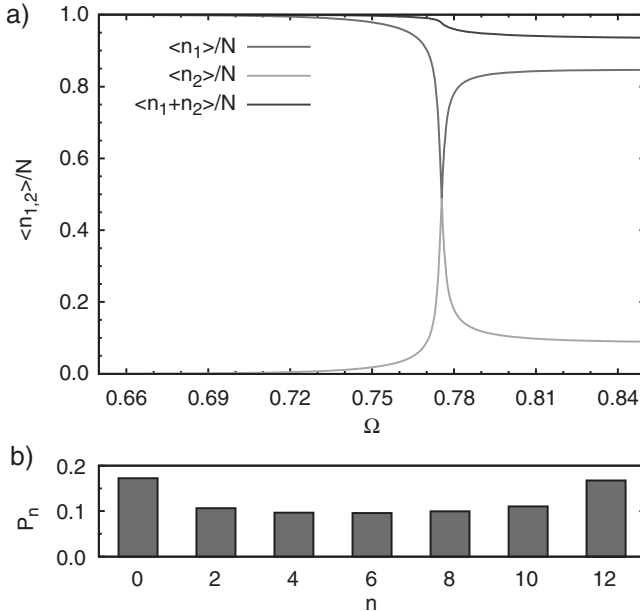


Figure 11.3 Structure of the ground state. (a) Variation of the relative populations n_1/N and n_2/N of the two most occupied states ψ_1 and ψ_2 of the SPDM. When Ω is sufficiently different from Ω_c , $n_1 \simeq N$, the system is well described by a single mode and the mean-field description is valid. Conversely, for $\Omega \simeq \Omega_c$, the two populations are comparable, corresponding to the case where a two-mode approximation is valid even in the entangled region. (b) Analysis of the state of the system at the critical point where $n_1 = n_2$, in terms of the square of the scalar products $P_n = |\langle n : \psi_1 ; N-n : \psi_2 | \Psi_0 \rangle|^2$. We obtain $|\langle E | \Psi_0 \rangle| = 0.92$. Both panels are plotted for $N = 12$, $g = 0.5$, and $A = 0.03$. From Dagnino *et al.* (2009b).

of the SPDM (see eqn (11.14)) are equal ($n_1 = n_2$). Thus the system is well described by a two-mode approximation since the two largest eigenvalues of the SPDM are much larger than the others, so that $n_1 = n_2 \simeq N/2$. As an example, for $N = 12$, $g = 0.5$, and $A = 0.03$, we obtain $n_1 = n_2 = 0.49 N$ at $\Omega_c = 0.776$, as shown in Figure 11.3. The ground state is a strongly correlated state that can be described (for even N) by

$$|E\rangle = [|N, 0\rangle + |N-2, 2\rangle + \dots + |0, N\rangle] / \sqrt{N/2 + 1}, \quad (11.21)$$

where $|n, m\rangle$ is the state with n (m) atoms in ψ_1 (ψ_2). Amazingly, the form of the ground state at Ω_c is practically independent of A , as long as $A \ll 1$. For a quantitative comparison of the exact ground state with the state in eqn (11.21), we display also in Figure 11.3 the squared scalar products $\langle n, N-n | \Psi_0 \rangle$ for a concrete value of $N = 12$. They are all zero for odd values of n (as expected from the parity of $|\Psi_0\rangle$) and approximately constant for even values of n .

Note that the ground state at Ω_c is quite different from a ‘Schrödinger cat’ state, that is $(|N, 0\rangle + |0, N\rangle)/\sqrt{2}$, or a ‘twin’ state $|N/2, N/2\rangle$. Although there are various ways of

defining entanglement for identical particles (for a review see Eckert *et al.* (2002)), according to the concept of mode entanglement, the state of eqn (11.21) is maximally entangled. This can be clearly seen by tracing the state of eqn (11.21) over one of the two modes and observing that the von Neumann entropy of the reduced density matrix reaches the maximal value $S \sim \log(N)$ (see Chapter 12).

11.3. Gauge symmetry in the lattice

Before turning to the main topic of the chapter—ultracold atoms in artificial gauge fields—we review in some detail the main aspects of gauge invariance related to lattices. Once more, the similarity between electronic systems in crystals (periodic lattices) and atoms in optical lattices can lead to analogous phenomena and, correspondingly, to atoms in optical lattices exhibiting similar physics to that encountered in electronic systems for Abelian fields. Moreover, atoms in optical lattices can be made to tunnel in a non-commutative way, leading to novel effects related to non-Abelian gauge fields. The distinction between the Abelian and non-Abelian cases will be clarified later using the gauge-invariant Wilson loop.

11.3.1 Classical external gauge fields

In what follows, we assume that the gauge fields are classical, external and do not correspond to dynamical variables, i.e. they are not influenced by atomic motion. Such a situation corresponds to the gauge potentials realized in ultracold gases, and is analogous to the one encountered in atomic or condensed-matter physics when considering interactions of matter with electromagnetic fields (Abelian gauge fields) under the following assumptions:

- that electromagnetic fields can be regarded as classical, i.e. quantum fluctuations can be neglected
- that electromagnetic fields can be regarded as external and the back influence of matter onto the electromagnetic fields is negligible.

Such a setting typically corresponds to strong electric or magnetic fields, either static or oscillating, such as a maser or laser field. In this case one can study the quantum dynamics of matter under this type of field. The requirements above can also be considered in the context of non-Abelian gauge fields, as widely studied in gauge field theory (see, for example, Rubakov (2002)). Interesting examples of classical external gauge fields (CEGFs) range from fields of constant strength to fields carrying topological character, such as Polyakov monopoles.

11.3.2 Gauge invariance in Abelian classical external gauge fields: the continuum case

Let us examine first a $U(1)$ gauge field in the absence of a lattice and focus on the non-relativistic limit. This could be, for instance, an electromagnetic field. For simplicity, we consider that the gauge potentials give rise to static magnetic fields only and we assume the scalar (electrostatic) potential to be zero (i.e. a vanishing electric field). Generalizations of the following concepts for more general gauge potentials are straightforward.

The second quantized Hamiltonian describing particles subjected to a $U(1)$ CEGF reads:

$$\hat{H} = \frac{1}{2m} \int d\mathbf{r} \hat{\psi}^\dagger(\mathbf{r}) \left(-i\hbar\nabla - \frac{e}{c} \mathbf{A}(\mathbf{r}) \right)^2 \hat{\psi}(\mathbf{r}) + \frac{g}{2} \int d\mathbf{r} \hat{\psi}^\dagger(\mathbf{r}) \hat{\psi}^\dagger(\mathbf{r}) \hat{\psi}(\mathbf{r}) \hat{\psi}(\mathbf{r}), \quad (11.22)$$

where $\hat{\psi}(\mathbf{r})$, $\hat{\psi}^\dagger(\mathbf{r})$ are annihilation and creation operators of the (single component) matter field, $\mathbf{A}(\mathbf{r})$ is the vector potential, and g is the coupling constant for contact interactions.

The Hamiltonian's spectrum is invariant with respect to gauge transformations, in which the matter fields undergo a local unitary transformation:

$$\hat{\psi}(\mathbf{r}) \rightarrow e^{i\phi(\mathbf{r})} \hat{\psi}(\mathbf{r}), \quad (11.23)$$

and the vector potential transforms according to

$$\mathbf{A}(\mathbf{r}) \rightarrow \mathbf{A}(\mathbf{r}) + \frac{c\hbar}{e} \nabla \phi(\mathbf{r}). \quad (11.24)$$

In this context, the magnetic field $\mathbf{B} = \nabla \times \mathbf{A}$ defines a gauge-invariant field. Note that the interaction term in eqn (11.22) is invariant under the gauge transformation of eqn (11.23). Generalizations to other types of gauge-invariant interaction are also straightforward.

11.3.3 Gauge invariance in non-Abelian classical external gauge fields: the continuum case

One can easily extend the considerations above to the situation in which the components of the gauge potential are expressed as non-commuting unitary matrices. The second quantized Hamiltonian describing particles subjected to a $U(N)$ CEGF reads

$$\hat{H} = \frac{1}{2m} \int d\mathbf{r} \hat{\Psi}^\dagger(\mathbf{r}) \left(-i\hbar\nabla - \frac{e}{c} \mathbf{A}(\mathbf{r}) \right)^2 \hat{\Psi}(\mathbf{r}) + \frac{g}{2} \int d\mathbf{r} \hat{\Psi}^\dagger(\mathbf{r}) (\hat{\Psi}^\dagger(\mathbf{r}) \hat{\Psi}(\mathbf{r})) \hat{\Psi}(\mathbf{r}), \quad (11.25)$$

where $\hat{\Psi}(\mathbf{r})$ and $\hat{\Psi}^\dagger(\mathbf{r})$ are now annihilation and creation operators of matter fields with N components, $\mathbf{A}(\mathbf{r})$ is the non-Abelian vector potential, and g is the coupling constant for the contact interactions. The interaction term is now invariant with respect to the $U(N)$ transformations of the matter fields, which are described below.

The Hamiltonian's spectrum is invariant with respect to $U(N)$ gauge transformations, in which the matter fields undergo a local unitary $U(N)$ transformation and the vector potential undergoes the gauge change,

$$\hat{\Psi}(\mathbf{r}) \rightarrow T(\mathbf{r}) \hat{\Psi}(\mathbf{r}), \quad (11.26)$$

$$\mathbf{A}(\mathbf{r}) \rightarrow T(\mathbf{r}) \mathbf{A}(\mathbf{r}) T^\dagger(\mathbf{r}) + \frac{ic\hbar}{e} T(\mathbf{r}) \nabla T^\dagger(\mathbf{r}). \quad (11.27)$$

The corresponding non-Abelian ‘magnetic’ field is defined by

$$\mathbf{B}(\mathbf{r}) = \nabla \times \mathbf{A}(\mathbf{r}) - \frac{ie}{c\hbar} \mathbf{A}(\mathbf{r}) \times \mathbf{A}(\mathbf{r}), \quad (11.28)$$

and transforms according to

$$\mathbf{B}(\mathbf{r}) \rightarrow T(\mathbf{r})\mathbf{B}(\mathbf{r})T^\dagger(\mathbf{r}). \quad (11.29)$$

Note that the magnetic field no longer describes a gauge-invariant quantity in this context.

11.3.4 Gauge invariance in Abelian classical external gauge fields: the lattice case

The concept of gauge invariance can also be extended to lattice systems (Montvay and Münster, 1997; Rothe, 2005), where the gauge transformation is defined for the on-site field operators. For instance, the Hubbard Hamiltonian describing particles on a lattice subjected to an Abelian gauge field reads:

$$\hat{H} = -t \sum_{\langle i,j \rangle} \left[e^{i\phi_{ij}} \hat{b}_i^\dagger \hat{b}_j + h.c. \right] + \frac{V}{2} \sum_i \hat{b}_i^\dagger \hat{b}_i^\dagger \hat{b}_i \hat{b}_i, \quad (11.30)$$

where \hat{b}_i (\hat{b}_i^\dagger) annihilates (creates) a particle on the site i , the phase factors $\exp(i\phi_{ij})$ are associated with the tunneling between the nearest-neighboring sites $j \rightarrow i$, t is the tunneling amplitude, and V is the coupling constant for the on-site interactions. Here we focus on a 2D square lattice, but the following discussion is valid in general.

In LGTs, the gauge transformation is naturally defined as an on-site $U(1)$ transformation of the field operators,

$$\hat{b}_j \rightarrow \hat{b}'_j = e^{i\chi_j} \hat{b}_j. \quad (11.31)$$

The Hamiltonian is modified under such a transformation and involves new tunneling phase factors given by

$$\phi_{ij} \rightarrow \phi'_{ij} = \phi_{ij} + \chi_i - \chi_j = \phi_{ij} + \Delta\chi_i. \quad (11.32)$$

Note that eqn (11.32) is recognized as a discrete form of the gauge transformation of eqn (11.24). As in the continuum case, the Hamiltonian’s spectrum is left invariant under the gauge transformation in eqns (11.31) and (11.32). When a particle hops around an elementary plaquette denoted by \square , it undergoes a unitary transformation

$$|\psi\rangle \rightarrow W(\square)|\psi\rangle, \quad (11.33)$$

where

$$W(\square) = e^{i\phi_{12}(\square)} e^{i\phi_{23}(\square)} e^{i\phi_{34}(\square)} e^{i\phi_{41}(\square)}, \quad (11.34)$$

and where the plaquette’s vertices are situated at neighboring sites $j = 1, 2, 3, 4$, and enumerated in an oriented manner. This quantity, called the Wilson loop, is therefore associated to the plaquette \square , and is defined unambiguously on the lattice by orienting each plaquette in the same way (say clockwise). Obviously, the Wilson loops are invariant under the local gauge transformations and consequently the set of Wilson loops $\{W(\square)\}$

determines the physics completely. Alternatively, the physics is governed by the cumulative phases

$$\Phi(\square) = \phi_{12}(\square) + \phi_{23}(\square) + \phi_{34}(\square) + \phi_{41}(\square), \quad (11.35)$$

that express the Aharonov–Bohm effect (i.e. the phase acquired by the wave function of a charged particle along a closed contour as a consequence of the magnetic flux) : $\Phi(\square)$ is also a gauge-invariant quantity and represents the magnetic flux through the plaquette \square in atomic units. Given a set of Wilson loops $\{W(\square)\}$ (or fluxes $\{\Phi(\square)\}$) on the lattice, there exists a choice of phases $\{\phi_{ij}(\square)\}$ such that eqn (11.34) is satisfied globally, i.e. for all loops \square . In fact, there are infinitely many families of local phases $\{\phi_{ij}(\square)\}$ that lead to the same physics determined by the given set of Wilson loops, $\{W(\square)\}$. The latter statement is always valid when open boundary conditions are applied to the lattice. In the case of closed surfaces (such as lattices with periodic boundary conditions, i.e. lattices forming a torus or symplexes lying on the surface of a sphere) there is an additional physical requirement: the total magnetic flux through the closed surface must be zero (in order to verify the Maxwell equation $\nabla \cdot \mathbf{B} = 0$) unless the system presents magnetic monopoles. For rigorous proofs of these statements see for instance Lieb (1992), Lieb (1994), and Macris and Nachtergale (1996).

11.3.5 Gauge invariance in non-Abelian classical external gauge fields: the lattice case

Non-Abelian gauge structures can also be found in non-relativistic quantum mechanics. As pointed out by Wilczek and Zee (1984) they arise when the wave functions have several components. The Hubbard Hamiltonian that describes particles evolving on a lattice and subjected to a $U(N)$ gauge field reads:

$$\hat{H} = -t \sum_{\langle i,j \rangle} \left[\hat{b}_i^\dagger U_{ij} \hat{b}_j + h.c. \right] + \frac{V}{2} \sum_i \hat{b}_i^\dagger (\hat{b}_i^\dagger \hat{b}_i) \hat{b}_i, \quad (11.36)$$

where \hat{b}_i , \hat{b}_i^\dagger are the N -component annihilation and creation operators of particles on site i , U_{ij} are the unitary operators associated with the tunneling from the nearest-neighboring sites $j \rightarrow i$, and V is the coupling constant for the on-site interactions.

The on-site gauge transformation is now defined as a $U(N)$ transformation acting on the field operators,

$$\hat{b}_j \rightarrow \hat{b}'_j = T_j \hat{b}_j, \quad (11.37)$$

where $T^\dagger T = TT^\dagger = \hat{1}$. The transformed Hamiltonian involves new tunneling operators given by

$$U_{ij} \rightarrow \hat{T}_i^\dagger U_{ij} \hat{T}_j. \quad (11.38)$$

The Hamiltonian's spectrum is left invariant under the gauge transformation of eqns (11.37) and (11.38). Now when a particle hops around an elementary plaquette it undergoes a

unitary transformation

$$|\psi\rangle \rightarrow U(\square)|\psi\rangle, \quad (11.39)$$

where

$$U(\square) = U_{12}(\square)U_{23}(\square)U_{34}(\square)U_{41}(\square). \quad (11.40)$$

This loop operator is associated with the plaquette \square and is defined unambiguously on the lattice by orienting each plaquette in the same way and also by choosing the first link. Physically, the loop operator U expresses the non-Abelian Aharonov–Bohm effect (Shapere and Wilczek, 1989; Bohm *et al.*, 2002) that takes place in the system. This important effect accounts for the non-Abelian character of the system and is therefore observable when the loop operator cannot be reduced to a phase factor, $U = e^{i\theta}\hat{1}$. In the latter trivial case, the non-Abelian Aharonov–Bohm effect cannot take place and the system behaves as an Abelian one. Under a gauge transformation, the loop operator is modified according to

$$U \rightarrow T^\dagger UT, \quad (11.41)$$

and therefore this operator is not a gauge-invariant quantity. One can then consider, however, the trace of the loop operator,

$$W(\square) = \text{Tr}(U_{12}(\square)U_{23}(\square)U_{34}(\square)U_{41}(\square)), \quad (11.42)$$

which indeed defines the gauge-invariant quantity, and which is simply called a Wilson loop. Again, the set of Wilson loops $\{W(\square)\}$ determines the physics of the non-Abelian system.

Given a set of Wilson loops $\{W(\square)\}$ on the lattice (with open boundary conditions), there exists a choice of tunneling operators $\{U_{ij}(\square)\}$, such that eqn (11.42) is satisfied globally, i.e. for all loops \square . Moreover, there are infinitely many families of tunneling operators $\{U_{ij}(\square)\}$ that lead to the same physics determined by the given set of Wilson loops $\{W(\square)\}$. The statement above has to be modified if the lattice is spanned on a closed surface, etc.

11.3.6 Genuine non-Abelian field configurations

It is now easy to understand which field configurations are genuinely non-Abelian and which are not. Let us consider the case of a 2D lattice subjected to a $U(2)$ gauge potential. In the case in which all the loop operators are trivial and given by complex phase factors, $U(\square) = e^{i\theta(\square)}\hat{1}$, we can gauge out all the unitary tunneling operators U_{ij} and replace them by simple phase factors. The system then reduces to an Abelian system. For simplicity, let us consider the case in which the loop operators are all equal to the same phase, namely

$U(\square) = e^{i\theta}\hat{1}$ for all the loops \square . We start with the first plaquette and consider the local gauge transformation induced by the following unitary operators:

$$T_1^\dagger = \hat{1}, \quad (11.43)$$

$$T_2^\dagger = U_{12}, \quad (11.44)$$

$$T_3^\dagger = U_{12}U_{23}, \quad (11.45)$$

$$T_4^\dagger = U_{12}U_{23}U_{34}. \quad (11.46)$$

The resulting new tunneling operators are trivialized according to

$$U_{12}^{\text{new}} = T_1^\dagger U_{12} T_2 = \hat{1}, \quad (11.47)$$

$$U_{23}^{\text{new}} = T_2^\dagger U_{23} T_3 = \hat{1}, \quad (11.48)$$

$$U_{34}^{\text{new}} = T_3^\dagger U_{34} T_4 = \hat{1}, \quad (11.49)$$

$$U_{41}^{\text{new}} = T_4^\dagger U_{41} T_1 = U(\square) = e^{i\theta}\hat{1}. \quad (11.50)$$

This trivialization procedure can be extended to the plaquettes that have a common bond with the first one, and so on. Note that if one plaquette \square_j is characterized by a non-trivial loop operator, $U(\square_j) \neq e^{i\theta}\hat{1}$, such a gauging out is impossible!

From the above considerations, it follows that when $U = \pm e^{i2\pi\Phi}\hat{1}$, we can gauge out the unitary tunneling operators and reduce our problem to two independent Schrödinger equations for the two ‘flavor’ components. If $U = e^{i2\pi\Phi}\hat{1}$, each ‘flavor’ component evolves in a square lattice subjected to an Abelian magnetic field, with flux Φ . When $U = -e^{i2\pi\Phi}\hat{1}$, the system describes particles evolving on the π -flux lattice and subjected to an Abelian magnetic field, with flux $\Phi + \pi$. On the other hand, when the loop operator is non-trivial, $U(\square) \neq e^{i\theta}\hat{1}$, no such gauging out is possible and the system cannot be expressed as two independent Abelian models. Moreover, in this case the system exhibits true non-Abelian effects such as the aforementioned non-Abelian Aharonov–Bohm effect. In that case, the system can be used for non-Abelian interferometry, in which the final effect of an obstacle (a unitary operator acting on the particle’s wave function) depends not only on the nature of the obstacle but also on the particle’s path and obstacle’s location.

For the examples considered in this book, the Abelian and non-Abelian cases are distinguished through a very simple criterion illustrated for a specific choice of $SU(2)$ gauge fields (discussed in Section 11.6) in Figure 11.4: if the Wilson loop’s magnitude equals two, $|W| = |\text{Tr } U| = 2$, then the loop operator is trivial, namely $U = e^{i\theta}\hat{1}$. In this case, the system reduces to two independent Abelian systems. In order to apply this criterion, we need to demonstrate the following lemma:

Lemma: Given a 2×2 unitary matrix $U \in U(2)$, then if $|\text{Tr } U| = 2 \iff U = e^{i\theta}\hat{1}$.

Proof:

(\Leftarrow) If $U = e^{i\theta}\hat{1}$, then of course $|\text{tr } U| = |e^{i\theta}2| = 2$.

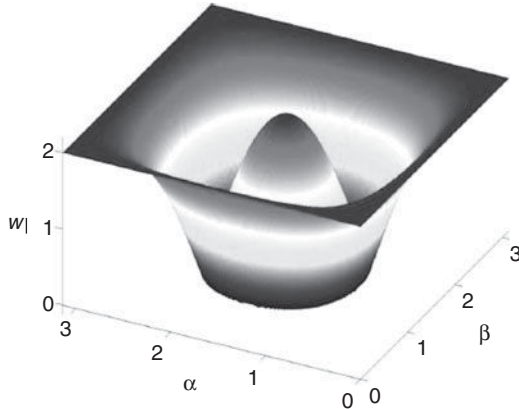


Figure 11.4 Wilson loop magnitude as a function of the parameters characterizing the gauge fields $|W| = |W(\Phi_\alpha, \Phi_\beta)|$. The Abelian regime is determined by the criterion $|W| = 2$. From Goldman *et al.* (2009b).

(\Rightarrow) We now show that if $|\text{tr}U| = 2$ then U must have the trivial form $U = e^{i\theta}\hat{1}$. Since $U \in U(2)$, its eigenvalues $\lambda_1 = e^{i\theta_1}$ and $\lambda_2 = e^{i\theta_2}$ lie on the unit circle and we have that

$$|\text{Tr}U| = |\text{Tr } T^\dagger UT| = |\lambda_1 + \lambda_2| = |e^{i\theta_1} + e^{i\theta_2}|, \quad (11.51)$$

$$= \sqrt{(\cos \theta_1 + \cos \theta_2)^2 + (\sin \theta_1 + \sin \theta_2)^2}, \quad (11.52)$$

$$= \sqrt{2(1 + \cos(\theta_1 - \theta_2))}, \quad (11.53)$$

where the unitary matrix $T \in U(2)$ diagonalizes the matrix U . Therefore the hypothesis $|\text{Tr}U| = 2$ is satisfied if

$$\theta_1 - \theta_2 = 2\pi n, \quad (11.54)$$

where n is an integer. Under this condition, $T^\dagger UT = \text{diag}(\lambda_1) = e^{i\theta}\hat{1}$, where $e^{i\theta} = \lambda_1 = \lambda_2$. Eventually this shows that $U = e^{i\theta}\hat{1}$, since $TT^\dagger = T^\dagger T = \hat{1}$. \square

11.4. Lattice gases in ‘artificial’ Abelian gauge fields

In order to create the effect of a constant magnetic field in a 2D square lattice of periodicity a , it is necessary to control the phases of the hopping matrix elements. The Schrödinger equation of a single particle in a 2D lattice subjected to an external gauge potential is analysed in the famous paper of Hofstadter (1976). Using Luttinger’s theorem (Luttinger, 1951), which states that one can solve the problem of a periodic system under an external

magnetic field $\hbar\mathbf{k} \rightarrow -i\hbar\nabla - e\mathbf{A}$ in terms of the Bloch functions of the unperturbed (without external field) systems. The Hofstadter equation reads:

$$\begin{aligned} E\psi(x, y) = & -t_a[e^{-i\frac{ea}{\hbar c}A_x}\psi(x+a, y) + e^{i\frac{ea}{\hbar c}A_x}\psi(x-a, y)] \\ & - t_b[e^{-i\frac{ea}{\hbar c}A_y}\psi(x, y+a) + e^{i\frac{ea}{\hbar c}A_y}\psi(x, y-a)], \end{aligned} \quad (11.55)$$

where $\psi(x, y)$ is the wave function, \mathbf{A} is the vector potential, t_a (resp. t_b) is the tunneling amplitude in the x (resp. y) direction, and a is the lattice spacing. The choice of \mathbf{A} determines the magnetic field \mathbf{B} , which in turn determines the behavior of the system. For a uniform field in the z direction $\mathbf{B} = Be_z$, one may choose the potential $\mathbf{A} = (0, Bx, 0)$ and tunnelings in the y -direction acquire phases. This makes the problem effectively 1D and by using the ansatz $\psi(ma, na) = e^{i\nu n}g(m)$, where $x = ma$, $y = na$, $\varepsilon = -E/t$, and $\alpha = Bea^2/ch$, eqn (11.55) can be transformed into Harper’s equation (Harper, 1955):

$$g(m+1) - g(m-1) + 2\cos(2\pi m\alpha - \nu)g(m) = \varepsilon g(m) \quad (11.56)$$

Note that $\alpha = Bea^2/ch$ is a crucial parameter that represents the number of magnetic flux quanta per unit cell. Similarly to the case of our discussion of the Anderson localization (see Section 9.2), it is useful to rewrite this equation in the form of recurrence

$$\begin{pmatrix} g_{m+1} \\ g_m \end{pmatrix} = M_m \begin{pmatrix} g_m \\ g_{m-1} \end{pmatrix} = \begin{pmatrix} \varepsilon - 2\cos(2\pi m\alpha - \nu) & -1 \\ 1 & 0 \end{pmatrix} \begin{pmatrix} g_m \\ g_{m-1} \end{pmatrix}. \quad (11.57)$$

Note that the 2×2 matrices M_m are unimodular, i.e. have determinants equal to one. Note also that when $\alpha = p/q$ is rational, with p, q being relatively prime integers, the problem becomes q -periodic. Starting with say, $m = 1$ and applying the recurrence to the left, we obtain

$$\begin{pmatrix} g_{m+1} \\ g_m \end{pmatrix} = M_m M_{m-1} \dots M_2 M_1 \begin{pmatrix} g_1 \\ g_0 \end{pmatrix}. \quad (11.58)$$

It is useful then to define the product of q matrices

$$Q = M_q M_{q-1} \dots M_2 M_1, \quad (11.59)$$

and transfer, so to speak, the eigenvalue problem to Q . For the periodic problem we expect the solutions to be delocalized but bounded. Since $\det Q = 1$, the product of eigenvalues of Q is one. In order to avoid the exponential growth of solutions, both eigenvalues must then have a unit absolute value, and one is the complex conjugate of another. That, in turn, is obviously equivalent to the condition

$$|\text{Tr } Q(\varepsilon, \nu)| \leq 2. \quad (11.60)$$

From the cyclic property of the trace one immediately obtains the result that

$$\mathrm{Tr}Q(\varepsilon, \nu) = \mathrm{Tr} \prod_{m=1}^q M_m = \mathrm{Tr} \prod_{m=m_0}^{(q+m_0)\bmod q} M_m.$$

This implies that we can always shift ν by $2\pi\alpha m_0$ without changing $\mathrm{Tr}Q(\varepsilon, \nu)$, i.e. the latter trace is periodic in ν with a period $2\pi/q$. This means that it is composed of the Fourier components $\pm kq\nu$ with k an integer. But, $\mathrm{Tr}Q(\varepsilon, \nu)$ can only contain $k = -1, 0, 1$ Fourier components, and, moreover, $k = \pm 1$ components cannot depend on ε (they can arise only from products of q terms of the form $2 \cos(2\pi m\alpha - \nu)$, or better to say $\exp(\pm 2\pi im\alpha \mp i\nu)$ in the definition of Q). An important implication is thus

$$\mathrm{Tr}Q(\varepsilon, \nu) = \mathrm{Tr}Q(\varepsilon) + 2f(\nu), \quad (11.61)$$

where for compactness of notation we have introduced $Q(\varepsilon) = Q(\varepsilon, 1/2q)$ and $f(\nu) = \cos(2\pi q\nu)$, which is a periodic function with a period $2\pi/q$ and a unit amplitude. In order to determine the spectrum we need to ask which values of ε are physical, i.e. admit physical solutions that may oscillate but cannot grow exponentially. Since $-2 \leq 2f(\nu) \leq 2$, eqn 11.60 can be rewritten as:

$$|\mathrm{Tr}Q(\varepsilon, \nu)| \leq 4. \quad (11.62)$$

Since the trace of $Q(\varepsilon)$ is always a polynomial of degree q of ε , the above condition, actually determining the spectrum, is generically fulfilled in q distinct regions of the ε axis. In other words, when $\alpha = p/q$, the Bloch band always breaks up precisely into q distinct energy bands. This is the first step toward understanding the fractal, yet symmetric, form of the spectrum.

Indeed, while for $\alpha = 0$ there is a single band, for rational values of the magnetic flux $\alpha = \frac{ea^2B}{hc}$ per elementary plaquette, i.e. when the eigenvalue problem becomes periodic, the bands form the famous Hofstadter butterfly (see Figure 11.5). Note that in order to consider this spectrum, one has to assume a strictly non-zero value of α , i.e. magnetic fields $B \sim 1/a^2$ which, in the continuum limit $a \rightarrow 0$, become ultra-intense.

The physical properties of ultracold gases in ‘artificial’ magnetic fields are, as expected, extremely rich. For instance, one may load the lattice with a cold BEC, or add disorder, and observe how the single-atom properties of the spectrum change in weakly interacting or weakly disordered systems. Jaksch and Zoller (2003) were the first to suggest such ‘artificial’ magnetic field effects in lattice gases. The modifications of the butterfly due to interactions, disorder, or both can be measured as proposed in Jaksch and Zoller (2003). We discuss in more detail the generalization of their proposal to the case of non-Abelian fields in the next section.

11.4.1 ‘Artificial electromagnetism’ for neutral atoms

There are several alternative ways to achieve ‘artificial electromagnetism’ for neutral atoms, each of which leads to its own plethora of physical phenomena. We list here only a few of the early proposals.

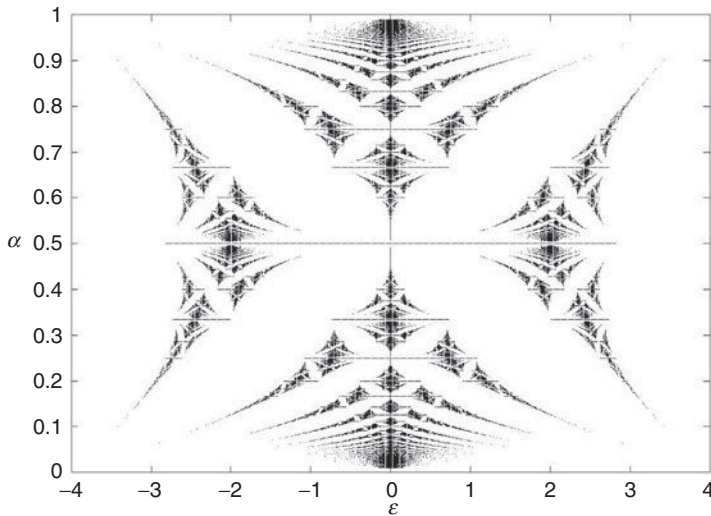


Figure 11.5 The famous Hofstadter butterfly: energy bands of a 2D periodic system under an external magnetic field plotted for rational values of the magnetic flux α . Eigenenergies in natural units plotted versus magnetic flux per plaquette with $\alpha_i = p_i/q_i, \in [0, , 1]$ with $q \leq 100$. The lowest Bloch band splits into sub-bands and forms a fractal for a set of all of them.

- Artificial magnetic fields for atoms with three internal states in three different lattices were proposed in Mueller (2004), generalizing the method of Jaksch and Zoller (2003). In contrast to the Jaksch–Zoller approach (discussed in the next section), this approach does not use lattice tilting, but at the cost of a more complicated laser configuration. Since the fields are ‘artificial’ they do not even need to fulfill the Maxwell equations and can thus lead to physical realizations of otherwise unphysical effects. Mueller has proposed, for instance, time-dependent realizations of a hopping-matrix element on a 1D ring that leads to an ‘Escher staircase’: a single particle in such a ring undergoes acceleration, limited only by the Umklapp process: when the de Broglie wavelength of the particle becomes equal to the lattice constant, the matter wave is Bragg reflected off the lattice and reverses its direction.
- Sørensen *et al.* (2005) have proposed another method that also employs time-dependent hopping-matrix elements along with a large oscillating quadrupolar potential. These authors performed exact diagonalizations of the resulting Bose–Hubbard model in the limit of hard-core bosons for N up to 5. In the limit of small α and low densities, the continuum limit may be applied and the model reduces to a system of bosons in a magnetic field with contact interactions. For filling factor $\frac{1}{2}$ (total angular momentum $L = 2N$), the Laughlin wave function is then the exact ground state (Haldane, 1983a; Haldane, 1983b). The numerical calculations show that the exact ground state remains very similar to the Laughlin state for $\alpha < 0.3$. Preparation of such a Laughlin state in the lattice may be achieved by first creating a Mott state with one atom per site in a superlattice with the larger period. In this way low density is achieved while the atoms

are quenched and not affected by the ‘magnetic’ field. By turning off the superlattice, the Mott state melts into a Laughlin liquid.

- Palmer and Jaksch studied high field FQHE in optical lattices. They considered the value of $\alpha \simeq \alpha_c = l/n$, where l, n are small integers, and derived the corresponding effective Hamiltonian in the continuum limit, which for $\alpha_c = \frac{1}{2}$ reduces to a model similar to a bilayer FQHE system (Ezawa, 2000). The corresponding ground state in homogeneous systems (in the absence of trapping potential) is the so-called 221-state, constructed as the Laughlin state for $\nu = \frac{1}{2}$ for particles from the same layer, and for $\nu = 1$ for particles from different layers. Denoting the coordinates as z_i, s_j , the wave function for $N = 2M$ atoms is

$$\Psi(z_1, \dots, z_M, s_1, \dots, s_M) \propto \prod_{i \neq j} (z_i - z_j)^2 \prod_{i \neq j} (s_i - s_j)^2 \prod_{i,j} (z_i - s_j). \quad (11.63)$$

The angular momentum of this state is $L = 2M(M - 1) + M^2$, and the filling factor $\nu = \frac{2}{3}$. Interestingly, the Hall current in such states in the presence of the trap might exhibit unexpected sign changes.

- Burkov and Demler (2006) have recently studied ‘vortices’ in a dice lattice induced by ‘magnetic field’. They have shown the fascinating possibility of the creation of a vortex-Peierls state (a bosonic analog of valence-bond solids). In addition, rotating optical lattices have been considered by several authors: Polini *et al.* (2004, 2005) proposed a realization of a fully frustrated XY model with cold atoms in optical lattices, while Bhat *et al.* (2006) studied ground states of various symmetries for rotating 4×4 lattices.

11.5. Lattice gases in ‘artificial’ non-Abelian gauge fields

The straightforward extension to a $U(2)$ non-Abelian gauge field in a 2D lattice, as specifically considered in Osterloh *et al.* (2005), leads to the $U(2)$ generalization of the Harper equation (11.56):

$$\sigma_x g(m+1) - \sigma_x g(m-1) + 2 \cos(2\pi m\alpha - \nu) g(m) = \varepsilon g(m), \quad (11.64)$$

where $g(m)$ is the two-component wave function obtained by using the ansatz $\psi(ma, na) = e^{i\nu n} g(m)$, with $x = ma$, $y = na$, and $\varepsilon = -E/t$; σ_x is the Pauli matrix, and the ‘magnetic flux’ matrix $\alpha = \text{diag}[\alpha_1, \alpha_2]$. The above equation was derived assuming that:

- tunneling in the x direction is laser assisted but spatially constant and governed by $U_x = \sigma_x$
- tunneling in the y direction depends on the x (m) variable and is governed by $U_y(m) = \exp(2\pi i m \text{diag}[\alpha_1, \alpha_2])$.

To obtain the generalized Harper equation, one needs to perform the Fourier transform with respect to y , or in other words make a plane-wave ansatz with quasimomentum ν

in the y direction. The generalized Harper equation (11.64) is far more complex than the corresponding Abelian Harper one. We can still consider a recurrence equation, but now it is a four-component equation,

$$\begin{pmatrix} g_{m+1} \\ g_m \\ g_m \\ g_{m-1} \end{pmatrix} = M_m \begin{pmatrix} g_m \\ g_{m-1} \end{pmatrix} = \begin{pmatrix} \sigma_x[\varepsilon - 2\cos(2\pi m\alpha - \nu)] & -1 \\ 1 & 0 \end{pmatrix} \begin{pmatrix} g_m \\ g_{m-1} \end{pmatrix}. \quad (11.65)$$

For the particular choice of non-Abelian potentials, it is useful to consider a double iteration of the recurrence (11.65). One then obtains

$$\begin{pmatrix} g_{m+2} \\ g_{m+1} \\ g_m \\ g_{m-1} \end{pmatrix} = \begin{pmatrix} \sigma_x f(m+1) & -1 \\ 1 & 0 \end{pmatrix} \begin{pmatrix} \sigma_x f(m) & -1 \\ 1 & 0 \end{pmatrix} \begin{pmatrix} g_m \\ g_{m-1} \end{pmatrix}, \quad (11.66)$$

where $f(m) = [\varepsilon - 2\cos(2\pi(m)\alpha - \nu)]$. Readers will easily convince themselves that the resulting 4×4 equation has a block structure and reduces to two two-uncoupled equations. Still, the only straightforward method to analyse them is numerical. Given each $\alpha_i = p_i/q_i$ rational, the problem is now Q -periodic (where Q equals the smallest common multiple of q_1 and q_2). The spectrum shows a band structure and is bounded by two hyperplanes (Figure 11.6). It exhibits a very complex arrangement of holes of finite measure and various sizes, which we call the Hofstadter ‘moth’. Although a rigorous proof cannot be provided, the ‘moth’ is reminiscent of a fractal structure. This fractal structure should be very sensitive to any sort of perturbation because of the finite size of the system, external trapping potential etc.) on very small scales. But, since the holes are true 3D objects with finite volume, on a larger scale the spectrum will be more robust to perturbations than the Hofstadter ‘butterfly’. Very recently, the same gauge fields were used to investigate metal–insulator

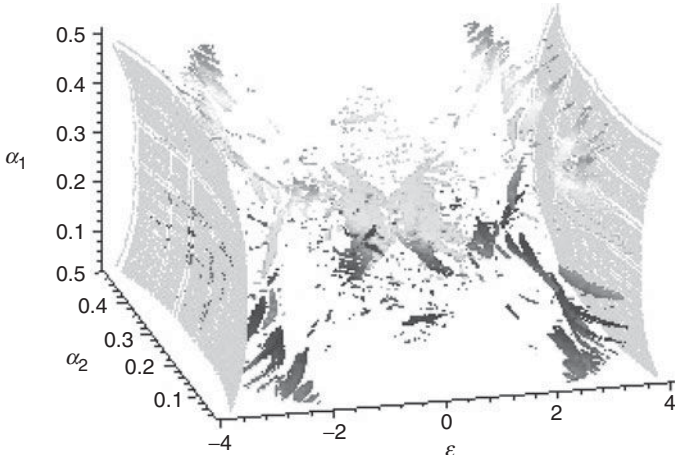


Figure 11.6 The Hofstadter ‘moth’ spectrum, i.e. the energy spectrum of a 2D periodic system under an external non-Abelian gauge field. Forbidden eigenenergies ε are plotted versus $\alpha_i = p_i/q_i, \in [0, = 0.5]$ ($i = 1, 2$), where $q_i \leq 41$ and $\alpha_1 \neq \alpha_2$. From Osterloh *et al.* (2005).

transitions for cold atoms (Satija *et al.*, 2006) and the integer quantum Hall effect (Goldman and Gaspard, 2007).

The method of Osterloh *et al.* (2005) can easily be generalized to external gauge potentials of the form

$$A_i(x, y) = a_i + b_i(x/a) + c_i(y/a), \quad (11.67)$$

with $i = x, y$ and a_i, b_i, c_i being essentially arbitrary $n \times n$ matrices. Furthermore, local disorder may be introduced in a controlled way allowing for small fluctuations of the matrices a_i, b_i, c_i . In particular, disorder can be made annealed, i.e. changing on a timescale comparable with the relevant timescales of the system and thus mimicking thermal fluctuations. It can be of significant amplitude provided it does not drive the assisting laser system out of resonance. Moreover, more complicated spatial dependence, e.g. piecewise linearity of \mathbf{A} , is feasible using static electric fields, laser-induced potentials, etc. Additional lasers may introduce local and, in general, time-dependent unitaries. Such transformations would generate arbitrary local temporal components of the gauge potential $A_0(x, y)$. Although for Yang–Mills fields in (2+1)D this component may be gauged out by adapting the Weyl or strict temporal gauge (Schulz, 2000), the corresponding gauge transformations may introduce more complex spatial and temporal forms in the remaining two components of \mathbf{A} .

In the limit of weak fields, the continuum limit may be used, and the single-particle Hamiltonian reduces to that of a particle in the gauge field corresponding to the above potential:

$$H = \frac{1}{2m} [(p_x - A_x(x, y))^2 + (p_y - A_y(x, y))^2]. \quad (11.68)$$

The non-Abelian gauge fields and Hofstadter ‘moth’ are interesting not only for fundamental reasons: they also offer a fascinating possibility of observing the non-Abelian Aharonov–Bohm effect and realizing non-Abelian atom interferometry and non-Abelian non-linear atom optics (Osterloh *et al.*, 2005; Jacob and Santos, 2006). Phase shifts in non-Abelian interferometers will correspond to matrices and will depend not only on the perturbations of the trajectories of the interfering particles but also the specific locations of these perturbations. Other effects include generation of magnetic monopoles (Pietilä and Möttönen, 2009), non-Abelian atom optics (Juzeliūnas *et al.*, 2008a), quasi-relativistic effects (Juzeliūnas *et al.*, 2008b), or even the modification of metal–insulator transitions (Satija *et al.*, 2006).

11.6. Integer quantum Hall effect and emergence of Dirac fermions

Low-energy excitations of fermionic lattice systems are usually governed by the non-relativistic Schrödinger equation. However, this description must be profoundly altered in the vicinity of Dirac points, where the energy bands display conical singularities and quasiparticles become massless relativistic fermions. Such remarkable behavior can be induced, for example, by a honeycomb geometry (Semenoff, 1984; Novoselov *et al.*, 2005;

Zhang *et al.*, 2005; Zhu *et al.*, 2007; Castro Neto *et al.*, 2009) or by an additional, either uniform (Wen, 2004) or staggered magnetic field (Lim *et al.*, 2008; Hou *et al.*, 2009).

The natural playground for the emergence of Dirac fermions is, however, provided by multi-component fermionic atoms subjected to artificial non-Abelian gauge fields. In what follows, we describe how the physical properties of massless relativistic fermions are completely characterized by the non-Abelian features of the external gauge fields. Furthermore, the anisotropy of the underlying Minkowski space-time can be controlled externally, producing an anomalous quantum Hall effect characterized by an squeezed Landau vacuum. We follow closely our work as presented in Goldman *et al.* (2009*b*).

11.6.1 Lattice gauge fields with constant Wilson loops

We consider a system of two-component (two-color) fermionic atoms trapped in an optical square lattice with sites at $\mathbf{r} = (n, m)a$, where a is the lattice spacing and $n, m \in \mathbb{Z}$. In the non-interacting limit, which can be obtained by means of Feshbach resonances, fermions freely hop between neighboring sites. The addition of an external gauge potential \mathbf{A} modifies the hopping Hamiltonian according to the Peierls substitution

$$\hat{H} = -t \sum_{\langle \mathbf{r}, \mathbf{r}' \rangle} \sum_{\tau \tau'} \hat{c}_{\tau'}^{\dagger}(\mathbf{r}') e^{-i \frac{\mathbf{r}'}{\mathbf{r}} \cdot \mathbf{A} \cdot \mathbf{d}\mathbf{l}} \hat{c}_{\tau}(\mathbf{r}) + \text{h.c.}, \quad (11.69)$$

where t is the hopping amplitude and $\hat{c}_{\tau}(\mathbf{r})$ is the fermionic field operator in color component $\tau = 1, 2$ (we have set $\hbar = e = 1$). Our set-up features an external gauge potential with both commutative and non-commutative components $\mathbf{A} = \frac{B_0}{2}(-y, x) + a(B_{\alpha}\sigma_y, B_{\beta}\sigma_x)$, where $B_0, B_{\alpha}, B_{\beta}$ are controllable parameters and $\sigma_{x,y}$ are Pauli matrices. Accordingly the hoppings are accompanied by non-trivial unitary operators,

$$U_x(m) = e^{-i\pi\Phi m} e^{i\Phi_{\alpha}\sigma_y} \quad (11.70)$$

$$U_y(n) = e^{i\pi\Phi n} e^{i\Phi_{\beta}\sigma_x},$$

where $\Phi = B_0 a^2$ is the Abelian magnetic flux and $\Phi_{\alpha,\beta} = B_{\alpha,\beta} a^2$ are the non-Abelian fluxes (see Figure 11.7(a)).

Let us note that the gauge fields considered here provide non-Abelian analogs of homogeneous magnetic fields since they are characterized by constant Wilson loops. Indeed, atoms hopping around an elementary plaquette undergo a unitary transformation $U = U_x(m)U_y(n+1)U_x^{\dagger}(m+1)U_y^{\dagger}(n)$, explicitly given by

$$U = e^{i2\pi\Phi} (c_1 \mathbb{I} + c_2 \sigma_z + c_3 \sigma_y + c_4 \sigma_x), \quad (11.71)$$

where the constants $\{c_j\}$ are given by:

$$c_1 = \cos^2 \Phi_{\alpha} + \cos 2\Phi_{\beta} \sin^2 \Phi_{\alpha}, \quad (11.72)$$

$$c_2 = \frac{i}{2} \sin 2\Phi_{\alpha} \sin 2\Phi_{\beta}, \quad (11.73)$$

$$c_3 = i \sin 2\Phi_{\alpha} \sin^2 \Phi_{\beta}, \quad (11.74)$$

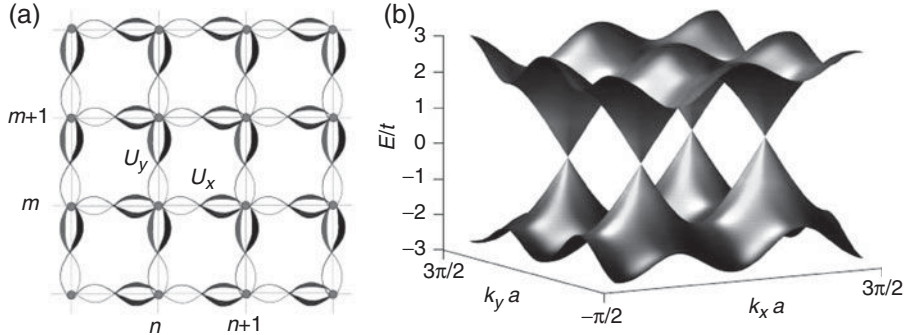


Figure 11.7 (a) Square lattice subjected to a non-Abelian gauge potential. This external field induces state-dependent hoppings described by the $U(2)$ operators U_x and U_y . (b) Energy bands close to the π -flux regime ($\Phi_\alpha = \frac{\pi}{2} + 0.1$, $\Phi_\beta = \frac{\pi}{2} - 0.1$), with vanishing Abelian flux $\Phi = 0$. The bands touch at four Dirac points inside the first Brillouin zone, where the energy scales linearly with momenta $E \sim k$.

$$c_4 = -i \sin^2 \Phi_\alpha \sin 2\Phi_\beta. \quad (11.75)$$

For specific values of $\Phi_{\alpha,\beta}$, the loop matrix reduces to a phase factor and reproduces the Abelian π -flux ($\Phi_\alpha = \Phi_\beta = \frac{\pi}{2}$) or Hofstadter ($\Phi_\alpha = \Phi_\beta = 0$) models (Hofstadter, 1976; Wen, 2004). However, in general cases it is a non-trivial $U(2)$ operator, exhibiting non-Abelian properties such as the non-Abelian Aharonov–Bohm effect (see Figure 11.4). As already shown in Lemma 1, the gauge-invariant Wilson loop $W = \text{Tr } U$ provides a clear distinction between the Abelian ($|W| = 2$) and non-Abelian ($|W| < 2$) regimes. The Wilson loop is homogeneous and the corresponding spectrum exhibits well-developed gaps (Goldman *et al.*, 2009*b*) between the bands.

11.6.2 Emergence of Dirac fermions

In order to isolate non-Abelian effects, we first consider the regime of vanishing Abelian flux $\Phi = 0$. The Hamiltonian is diagonalized in momentum space and the fermion gas becomes a collection of non-interacting quasiparticles whose energies are shown in Figure 11.7(b). Close to the marginally Abelian regime ($\Phi_\alpha, \Phi_\beta \approx \frac{\pi}{2}$), the spectrum develops four independent conical singularities $\mathbf{k}_D \in \{(0,0), (\frac{\pi}{a},0), (0,\frac{\pi}{a}), (\frac{\pi}{a},\frac{\pi}{a})\} \in \text{BZ}$ (the Brillouin zone), which correspond to massless relativistic excitations at half filling. Around these points $\mathbf{p} = \mathbf{k} - \mathbf{k}_D$, the low-energy properties are accurately described by a Dirac Hamiltonian

$$H_{\text{eff}} = \sum_{\mathbf{p}} \Psi_{\mathbf{p}}^\dagger H_D \Psi_{\mathbf{p}}, \quad H_D = c_x \alpha_x p_x + c_y \alpha_y p_y, \quad (11.76)$$

where $\Psi_{\mathbf{p}} = (c_{1\mathbf{p}}, c_{2\mathbf{p}})$ is the relativistic spinor, the Dirac matrices α_x, α_y fulfill $\{\alpha_j, \alpha_k\} = 2\delta_{jk}$ (e.g. around $\mathbf{k}_D = (0, \pi/a)$, $\alpha_x = \sigma_y$, and $\alpha_y = \sigma_x$), and $c_x = 2at \sin \Phi_\alpha$ and $c_y = 2at \sin \Phi_\beta$ represent the effective speed of light. The control over the non-Abelian fluxes $\Phi_{\alpha,\beta}$

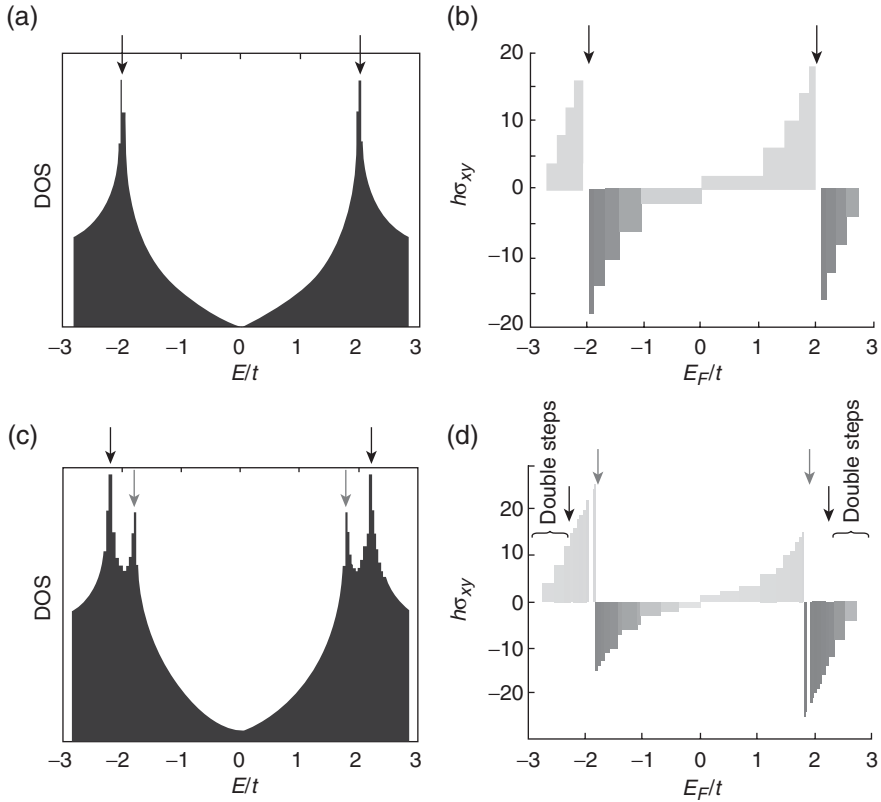


Figure 11.8 (a) Density of states in the π -flux regime $\Phi_\alpha = \Phi_\beta = \frac{\pi}{2}$ when $\Phi = 0$. (b) Hall conductivity in units of h^{-1} as a function of the Fermi energy in the same regime for $\Phi = \frac{1}{41}$. Black arrows indicate the Van Hove singularities (VHSs). (c) Density of states close to the π -flux regime $\Phi_\alpha = \frac{\pi}{2} + 0.1$ and $\Phi_\beta = \frac{\pi}{2} - 0.1$ when $\Phi = 0$. (d) Hall conductivity $h\sigma_{xy} = h\sigma_{xy}(E_F)$ in the same regime as (c) for $\Phi = \frac{1}{41}$. Dark and light arrows respectively designate the VHSs $E_{\text{red}}^{\text{VHS}}$ and $E_{\text{green}}^{\text{VHS}}$ (cf. Eq. (11.79)).

offers the exotic opportunity to modify the structure of the underlying Minkowski space-time, reaching anisotropic situations where $c_x \neq c_y$. Hence, non-Abelian optical lattices provide a quantum optical analog of relativistic quantum electrodynamics (QED), where the emerging fermions and the properties of the corresponding space-time rely on the non-Abelian features of the external fields. Furthermore, it is also possible to observe a transition between relativistic and non-relativistic dispersion relations as the energy is increased. This abrupt change of the quasiparticle nature is revealed by van Hove singularities (VHSs) in the density of states, as shown in Figure 11.8(a)–(c).

11.6.3 Transport and the integer quantum Hall effect

The transport properties of 2D Fermi gases subjected to external gauge fields are characterized by the optical-lattice analog of the well-known quantum Hall effect (Stone, 1992).

In this context, the transverse Hall conductivity measures the response of the system to a static force, e.g. a lattice acceleration, and takes on quantized values $\sigma_{xy} = \frac{\nu}{h}$, with $\nu \in \mathbb{Z}$, when the Fermi energy E_F lies in a gap (Goldman *et al.*, 2009b). Quite unexpectedly, the quantized conductivity of cold gases can be directly observed through density measurements (Umucalilar *et al.*, 2008).

Non-Abelian effects have dramatic consequences on the quantum Hall effect when an additional Abelian flux Φ is applied to the system. The quantized values of the transverse conductivity are calculated using second-order perturbation theory, i.e. calculating the linear response of the system to the applied voltage (force). Amazingly, the result is that the transverse conductivity is the sum of topological invariants associated with each energy band n , the so-called Chern numbers C_n (Kohmoto, 1985),

$$\sigma_{xy} = - \sum_{E_n < E_F} \frac{i}{2\pi h} \int_{\text{BZ}} \text{tr } \mathcal{F}(\psi_n) \mathbf{d}\mathbf{k}, \quad (11.77)$$

where $\mathcal{F}(\psi_n) = \langle \partial_{k_x} \psi_n | \partial_{k_y} \psi_n \rangle - \langle \partial_{k_y} \psi_n | \partial_{k_x} \psi_n \rangle$ is the Berry’s curvature of the band E_n . For a detailed pedagogical derivation of this formula we refer to the excellent book by Goldman (2009). The calculation of the Chern numbers is not an easy task; here they are computed numerically by discretizing the Brillouin zone (Fukui *et al.*, 2005). An LGT method allows determination of the Berry’s curvature

$$\begin{aligned} \mathcal{F}_{xy}(\mathbf{k}_l) &= \ln T_x(\mathbf{k}_l) T_y(\mathbf{k}_l + \hat{\mathbf{x}}) T_x(\mathbf{k}_l + \hat{\mathbf{y}})^{-1} T_y(\mathbf{k}_l)^{-1}, \\ T_\mu(\mathbf{k}_l) &= \langle \psi_n(\mathbf{k}_l) | \psi_n(\mathbf{k}_l + \hat{\mu}) \rangle, \end{aligned} \quad (11.78)$$

and subsequently the Chern number $C = \frac{i}{2\pi} \sum_l \mathcal{F}_{xy}(\mathbf{k}_l)$. The Chern number is an integer and has contributions from all bands below the gap.

Remarkably, the sequence of Hall plateaus is extremely sensitive to the values of the non-Abelian fluxes. In the Abelian regime, $\Phi_\alpha = \Phi_\beta = 0$, we observe that the Hall conductivity follows the usual IQHE $\sigma_{xy} = \frac{2\nu}{h}$, where the factor 2 is due to color-degeneracy. Conversely, in the π -flux regime ($\Phi_\alpha = \Phi_\beta = \frac{\pi}{2}$) illustrated in Figure 11.8(b), we obtain a completely different sequence of Hall plateaus where $\sigma_{xy} = \frac{4}{h}(\nu + \frac{1}{2})$ around $E_F = 0$, as recently observed in graphene (Zhang *et al.*, 2005). This sequence is characterized by sudden changes of sign across the VHS situated at $E = \pm 2$ and by unusual double steps, which can be traced back to the underlying low-energy relativistic excitations. As the gauge fluxes vary in the vicinity of the π -flux point ($\Phi_\alpha = \frac{\pi}{2} + \epsilon$ and $\Phi_\beta = \frac{\pi}{2} - \epsilon$), the system enters the non-Abelian regime and the Hall plateaus are modified (see Figure 11.8(d)). Indeed, most of the degeneracies induced by the Dirac points are lifted and the anomalous double steps around $E_F = 0$ are progressively destroyed. However, striking behavior occurs: as the non-Abelian fluxes are varied, the two VHSs originally situated at $E = \pm 2$ in the π -flux point are split into four

$$E_{\text{red}}^{\text{VHS}} = \pm 2(1 + \cos \Phi_\beta), \quad E_{\text{green}}^{\text{VHD}} = \pm 2(1 + \cos \Phi_\alpha), \quad (11.79)$$

as illustrated in Figure 11.8(c) for $\epsilon = 0.1$. Surprisingly enough, anomalous double steps in the plateau sequence reappear at higher energies outside the two *dark arrow* VHSs, while

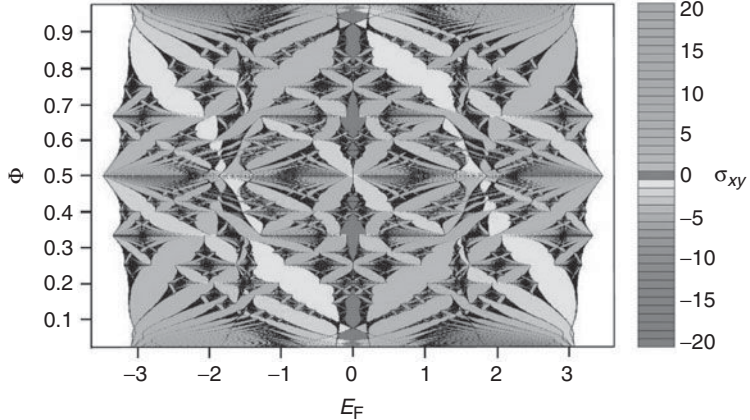


Figure 11.9 Spectrum $E = E(\Phi)$ and phase diagram for $\alpha = 1$, $\beta = 2$, and $\Phi = \frac{p}{q}$ with $q < 97$. Light (dark) colors correspond to positive (negative) values of the quantized conductivity. The darkest color corresponds to a null transverse conductivity. For $\Phi \ll 1$, the quantized conductivity evolves monotonically, but suddenly changes sign around the van Hove singularities located at $E \simeq \pm 1$ (see the alternation of light and dark colors). The Fermi energy is expressed in units of the hopping parameter t and the transverse conductivity is expressed in units of $1/h$.

the *light arrow* VHSs induce a sudden change of sign (see Figure 11.8(c) and (d)). It is interesting to note that the anomalous behavior persists in the high-energy regime and that this effect can be probed by varying the parameter Φ_β . The temperature required to observe these plateaus should be smaller than the spectral gaps, namely $T \sim 10$ nK. In Figure 11.9 we present a cumulative phase diagram where different colors denote different integer values of the Hall conductivity for $\alpha = 1$, $\beta = 2$, and $\Phi = \frac{p}{q}$, with $q < 97$. This figure can also be viewed as a plot of the Hofstadter butterfly spectrum obtained at fixed values of α and β .

11.6.4 Effective Jaynes–Cummings model

To identify the non-Abelian features in this anomalous quantum Hall effect, we introduce the Abelian flux Φ into the Dirac Hamiltonian (eqn (11.76)) by minimal coupling $\mathbf{p} \rightarrow \mathbf{p} + \frac{B_0}{2}(-y, x)$, and obtain

$$\hat{H}_D = (g_- \sigma^+ \hat{a} + g_- \sigma^- \hat{a}^\dagger) + (g_+ \sigma^+ \hat{a}^\dagger + g_+ \sigma^- \hat{a}), \quad (11.80)$$

where $\sigma^+ = |\chi_1\rangle\langle\chi_2|$, $\sigma^- = |\chi_2\rangle\langle\chi_1|$ are color-flip operators, $g_\pm = (c_y \pm c_x)(B_0/2)^{1/2}$, and the right-handed $a = (a_x - ia_y)/\sqrt{2}$ and left-handed $b = (a_x + ia_y)/\sqrt{2}$ (chiral) operators are defined in terms of the usual cartesian modes $a_j = \sqrt{\frac{\omega}{2}}(x_j + \frac{1}{\omega}p_j)$, where $\omega = B_0/2$.

In the isotropic limit $g_- = 0$, the Hamiltonian consists of an anti-Jaynes–Cummings term, a well-known interaction in quantum optics (Jaynes and Cummings, 1963) that leads to the usual relativistic Landau levels recently observed in graphene (Castro Neto *et al.*, 2009). Conversely, in the non-Abelian regime $g_- \neq 0$, the Hamiltonian becomes

a simultaneous combination of Jaynes–Cummings and anti-Jaynes–Cummings terms, producing a new type of Landau levels. These novel levels are obtained by means of a Bogoliubov squeezing transformation $S(\zeta) = e^{\frac{\zeta}{2}(a^2 - (a^\dagger)^2)}$, with $\zeta = -\tanh^{-1}(g_-/g_+)$, leading to the energy spectrum

$$E_{\text{LLL}} = 0, \quad E_n^\pm = \pm \sqrt{(2B_0 c_x c_y)n}, \quad n = 1, 2 \dots \quad (11.81)$$

and corresponding eigenstates

$$\begin{aligned} |\text{LLL}\rangle &= |\chi_2\rangle S^\dagger(\zeta)|\text{vac}\rangle, \\ |E_n^\pm\rangle &= \frac{1}{\sqrt{2}}|\chi_1\rangle S^\dagger(\zeta)|n-1\rangle \pm \frac{1}{\sqrt{2}}|\chi_2\rangle S^\dagger(\zeta)|n\rangle, \end{aligned} \quad (11.82)$$

with $|n\rangle = (n!)^{-1/2}(a^\dagger)^n|\text{vac}\rangle$ being the usual Fock states. Accordingly, the effect of non-Abelian fields is to squeeze the usual Landau levels. In particular, the LLL is a zero-energy mode characterized by a colored squeezed vacuum, which is in clear contrast with its Abelian counterpart, the latter being simply the vacuum. Besides, this LLL exhibits half the degeneracy of the remaining excited states $n \geq 1$ (Gusynin and Sharapov, 2005), and leads to the so-called anomalous half-integer quantum Hall effect

$$\sigma_{xy} = \pm \frac{g}{h} \left(\nu + \frac{1}{2} \right), \quad (11.83)$$

where the filling factor ν is defined as the integer part of $[E_F^2/2B_0 c_x c_y]$, and g is the Dirac point degeneracy. Let us stress that the non-Abelian fluxes modify the Hall plateaus in a non-trivial manner as already illustrated by the numerical results presented, for instance, in Fig. 11.9. In particular, the Hall conductivity in eqn (11.83) predicts the anomalous half-integer plateaus represented in Figure 11.8(b), where the conical singularities are four-fold degenerate $g = 4$. Conversely, in the non-Abelian case shown in Figure 11.8(d), the degeneracy is lifted to $g = 1$ and the size of the steps is modified accordingly.

This anomalous quantum Hall effect is essentially a single-particle phenomenon that relies on the peculiar properties of the LLL (see Fig. 11.10). Additionally, further non-Abelian anomalies can also be found at the many-particle level, where an exotic Laughlin wave function (Laughlin, 1983) can be obtained.

11.7. Fractional quantum Hall effect in non-Abelian fields

Another fascinating possibility relates to the creation of novel FQHE states, which would be associated with fractional non-Abelian excitations. For instance, moving a pseudo-hole around the origin should induce a non-Abelian Berry ‘phase’ described by a non-trivial matrix (Shapere and Wilczek, 1989). One would expect that a pseudo-hole in such a model would transform according to the non-Abelian representations of the permutation group, or more precisely Artin’s braid group, which in 2D considers particle exchange along the topologically distinct paths that avoid other particles. The studies of non-Abelian FQHE in such fields has just begun.

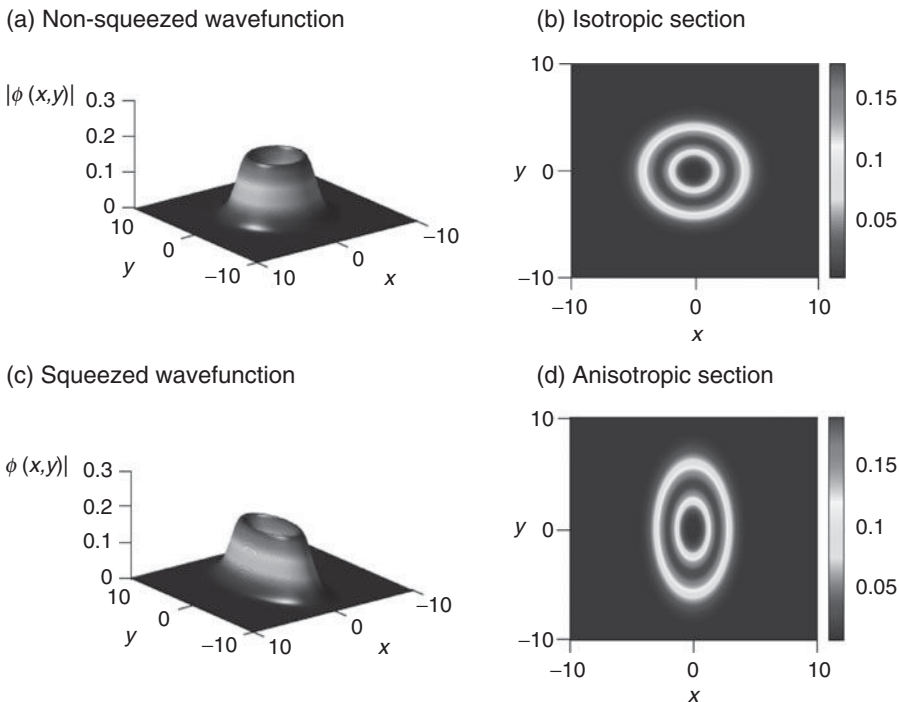


Figure 11.10 Vortex-like single-particle wave functions of the lowest Landau level (LLL) $\phi_{\text{LLL}}^m(x, y)$ for $m = 4$. (a) and (b) show the isotropic limit $c_x = c_y$; (c) and (d) show the anisotropic regime $c_y = 2c_x$. Note that distances are measured in units of the magnetic length l_B .

There has been a long quest for non-Abelian anyons reported in the condensed-matter literature, but there have been no clear experimental observations so far. The most prominent candidates are electronic (fermionic) $\nu = \frac{5}{2}$ FQHE states. Although this state has been observed in experiments, its non-Abelian character has not been demonstrated. Moore and Read (Moore and Read, 1991; Read and Rezayi, 1996) and independently Greiter, Wen and Wilczek (Greiter *et al.*, 1991) proposed an explanation in terms of the ‘Pfaffian state’ (see also (Das Sarma and Pincuk, 1997)). Recently, however, Töke and Jain (2006) proposed an alternative ‘composite fermion’ model of the $\nu = \frac{5}{2}$ state, which does not relate to non-Abelian statistics in any obvious manner. On the other hand, for bosons, a promising candidate is the $\nu = \frac{3}{2}$ state for the so-called Read–Rezayi sequence of incompressible correlated liquids. This state seems to be a true ground state for the rapidly rotating gas of bosons interacting via contact (Van der Waals) forces with a moderate amount of dipolar interaction (Rezayi *et al.*, 2005). Such a situation may be achieved, for instance, with Bose-condensed chromium (Griesmaier *et al.*, 2005). Non-Abelian FQHE, due its profound non-commutative character, could provide further experimentally feasible examples of non-Abelian anyons (for pedagogical reviews see Read and Moore (1992) and Ardonne and Schoutens (2007)). Indeed, very recently in Burrello and Trombettoni (2010) some of these questions were addressed and partially answered. We sketch their main results below.

11.7.1 Single-particle Hamiltonian

Let us consider in the following the continuum limit of the lattice theory, i.e. atoms not in the lattice, but in a 2D trap subjected to $SU(2)$ gauge fields. The atoms have two different internal (hyperfine, Zeeman...) levels, which we denote $|\uparrow\rangle$ and $|\downarrow\rangle$. The single-atom Hamiltonian in the presence of a non-Abelian gauge potential \vec{A} reads:

$$H = (p_x + A_x)^2 / 2m + (p_y + A_y)^2 / 2m \equiv H_a + H_{na}. \quad (11.84)$$

In the Hamiltonian in eqn (11.84) one can clearly distinguish an Abelian term proportional to the identity H_a and the non-Abelian off-diagonal term H_{na} (the units are taken to have mass $\frac{1}{2}$). The vector potential (A_x, A_y) chosen by Burrello and Trombettoni is essentially the same as the one used in the previous section, corresponding to a constant Wilson loop:

$$A_x = q\sigma_x - \frac{B}{2}y, \quad A_y = q\sigma_y + \frac{B}{2}x, \quad (11.85)$$

where the σ s are the 2×2 Pauli matrices. Here, the parameter q measures the strength of the non-Abelian contribution and B is an artificial standard magnetic, i.e. Abelian, gauge field. When $q = 0$, the usual Landau levels are retrieved (Cooper, 2008), although they are doubly degenerate.

Using the complex variables $z = x - iy$ and $\bar{z} = x + iy$, one can rewrite H_a and H_{na} as

$$H_a = 2q^2 + B + \frac{1}{4}\hat{d}^\dagger\hat{d}, \quad H_{na} = q \begin{pmatrix} 0 & -\mathbb{I} \\ \mathbb{I}^\dagger & 0 \end{pmatrix}, \quad (11.86)$$

where the creation and annihilation operators are $\hat{d}^\dagger = B\bar{z} - 4\partial_z$ and $\hat{d} = Bz + 4\partial_{\bar{z}}$. These operators describe the eigenstates of H_a , i.e. the standard Landau levels for a magnetic field B , $\psi_{n,m} = \hat{d}^\dagger^n (z^m e^{-B|z|^2/4})$, with energy eigenvalues $E_n = 2q^2 + 2B(n + \frac{1}{2})$.

The non-Abelian part of the Hamiltonian H_{na} corresponds to a Jaynes–Cummings coupling between subsequent Landau levels, as discussed in the previous section. In particular, H_{na} is analogous to the Hamiltonian obtained in Goldman *et al.* (2009b) starting from the Dirac equation in an anisotropic regime. Therefore, it leaves a single family of uncoupled states corresponding to the LLL, $\psi_{0,m} |\downarrow\rangle$, and, otherwise, its eigenstates take the form $\psi_{n-1} |\uparrow\rangle \pm \psi_n |\downarrow\rangle$. Using these wave functions, one diagonalizes the whole single-particle Hamiltonian H obtaining the eigenvalues

$$\varepsilon_n^\pm = 2Bn + 2q^2 \pm \sqrt{B^2 + 8q^2Bn}, \quad (11.87)$$

and the corresponding eigenstates

$$\chi_n^\pm \propto \left(B + 2q\sqrt{2Bn} \mp \sqrt{B^2 + 8q^2Bn} \right) \psi_{n-1} |\uparrow\rangle + \quad (11.88)$$

$$\left(B - 2q\sqrt{2Bn} \pm \sqrt{B^2 + 8q^2Bn} \right) \psi_n |\downarrow\rangle, \quad (11.89)$$

where the ψ_k are the wave functions in the k th Landau level such that $2\sqrt{2Bn}\psi_n = id^\dagger\psi_{n-1}$ due to the Jaynes–Cummings coupling. One immediately observes that there is

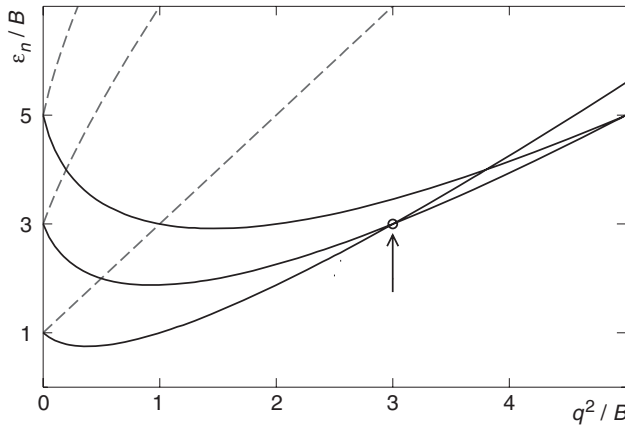


Figure 11.11 Energies of the first six eigenstates as a function of q^2/B . The n th Landau level is split by the non-Abelian contribution of the external field in χ_{n+1}^- (black solid) and χ_n^+ (red dashed); for $q = 0$ one recovers the usual Landau levels, while for $q^2/B = 3$ there is a degeneracy of the Landau levels (indicated by a circle). From Burrello and Trombettoni (2010).

a correspondence between the standard Landau levels in a magnetic field and the states χ : every Landau level is split in two parts corresponding to χ_{n-1}^+ and χ_n^- . For $q \rightarrow 0$ their energies merge $\sim E_{n-1} \pm 4q^2n$. The energy spectrum of eqn (11.87) is plotted in Figure 11.11.

It is easy to see that χ_1^- is the ground-state family of the system for $q^2 < 3B$. At $q^2 = 3B$ the phenomenon known in quantum optics as a *superradiant phase transition* occurs, and a new state becomes the ground state; we direct the reader to the original publication for the analysis of this very interesting case. To describe the states in χ_1^- one introduces the operator $\mathcal{G}_1 \equiv c_{\uparrow,1}\sigma_x + c_{\downarrow,1}d^\dagger$, with

$$\begin{aligned} c_{\uparrow,n} &= B + 2q\sqrt{2Bn} + \sqrt{B^2 + 8q^2Bn}, \\ c_{\downarrow,n} &= i \frac{B - 2q\sqrt{2Bn} - \sqrt{B^2 + 8q^2Bn}}{2\sqrt{2Bn}}. \end{aligned}$$

Thus one can describe every state from the ground-state family as

$$\chi_1^- = \mathcal{G}_1 \left(P(z) e^{-\frac{B}{4}|z|^2} |\downarrow\rangle \right), \quad (11.90)$$

where P is a generic polynomial in z .

11.7.2 Two-body interactions

Let us now introduce two-body intra-species repulsive interactions, H_I , such as for instance dipole-dipole interactions while we assume that the interspecies interactions vanish

(for instance, by means of Feshbach resonance). The task is to find the ground state of the many-body Hamiltonian

$$\mathcal{H} = \sum_i^N H_i + H_I. \quad (11.91)$$

Using the analogy to the standard FQHE, for fermions one finds for $q^2 < 3B$ that the state

$$\Psi^{(m)} = \prod_{j \leq N} \mathcal{G}_{1;j} \Lambda_N^{(m)} \quad (11.92)$$

is a ground state of the Hamiltonian \mathcal{H} . Here,

$$\Lambda_N^{(m)} = \prod_{i < j}^N (z_i - z_j)^m e^{-\frac{B}{4} - \frac{N}{i} |z_i|^2} |\downarrow\downarrow \dots \downarrow\rangle \quad (11.93)$$

denotes the Laughlin wave function with m odd. For repulsive bosons, the form of eqn (11.92) holds with $m \geq 2$ and even. The state $\Psi^{(m)}$ is a non-Abelian deformation of the usual Laughlin states and it describes an incompressible fluid of spin- $\frac{1}{2}$ particles with constant density in the thermodynamical limit. One can study excitations of such a state such as, for instance, pairs of quasi-holes,

$$\Psi_{\zeta_1, \zeta_2}^{(m,k)} = \prod_{i \leq N} \mathcal{G}_{1;i} (z_i - \zeta_1)^k (z_i - \zeta_2)^k \Lambda_N^{(m)}. \quad (11.94)$$

Obviously, the Berry phase due to the adiabatic exchange of the pair of quasi-holes ζ_1 and ζ_2 is the same of the one characterizing the corresponding quasi-holes in a simple Laughlin state. Therefore, excitations are Abelian anyons (Arovas *et al.*, 1984).

The situation turns out to be even more interesting at the critical point, when the ground state of the Jaynes–Cummings model is degenerate. This leads, of course, to additional degeneracy of the effective LLL. Burrello and Trombettoni (2010) argue that the ground state of the systems will then become Pfaffian-like, and that it will exhibit non-Abelian quasihole and quasiparticle excitations.

11.8. Ultracold gases and lattice gauge theories

A compelling subject is the possibility of using ultracold atoms for simulations of lattice gauge theories in (2+1)D. The main difference is that in LGTs the gauge fields are dynamical variables, whereas they are obviously not in the schemes presented so far with ultracold gases. Moreover, the schemes are realized in real rather than in imaginary time, which is the usual case for LGTs. Nevertheless, a big advantage of the previous proposals is that given a gauge field configuration, the dynamics of matter fields in real time are given for free. By generating various configurations of gauge fields, one may try to ‘mimic’ the Monte Carlo sampling of LGT in the limit in which gauge fields affect the matter fields, but not vice versa. Averaging over both, annealed disorder and quantum fluctuations should approximate the

statistical average in LGT. Such an approach requires that the configurations generated represent the characteristic or statistically relevant characteristics of corresponding LGT phases. For instance, configurations in the confinement sector should exhibit an area law fulfilled by Wilson loops, appropriate distributions of vortices, Abelian magnetic monopoles, instantons, merons, calorons, etc. (for recent reviews, see Baig and Colet (1986), Greensite (2003), and Engelhardt (2004)).

The situation is much better when we turn to Abelian LGTs since they reduce, in some limits, to models with ring-exchange interactions that involve the product of operators over an elementary plaquette of the underlying lattice. A model involving spin for a multicomponent Bose or Fermi gas, in the Mott limit, with one particle per site, and in a triangular lattice was formulated in Pachos and Rico (2004). Due to the fact that in a triangular lattice, tunneling from one site to another may occur directly or via the remaining third site, the three-spin interactions are of third order on the t/U expansion. However, since in the Mott limit $(t/U)^3 \ll 1$, the energy scales involved in the process are very small, implying very long timescales. A different model that realizes ring interactions has been reported in Büchler *et al.* (2005). These authors considered a standard one-component Bose–Hubbard model in a square (cubic) lattice, described by the Hamiltonian H_{BH} , coupled to a lattice of diatomic ‘molecules’ trapped in the center of each plaquette as shown in Fig. 11.12. There, the coupling to the molecular state (of d -symmetry) takes the form:

$$H_m = \nu \sum_{\text{plaquettes}} m^\dagger m + g \sum_{\text{plaquettes}} [m^\dagger (b_1 b_3 - b_2 b_4) + h.c.] . \quad (11.95)$$

Two atoms may perform a Raman transition to a molecular state with the coupling g ; ν denotes detuning of this transition. Perturbative elimination of the molecules leads to the

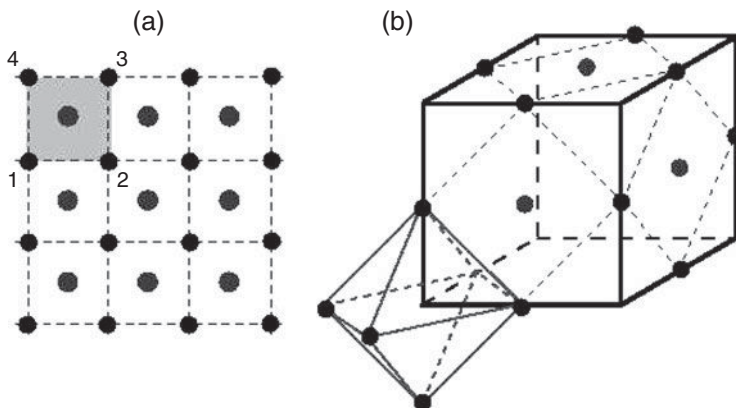


Figure 11.12 A scheme to realize ring-exchange interactions using a single-component Bose–Hubbard model in a square (cubic) lattice coupled to lattice of ‘molecules’. Redrawn from Büchler *et al.* (2005) by courtesy of the authors.

effective ring-exchange Hamiltonian for bosons:

$$H_{RE} = K \sum_{\text{plaquettes}} \left(b_1^\dagger b_2 b_3^\dagger b_4 + b_4^\dagger b_3 b_2^\dagger b_1 - n_1 n_2 - n_3 n_4 \right). \quad (11.96)$$

More precisely, the model can be realized using atoms with two internal states: one state trapped in the square (cubic) lattice and described by the simple Bose–Hubbard model, and a second one trapped in the centres of the plaquettes in a site potential that is not symmetric, but rather has a point symmetry of the lattice. ‘Molecules’ are build from two atoms in that second internal state and have d -symmetry.

The model described by the Bose–Hubbard Hamiltonian H_{BH} plus H_m is a promising candidate for a deconfined quantum critical point in two dimensions (Senthil *et al.*, 2004). This is because it undergoes (most probably) a quantum phase transition between the bosonic superfluid phase (which occurs when $\nu \gg g$ and $t \gg g^2/\nu$, and which breaks the $U(1)$ -symmetry) and a molecular ‘density wave’ (stripes) phase (which occurs in the opposite limit, when $\nu < 0$ and $|\nu| \gg t, g$, and which breaks the translational symmetry). Both in two and three dimensions, this model describes a $U(1)$ gauge theory and is likely to exhibit a variety of quantum phases, such as $U(1)$ deconfined insulator, $U(1)$ deconfined phase, etc. (Alet *et al.*, 2006; Hermelé *et al.*, 2004).

Later on, Tewari *et al.* used a dipolar Bose gas in 2D kagomé or 3D pyrochlore lattice to simulate the compact $U(1)$ lattice gauge theory (Tewari *et al.*, 2006). Such a model is well described by an extended Bose–Hubbard Hamiltonian, as discussed in Chapter 8. In the limit in which on-site interactions, U , are comparable to the nearest-neighbor interactions V and both are strong; the physics is dominated by the configurations where the fluctuations in the number of atoms in all elementary plaquettes is zero. In the lowest relevant order of perturbation theory, $(t/U)^3$, one obtains a Hamiltonian with a ‘ring-exchange’ term on a dual hexagonal lattice. This model reduces directly to the $U(1)$ LGT, and allows us to realize various fractionalized topological phases. Moreover, the authors described methods of detecting signatures of the emergent $U(1)$ Coulomb phase, terming it ‘emergence of artificial light in an optical lattice’.

More recently, Weimer *et al.* proposed a model in which they show how laser-excited Rydberg atoms in optical or magnetic lattices with large spacing can provide an efficient implementation of a universal quantum simulator for spin models involving (high-order) n -body interactions. Such models include Hamiltonians involving n -particle constraints, such as the Kitaev toric code (Kitaev, 2003; Kitaev, 2006) (see also Chapter 13), color code (Bombin and Martin-Delgado, 2008), and LGTs with spin-liquid phases (see Moessner and Sondhi (2001b), Motrunich and Senthil (2002), Hermelé *et al.* (2004), and Levin and Wen (2005)). A schematic setup of the system is shown in Figure 11.13. Amazingly, this scheme has been recently realized with . . . a small systems of ultracold ions (Lanyon *et al.*, 2011; Berreiro *et al.*, 2011).

11.9. Generation of ‘artificial’ gauge fields

In this section we discuss some of the proposals for generation of ‘artificial’ or ‘synthetic’ gauge fields. A very pedagogical and complete presentation of this subject can be found in

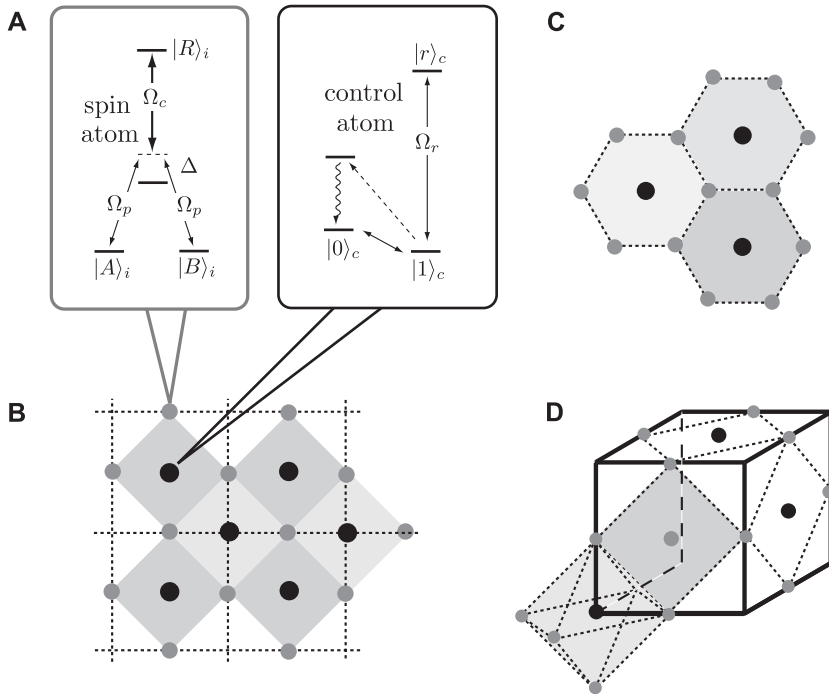


Figure 11.13 Setup of the system. (a) Two internal states $|A\rangle_i$ and $|B\rangle_i$ give rise to an effective spin degree of freedom. These states are coupled to a Rydberg state $|R\rangle_i$ in two-photon resonance, establishing an electromagnetic-induced transparency condition. On the other hand, the control atom has two internal states $|0\rangle_c$ and $|1\rangle_c$. The state $|1\rangle_c$ can be coherently excited to a Rydberg state $|r\rangle_c$ with Rabi frequency Ω_r , and can be optically pumped into the state $|0\rangle_c$ for initializing the control qubit. (b) For the toric code, the system atoms are located on the links of a 2D square lattice, with the control qubits in the centre of each plaquette for the interaction A_p and on the sites of the lattice for the interaction B_s . Set-up required for the implementation of the color code (c) and the $U(1)$ lattice gauge theory. Redrawn after Weimer *et al.* (2010) by courtesy of the authors.

the excellent review of Dalibard *et al.* (2010). In our initial classification, we separate the main proposals into four different classes.

11.9.1 Proposals employing rapidly rotating ultracold gases

As is well known, and as we have discussed in previous sections, rapidly rotating trapped ultracold gases provide a straightforward way to realize standard 'artificial', or better to say, Abelian magnetic fields (see, for example, Fetter (2009)). In order to create such magnetic fields, typically one considers a quasi-single-component ('spinless') 2D gas of N atoms confined in a harmonic trap of frequency ω_\perp and rotating in the XY plane around the z -axis with frequency Ω . For moderate rotations $\Omega < \omega_\perp$ in macroscopic atomic clouds, an Abrikosov vortex lattice is formed (Madison *et al.*, 2000; Abo-Shaeer *et al.*, 2001).

As Ω approaches ω_{\perp} , the vortex lattice melts and the system evolves through a sequence of states that have been identified in the literature as highly correlated quantum liquids (Wilkin *et al.*, 1998; Wilkin and Gunn, 2000; Paredes *et al.*, 2001).

The various regimes of rapidly rotating gases can be described in the terminology of the FQHE. A crucial role is played by the direct analog of the Landau level filling factor ν , in the FQHE (see Section 1.3), which can be related to the number of vortices N_v by $\nu = N/N_v$ in the BEC mean-field description (valid for large systems and moderate rotations). Indeed, most of the literature on rapidly rotating ultracold gases considers relatively large systems and even the thermodynamic limit. The stability of the cloud in a harmonic trap requires $\Omega < \omega_{\perp}$, since otherwise centrifugal forces drag the atoms away from the trap. Observation of the Laughlin states requires, on the other hand, to remain in the LLL. This in turn can be assured only if $\Omega - \omega_{\perp} = O(1/N)$, i.e. it requires a very precise control of the delicate balance between Ω and ω_{\perp} . Unfortunately, in the case of contact (short-range Van der Waals) interactions pseudohole excitations of the Laughlin state have vanishing interaction energy, similar to the Laughlin state itself; they can differ only by the angular momentum contribution $\propto \Omega - \omega_{\perp} = O(1/N)$, i.e. they vanish at large N . Despite progress having been made in experimental studies of vortex lattices (Coddington *et al.*, 2003; Schweikhard *et al.*, 2004b) and the first steps having been taken toward reaching LLL physics (Schweikhard *et al.*, 2004a; Simula *et al.*, 2005; Stock *et al.*, 2005), experiments have not yet reached this regime.

While the first studies only considered the LLL for strong enough rotation (Wilkin and Gunn, 2000; Paredes *et al.*, 2001), attention has latterly been paid to edge excitations and topological order too (Cazalilla *et al.*, 2005). Recently, correlated liquids at $\nu = k/2$ for $k = 1, 2, 3, \dots$ and for $\nu \leq \nu_c \simeq 6 - 10$ have been discussed (Cooper *et al.*, 2001; Sinova *et al.*, 2002; Regnault and Jolicoeur, 2004a; Regnault and Jolicoeur, 2004b). These states resemble, to a great extent, the states from the Rezayi–Read hierarchy (Read and Rezayi, 1999): $k = 1$ is the Laughlin state, $k = 2$ is the Moore–Read paired state (Moore and Read, 1991; Cazalilla *et al.*, 2005), etc. Rezayi *et al.* (2005) have recently shown that the presence of a small amount of dipole–dipole interaction unambiguously makes the Rezayi–Read state with $k = 3$ the ground state. This state is particularly interesting, since its excitations are both fractional and non-Abelian. The validity of the LLL approximation for rotating gases is also discussed in Morris and Feder (2006).

Finally, it is worth noticing that the problems related to the short-range nature of the Van der Waals forces can be overcome by using optical traps that are more rigid than harmonic ones, which is technically difficult but in principle possible. Yet another promising idea is to use dipolar gases, i.e. gases that interact via magnetic or electric dipole moments (for a review see Baranov *et al.* (2002)). Rotating dipolar bosonic gases are expected to exhibit exotic behavior in the weakly interacting regime (Cooper *et al.*, 2005), whereas fermionic dipolar gases have a finite gap for the $\nu = \frac{1}{3}$ Laughlin state (Baranov *et al.*, 2005). Unfortunately, the results of Baranov *et al.* (2005) are much overestimated, as pointed out in Grass *et al.* (2011). Still, the gap can be quite significant when the dipolar Fermi gas is subjected to non-Abelian gauge fields. We refer the reader to the recent review by Lahaye *et al.* (2009) and the chapter on dipolar gases for more details about the recent progress in realizing such systems, either in a dipolar gas of chromium atoms with large magnetic dipoles (Stuhler *et al.*, 2005) or with an ultracold gas of heteronuclear molecules with large electric dipole moments (Ni *et al.*, 2008).

11.9.2 Proposals employing Berry’s phase

A completely different approach to creating ‘artificial’ magnetic fields in ultracold gases employs quantum optical effects of three-level atomic systems: electromagnetically induced transparency, ‘slow light’, dark states, stimulated Raman adiabatic population transfer (STIRAP) etc. The interaction of the internal atomic degrees of freedom with the external fields can lead to vortex nucleation. A first proposal to exploit quantum-optic effects considered a two-component BEC to transfer atoms from one internal state to another using STIRAP and a coupling that is (i) spatially odd in one dimension to create dark solitons and (ii) spatially chiral to create vortices, the latter being achieved simply with a Raman coupling employing two perpendicular standing waves (Dum *et al.*, 1998). Similar although much more elaborate ideas have been proposed in (Juzeliūnas and Öhberg, 2004; Juzeliūnas *et al.*, 2005a; Juzeliūnas *et al.*, 2005b; Juzeliūnas *et al.*, 2006) in a very versatile method that can be used to reach the IQHE (Öhberg *et al.*, 2005) and even regimes of FQHE in planar geometries (Juzeliūnas *et al.*, 2006), as well as to generate non-Abelian gauge fields (Ruseckas *et al.*, 2005).

In fact these methods can be viewed as a way of employing the geometrical potentials induced by laser fields by exploiting the spatial variations of the external laser fields and separating internal and external atomic degrees of freedom. Here we follow Günter *et al.* (2009) and sketch a very recent version of this approach. The starting point is to assume that atoms are in a ground state g (with angular momentum $J_g > 0$), which, in the absence of any external perturbation, is degenerate. When there is an external laser field, the degeneracy is lifted and one can consider that the atomic energy eigenstates denoted by $|\psi_\alpha\rangle$ ($\alpha = 0, \dots, 2J_g$), which are linear combinations of the Zeeman substates $|g, J_g, m\rangle$ ($m = -J_g, \dots, J_g$), acquire a spatial dependence due to the spatial variation of the external laser fields, leading to a Berry phase (Berry, 1984; Shapere and Wilczek, 1989). This, as we have seen, corresponds to a gauge field $\{\mathbf{A}, U\}$, which in this case appears in the effective Hamiltonian of center of mass motion. Assuming the system remains in $|\phi_0\rangle$,

$$H = \frac{[\mathbf{p} - q\mathbf{A}(\mathbf{r})]^2}{2m} + E_0(\mathbf{r}) + U(\mathbf{r}), \quad (11.97)$$

where m is the atomic mass, and

$$\mathbf{A} = i\hbar\langle\psi_0|\nabla(|\psi_0\rangle)\rangle, \quad U = \frac{\hbar^2}{2m} \sum_{\alpha \neq 0} |\langle\psi_0|\nabla(|\psi_\alpha\rangle)\rangle|^2, \quad (11.98)$$

with the charge $q = 1$. As mentioned, there are several ways to create gauge fields with laser beams in this manner.

In particular, the proposal of Juzeliūnas *et al.* (2006) uses a Λ level scheme configuration with two counter propagating beams to drive the two transitions of the atom (see Figure 11.14(a)). If the two beams are assumed to be circularly polarized (with positive and negative helicity respectively), and both the ground (g) and the excited (e) states have unit angular momentum ($J_g = J_e = 1$), the configuration permits us to take a ‘dark’ superposition of the states $|g, J_g, m = \pm 1\rangle$ as the candidate state $|\psi_\alpha\rangle$ for the Berry-phase. However, for most alkali-metal atoms this scheme is, in principle, difficult to implement,

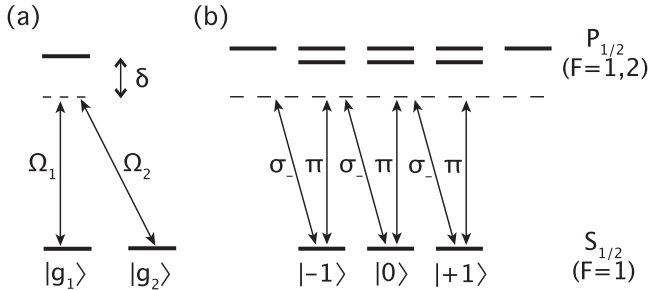


Figure 11.14 (a) Λ -type system used as a simple model of the atom–laser coupling. (b) Atomic scheme relevant for a $\frac{3}{2}$ nuclear spin, as for ^{87}Rb or ^{23}Na . From Günter *et al.* (2009).

since the hyperfine splitting of the relevant excited manifold is very small, easily leading to a superposition with states with different angular momenta. This, together with the fact that there will be heating due to spontaneous emission will eventually screen the effect of the ‘artificial’ magnetic field. Nevertheless, such a scheme has been realized quite successfully with bosonic ^{87}Rb atoms, creating an Abelian gauge field (see Lin *et al.* (2009a, 2009b) and also Dutta *et al.* (1999) for early attempts). Very recently, Spielman’s group reported realization of spin–orbit coupling, equivalent to a non-Abelian gauge field, using a similar method.

In Günter *et al.* (2009), the authors propose a simpler planar scheme to overcome the limitations mentioned above. This involves crossing two laser beams, far-detuned from the atomic resonance transition, resulting in an effective gauge field that varies smoothly over the area of the atomic cloud and allows for the observation of several vortices in a cold interacting spinor Bose gas.

Let us illustrate their explicit calculations for the simple case of a three-level Λ system (Günter *et al.*, 2009). The Λ scheme of Figure 11.14(a) shows the two ground states $|g_1\rangle$ and $|g_2\rangle$, which are coupled to the excited state by laser fields with spatially varying Rabi frequencies $\Omega_1(\mathbf{r})$ and $\Omega_2(\mathbf{r})$, respectively. The Hamiltonian for an atom in the light field at any point \mathbf{r} reads

$$H = \frac{\mathbf{p}^2}{2m} + V(\mathbf{r}) + H_{\text{AL}}(\mathbf{r}). \quad (11.99)$$

The atom is confined in a 2D trapping potential $V(\mathbf{r}) = (\omega_x^2 x^2 + \omega_y^2 y^2)/2m$. The interacting part of the Hamiltonian H_{AL} acts on the internal degrees of freedom only and describes the atom–laser coupling. Using the rotating wave approximation, it can be written as

$$H_{\text{AL}} = \hbar \begin{pmatrix} 0 & 0 & \Omega_1/2 \\ 0 & 0 & \Omega_2/2 \\ \Omega_1^*/2 & \Omega_2^*/2 & -\delta \end{pmatrix}, \quad (11.100)$$

where $\delta = \omega_L - \omega_A$ is the detuning of the laser frequency ω_L with respect to the atomic resonance frequency ω_A . We assume the atom to be initially prepared in the eigenstate of H_{AL}

$$|\psi_0(\mathbf{r})\rangle = \cos(\theta/2)|g_1\rangle + e^{-i\phi}\sin(\theta/2)|g_2\rangle \quad (11.101)$$

where $\cos\theta = (|\Omega_1|^2 - |\Omega_2|^2)/\Omega^2$, $e^{i\phi}\sin\theta = -2\Omega_1^*\Omega_2/\Omega^2$ and $\Omega = (|\Omega_1|^2 + |\Omega_2|^2)^{1/2}$. Here $|\psi_0\rangle$ is a non-coupled (dark) state, which is separated from the next eigenstate by an energy given by $\varepsilon = \hbar\Omega^2/4\delta$ in the low-intensity limit $\Omega \ll |\delta|$. The gauge potentials (eqn (11.98)) can be explicitly written as

$$\mathbf{A}(\vec{r}) = \frac{\hbar}{2}(1 - \cos\theta)\nabla\phi, \quad (11.102)$$

$$U(\vec{r}) = \frac{\hbar^2}{8M} [(\nabla\theta)^2 + \sin^2\theta(\nabla\phi)^2]. \quad (11.103)$$

It is worth pointing out that using off-resonant lasers also imposes limitations on the schemes that can lead to a non-trivial gauge field. For instance, if a frequency detuning is large compared to the hyperfine splitting of the excited manifold, the nuclear spin becomes irrelevant for the description of the excited state. Consider, for example, the D_1 transition between the states $S_{1/2}$ and $P_{1/2}$ of an alkali-metal atom, which is sketched in Figure 11.14(b) for the case of a nuclear spin $\frac{3}{2}$, as for ^{87}Rb or ^{23}Na . Since only the electronic angular momentum is relevant for evaluating the matrix elements of the atom–laser coupling, the energy-level structure can be regarded as a simple $J_g = \frac{1}{2} \leftrightarrow J_e = \frac{1}{2}$ system. At the same time this restricts the polarizations of the laser beams that can be applied to create the internal superposition state: A spin flip from $m = -\frac{1}{2}$ to $m = +\frac{1}{2}$, for instance, corresponds to an angular momentum transfer of $+\hbar$, so a two-photon transition requires light with circular (σ_- or σ_+) as well as with linear (π) polarization. Note also that the detuning cannot be large compared to the *fine* structure splitting between the $P_{1/2}$ and $P_{3/2}$ manifolds, since otherwise one is left with an effective $J_g = 0 \leftrightarrow J_e = 1$ transition where no coherent level superposition is generated by the atom–light interaction.

A simple implementation scheme to generate such a gauge field employs two far-detuned crossed Gaussian laser beams, similar to the scheme of Dum *et al.* (1998). One takes the beams to be σ_- and π (or equivalently σ_+ and π) polarized. Moreover, it is assumed that the beams are also displaced by a distance $\pm a$ (of the order of the beam waists) from the x - and the y -axis, respectively, as shown in Figure 11.15, in order to obtain a non-vanishing magnetic field at the origin. The Rabi frequencies are $\Omega_1(\mathbf{r}) = \Omega_0 \exp[ikx - (y - a)^2/w^2]$ and $\Omega_2(\mathbf{r}) = \Omega_0 \exp[iky - (x + a)^2/w^2]$, where w denotes the waist of the beams and k the wave vector. By expanding the matrix in eqn (11.100) up to second order around the origin, one obtains

$$\mathbf{A}(\mathbf{r}) = \hbar k(\mathbf{e}_y - \mathbf{e}_x)[1/2 - a(x + y)/w^2] \quad (11.104)$$

$$\mathbf{B}(\mathbf{r}) = \nabla \times \mathbf{A} = \frac{2\hbar ka}{w^2} \mathbf{e}_z,$$

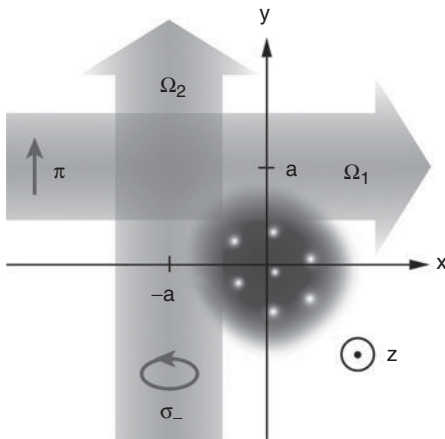


Figure 11.15 Planar scheme to create a gauge field for atoms using two crossed far-detuned laser beams displaced by a distance $\pm a$ from the centre position of the atomic cloud. From Günter *et al.* (2009).

and the scalar potential up to second order becomes

$$U(\mathbf{r}) = \frac{\hbar^2 k^2}{4m} - \frac{1}{2} m \omega_c^2 \left(\frac{x+y}{\sqrt{2}} \right)^2, \quad (11.105)$$

which reduces the trapping frequency along the axis $x = y$.

11.9.3 Proposals employing rotating optical microtraps

Despite their simplicity, geometrical potentials barely allow the regime of truly strong artificial magnetic fields to be reached. For this reason atomic gases in optical lattices or arrays of optical traps perhaps still provide the best candidates to achieve IQFE and FQHE. There are two possible ways of reaching the regime of Laughlin liquids in these proposals. A very promising one uses atoms in an array of rotating optical microtraps, either in an optical lattice (see Bloch *et al.* (2008) and Sarajlic *et al.* (2009)) or in an array of rotating traps generated by an array of microlenses (Birkl *et al.*, 2001) or an array of laser beams (Yavuz *et al.*, 2006).

In such arrangements, it is natural to study independent mesoscopic or even microscopic systems of a few atoms at each lattice site, i.e. avoid the problems of large N . The lattice plays an important role, however. First of all, one can prepare an equal number of atoms at each site by using a Mott transition, and then turn the intersite hopping off. Second, the measurement and detection procedures could automatically be applied to many copies of the same meso- or micro-system. Such experiments demand a careful theoretical analysis of few-atom systems, possibly using exact methods such as exact diagonalization in the presence of a trap. This permits the study, for example, of the adiabatic path to fractional quantum Hall states (Popp *et al.*, 2004) or, as we discussed in Section 11.2, the appearance of ordered

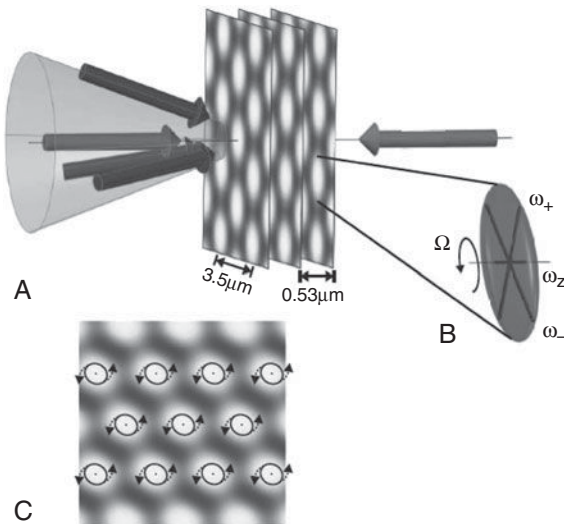


Figure 11.16 Simulation of a magnetic field at the rotating minima of an optical lattice potential. (A) Bose-condensed atoms are loaded into a deep optical lattice formed by the superposition of a 2D lattice (blue beams) and a standing wave along its normal (red beams). The optical phases of the 2D lattice beams are modulated in time to produce lattice sites which, near the lattice potential minima, rotate at a rate comparable to the trapping frequency for atoms confined there. (B) The potential near each site approximates a strongly oblate harmonic oscillator, whose principle axes rotate in the plane normal to the direction of tightest confinement at a frequency $\Omega \sim \omega_{\pm}$. (C) Although the local potential near each site rotates, the overall lattice structure remains constant. From Gemelke *et al.* (2010).

structures (vortices, vortex arrays, Wigner crystals) in systems of few bosonic atoms. In Figure 11.2 an example of such structures obtained from a pair-correlation function in the Laughlin states is shown. Similar studies (going even beyond the LLL approximation) for bosonic and fermionic atoms have been reported in several studies (Romanovsky *et al.*, 2004; Yannouleas and Landman, 2004; Romanovsky *et al.*, 2006).

Experimental work in small rotating clusters of interacting bosonic atoms (see Figure 11.16) have demonstrated that quantum ground states being precursors of topological states of electronic systems, such as FQHE states, can be created (Gemelke *et al.*, 2010).

11.9.4 Proposals employing laser-induced gauge fields in optical lattices

Finally, let us turn to another way of creating topological order and highly-correlated liquids, without using rotation or geometrical light potentials. Instead, the task will be achieved by appropriately designed control of tunneling in optical lattices. The pioneering theoretical attempts to simulate 'artificial' gauge fields in ultracold atom laboratories (see Jaksch and Zoller (2003) and Osterloh *et al.* (2005)) were based on such a scheme.

Jaksch–Zoller–Osterloh proposal The application of state-dependent, laser-assisted tunneling (see Liu *et al.* (2004)) and coherent transfer between internal states allows us to generate Abelian gauge fields as first proposed by Jaksch and Zoller (2003) and to create ‘artificial external magnetic fields’ corresponding to non-Abelian $U(n)$, $SU(n)$, or even $GL(n)$ gauge fields by using atoms with more internal states (Osterloh *et al.*, 2005). As we have discussed at length, in this case the tunneling amplitudes are replaced by (unitary) matrices whose product around a plaquette is non-trivial and whose mean trace (Wilson loop) is not equal to n (Montvay and Münster, 1997; Rothe, 1998). In what follows we explicitly derive such models.

We consider an atomic gas in a 3D optical lattice and assume that tunneling is completely suppressed in the z direction, so that we effectively deal with an array of 2D lattice gases and we are able to restrict ourselves to one copy. The atoms occupy two internal hyperfine states $|g\rangle$, $|e\rangle$, and the optical potential traps them in the states $|g\rangle$ and $|e\rangle$ in every second column, i.e. for the y coordinate equal to $\dots, n-1, n+1, \dots$ ($\dots, n, n+2, \dots$). The resulting 2D lattice thus has the spacing $\lambda/2$ ($\lambda/4$) in the x (y) direction. The tunneling rates in the x direction are due to kinetic energy; they are spatially homogeneous and assumed to be equal for both hyperfine states. The lattice is tilted in the y direction, which introduces an energy shift Δ between neighboring columns. Tilting can be achieved by accelerating the lattice or by placing it in a static electric field. By doing this, standard tunneling rates due to kinetic energy are suppressed in the y direction. Instead, tunneling is laser-assisted and driven by two pairs of lasers resonant for Raman transitions between $|g\rangle$ and $|e\rangle$, i.e. $n \leftrightarrow n \pm 1$. This can be achieved because the offset energy for both transitions is different and equals $\pm\Delta$. Detunings of the lasers are chosen in such a way that the effect of tilting is cancelled in the rotating frame of reference. The lasers generate running waves in the $\pm x$ direction, so that the corresponding tunneling rates acquire local phases $\exp(\pm iq_x)$.

In order to realize ‘artificial’ non-Abelian fields in a similar scheme, one may use atoms with degenerate Zeeman sublevels in the hyperfine ground-state manifolds $|g_i\rangle$, and $|e_i\rangle$ with $i = 1, \dots, n$, whose degeneracy is lifted in external magnetic fields. These states may be thought of as ‘colors’ of the gauge fields. Promising fermionic candidates with these properties are heavy alkali atoms, for instance ^{40}K atoms in states $F = \frac{9}{2}, m_F = \frac{9}{2}, \frac{7}{2}, \dots$, and $F = \frac{7}{2}, m_F = -\frac{7}{2}, -\frac{5}{2}, \dots$; in particular, they allow realization of ‘spin’-dependent lattice potentials and hopping (Liu *et al.*, 2004).

Having identified the ‘colors’, one modifies the scheme of Jaksch and Zoller (2003) in the following way: laser-assisted tunneling rates along the y -axis should depend on the internal state, although not necessarily in the sense of Liu *et al.* (2004). For a given link $|g_i\rangle$ to $|e_i\rangle$, tunneling should be described by a non-trivial unitary matrix $U_y(x)$ being a member of the ‘color’ group ($U(n)$, $SU(n)$, $GL(n)$ etc.). For unitary groups, the tunneling matrix $U_y(x)$ can be represented as $\exp(i\tilde{\alpha}A_y(x))$. Here, $\tilde{\alpha}$ is real and $A_y(x)$ is a Hermitian matrix from the gauge algebra, e.g. $u(N)$ or $su(N)$. Since transitions from $|g_i\rangle$ to $|e_i\rangle$ correspond to different frequencies for each i , they are driven by different running wave lasers, and may attain different phase factors $\exp(\pm iq_i x)$.

In order to create gauge potentials that cannot simply be reduced to two independent Abelian components, tunneling in the x direction should be described by a tunneling matrix U_x , which fulfills $[U_x, U_y(x)] \neq 0$, so that a genuine non-Abelian character of the fields is assured. We stress that all elements of this scheme, as shown in Figure 11.17, are experimentally accessible.

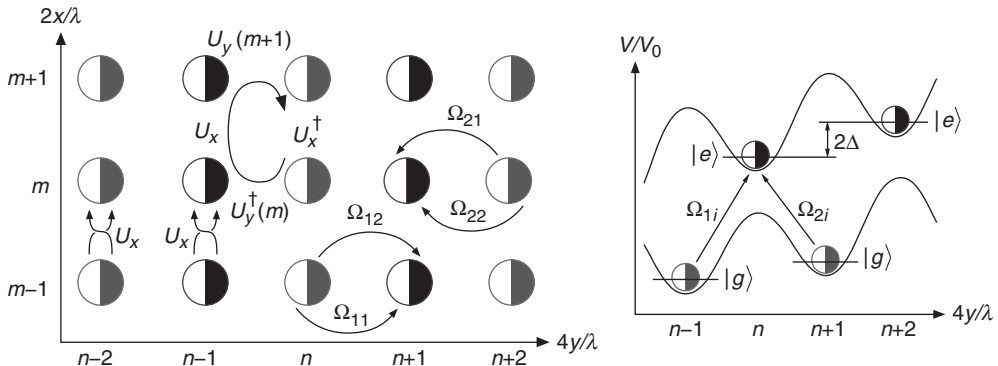


Figure 11.17 Optical lattice setup for $U(2)$ gauge fields: red and blue open semicircles (closed semicircles) denote atoms in states $|g_1\rangle$ and $|g_2\rangle$, respectively ($|e_1\rangle$ and $|e_2\rangle$). Left: hopping in the x direction is laser assisted and allows for unitary exchange of colors; it is described by the same unitary hopping matrix U_x for both $|g_i\rangle$ and $|e_i\rangle$ states. Hopping along the y direction is also laser assisted and attains ‘spin-dependent’ phase factors. Right: trapping potential in y direction. Adjacent sites are set off by an energy Δ due to the lattice acceleration, or a static inhomogeneous electric field. The lasers Ω_{1i} are resonant for transitions $|g_{1i}\rangle \leftrightarrow |e_{2i}\rangle$, while Ω_{2i} are resonant for transitions between $|e_{1i}\rangle \leftrightarrow |g_{2i}\rangle$ due to the offset of the lattice sites. Because of the spatial dependence of $\Omega_{1,2}$ (running waves in $\pm x$ direction), the atoms hopping around the plaquette get the unitary transformation $U = U_y^\dagger(m)U_xU_y(m+1)U_x^\dagger$, where $U_y(m) = \exp(2\pi im \text{ diag}[\alpha_1, \alpha_2])$, as indicated in the left-hand figure. See Osterloh *et al.* (2005). Figure in color online.

Spielman atom-chip proposal The fully optical implementations of the above schemes with non-radioactive alkaline fermions suffer from excessive spontaneous emission. In the remainder of this section we present in some detail the experimental proposal of Spielman *et al.* (Goldman *et al.*, 2010). This also uses optical lattices coupled with Raman-stimulated hopping, as sketched in Figure 11.18(c) and (d), but it combines state-independent optical potentials with micron-scale state-dependent magnetic potentials near the surface of an atom chip. We focus on harmonically trapped quantum degenerate ${}^6\text{Li}$ systems about $5\ \mu\text{m}$ above an atom chip’s surface, with an equal lattice period $d = 2\ \mu\text{m}$ along \hat{x} and \hat{y} . We use $\hbar k_L = \pi\hbar/d$ and $E_L = \hbar^2 k_L^2/2m = h \times 8.3\ \text{kHz}$ —the recoil momentum $\hbar k_R = 2\pi\hbar/\lambda$ and recoil energy, where λ is the optical wavelength not the lattice period, $\lambda/2$ for counter propagating lasers. The scheme is equally applicable to ${}^{40}\text{K}$.

The proposal for realizing an atomic model with a $SU(2)$ gauge structure requires four atomic states, denoted $|g_1\rangle, |g_2\rangle, |e_1\rangle$, and $|e_2\rangle$, with very specific properties as outlined below:

- (i) All of the atomic states experience a primary lattice potential $V_1(x) = V_x \sin^2(kx)$ along the x -axis. When the lattice depth $V_x = 6E_L \approx h \times 50\ \text{kHz}$, this a hopping matrix element $t \approx 0.05E_L \approx h \times 400\ \text{Hz}$. An additional, much weaker lattice $V_2(x) = 2\lambda_{\text{stag}} \sin^2(kx/2)$ slightly staggers the primary lattice. We take $\lambda_{\text{stag}} \sim t \ll V_x$. Figure 11.18(b) shows two pairs of $\lambda = 1064\ \text{nm}$ lasers, slightly detuned from each other, incident on the reflective surface of the atom chip. These beams produce lattices with period $\lambda/2 \sin\theta$. For our base $2\ \mu\text{m}$ lattice period, we choose the

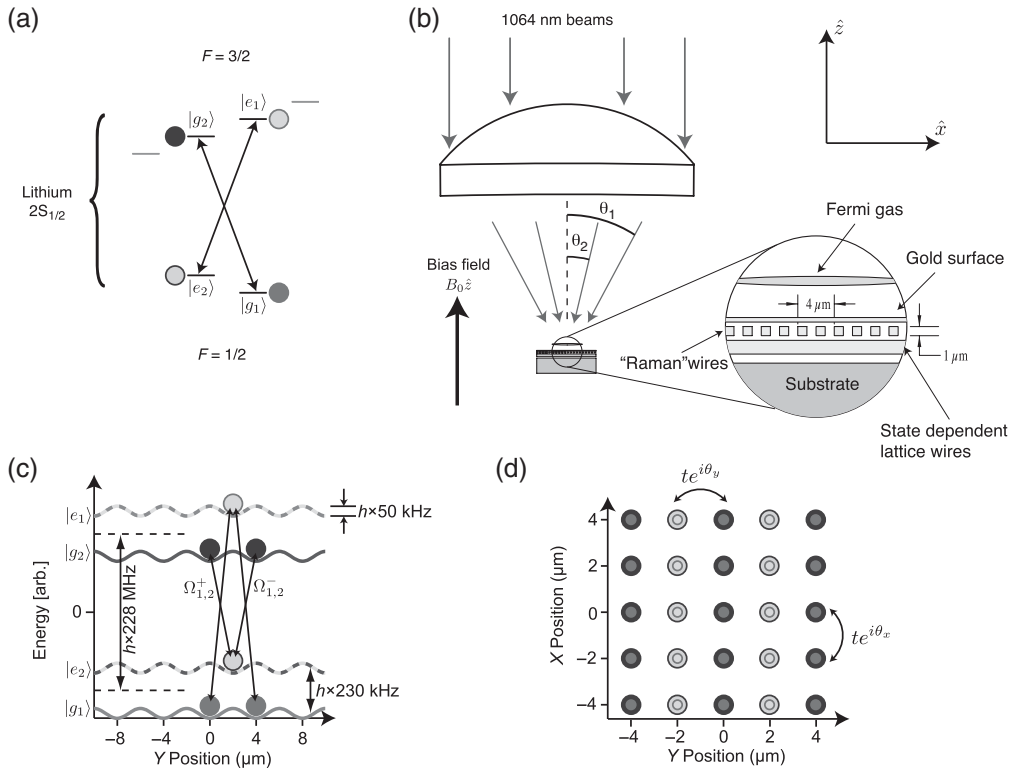


Figure 11.18 Experimental realization using an atom-chip and resulting model. (a) Level diagram identifying the four required states from within the ground $2S_{1/2}$ electronic manifold of fermionic ${}^6\text{Li}$. Each of the state-pairs $\{|g_1\rangle, |g_2\rangle\}$ and $\{|e_1\rangle, |e_2\rangle\}$ are chosen to be a pair of clock states (states with the same magnetic moment), and the indices 1 and 2 label the $SU(2)$ degree of freedom. Moreover, the $|g_{1,2}\rangle$ and $|e_{1,2}\rangle$ pairs have opposite magnetic moments, so they feel opposite-signed magnetic potentials. (b) Explicit experimental layout showing the origin of optical (state-independent) and magnetic (state-dependent) potentials and coupling fields. First, a state-independent, staggered lattice along \hat{x} is formed by the separate interference of two pairs of $\lambda = 1064 \text{ nm}$ laser beams slightly detuned from each other to eliminate cross-interference. The respective intersection angles are chosen so the lattice periods differ by a factor of two. Both beams reflect from the chip-surface and form vertically aligned lattices, trapping the degenerate Fermi gas about $5 \mu\text{m}$ above the surface. The inset shows the chip geometry, from top to bottom: a reflective chip surface, gold wires aligned along \hat{y} with a $1\text{-}\mu\text{m}$ spacing along \hat{x} (producing the $|g\rangle$ - $|e\rangle$ coupling), and finally gold wires aligned along \hat{x} with a $2\text{-}\mu\text{m}$ spacing (producing the state-dependent lattice). (c) Computed atomic potentials and coupling matrix elements. (d) The resulting lattice with couplings schematically illustrated. From Goldman *et al.* (2010).

incident angles to be $\theta_1 \approx 15^\circ$ and $\theta_2 \approx 7.5^\circ$ and in this way we realize the required lattice potentials, as shown in Figure 11.18. These beams also produce a lattice along \hat{z} , with a 550-nm period confining the fermions to a 2D plane.

- (ii) The states $|g\rangle$ and $|e\rangle$ experience oppositely-signed lattice potentials along y -axis, as in Figure 11.18(c). This can be directly implemented with the Zeeman shift $g\mu_B|B|$ of atoms, provided that $|g_{1,2}\rangle$ and $|e_{1,2}\rangle$ have equal but opposite magnetic moments g (i.e. are each on clock transitions). Figure 11.18(a) shows such a choice for ${}^6\text{Li}$, where $|g_1\rangle = |F = \frac{1}{2}, m_F = \frac{1}{2}\rangle$, $|g_2\rangle = |\frac{3}{2}, -\frac{1}{2}\rangle$, $|e_1\rangle = |\frac{3}{2}, \frac{1}{2}\rangle$, and $|e_2\rangle = |\frac{1}{2}, -\frac{1}{2}\rangle$. For this selection of states, at a bias field $B = 0.25$ G, the magnetic moments are correctly signed and differ by less than 1% in magnitude. The state-dependent lattice in Figure 11.18(c) can be directly realized using the Zeeman shift of an array of current-carrying wires with alternating $+I$ and $-I$ currents, spaced by a distance d (repeating with full period $2d = 4 \mu\text{m}$). Because the evanescent magnetic field decays exponentially $\propto \exp(-2\pi h/d)$, the height h of the atoms above the surface must be comparable to d . A modest $I = 5 \mu\text{A}$ current in wires $3 \mu\text{m}$ below the chip surface ($8 \mu\text{m}$ from the atoms) produces a $6E_R$ Zeeman lattice with a negligible 3 Hz hopping-matrix element.
- (iii) The model also requires hopping along they-axis with a phase depending on x : $t \exp(iqx)$. This can be realized with an additional grid of wires spaced by $d = 2 \mu\text{m}$ along x , with currents I_n . This provides *moving* Zeeman lattices with wavevector q (leading to effective Raman coupling) when $I_n = I_0 \sin(qnd - \omega t)$. The $\omega/2\pi \approx 228 \pm 0.23$ MHz transitions, indicated with arrows in Figure 11.18(c), $|e_1\rangle \rightarrow |g_1\rangle$ and $|e_2\rangle \rightarrow |g_2\rangle$, are independently controllable in phase, amplitude, and wavevector by commanding two concurrent running waves at the indicated resonant frequency. One can restrict to the case of equal amplitude and wavevector. The maximum wavevector q of this moving lattice is Nyquist-limited by $1/2d$. An additional contribution to the hopping along x that mixes the $|e\rangle$ and $|g\rangle$ states can be realized in a similar manner.
- (iv) Lastly, a potential gradient along y detuning the Raman beams into resonance is produced by simply shifting the center of the harmonic potential—equivalent to adding a linear gradient potential.

The proposal above represents the current experimental state of the art and is only one example. Recently there have been many other approaches developed that are ‘spontaneous-emission-proof’. We mention here in particular the superlattice approach developed in Gerbier and Dalibard (2010) and Mazza *et al.* (2010), since it allows for generation of $SU(4)$ gauge fields in three dimensions, and studies of 3D topological insulators, Wilson fermions, and axion quantum electrodynamics (Bermudez *et al.*, 2010). A recent, very detailed paper (Mazza *et al.*, 2011) describes a true ‘toolbox’ for generating $SU(N)$ gauge fields in two and three dimensions, as well as realizing various kinds of topological insulators on demand.

12

Many-body physics from a quantum information perspective

The interface between quantum information and many-body systems has become an extremely active research arena. Starting from the pioneering proposal of Jaksch and coauthors of using ultracold lattice gases for quantum information purposes (Jaksch *et al.*, 1999) and followed by the studies relating quantum phase transitions with entanglement (Osborne and Nielsen, 2002a; Osborne and Nielsen, 2002b; Osterloh *et al.*, 2002), a plethora of new studies either regarding many-body systems from a quantum information perspective or using many-body systems for quantum computation have appeared. The next two chapters focus on these two major subjects. Proposals for quantum computation and information tasks using many-body systems are presented in Chapter 13, while here we deal with the analysis of quantum correlations in condensed-matter and many-body phenomena using quantum information concepts. In order to make the book self-contained, we begin, after a short introduction, with a ‘crash course’ in quantum information in Section 12.2. In Section 12.3, we consider quantum phase transitions from a quantum information perspective. In Section 12.4, we discuss in detail area laws, i.e. laws that characterize correlations and entanglement in physically relevant many-body states. These laws entail statements about computational complexity of the corresponding Hamiltonians. Finally, Section 12.5 is devoted to the concept of MPSs and their generalizations, projected entangled pairs states (PEPS), and tensor networks states (TNS). These states provide, on one hand, a very useful ansatz for numerical applications and, on the other, a powerful tool for a theoretical understanding of the role of entanglement in quantum many-body theory.

12.1. Introduction

Quantum theory, formalized in the first few decades of the twentieth century, contains elements that are radically different from those used in the classical description of Nature. An important aspect in these fundamental differences is the existence of quantum correlations. In the classical description of Nature, full knowledge of the parts is equivalent to full knowledge of the whole. Thus, for a system formed of different subsystems, complete knowledge of the subsystems implies complete knowledge of the whole system. This is no longer true in the quantum realm where there exist states of composite systems for which we might have the complete information, while our knowledge about the composing subsystems’ states might be completely random. The paradoxical structure of such composite states is referred to as ‘entanglement’, a concept that can be traced back to the manuscripts

of Schrödinger around 1932. One may reach some paradoxical conclusions if one applies a classical description to states that have characteristic quantum signatures. During the last two decades it was realized that these fundamentally non-classical states, also described as ‘entangled states’, can provide us with something other than just paradoxes: they may be used to perform tasks that cannot be achieved with classical states. As benchmarks of the usefulness of entangled states one might mention the spectacular discoveries of (entanglement-based) quantum cryptography (Ekert, 1991), quantum dense coding (Bennett and Wiesner, 1992), quantum teleportation (Bennett *et al.*, 1993), and quantum purification (Bennett *et al.*, 1996*b*) among others.

Our knowledge and understanding of entanglement is still far from complete, although significant progress has been made in recent years (for a recent and very complete review see Horodecki *et al.* (2009)). In the next section we review the basic notions of entanglement in bipartite composite systems. Then we define formally what entangled states are, present some important criteria to discriminate entangled states from separable ones, and show how they can be classified according to their capability to perform some precisely defined tasks.

12.2. Crash course on quantum information

12.2.1 Bipartite pure states: Schmidt decomposition

We primarily consider bipartite systems here. These are traditionally associated with two observers called Alice (A) and Bob (B), who can be located in distant spatial regions. Let Alice’s physical system belong to the Hilbert space \mathcal{H}_A and that of Bob to \mathcal{H}_B . The joint physical system of Alice and Bob is then described in the tensor product Hilbert space $\mathcal{H}_A \otimes \mathcal{H}_B$.

Def. 12.1: A pure state of a bipartite system, i.e. a projector $|\psi_{AB}\rangle\langle\psi_{AB}|$ on a vector $|\psi_{AB}\rangle \in \mathcal{H}_A \otimes \mathcal{H}_B$, is a product state iff $|\psi_{AB}\rangle = |\psi_A\rangle \otimes |\psi_B\rangle$, that is, iff the states of the local subsystems are also pure states. Pure states that cannot be written in this form are called pure entangled states.

A paradigmatic example of an entangled state is the singlet state: $|\psi_{AB}^-\rangle = (|0_A\rangle \otimes |1_B\rangle - |1_A\rangle \otimes |0_B\rangle)/\sqrt{2}$, where $|0\rangle$ and $|1\rangle$ are two orthonormal states in Alice’s and Bob’s subspaces (in a more compact notation $|\psi_{AB}^-\rangle = (|01\rangle - |10\rangle)/\sqrt{2}$). Operationally, product states correspond to those states that can be *locally* prepared by Alice and Bob at two separate locations. Entangled states can, however, be prepared only after the particles of Alice and Bob have interacted either directly or by means of an ancillary system. A very useful representation of bipartite pure states is the so-called Schmidt representation.

Theorem 12.1 Schmidt decomposition: Every $|\psi_{AB}\rangle \in \mathcal{H}_A \otimes \mathcal{H}_B$ can be represented in an appropriately chosen basis as:

$$|\psi_{AB}\rangle = \sum_{i=1}^M a_i |e_i\rangle \otimes |f_i\rangle, \quad (12.1)$$

where $|e_i\rangle$ ($|f_i\rangle$) form a part of an orthonormal basis in \mathcal{H}_A (\mathcal{H}_B), $a_i > 0$, $\sum_{i=1}^M a_i^2 = 1$, and $M \leq \dim(\mathcal{H}_A), \dim(\mathcal{H}_B)$.

The positive numbers a_i are known as the Schmidt coefficients of $|\psi_{AB}\rangle$. Note that pure product states correspond to those states whose Schmidt decomposition has one and only one Schmidt coefficient. If the decomposition has more than one Schmidt coefficient, the state is entangled. Notice also that the squares of the Schmidt coefficients of a pure bipartite state $|\psi_{AB}\rangle$ are the eigenvalues of either of the reduced density matrices $\rho_A (= \text{Tr}_B \rho_{AB} = \sum_i \langle f_i | \rho_{AB} | f_i \rangle)$ and $\rho_B (= \text{Tr}_A \rho_{AB} = \sum_i \langle e_i | \rho_{AB} | e_i \rangle)$ of $|\psi_{AB}\rangle$. Thus whether a given pure bipartite state is separable or entangled is straightforward: the state is separable if the reduced density matrices are pure or equivalently a bipartite pure state is separable if it has only a single Schmidt coefficient.

12.2.2 Bipartite mixed states: separable and entangled states

The question of whether a mixed state is separable or not is much harder and, currently, it lacks a complete answer, even for composite systems of dimension as low as $\mathbb{C}^2 \otimes \mathbb{C}^4$. Let us consider the following preparation procedure of a bipartite state between Alice and Bob. Suppose Alice prepares her physical system in the state $|e_i\rangle$ and Bob prepares his system in the state $|f_i\rangle$. The description of their joint physical system is given by:

$$\rho_{AB} = |e_i\rangle\langle e_i| \otimes |f_i\rangle\langle f_i|. \quad (12.2)$$

Assume now that they can communicate over a classical channel (a phone line, for example). So, whenever Alice prepares the state $|e_i\rangle$ ($i = 1, 2, \dots, K$), which she does with probability p_i , she communicates that to Bob, and correspondingly Bob prepares his system in the state $|f_i\rangle$ ($i = 1, 2, \dots, K$). The joint state they have prepared is then

$$\rho_{AB} = \sum_{i=1}^K p_i |e_i\rangle\langle e_i| \otimes |f_i\rangle\langle f_i|, \quad (12.3)$$

where $\sum_i p_i = 1$ and $\forall p_i > 0$. It is important to point out here that the state displayed in eqn (12.3) is the most general state that Alice and Bob will be able to prepare by acting locally in their own subsystems and communicating between them classically. Such operations consisting of local operations plus classical communication are termed as LOCC. The formal definition of separability formulated in the seminal paper by R.F. Werner (1989) can be now stated.

Def. 12.2: A mixed state ρ_{AB} is separable if and only if it can be represented as a convex combination of the product of projectors on local states as stated in eqn (12.3). Otherwise, the mixed state is said to be entangled.

Entangled states, therefore, cannot be prepared locally by two parties even after communicating over a classical channel. To prepare such states, the physical systems must be brought together to interact.¹ Mathematically, a non-local unitary operator must *necessarily* act on

¹Due to the existence of the phenomenon of entanglement swapping (Żukowski *et al.*, 1993), one must suitably enlarge the notion of preparation of entangled states. So an entangled state between two particles can be prepared if and only if, either the two particles (call them A and B) themselves come together to interact at a time in the past, or two *other* particles (call them C and D) do the same, with C (D) having interacted beforehand with A (B).

the physical system described by $\mathcal{H}_A \otimes \mathcal{H}_B$ to produce an entangled state from an initial separable state. A non-local unitary operator on $\mathcal{H}_A \otimes \mathcal{H}_B$ is a unitary operator that cannot be expressed as $U_A \otimes U_B$, (with U_A (U_B) being a unitary operator acting on \mathcal{H}_A (\mathcal{H}_B)).

The general question of whether a given arbitrary bipartite state is separable or not turns out to be quite involved, since the decomposition presented in eqn (12.3) is not unique. Among the difficulties, notice that for an arbitrary state ρ_{AB} there is no stringent bound on the value of K in eqn (12.3), which is only limited by the Caratheodory theorem to $K \leq (\dim \mathcal{H})^2$, with $\mathcal{H} = \mathcal{H}_A \otimes \mathcal{H}_B$ (see Horodecki (1997) and Horodecki *et al.* (2009)). This bound implies that if ρ_{AB} is separable, then it admits a decomposition into projectors onto product states with $\leq K$ terms. Although the general answer to the separability problem still eludes us, there has been significant progress in recent years and we will review some of the advances below.

12.2.3 Operational entanglement criteria

To determine whether a mixed state is separable or not, some operational entanglement criteria providing necessary but not sufficient conditions for separability have been found. In particular we discuss here, because of its importance, the partial transposition criterion (Peres, 1993; Horodecki *et al.*, 1996a) and the majorization criterion (Nielsen and Kempe, 2001). There are several other criteria that will not be discussed here, see e.g. Horodecki and Horodecki (2000) and Rudolph (2003). Up to now, an operational criterion for detecting entanglement of an arbitrary given mixed state and which is both necessary and sufficient is still lacking. By operational we mean that the criterion is state-independent. There are, however, efficient numerical checks for such tasks. Using a semidefinite programming approach, it has been shown that separability can be tested in a finite number of steps, although there is no limit on the number of steps needed (Doherty *et al.*, 2002; Hulpke and Bruß, 2005). This means that these checks become extremely complex at high dimensions and in fact it has been shown that in general (i.e. without the restriction on dimensions) the separability problem belongs to the computational complexity class of NP-hard problems (Gurvits, 2003).

Partial transposition criterion We start by defining the operation of partial transposition.

Def. 12.3: Let ρ_{AB} be a completely arbitrary density matrix of a bipartite system. Without losing generality it can be expressed as

$$\rho_{AB} = \sum_{i,j=1}^{N_A} \sum_{\mu,\nu=1}^{N_B} a_{ij}^{\mu\nu} (|i\rangle\langle j|)_A \otimes (|\mu\rangle\langle \nu|)_B, \quad (12.4)$$

where $\{|i\rangle\}$ ($\{|\mu\rangle\}$) with $i = 1, 2, \dots, N_A$, $N_A \leq \dim \mathcal{H}_A$ ($\mu = 1, 2, \dots, N_B$, $N_B \leq \dim \mathcal{H}_B$) is a set of orthonormal vectors in \mathcal{H}_A (\mathcal{H}_B). The partial transposition ρ_{AB}^{TA} of ρ_{AB} with respect to subsystem A , is defined as:

$$\rho_{AB}^{TA} = \sum_{i,j=1}^{N_A} \sum_{\mu,\nu=1}^{N_B} a_{ij}^{\mu\nu} (|j\rangle\langle i|)_A \otimes (|\mu\rangle\langle \nu|)_B. \quad (12.5)$$

A similar definition exists for the partial transposition of ρ_{AB} with respect to Bob's subsystem. Notice that $\rho_{AB}^{T_B} = (\rho_{AB}^{T_A})^T$. Although the partial transposition depends upon the choice of the local basis in which ρ_{AB} is written, its eigenvalues are basis-independent. We say that a state has positive partial transposition (PPT), whenever $\rho_{AB}^{T_A} \geq 0$, i.e. the eigenvalues of $\rho_{AB}^{T_A}$ are non-negative. Otherwise, the state is said to be non-positive under partial transposition (NPT). Note that transposition is equivalent to time-reversal.

Theorem 12.2 (Peres, 1993): *If a state ρ_{AB} is separable, then*

$$\rho_{AB}^{T_A} \geq 0 \quad \text{and} \quad \rho_{AB}^{T_B} = \left(\rho_{AB}^{T_A} \right)^T \geq 0.$$

Proof: Since ρ_{AB} is separable, it can be written as

$$\rho_{AB} = \sum_{i=1}^K p_i |e_i\rangle\langle e_i| \otimes |f_i\rangle\langle f_i| \geq 0. \quad (12.6)$$

Now performing the partial transposition with respect to A, we have

$$\rho_{AB}^{T_A} = \sum_{i=1}^K p_i (|e_i\rangle\langle e_i|)^T \otimes |f_i\rangle\langle f_i| = \sum_{i=1}^K p_i |e_i^*\rangle\langle e_i^*| \otimes |f_i\rangle\langle f_i| \geq 0. \quad (12.7)$$

Note that in eqn (12.7), we have used the fact that $A^\dagger = (A^*)^T$. \square

The above definition leads to the PPT criterion:

PPT criterion: For an arbitrary bipartite state ρ_{AB} , a negative eigenvalue of any of its partial transpositions ($\rho_{AB}^{T_{A/B}}$) implies that the state is entangled. Such state is said to be NPT, that is, non-positive defined in front of partial transposition.

The partial transposition criterion provides a straightforward manner to detect all entangled states that are NPT. Let us illustrate the above criterion with the singlet, for which, trivially, the partial transposition reads;

$$\rho_{AB}^{T_A} = (|\psi_{AB}^-\rangle\langle\psi_{AB}^-|)^{T_A} = \begin{pmatrix} 0 & 0 & 0 & -1 \\ 0 & 1 & 0 & 0 \\ 0 & 0 & 1 & 0 \\ -1 & 0 & 0 & 0 \end{pmatrix}, \quad (12.8)$$

and has eigenvalues $\lambda = \pm 1$.

The class of NPT entangled states is huge. It turns out, however, that there exist PPT states that are also entangled (see Horodecki (1997) and also Horodecki *et al.* (2009)). Moreover, the set of PPT entangled states is not a set of measure zero (Życzkowski *et al.*, 1998). It is, therefore, important to have further independent criteria of entanglement to detect entangled PPT states. It is worth mentioning that PPT states that are entangled

form the only known examples of the ‘bound entangled states’, i.e. states from which one cannot distil entanglement via local operations and classical communications, even if one has an unlimited number of copies of them (see Horodecki *et al.* (1998) and Horodecki *et al.* (2009)). The conjecture of the existence of NPT ‘bound entangled’ states is one of the most challenging open problems in quantum information theory (DiVincenzo *et al.*, 2000; Dür *et al.*, 2000). It is important to observe that both separable and PPT states form convex sets. While Theorem 12.2 imposes a necessary but not sufficient condition of separability in any arbitrary dimension, for some special cases the partial transposition criterion is both a necessary and sufficient condition for separability:

Theorem 12.3 (Horodecki *et al.*, 1996a): *In $\mathbb{C}^2 \otimes \mathbb{C}^2$ or $\mathbb{C}^2 \otimes \mathbb{C}^3$, a state ρ is separable if and only if $\rho^{T_A} \geq 0$.*

Majorization The partial transposition criterion, although powerful, is not able to detect all entangled states. It is therefore necessary to find other independent criteria. The majorization criterion that we discuss now is *not* more powerful in detecting entanglement than partial transposition (Hiroshima, 2003). In other words, if a state is not detected by the PPT criterion, neither will it be by the majorization criterion. This criterion has, however, independent roots and gives some insight into the thermodynamic properties of entanglement. Before presenting the criterion we define majorization (Marshall and Olkin, 1979).

Def. 12.4: Let $x = (x_1, x_2, \dots, x_d)$, and $y = (y_1, y_2, \dots, y_d)$ be two probability distributions, arranged in decreasing order, i.e. $x_1 \geq x_2 \geq \dots \geq x_d$ and $y_1 \geq y_2 \geq \dots \geq y_d$. Then we say ‘ x is majorized by y ’, denoted as $x \prec y$, if

$$\sum_{i=1}^l x_i \leq \sum_{i=1}^l y_i, \quad (12.9)$$

where $l = 1, 2, \dots, d-1$ and equality holds when $l = d$.

Theorem 12.4 (Nielsen and Kempe, 2001): *If a state ρ_{AB} is separable, then*

$$\lambda(\rho_{AB}) \prec \lambda(\rho_A) \quad \text{and} \quad \lambda(\rho_{AB}) \prec \lambda(\rho_B), \quad (12.10)$$

where $\lambda(\rho_{AB})$ is the set of eigenvalues of ρ_{AB} , and $\lambda(\rho_A)$ and $\lambda(\rho_B)$ are the sets of eigenvalues of the corresponding reduced density matrices of the state ρ_{AB} , where all the sets are arranged in decreasing order.

The majorization criterion implies that a given bipartite state is entangled if eqn (12.10) is violated. Let us notice an interesting relation between the majorization and the entropy. To this end, we recall that while the global state of the singlet is pure, the local states $\rho_{A(B)} = \text{Tr}_{B(A)}(|\psi^-\rangle_{AB}\langle\psi^-|)$ are maximally mixed. In particular, this implies that the von Neumann entropy of the singlet is lower than any of its reductions, where the von Neumann entropy of ρ is $S(\rho) = -\text{Tr}\rho\log_2\rho$. Since the von Neumann entropy can also be used to quantify disorder in a quantum state, this indicates that there are bipartite quantum states for which the global disorder can be smaller than the disorder of any of the

local subsystems. This is clearly a non-classical effect, as for two classical random variables the Shannon entropy² of the joint distribution cannot be smaller than the Shannon entropy of each of them. In Horodecki *et al.* (1996b), it was shown that a similar fact holds for separable states:

Theorem 12.5: *If a state ρ_{AB} is separable, then*

$$S(\rho_{AB}) \geq S(\rho_A) \quad \text{and} \quad S(\rho_{AB}) \geq S(\rho_B), \quad (12.11)$$

S being the von Neumann entropy.

Although the von Neumann entropy is an important notion for quantifying ‘disorder’, the theory of majorization is a more stringent quantifier (Marshall and Olkin, 1979): For two probability distributions x and y , $x \prec y$ if and only if $x = Dy$, where D is a doubly stochastic matrix.³ Moreover, $x \prec y$ implies that $H(\{x_i\}) \geq H(\{y_i\})$. Quantum mechanics therefore allows the existence of states for which global ‘disorder’ is greater than local ‘disorder’ even in the sense of majorization. A density matrix that satisfies eqn (12.10), automatically satisfies eqn (12.11). In this sense, Theorem 12.4 is a generalization of Theorem 12.5.

12.2.4 Non-operational entanglement criteria

We move now into the mathematical formalism of maps to show that the Hahn–Banach theorem can be used to obtain a very elegant entanglement criterion known as ‘entanglement witnesses’ (Terhal, 2001). We also introduce the notion of positive maps, and present the entanglement criterion based on it. Both criteria are ‘non-operational’, meaning that the criteria are not state-independent, as they were the previous ones. Nevertheless they provide an important insight into the structure of the set of entangled states. Moreover, the concept of entanglement witnesses can be used, and has been used, to detect entanglement experimentally, performing only a few *local* measurements and assuming some prior knowledge of the density matrix (Guhne *et al.*, 2002; Bourennane *et al.*, 2004).

Entanglement witnesses Crucial to the concept of entanglement witnesses, is the Hahn–Banach theorem, which we present here without proving it (see Alt (1985)):

Theorem 12.6: *Let S be a convex compact set in a finite dimensional Banach space. Let ρ be a point in the space with $\rho \notin S$, then there exists a hyperplane that separates ρ from S .*

A hyperplane denotes a linear subspace whose dimension smaller by one than the dimension of the space itself. The theorem is schematically illustrated in Figure 12.1. Let us characterize the hyperplane by an vector W orthogonal to it and with W chosen such that it points towards the convex set S . Every state ρ can be parametrized by its distance from the plane by projecting ρ onto the chosen orthonormal vector and using the trace as scalar product, i.e. $\text{Tr}(W\rho)$. This measure is either positive, zero, or negative. We now

²The Shannon entropy of a random variable X , taking up values X_i with probabilities p_i , is given by $H(X) = H(\{p_i\}) = - \sum_i p_i \log_2 p_i$.

³A matrix $D = (D_{ij})$ is said to be doubly stochastic if $D_{ij} \geq 0$ and $\sum_i D_{ij} = \sum_j D_{ij} = 1$.

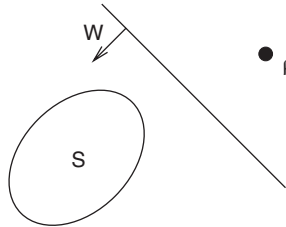


Figure 12.1 Schematic picture of the Hahn–Banach theorem. The (unique) unit vector orthonormal to the hyperplane can be used to define *right* and *left* with respect to the hyperplane by using the sign of the scalar product.

suppose that S is the convex compact set of all separable states. According to our choice of basis in Figure 12.1, every separable state has a positive distance while there are some entangled states with a negative distance. This leads to the concept of entanglement witness: an observable that detects a given entangled state ρ and hence the name.

Def. 12.5: A Hermitian operator W is called an entanglement witness (EW) iff $\text{Tr}(W\sigma) \geq 0$, $\forall \sigma \in S$ (separable set) and there exists at least one $\rho \notin S$ such that $\text{Tr}(W\rho) < 0$.

The following lemma and observation are useful for exploiting the properties of witness operators.

Lemma 12.1: $\text{Tr}(\rho_{AB}^{T_A} \sigma_{AB}) = \text{Tr}(\rho_{AB} \sigma_{AB}^{T_A})$.

Observation 12.1: The space of linear operators acting on \mathcal{H} (denoted by $\mathcal{B}(\mathcal{H})$) is itself a Hilbert space, with the (Euclidean) scalar product

$$\langle A | B \rangle = \text{Tr}(A^\dagger B) \quad A, B \in \mathcal{B}(\mathcal{H}). \quad (12.12)$$

This scalar product is equivalent to writing A and B row-wise as vectors, and scalar-multiplying them:

$$\text{Tr}(A^\dagger B) = \sum_{ij} A_{ij}^* B_{ij} = \sum_{k=1}^{(\dim \mathcal{H})^2} a_k^* b_k. \quad (12.13)$$

With the help of the above lemma (Lemma 12.1) we can show now how the structure of the witness operator W can resolve properties of the entangled state ρ detected by W .

Def. 12.6: An EW is decomposable if and only if there exist operators P, Q with

$$W = P + Q^{T_A}, \quad P, Q \geq 0. \quad (12.14)$$

Lemma 12.2: A decomposable EW cannot detect PPT entangled states.

Proof: Let δ be a PPT entangled state and W be a decomposable EW. Then

$$\mathrm{Tr}(W\delta) = \mathrm{Tr}(P\delta) + \mathrm{Tr}(Q^{T_A}\delta) = \mathrm{Tr}(P\delta) + \mathrm{Tr}(Q\delta^{T_A}) \geq 0. \quad (12.15)$$

Here we used Lemma 12.1. \square

Def. 12.7: An EW is called non-decomposable entanglement witness (nd-EW) if and only if there exists at least one PPT entangled state that is detected by the witness.

Using these definitions, we can now restate the consequences of the Hahn–Banach theorem in several ways:

Theorem 12.7 (Woronowicz, 1976; Choi, 1982; Horodecki *et al.*, 1996a; Lewenstein *et al.*, 2000; Terhal, 2001):

1. ρ is entangled if and only if, there exist a witness, W , s.t. $\mathrm{Tr}(\rho W) < 0$.
2. ρ is a PPT entangled state if and only if there exist a nd-EW, W , s.t. $\mathrm{Tr}(\rho W) < 0$.
3. σ is separable if and only if \forall EW, W , s.t. $\mathrm{Tr}(W\sigma) \geq 0$.

Notice that although, from a theoretical point of view, the theorem is quite powerful and elegant, it does not provide a way to construct the appropriate witness operator given a state ρ . As schematically shown in Figure 12.2, different witness operators detect entanglement for different sets of states. In what follows we give some examples of how such witnesses can be constructed.

- *Example 1.* Let us construct a witness operator in the simplest possible composite system $\mathbb{C}^2 \otimes \mathbb{C}^2$. To this end, we take a maximal entangled pure state in this space (i.e. those with all Schmidt coefficients equal), for instance $|\phi^+\rangle = \frac{1}{\sqrt{2}}(|00\rangle + |11\rangle)$.

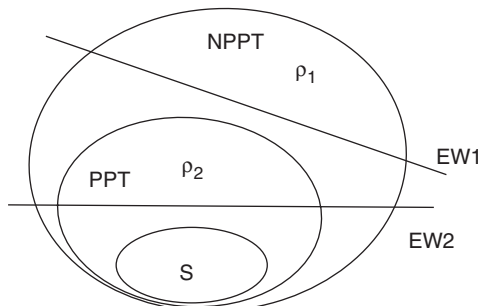


Figure 12.2 Schematic view of the Hilbert-space with two states ρ_1 and ρ_2 and two witnesses $EW1$ and $EW2$. $EW1$ is a decomposable EW and detects only NPT states, such as ρ_1 . $EW2$ is a non-decomposable EW and it also detects some PPT states, such as ρ_2 . Note that none of the witnesses detects *all* entangled states.

A witness operator is immediately obtained from $W = Q^{T_A} = (|\phi^+\rangle\langle\phi^+|)^{T_A}$, where

$$Q = \begin{pmatrix} \frac{1}{2} & 0 & 0 & \frac{1}{2} \\ 0 & 0 & 0 & 0 \\ 0 & 0 & 0 & 0 \\ \frac{1}{2} & 0 & 0 & \frac{1}{2} \end{pmatrix} \quad \text{and} \quad Q^{T_A} = \begin{pmatrix} \frac{1}{2} & 0 & 0 & 0 \\ 0 & 0 & \frac{1}{2} & 0 \\ 0 & \frac{1}{2} & 0 & 0 \\ 0 & 0 & 0 & \frac{1}{2} \end{pmatrix}. \quad (12.16)$$

It is straightforward to verify that indeed $W = Q^{T_A}$ is a witness operator, since for any product state $|e, f\rangle = |e\rangle|f\rangle$, $\text{Tr}(W|e, f\rangle\langle e, f|) \geq 0$ and therefore using the convexity of the set of separable states, the expectation value is positive for any separable state. Then, using $|\psi^-\rangle = \frac{1}{\sqrt{2}}(|01\rangle - |10\rangle)$, we can rewrite the witness:

$$W = Q^{T_A} = \frac{1}{2} (I - 2|\psi^-\rangle\langle\psi^-|). \quad (12.17)$$

This witness now detects $|\psi^-\rangle$ since $\text{Tr}(W|\psi^-\rangle\langle\psi^-|) = -1/2$.

- *Example 2.* Our example here follows trivially from the fact that any decomposable witness $W' = P + Q^{T_A}$ for all separable states σ fulfils

$$\text{Tr}(W'\sigma) \geq 0. \quad (12.18)$$

Proof: If σ is separable, then it can be written as a convex sum of product vectors. So if eqn (12.18) holds for any product vector $|e, f\rangle$, any separable state will also satisfy the same:

$$\begin{aligned} \text{Tr}(W'|e, f\rangle\langle e, f|) &= \langle e, f|W'|e, f\rangle \\ &= \underbrace{\langle e, f|P|e, f\rangle}_{\geq 0} + \underbrace{\langle e, f|Q^{T_A}|e, f\rangle}_{\geq 0}, \end{aligned} \quad (12.19)$$

because

$$\langle e, f|Q^{T_A}|e, f\rangle = \text{Tr}(Q^{T_A}|e, f\rangle\langle e, f|) = \text{Tr}(Q|e^*, f\rangle\langle e^*, f|) \geq 0. \quad (12.20)$$

Here we used Lemma 12.1 and $P, Q \geq 0$. This argument shows that $W = Q^{T_A}$ is a suitable witness also. \square

Positive maps So far, we have only considered states belonging to a Hilbert space \mathcal{H} , and operators acting on the same Hilbert space. However, the space of operators $\mathcal{B}(\mathcal{H})$ also has a Hilbert-space structure. We now look at transformations of operators, the so-called ‘maps’, which can be regarded as *superoperators*. As we will see, this will lead us to an important characterization of entangled and separable states. We start by defining linear maps:

Def. 12.8: A linear, self-adjoint map ϵ is a transformation

$$\epsilon : \mathcal{B}(\mathcal{H}_B) \rightarrow \mathcal{B}(\mathcal{H}_C),$$

which is linear, i.e.

$$\epsilon(\alpha O_1 + \beta O_2) = \alpha\epsilon(O_1) + \beta\epsilon(O_2), \quad \forall O_1, O_2 \in \mathcal{B}(\mathcal{H}_B),$$

where α, β are complex numbers, and maps Hermitian operators onto Hermitian operators, i.e.

$$\epsilon(O^\dagger) = (\epsilon(O))^\dagger, \quad \forall O \in \mathcal{B}(\mathcal{H}_B).$$

For brevity, we will only write ‘linear map’, instead of ‘linear self-adjoint map’. The following definitions help to further characterize linear maps.

Def. 12.9: A linear map ϵ is called trace preserving if

$$\text{Tr}(\epsilon(O)) = \text{Tr}(O), \quad \forall O \in \mathcal{B}(\mathcal{H}_B). \quad (12.21)$$

Def. 12.10: A linear, self-adjoint map ϵ is called positive if

$$\forall \rho \in \mathcal{B}(\mathcal{H}_B), \quad \rho \geq 0 \quad \Rightarrow \quad \epsilon(\rho) \geq 0. \quad (12.22)$$

Positive maps therefore have therefore the property of mapping positive operators onto positive operators. It turns out that by considering maps that are a tensor product of a positive operator acting on subsystem A and the identity acting on subsystem B (or vice versa), one can learn about the properties of the composite system.

Def. 12.11: A positive linear map ϵ is completely positive if for any tensor extension of the form

$$\epsilon' = \mathcal{I}_A \otimes \epsilon,$$

where

$$\epsilon' : \mathcal{B}(\mathcal{H}_A \otimes \mathcal{H}_B) \rightarrow \mathcal{B}(\mathcal{H}_A \otimes \mathcal{H}_C),$$

ϵ' is positive. Here \mathcal{I}_A is the identity map on $\mathcal{B}(\mathcal{H}_A)$.

Let us illustrate this with some examples of completely positive (example 1) and positive, but not completely positive (example 2) maps.

- *Example 1: Hamiltonian evolution of a quantum system.* Let $O \in \mathcal{B}(\mathcal{H}_B)$, U a unitary matrix, and define ϵ as:

$$\begin{aligned}\epsilon : \mathcal{B}(\mathcal{H}_B) &\rightarrow \mathcal{B}(\mathcal{H}_B) \\ \epsilon(O) &= UOU^\dagger.\end{aligned}\tag{12.23}$$

As an example for this map, consider the time-evolution of a density matrix. It can be written as $\rho(t) = U(t)\rho(0)U^\dagger(t)$, i.e. in the form given above. Clearly this map is linear, self-adjoint, positive and trace-preserving. It is also completely positive, because for $0 \leq \rho_{AB} \in \mathcal{B}(\mathcal{H}_A \otimes \mathcal{H}_B)$,

$$(\mathcal{I}_A \otimes \epsilon)\rho_{AB} = (\mathcal{I}_A \otimes U)\rho_{AB}(\mathcal{I}_A \otimes U^\dagger) = \tilde{U}\rho_{AB}\tilde{U}^\dagger,\tag{12.24}$$

where \tilde{U} is unitary. But then $\langle \psi | \tilde{U}\rho_{AB}\tilde{U}^\dagger | \psi \rangle \geq 0$ if and only if $\langle \psi | \rho_{AB} | \psi \rangle \geq 0$ (since the scalar product is not changed by unitary evolution).

- *Example 2: Transposition.* An example of a positive, but not completely positive map is the transposition T defined as:

$$\begin{aligned}T : \mathcal{B}(\mathcal{H}_B) &\rightarrow \mathcal{B}(\mathcal{H}_B) \\ T(\rho) &= \rho^T.\end{aligned}\tag{12.25}$$

Of course this map is positive, but it is not completely positive, because

$$(\mathcal{I}_A \otimes T)\rho_{AB} = \rho_{AB}^{T_B},\tag{12.26}$$

and we know that there exist states for which $\rho \geq 0$ but $\rho^{T_B} \not\geq 0$.

We can now define what a decomposable map is:

Def. 12.12: A positive map is called decomposable if and only if it can be written as

$$\epsilon = \epsilon_1 + \epsilon_2 T,\tag{12.27}$$

where ϵ_1, ϵ_2 are completely positive maps and T is the operation of transposition.

12.2.5 Positive maps and entangled states

Partial transposition can be regarded as a particular case of a map that is positive but not completely positive. We have already seen that this particular positive but not completely positive map gives us a way to discriminate entangled states from separable states. The theory of positive maps provides us with stronger conditions for separability, as shown in Horodecki *et al.* (1996a).

Theorem 12.8: A state $\rho \in \mathcal{B}(\mathcal{H}_A \otimes \mathcal{H}_B)$ is separable if and only if for all positive maps

$$\epsilon : \mathcal{B}(\mathcal{H}_B) \rightarrow \mathcal{B}(\mathcal{H}_C), \quad (12.28)$$

we have

$$(\mathcal{I}_A \otimes \epsilon)\rho \geq 0. \quad (12.29)$$

Proof: $[\Rightarrow]$ As ρ is separable, we can write it as

$$\rho = \sum_{k=1}^K p_k |e_k\rangle\langle e_k| \otimes |f_k\rangle\langle f_k|, \quad (12.30)$$

for some $K > 0$. On this state, $(\mathcal{I}_A \otimes \epsilon)$ acts as

$$(\mathcal{I}_A \otimes \epsilon)\rho = \sum_{k=1}^P p_k |e_k\rangle\langle e_k| \otimes \epsilon(|f_k\rangle\langle f_k|) \geq 0, \quad (12.31)$$

where the last \geq follows because $|f_k\rangle\langle f_k| \geq 0$ and ϵ is positive.

$[\Leftarrow]$ The proof in this direction is not as easy as the only-if direction. We shall prove it at the end of this section. Theorem 12.8 can also be restated in the following form:

Theorem 12.9 (Horodecki *et al.*, 1996a): A state $\rho \in \mathcal{B}(\mathcal{H}_A \otimes \mathcal{H}_B)$ is entangled if and only if there exists a positive map $\epsilon : \mathcal{B}(\mathcal{H}_B) \rightarrow \mathcal{B}(\mathcal{H}_C)$, such that

$$(\mathcal{I}_A \otimes \epsilon)\rho \not\geq 0. \quad (12.32)$$

Note that eqn (12.32) can never hold for maps ϵ that are completely positive (while for non-positive maps it may hold even for separable states). Hence positive but not completely positive maps can be used to detect entanglement.

In order to complete the proof of Theorem 12.8, we first introduce the Jamiołkowski isomorphism (Jamiołkowski, 1972; Choi, 1982) between operators and maps: given an operator $E \in \mathcal{B}(\mathcal{H}_B \otimes \mathcal{H}_C)$, and an orthonormal product basis $|k, l\rangle$, we define a map by

$$\epsilon : \mathcal{B}(\mathcal{H}_B) \rightarrow \mathcal{B}(\mathcal{H}_C),$$

$$\epsilon(\rho) = \sum_{k_1, l_1, k_2, l_2} {}_{BC}\langle k_1 l_1 | E | k_2 l_2 \rangle_{BC} |l_1\rangle_{CB} \langle k_1 | \rho | k_2 \rangle_{BC} \langle l_2|, \quad (12.33)$$

or in short form,

$$\epsilon(\rho) = \text{Tr}_B(E\rho^{T_B}). \quad (12.34)$$

This shows how to construct the map ϵ from a given operator E . To construct an operator E from a given map ϵ we use the state

$$|\psi^+\rangle = \frac{1}{\sqrt{M}} \sum_{i=1}^M |i\rangle_B |i\rangle_B, \quad (12.35)$$

where $M = \dim \mathcal{H}_B$, to obtain

$$E = M (I_B \otimes \epsilon) (|\psi^+\rangle \langle \psi^+|). \quad (12.36)$$

This isomorphism between maps and operators results in the following properties:

Theorem 12.10 (Jamiolkowski, 1972; Woronowicz, 1976; Horodecki *et al.*, 1996*a*; Lewenstein *et al.*, 2000; Terhal, 2001):

1. $E \geq 0$ if and only if ϵ is a completely positive map.
2. E is an entanglement witness if and only if ϵ is a positive map.
3. E is a decomposable entanglement witness if and only if ϵ is decomposable.
4. E is a non-decomposable entanglement witness if and only if ϵ is non-decomposable and positive.

The demonstration of Theorem 12.10 is lengthy but straightforward (see, for example, Horodecki *et al.* (2009)). To prove the \Leftarrow direction of Theorem 12.8 or, equivalently, the \Rightarrow direction of Theorem 12.9, we have to show that if ρ_{AB} is entangled there exists a positive map $\epsilon : \mathcal{B}(\mathcal{H}_A) \rightarrow \mathcal{B}(\mathcal{H}_C)$ such that $(\epsilon \otimes \mathcal{I}_B) \rho_{AB}$ is not positive definite. If ρ_{AB} is entangled, then there exists an entanglement witness W_{AB} such that

$$\text{Tr}(W_{AB}\rho_{AB}) < 0 \quad \text{and} \quad \text{Tr}(W_{AB}\sigma_{AB}) \geq 0, \quad (12.37)$$

for all separable σ_{AB} . W_{AB} is an entanglement witness (which detects ρ_{AB}) if and only if W_{AB}^T (note the complete transposition) is also an entanglement witness (which detects ρ_{AB}^T).

We define a map by

$$\epsilon : \mathcal{B}(\mathcal{H}_A) \rightarrow \mathcal{B}(\mathcal{H}_C), \quad (12.38)$$

$$\epsilon(\rho) = \text{Tr}_A(W_{AC}^T \rho_{AB}^{TA}), \quad (12.39)$$

where $\dim \mathcal{H}_C = \dim \mathcal{H}_B = M$. Then

$$(\epsilon \otimes \mathcal{I}_B)(\rho_{AB}) = \text{Tr}_A(W_{AC}^T \rho_{AB}^{TA}) = \text{Tr}_A(W_{AC}^T \rho_{AB}) = \tilde{\rho}_{CB}, \quad (12.40)$$

where we have used Lemma 12.1 and the fact that $T = T_A \circ T_C$. To complete the proof one has to show that $\tilde{\rho}_{CB} \not\geq 0$, which can be done by showing that ${}_{CB}\langle \psi^+ | \tilde{\rho}_{CB} | \psi^+ \rangle_{CB} < 0 = \text{Tr}(W_{AB}\rho_{AB})$, where $|\psi^+\rangle_{CB} = \frac{1}{\sqrt{M}} \sum_i |ii\rangle_{CB}$, with $\{|i\rangle\}$ being an orthonormal basis. \square

12.2.6 Entanglement measures

The partial transposition criterion provides a tool to check whether a given state is entangled or not. Entanglement measures, on the other hand, try to quantify *how much* entanglement a given state has, once we know that it is entangled. This quantification is necessary, not only because entanglement is viewed as a resource in quantum information theory, but also as a way to classify the states. There are several complementary ways to quantify entanglement. Here, we present three possible ways to do so.

Entanglement of formation (Bennett *et al.*, 1996a) Consider a bipartite pure state $|\psi_{AB}\rangle$ shared between Alice and Bob. Given $nE(\psi_{AB})$ copies of the singlet state shared between Alice and Bob, they can, by means of LOCC, transform them into n copies of the state $|\psi_{AB}\rangle$, if n is large enough and where:

$$E(\psi_{AB}) = S(\rho_A) = S(\rho_B), \quad (12.41)$$

with ρ_A and ρ_B being the local density matrices of $|\psi_{AB}\rangle$. Here $S(\rho)$ denotes the von Neumann entropy. Note that for separable (pure) states, E vanishes. If the state $|\psi_{AB}\rangle$ describes a $\mathbb{C}^{d_1} \otimes \mathbb{C}^{d_2}$ system, then E ranges from 0 to $\log_2 d$, where $d = \min\{d_1, d_2\}$. A state is called maximally entangled in $\mathbb{C}^{d_1} \otimes \mathbb{C}^{d_2}$ if its E is $\log_2 d$. Thus since the singlet state is a maximally entangled state in $\mathbb{C}^2 \otimes \mathbb{C}^2$, its entanglement is unity. The entanglement of a singlet is also-called an *ebit* and it is used as a unit of reference.

With the above terminology we can, therefore, say that if the state $|\psi_{AB}\rangle$ has $E(\psi_{AB})$ ebits, this is the minimum number of singlets required to prepare a copy of the state $|\psi_{AB}\rangle$ and thus, we call $E(\psi_{AB})$ the ‘entanglement of formation’ of $|\psi_{AB}\rangle$.

For (bipartite) pure states, the entanglement of formation is essentially the only (asymptotic) measure of entanglement, as the singlet state can be locally obtained from a pure state at the same asymptotic rate (Bennett *et al.*, 1996a).

Let us now define this measure for mixed states (Bennett *et al.*, 1996b). Since any mixed state can be expressed as a mixture (convex combination) of pure states:

$$\rho_{AB} = \sum_i p_i |\psi_{AB}^i\rangle \langle \psi_{AB}^i|, \quad (12.42)$$

one is tempted to define the entanglement of formation as its average $\sum_i p_i E(\psi^i)$. However, a mixed state can be decomposed into pure states in an infinite number of ways. In other words, the above decomposition is not canonical, neither do the pure states appearing in the decomposition have to be orthonormal. The entanglement of formation E_F of ρ_{AB} is defined as the minimum over all such averages (Bennett *et al.*, 1996b):

$$E_F(\rho_{AB}) = \min \sum_i p_i E(\psi_{AB}^i), \quad (12.43)$$

where the minimum is taken over all decompositions of ρ_{AB} into pure states. Generally, problems involving optimization (minimization or maximization over a set) are extremely hard and hence to find E_F for an arbitrary state is not normally possible. A constructive procedure for calculating the entanglement of formation of any mixed state in $\mathbb{C}^2 \otimes \mathbb{C}^2$ was

provided in Hill and Wootters (1997) and Wootters (1998). For states in higher dimensions, the entanglement of formation (or, even more difficult, the asymptotic entanglement cost for many copies) has been calculated for only a few rare instances using certain symmetries.

Concurrence (Hill and Wootters, 1997) The entanglement of formation of an arbitrary state in $\mathbb{C}^2 \otimes \mathbb{C}^2$ is given by:

$$E_F(\rho) = H\left(\frac{1 + \sqrt{1 - C^2}}{2}\right), \quad (12.44)$$

where

$$C = C(\rho) = \max \{0, \lambda_1 - \lambda_2 - \lambda_3 - \lambda_4\}, \quad (12.45)$$

and $H(\cdot)$ is the binary entropy function, defined for $0 \leq x \leq 1$ as $H(x) = -x \log_2 x - (1-x) \log_2(1-x)$. The λ_i are the eigenvalues (with λ_1 being the largest) of the Hermitian matrix $\left(\rho^{\frac{1}{2}} \tilde{\rho} \rho^{\frac{1}{2}}\right)^{\frac{1}{2}}$, where $\tilde{\rho} = \sigma_y \otimes \sigma_y \rho^* \sigma_y \otimes \sigma_y$, with the complex conjugation over ρ being taken in the σ_z eigenbasis. For ρ_{AB} acting in $\mathbb{C}^2 \otimes \mathbb{C}^2$, the quantity $C(\rho_{AB})$ is called the concurrence. Moreover, the entanglement of formation and the concurrence are monotonically non-decreasing functions of each other, with both quantities ranging from 0 to 1. For this reason, in $\mathbb{C}^2 \otimes \mathbb{C}^2$ we can also use the concurrence as a measure of entanglement.

Logarithmic negativity The partial transposition criterion, which is easily computable, can also be used to define a useful measure of entanglement. To define the measure, we introduce first the so-called negativity. The negativity $N(\rho_{AB})$ of a bipartite state ρ_{AB} is defined as the absolute value of the sum of the negative eigenvalues of $\rho_{AB}^{T_A}$. The logarithmic negativity (LN) is defined as in Vidal and Werner (2002):

$$E_N(\rho_{AB}) = \log_2(2N(\rho_{AB}) + 1). \quad (12.46)$$

For two-qubit states, $\rho_{AB}^{T_A}$ has at most one negative eigenvalue (Sanpera *et al.*, 1998). Moreover, it follows from our discussion in previous subsections that for states in $\mathbb{C}^2 \otimes \mathbb{C}^2$ and $\mathbb{C}^2 \otimes \mathbb{C}^3$, a positive LN implies that the state is entangled while $E_N = 0$ implies that the state is separable.

The LN has an operational interpretation in terms of another measure related to the entanglement of formation (Audenaert *et al.*, 2003) and is, moreover, an entanglement monotone, i.e. it does not increase under deterministic LOCC (Plenio *et al.*, 2005). However, it is not a convex function of the states.

12.3. Quantum phase transitions and entanglement

Over the past few years, the question of whether quantum phase transitions can be understood from the perspective of quantum information has been posed and positively

answered, at least in part. Quantum phase transitions are non-analyticities in the ground-state energy of physical systems, which can typically be described as follows (see, for example, Sachdev (1999)). Consider a system defined on some lattice, and described by a Hamiltonian of the form

$$H = H_0 + \lambda H_1, \quad (12.47)$$

where $[H_0, H_1] \neq 0$. The parameter λ has to be visualized as an external parameter, which can be changed by an experimenter. In the limit of an infinite lattice, as the system crosses a certain value of λ (λ_c), the ground state has a qualitative change. If there is an associated non-analyticity in the ground-state energy (or, more generally, in some other physical observable) at $\lambda = \lambda_c$, then the system is said to have a quantum phase transition at that point. Since the transition occurs in the ground state, so that the system is at zero temperature, the transition is driven by quantum fluctuations and not by thermal fluctuations as in classical phase transitions. This is the reason why it is called a ‘quantum’ phase transition.

The study of the entanglement content in strongly correlated systems has been, since the end of the 1990s, a very dynamic subject of research (for an extended set of references see, for example, Lewenstein *et al.* (2007) and Amico *et al.* (2008)). It was realized in Osborne and Nielsen (2002a), Osborne and Nielsen (2002b), and Osterloh *et al.* (2002) that quantum phase transitions are related to entanglement by analysing the entanglement of a solvable model like the (infinite) XY spin- $\frac{1}{2}$ chain when the system passes through a quantum phase transition. Ideally, such a study should consider all types of entanglement, namely bipartite and multipartite, but the characterization of multiparticle entanglement is presently far from being complete and understood. For this reason, only the entanglement between nearest neighbors in the ground state of the spin chain—something that requires computation of the entanglement of (mixed) states in $\mathbb{C}^2 \otimes \mathbb{C}^2$ by means, for instance, of the concurrence—was considered. The entanglement between one spin and the rest of the chain was considered in, for example, Osborne and Nielsen (2002b), Zanardi (2002), and Zanardi and Wang (2002), and the study of scaling—how the entanglement of a block of n spins with the rest of the system behaves as n increases—was initiated in Vidal *et al.* (2003b). We discuss this topic briefly in Section 12.3.2, and in more detail in Section 12.4. Yet another type of scaling was considered later in Verstraete *et al.* (2004b) by using the concept of ‘localizable entanglement’; we come back to it in Section 12.3.3.

12.3.1 Scaling of entanglement in the reduced density matrix

The first system for which the scaling of entanglement near a quantum phase transition was considered is a system of spin- $\frac{1}{2}$ particles on a chain, described by the XY Hamiltonian:

$$H_{XY} = -\frac{J}{2} \sum_i [(1-\gamma)\sigma_i^x \sigma_{i+1}^x + (1+\gamma)\sigma_i^y \sigma_{i+1}^y] - h \sum_i \sigma_i^z, \quad (12.48)$$

with $J > 0$, $h > 0$, and $0 < \gamma \leq 1$. This system is known to undergo a quantum phase transition as the parameter $\lambda = \frac{J}{2h}$ passes over $\lambda = \lambda_c \equiv 1$ (for a detailed derivation see for instance Sachdev (1999) and Chapter 5). It was proposed that this quantum phase transition

may be analysed by looking at the behavior of the entanglement in the two-site states (the state obtained by tracing over all except two sites of the chain) of the ground state of the system as it goes through the quantum phase transition (Osborne and Nielsen, 2002a, 2002b; Osterloh *et al.*, 2002). In particular, in the case of the Ising Hamiltonian ($\gamma = 1$) on an infinite chain, the λ -derivative of the nearest-neighbor concurrence diverges as:

$$\partial_\lambda C_1 = \frac{8}{3\pi^2} \ln |\lambda - \lambda_c|, \quad (12.49)$$

(up to an additive constant) as λ approaches λ_c , as schematically shown in Figure 12.3 (Osterloh *et al.*, 2002). The subindex on the concurrence C_1 indicates the fact that the nearest-neighbor entanglement, in the middle of the chain, is calculated. The finite size scaling, i.e. the dependence of $\partial_\lambda C_1$ on the number of spins in the system is also shown in Figure 12.3. Further studies of two-site entanglement to characterize quantum phase transition can be found in recent reviews, such as Amico *et al.* (2008).

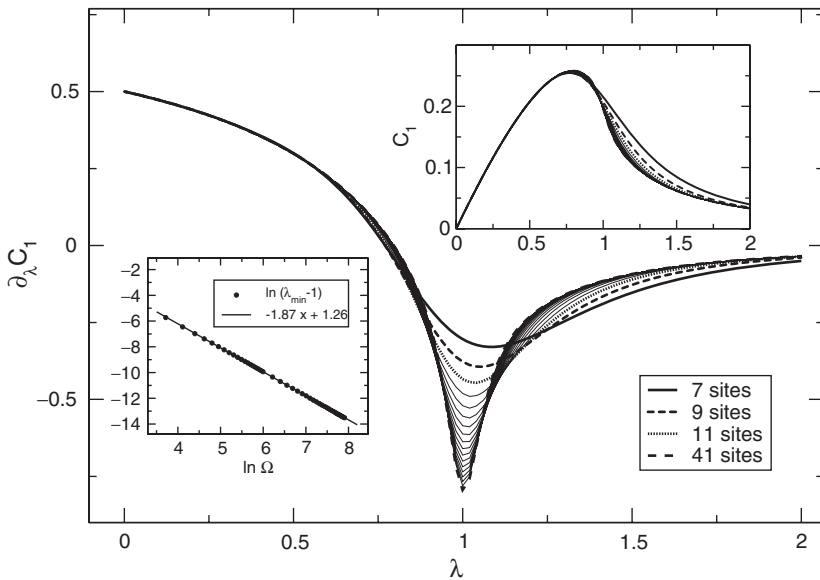


Figure 12.3 Scaling of nearest-neighbor entanglement in the ground state of the transverse Ising Hamiltonian on a chain. The inset at the right shows the nearest-neighbor concurrence entanglement for an infinite system. The main figure shows its derivative, plotted against the parameter λ for chains of different length $L = 11, 41, 101, 251, 401, \infty$ and showing that as the system size increases the minimum gets more pronounced. Bottom left inset: the position λ_{\min} of the minimum of $\partial_\lambda C_1$ in the main figure changes with the total number of sites. The current inset shows the plot of the logarithm of $\lambda_{\min} - 1$ against the logarithm of the total number of sites (denoted in this figure by $\ln \Omega$). Redrawn after Osterloh *et al.* (2002) by courtesy of the authors.

12.3.2 Entanglement entropy: scaling of block entanglement

A different approach to study genuine quantum correlations in strongly correlated systems was considered in Vidal *et al.* (2003b), whose idea was to consider a block of spins of the ground state and analyse its entanglement with the rest of the system as the block size increases. Since the ground state is a pure state, a good measure of entanglement of a block of spins with the rest of the system is the von Neumann entropy of the block of spins. This has been termed the entanglement entropy (EE) of the model. The models considered in Vidal *et al.* (2003b) (see also Latorre *et al.* (2004)) were the 1D XY and XXZ models, the latter described by the following Hamiltonian:

$$H_{XXZ} = \sum_i (\sigma_i^x \sigma_{i+1}^x + \sigma_i^y \sigma_{i+1}^y + \Delta \sigma_i^z \sigma_{i+1}^z - \lambda \sigma_i^z). \quad (12.50)$$

It was shown that when the system was not critical (away from any quantum phase transitions), EE saturates to a constant as a function of the block size. However, near the criticality EE diverges logarithmically with the size of the block. Similar behavior was seen to be true for the Affleck–Kennedy–Lieb–Tasaki valence-bond solid model (Fan *et al.*, 2004). Indeed, the logarithmic scaling shown by the entanglement entropy in the critical regime is a sign of the conformal symmetry of the system. Conformal field theory techniques were used to evaluate the behavior of the block entanglement for infinite chains near criticality and to link it to the central charge of the effective theory (Korepin, 2004). The central charge in a conformal field theory is a quantity that characterizes the universality class of the quantum phase transition. In Its *et al.* (2005) the limiting EE for an infinite chain governed by the XY model was evaluated.

In fact, the scaling of EE for 1D chains is an example of a more general behavior, termed ‘area laws’, which are present in different branches of physics. For many quantum systems governed by local Hamiltonians, their respective relevant quantum states (ground and/or thermal) exhibit such laws away from the criticality. In D spatial dimensions, the area law indicates that EE of a block of size L^D scales as L^{D-1} , hence its name. Much less is known about the scaling of entanglement at criticality at dimensions larger than one. For harmonic systems (governed by bilinear Hamiltonians) a lot of results have been obtained about the relation between entanglement entropy and area (Plenio *et al.*, 2005; Cramer *et al.*, 2006). The same is true of fermionic harmonic systems (Wolf, 2006; Gioev and Klich, 2006; Verstraete *et al.*, 2006; Riera and Latorre, 2006). The situation is, of course, more complex for systems with long-range or non-local interactions. An unbounded increase of the entanglement entropy was obtained for a lattice of spins that interact via some long-range Ising-type interaction (Dür *et al.*, 2005). Because of their importance in various areas of physics, we discuss the present status of area laws in Section 12.4.

12.3.3 Entanglement localization

In contrast to the entanglement measures above, the entanglement localization does not focus on the entanglement between two nearby sites but rather introduces the idea of ‘long-range’ entanglement. For a given multiparty state $\rho_{1,2,\dots,N}$ of N parties, the localizable entanglement (LE) (Verstraete *et al.*, 2004b) is the maximum average entanglement that can be made to be shared between two pre-determined parties (say, 1 and 2) by local

measurements and classical communication between the rest of the parties. Still, one has to state which entanglement measure should be considered in finding the average entanglement. The definition of the LE goes as follows: consider a pure state $|\psi\rangle$ of N qubits. The localizable entanglement $E_{ij}(\psi)$ is then variationally defined as the maximal amount of entanglement that can be created (i.e. localized) on average between the spins i and j by performing local measurements on the other spins. More specifically, every measurement basis specifies a pure-state ensemble $\mathcal{E} = \{p_s, |\phi_s\rangle\}$ consisting of at least $2^{(N-2)}$ elements counted by the index s . Here p_s denotes the probability of obtaining the two-spin state $|\phi_s\rangle$ after performing the measurement $|s\rangle$ on the assisting spins of the N -partite spin system considered. The LE is then defined as

$$E_{ij} = \max_{\mathcal{E}} \sum_s p_s E(|\phi_s\rangle), \quad (12.51)$$

where $E(|\phi_s\rangle)$ denotes the entanglement of $|\phi_s\rangle$. As already stated, for bipartite states of two qubits all entanglement measures are essentially equivalent. Verstraete *et al.* (2004b) used the concurrence (see Section 12.2.6) due to its connection with correlation functions, as we shall see below.

Quantum correlations for qubits are defined as

$$Q_{\alpha\beta}^{ij} = \langle\psi|\sigma_{\alpha}^i \otimes \sigma_{\beta}^j|\psi\rangle - \langle\psi|\sigma_{\alpha}^i|\psi\rangle\langle\psi|\sigma_{\beta}^j|\psi\rangle, \quad (12.52)$$

where i, j denote the positions of the spins of interest and α, β label the Pauli matrices. It is easy to check that the maximal correlation function for a pure state of two qubits is equal to its concurrence $C(|\psi\rangle = a|00\rangle + b|01\rangle + c|10\rangle + d|11\rangle) = 2|ad - bc|$. The basis in which the maximal possible correlation is measured is found by calculating the singular value decomposition (SVD) of the 3×3 matrix $Q_{\alpha\beta}$; the largest singular value corresponds to the spin directions that attain the maximal possible correlation.

Since LE is variationally defined it is, in general, very difficult to calculate. Moreover, in large spin systems one frequently does not have an explicit parametrization of the state under consideration; instead one has access to the one- and two-particle correlation functions (which parametrize completely the two-qubit reduced density operator). It would, therefore, be interesting to derive tight upper and lower bounds to the LE solely based on this information. The upper bound can readily be obtained using the concept of entanglement of assistance (DiVincenzo *et al.*, 1998), defined as the maximum average entanglement of all pure-state ensembles realising a given mixed state, and which is quite analogous to LE, except that in the former case, global and/or joint measurements are permitted. In Laustsen *et al.* (2003), the entanglement of assistance was calculated as follows: given the reduced density operator ρ_{ij} and its square root X , i.e. $\rho_{ij} = XX^\dagger$, the entanglement of assistance $E_{ij}(\psi)$ measured by the concurrence is equal to the trace norm $\text{Tr}|X^T(\sigma_y \otimes \sigma_y)X|$. The lower bound is more difficult to calculate. To this end, the following theorem was proven in Verstraete *et al.* (2004b):

Theorem 12.11: *For a given a state, pure or mixed, of N qubits with classical correlation $Q_{\alpha\beta}^{ij}$ between the spins i and j and directions α, β there exist always other directions in which one can measure the other spins without making this specific correlation to decrease, on average.*

Proof: First, one should note that it is sufficient to consider mixed states of three qubits. A mixed three-qubit state ρ can be parametrized with four 4×4 blocks

$$\rho = \begin{bmatrix} \rho_1 & \sigma \\ \sigma^\dagger & \rho_2 \end{bmatrix}. \quad (12.53)$$

Without loss of generality, one considers the Q_{zz}^{12} correlations. These are completely determined by the diagonal elements of the density operator $\rho_1 + \rho_2$. A von Neumann measurement in the $|\pm\rangle := \cos(\theta/2)|0\rangle \pm \sin(\theta/2)\exp(\pm i\phi)|1\rangle$ basis on the third qubit results in Hermitian unnormalized two-qubit operators

$$\begin{aligned} X_\pm &= \frac{\rho_1 + \rho_2}{2} \pm \cos(\theta) \frac{\rho_1 - \rho_2}{2} \\ &\quad \pm \sin(\theta) \left(\cos(\phi) \frac{\sigma + \sigma^\dagger}{2} + \sin(\phi) \frac{i(\sigma - \sigma^\dagger)}{2} \right). \end{aligned} \quad (12.54)$$

Defining $p_\pm = \text{Tr}(X_\pm)$, one now has to prove that there always exist parameters θ, ϕ such that the correlation, on average, does not decrease:

$$p_+|Q_{zz}(X_+/p_+)| + p_-|Q_{zz}(X_-/p_-)| \geq |Q_{zz}(X_+ + X_-)|. \quad (12.55)$$

Assuming, without loosing generality, that $\alpha = Q_{zz}(X_+ + X_-)$ is positive and taking the following parametrization

$$\bar{x} := [\cos(\theta); \sin(\theta) \cos(\phi); \sin(\theta) \sin(\phi)], \quad (12.56)$$

the inequality to be proven becomes:

$$x^{\star T} \left[\alpha \left(c^* - \frac{\beta^*}{\alpha} \right) \left(c^* - \frac{\beta^*}{\alpha} \right)^T + Q - \frac{\beta^* \beta^{*T}}{\alpha} \right] x \geq 0, \quad (12.57)$$

where c^* is such that $p_\pm = (1 \pm c^{\star T} x^*)/2$, and β^*, Q are respectively defined as matrices of sizes 3×1 and 3×3 , corresponding to the blocks of the matrix

$$S = R^T (\sigma_y \otimes \sigma_y) R = \begin{bmatrix} \alpha & \beta^{*T} \\ \beta^* & Q \end{bmatrix}, \quad (12.58)$$

where the star denotes complex conjugation. R is the real 4×4 matrix whose columns consist of the diagonal elements of the matrices $(\rho_1 + \rho_2)$, $(\rho_1 - \rho_2)$, $(\sigma + \sigma^\dagger)$, $i(\sigma - \sigma^\dagger)$. Due to Sylvester's law of inertia (Horn and Johnson, 1985), we know that S has two positive and two negative eigenvalues. The 3×3 matrix $Q - \beta^* \beta^{*T}/\alpha$, (the so-called Schur complement of α), corresponds to a principal 3×3 block of the matrix S^{-1} . Due to the interlacing properties of eigenvalues of principal blocks (Horn and Johnson, 1985), it follows that it has either two positive and one negative eigenvalue, or two negative and one positive one.

We can then always choose x^* corresponding to the positive eigenvalues so eqn (12.57) is trivially fulfilled. \square

The theorem above immediately gives a lower bound to the LE. Consider the state $|\psi\rangle$ and measure $N - 3$ qubits in such a way that the resulting correlations do not decrease (as shown above). The final state of the remaining two qubits has a concurrence equal to the maximal correlation, i.e. LE must, by definition, be larger than its correlation. Moreover, the theorem above indicates the strategy of the measurements allows us to reach the bound.

Using the concept of LE, a related ‘entanglement length’ ξ_E was introduced in Verstraete *et al.* (2004a). This is the typical length scale at which it is possible to create maximally entangled states by performing measurements at the rest of the parties. To be more specific, in the case of a spin chain let $E_{i,i+n}$ be the LE that can be made to share between the i th and the $(i+n)$ th spins of the chain. Assuming that $E_{i,i+n}$ decays exponentially with n , the entanglement length of the chain is defined by:

$$\xi_E^{-1} = \lim_{n \rightarrow \infty} \left(\frac{-\ln E_{i,i+n}}{n} \right). \quad (12.59)$$

If the decay of $E_{i,i+n}$ is non-exponential, then the entanglement length is infinite. A similar definition was given by Aharonov (2000), who considered a transition from quantum to classical physics. The definition of entanglement length is analogous to that of correlation length: if the correlation $\langle O_i O_{i+n} \rangle$ between two observables O_i and O_{i+n} decays exponentially, then the correlation length ξ_C is defined by:

$$\xi_C^{-1} = \lim_{n \rightarrow \infty} \left(\frac{-\ln \langle O_i O_{i+n} \rangle}{n} \right). \quad (12.60)$$

From the theorem proved above, it immediately follows that a diverging correlation length implies a diverging entanglement length. However, the converse is not true in general. One clear example is provided by gapped spin systems governed by the one-parameter family of modified Affleck–Kennedy–Lieb–Tasaki (AKLT) models (Affleck *et al.*, 1987), which, having a finite correlation length, have been proven to have a diverging entanglement length (Verstraete *et al.*, 2004a). It is instructive to analyse this example in some detail. Consider an open chain of N spin-1 particles at positions $1, 2, \dots, N$, with spin- $\frac{1}{2}$ particles at the two ends of the chain; say at locations 0 and $N + 1$. The AKLT Hamiltonian is given by

$$H^{\text{AKLT}} := \sum_{k=0}^N \left(\vec{S}_k \vec{S}_{k+1} + \frac{1}{3} (\vec{S}_k \vec{S}_{k+1})^2 + \frac{2}{3} \right) := \sum_{k=0}^N X_{k,k+1}^{\text{AKLT}} \quad (12.61)$$

with $\vec{S} = (S_x, S_y, S_z)$ denoting spin-1 operators.

The ground state of this Hamiltonian is obtained by representing each spin-1 system $(1 \dots N)$ by two spin- $\frac{1}{2}$ ($\bar{1}, 1, \bar{2}, 2, \dots$) systems and projecting them on the 3D symmetric subspace (see Figure 12.4). The Hamiltonian can be expressed in terms of $X_{k,k+1}^{\text{AKLT}}$, each

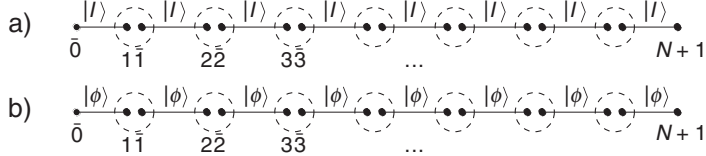


Figure 12.4 (a) The valence-bond ground state of the AKLT model. Each edge represents a singlet and the dashed circle corresponds to a projection onto the symmetric subspace. (b) A deformed AKLT model where the singlets are replaced by non-maximally entangled states $|\phi\rangle$. From Verstraete *et al.* (2004a).

term corresponding to a projector on a 5D subspace of the 9D space of two spin-1 particles, corresponding to the total spin of the pair being equal to 2. Let $|I\rangle$ be the singlet of two spin- $\frac{1}{2}$ particles $|I\rangle = |01\rangle - |10\rangle$ and A the 3×4 operator that projects a two spin- $\frac{1}{2}$ system onto its symmetric subspace. The (unique) ground state of H^{AKLT} can be written as

$$|V\rangle = (\otimes_{k=1}^N A_{\bar{k}k}) |I\rangle_{\bar{0}1} |I\rangle_{\bar{1}2} \cdots |I\rangle_{\bar{N}N+1}. \quad (12.62)$$

Now, we consider a one-parameter family of the deformed AKLT Hamiltonian (Verstraete *et al.*, 2004b):

$$H(\phi) = \sum_{k=0}^N X_{k,k+1}(\phi), \quad (12.63)$$

$$X_{k,k+1}(\phi) = ((\Sigma_k^\phi)^{-1} \otimes \Sigma_{k+1}^\phi) X_{k,k+1}^{\text{AKLT}} ((\Sigma_k^\phi)^{-1} \otimes \Sigma_{k+1}^\phi),$$

with Σ_k^ϕ defined as

$$\Sigma_k^\phi = \mathbf{1}_k + (\cosh(\phi) - 1) S_k^z + \sinh(\phi) (S_k^z)^2. \quad (12.64)$$

The AKLT model then corresponds to $\phi = 0$, and the deformation breaks the $O(3)$ rotational symmetry to $O(2)$. In the limit of $\phi \rightarrow \pm\infty$, the unique ground state is a product state with all individual spin eigenstates of S_k^z with eigenvalue 0. The unique ground state is completely specified by replacing A in eqn (12.62) by

$$A = \begin{pmatrix} \exp(\phi) & 0 & 0 & 0 \\ 0 & \frac{\exp(-\phi)}{\sqrt{2}} & \frac{\exp(\phi)}{\sqrt{2}} & 0 \\ 0 & 0 & 0 & \exp(-\phi) \end{pmatrix}. \quad (12.65)$$

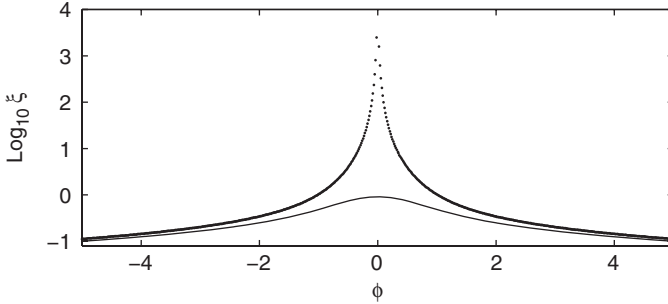


Figure 12.5 Correlation length ξ_C (solid) and entanglement length ξ_E (dotted) for the ground state of the deformed AKLT Hamiltonians $H(\phi)$ (12.63). From Verstraete *et al.* (2004a).

The correlation functions and the LE can be exactly calculated for the end points of the chain. The associated correlation length ξ_C and the entanglement length ξ_E are given by

$$\xi_C = 1/\ln \left| \sqrt{\cosh(2\phi)^2 + 3} + \cosh(2\phi) \right|, \quad (12.66)$$

$$\xi_E = 1/\ln \left| \frac{\sqrt{\cosh(2\phi)^2 + 3} + \cosh(2\phi)}{3} \right|, \quad (12.67)$$

and are shown in Figure 12.5. One observes that the quantity ξ_C always remains finite and attains its maximum for $\phi = 0$. In contrast, ξ_E is always strictly larger than ξ_C . Moreover, it diverges at the AKLT point $\phi \rightarrow 0$. This clearly shows a novel type of quantum phase transition to which the correlation functions are not sensitive. Obviously it is related to the $O(3) \rightarrow O(2)$ symmetry-breaking at $\phi = 0$.

12.4. Area laws

Area laws play a very important role in many areas of physics, since generically the relevant states of physical systems described by local Hamiltonians (both quantum and classical) fulfil them. The interest in this area goes back to the seminal works on the free Klein–Gordon equation (Bombelli *et al.*, 1986; Srednicki, 1993), where it was suggested that the area law of geometric entropies might be related to the physics of black holes and, in particular, the Bekenstein–Hawking entropy proportional to the black hole surface (Bekenstein, 1973, 2004; Hawking, 1974). The related *holographic principle* (Bousso, 2002) states that information (entropy) about a region of space can be represented by a theory that is restricted to the boundary of that region.

In recent years there has been a real explosion of studies of area laws in many-body physics, and there are excellent reviews (see for example Eisert *et al.* (2010)), and special issues of journals (Calabrese *et al.*, 2009) devoted to this subject. As pointed out in Eisert *et al.* (2010), the interest in area laws is particularly motivated by the following issues:

- the holographic principle and the entropy of the black holes
- quantum correlations in many-body systems
- computational complexity of quantum many-body systems
- characterization of certain many-body topological systems.

While the first topic is outside the scope of this book, we shall discuss the consequences of area laws for the others. We start by analysing the entropy for a generic bipartite pure states.

12.4.1 Mean entanglement of bipartite states

Let us first consider a *generic* pure state in a Hilbert space in $\mathbb{C}^m \otimes \mathbb{C}^n$ ($m \leq n$). Such a generic state (normalized, i.e. unit vector) has a form

$$|\Psi\rangle = \sum_{i=1}^m \sum_{j=1}^n \alpha_{ij} |i\rangle |j\rangle, \quad (12.68)$$

where the complex numbers α_{ij} may be regarded as random variables distributed uniformly on a hypersphere, i.e. distributed according to the probability density

$$P(\alpha) \propto \delta \left(\sum_{i=1}^m \sum_{j=1}^n |\alpha_{ij}|^2 - 1 \right), \quad (12.69)$$

with the only constraint being the normalization. As we shall see below, such a generic state fulfills, on average, a ‘volume’ rather than area law.

To this end, we introduce a somewhat more rigorous description and prove that, on average, the entropy of one of the subsystems of an generic bipartite pure state in $\mathbb{C}^m \otimes \mathbb{C}^n$ ($m \leq n$) is almost maximal for sufficiently large n . In other words, typical pure states in $\mathbb{C}^m \otimes \mathbb{C}^n$ are almost maximally entangled. This ‘typical behavior’ of pure states happens to be completely *atypical* for ground states of local Hamiltonians with a energy gap between ground and first excited eigenstates.

Rigorously speaking, the average with respect to the distribution of eqn (12.69) should be taken with respect to the unitarily invariant measure on the projective space $\mathbb{C}P^{mn-1}$. This is a unique measure generated by the Haar measure on the unitary group. It follows then that the eigenvalues of the first subsystem λ_i of a randomly generated pure state $|\psi_{AB}\rangle$ are distributed according to the following probability distribution:

$$P_{m,n}(\lambda_1, \dots, \lambda_m) = C_{m,n} \delta \left(\sum_i \lambda_i - 1 \right) \prod_i \lambda_i^{n-m} \prod_{i < j} (\lambda_i - \lambda_j)^2, \quad (12.70)$$

where the delta function is responsible for the normalization, and the normalization constant reads

$$C_{m,n} = \frac{\Gamma(mn)}{\prod_{i=0}^{m-1} \Gamma(n-i)\Gamma(m-i+1)}, \quad (12.71)$$

with Γ being the well-known Euler gamma function.

Theorem 12.12: Let $|\psi_{AB}\rangle$ be a bipartite pure state from $\mathbb{C}^m \otimes \mathbb{C}^n$ ($m \leq n$) chosen at random according to the Haar measure on the unitary group, and $\rho_A = \text{Tr}_B |\psi_{AB}\rangle\langle\psi_{AB}|$ its subsystem acting on \mathbb{C}^m . Then

$$\langle S(\rho_A) \rangle \approx \log m - \frac{m}{2n}. \quad (12.72)$$

Proof: In what follows we sketch an intuitive proof without involving a detailed mathematical discussion. For more rigorous proofs see Page (1993), Foong and Kanno (1994), and Sen (1996). Our aim is to estimate the following quantity:

$$\langle S(\rho_A) \rangle = - \int \left(\sum_{i=1}^m \lambda_i \log \lambda_i \right) P(\lambda_1, \dots, \lambda_m) d\lambda_1 \dots d\lambda_m, \quad (12.73)$$

where the probability distribution $P(\lambda_1, \dots, \lambda_m)$ is given by eqn (12.70). We can always write the eigenvalues λ_i as $\lambda_i = \frac{1}{m} + \delta_i$, where $\delta_i \in \mathbb{R}$ and $\sum_i \delta_i = 0$. We can now expand the logarithm into the Taylor series

$$\begin{aligned} \log \left(\frac{1}{m} + \delta_i \right) &= -\log m + m\delta_i - \frac{1}{2}m^2\delta_i^2 + \frac{1}{3}m^3\delta_i^3 - \dots \\ &= -\log m + \sum_{k=1}^{\infty} \frac{(-1)^{k-1}}{k} (m\delta_i)^k. \end{aligned} \quad (12.74)$$

Applying eqn (12.74) to the von Neumann entropy of ρ_A , one obtains

$$S(\rho_A) = \log m - \frac{m}{1 \cdot 2} \sum_i \delta_i^2 + \frac{m^2}{2 \cdot 3} \sum_i \delta_i^3 - \frac{m^3}{3 \cdot 4} \sum_i \delta_i^4 - \dots \quad (12.75)$$

Thus the average entropy can be written as

$$\langle S(\rho_A) \rangle = \log m - \frac{m}{1 \cdot 2} \left\langle \sum_i \delta_i^2 \right\rangle + \frac{m^2}{2 \cdot 3} \left\langle \sum_i \delta_i^3 \right\rangle - \frac{m^3}{3 \cdot 4} \left\langle \sum_i \delta_i^4 \right\rangle - \dots \quad (12.76)$$

Let us now notice that $\text{Tr} \rho_A^2 = \sum_i \lambda_i^2 = \sum_i (\delta_i + 1/m)^2 = \sum_i \delta_i^2 + 1/m$ and, therefore, $\sum_i \delta_i^2 = \text{Tr} \rho_A^2 - 1/m$. Substituting this in the above expression and assuming than one can omit the terms with higher powers of δ_i , leads to

$$\langle S(\rho_A) \rangle \approx \log m - \frac{m}{2} \left\langle \text{Tr} \rho_A^2 - \frac{1}{m} \right\rangle. \quad (12.77)$$

Since the $\text{Tr } \rho_A^2$ denotes the purity of ρ_A , its average (calculated by Lubkin (1978)) reads

$$\langle \text{Tr } \rho_A^2 \rangle = \frac{m+n}{mn+1}. \quad (12.78)$$

Substitution into eqn (12.77) leads to the desired results completing the proof. \square

It should be pointed out that it is possible to obtain an exact analytic expression for $\langle S \rangle$:

$$\langle S(\rho) \rangle = \Psi(mn+1) - \Psi(n+1) - \frac{m-1}{2n} \quad (12.79)$$

with Ψ denoting the bigamma function.⁴ Now using the fact that $\Psi(z+1) = \Psi(z) + 1/z$ and the asymptotic properties of the bigamma function, $\Psi(z) \approx \ln z$, we obtain the desired result (Page, 1993; Foong and Kanno, 1994; Sen, 1996).

Let us also note that the exact result of Lubkin (12.78) can be estimated by relaxing the normalization constraint in the distribution of eqn (12.69), and replacing it with a product of independent Gaussian distributions $P(\alpha) = \prod_{i,j} (nm/\pi) \exp[-nm|\alpha_{ij}|^2]$, with $\langle \alpha_{ij} \rangle = 0$ and $\langle |\alpha_{ij}|^2 \rangle = 1/nm$. The latter distribution, according to the central limit theorem, tends for $nm \rightarrow \infty$ to a Gaussian distribution, for $\sum_{i=1}^m \sum_{j=1}^n |\alpha_{ij}|^2$ centred at 1, with a width $\simeq 1/\sqrt{nm}$. One then straightforwardly obtains $\langle \text{tr} \rho_A \rangle = 1$, and after a little more tedious calculation $\langle \text{tr} \rho_A^2 \rangle = (n+m)/nm$, which agrees asymptotically with the Lubkin result for $nm \gg 1$.

12.4.2 Area laws in a nutshell

In what follows we shall be concerned with lattices $L \subseteq \mathbb{Z}^D$ with D denoting the spatial dimension. At each site we have, in general, a quantum d -dimensional physical system (one can, however, also consider classical lattices, in which case we have a d -dimensional classical spin at each site, with the configuration space \mathbb{Z}_d). The distance between two sites x and y of the lattice is defined as

$$\mathcal{D}(x, y) = \min_{1 \leq i \leq D} |x_i - y_i|, \quad (12.80)$$

and, accordingly, we define the distance between two disjoint regions X and Y of L as the minimal distance between all pairs of sites $\{x, y\}$, where $x \in X$ and $y \in Y$, i.e., $\mathcal{D}(X, Y) = \min_{x \in X} \min_{y \in Y} \mathcal{D}(x, y)$. We denote by \mathcal{R} some region of L , and we define its boundary $\partial \mathcal{R}$ as all sites belonging to \mathcal{R} for which the distance to $L \setminus \mathcal{R}$ (the complement of \mathcal{R}) is one. Formally, $\partial \mathcal{R} = \{x \in R | \mathcal{D}(x, L \setminus \mathcal{R}) = 1\}$. Finally, we denote by $|\mathcal{R}|$ the number of sites in the region \mathcal{R} , as schematically shown in Figure 12.6

We can now add some physics to our lattice by assuming that interactions between the sites of L are governed by some Hamiltonian H . We can divide the lattice L into

⁴The bigamma function is defined as $\Psi(z) = \Gamma'(z)/\Gamma(z)$ and for natural $z = n$ it takes the form $\Psi(n) = -\gamma + \sum_{k=1}^{n-1} (1/k)$ with γ being the Euler–Mascheroni constant, the exact value of which is not necessary for our consideration as it vanishes in eqn (12.79).

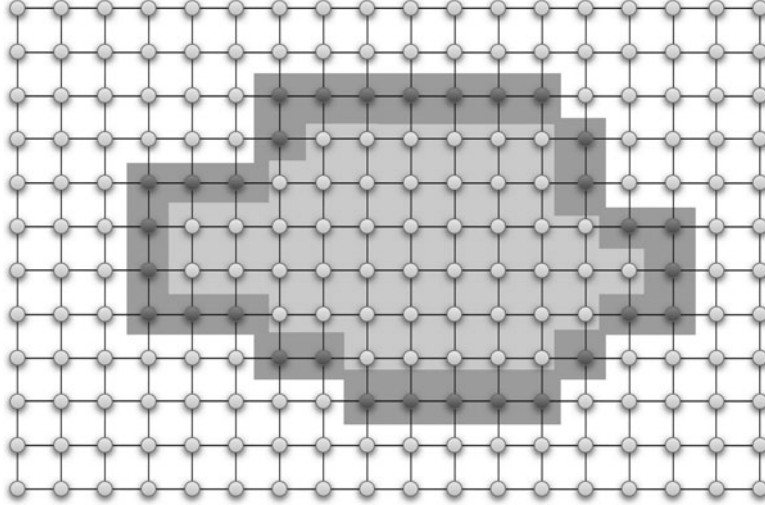


Figure 12.6 Schematic representation of a lattice system L , an arbitrary region \mathcal{R} (denoted by a light gray background) with size $|\mathcal{R}|$, and its boundary $\partial\mathcal{R}$ (denoted by a dark gray background).

two parts: the region \mathcal{R} and its complement $L \setminus \mathcal{R}$. Roughly speaking, the aim is now to determine the scaling of the entropy of some region \mathcal{R} with its size $|\mathcal{R}|$. If the entropy scales at most as the boundary area, i.e. if

$$S(\rho_{\mathcal{R}}) = O(|\partial\mathcal{R}|) \quad (12.81)$$

holds, then we say that it satisfies an area law.

Area laws in one-dimensional systems Let us start from the simplest case of $D = 1$ lattices. Now $L = \{1, \dots, N\}$ and let \mathcal{R} be a subset of L consisting of n contiguous spins starting from the first site, i.e. $\mathcal{R} = \{1, \dots, n\}$ with $n < N$. In this case, the boundary $\partial\mathcal{R}$ of the region \mathcal{R} contains either one or two spins, depending on which boundary conditions we deal with: open or periodic. Therefore, the area law is extremely simple in this case and reads

$$S(\rho_{\mathcal{R}}) = O(1). \quad (12.82)$$

In general, all local gapped systems (away from criticality) satisfy the above law, while there is a logarithmic divergence of the entanglement entropy when the system is critical. The first part of the above statement has been rigorously proven in Hastings (2007). There, it is specifically considered a short-range (i.e. local interactions) and translational-invariant Hamiltonian,

$$H = \sum_{i \in L} H_{i,i+1}, \quad (12.83)$$

where each $H_{i,i+1}$ has non-trivial support only on sites i and $i + 1$. Furthermore, it is also assumed that the operator norm of all terms in eqn (12.83) are upper bounded by some positive constant J , i.e. $\|H_{i,i+1}\| \leq J$ for each i . In other words, one assumes that the interaction strength between the i th site and its nearest neighbors is not greater than some constant. Under these premises it can be shown, using the Lieb–Robinson bound (Lieb and Robinson, 1972), that there is a sound velocity of system v , and a typical length scale ξ_C such that any pair of operators A and B , with support on sets X and Y respectively, fulfill

$$\|[A(t), B]\| \leq c|X|\|A\|\|B\|\exp[\xi_c \mathcal{D}(X, Y)], \quad (12.84)$$

for a time $|t| \leq l/v$. Here $\mathcal{D}(X, Y)$ is the distance between the sets, as defined before, c is a numeric constant of order unity, and $A(t) = \exp(iHt)A\exp(-iHt)$. The velocity of sound is of the order of J and ξ_c is of the order of unity.

Theorem 12.13: *Area law for local gapped 1D systems (Hastings, 2007). Let L be a 1D lattice with sites $i = 1, \dots, N$ and on each site there is a d -dimensional Hilbert space, and let H be a local Hamiltonian as in eqn (12.83). Assuming that H has a unique ground state separated from the first excited states by the energy gap $\Delta E > 0$, the entropy of any region \mathcal{R} of L satisfies*

$$S(\rho_{\mathcal{R}}) \leq 6c_0\xi 2^{6\xi \ln d} \ln \xi \ln d, \quad (12.85)$$

with c_0 denoting some constant of order unity and $\xi = \max\{2v/\Delta E, \xi_C\}$.

Let us remark that both constants appearing in the above theorem come from the Lieb–Robinson bound (see Lieb and Robinson (1972) and also Masanes (2009) for the recent simple proof of this bound). The theorem tells us that when a 1D system with local interactions (eqn (12.83)) is away from the criticality ($\Delta E > 0$), the entropy of \mathcal{R} is bounded by some constant independent of $|\mathcal{R}|$, even if this bound does not have to be tight. A similar scaling occurs for the Rényi entropies.

Of course, a natural question is to ask if there are gapped systems with long-range interactions that violate eqn (12.82). This question was affirmatively answered in Dür *et al.* (2005) and Eisert and Osborne (2006), where examples of one-dimensional models with long-range interactions, non-zero energy gap, and scaling of entropy as $S(\rho_{\mathcal{R}}) = \xi \log_2 n + O(1)$ were given. The second question one could pose is about the behavior of the entropy when the gap ΔE goes to zero and the system becomes critical. Numerous analytical and numerical results show that one usually observes logarithmic divergence of $S(\rho_{\mathcal{R}})$ with the size of the region \mathcal{R} . Here we recall only the results (see also the recent reviews by Eisert *et al.* (2010) and Calabrese *et al.* (2009)) given for the XY model is a transverse magnetic field as described in eqn (12.48), with the anisotropy parameter $0 \leq \gamma \leq 1$ and the magnetic field $h \in \mathbb{R}$. In the case of vanishing anisotropy ($\gamma = 0$) we have the isotropic XY model or the XX model for short. For $\gamma = 1$ the above Hamiltonian recovers the well-known Ising Hamiltonian in a transverse field. Let us finally mention that the Hamiltonian H_{XY} is critical when either $\gamma = 0$ and $|h| \leq 2$ (the critical XX model) or for $|h| = 2$.

It was shown in a series of papers (Jin and Korepin, 2004; Its *et al.*, 2005; Keating and Mezzadri, 2005) that for the critical XX model (that is when $\gamma = 0$ and $|h| \leq 2$) the entropy

of the region $\mathcal{R} = \{1, \dots, n\}$ scales as

$$S(\rho_{\mathcal{R}}) = \frac{1}{3} \log_2 n + O(1). \quad (12.86)$$

Then, in the case of the critical Ising model ($\gamma = 1$) it can be shown that the entropy scales logarithmically, i.e. $S(\rho_{\mathcal{R}}) = \Omega(\log_2 n)$.

A vast amount of work on the logarithmic scaling of the block entropy using conformal field theory (CFT) methods has recently appeared (see e.g. Calabrese *et al.* (2009) and references therein). Quite generally, it has been shown that for the 1D critical systems whose scaling limit is described by a CFT, the block entropy at criticality scales as:

$$S(\rho_I) = \frac{c}{3} \log(|I|/a), \quad (12.87)$$

where c is the so-called *central charge* of the underlying CFT, and a corresponds to the lattice constant for lattice systems (cut-off). Similar scalings hold also for the Rényi entropies $S_\alpha(\rho) = 1/(1-\alpha) \log \text{Tr } \rho^\alpha$ at criticality

$$S_\alpha(\rho_I) \simeq \frac{c}{6} \left(1 + \frac{1}{\alpha}\right) \log(|I|/a). \quad (12.88)$$

This expression can even be generalized to the case away from but close to the criticality, where

$$S(\rho_I) = \frac{c}{3} \log(|\xi_C|/a), \quad (12.89)$$

where ξ_C is the correlation length.

The situation is much more complex in higher dimensions and so far there are no general rules. However, some general results hold in any dimension but require strong assumptions. Below we follow the work presented in Wolf *et al.* (2008) and Masanes (2009).

Area laws in classical systems for mutual information A sensible problem is to ask whether classical systems follow area laws as well. Classical correlations are very well quantified by the *mutual information*, which tells us, given two random classical variables X (with probability distribution $\{p_x\}$) and Y (with probability distribution $\{p_y\}$), how much information X and Y have in common. Following the notation we have already used, let A and $B = S \setminus A$ denote two subsystems of a physical system S . Let p^A and p^B be the marginals of the joint probability distribution p^{AB} . Then, the (classical) correlations between A and B are given by

$$I(A : B) = H(A) + H(B) - H(AB), \quad (12.90)$$

where $H(X) = \sum_i p_i^X \log p_i^X$ indicates the Shannon entropy.⁵

⁵Recall that given a random variable $\{X\} = \{X_1, X_2, \dots, X_n\}$, with a probability distribution $\{p_1, p_2, \dots, p_n\}$, the Shannon entropy quantifies our uncertainty about X_i before we actually learn its value.

Coming back to our problem, we denote by L a lattice of interactions of the system and we assume a d -dimensional classical spin (\mathbb{Z}_d) on each site. We divide the lattice into two parts A and B , and we denote the boundaries of these sets as ∂A and ∂B . Then, we can state:

Theorem 12.14 Area law for classical Gibbs states (Wolf *et al.*, 2008):

Let L be a lattice with a d -dimensional classical spin in each site. Let p be a probability distribution on L such that $p(x_a|x_b, x_c) = p(x_a|x_c)$ if c separates a from b , with $a, b, c \subset L$. Then if $L = A \cup B$, it holds that

$$I(A : B) \leq |\partial A| \log d. \quad (12.91)$$

Proof: Notice that when there is a region C that separates regions A and B , then $p(x_a|x_c, x_b) = p(x_a|x_c)$ due to the Markovian property. Using the definition of conditional probability, the latter can be rewritten as

$$p(x_a, x_b, x_c) = \frac{p(x_a, x_c)p(x_b, x_c)}{p(x_c)}. \quad (12.92)$$

Now, let A and B be two regions such that $L = A \cup B$ and let $\bar{A} = A \setminus \partial A$ and $\bar{B} = B \setminus \partial B$. Since ∂A separates A from ∂B we can use eqn (12.92) to obtain

$$\begin{aligned} H(AB) &= H(\bar{A}\partial AB) = - \sum_{x_{\bar{A}}, x_{\partial A}, x_B} p(x_{\bar{A}}, x_{\partial A}, x_B) \log p(x_{\bar{A}}, x_{\partial A}, x_B) \\ &= - \sum_{x_{\bar{A}}, x_{\partial A}} p(x_{\bar{A}}, x_{\partial A}) \log p(x_{\bar{A}}, x_{\partial A}) - \sum_{x_{\partial A}, x_B} p(x_{\partial A}, x_B) \log p(x_{\partial A}, x_B) \\ &\quad + \sum_{x_{\partial A}} p(x_{\partial A}) \log p(x_{\partial A}) \\ &= H(A) + H(\partial AB) - H(\partial A). \end{aligned} \quad (12.93)$$

Since ∂B separates ∂A from B , the same reasoning may be applied to the second term of the right-hand side of the above, obtaining $H(\partial AB) = H(\partial A\partial B) + H(B) - H(\partial B)$. This, together with eqn (12.93), gives

$$H(AB) = H(A) + H(B) + H(\partial A\partial B) - H(\partial A) - H(\partial B), \quad (12.94)$$

which in turn, after application to eqn (12.90), allows us to write

$$I(A : B) = I(\partial A : \partial B). \quad (12.95)$$

This means that whenever the probability distribution p has the above Markovian property, correlations between A and B are the same as between its boundaries. Now, we know that the mutual information can be expressed

through the conditional Shannon entropy⁶ as $I(X : Y) = H(X) - H(X|Y)$. Since $H(X|Y)$ is always non-negative, we have the following inequality:

$$I(\partial A : \partial B) \leq H(\partial A). \quad (12.96)$$

To obtain eqn (12.91) it suffices to notice that $H(A)$ is upper-bounded by the Shannon entropy of independently and identically distributed probabilities. \square

Since all classical Gibbs distributions with finite-range interactions fulfill the Markov property, they satisfy the above area law for mutual information. Can the same conclusion be drawn in the case of quantum thermal states where the Markov property does not hold in general? With the aim of analysing this question, we denote as L a lattice consisting of d -dimensional quantum systems with some interactions given by some Hamiltonian H . As a measure of correlations we use *quantum mutual information* $I(A : B) = S(\rho_A) + S(\rho_B) - S(\rho_{AB})$, where, as previously, S denotes the von Neumann entropy.

Theorem 12.15 Area laws for quantum thermal states (Wolf *et al.*, 2008; Masanes, 2009): *Let L be a lattice consisting of d -dimensional quantum systems divided into parts A and B ($L = A \cup B$). For any Gibbs state ($\beta > 0$) of a local Hamiltonian H , it holds that*

$$I(A : B) \leq \beta \text{Tr}[H_\partial(\rho_A \otimes \rho_B - \rho_{AB})]. \quad (12.97)$$

Proof: The thermal state ρ_β , with $\beta > 0$ (β is the inverse of the temperature), minimizes the free energy $F(\rho) = \text{Tr}(H\rho) - (1/\beta)S(\rho)$ and therefore $F(\rho_\beta) \leq F(\rho_\beta^A \otimes \rho_\beta^B)$, with $\rho_\beta^A = \text{Tr}_B \rho_\beta$. This allows us to estimate the entropy of ρ_β as

$$\begin{aligned} S(\rho_\beta) &= \beta [\text{Tr}(H\rho_\beta) - F(\rho_\beta)] \\ &\geq \beta [\text{Tr}(H\rho_\beta) - F(\rho_\beta^A \otimes \rho_\beta^B)] \\ &= \beta [\text{Tr}(H\rho_\beta) - \text{Tr}(H\rho_\beta^A \otimes \rho_\beta^B)] + S(\rho_\beta^A \otimes \rho_\beta^B) \\ &= \beta [\text{Tr}(H\rho_\beta) - \text{Tr}(H\rho_\beta^A \otimes \rho_\beta^B)] + S(\rho_\beta^A) + S(\rho_\beta^B), \end{aligned} \quad (12.98)$$

where the last equality follows from additivity of the von Neumann entropy $S(\rho \otimes \sigma) = S(\rho) + S(\sigma)$. Substituting eqn (12.98) into the formula for mutual information we obtain:

$$I(A : B) \leq \beta [\text{Tr}(H\rho_\beta^A \otimes \rho_\beta^B) - \text{Tr}(H\rho_\beta)]. \quad (12.99)$$

Let us now write the Hamiltonian as $H = H_A + H_\partial + H_B$, where H_A and H_B denote all the interaction terms within the regions A and B respectively, while H_∂ stands for interaction terms connecting these two regions. One immediately notices that $\text{Tr}[H_{A(B)}(\rho_\beta^A \otimes \rho_\beta^B - \rho_\beta)] = 0$ and only the H_∂ part of H contributes to the right-hand side of eqn (12.99). This finishes the proof. \square

⁶The conditional Shannon entropy is defined as $H(A|B) = H(A, B) - H(B)$.

General area laws In the previous sections we have seen that the ground state of gapped 1D local Hamiltonians always satisfies an area law. In what follows we show that, under some assumptions, general area laws can be proven for general lattices (Masanes, 2009). Some bounds on the von Neumann entropy of a region ρ_R of a given system for arbitrary Hamiltonians with finite-range interactions in a D -dimensional lattice can be found by realising that the eigenstates of the system have a well-defined global energy, but since they are not eigenstates of the region \mathcal{R} they should fluctuate inside it.

Let us denote by \mathcal{R} the region of interest (bulk) where the entropy is going to be measured and let \mathcal{X} and $\bar{\mathcal{X}}$ be two disjoint regions of the lattice such that $|\mathcal{X}| \leq |\bar{\mathcal{X}}|$. Let the distance between both these regions be $2l$, as shown schematically in Figure 12.7. The eigenstates of an arbitrary Hamiltonian H with support on $\mathcal{X} \cup \bar{\mathcal{X}}$ have a well-defined global energy, but inside the region \mathcal{X} of the lattice the energy may fluctuate. It was shown by Masanes (2009) that these fluctuations can be observed by measuring the exterior of the region and a superficial shell inside the region, $\bar{\mathcal{X}} \cup \mathcal{S}$, separated from the region \mathcal{R} by a distance l . One can impose a condition on the ground state: if the operator X has support on the region \mathcal{R} , which is separated from the support of the operator Y by a distance l , then one demands that the connected correlation function decays at least as

$$|\langle XY \rangle - \langle X \rangle \langle Y \rangle| \leq (l - \xi \ln |\mathcal{R}|)^D \quad (12.100)$$

where ξ is a constant. This implies that the energy fluctuations inside \mathcal{X} cannot be seen in its bulk, denoted by \mathcal{R} (see Figure 12.7). In turn, this fact provides a characterization for the approximate support of the global ground state inside the region \mathcal{R} . Let by $H_{\mathcal{X}}$ refer to the part of the global Hamiltonian H that acts only on sites from \mathcal{X} . Obviously, $H_{\mathcal{X}}$ have their own eigenvalues e_n and eigenstates $|\psi_n\rangle$. The number of eigenenergies of $H_{\mathcal{X}}$ lower

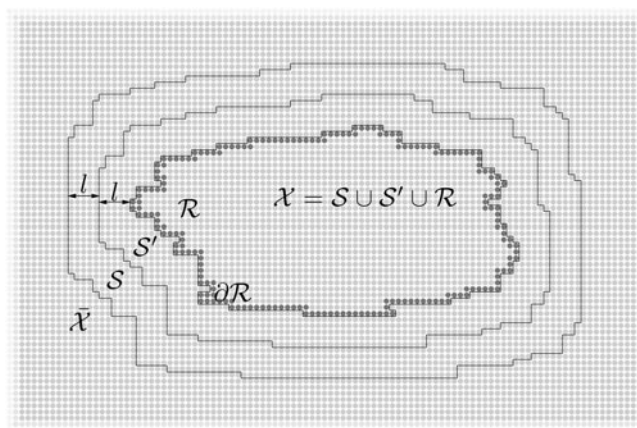


Figure 12.7 \mathcal{R} is the chosen region where the entropy is estimated; the sites belonging to its boundary $\partial\mathcal{R}$ are darker. \mathcal{S} and \mathcal{S}' are two superficial shells with thickness l outside \mathcal{R} ; $\mathcal{X} = \mathcal{S} \cup \mathcal{S}' \cup \mathcal{R}$ is the extended region, $\bar{\mathcal{X}}$ is the exterior of \mathcal{X} . From Masanes (2009).

than e is assumed to be bounded by

$$\Omega_{\mathcal{X}}(e) \leq (\tau|\mathcal{X}|)^{\gamma(e-e_0)+\eta|\partial\mathcal{X}|}, \quad (12.101)$$

where e_0 is the lowest eigenvalue and τ, γ , and η are some constants independent of \mathcal{X} . This condition is only assumed for $e \sim |\partial\mathcal{X}|$. This bound on the eigenstates gives an upper bound of the support subspace that can be used to bound the von Neumann entropy in the reduced region \mathcal{R} .

Theorem 12.16 (Masanes, 2009): *Let \mathcal{R} be some arbitrary (even disjoint) region of a lattice L . Then assuming that both the correlations and the eigenvalues of the $H_{\mathcal{R}}$ are bounded, the entropy of the reduced density matrix $\rho_{\mathcal{R}}$ satisfies*

$$S(\rho_{\mathcal{R}}) = \text{Tr}(-\rho_{\mathcal{R}} \ln \rho_{\mathcal{R}}) \leq \text{const}|\partial\mathcal{R}| \ln |\mathcal{R}|. \quad (12.102)$$

Proof: Let $|\psi_n\rangle$ and e_n denote the eigenvectors and ordered eigenvalues ($e_0 \leq e_1 \leq \dots \leq e_n \leq \dots$) of $H_{\mathcal{R}}$. It is clear that the ground state $|\Psi_0\rangle$ of H can be written as $|\Psi_0\rangle = \sum_{i,j} \alpha_{ij} |\psi_i\rangle |\varphi_j\rangle$, where the vectors $|\varphi_j\rangle$ constitute some basis in the Hilbert space corresponding to the region $L \setminus \mathcal{R}$. One may always denote $|\tilde{\varphi}_i\rangle = \sum_j \alpha_{ij} |\varphi_j\rangle$, and then

$$|\Psi_0\rangle = \sum_i \sqrt{\mu_i} |\psi_i\rangle |\tilde{\varphi}_i\rangle, \quad (12.103)$$

where $\mu_i = 1/\langle \tilde{\varphi}_i | \tilde{\varphi}_i \rangle = 1/\sum_j |\alpha_{ij}|^2 \geq 0$ and they add up to unity. The vectors $|\tilde{\varphi}_i\rangle$ in general do not have to be orthogonal and therefore eqn (12.103) is not the Schmidt decomposition of $|\Psi_0\rangle$. Nevertheless, one may show that tracing out the $L \setminus \mathcal{R}$ subsystem, the entropy of the density matrix acting on \mathcal{R} is upper-bounded as:

$$S(\rho_{\mathcal{R}}) \leq - \sum_i \mu_i \ln \mu_i. \quad (12.104)$$

The aim is to maximize the right-hand side of the above equation under the following conditions imposed on μ_i . First, the locality of our Hamiltonian means that $\langle H_{\mathcal{R}} \rangle \leq e_0 + J3^D|\partial\mathcal{R}|$, i.e. it is bounded by the bulk contribution and the contribution of the boundary terms; we assume that in a given site at the boundary there are no more than 3^D of such terms, and that each is bounded by J , implying the following condition for the probabilities μ_i :

$$\sum_i \mu_i \tilde{e}_i \leq J3^D|\partial\mathcal{R}|, \quad (12.105)$$

with $\tilde{e}_i = e_i - e_0$. Second, the modified version of the second assumption allows us to infer that for any eigenvalue e_n the inequality $i \leq c_2(\tau|R|)^{\gamma e_i + \eta|\partial R|}$ holds.

Substitution in eqn (12.105) gives:

$$\sum_i \mu_i \ln i \leq \Theta, \quad (12.106)$$

where Θ is a bound depending linearly on $|\partial\mathcal{R}| \ln |\mathcal{R}|$.

Since our aim is to maximize the right-hand side of eqn (12.104) under two conditions, namely inequality (12.106) and the normalization of μ_i , it is enough to consider only the worst case—eqn (12.106) being an equality. The Lagrange multiplier method tells us that under these conditions we need to seek the probabilities of the form $\mu_n = \alpha n^{-\beta}$, with $\alpha, \beta \geq 0$ being the Lagrange multipliers. The above conditions lead us then to the set of equations:

$$\alpha \sum_n \frac{1}{n^\beta} = 1 \quad \alpha \sum_n \frac{\ln n}{n^\beta} = \Theta. \quad (12.107)$$

Thus, maximization of the right hand side of eqn (12.104)—provided that both of the above equalities hold—gives maximization of the right hand side of (12.104), and we obtain that

$$S(\rho_{\mathcal{R}}) \leq \text{const} |\partial\mathcal{R}| \ln |\mathcal{R}|, \quad (12.108)$$

which finishes the proof. \square

12.5. The world according to tensor networks

Quantum many-body systems are, in general, difficult to describe: specifying an arbitrary state of a system with N two-level subsystems requires 2^N complex numbers. For a classical computer this presents not only storage problems but also computational ones, since simple operations such as calculating the expectation value of an observable would require an exponential number of operations. However, we know that completely separable states can be described with about N parameters—indeed, they correspond to classical states. Therefore, what makes a quantum state difficult to describe are quantum correlations, or entanglement. We have already seen that even if, in general, the entropy of a subsystem of an arbitrary state is proportional to the volume, there are some special states that obey an entropic area law. Intuitively, and given the close relation between entropy and information, we could expect that states following an area law could be described (at least approximately) with much less information than a general state. We also know that such low-entanglement states are few, albeit interesting—we only need an efficient and practical way to describe and parametrize them. In Section 12.3 we analysed the ground state of the spin-1 chain AKLT Hamiltonian, and observed that the ground state can be written compactly in a very particular way: by replacing each physical particle of spin-1 in the chain by two spin- $\frac{1}{2}$ particles, each of them being maximally entangled with its counterpart spin- $\frac{1}{2}$ in the left- or right-neighbor spin, and finally projecting back the resulting state to the physical spin-1 particles. Such a construction can be understood as an example of a ‘tensor

network representation' or matrix product representation of a quantum state (MPS), an idea introduced in the seminal paper of Fannes *et al.* (1992) for finitely correlated systems as a generalization of the AKLT example. Moreover, the example illustrates the close link between the fulfillment of an area law and the efficient representation of the state. This link is indeed deep in the roots of numerical methods, such as DMRG, that are used in condensed matter to efficiently find ground states. In this last section we discuss at length such a link, which provides a novel perspective to our understanding of ground states of many-body Hamiltonians, as well as to their efficient representation or simulatability. The entanglement content of the state is the key parameter for an efficient representation, and it is a stringent requirement for studying the dynamics of many-body quantum systems. An excellent detailed discussion of recent developments of tensor network representations can be found in Perez-García *et al.* (2007). Here we follow it closely.

12.5.1 The tensor network representation of quantum states

Consider a completely general pure state of a system with N d -level particles,

$$|\psi\rangle = \sum_{i_1, i_2, \dots, i_N=1}^d c_{i_1, i_2, \dots, i_N} |i_1, i_2, \dots, i_N\rangle. \quad (12.109)$$

When the state is separable (has no entanglement), the coefficient $c_{i_1, i_2, \dots, i_N} = c_{i_1}^1 c_{i_2}^2 \dots c_{i_N}^N$, where now all the coefficients c are scalars. In this case, the locality of the information (i.e. the set of coefficients $c_{i_k}^k$ for each site k is independent of the others) is the key to the efficiency with which separable states can be represented. Could this locality be kept in some way, even when the state is not separable and the N parties are quantum-correlated? How could that be, in the case that there are only nearest-neighbor interactions? Is it possible in this case to represent the ground state of the many-body system by a tensor at each site of the lattice, with one index of the tensor for every physical neighbor and another index for the physical states of the particle? This is exactly the representation we used in Section 12.3 for the AKLT state. The ground state of a 1D chain with short-range interactions and open boundary conditions can therefore be written as

$$|\psi\rangle = \sum_{i_1, i_2, \dots, i_N=1}^d \left[A_{i_1}^{[1]} A_{i_2}^{[2]} \dots A_{i_N}^{[N]} \right] |i_1, i_2, \dots, i_N\rangle, \quad (12.110)$$

where $A_{i_k}^{[k]}$ stands for a matrix with dimensions $D_k \times D_{k+1}$, and, at the ends of the chain, $A_{i_1}^{[1]}$ and $A_{i_N}^{[N]}$ are vectors. If the state we represent is translational invariant and it has periodic boundary conditions, eqn (12.111) becomes

$$|\psi\rangle = \sum_{i_1, i_2, \dots, i_N=1}^d \text{Tr} \left[A_{i_1}^{[1]} A_{i_2}^{[2]} \dots A_{i_N}^{[N]} \right] |i_1, i_2, \dots, i_N\rangle, \quad (12.111)$$

where now the $A_{i_k}^{[k]} = A_i$ are the same on each site. Therefore, the state is represented by a product of matrices, and hence the name matrix product state or MPS.

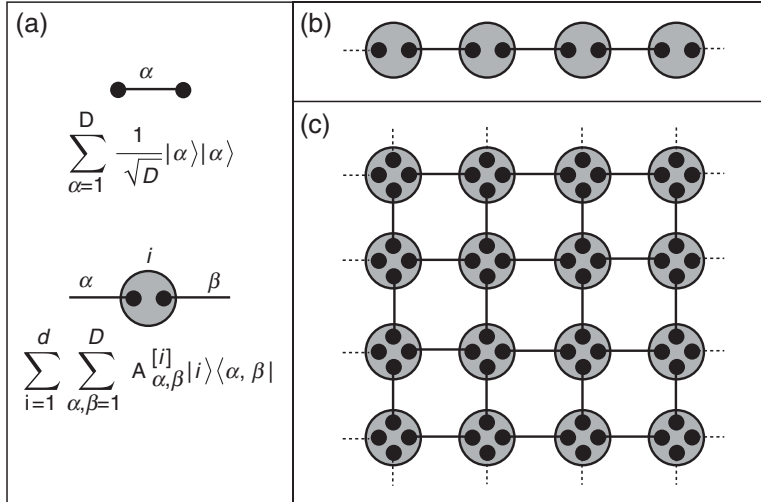


Figure 12.8 Schematic representation of a tensor network. (a) The meaning of the elements in the representation, namely the solid line joining two virtual particles in different sites means the maximally entangled state between them; the grey circle represents the map from virtual particles in the same site to the physical index. (b) A 1D tensor network or matrix product state. (c) How the scheme can be extended intuitively to two dimensions, where a projected entangled pair state contains four virtual particles per physical site. From Augusiak *et al.* (2012).

One useful way of understanding the motivations for this representation is to think of a valence-bond picture. Imagine that we replace every particle at the lattice by a pair (or more in higher dimensions) of particles of dimensions D that are in a maximally entangled state with their corresponding partners in a neighboring site (see Figure 12.8). Then, by applying a projecting map from these virtual particles into the real ones,

$$A = \sum_{i=1}^d \sum_{\alpha, \beta=1}^D A_{\alpha, \beta}^{[i]} |i\rangle \langle \alpha, \beta| \quad (12.112)$$

we obtain a state that is expressed as in eqn (12.111). Here Greek indices indicate virtual systems and Roman ones the physical system. One can show that any state $|\psi\rangle \in \mathbb{C}^{d \otimes N}$ can be written in this way, with $D = \max_m D_m, D_m \leq d^{N/2}$. Furthermore, an MPS can always be found such that (Vidal, 2003a; Perez-García *et al.*, 2007)

- $\sum_i A_i^{\dagger[k]} A_i^{[k]} = 1_{D_k}$, for $1 \leq k \leq N$
- $\sum_i A_i^{\dagger[k]} \Lambda^{[k-1]} A_i^{[k]} = \Lambda^{[k]}$, for $1 \leq k \leq N$
- for open boundary conditions $\Lambda^{[0]} = \Lambda^{[N]} = 1$, and $\Lambda^{[k]}$ is a $D_{k+1} \times D_{k+1}$ positive diagonal matrix of full rank with $\text{Tr}\Lambda^{[k]} = 1$.

In fact, $\Lambda^{[k]}$ is a matrix whose diagonal components $\lambda_n^k, n = 1..D_k$, are the non-zero eigenvalues of the reduced density matrix obtained by tracing out the particles from $k+1$

to N ; in other words, the Schmidt coefficients of a bipartition of the system at site k . An MPS with these properties is said to be in its canonical form (see also Chapter 5).

Indeed, it is not difficult to see that eqn (12.111) is actually a faithful representation of all possible states, provided the bond matrix D is large enough. In this sense, the generic MPS representation is nothing but another representation that is obtained by a recurrent application of the Schmidt decomposition of the state written in eqn (12.109). This representation is as complex as any other, but it becomes advantageous and efficient when the virtual bond dimension D is small, i.e. when the state is said to have an MPS representation. Also, every translationally-invariant pure state in a finite chain with periodic boundary conditions has an MPS representation. The reason is that when entanglement in a bipartite splitting is small (but finite), most of the Schmidt coefficients are either zero or decay rapidly to zero. Then, if $|\psi\rangle$ contains little entanglement, we can obtain a very good approximation to it by truncating the matrices A to a rank D much smaller than the maximum allowed by the above theorem, $d^{N/2}$. In fact, the validity of approximating a quantum state by an MPS state has been proved (Verstraete and Cirac, 2006):

Theorem 12.18: *Given an arbitrary state $|\psi\rangle$, there exists an MPS $|\psi_D\rangle$ with bond dimension D such that $\||\psi\rangle - |\psi_D\rangle\| < 2 \sum_{\alpha=1}^{N-1} \epsilon_\alpha(D)$, where $\epsilon_\alpha(D) = \sum_{i=D+1}^{d^{\min(\alpha, N-\alpha)}} \lambda_i^{[k]}$.*

Proof: Let us assume that the MPS is in its canonical form with $D = 2^{N/2}$. We can now define a projector into the virtual bond dimension $P = \sum_{k=1}^D |k\rangle\langle k|$ and a trace-preserving completely positive map acting on the space of $D \times D$ matrices given by $\varepsilon_m(X) = \sum_i A_i^{\dagger[m]} X A_i^{[m]}$. With these tools one can write the overlap

$$\langle \psi | \psi_D \rangle = \text{Tr} \left[\varepsilon_2(\dots \varepsilon_{N-2}(\varepsilon_{N-1}(\Lambda^{[N-1]} P) P) \dots) P \right]. \quad (12.113)$$

By defining $Y^{[k]} = \varepsilon_k(Y^{[k+1]} P)$, with $Y^{[N-1]} = \Lambda^{[N-1]} P$, and using the fact that $\text{Tr}|\varepsilon(X)| \leq \text{Tr}|X|$, we can see that

$$\begin{aligned} \text{Tr}|\Lambda^{[k]} - Y^{[k]}| &= \text{Tr}|\varepsilon_k(\Lambda^{[k+1]} - Y^{[k+1]} P)| \\ &\leq \text{Tr}|\Lambda^{[k+1]} - Y^{[k+1]}| + \text{Tr}|\Lambda^{[k+1]}(1 - P)|, \end{aligned} \quad (12.114)$$

where the last term is equal to $\sum_{\alpha=D+1}^{2^{N/2}} \lambda_\alpha^{[k]}$. Finally, applying this last inequality recursively from $N-1$ to 2, and using the fact that $\langle \psi_D | \psi_D \rangle \leq 1$, one can obtain the desired bound on $\langle \psi | \psi_D \rangle$. \square

Theorem 12.18 shows that there is an efficient MPS representation of the state that reproduces with accuracy the non-local properties of the system, such as the correlation length. This is very powerful in the context of numerical simulations of quantum states: it gives a controllable handle on the precision of the approximation by MPS. In practice what we are saying is that for the representation to be efficient the Schmidt coefficients λ need

to decay faster than polynomial. However, one can be more precise and give bounds on the error of the approximation in terms of the Rényi entropies (Schuch *et al.*, 2007):

Lemma 12.3. *Let $S_\alpha(\rho) = \log(\text{Tr}\rho^\alpha)/(1-\alpha)$, the Rényi entropy of a reduced density matrix ρ , with $0 < \alpha < 1$. Denote $\epsilon(D) = \sum_{i=D+1}^{\infty} \lambda_i$, with λ_i the eigenvalues of ρ in decreasing order. Then,*

$$\log(\epsilon(D)) \leq \frac{1-\alpha}{\alpha} \left(S_\alpha(\rho) - \log \frac{D}{1-\alpha} \right). \quad (12.115)$$

We have not yet explained which quantum states can be efficiently simulated by MPS. For example, one case of interest where we could expect the method to fail is near quantum critical points where correlations (and entanglement) are singular and might diverge. However, at least in 1D systems, the following is true:

Theorem 12.19 (Verstraete and Cirac, 2006): *In one dimension there exists a scalable, efficient MPS representation of ground states even at criticality.*

Proof: In one dimension, the worst case of growth of the entropy of a subsystem of size L —exactly at criticality—is given by

$$S_\alpha(\rho_L) \simeq \frac{c + \tilde{c}}{12} \left(1 + \frac{1}{\alpha} \right) \log L. \quad (12.116)$$

Let us take the length L to be half the chain, $N = 2L$. By means of the previous discussion, we can find a MPS $|\psi_D\rangle$ such that its distance from the ground state $|\psi_{GS}\rangle$ is bounded as $\| |\psi_{GS}\rangle - |\psi_D\rangle \| \leq \epsilon_0/L$, with ϵ_0 constant. Now, let D_L be the minimal virtual bond dimension needed for this precision, i.e. $\| |\psi_{GS}\rangle - |\psi_D\rangle \| \leq 2 \times 2L \epsilon_{\max}(D)$. We demand that

$$\begin{aligned} \epsilon_{\max}(D) &\leq \frac{\epsilon_0}{4L^2} \\ &\leq \exp \left[\frac{1-\alpha}{\alpha} \left(\frac{c + \tilde{c}}{12} \frac{1+\alpha}{\alpha} \log L - \log \frac{D_L}{1-\alpha} \right) \right], \end{aligned} \quad (12.117)$$

from which we can extract

$$D_L \leq \text{const } \left(\frac{L^2}{\epsilon_0} \right)^{\frac{\alpha}{1-\alpha}} L^{\frac{c+\tilde{c}}{12} \frac{1+\alpha}{\alpha}} \propto \text{poly}(L), \quad (12.118)$$

which finishes the proof. \square

Establishing that there is an efficient representation of the ground state is not enough: we must also know if it is possible to find it efficiently too. In 1D gapped systems, the gap Δ typically scales polynomially, which means that the DMRG and MPS methods should converge reasonably quickly. One can, however, formalize the regime of efficiency of MPS as a function of how the different Rényi entropies scale with subsystem size (Schuch *et al.*, 2007). In Table 12.1 we summarize the currently known regimes where the MPS approach is appropriate or otherwise.

Table 12.1 Relation between the scaling of the block Rényi entropies and the approximability by MPS. In the ‘undetermined’ region nothing can be said about approximability just from looking at the scaling. From Schuch *et al.* (2007).

$S_{\alpha \sim}$	const	$\log L$	$L^{\kappa} (\kappa < 1)$	L
$S_{\alpha < 1}$	approximable			
$S \equiv S_1$			determined	
$S_{\alpha > 1}$	undetermined			inapproximable

12.5.2 Examples of MPS and PEPS

Let us present here a few examples (Perez-García *et al.*, 2007) and models to clarify the above concepts and to show the power of MPS and, more generally, the potential for tensor network representations of ground states of quantum many-body systems.

AKLT model As discussed above, a well-known model with a finite excitation gap and exponentially decaying spin-correlation functions was introduced by Affleck, Kennedy, Lieb, and Tasaki (Affleck *et al.*, 1987, 1988a): the so-called AKLT model. It corresponds to a concrete point of the Heisenberg bilinear–biquadratic model describing a chain of spin-1 particles. The AKLT Hamiltonian is

$$H = \sum_i \mathbf{S}_i \cdot \mathbf{S}_{i+1} + \frac{1}{3} (\mathbf{S}_i \cdot \mathbf{S}_{i+1})^2, \quad (12.119)$$

where we now consider periodic boundary conditions. For $S = 1$, the local Hilbert space of each spin has three states and thus $d = 3$. The ground state of this Hamiltonian can be written compactly using a translationally invariant MPS with bond dimension $D = 2$; specifically

$$A_{-1} = \sigma_x, \quad A_0 = \sqrt{2}\sigma^+, \quad A_1 = -\sqrt{2}\sigma^-, \quad (12.120)$$

where $\sigma^\pm = \sigma_x \pm i\sigma_y$ and σ_i ($i = x, y, z$) are the Pauli matrices.

Majumdar-Gosh model A paradigmatic example of a frustrated 1D spin chain is the Majumdar-Gosh (Majumdar and Ghosh, 1969) or $J_1 - J_2$ Heisenberg model with nearest-and next-to-nearest-neighbor interactions:

$$H = \sum_i (2\sigma_i \sigma_{i+1} + \sigma_i \sigma_{i+2}), \quad (12.121)$$

where in this example we have set $J_1 = 2$ and $J_2 = 1$. The ground state of this model is composed of singlets between nearest-neighbor spins. However, since the state must be translationally invariant, we must include a superposition of singlets between even-odd

spins and ‘shifted’ singlets between odd–even spins. The state can be written compactly in MPS form using $D = 3$ and:

$$A_0 = \begin{pmatrix} 0 & 1 & 0 \\ 0 & 0 & -1 \\ 0 & 0 & 0 \end{pmatrix}, \quad A_1 = \begin{pmatrix} 0 & 0 & 0 \\ 1 & 0 & 0 \\ 0 & 1 & 0 \end{pmatrix}. \quad (12.122)$$

Greenberger–Horne–Zeilinger states A relevant state for quantum information theory is the Greenberger–Horne–Zeilinger (GHZ) state, which for N spin- $\frac{1}{2}$ particles can be written as

$$|\text{GHZ}\rangle = \frac{|0\rangle^{\otimes N} + |1\rangle^{\otimes N}}{\sqrt{2}}. \quad (12.123)$$

GHZ states are considered important because for many entanglement measures they are maximally entangled, but by measuring or tracing out any qubit a classical state is obtained (although with correlations). GHZ states can be written using $D = 2$ MPS, specifically $A_{0,1} = 1 \pm \sigma_z$. The ‘antiferromagnetic’ GHZ state is simple: $A_{0,1} = \sigma^\pm$.

Cluster states in 1D These are the states relevant for one-way quantum computing (see Chapter 13). They correspond to the unique ground state of the three-body Hamiltonian

$$H = \sum \sigma_{i-1}^z \sigma_i^x \sigma_{i+1}^z, \quad (12.124)$$

and can be represented by MPS using $D = 2$ and

$$A_0 = \begin{pmatrix} 0 & 0 \\ 1 & 1 \end{pmatrix}, \quad A_1 = \begin{pmatrix} 1 & -1 \\ 0 & 0 \end{pmatrix}. \quad (12.125)$$

Classical superposition of matrix product states Imagine we have a classical Hamiltonian

$$H = \sum_{(i,j)} h(\sigma_i, \sigma_j), \quad (12.126)$$

where σ_i , $i = 1, \dots, d$ are the components of a vector $\boldsymbol{\sigma}$ and $h(\sigma_i, \sigma_j)$ are local interactions. The partition function of such a model at a given inverse temperature β is

$$Z = \sum_{\{\boldsymbol{\sigma}\}} \exp(-\beta H(\boldsymbol{\sigma})), \quad (12.127)$$

where the sum is over all possible configurations of the vector $\boldsymbol{\sigma}$. Let us now define a quantum state $|\psi_\beta\rangle$ whose amplitude for a given state of the computational basis

corresponds to the term in the partition function for that state:

$$\begin{aligned} |\psi_\beta\rangle &= \frac{1}{\sqrt{Z}} \sum_{\{\sigma\}} \exp\left(-\frac{\beta}{2} H(\sigma)\right) |\sigma_1 \dots \sigma_N\rangle \\ &= \frac{1}{\sqrt{Z}} \sum_{\{\sigma\}} \prod_{(i,j)} \exp\left(-\frac{\beta}{2} h(\sigma_i, \sigma_j)\right) |\sigma_1 \dots \sigma_N\rangle. \end{aligned} \quad (12.128)$$

We shall now define a map P in the same manner as in the valence-bond states explained above. This maps C^{d^2} to C^2 such that

$$P|s, k\rangle = |s\rangle \langle \varphi_s|k\rangle, \quad (12.129)$$

where we have defined

$$\sum_{\alpha=1}^d \langle \varphi_s|\alpha\rangle \langle \varphi_{\tilde{s}}|\alpha\rangle = \exp\left(-\frac{\beta}{2} h(s, \tilde{s})\right). \quad (12.130)$$

Let us visualize what happens when we insert these back into the classical superposition state $|\psi_\beta\rangle$. We focus, for a moment, on a 1D system:

$$\begin{aligned} |\psi_\beta\rangle &= \frac{1}{\sqrt{Z}} \sum_{\sigma_1, \dots, \sigma_N} \exp\left(-\frac{\beta}{2} h(\sigma_1, \sigma_2)\right) \dots \exp\left(-\frac{\beta}{2} h(\sigma_{N-1}, \sigma_N)\right) |\sigma_1 \dots \sigma_N\rangle \\ &= \frac{1}{\sqrt{Z}} \sum_{\sigma_1, \dots, \sigma_N} \sum_{\alpha_1=1}^d \langle \varphi_{\sigma_1}|\alpha_1\rangle \langle \varphi_{\sigma_2}|\alpha_1\rangle \sum_{\alpha_2=1}^d \langle \varphi_{\sigma_2}|\alpha_2\rangle \langle \varphi_{\sigma_3}|\alpha_2\rangle \dots |\sigma_1 \dots \sigma_N\rangle \\ &= \frac{1}{\sqrt{Z}} \sum_{\sigma_1, \dots, \sigma_N} \sum_{\alpha_1=1}^d \sum_{\alpha_2=1}^d \dots \langle \varphi_{\sigma_1}|\alpha_1\rangle [\langle \varphi_{\sigma_2}|\alpha_1\rangle \langle \varphi_{\sigma_2}|\alpha_2\rangle] [\langle \varphi_{\sigma_3}|\alpha_2\rangle \dots |\sigma_1 \dots \sigma_N\rangle], \end{aligned} \quad (12.131)$$

and we can replace $\langle \varphi_{s_i}|\alpha\rangle \langle \varphi_{s_i}|\beta\rangle = A_{s_i, \alpha, \beta}^{(i)}$, thus expressing the classical thermal superposition state as an MPS. These states have some important properties:

- (i) they obey strict area laws
- (ii) they allow to calculate classical and quantum correlations
- (iii) they are ground states of local Hamiltonians.

Property (i) should be obvious by now, since we have explicitly shown the MPS form of the state. We can easily show property (ii) for Ising models. A classical correlation function f must be evaluated with the partition function, $\langle f(\sigma) \rangle = \sum_{\sigma} f(\sigma) e^{-\beta H(\sigma)}/Z$, but this is just the expectation value of an operator made by changing the argument of f into σ_z operators and evaluated with $|\psi_\beta\rangle$. Since it is the expectation value of a MPS, it is efficient to compute. We will demonstrate property (iii) in detail in the next paragraph.

Classical kinetic models Let us consider a system made out of classical spins, whose configurations we label by σ . If we denote $P(\sigma, t) = P(\sigma, t, \sigma_0, t_0)$, the probability of finding the system in state σ at time t given that it was in state σ_0 at time t_0 , the system we will consider has a dynamic described by a master equation

$$\dot{P}(\sigma, t) = \sum_{\sigma' \neq \sigma'} W(\sigma, \sigma') P(\sigma', t) - \sum_{\sigma' \neq \sigma} W(\sigma', \sigma) P(\sigma, t), \quad (12.132)$$

where $W(\sigma, \sigma')$ is the transition rate from state σ' to state σ . This equation defines a kinetic model, and it is clearly a Markov process since at time t there is no dependence of P on its history. In the following we consider only systems that obey a detailed balance rule, i.e.

$$W(\sigma, \sigma') e^{-\beta H(\sigma')} = W(\sigma', \sigma) e^{-\beta H(\sigma)}. \quad (12.133)$$

With this condition, the stationary state of the master equation, (eqn (12.132))—that is, the one that fulfils $\dot{P}_{st}(\sigma, t) = 0$ —is simply $P_{st}(\sigma) = e^{-\beta H(\sigma)} / Z$.

To demonstrate that classical superposition MPS are ground states of local Hamiltonians (corresponding to property (iii) above), we must do some changes of variables. Replacing $\psi(\sigma, t) = e^{\beta H(\sigma)/2} P(\sigma, t)$ in the master equation, (eqn (12.132)), we obtain:

$$\begin{aligned} \dot{\psi}(\sigma, t) &= \sum_{\sigma'} e^{\beta H(\sigma)/2} W(\sigma, \sigma') P(\sigma', t) - W(\sigma', \sigma) e^{\beta H(\sigma)/2} e^{-\beta H(\sigma)/2} \psi(\sigma, t), \\ &= \sum_{\sigma'} e^{\beta H(\sigma)/2} W(\sigma, \sigma') e^{-\beta H(\sigma')/2} \psi(\sigma', t) - W(\sigma', \sigma) \psi(\sigma, t). \end{aligned} \quad (12.134)$$

Because of detailed balance, $e^{\beta H(\sigma)/2} W(\sigma, \sigma') e^{-\beta H(\sigma')/2} = e^{\beta H(\sigma')/2} W(\sigma', \sigma) e^{-\beta H(\sigma)/2}$, we can write eqn (12.134) as

$$\dot{\psi}(\sigma, t) = \sum_{\sigma'} H_\beta(\sigma, \sigma') \psi(\sigma', t), \quad (12.135)$$

where H_β is a Hermitian matrix, i.e. we can interpret eqn (12.135) as an ‘imaginary-time’ Schrödinger equation with Hamiltonian H_β . Furthermore, because of the conservation of probability, H_β can only have non-negative eigenvalues, which means that the stationary state P_{st} with eigenvalue zero must be a ground state. The associated ψ_{st} is the classical superposition MPS that we were looking for.

However, so far we have not said anything about H_β . Let us consider a well known example, the so-called Glauber model (Glauber, 1963c) or, more generally, the kinetic Ising model (Kawasaki, 1972; Hilhorst *et al.*, 1972; Haake, 2010), where $H = -J \sum_{\langle ij \rangle} \sigma_i \sigma_j$. Denoting P_i the flip operator of the i th spin, ($P_i \sigma_i = -\sigma_i$) and h_i the local field of spin i induced by its neighbors ($h_i = \sum_{j, \langle i,j \rangle} \sigma_j$), the master equation for Glauber’s model becomes

$$\dot{P}(\sigma, t) = \sum_i (1 - P_i)(1 - \tanh(\beta \sigma_i h_i)) P(\sigma, t). \quad (12.136)$$

By applying the above change of variables, the Hamiltonian associated to this model is

$$H_\beta = \sum_i \left[(1 - \tgh(\beta \sigma_i^z h_i(\sigma^z)) - \frac{2\sigma_i^z}{\cosh(\beta h_i(\sigma^z))} \right]. \quad (12.137)$$

This Hamiltonian, and others that can be derived in this way, are typically local and gapped except at a critical temperature β_c where the gap vanishes with a critical exponent z that characterizes the model. In one dimension $\beta_c = \infty$, but for larger dimensions this model has a finite critical temperature.

We have seen thus far how the master equation of a classical spin model (that obeys the detailed balance condition) can be associated with a quantum Hamiltonian with some interesting critical properties. The ground state of this Hamiltonian, as we have seen, obeys a strict area law and can be written efficiently as an MPS. Nevertheless, the underlying model is still classical. In Augusiak *et al.* (2010a), the authors considered a generalization of this and similar classical models to the quantum domain, retaining the same structure that leads to associated Hamiltonians that obey area laws. A similar approach has been applied for classical random exclusion processes in Temme *et al.* (2009).

13

Quantum information with lattice gases

13.1. Introduction

Computer technology has evolved over the years through a sequence of physical realizations: from gears to relays, from relays to valves, then to transistors, and now to integrated circuits. We are used to think about computational processes as mathematical operations but, under close scrutiny, performing a computation is essentially a physical process. This statement was coined and formalized by Rolf Landauer in the 1980s. Landauer asserted that information processing is intrinsically linked to a physical process rather than to an abstract concept and therefore follows the laws of physics. Within this framework, radically novel computational models have emerged with the recognition that entanglement is a resource that can be manipulated to process, store, and transfer information. The seminal contribution of Deutsch (1985) laid the foundations of quantum computation. In his contribution, he envisioned a computer behaving as a quantum object, which could, for instance, exist in a superposition of states. Each state could coherently follow a distinct computational path and interfere to produce a final output. Such a computer should follow the laws of quantum physics to perform operations. The first quantum algorithm, the so-called ‘Deutsch–Jozsa’ algorithm, demonstrated that this prototype computer could solve a ‘toy’ problem more efficiently than any classical computer will ever do (Deutsch and Jozsa, 1992). In 1994, Shor discovered a quantum algorithm that can efficiently factorize integers into their prime factors (Shor, 1994). Factorization of large numbers is believed to be intractable by any classical computer. Shor’s algorithm had tremendous consequences since factorization has not only pure academic interest: it is also the problem that underpins the security of many classical public-key cryptosystems. In particular, the most popular encryption method, RSA (Rivest *et al.*, 1979), bases its security on the difficulty of factorizing large numbers into prime factors.

In 1982, the Nobel Prize winner Richard P. Feynman (Feynman, 1982) pointed out the impossibility of classical computers—no matter how powerful—simulating some complex quantum systems driven by quantum physics laws. He envisioned that in order to understand and predict the properties of complex systems one should use a model prototype that is highly controllable and versatile and which permits easy simulation of a number of different systems, i.e. a quantum simulator.

As we have seen in previous chapters, cold atoms in optical lattices are very well suited to simulate various condensed-matter models and have become probably the best candidates to be quantum simulators. In this chapter we focus on their potential as universal quantum

computers assuming that atoms are used to construct quantum bits. In DiVincenzo (2000), the minimal requirements that a physical system should fulfill in order to become a quantum computer were summarized. The candidate system has to:

- (i) be scalable, with well-defined qubits,
- (ii) be initializable to a simple fiducial state,
- (iii) have long decoherence times compared to the gate operation time,
- (iv) have a universal set of quantum gates,
- (v) have a qubit-specific measurement.

One can add to the list that the system should permit an efficient correction of errors—unavoidable in any computation. Atoms loaded in optical lattices provide systems with a large number of qubits, an advantageous property for a highly scalable quantum computer. On the other hand, the difficulty in individually addressing the atoms is compensated by the simplicity of operating on all atoms simultaneously. Moreover, the first experimental methods with single-atom addressability in optical lattices have been reported recently (Gericke *et al.*, 2008; Würtz *et al.*, 2009; Bakr *et al.*, 2009, 2010; Sherson *et al.*, 2010) as discussed in Chapter 14.

Neutral atoms, furthermore, couple weakly to the environment and have relatively long coherence times compared to typical timescales of their internal dynamics. However, when atoms are brought to a superposition state or, even further, to an entangled state, they become very fragile with respect to decoherence, which tends to destroy any quantum superposition. The larger the entangled system, the faster it will decohere. To fight against decoherence, the qubits have to be ‘protected’ by preparing them in quantum states that are robust against external perturbations and providing adequate error correction codes to correct the systematic errors that appear in unitary transformations.

Theoretically, there are several well established models of quantum computation. The quantum circuit model, first introduced by Deutsch (1989) is a generalization of a classical network, with information is processed by logic (quantum) gates and gates are connected by quantum wires. Recall that a logic gate operates between an input state and an output state according to a truth table. A set of gates is called universal if any computation can be performed with arbitrary precision by a network containing only replicas of that set. The quantum circuit model uses a set of universal logical quantum gates to perform any computation.

A particularly appropriate approach that exploits the massive parallelism of atomic lattice systems to perform quantum computation is measurement-based quantum computation, also called the one-way quantum computer, which was introduced by Raussendorf and Briegel (2001a). This is a model that relies on an adaptive sequence of measurements of single particles in a highly entangled state to perform computation. It requires the capability to create a cluster state—a large multipartite quantum state able to reproduce any “small” entangled state—to perform local single operations.

Topological quantum information, first introduced by Kitaev in 1997 (Kitaev, 1997, 2003, 2006), is a novel approach, which uses the hidden topological order related to the global properties of some systems to encode and process information globally, thus providing a fault-tolerant method. There are other well-studied models of quantum computation and the present list is by no means exhaustive. Some of these approaches are proven to have the same computational power, and one can conjecture that any model based on quantum

physics will have the same computational capabilities. Furthermore, all aim to achieve a scalable quantum computer that is robust and efficient with respect to decoherence and systematic errors. Ultracold gases in optical lattices appear well-suited in particular to the quantum circuit model, the one-way quantum computer, and the topological quantum computer. These are the models of quantum information that we shall discuss in some detail below.

Finally, let us point out also that there are several proposals for implementing quantum computation in other AMO systems, with the most prominent and promising one put forward by Cirac and Zoller in 1995 (Cirac and Zoller, 1995). A Cirac–Zoller computer uses cold trapped ions interacting with laser beams. Currently 8–14 ions can be simultaneously entangled and used to perform quantum operations (Gulde *et al.*, 2003) and to study decoherence (Monz *et al.*, 2011) with higher fidelity than any other known system. However, the scalability of such system is a complicated issue. By increasing the number of trapped ions the individual addressing of the ions becomes technically very hard. Promising approaches to scalability, on the other hand, are offered by the optical microtrap proposal of G. Birkh (Birkh and Fortagh, 2007) and the recent proposal of P. Grangier and co-workers (Gaëtan *et al.*, 2009). Both these proposals concern neutral atoms, though.

13.2. Quantum circuit model in optical lattices

The basic unit of quantum information is the quantum bit or qubit, a two-level system or spin- $\frac{1}{2}$ particle described by the simplest Hilbert space \mathbb{C}^2 , with an orthogonal canonical basis (sometimes called computational basis) denoted by $|0\rangle$ and $|1\rangle$. In order to store, process, and read the output of a computation, a quantum register is also needed. A quantum register is a quantum state composed of a string of n -qubits in a Hilbert space of dimension 2^n represented by

$$\Psi(1, 2, \dots, n) = \sum_{k=1}^{2^n} c_{1,2,\dots,n}^k |x_1 x_2 \dots x_n\rangle_k, \quad (13.1)$$

where k labels the configuration of qubits. A computation is implemented in a similar way to the classical case: by means of logical operations or gates. A gate is completely specified by a truth table, which uniquely defines a Boolean operation:

$$\begin{aligned} f : B \times B &\rightarrow B, \\ (a_0, a_1) &\rightarrow f(a_0, a_1), \end{aligned} \quad (13.2)$$

where $B = \{0, 1\}$ is the set of allowed Boolean values. In a quantum computer each gate corresponds to a unitary evolution acting on the qubits. A computation can be associated with a concatenation U_i, \dots, U_l of unitary operations applied on the whole quantum register

$$\Psi_{out}(1, 2, \dots, n) = U_i, \dots, U_l \Psi_{in}(1, 2, \dots, n). \quad (13.3)$$

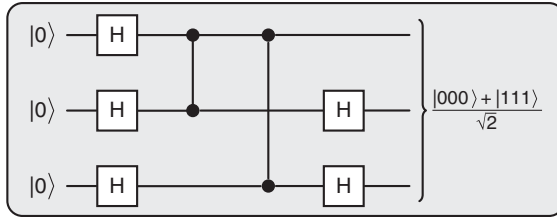


Figure 13.1 Schematic representation of a quantum circuit composed of a sequence of one-qubit Hadamard (H) gates plus two-qubit CNOT gates to create a Greenberger–Horne–Zeilinger state.

Universality refers to the minimal resources needed to implement any unitary operation U , and hence any computation. Universal quantum computation requires the ability to generate qubits in arbitrary superpositions, i.e. $|x\rangle = |a\rangle + |b\rangle \equiv a|0\rangle + b|1\rangle$, $a, b \in \mathbb{C}$ (one-qubit gates) plus the capability to create entanglement between two qubits, i.e. two-qubit gates. In Barenco (1995) it was shown that these two types of gate are enough to form a universal set, meaning that any reversible computation, no matter how complex, can be decomposed as a sequence of single-qubit operations and two-qubit operations acting on the quantum register. A quantum circuit corresponds to the concatenation of such gates that results in the desired output, as shown schematically in Figure 13.1.

It can be easily shown that any 2×2 unitary matrix (one-qubit gate) can be decomposed as a sequence of rotations (Nielsen and Chuang, 2000):

$$U = e^{i\alpha} \begin{pmatrix} e^{-i\beta/2} & 0 \\ 0 & e^{i\beta/2} \end{pmatrix} \begin{pmatrix} \cos(\gamma/2) & -\sin(\gamma/2) \\ \sin(\gamma/2) & \cos(\gamma/2) \end{pmatrix} \begin{pmatrix} e^{-i\delta/2} & 0 \\ 0 & e^{i\delta/2} \end{pmatrix}, \quad (13.4)$$

where $\alpha, \beta, \gamma, \delta$ are real-valued. Among one-qubit gates, the Hadamard gate, denoted by H, is very useful for creating superpositions $H|0\rangle = (1/\sqrt{2})|0\rangle + |1\rangle$, where the corresponding unitary matrix is written

$$U_H = \frac{1}{\sqrt{2}} \begin{pmatrix} 1 & 1 \\ 1 & -1 \end{pmatrix}. \quad (13.5)$$

A non-trivial entangling two-qubit gate is the so-called CNOT gate, which corresponds to a unitary evolution U_{CNOT} , whose matrix in the computational basis $\{|00\rangle, |01\rangle, |10\rangle, |11\rangle\}$ is

$$U_{CNOT} = \begin{pmatrix} 1 & 0 & 0 & 0 \\ 0 & 1 & 0 & 0 \\ 0 & 0 & 0 & 1 \\ 0 & 0 & 1 & 0 \end{pmatrix}. \quad (13.6)$$

In a more compact form this can be written $|x_1\rangle|x_2\rangle \rightarrow |x_1\rangle|x_1 \oplus x_2\rangle$, where the direct sum indicates addition modulo 2. The first qubit, whose value never changes, is conventionally called the control qubit, while the second is the target. The CNOT and the rotation

one-qubit gates are universal in the stricter sense: for fixed k , any k -qubit gate can be composed out of a fairly small number of CNOT and one-qubit rotation gates. Let us illustrate the meaning of universality with an example: we would like to implement the SWAP operation consisting of swapping the value of the first qubit and the value of the second, i.e. $U(|x_1\rangle|x_2\rangle) \rightarrow |x_2\rangle|x_1\rangle$, with $|x_i\rangle = a_i|0\rangle + b_i|1\rangle$. We can achieve such a task by the concatenation of CNOT gates as follows (Nielsen and Chuang, 2000):

$$\begin{aligned} \text{CNOT}_{12} \quad (|x_1\rangle|x_2\rangle) &= |x_1\rangle|x_1 \oplus x_2\rangle, \\ \text{CNOT}_{21} \quad (|x_1\rangle|x_1 \oplus x_2\rangle) &= |x_1 \oplus (x_1 \oplus x_2)\rangle|x_1 \oplus x_2\rangle = |x_2\rangle|x_1 \oplus x_2\rangle, \\ \text{CNOT}_{12} \quad (|x_2\rangle|x_1 \oplus x_2\rangle) &= |x_2\rangle|x_1\rangle, \end{aligned} \quad (13.7)$$

where the sub-indices $\{1, 2\}$ label the qubits and the first subindex in the CNOT operation indicates the control qubit. Another universal and very useful two-qubit gate is the so-called U_{phase} gate, whose truth table in the computational basis reads:

$$\begin{aligned} |0\rangle_1|0\rangle_2 &\rightarrow |0\rangle_1|0\rangle_2, \\ |0\rangle_1|1\rangle_2 &\rightarrow |0\rangle_1|1\rangle_2, \\ |1\rangle_1|0\rangle_2 &\rightarrow |1\rangle_1|0\rangle_2, \\ |1\rangle_1|1\rangle_2 &\rightarrow \exp^{i\phi}|1\rangle_1|1\rangle_2. \end{aligned} \quad (13.8)$$

13.2.1 Two-qubit gates employing cold collisions

How are these gates implemented with ultracold atoms? The first proposal to implement quantum logical operations using ultracold gases in optical lattices was made in Jaksch *et al.* (1999), assuming an optical lattice loaded with a single atom per site, each atom with two internal states. Since interactions between atoms are normally very short-range, the authors proposed to enhance the interactions by bringing the atoms together with time-dependent trapping potentials and then use controlled collisions between the atoms to implement the U_{phase} gate. The starting point of this protocol is a Bose–Hubbard model for two species or two internal states, $|a\rangle$ and $|b\rangle$:

$$\begin{aligned} \hat{H} = \sum_i &\left[\omega^a(t)\hat{a}_i^\dagger\hat{a}_i + \omega^b(t)\hat{b}_i^\dagger\hat{b}_i \right] \\ &+ \sum_i \left[\frac{U^{aa}(t)}{2}\hat{a}_i^\dagger\hat{a}_i^\dagger\hat{a}_i\hat{a}_i + \frac{U^{bb}(t)}{2}\hat{b}_i^\dagger\hat{b}_i^\dagger\hat{b}_i\hat{b}_i \right] + \sum_{ij} \frac{U_{ij}^{ab}(t)}{2}\hat{a}_i^\dagger\hat{a}_i\hat{b}_j^\dagger\hat{b}_j, \end{aligned} \quad (13.9)$$

Here \hat{a}_i (\hat{a}_i^\dagger) and \hat{b}_i (\hat{b}_i^\dagger) are the annihilation (creation) operators of atoms in the internal level $|a\rangle$ ($|b\rangle$) for an atom in the ground state of the potential well at position i . In the above expression direct tunneling has been neglected. The first and second terms contain the offset energy due to the different trapping potentials experienced by atoms in states $|a\rangle$ and $|b\rangle$. The other terms correspond to interaction of atoms of type a , U^{aa} , of type b , U^{bb} , and finally nearest-neighbor interactions between both species, U^{ab} . The implementation of the U_{phase}

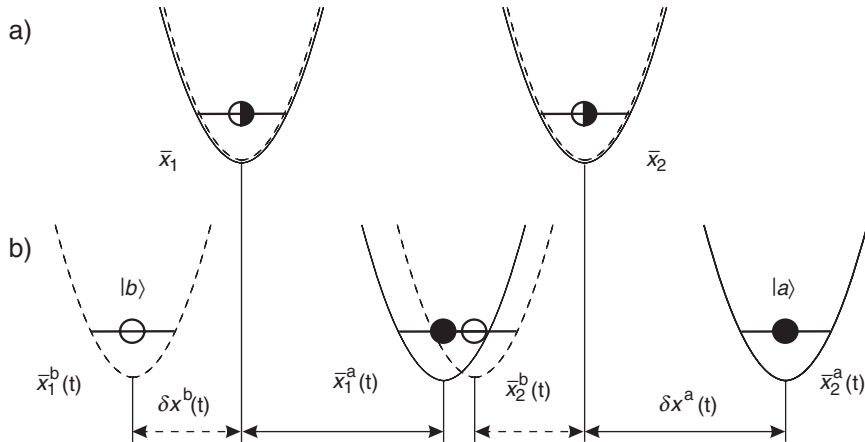


Figure 13.2 Schematic representation of the gate operation. Solid and dashed lines represent potentials felt by the atoms 1 and 2 in states $|a\rangle$ and $|b\rangle$, respectively. By shifting the potentials, the pair of atoms in the middle experiences a collisional shift. From Jaksch *et al.* (1999).

gate requires internal state-dependent potentials, so that the atoms in different internal states feel different potentials (see Figure 13.2). This can be achieved in an optical lattice formed by two linearly polarized counter-propagating traveling waves with the electric fields forming an angle 2θ (lin \angle lin configuration). The resulting electric field is a superposition of right and left circular standing waves (σ^\pm):

$$\mathbf{E}^+(z, t) = E_0 \exp^{-i\nu t} [\sigma^+ \sin(kz + \theta) + \sigma^- \sin(kz - \theta)], \quad (13.10)$$

with σ^\pm denoting unit vector of right and left circular polarization. Jaksch *et al.* (1999) focus on alkaline atoms with nuclear spin equal to $\frac{3}{2}$, and consider as states of interest the hyperfine states of the ground state $S_{1/2}$, $|a\rangle = |F = 1, m_F = 1\rangle$ and $|b\rangle = |F = 2, m_F = 2\rangle$. By tuning the lasers between $P_{1/2}$ and $P_{3/2}$ levels, the polarizabilities of states $m_S = \pm \frac{1}{2}$ due to σ^\mp vanish, whereas the ones due to σ^\pm are identical. The optical potential for these two states reads $V_{m_S=\pm 1/2} = \alpha |E_0|^2 \sin^2(kz \pm \theta)$. Decomposing $|a\rangle$ and $|b\rangle$ in the basis of the fine-structure ground states, one finds that $|b\rangle$ has only component $+\frac{1}{2}$ and therefore feels only potential $V_{m_S=1/2}$. In contrast, $|a\rangle$ has overlap with both fine-structure ground states and feels a combination of $V_{m_S=1/2}$ and $V_{m_S=-1/2}$. By varying the angle θ in time, from $\frac{\pi}{2}$ (0) to 0 ($\frac{\pi}{2}$), the optical potentials for the two species move in opposite directions, approaching (separating from) one another.

The protocol to implement a U_{phase} gate is schematically indicated in Figure 13.2 for two adjacent atoms, each initially prepared as a superposition of their internal states. Initially, the potential wells are sufficiently separated so that there is no interaction between the atoms. The potentials are then moved along certain trajectories toward each other, so that the atoms interact for a certain time if they are in a different internal state, or do not interact at all if they are in the same internal state. Finally the wells are restored to their

initial positions. The potential wells are moved adiabatically, so that the atoms remain in the respective ground states of the wells.

It is assumed that:

- (i) there is no sloshing motion of the atoms in the wells when the latter are moved
- (ii) the potentials are moved so that the atoms remain in the ground state (adiabaticity condition)
- (iii) the velocity of the atoms in the vibrational ground state is sufficiently small that the zero-energy s -wave scattering approximation is valid.

Then, the trajectories, i.e. $\theta(t)$, are chosen in such a way that the two atoms 1 and 2 collide only if they are in the states $|a\rangle$ and $|b\rangle$, respectively. The evolution of the two atoms under the desired trajectories will result in a unitary transformation corresponding to

$$\begin{aligned} |a\rangle_1|a\rangle_2 &\rightarrow \exp^{2i\phi_a} |a\rangle_1|a\rangle_2, \\ |a\rangle_1|b\rangle_2 &\rightarrow \exp^{i(\phi_a+\phi_b+\phi_{ab})} |a\rangle_1|b\rangle_2, \\ |b\rangle_1|a\rangle_2 &\rightarrow \exp^{i(\phi_b+\phi_a)} |b\rangle_1|a\rangle_2, \\ |b\rangle_1|b\rangle_2 &\rightarrow \exp^{2i\phi_b} |b\rangle_1|b\rangle_2, \end{aligned} \quad (13.11)$$

where the motional states remain unchanged, and there is only a conditional phase ϕ_{ab} . All other phases are dynamical and can be absorbed into the definition of the state. The above unitary corresponds thus to a universal U_{phase} gate. Other proposals to perform quantum computation with atoms in optical lattices using cold collisions in different configurations can be found for instance in Lewenstein *et al.* (2007).

13.2.2 Two-qubit gates employing exchange and superexchange interactions

In the recent years, new tools have appeared for trapping and manipulating the state of the atoms and hence their interactions, leading to novel ways of entangling and constructing universal quantum gates. These new proposals rely heavily on the use of double-well lattices, i.e. lattices whose unit cells contain two sites. This has opened the possibility of isolating and individually addressing pairs of atoms, hence allowing manipulation of the interactions between them. In the original proposals, the goal was to allow only for collisions between specific spins or internal states of atoms, by having state-dependent motion, interaction, or excitations. A different approach to achieve a quantum gate is to exploit the statistical nature of the particles and their inherent symmetry properties. This permits control of the spin–spin interactions between atoms using exchange and superexchange interactions.

In this spirit, a seminal experiment by Porto and collaborators (Anderlini *et al.*, 2007) demonstrated controlled exchange interactions between pairs of atoms when they are forced to be in the same location. This permits creation of two-qubit gates between neighboring atoms in the double well potential, in a controlled manner and with coherence times of the order of milliseconds, as schematically shown in Figure 13.3(a). To illustrate the working scheme of a two-qubit gate with bosons, the authors considered a pair of ^{87}Rb atoms, each occupying the single-particle vibrational ground state of two adjacent potential wells, denoted as left (L) and right (R), with spatial wave functions $\phi_\nu(x)$, with $\nu = L, R$.

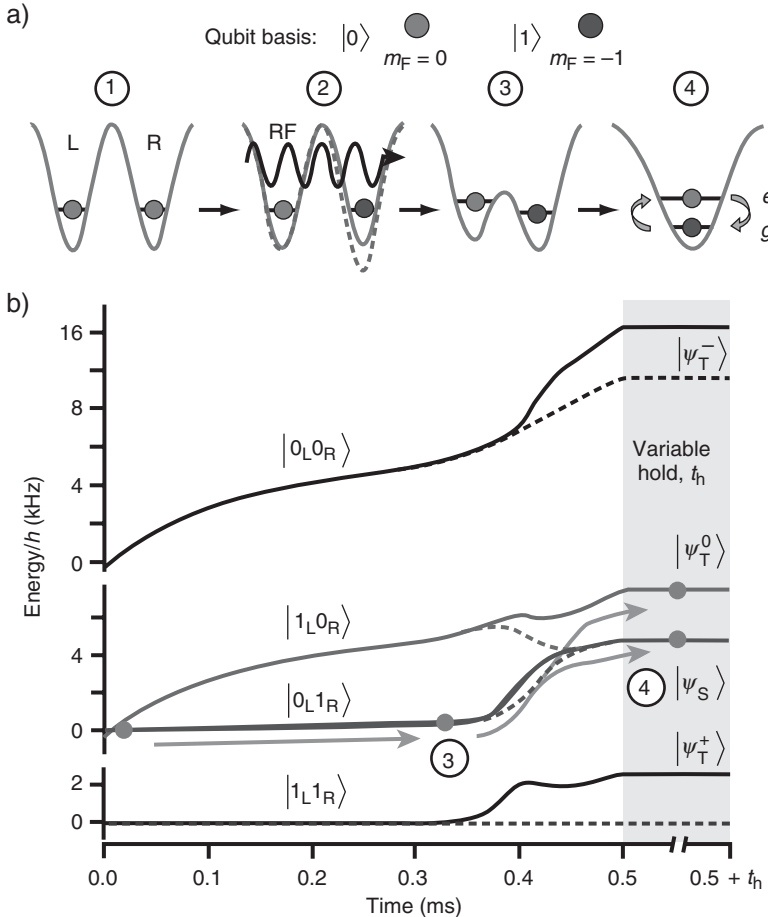


Figure 13.3 (a) Schematic illustration of the sequence of operations used by Porto and collaborators to realize a two-qubit gate. (b) Time evolution during the gate sequence of the interacting (solid lines) and non-interacting (dashed lines) two-particle energies, where the mixing of the two logic qubit states $|0_L, 1_R\rangle$ and $|1_L, 0_R\rangle$ can be seen. From Anderlini *et al.* (2007).

The atoms, moreover, have two internal Zeeman states, which are denoted as $|0\rangle$ and $|1\rangle$, and they are prepared in the state $|q\rangle = a|0\rangle + b|1\rangle$ with $a, b \in \mathbb{C}$. Thus, the full single-atom wave function is

$$|q_\nu\rangle = \phi_\nu(x)|q\rangle. \quad (13.12)$$

To initiate the interaction, the L and R sites are merged into a single site, so that the spatial probability distributions of atoms overlap. The merging process is done in such a way that the atoms in L and R wells are adiabatically transferred to the vibrational excited

state (e) and ground state (g) of the single well, respectively. In the merged trap

$$\begin{aligned}\phi_L(x) &\rightarrow \phi_e(x), \\ \phi_R(x) &\rightarrow \phi_g(x).\end{aligned}\tag{13.13}$$

Since the two qubits are encoded by identical bosons, the full two-particle wave function must be symmetric under particle exchange. In the merged trap it reads

$$|q_L, p_R\rangle = \phi_L(x_1)|q\rangle_1 \otimes \phi_R(x_2)|p\rangle_2 + \phi_L(x_2)|q\rangle_2 \otimes \phi_R(x_1)|p\rangle_1,\tag{13.14}$$

where 1 and 2 label the atoms. The symmetrized states, $|0_L, 0_R\rangle, |0_L, 1_R\rangle, |1_L, 0_R\rangle, |1_L, 1_R\rangle$, form the most appropriate computational basis to identify the qubit straightforwardly. However, when the atoms interact in the merged trap, the symmetrized energy eigenstates are no longer in the computational basis. A new expression for the total wave function can be easily rewritten in a new basis by factorizing the spatial and the spin parts into singlet and triplet components

$$\begin{aligned}|\psi_S\rangle &= \phi_S(x_1, x_2)|S\rangle = (|1_e, 0_g\rangle - |0_e, 1_g\rangle)/\sqrt{2}, \\ |\psi_T^0\rangle &= \phi_T(x_1, x_2)|T^0\rangle = (|1_e, 0_g\rangle + |0_e, 1_g\rangle)/\sqrt{2}, \\ |\psi_T^-\rangle &= \phi_T(x_1, x_2)|T^-\rangle = |0_e, 0_g\rangle, \\ |\psi_T^+\rangle &= \phi_T(x_1, x_2)|T^+\rangle = |1_e, 1_g\rangle.\end{aligned}\tag{13.15}$$

So, if the spatial part is antisymmetric, the spin part should also be antisymmetric under exchange of particles, but if the spatial part is symmetric under exchange of particles, the spin part must be symmetric too. These two configurations have, however, quite different interacting energies. If the two atoms are in the antisymmetric spatial configuration, they do not interact since there is no wave function overlapping. If, on the other hand, they are in any configuration within the triplet spatial state, there is a interaction energy arising from the overlap of the spatial wave functions in the ground and first vibrational excited states of the merged trap $U_{eg} = (8\pi\hbar^2 a_s/m) \int |\phi_e(x)|^2 |\phi_g(x)|^2 d^3x$, with a_s being the scattering length and m the mass. This difference in energy, which depends on the spatial configuration, can be seen as an effective spin–spin interaction $\boldsymbol{\sigma}_e \boldsymbol{\sigma}_g$, with $\boldsymbol{\sigma}$ being the vector of the Pauli spin operators acting on the qubit basis for the atom in the different vibrational modes. Such an interaction can give rise to a spin-exchange oscillation between the qubit states $|0_e, 1_g\rangle, |1_e, 0_g\rangle$. To experimentally observe this effective spin–spin interaction, after a given time $\tau = \pi\hbar/U_{eg}$, the two traps are subsequently separated and one observes that this effective spin–spin interaction has led to an exchange between the internal states of the qubits associated with $\phi_e(x)$ and $\phi_g(x)$. One has realized nothing other than a SWAP operation in the spin degree of freedom. If the merged lattice is returned to a double-well lattice at half period of the SWAP oscillation, an entangling operation that has no classical analog, denoted as $\sqrt{\text{SWAP}}$, is produced.

In the experiment of National Institute of Standards and Technology (NIST) (Anderlini *et al.*, 2007), oscillations corresponding up to 12 applications of the SWAP operation

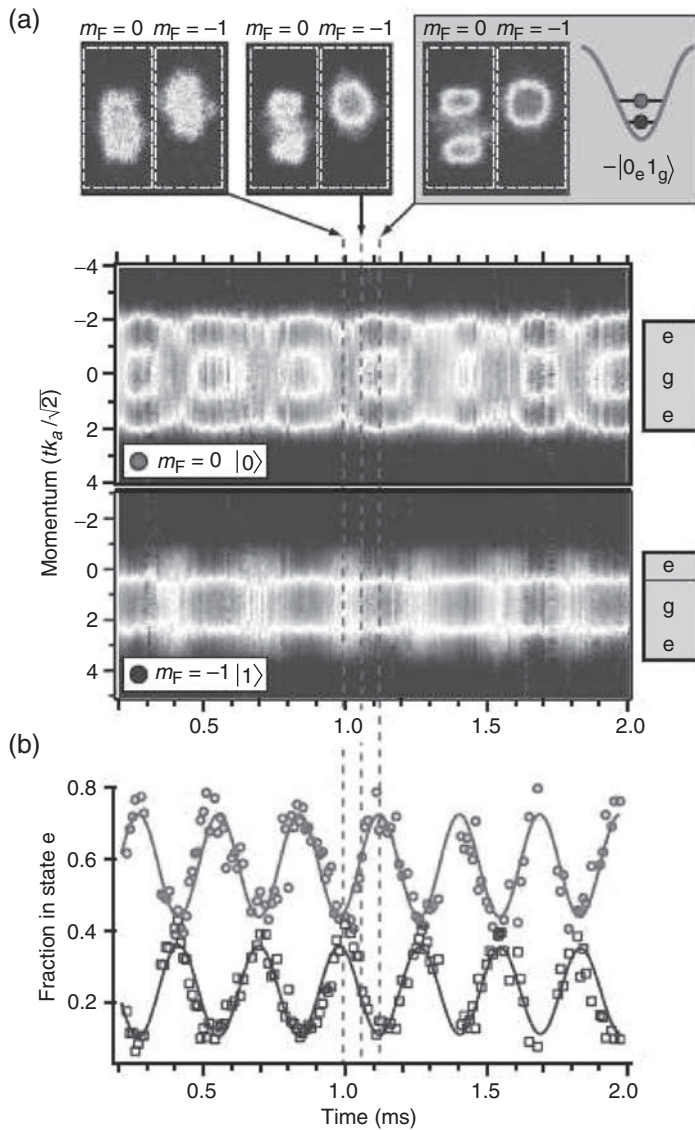


Figure 13.4 (a) Absorption images as a function of time in the single-well configuration. (b) Fraction of total population in the e -state versus time; exchange oscillations are clearly seen for many periods. From Anderlini *et al.* (2007).

between the spins of the adjacent sites without damping or decoherence have been observed (Figure 13.4).

One can also produce an effective spin–spin interaction $H_{\text{eff}} = -J \sum \boldsymbol{\sigma}_i \boldsymbol{\sigma}_j$ without bringing the atoms together in a merged trap, but instead by means of superexchange interactions, that is, virtual tunneling (Trotzky *et al.*, 2008). The interactions between

atoms trapped in two adjacent sites of the optical lattice can be made analogous to the interactions between atomic spins in magnetic materials. For quantum information processing, superexchange interactions can also be used to implement entangling quantum gates. Furthermore, they can be used to create massive entanglement in an optical lattice to directly generate cluster states. As we shall discuss in Section 11.3, superexchange interactions can be used to encode qubits in a manifold with vanishing magnetization, making them more robust in the face of external fluctuations than states created via controlled collisions. To fight against decoherence, either the quantum states have to be naturally protected or the gates have to be operated on timescales much shorter than typical decoherence times. For the collision approach that we outlined in Section 13.2.1, the interaction times cannot be made shorter than the vibrational oscillation frequency, so as to avoid entanglement with the motional states. This implies timescales of the order of a few microseconds, which is too long. A promising route to overcome this problem and obtain faster gates is to use Rydberg atoms (Jaksch *et al.*, 2000; Saffman *et al.*, 2010), or electric dipole–dipole interactions in polar molecules (Micheli *et al.*, 2006), or dipole blockade (Møller *et al.*, 2008).

13.3. One-way quantum computer with lattice gases

Let us now consider a different quantum information model based on single-particle measurements. The one-way quantum computer model (also referred to as ‘measurement-based quantum computation’) was proposed by Raussendorf and Briegel (2001a, 2001b), and is schematically depicted in Figure 13.5. The authors demonstrated that any algorithm implemented in a quantum circuit can be efficiently implemented by performing a sequence of adaptive single-particle measurements, together with single local-particle unitary operations acting on a specific initial state called a *cluster state*. A universal cluster state is a highly entangled multipartite state, which provides a resource sufficient

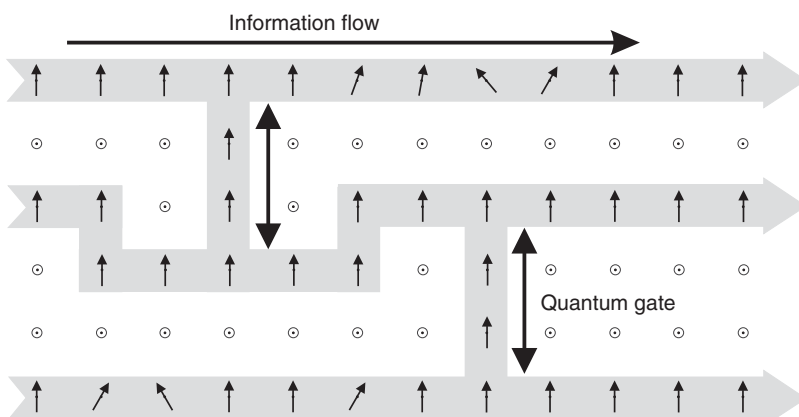


Figure 13.5 Schematic representation of the one-way quantum computer. Redrawn after Raussendorf and Briegel (2001a), by courtesy of the authors.

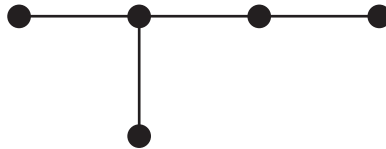


Figure 13.6 An example of a graph. In this case, it has five vertices and four edges. The vertices represent qubits and the edges represent Ising interactions between them.

to carry out any computation. To create universal 2D cluster states (1D cluster states are not universal, since they do not allow for generation of all possible entangled states), interactions and hence entanglement between neighboring atoms along both the vertical and the horizontal directions should take place, taking into account that the highly entangled state should not decohere during the whole sequence of steps of the computation. Because of the essential role of measurements, the one-way quantum computer is irreversible, hence its name. Cluster states could be efficiently created in lattice atomic systems by quantum Ising-type interactions after preparing the system in a specific initial product state.

In order to define cluster states (Raussendorf and Briegel, 2001*b*), let us consider an arbitrary graph made up of N ‘vertices’, identified with the qubits making up the quantum computer, and a certain number of ‘edges’ connecting the vertices, the latter corresponding to Ising interactions between the qubits. This is schematically depicted in Figure 13.6.

The terminology used here comes from graph theory (see, for example, Deo (1974)), and because of this cluster states are also-called ‘graph states’. Suppose that the qubits are spin-half particles, and that each is prepared in the state $|+\rangle = (|0\rangle + |1\rangle)/\sqrt{2}$, where $|0\rangle$ and $|1\rangle$ denote the spin-up and spin-down states along the z direction, respectively. We apply an Ising interaction given by the Hamiltonian

$$H = -J \sum_{(k,l)} \sigma_k^z \sigma_l^z, \quad (13.16)$$

between the qubits, where the summation runs over all pairs (k, l) of sites that are connected by edges in the graph. After a certain finite time $\tau = \frac{\pi}{4J}$, the state

$$H |\phi_C\rangle = \prod_{k,l} (U)_{kl} |+\rangle^{\otimes N} \quad (13.17)$$

is created. Here $(U)_{kl}$ is a just the U_{phase} gate (see eqn (13.8)), defined as

$$\begin{aligned} |0\rangle|0\rangle &\rightarrow |0\rangle|0\rangle, \\ |0\rangle|1\rangle &\rightarrow |0\rangle|1\rangle, \\ |1\rangle|0\rangle &\rightarrow |1\rangle|0\rangle, \\ |1\rangle|1\rangle &\rightarrow i|1\rangle|1\rangle, \end{aligned} \quad (13.18)$$

acting on the spins k and l . The product on the right-hand side of eqn (13.17) again runs over all pairs (k, l) of sites that are connected by edges in the graph. The state $|\phi_C\rangle$ is the cluster

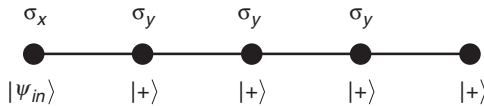


Figure 13.7 A graph to implement the Hadamard gate.

state of the given graph. These states have several interesting properties. Perhaps the most interesting is that for sufficiently large 2D graphs, the corresponding cluster states can be used as a substrate for quantum computational tasks. More specifically, any quantum gate can be implemented with this resource, simply by performing measurements on the different spins of a suitably chosen graph, where it is assumed that the choice of a measurement basis on a particular spin may depend on outcomes of previous measurements on other spins.

Let us illustrate these statements with an example from Raussendorf and Briegel (2001*a*) of how to implement the Hadamard gate H (eqn (13.5)), whose action on the computational basis is:

$$\begin{aligned} |0\rangle &\rightarrow (|0\rangle + |1\rangle)/\sqrt{2}, \\ |1\rangle &\rightarrow (|0\rangle - |1\rangle)/\sqrt{2}. \end{aligned} \quad (13.19)$$

We will use a graph of five vertices in a chain as shown in Figure 13.7. Suppose that at a certain point of computation, we obtain the input state $|\psi_{in}\rangle$, which we want to transform into $H|\psi_{in}\rangle$, with H being the Hadamard gate. The input state is initially at the extreme left and the rest of the spins are initially in the state $|+\rangle$. Ising interactions between nearest-neighbors (as depicted in the figure by the edges) for the required amount of time results in an entangled state of the five spins. Subsequently, measurements are performed on all spins except that on the extreme right, in the eigenbasis of the operator indicated and over the corresponding vertices in the figure. This results in the state $H|\psi_{in}\rangle$ of the spin at the extreme right.

A five-spin graph and corresponding measurements implementing an arbitrary single-qubit gate, together with a 15-spin graph implementing the CNOT gate, can also be found in Raussendorf and Briegel (2001*a, b*). There is a vast literature on one-way quantum computers and the theory of cluster states. For nice tutorials we refer the reader to Browne and Briegel (2006) and Van den Nest *et al.* (2007).

13.3.1 Decoherence-free schemes

The preparation of cluster states has been demonstrated using optical lattices, where the logical qubits are stored directly in individual spins and with controlled collisions used to implement a controlled-phase gate between neighboring spins (Mandel *et al.*, 2003). However, such a scheme suffers severely from decoherence. Obviously, the fight against decoherence concerns all of the quantum computing schemes, and the solutions discussed below can be applied for various computational schemes, not necessarily just the one-way computer.

To fight the problem of decoherence, resilient encoding schemes using four internal states of atoms plus an extra blue laser have been proposed (Kay *et al.*, 2006). Another way is

to use periodic arrays of double-well potentials (see Section 13.2.2), where robust schemes using only two internal Zeeman levels are possible. In such schemes, each double well traps two two-level atoms (spin- $\frac{1}{2}$) to encode a logical qubit. The logical space is then spanned by the singlet and triplet states of the two spin- $\frac{1}{2}$ particles along the quantization axis, e.g. $z |S\rangle = 1/\sqrt{2}(|\uparrow,\downarrow\rangle - |\downarrow,\uparrow\rangle)$ and $T_0 = 1/\sqrt{2}(|\uparrow,\downarrow\rangle + |\downarrow,\uparrow\rangle)$. Since these two states have a zero z component of the total spin, such encoding is insensitive to fluctuations of the magnetic field along the quantization axis (Anderlini *et al.*, 2007). In practice, such a scheme is well suited for robust controlled interactions along one, say horizontal, direction. However, in order to create a universal 2D cluster state, interactions between atoms along both vertical and horizontal directions should be performed in such a way that robustness is preserved.

A possible way to overcome this fragility using superexchange interactions in a periodic array of double-well potentials is to use four physical qubits (four two-level atoms) to encode the logical qubit into the two-fold singlet subspace with $S_{\text{tot}} = 0$ (Jiang *et al.*, 2009). By superimposing two optical lattice potentials with short and long wavelengths differing by a factor of two along both horizontal and vertical directions, a periodic array of 2×2 plaquettes is formed, as shown in Figure 13.8. Thus by doubling the physical resources in comparison to the two-physical-qubit encoding previously mentioned, it is possible to obtain the desired encoding that is decoherence-free against uniform magnetic-field fluctuations in arbitrary directions (Jiang *et al.*, 2009). In such a configuration, also called a ‘supercoherent qubit’, tunable Heisenberg superexchange interactions between neighboring spins, including the diagonal and off-diagonal ones, are sufficient for universal quantum computation. The dynamics of a single plaquette is described by an effective Hamiltonian obtained from

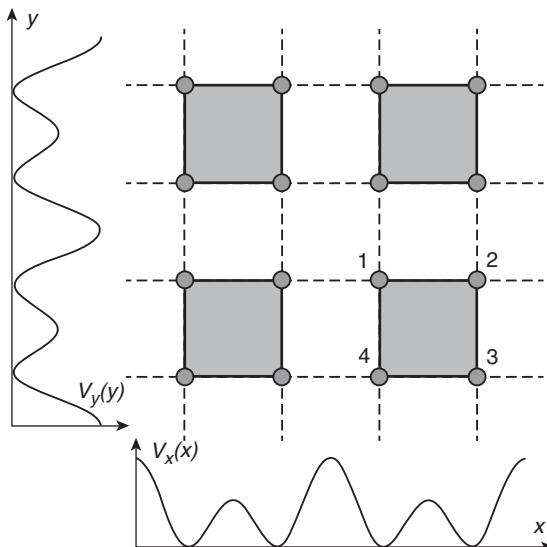


Figure 13.8 The optical superlattice consists of a periodic array of 2×2 plaquettes. The intraplaquette coupling is represented by the solid lines and the inter-plaquette coupling by the dashed ones. From Jiang *et al.* (2009).

the Bose–Hubbard model, with spin-independent tunneling and interactions. Assuming on-site interactions U that are much larger than tunneling t , so that particle tunneling only occurs virtually between neighboring sites giving raise to a superexchange coupling, the Bose–Hubbard Hamiltonian reduces to the effective Hamiltonian

$$H_{\text{eff}} = -J_H(\boldsymbol{\sigma}_1\boldsymbol{\sigma}_2 + \boldsymbol{\sigma}_3\boldsymbol{\sigma}_4) - J_V(\boldsymbol{\sigma}_2\boldsymbol{\sigma}_3 + \boldsymbol{\sigma}_4\boldsymbol{\sigma}_1), \quad (13.20)$$

where $\boldsymbol{\sigma}_i$ refers as usual to the Pauli operators at site i . The coupling strengths are easily obtained from the Bose–Hubbard model with second-order perturbation theory, and are $J_{H/V} = t_{H/V}^2/U$ where $t_{H/V}$ denotes the tunneling along the corresponding directions and U is the interaction energy. The logical qubit subspace reads:

$$\begin{aligned} |0\rangle &= |S\rangle_{2,3}|S\rangle_{4,1}, \\ |1\rangle &= \frac{1}{\sqrt{3}} [|T_+\rangle_{2,3}|T_-\rangle_{4,1} - |T_0\rangle_{2,3}|T_0\rangle_{4,1} + |T_-\rangle_{2,3}|T_+\rangle_{4,1}], \end{aligned} \quad (13.21)$$

where we have followed the notation given in eqn (13.15) for the singlet and triplet. With such encoding it is possible to perform one- and two-qubit operators without leaving the decoherence-free subspace (Jiang *et al.*, 2009).

13.4. Topological quantum computing in optical lattices

A different model of quantum computation, based on statistical properties of topological states of matter, was put forward by Kitaev early in 1997 (Kitaev, 1997, 2003). Topological quantum computation is conceptually different from previous models. Here, information is encoded globally and logical qubits no longer correspond to individual atoms with two internal states. The idea underneath topological order for quantum computation is that such systems are physically built on a mechanism for error correction without resorting to external resources for this task. Topological properties thus provide a fault-tolerant method for quantum computation and quantum memories. Kitaev demonstrated that some topological anyonic systems can efficiently simulate a quantum circuit. Later, in Freedman *et al.* (2003) it was shown that a system of anyons can be simulated efficiently by a quantum circuit. The anyon quantum computer and the quantum circuit model thus have equivalent computational power. Recent reviews concerning topological quantum computation can be found in Preskill (2004) and Nayak *et al.* (2008), where an extensive bibliography is provided. Typically, ‘a topological computation’ consists of creating quasiparticles with fractional statistics (anyons), constructing qubits by combining them (fusion rules), perform gates by braiding them, and finally obtaining the output of the computation by measuring their final state. Braiding refers to trajectories on which the final positions of the particles are equal to the initial ones but some particles might swap positions with some others. In the simplest case, with only two identical particles, the braiding between them means

$$\Psi(\vec{r}_1, \vec{r}_2) = e^{i\theta}\Psi(\vec{r}_2, \vec{r}_1). \quad (13.22)$$

Spin and statistics are concepts that go hand in hand. If $\theta = 0, (\pi)$, one speaks about bosons (fermions). For *any* other value of the phase θ , one speaks about *any*-ons. Thus, anyons refer to (quasi)particles that acquire a non-trivial topological phase when they braid. Furthermore, if the phase θ is not just a number but rather a matrix (or a tensor) acting on some internal degrees of freedom of the particles, one deals with non-Abelian anyons, since matrices in general do not commute. In three dimensions, particles and quasiparticles (excitations) are either bosons or fermions, the reason being the topological property of the 3D rotation group $SO(3)$, in which a rotation by 4π is topologically equivalent to the identity and therefore the only possible eigenvalues of a 2π rotation are +1 (bosons with integer spin) or -1 (fermions with half-integer spin). The 2D rotation group $SO(2)$ does not have this topological property, and braiding in two dimensions can lead to any value of the phase in eqn (13.22). The connection between statistics and braiding requires the creation of many-body excitations, or quasiparticles, since even when confined in a 2D geometry, electrons, protons, neutrons, atoms, or photons remain as being either fermions or bosons. However, if a 2D confined many-body system (composed of fermions or bosons) has localized excitations of its quantum-mechanical ground state—known as quasiparticles—then these quasiparticles can be anyons (Nayak *et al.*, 2008). As a final remark, one should not confuse the braiding phase (one particle winding around another) with the geometrical phase (Berry phase) acquired by a particle as it performs a closed loop.

In the general case of N identical particles, all the trajectories that take the particles from their initial positions at some initial time t_i to their same final positions at time t_f correspond to the elements of the braid group (Nayak *et al.*, 2008). The braid group can be represented algebraically in terms of generators σ_i , with $1 < i < (N - 1)$, where σ_i is a counterclockwise exchange between particles i and $i + 1$. Correspondingly σ_i^{-1} is a clockwise exchange between the i th and the $i + 1$ th particle. The braid group, $\{\sigma\}$, resembles the permutation group S_N , but since $\sigma_i^2 \neq 1$ the braiding group is infinite, in contrast to the permutation group, which has $N!$ elements.

The formation of a different type of anyon by bringing together two anyons is called a fusion rule. In sharp contrast with the previous models of quantum computation, the logical qubit here is a highly non-local entity composed of two or more locally separated anyons. For instance, the simplest universal topological model demands three anyonic quasiparticles to encode a logical qubit. The two states of the qubit correspond to different internal states of the quasiparticles. Gate operations are performed by braiding quasiparticles around each other in a defined way. A final measurement of the state of the system after the various braidings, corresponding to the appropriate gates that have operated, provides the result of the computation. Such a measurement is not a straightforward task. To this end, different proposals of anyonic interferometry have recently appeared (Jiang *et al.*, 2008b).

Which systems can be prepared in a topological state? Systems with topological order should fulfil two requirements. First, they have to have a degenerate ground state whose degeneracy is related to the global properties of the system (topology), in contrast to symmetries, which are linked to local properties. For a system in a topological phase, all observable properties are invariant in the face of small deformations of the space-time manifold where the system lives (diffeomorphisms). Second, the system should be gapped (in the thermodynamical limit) separating the ground state(s) from the low-energy excitations. The presence of such a gap should protect the system from external deformations if these are small and, therefore, from decoherence, which is nothing but the effect of a local operator.

These conditions are necessary but not sufficient, and search for topological states of matter is an active research area in many-body physics and quantum information. As we shall see later, in a 2D system of ultracold bosons or fermions, is it possible to have low-energy quasiparticle (excitations) corresponding to local disturbances of the ground state (vortices), which have anyonic statistics.

13.4.1 Kitaev codes

The toric code In this subsection we shall review the two topological models presented by Kitaev, which are often termed ‘topological codes’, due to their relation to quantum error correcting codes: the toric code created by a spin lattice in a torus geometry and the code formed by a planar honeycomb spin lattice. The first of these has Abelian anyonic excitations, while in the second case the excitations can be non-Abelian. The toric code (Kitaev, 1997) is an idealized Hamiltonian designed with the purpose of having anyonic excitations. Here we follow Kitaev (1997) and Preskill (2004) to explain its main features. The system is formed by spin- $\frac{1}{2}$ particles or qubits sitting at the links between the sites of a 2D square lattice, whose boundary conditions match the geometry of a doughnut, or torus. The Hamiltonian describing the system is

$$H = -J \left(\sum_P Z_P + \sum_S X_S \right), \quad (13.23)$$

with $J > 0$. The Hamiltonian is split between plaquette operators with index P , being given by $Z_P = \otimes_{j \in P} \sigma_j^z$, i.e. the tensorial product of the four spins belonging to the plaquette, and star (sites) operators, with index S , given by $X_S = \otimes_{j \in S} \sigma_j^x$, being the tensorial product of the four spins that meet at one site (vertex) (see Figure 13.9).

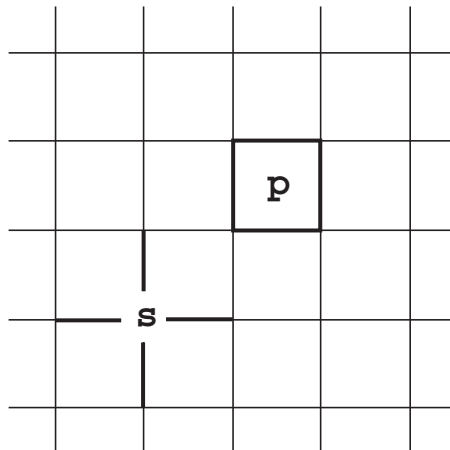


Figure 13.9 Schematic representation of a star (s) and a plaquette (p) in the Kitaev code, corresponding to a square lattice on a torus. Redrawn after Kitaev (2003) by courtesy of the authors.

It is easy to see that different plaquette operators and different star operators commute,

$$[H, Z_P] = [H, X_S] = [Z_P, X_S] = 0, \quad (13.24)$$

so that the ground state of the Hamiltonian, $|\psi_0\rangle$ is the simultaneous eigenstate of all the various Z_P and X_S with eigenvalue +1; that is, the ground-state manifold is defined by $\mathbb{M} = \{|\psi_0\rangle \text{ s.t. } Z_p|\psi_0\rangle = X_S|\psi_0\rangle = |\psi_0\rangle\}$. For these reasons, the Z_P and X_S are called stabilizers in the error-correction context. Moreover, the stabilizers fulfill $\Pi_S X_S = 1$ and $\Pi_P Z_P = 1$, so that the number of independent stabilizers in a lattice of dimension $L = n \times n$ with $2n^2$ spins is $2n^2 - 2$. We see that in this model there are two different types of ‘particles’: ‘star’ and ‘plaquette’ excitations. An eigenvector of the Hamiltonian is an eigenvector of all stabilizers X_S and Z_P , so an excitation means that either $Z_P|\psi\rangle = |\psi\rangle$ or $X_S|\psi\rangle = |\psi\rangle$ is violated. There are two types of localized excitations: plaquette excitations corresponding to an eigenvalue of $Z_P = -1$, and star excitations corresponding to an eigenvalue of $X_S = -1$. Since $\Pi_S X_S = 1$ and $\Pi_P Z_P = 1$, a single excitation cannot occur and excitations always occur in pairs. These excitations are created by spin-flips. A z spin-flip acting on a link creates a pair of star excitations on the two sites joined by the link. In the same way, an X error acting on a link creates a pair of plaquette excitations on the two plaquettes that share that link. The energy gap, J , corresponds to the cost of creating a pair of either type. What makes this an anyon model is that a non-trivial topological phase is acquired when a star-excitation is winding around a plaquette-excitation. There are two possible ways of winding on the torus surface: one corresponds to cycling the torus along the x direction, and the other along the y direction. These two types of windings (which correspond to strings that cannot be contracted) are represented by unitary operators $Z = \prod_{j \in \mathcal{C}_z} \sigma_j^z$ for the plaquette and $X = \prod_{j \in \mathcal{C}_x} \sigma_j^x$ for the sites where \mathcal{C}_z is a loop on the lattice (i.e. plaquettes) and \mathcal{C}_x is a loop in the dual lattice (i.e. stars) (see Figure 13.10 (a)). Moving a plaquette particle around the torus along the x direction is equivalent to applying the operator $Z_{\mathcal{C}_x}$ and so forth. Equivalently, moving a plaquette around a path t in the lattice corresponds to apply the string-operator $\prod_{j \in t} \sigma_j^z$; the same applies if we move a star particle along the dual lattice t' . If we now move a star particle around a plaquette particle (this can be done in the plane—we do not need a torus) we obtain

$$\begin{aligned} |\Psi_{\text{initial}}\rangle &= \prod_{j \in t} \sigma_j^z |\Psi^x(q)\rangle \\ |\Psi_{\text{final}}\rangle &= \prod_{j \in t'} \sigma_j^x \prod_{j \in t} \sigma_j^z |\Psi^x(q)\rangle = -|\Psi_{\text{initial}}\rangle \end{aligned} \quad (13.25)$$

since the two string operators anticommute and $\prod_{j \in t'} \sigma_j^x |\Psi^x(q)\rangle = |\Psi^x(q)\rangle$. So, there is an anyonic exchange of the phase, since x particles and z particles acquire a non-trivial phase when they braid one to each other. The ground-state manifold is given in a compact form by $\mathbb{M} = \text{span}\{T_{\mathcal{C}_x}^i T_{\mathcal{C}_z}^j |\psi_0\rangle; i, j = p, s\}$ (with $T_{\mathcal{C}_x}^p = Z$) and

$$|\psi_0\rangle = \sqrt{|G|} \sum_{g \in G} g |\mathbf{0}\rangle, \quad (13.26)$$

where g is a string of star operators, i.e. a product of σ^x Pauli operators on a set of spins whose corresponding edges in the lattice form a connected string, and $|\mathbf{0}\rangle = |0, 0, \dots, 0\rangle$ is the

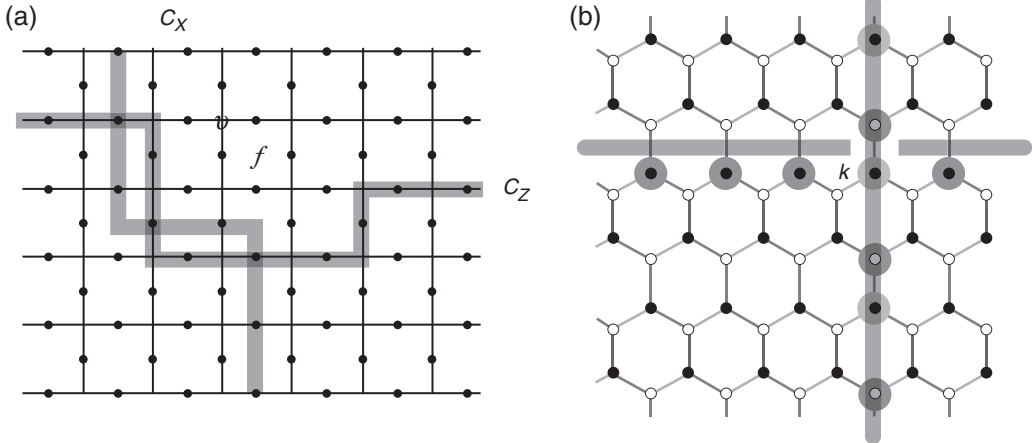


Figure 13.10 Schematic representation of (a) the toric code and (b) honeycomb lattice code and non-trivial windings in both cases. Redrawn after Jiang *et al.* (2008b) by courtesy of the authors.

vacuum reference state with all spins pointing to $+z$ direction. For a lattice with $L = n \times n$ sites and $2n^2$ spins sitting on the links of the square lattice, G is the Abelian group of all star operators generated under tensor multiplication. Due to the periodic boundary conditions, $|G| = 2n^2 - 1$ (Kitaev, 2003; Tsomokos *et al.*, 2009; Jiang *et al.*, 2008b).

The topological degeneracy is compactly expressed as $\dim(\mathbb{M}) = 2^{2g+h}$, where g is the number of genus (holes in the lattice regarded as a Riemann surface) and h denotes the ‘true’ holes. For the torus without the ‘true’ holes, $g = 1, h = 0$, the ground state has the degeneracy 4.

The honeycomb code The toric code is somewhat baroque, with four spin interactions and torus geometry. A spin model with only nearest-neighbor interactions in a planar honeycomb lattice (as depicted in Figure 13.10(b)) was proposed and solved in Kitaev (2006). This model can have non-Abelian anyons, although not the ones that are computationally universal. In the honeycomb model, the interactions between nearest neighbors are of the type XX, YY, or ZZ depending on the direction of the link, and the strength of the interactions is not necessarily equal for all links. In this model, a spin- $\frac{1}{2}$ particle is sitting at each site of the lattice. The model can be solved exactly by transforming it back to the previous toric code. The phase diagram in the parameter space shows that there exist gapped *A*-phases, whose excitations are Abelian anyons. However, in a different regime of the coupling parameters, there is also another phase *B* that is gapless, but can acquire a gap if there is an external magnetic field. In this latter case, the excitations are non-Abelian anyons. A very nice self-contained and detailed explanation of the model can be found in the original reference of Kitaev (2006), which we closely follow here.

The Hamiltonian of the system is given by

$$H = -J_x \sum_{x\text{-links}} \sigma_j^x \sigma_k^x - J_y \sum_{y\text{-links}} \sigma_j^y \sigma_k^y - J_z \sum_{z\text{-links}} \sigma_j^z \sigma_k^z. \quad (13.27)$$

The solution of the model is found by reducing the Hamiltonian to a free real (Majorana) fermionic system. The quasiparticles of the system may be characterized as fermions and \mathbb{Z}_2 vortices. In phase *A* the fermions have an energy gap and the vortices are bosons; braiding one around the other gives a topological phase factor of -1 . In the *B* phase, a gap in the fermionic spectrum can be opened by adding an external magnetic field. The vortices then become then non-Abelian anyons. In Section 13.4.2 we detail how to create non-Abelian anyons in a 2D square fermionic lattice. The different statistics of vortices in the two phases is related to the different topology of the fermionic pairing.

Let us come back to the Hamiltonian in eqn (13.27). By introducing the following notation

$$K_{jk} = \begin{cases} \sigma_j^x \sigma_k^x & \text{if } (j, k) \text{ is an } x\text{-link,} \\ \sigma_j^y \sigma_k^y & \text{if } (j, k) \text{ is an } y\text{-link,} \\ \sigma_j^z \sigma_k^z & \text{if } (j, k) \text{ is an } z\text{-link,} \end{cases} \quad (13.28)$$

and

$$J_{jk} = \begin{cases} J_x & \text{if } (j, k) \text{ is an } x\text{-link,} \\ J_y & \text{if } (j, k) \text{ is an } y\text{-link,} \\ J_z & \text{if } (j, k) \text{ is an } z\text{-link,} \end{cases} \quad (13.29)$$

we get $H = -\sum_{nn} J_{jk} K_{jk}$. It is not difficult to prove that, remarkably, all operators K_{jk} commute with the lattice plaquette operators, which are labeled by p and defined as

$$W_p = \sigma_1^x \sigma_2^y \sigma_3^z \sigma_4^x \sigma_5^y \sigma_7^z = K_{12} K_{23} K_{34} K_{45} K_{56} K_{61} \quad (13.30)$$

and as before $[W_p, W'_p] = 0 = [H, W_p] = [K_{jk}, W_p]$. Now one first divides the total Hilbert space into eigenspaces of W_p , which are also invariant subspaces of the Hamiltonian H . Each operator W_p has eigenvalues ± 1 , so the Hilbert space can be written as a direct sum of each of the invariant subspaces as

$$\mathbb{H} = \otimes_{w_1, \dots, w_m} \mathbb{H}_{w_1, \dots, w_m}, \quad (13.31)$$

where m is the number of plaquettes and each sector corresponds to the choice of the eigenvalue $w_p = 1$ or $w_p = -1$ for each plaquette p . The degrees of freedom within each sector can be described as real Majorana fermions, and the restricted Hamiltonian becomes quadratic in the Majorana representation.

Majorana representation: To this end, we recall that a fermionic system with n modes described by creation and annihilation operators \hat{a}_k^\dagger and \hat{a}_k can be described by Majorana operators \hat{c}_k with the following transformation

$$\begin{pmatrix} \hat{a}_k \\ \hat{a}_k^\dagger \end{pmatrix} \rightarrow \begin{cases} \hat{c}_{2k-1} = \hat{a}_k + \hat{a}_k^\dagger \\ \hat{c}_{2k} = -i(\hat{a}_k - \hat{a}_k^\dagger). \end{cases} \quad (13.32)$$

The Majorana operators are Hermitian and fulfill $\hat{c}_k^2 = 1$ and $\hat{c}_k \hat{c}_l = -\hat{c}_l \hat{c}_k$ if $k \neq l$. Each spin- $\frac{1}{2}$ mode, described by the operators $\{\hat{a}_\uparrow, \hat{a}_\uparrow^\dagger, \hat{a}_\downarrow, \hat{a}_\downarrow^\dagger\}$, has a representation with four

Majorana fermions, so that Majorana representation doubles the fermionic Fock space. At some point one has to project back to the physical space. In this new representation, let us write the Majorana fermions in a compact way as

$$\begin{aligned}\hat{b}^x &= \hat{a}_\uparrow + \hat{a}_\uparrow^\dagger, \\ \hat{b}^y &= -i(\hat{a}_\uparrow - \hat{a}_\uparrow^\dagger), \\ \hat{b}^z &= \hat{a}_\downarrow + \hat{a}_\downarrow^\dagger, \\ \hat{c} &= -i(\hat{a}_\downarrow - \hat{a}_\downarrow^\dagger).\end{aligned}\tag{13.33}$$

Conversely, the spin operators can now be written as:

$$\begin{aligned}\hat{\sigma}^x &= i\hat{b}^x\hat{c}, \\ \hat{\sigma}^y &= i\hat{b}^y\hat{c}, \\ \hat{\sigma}^z &= i\hat{b}^z\hat{c}, \\ \hat{D} &= -i\hat{\sigma}^x\hat{\sigma}^y\hat{\sigma}^z = \hat{b}^x\hat{b}^y\hat{b}^z\hat{c}.\end{aligned}\tag{13.34}$$

Here \hat{D} is a gauge operator fulfilling $[\hat{D}, \hat{\sigma}^\alpha] = 0$. The projection onto the physical space corresponds to demand $\hat{D} = 1$, and is done via the projector operator

$$\hat{P}_{\text{physical}} = \Pi_j \frac{1 + \hat{D}_j}{2}.\tag{13.35}$$

Within this Majorana representation, we notice that eqn (13.28) can be rewritten as

$$\hat{K}_{jk} = \hat{\sigma}_j^\alpha \hat{\sigma}_k^\alpha = (i\hat{b}_j^\alpha \hat{c}_j)(i\hat{b}_k^\alpha \hat{c}_k) = -i\hat{u}_{jk} \hat{c}_j \hat{c}_k,\tag{13.36}$$

where $\hat{u}_{jk} = i\hat{b}_j^\alpha \hat{b}_k^\alpha$. Obviously, \hat{u}_{jk} are Hermitian operators, but as we shall see below, they can be replaced by ± 1 . The reason is that they all commute one with another, as well as with the Hamiltonian $[\hat{u}_{jk}, \hat{H}] = 0$. Since $\hat{u}_{jk}^2 = 1$, we indeed see that \hat{u}_{jk} can be set to ± 1 , and presumably all equal to 1 if we are looking for the ground state.

In this way the Hamiltonian in eqn (13.27) is transformed into a quadratic Hamiltonian of the form

$$\hat{H}(A) = \frac{i}{4} \sum_{jk} A_{jk} \hat{c}_j \hat{c}_k,\tag{13.37}$$

where

$$A_{jk} = \begin{cases} 2J_{jk} u_{jk} & \text{if } j \text{ and } k \text{ are connected} \\ 0 & \text{otherwise} \end{cases}.\tag{13.38}$$

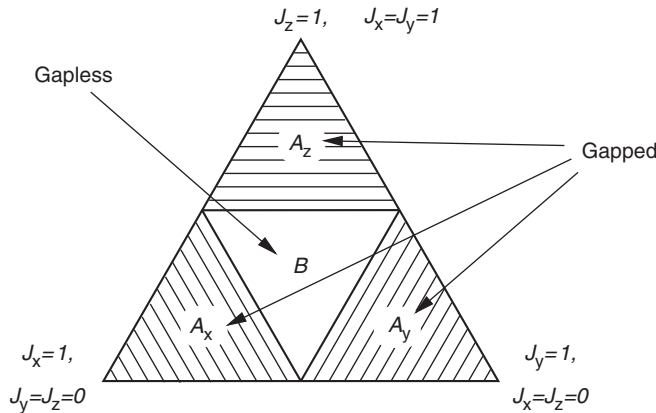


Figure 13.11 The phase diagram of the honeycomb model. Redrawn after Kitaev (2006) by courtesy of the authors.

Note that $A_{jk} = -A_{kj}$ is a real skew-symmetric matrix of size $n = 2m$, where m is the number of plaquettes in the lattice. The Hamiltonian in eqn (13.37) can be diagonalized via a Bogoliubov transformation. The phase diagram is schematically depicted in Figure 13.11. Two different phases A and B , characterized by the absence and the presence of a gap respectively, are found for different values of the initial couplings J_x, J_y, J_z .

Phases A are gapped and are related to each other by rotational symmetry. They differ in the way lattice translations act on anyonic states, so a continuous transition from one of the gapped phases to another is not possible. Phase B is gapless, but it acquires a gap in the presence of an external magnetic field. In a gapped phase, A , spin correlations decay exponentially and spatially separated quasiparticles cannot directly interact. But they interact topologically by braiding around each other (braiding rules). The excitations will correspond to fermions and vortices. When a fermion moves around the vortex the overall quantum state acquires a factor of -1 and corresponds to an Abelian anyon. As the A phase occurs when $|J_z| \gg |J_x| + |J_y|$, one can apply perturbation theory and consider the initial Hamiltonian (eqn (13.27)) as $H = H_0 + V$ where

$$H_0 = -J_z \sum_{z\text{-links}} \sigma_j^z \sigma_k^z, \quad V = -J_x \sum_{x\text{-links}} \sigma_j^x \sigma_k^x - J_y \sum_{y\text{-links}} \sigma_j^y \sigma_k^y. \quad (13.39)$$

The strong z links in the original model, eqn (13.27), become effective spins and can be associated with the links of a new square lattice. Perturbation theory is then applied up to the third order (which is the lowest relevant one), and the effective Hamiltonian becomes

$$H_{\text{eff}} = -\frac{J_x^2 J_y^2}{16 |J_z|^3} \sum_p W_p. \quad (13.40)$$

Finally, after a unitary transformation $U H_{\text{eff}} U^\dagger = H_{tc}$, the effective Hamiltonian becomes the toric code Hamiltonian of the previous subsection, see eqn (13.23). Let us finally

remark that in phase B , which is characterized by a gapless spectrum, due to long-range correlations there are no local and stable excitations. To make phase B gapped we need to add a perturbation that breaks the time-reversal T -symmetry. In this case, one finds chiral Majorana fermions that are similar to the edge modes in quantum Hall systems. It is then possible to show that in some cases a vortex must carry an unpaired Majorana mode, and these excitations are non-Abelian.

13.4.2 Anyonic systems with ultracold gases: p -wave superfluidity

In this section we illustrate in some detail how to create a topological state of matter using ultracold gases in the simpler lattices: a 2D square lattice with the same interaction strength along all directions. There are several models that potentially lead to topological phases. The most relevant from the perspective of ultracold gases are the simulation of the fractional quantum Hall effect (see Chapter 11 and references therein) and the p -wave superconductivity in a 2D geometry (Read and Green, 2000; Das Sarma and Pinczuk, 1997). Paredes and Bloch (2008) showed how minimal instances of topological phases can be achieved for just four spins encoded in an optical plaquette using a superlattice geometry. Such configuration permits creation of superpositions of singlet states leading to resonating valence-bond states, Laughlin states without the need to use a rotating frame, and string-net-condensed states, which could be detected using interferometric schemes. Here we will discuss in detail how to realize p -wave superfluidity using Bose–Fermi mixtures in an optical lattice.

Superfluids with p -symmetry are unconventional superfluids composed of pairs of fermions having a non-zero angular momentum. In the seminal paper of Read and Green (2000) it was demonstrated that the spectrum of an homogeneous p -wave superfluid in two dimensions should be linear, i.e. identical to the one of the Dirac equation, and also that it should contain zero-energy (Majorana) excitations with non-Abelian statistics, analogous to the ones found in $\nu = \frac{5}{2}$ fractional quantum Hall physics (Read and Green, 2000; Gurarie and Radzhovsky, 2007b). This is the most simple system in which a non-Abelian topological state can emerge from ground-state excitations of a many-body system. To achieve the regime we are interested in, strong p -wave interactions between fermions are needed. Normally interactions can be increased with the help of p -wave Feshbach resonances, but if one tries to implement the work of Read and Green (2000) in a fermionic gas confined in a 2D geometry, three-body collisions make the system highly unstable.

In this section we closely follow the work of Massignan *et al.* (2010), and investigate the topological properties of a *confined* 2D fermionic system in a finite optical lattice. Our system is described by an extended Hubbard model, with next-neighbor interactions; such interactions may appear for composite fermions in Fermi–Bose mixtures (as discussed in Chapter 5), or for fermionic dipolar molecules. In both cases one avoids using the lossy p -wave Feshbach resonances. The system exhibits non-Abelian states outside the homogeneous regime for intermediate interaction strengths. The way to progress is to use self-consistent Bogoliubov–de Gennes equations to characterize the topological vortex excitation of the p -wave superfluid.

The starting point is the Fermi–Hubbard Hamiltonian for spinless fermions with nearest-neighbor interactions U , which, due to the Pauli principle cannot collide in an s -wave channel. Restricting ourselves to the lowest band, the tight-binding Hamiltonian on a square

lattice with $N = L \times L$ sites reads:

$$\hat{H} = -\mu \sum_{i=1}^N \hat{c}_i^\dagger \hat{c}_i - t \sum_{\langle i,j \rangle} \hat{c}_i^\dagger \hat{c}_j - \frac{U}{2} \sum_{\langle i,j \rangle} \hat{c}_i^\dagger \hat{c}_i \hat{c}_j^\dagger \hat{c}_j. \quad (13.41)$$

Such a system may then be interpreted as an ensemble of fermionic composites (consisting of a fermion and a boson, or a bosonic hole) with chemical potential μ , hopping with energy $t > 0$ on an otherwise uniformly filled bosonic Mott state (for details see Chapter 5). Following the standard BCS treatment, one can introduce the p -wave gap function $\Delta_{ij} = U \langle \hat{c}_i \hat{c}_j \rangle$, which is naturally antisymmetric due to the anticommuting properties of the fermionic operators \hat{c}_i . Keeping only quadratic terms in the fluctuations around the mean field, the Hamiltonian may be diagonalized by means of the operators $\hat{\gamma}_n = \sum_i u_n(i) \hat{c}_i + v_n(i) \hat{c}_i^\dagger$ ($n = 1, \dots, 2N$), leading to the Bogoliubov–de Gennes (BdG) equations (see Gurarie and Radzhovsky, 2007b):

$$\begin{pmatrix} h_0 & -\hat{\Delta}^\dagger \\ -\hat{\Delta} & -h_0 \end{pmatrix} \begin{pmatrix} u_n \\ v_n \end{pmatrix} = E_n \begin{pmatrix} u_n \\ v_n \end{pmatrix}. \quad (13.42)$$

Here $h_0 u_n(i) = -\mu u_n(i) - t \sum_{\langle j,i \rangle} u_n(j)$ is the ideal-gas tight-binding Hamiltonian on the lattice, while the pairing operator $\hat{\Delta}$ satisfies $\hat{\Delta}^\dagger = -\hat{\Delta}^*$ and acts on the quasiparticle wave functions as $\hat{\Delta} u_n(i) = \sum_{\langle i,j \rangle} \Delta_{ij} u_n(j)$ (the two sums above run over j only). The $2N$ allowed energies appear in pairs of opposite sign since the Hamiltonian is symmetric under the exchange of $\{E_n, \psi_n\}$ with $\{-E_n, \sigma_1 \psi_n^*\}$, where σ_1 is the first Pauli matrix and $\psi_n = (u_n, v_n)^T$. As a consequence of this symmetry, if there exists a solution with $E_0 = 0$, the associated wave function may be chosen to satisfy the condition $u_0 = v_0^*$. The self-consistency condition or gap equation reads

$$\Delta_{ij} = U \langle \hat{c}_i \hat{c}_j \rangle = U \sum_{E_n > 0} u_n^*(i) v_n(j) \tanh \left(\frac{E_n}{2k_B T} \right), \quad (13.43)$$

with k_B the Boltzmann constant and T the temperature.

The total number of particles is

$$N_{\text{tot}} = \sum_i \langle \hat{c}_i^\dagger \hat{c}_i \rangle = \sum_{E_n > 0, i} [|v_n(i)|^2 + f(E_n)(|u_n(i)|^2 - |v_n(i)|^2)], \quad (13.44)$$

where $f(E)$ is the Fermi distribution and the lattice filling is $F = N_{\text{tot}}/N$. The dispersion relation for a homogeneous superfluid on a lattice with chiral ($p_x \pm i p_y$) order parameter $\Delta(\mathbf{k}) = \Delta_h [\sin(k_x a) \pm i \sin(k_y a)]$ reads (Iskin and Sá de Melo, 2005)

$$E(\mathbf{k}) = \sqrt{\xi^2 + |\Delta_h|^2 [\sin^2(k_x a) + \sin^2(k_y a)]}, \quad (13.45)$$

where $\xi = -\mu - 2t[\cos(k_x a) + \cos(k_y a)]$ and a is the lattice constant. This dispersion presents gapless points for three values of μ , i.e. $\mu = -4t, 0, 4t$. In the absence of interactions, these

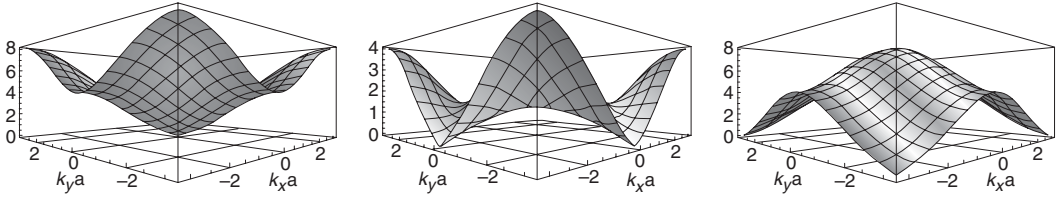


Figure 13.12 The dispersion relation $E(\mathbf{k})/t$ of a uniform chiral p-wave superfluid (here $\Delta_h = t$) vanishes linearly around the Dirac points appearing, from left to right, at $\mu = -4t, 0, 4t$. From Massignan *et al.* (2010).

values correspond respectively to average fillings of $F = 0, \frac{1}{2}, 1$. When $\Delta_h \neq 0$ the dispersion vanishes linearly around the gapless points, as depicted in Figure 13.12, i.e. it coincides with the dispersion relation of the Dirac relation.

Topological modes are known to arise as excitations bound to the core of a vortex in the order parameter. To model a vortex, one uses open boundary conditions and solves eqns (13.42) and (13.43) self-consistently by taking the initial ansatz for the gap

$$\Delta_{ij} = \chi[f_i e^{iw\theta_i} + f_j e^{iw\theta_j}]/2. \quad (13.46)$$

Here $f_i = r_i/\sqrt{r_i^2 + 2\sigma^2}$ is the amplitude of the gap around a vortex with core size σ and r_i and θ_i are the polar coordinates of site i with respect to the core. The chirality factor χ for anti-clockwise chirality $p_x + ip_y$ takes the values $\chi = \pm 1$ when $j = i \pm \hat{\mathbf{x}}$, and $\chi = \pm i$ when $j = i \pm \hat{\mathbf{y}}$. Finally, $w = \pm 1$ is the direction of rotation of the vortex with respect to the chirality.

In the absence of a confining potential, the physics in the lattice exhibits particle-hole symmetry around the half-filling point $\mu = 0$. For $\mu < 0$ ($\mu > 0$), one has $0 < F < \frac{1}{2}$ ($\frac{1}{2} < F < 1$), and the superfluid may be identified with a condensate of pairs of particles (holes). The gap function and the energy of the eigenstates depend only on the modulus of μ , but the wave functions u and v depend on its sign, since the two phases are topologically distinguishable. In free space, zero-energy modes appear when the chemical potential lies inside the continuum of states, the so-called weak-pairing phase. Correspondingly, in a lattice the weak-pairing phases are found for chemical potentials in the ranges $-4t < \mu < 0$ and $0 < \mu < 4t$ for particles and holes, respectively. At intermediate fillings and for sufficiently strong interactions ($t \lesssim U \lesssim 10t$), the modulus Δ_0 of the gap in the bulk (away from the vortex core) at $T = 0$ rises to values $\sim t$ indicating large pairing correlations and critical temperatures (since $T_c \sim \Delta_0$). The low-energy spectrum of the BdG Hamiltonian becomes linear, $|E_n| \sim n\omega_0$, where $n = 0, 1, 2, \dots$. In particular, there exists a quasi-Majorana fermion excitation ψ_0 with an extremely small eigenvalue, $E_0 \ll \Delta_0$. For very strong attraction ($U \gtrsim 10t$), the vortex core size shrinks below a lattice constant, and the lowest-energy excitation quickly loses its topological quasi-Majorana character. In Figure 13.13 we show a typical ψ_0 in the weak-pairing phase; similarly to the zero modes in free space (Read and Green, 2000; Tewari *et al.*, 2007; Gurarie and Radzhivsky, 2007b), it exhibits oscillations that are exponentially damped away from the vortex core. When the vortex

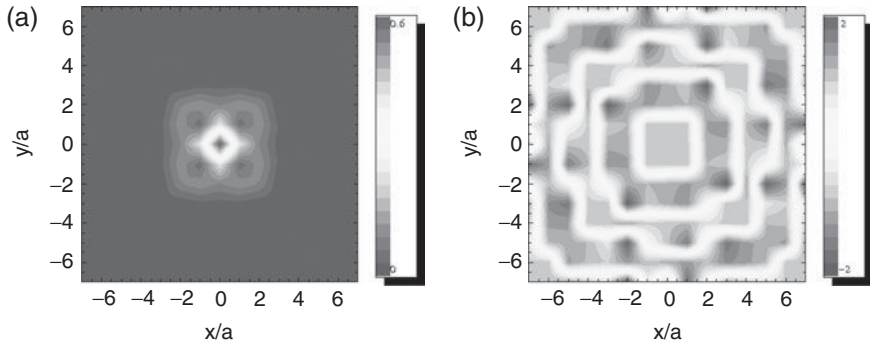


Figure 13.13 Wave function $u_0 = v_0^*$ at $F \sim \frac{1}{4}$, $w = -1$, and $U = 5t$ for a 25×25 lattice size. (a) The modulus is exponentially localized around the vortex core. (b) The phase plot evidences the shape of the nodes adapting to the lattice structure. From Massignan *et al.* (2010).

rotates in the (opposite to the) direction of the chirality, i.e. $w = +1$ ($w = -1$), $|\psi_0|$ has a node (a maximum) at the vortex core.

Finally, it should be noted that, to date, no direct evidence of anyonic states has been experimentally observed, and the accomplishment of such a goal is *per se* a big challenge.

13.5. Distributed quantum information

13.5.1 Classical attractor neural networks

We have seen that topological states of matter can provide robustness for quantum memories and quantum computation by storing information in a logical qubit that is distributed over the system and does not correspond to the physical qubit provided by the spin- $\frac{1}{2}$ particle. Here we want to comment on complex disordered models, such as spin models simulating neural network Hamiltonians, which are a prototype of parallel distributed memory (Amit, 1989; Mézard *et al.*, 1987) and have been intensively studied by physicists since the famous paper by Hopfield (Hopfield, 1984). These disordered systems with long-range interactions typically present a large number of metastable (free) energy minima, as in spin glasses (Mézard *et al.*, 1987). These states can be used to store information distributed over the whole system. The patterns stored have large basins of attraction in the thermodynamic sense, so that even fuzzy ones are recognized as perfect ones. For this reason, attractive neural networks (NNs) can be used as associative memory. At the same time, NNs are robust, so that destroying even a large part of the network does not necessarily diminish its performance. The properties listed above make NNs interesting for *distributed* quantum information, where quantum bits do not correspond to the internal states (spins) of individual particles, but rather to patterns of the internal states of a whole chain (all-up, all-down, half-up-half-down, etc.).

Let us remind the reader how the classical NN models are constructed. Following the works of Hopfield (1984) and Little (1974), a neuron can be viewed as an Ising spin with two possible states: ‘up’ ($S = +1$) and ‘down’ ($S = -1$), depending on whether the neuron

has or has not fired an electromagnetic signal in a given interval of time (Amit, 1989). The state of the network of N neurons at a certain time is defined by the instantaneous configuration of all the spins $\{S_i\}$ at this time. The dynamic evolution of these states is determined by the symmetric interactions among neurons, $J_{ij} = J_{ji}$. Also, full connectivity is assumed, i.e. every neuron can receive an input from any other, and can also send an output to it. The Hamiltonian reads:

$$H = -\frac{1}{2} \sum_{i,j}^N J_{ij} S_i S_j + h \sum_i^N S_i, \quad (13.47)$$

where h corresponds to an external magnetic field. The interactions are determined by the patterns or configurations of spins to be stored in the network. These patterns will be learned if the system is able to accommodate them as attractors, implying that a large set of initial configurations of the network will be driven dynamically to those patterns. A possible choice of the interactions is given by a so-called Hebbian learning rule,

$$J_{ij} = \frac{1}{N} \sum_{\mu=1}^p \xi_i^\mu \xi_j^\mu, \quad (13.48)$$

with $i \neq j$. The p sets of $\{\xi_i^\mu\} = \pm 1$ are the patterns to be stored. The network will have the capacity to store and retrieve information if the dynamical stable configurations (local minima) reached by the system $\{S_i\}$ are highly correlated with the learned ones $\{\xi_i^\mu\}$. Although the interactions have been constructed to guarantee that certain specified patterns are fixed points of the dynamics, the non-linearity of the dynamical process may induce additional attractors, the so-called spurious states.

Complex disordered systems offer at least two possible advantages for quantum computing. First, since they typically have a large number of different metastable (free) energy minima, such states might be used to store information distributed over the whole system, similarly to classical NN models (Amit, 1989). The information is thus naturally stored in a redundant way, like in error-correcting schemes (Shor, 1995; Steane, 1996). Second, in disordered systems with long-range interactions, the stored information is robust: metastable states have quite large basins of attraction in the thermodynamical sense.

13.5.2 Quantum attractor neural networks

It is interesting to ask if the concept of distributed information processing and memory storage can be applied to quantum systems. This would perhaps provide an alternative to robust topological memories and computers, and ensure error tolerance. The utility of such systems for quantum information has been addressed in Pons *et al.* (2007), where the following questions were posed:

- (i) Can one design a quantum system with many metastable states that can serve as quantum analog of the Hopfield model?
- (ii) Can one realize quantum gates with reasonable fidelity?

Both questions were answered affirmatively for the model that employs trapped ions and leads to an effective spin Hamiltonian (for more details see the subsection about ion-based quantum simulators in Chapter 10):

$$H = -\frac{1}{2} \sum_{i,j}^N J_{ij} S_i^z S_j^z + \sum_i^N h_i^z S_i^z + \sum_i^N h_i^x S_i^x. \quad (13.49)$$

Note that this model is quantum due the presence of the transverse field in the x direction.

The interactions in this model are given by

$$J_{ij} = \frac{1}{N} \sum_{\mu=1}^N \xi_i^\mu \xi_j^\mu / \Omega_\mu^2, \quad (13.50)$$

where the patterns *echo* the lowest-energy vibrational (phonon) modes of the system. Ω_μ are phonon frequencies. In Pons *et al.* (2007) it was shown that one can control the phonon dispersion relation by appropriately shaping the external trap potential. One can indeed realize situations where $\Omega_1 \simeq \Omega_2, \dots, \Omega_k \ll \Omega_{k+1}, \dots$, and so on. In such cases one deals with $2k$ quasi-degenerate ground states in the systems (the factor 2 is due to up-down symmetry). One can then code, say, two qubits in such systems by mapping the configurations of the left (right) half of the spins to the first (second) qubit.

In Pons *et al.* (2007) and Braungardt *et al.* (2007) it was indeed shown that by employing time- and space-dependence of the fields $h_i^x(t)$ and $h_i^z(t)$ in a 8–16 ion chain, one can indeed realize error-resistant distributed quantum computation. Unfortunately, at least for the model based on trapped ions, the scalability of such an approach remains problematic.

14

Detection of quantum systems realized with ultracold atoms

14.1. Introduction

The faithful preparation of quantum states in many-body systems, and detection of their properties, incorporated in quantum correlations, is one of the major challenges confronted by experiments with ultracold atoms. It is absolutely crucial for any potential implementation of quantum technology. The knowledge of ground-state properties and low-energy excitations are key ingredients required to describe the response of the system to external perturbations and its low-energy/entropy/temperature dynamics. In contrast to quantum state estimation, the primary goal of the detection of many-body systems is not the full reconstruction of the quantum state. This is so because strictly speaking the set of parameters required to describe quantum many-body systems scales exponentially with the number of particles, making the estimation almost always intractable. Many-body ground-state properties are often reflected through a set of *order parameters* given by local operators with non-vanishing expectation values. Such a set reflects the symmetries (order) embedded in the ground state. Transitions from one quantum phase to another are generally indicated by a sharp change of the order parameter, which is associated with spontaneous symmetry-breaking. This concept, introduced by Landau to explain phase transitions, is one of the cornerstones of modern physics. However, measuring order parameters is not always possible; even finding the appropriate set of order parameters to accurately describe a many-body ground state can be very hard or even meaningless. For instance, there are topological ground states that cannot be described by local order parameters. To signal the appearance of such quantum phases a highly non-local parameter, such as the string order parameter, is often necessary.

Correlations in many-body quantum systems can be analysed through ground-state properties, collective modes, and excitations. In many-body systems two different types of excitation co-exist: many-body collective excitations and single-particle ones. The latter correspond to the addition or removal of a single particle from the many-body ground state. Both types of excitation occur at different energy and momentum scales, but both of them provide valuable information about the ground-state properties. Probing the system with an external probe shows that at low momentum transfer, the collective excitations are typically responsible for the macroscopic response. At high momentum transfer, in contrast, the response comes typically from inelastic scattering from individual atoms. Remarkably, spectroscopic methods connect different aspects of the microscopic structure to the macroscopic response, which can be measured.

A standard method to measure excitations in condensed-matter systems is the linear response. Linear response refers to the perturbative response of a system when it is coupled linearly to a probe \hat{G} that delivers some momentum \mathbf{k} and energy $\hbar\omega$ to the system. The effect of the perturbative coupling

$$\hat{H}_{\text{pert}} = -\lambda \hat{G} e^{-i\omega t} + h.c. \quad (14.1)$$

is analysed through the fluctuations of another (or the same) physically relevant operator \hat{F} . In alkaline condensates, the first experiments to study excitations were done by deforming the harmonic trap that confined the condensate and letting the system evolve (Pitaevskii and Stringari, 2003). In general, the response of ultracold atomic systems to linear perturbations provides first-order (single-particle spectral function) and second-order (dynamical structure factor) correlation functions, which are defined as the Fourier transforms of the one-particle and two-particle correlations of a given operator \hat{F} , respectively. In the case of one-particle correlations, \hat{F} corresponds to the field operator $\hat{\Psi}$ and the measured correlations to a single-particle-density matrix $\langle \hat{\Psi}^\dagger(\mathbf{r}, t)\hat{\Psi}(\mathbf{r}', t') \rangle$. Two-particle correlations, meanwhile, account for density-density $\langle \hat{\rho}(\mathbf{r}, t)\hat{\rho}(\mathbf{r}', t') \rangle$ or spin-spin $\langle \hat{S}(\mathbf{r}, t)\hat{S}(\mathbf{r}', t') \rangle$ correlations. In the solid state, spectroscopic techniques such as angle-resolved photoemission spectroscopy (ARPES) and neutron scattering have become reference methods to provide insight into the excitations of the material through the spectral function or the dynamic structure factor, respectively. Photoemission spectroscopy for electronic systems allows us to probe the occupied single-particle states. The technique consists of counting the energy- and momentum-resolved photoelectrons ejected from a substance through the photoelectric effect.

The application of photoemission spectroscopy to cold Fermi gases was theoretically proposed in Dao *et al.* (2007), and experimentally realized in Stewart *et al.* (2008). Time-of-flight measurements and Raman spectroscopy also give insight into the single-particle correlation functions, while Bragg spectroscopy or shot-noise correlations involve two-particle excitations. All these methods will be discussed in this chapter. The relationship between each measurement and the correlation function is most explicit in scattering experiments, where the differential scattering cross-sections provide information about the correlations as a consequence of Fermi's golden rule, which, in the Born approximation, reads:

$$\frac{d^2\sigma}{d\Omega d\omega} \sim \Gamma_{i \rightarrow f} = \frac{2\pi}{\hbar} \sum_f p_i |\langle f | \hat{F} | i \rangle|^2 \delta(E_f - E_i), \quad (14.2)$$

where p_i is the probability of being in the initial state $|i\rangle$ and \hat{F} describes the way the external probe couples to the system. Typically, the probe couples an initial state $|i\rangle = |\mathbf{q}|n\rangle$ with a final state $|f\rangle = |\mathbf{q}'|m\rangle$, with $\mathbf{k} = \mathbf{q}' - \mathbf{q}$ being the momentum delivered by the probe and $|j\rangle$ with $j = n, m$ denoting the eigenstates of the many-body Hamiltonian $\hat{H}|j\rangle = E_j|j\rangle$ such that $E_m - E_n = \hbar\omega_{mn}$. The correlation function associated with the

observable \hat{F} reads:

$$C(\mathbf{r}, \mathbf{r}'; t, t') = \langle \mathcal{T}[\hat{F}(\mathbf{r}, t)\hat{F}^\dagger(\mathbf{r}', t')]\rangle = \sum_{n,m} \frac{e^{-\beta E_n}}{Z} e^{-i(E_n - E_m)(t-t')/\hbar} \langle m|\hat{F}|n\rangle \langle n|\hat{F}^\dagger|m\rangle, \quad (14.3)$$

where \mathcal{T} indicates the time-order product and $\beta = 1/k_B T$, with k_B being the Boltzmann constant and T being the temperature. The spectral function, measuring how many states contribute to the correlation function in a given energy interval, can be calculated by Fourier transforming eqn (14.3):

$$\bar{C}(\mathbf{k}, \omega) = \sum_{n,m} \frac{e^{-\beta E_n}}{Z} |\langle m|\hat{F}_\mathbf{k}|n\rangle|^2 \delta(\omega - \omega_{mn}), \quad (14.4)$$

which, for the single-particle and two-particle excitations, corresponds to the single-particle spectral function:

$$A(\mathbf{k}, \omega) = \sum_{n,m} \frac{e^{-\beta E_n}}{Z} |\langle m|\hat{\Psi}_\mathbf{k}^\dagger|n\rangle|^2 \delta(\omega - \omega_{mn}), \quad (14.5)$$

and the dynamic structure factor:

$$S(\mathbf{k}, \omega) = \sum_{n,m} \frac{e^{-\beta E_n}}{Z} |\langle m|\hat{\rho}_\mathbf{k}^\dagger|n\rangle|^2 \delta(\omega - \omega_{mn}), \quad (14.6)$$

respectively. In the case of ultracold atoms in optical lattices, the single-particle correlation function probes excitations of the system by adding or removing one particle. It is therefore described by the creation $\hat{\Psi}_\mathbf{k}^\dagger = \hat{b}_\mathbf{k}$ or annihilation operator $\hat{\Psi}_\mathbf{k} = \hat{b}_\mathbf{k}^\dagger$ of a single particle. In the two-particle excitation case, $\hat{\rho}_\mathbf{k}^\dagger = \sum_q \hat{b}_{\mathbf{q}+\mathbf{k}}^\dagger \hat{b}_\mathbf{q}$ is the density operator that creates an excitation with momentum \mathbf{k} by transferring particles from a state with quasimomentum \mathbf{q} to a state with quasimomentum $\mathbf{q} + \mathbf{k}$. Equations (14.5) and (14.6) at $T = 0$ reduce to:

$$A(\mathbf{k}, \omega) = \sum_m |\langle m|\hat{\Psi}_\mathbf{k}^\dagger|0\rangle|^2 \delta(\omega - \omega_{m0}), \quad (14.7)$$

$$S(\mathbf{k}, \omega) = \sum_m |\langle m|\hat{\rho}_\mathbf{k}^\dagger|0\rangle|^2 \delta(\omega - \omega_{m0}). \quad (14.8)$$

Thus, the dynamic structure factor, eqn (14.7) or (14.8) at $T = 0$, characterizes the scattering cross-section of inelastic processes where the probe transfers momentum $\hbar\mathbf{k}$ and energy $\hbar\omega$ to the system. Very importantly, sum rules and completion relations connect the moments of the structure factor to expectation values of relevant operators (Pitaevskii and Stringari, 2003; Roth and Burnett, 2004). In general, different detection methods may provide complementary information about different types of correlations embedded

in the many-body systems of interest. In the following we will discuss some of these methods:

- (i) time of flight, which provides a straightforward measurement of the Fourier transform of the two-point density correlation function by opening the trap that contains the many-body system and imaging it after free expansion (Bloch *et al.*, 2008)
- (ii) noise correlations after time-of-flight, which allow us to infer second and higher orders in the density-density correlations (Altman *et al.*, 2004; Bach and Rzążewski, 2004a; Bach and Rzążewski, 2004b),
- (iii) Bragg spectroscopy, providing a direct measure of the dynamic structure factor and allowing detection of the full momentum structure of the excitations
- (iv) optical Bragg diffraction, which has been used for detection of some types of magnetic ordering
- (v) single-atom detectors based on high-resolution fluorescence imaging
- (vi) quantum polarization spectroscopy, which could provide the dynamic spin-structure factor, as well as some other local order parameters.

14.2. Time of flight: first-order correlations

A particularly useful and easy way to obtain information about the state created with cold gases is via time-of-flight experiments (Bloch *et al.*, 2008). Time-of-flight measurements probe the single-particle Green's function at equal times $\langle \Psi^\dagger(\mathbf{r}, t)\Psi(\mathbf{r}', t) \rangle$, i.e., the one-body density matrix. Its Fourier transform is the momentum distribution $\hat{n}(\mathbf{q})$. A time-of-flight image of an ultracold gas is obtained by light absorption imaging after releasing the sample from the trap and letting the atoms fall due to gravitation for a certain time t_{tof} . The image is the result of a quantum measurement of the column-density distribution operator, i.e. the momentum density integrated along the laser axis (say the z -axis) after a time of flight t_{tof} . If the free-atom interaction cross-section of ultracold atoms is very small (i.e. if the sample is not very dense and the system is far from Feshbach resonances when the trap is turned off), atoms can be considered to fall freely and hence (neglecting the irrelevant shift due to gravity) the position of an atom after time of flight is given by $\vec{r}(t_{\text{tof}}) = \hbar t_{\text{tof}} \vec{q}/m$, where \vec{q} is the momentum of the atom in the trap. Thus, one can reinterpret the image as the outcome of a quantum measurement of the z -integrated momentum density operator of the sample in the trap, namely

$$\hat{n}(\mathbf{q}) = \int dq_z \hat{\Psi}^\dagger(\mathbf{q}, q_z) \hat{\Psi}(\mathbf{q}, q_z), \quad (14.9)$$

where $\hat{\Psi}(\mathbf{q}, q_z)$ ($\hat{\Psi}^\dagger(\mathbf{q}, q_z)$) is the Fourier transform of the annihilation (creation) field operator and \mathbf{q} now refers to a 2D momentum that is mapped onto the 2D image. By repeating the experiment, different images are obtained at each shot, which can be used to compute the averaged momentum density operator $\langle \hat{n}(\mathbf{q}) \rangle$. An example of time-of-flight imaging for a BEC of ${}^7\text{Li}$ is shown in Figure 14.1. In this case, since the molecular condensate is strongly interacting, the scattering length is decreased abruptly before the expansion in order to reduce the mean-field energy.

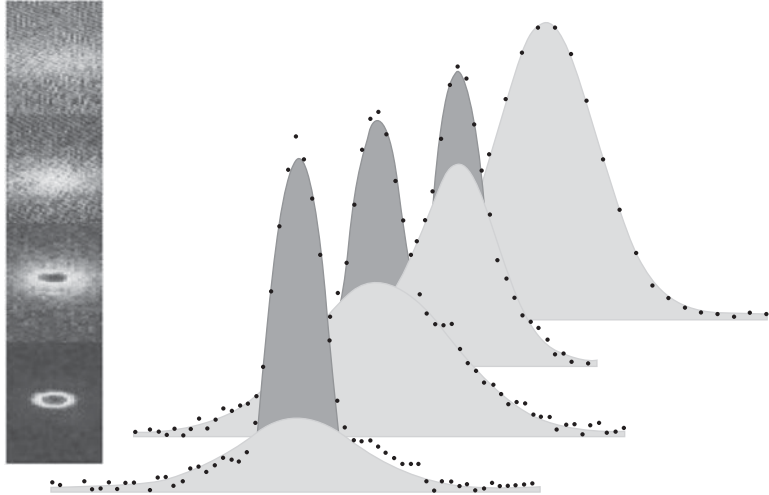


Figure 14.1 Time of flight (column density) in a molecular BEC of ${}^7\text{Li}$. Since the molecular BEC is strongly interacting, it is typically difficult to clearly distinguish between thermal and condensed fractions. To overcome this, one can abruptly change the scattering length before time-of-flight to a smaller value. This dramatically reduces the mean-field energy, and therefore the expansion of the condensed part, but leaves the thermal cloud unaffected. Figure and text by courtesy of Selim Jochim.

For a system of ultracold gases in an optical lattice consisting of N sites, the field operators can be expressed, in the tight binding regime, as a linear combination of Wannier functions $\hat{\Psi}(\mathbf{r}) = \sum_i w(\mathbf{r} - \mathbf{r}_i) \hat{a}_i$, where \mathbf{r}_i denotes the space coordinate of the i th lattice site, \hat{a}_i the atom annihilation operator at site i , and $w(\mathbf{r} - \mathbf{r}_i)$ denotes the corresponding Wannier function. Using a Gaussian ansatz for the Wannier functions, e.g. $w(\mathbf{r} - \mathbf{r}_i) = \frac{1}{(\pi)^{3/4} \sqrt{\sigma}} \exp^{-(\mathbf{r}-\mathbf{r}_i)^2/\sigma^2}$, the density correlation function can be expressed as

$$\langle \hat{n}(\mathbf{q}) \rangle \propto \frac{1}{N} \sum_{i,j} e^{i\mathbf{q}(\mathbf{r}_i - \mathbf{r}_j)} \delta_{z_i, z_j} \hat{a}_i^\dagger \hat{a}_j. \quad (14.10)$$

The position density distribution after time of flight represents a momentum distribution that reflects the first-order coherence properties of the in-lattice quantum state:

$$\langle n(\mathbf{r}) \rangle_{\text{t.of}} = \langle \hat{a}_{\text{t.of}}^\dagger(\mathbf{r}) \hat{a}_{\text{t.of}}(\mathbf{r}) \rangle_{\text{t.of}} \approx \langle \hat{a}^\dagger(\mathbf{q}) \hat{a}(\mathbf{q}) \rangle_{\text{trap}} = \langle \hat{n}(\mathbf{q}) \rangle_{\text{trap}}. \quad (14.11)$$

The momentum density probes states with a well-defined quasimomentum, such as a superfluid state in which atoms are completely delocalized over the whole lattice (Greiner *et al.*, 2002) or a BEC where long-range order in the amplitudes leads to a constant value of the first-order coherence function $\langle \hat{a}_i^\dagger \hat{a}_j \rangle \rightarrow \text{const}$, for $|\mathbf{r}_i - \mathbf{r}_j| \gg 1$. In these cases, by opening the trap and letting the atoms interfere, well-defined structures appear, as shown in Figure 14.2(a)–(f). On the other hand, states where atoms are localized on each lattice

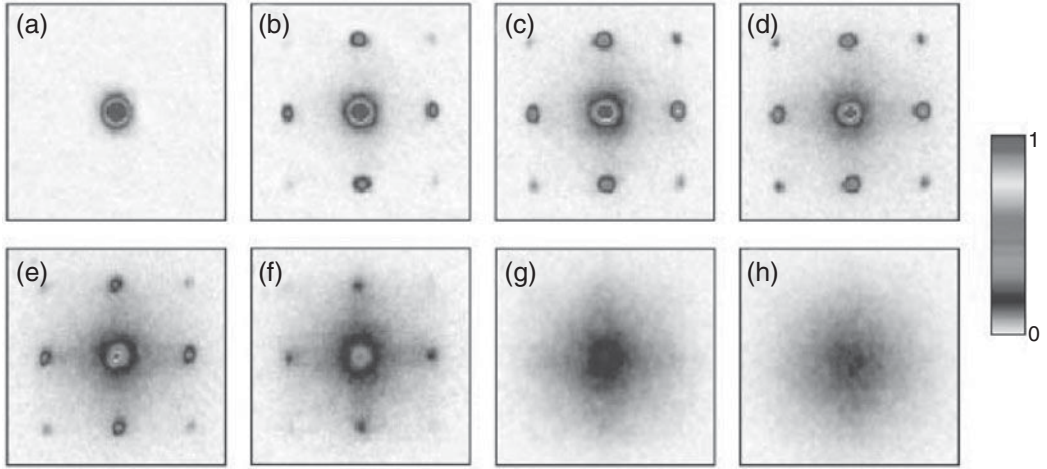


Figure 14.2 Absorption images after 15 ms of time of flight of a quantum degenerate gas of ^{87}Rb atoms released from a 3D optical lattice of increasing depth from (a) to (h). The images show the change of pattern due to the crossing of the superfluid–Mott-insulator quantum phase transition. From Greiner *et al.* (2002).

site have a loosely defined phase, and a not well-defined quasimomentum. This is the case in a Mott-insulator phase. As a consequence, an image after time of flight does not show any structure in the momentum density (Figure 14.2(g) and (h)).

14.3. Time of flight and noise correlations: higher-order correlations

In Section 14.2 we showed that Mott-insulator phases cannot be analysed by first-order correlations in time-of-flight experiments. However, they *can* be probed with two-point (density–density) correlation functions also obtained after time of flight (Bach and Rzążewski, 2004a; Bach and Rzążewski, 2004b; Altman *et al.*, 2004; Fölling *et al.*, 2005; Greiner *et al.*, 2005; Rom *et al.*, 2006). Assuming again that particles follow a ballistic expansion once the external traps are switched off, the density, as shown in two pixels taken after time-of-flight absorption of the same experimental realization, mirrors momentum correlations of the trapped system:

$$\langle \hat{n}(\mathbf{r})\hat{n}(\mathbf{r}') \rangle_{\text{tof}} \propto \langle \hat{n}(\mathbf{q})\hat{n}(\mathbf{q}') \rangle_{\text{trap}}. \quad (14.12)$$

Density–density correlations in momentum space read

$$\langle \hat{n}(\mathbf{q})\hat{n}(\mathbf{q}') \rangle \propto \frac{1}{N^2} \sum_{i,j,k,l} e^{i\mathbf{q}(\mathbf{r}_i-\mathbf{r}_j)} e^{i\mathbf{q}'(\mathbf{r}_k-\mathbf{r}_l)} \delta_{z_i,z_j} \delta_{z_k,z_l} \hat{a}_i^\dagger \hat{a}_j \hat{a}_k^\dagger \hat{a}_l, \quad (14.13)$$

where \mathbf{r}_m ($m = i, j, k, l$) denotes the space coordinate of the m th lattice site. Note that here again, the momentum \mathbf{q} refers to the 2D momentum and we have taken into account in

the sum the z -axis integration of the momentum density operator $\delta_{z_i,z_j}\delta_{z_k,z_l}$. The spatially averaged density–density correlation function, which gives the conditional probability of finding two particles at two positions separated by a distance $\mathbf{d} = \mathbf{r} - \mathbf{r}'$ averaged over all such positions, reads:

$$g^2(\mathbf{d}) = \frac{\int d\mathbf{r} \langle \hat{n}(\mathbf{r} + \mathbf{d}/2)\hat{n}(\mathbf{r} - \mathbf{d}/2) \rangle}{\int d\mathbf{r} \langle \hat{n}(\mathbf{r} + \mathbf{d}/2) \rangle \langle \hat{n}(\mathbf{r} - \mathbf{d}/2) \rangle} - 1, \quad (14.14)$$

where $\hat{n}(\mathbf{r})$ is the column density from a single absorption image and $\langle \cdot \rangle$ denotes the statistical average over a set of independently acquired images. The factor 1, corresponding to the autocorrelation function, is included to normalize the correlation function $g^{(2)}$ to zero if the state is uncorrelated.

We analyse now what happens for an ideal bosonic Mott insulator described by a product of Fock states with a fixed number of particles per site, i.e. $|\text{MI}\rangle = |n\rangle^{\otimes N}$, or for a fermionic band insulator. In both cases, the number of particles per site is fixed. Applying eqn (14.14) to the bosonic or fermionic cases leads to the following density–density correlation function probe at a distance \mathbf{d} :

$$g_{\text{MI}}^{(2)}(\mathbf{d}) = \pm \frac{1}{N^2} \sum_{i,j} e^{i\mathbf{d}(\mathbf{r}_i - \mathbf{r}_j)} \delta_{z_i,z_j}, \quad (14.15)$$

where \mathbf{r}_m ($m = i, j$) denotes the space coordinates of the m th lattice site, i.e. $\mathbf{r}_m = (x_m, y_m, z_m)$. For a regular 3D cubic lattice of period a , this function exhibits peaks when the momentum difference $\mathbf{q} - \mathbf{q}'$ is equal to a vector of the reciprocal lattice $\mathbf{d} = 2\pi(n_x, n_y)/a$, where n_x and n_y are integers. The above equation shows that there are correlations ($g^{(2)} > 0$) or anticorrelations ($g^{(2)} < 0$) in the density–density expectation value for bosons or fermions, respectively. The positive (negative) peaks correspond to the bunching (antibunching) effect, which depends on quantum statistics. Indeed, this is the atomic equivalent of the celebrated Hanbury Brown and Twiss effect (Hanbury Brown and Twiss, 1956), showing bunching of photons, and its analog for electrons (Henny *et al.*, 1999; Oliver *et al.*, 1999). The bunching and antibunching effects in ultracold atoms have recently been experimentally observed (Fölling *et al.*, 2005; Rom *et al.*, 2006; Schellekens *et al.*, 2005). The bunching of bosons is displayed in Figure 14.3 for the bosonic Mott state, while antibunching for fermions (negative peaks) is shown in Figure 14.4. Notice that the correlation function used in the experiments neglects the autocorrelation function in eqn (14.14) and hence the difference in scales. The method of noise correlations can be straightforwardly extended to any density correlation order, but above second order the correlation signal is so small that single-atom detectors are necessary (see Section 14.6). The noise-correlation method can also probe different internal states, but is highly destructive.

14.4. Bragg spectroscopy

The establishment of the Bragg scattering as a spectroscopic technique for ultracold atoms goes back to the late 1990s (Stenger *et al.*, 1999; Stamper-Kurn *et al.*, 1999). Bragg scattering, where two momentum states of the same ground state are connected by a stimulated two-photon process, provides a direct measure of the dynamic structure factor,

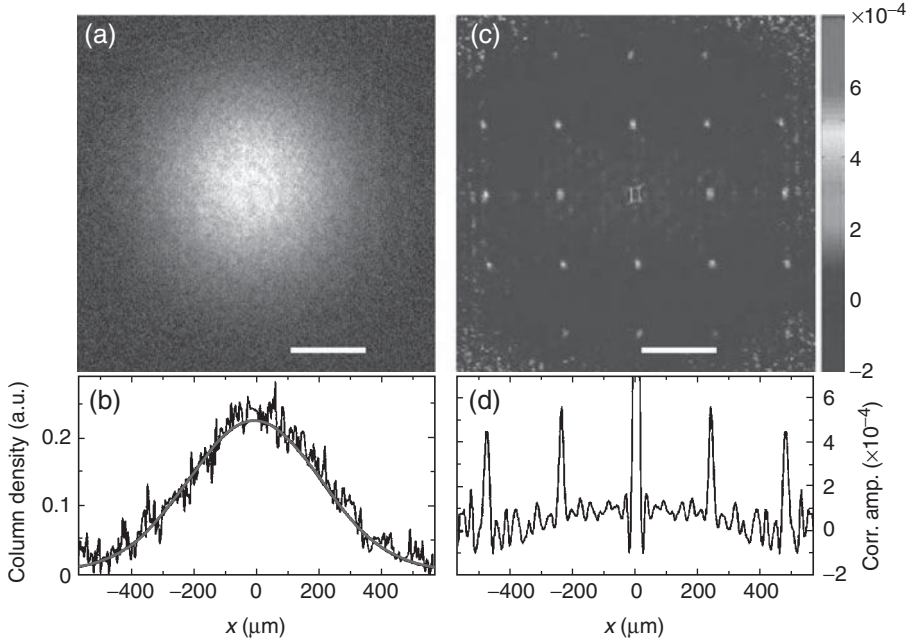


Figure 14.3 Noise correlations of an MI released from a 3D optical lattice. (a) 2D column density distribution (single-shot absorption image) of a Mott insulator released from a 3D optical lattice. (b) Horizontal section through the center of the image in (a) and Gaussian fit to the average over several independent images. (c) Spatial noise correlation function obtained from the set of independent images used in (a). (d) Horizontal section through the center of the pattern shown in (c) revealing a Hanbury Brown and Twiss type of bunching of the bosonic atoms. From Fölling *et al.* (2005).

i.e. the Fourier transform of the density–density correlation function. In the presence of optical lattices, Bragg spectroscopy offers the possibility of studying the full momentum structure of the excitations (Ernst *et al.*, 2010). The way it works is schematically depicted in Figure 14.5. Two phase-locked laser beams with wave vectors \mathbf{k}_1 and \mathbf{k}_2 , and frequencies ω_1 and ω_2 intersect on the sample, forming an angle Θ . In this situation, the initial and final states of atoms are resonantly coupled with a momentum difference of $\hbar\mathbf{k}_{\text{Bragg}} = \mathbf{k}_1 - \mathbf{k}_2$ and energy difference $\delta = \hbar E_{\text{Bragg}} = \hbar(\omega_2 - \omega_1)$, due to momentum and energy conservation. During the Bragg process, the atoms absorb photons from one beam, and are stimulated to emit photons into the second pulse. Importantly, the transfer of momentum can be tuned independently of the energy transfer by changing the angle between the two beams. Assuming that both lasers have similar wavelengths, $|\mathbf{k}| \simeq |\mathbf{k}_1| \simeq |\mathbf{k}_2|$:

$$\mathbf{k}_{\text{Bragg}} = (\mathbf{k}_1 - \mathbf{k}_2) \simeq 2|\mathbf{k}|(\sin \Theta/2)(\mathbf{e}_1 - \mathbf{e}_2), \quad (14.16)$$

where \mathbf{e}_1 and \mathbf{e}_2 are the unit vectors in the propagation direction of the two beams. Bragg scattering thus allows us to scan, for a given momentum transfer, a different interval of energies providing the excitation spectrum of the complete Brillouin zone.

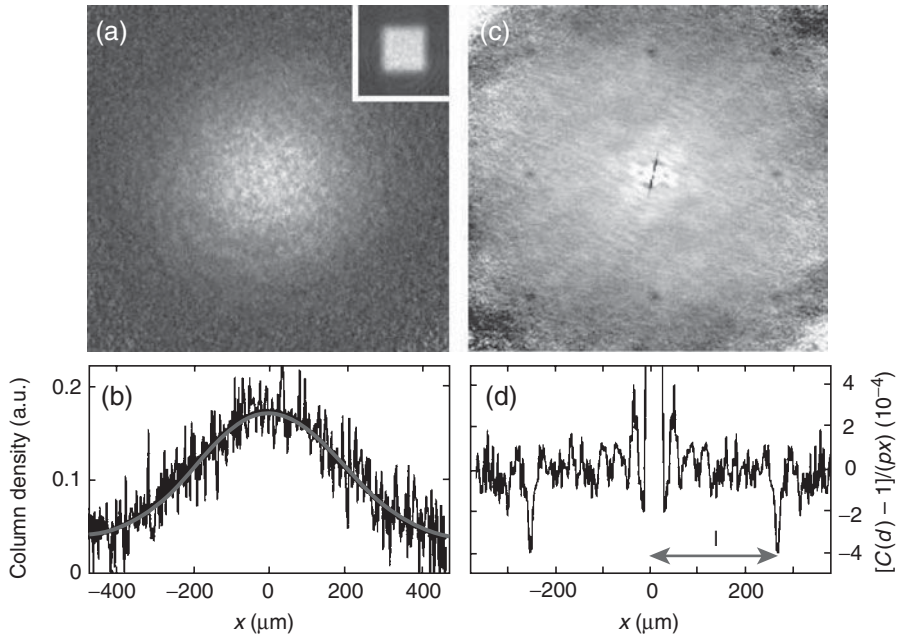


Figure 14.4 Noise correlations of a band-insulating Fermi gas. The inset in (a) shows the Brillouin-zone-mapping of the cloud. The images shown are the equivalents of the bosonic case shown in Figure 14.3. Note that instead of the correlation (bunching) peaks observed in Figure 14.3, the fermionic quantum gas shows a Hanbury Brown and Twiss type antibunching effect, with dips in the observed correlation function. From Rom *et al.* (2006).

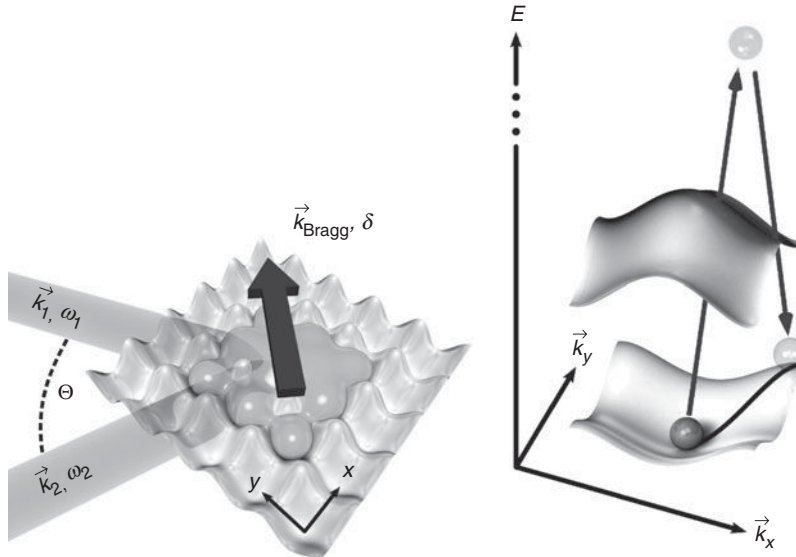


Figure 14.5 Schematic representation of two-photon Bragg scattering process in real space (left panel) and momentum space (right panel). Redrawn after Ernst *et al.* (2010) by courtesy of the authors.

Experimentally (Ernst *et al.*, 2010), for each $\mathbf{k}_{\text{Bragg}}$ and depth of the optical lattice, the energy difference δ is varied and the resonance spectrum is measured. The resonance can be determined by two different methods: energy transfer and coherent momentum transfer mapping (CMTM).

In the energy transfer method (Clément *et al.*, 2010; Ernst *et al.*, 2010), atoms in the optical lattice are illuminated by the two Bragg beams for a short interval of time (around 3–6 ms) in order to transfer energy to the system. Then, the system is allowed to rethermalize before both the optical lattice and the confining potential are switched off and the atoms expand. With a time-of-flight image, one can evaluate the energy absorbed by the atomic sample from the Bragg beams. The excitation spectrum is obtained by monitoring the energy absorbed as a function of the relative energy difference between the two Bragg beams at a given momentum transfer $\mathbf{k}_{\text{Bragg}}$.

The CMTM technique (Ernst *et al.*, 2010) allows us to study the coherent composition of the excitations by projecting the quasimomentum states onto real momentum states. This is achieved by switching off the lattice and the confining potential immediately after the application of the Bragg pulses. In this situation, the momentum $\hbar\mathbf{k}_{\text{Bragg}}$ transferred to a fraction of atoms becomes visible by the separation of clouds during time of flight. Using absorption images it is possible to determine the fraction of transferred atoms at $\mathbf{k}_{\text{Bragg}}$ and the reduction of atoms at $\mathbf{k} = 0$ as a function of the energy difference of the two Bragg beams, thus resulting in the resonance spectrum. Bragg spectroscopy has been used to study low-momentum excitations in optical lattices, to characterize phonon-like behavior and to determine the speed of sound. Also, using the CMTM technique, Bogoliubov modes have been observed allowing a determination of the range of validity of the Bogoliubov theory. The linear response of an interacting 1D gas across the SF–MI transition has also been investigated (Clément *et al.*, 2010; Pupillo *et al.*, 2006) in a first attempt to characterize the excitation spectrum, the phase transition, and the temperature of the sample. Interestingly, Bragg spectroscopy can also be used outside the linear-response regime, as demonstrated in Bissbort *et al.* (2011), where it was shown that Bragg spectroscopy is a suitable method for probing not only the quasiparticle structure of Bogoliubov modes with full momentum resolution, but also more exotic collective-amplitude mode excitations, such as the predicted gapped Higgs mode (Huber *et al.*, 2007) in the superfluid regime.

14.5. Optical Bragg diffraction

Spin- or internal atomic structure resolution demands that the probe is capable of coupling differently to the different spin components. The proposals for detecting magnetic ordering in an atomic gas mostly rely on the fact that appropriately tuned light couples differently to the different spin components as demonstrated in Partridge *et al.* (2006) and Shin *et al.* (2006). Combining this selectivity with detection methods based on direct images of individual sites in optical lattices, the magnetic ordering can be resolved, as we will discuss in the next section. Recently, it has been proposed that optical Bragg diffraction could be also used to detect some types of magnetic ordering (Corcovilos *et al.*, 2010). Bragg diffraction of light has a long history, and was first applied to detect crystalline order of non-degenerate gases in optical lattices (Birkel *et al.*, 1995; Weidemüller *et al.*, 1995). This technique, similar to neutron scattering in solid-state physics, is non-destructive and done

in situ. Corcovilos *et al.* (2010) consider atoms in two hyperfine states (\uparrow, \downarrow) separated in energy by $2\Delta_0$, having optical resonance transitions available for imaging with linewidth Γ , and confined in a 3D optical lattice. The quantization axis is defined by an external magnetic field that tunes the interactions between atoms via a Feshbach resonance. To maximize the sensitivity to the spin order, neglect bulk dispersive effects, and reduce the absorption, the probe light frequency is tuned to halfway between the levels. In the Born approximation, for low probe intensity and low optical density, the differential scattering cross-section, assuming elliptical polarization for the incoming photon and half filling $n_{i\uparrow} = n_{i\downarrow}$, reads (Corcovilos *et al.*, 2010):

$$\begin{aligned} \frac{d\sigma(\mathbf{K})}{d\Omega} &= \frac{9}{16k^2}(1 + \cos^2\theta)(1 + \cos^2\theta')e^{-2W} \\ &\times [\alpha(\delta_\uparrow, \delta_\downarrow)C(\mathbf{K}) + \beta(\delta_\uparrow, \delta_\downarrow)S(\mathbf{K})], \end{aligned} \quad (14.17)$$

where $\mathbf{K} = \mathbf{k}_i - \mathbf{k}_f$ is the difference between the incoming and outgoing wave vector of the photons, $C(\mathbf{K}) = \sum_{i,j} \exp(-i\mathbf{K}(\mathbf{r}_j - \mathbf{r}_i))$ is the crystalline structure factor, and $S(\mathbf{K}) = \sum_{i,j} \exp(-i\mathbf{K}(\mathbf{r}_j - \mathbf{r}_i))\langle S_i^z S_j^z \rangle$ is the spin structure factor, where $S_i^z = 1/2(n_{i\uparrow} - n_{i\downarrow})$. The angles $\theta(\theta')$ refer to the angles between the magnetization axis and the wave vector incoming (outgoing) photons. The phase shifts δ_σ with $\sigma = \uparrow, \downarrow$ are related to the linewidth and the detuning of the optical transition according to the expression

$$\tan(\delta_\sigma) = -\Gamma/2\Delta_\sigma.$$

Finally, $\exp(-2W)$ is the Debye–Waller factor due to the zero-point motion of the atoms around the lattice sites. The coefficients $\alpha(\delta_\uparrow, \delta_\downarrow)$ and $\beta(\delta_\uparrow, \delta_\downarrow)$ are related to the scattering amplitudes of individual atoms in the two spin states \uparrow and \downarrow . These coefficients can be written down in a very simple way in the considered case, $\delta_\uparrow = -\delta_\downarrow$, that is, when the optical detuning is at halfway between the levels, i.e. $\Delta_\uparrow = -\Delta_\downarrow = \Delta_0$ (Corcovilos *et al.*, 2010):

$$\begin{aligned} \alpha(\delta_\uparrow, \delta_\downarrow) &\approx \left(\frac{\Gamma}{2\Delta_0}\right)^4, \\ \beta(\delta_\uparrow, \delta_\downarrow) &\approx 4\left(\frac{\Gamma}{2\Delta_0}\right)^2. \end{aligned} \quad (14.18)$$

Therefore, $\Gamma < 2\Delta_0$ implies $\alpha(\delta_\uparrow, \delta_\downarrow) \ll \beta(\delta_\uparrow, \delta_\downarrow)$. Then, the whole strength of the method relies on the fact that, in such conditions, for a detuning with opposite sign but equal value between the two spin components, the contribution of the crystalline structure factor from the differential cross-section (eqn (14.17)) cancels out and therefore the method provides a signal that permits determination of the spin structure factor $S(\mathbf{K})$. Bragg diffraction peaks, corresponding to the maxima of eqn (14.17), occur when $\mathbf{K} = \mathbf{Q}$, with \mathbf{Q} being a reciprocal vector of the lattice. Thus, as shown in Corcovilos *et al.* (2010), information about the degree of ordering can be obtained by measuring the ratio of the intensities of the Bragg peak corresponding to cubic ordering and the Bragg peak indicating antiferromagnetic ordering. Therefore, optical Bragg diffraction can be a valuable tool to study, for instance, Néel ordering in fermionic systems.

14.6. Single-atom detectors

The possibility of probing a quantum gas in an optical lattice with single atom/single lattice site resolution has been a long-pursued goal in the ultracold community. Such measurements should give access to particle–particle correlation functions of any order, thus providing an extremely powerful tool for characterization and preparation of strongly correlated quantum states. This includes access towards the detection of topological states characterized by non-local operators. The first attempts in this direction were realized by imaging single sites in 1D and 2D optical lattices with many atoms per site (Boiron *et al.*, 1998; Scheunemann *et al.*, 2000), and in small 1D and 2D arrays of few sites with single atoms (Bergamini *et al.*, 2004; Miroshnychenko *et al.*, 2006). The first results of single-atom spectroscopy in 3D optical lattices were reported by the group of D. Weiss (Nelson *et al.*, 2007) using a diffraction-limited objective with a depth of field shallow enough that only one plane of atoms was in focus at a time. More recently, in Gemelke *et al.* (2009), in-situ imaging of an atomic Mott insulator with one atom per site was realized in a 2D lattice. In both experiments (Nelson *et al.*, 2007; Gemelke *et al.*, 2009) the period of the optical lattice was of the order of $5\text{ }\mu\text{m}$. The separation of two atoms down to nearest neighbors in a sparsely occupied 1D optical lattice with a period of 433 nm has also been reported (Karski *et al.*, 2009). Single-site addressability in 1D and 2D optical lattices with spatial resolution of less than $1\text{ }\mu\text{m}$ has been successfully demonstrated using electron microscopy (Gericke *et al.*, 2008; Würtz *et al.*, 2009).

However, in order to reach the strongly correlated regime, the tunneling strength t has to be comparable with the on-site interactions ($t \approx U$) and larger than the temperature of the system. This implies optical lattices with typical lattice periods well below the micron level. In this context, an in-situ single-atom–single-lattice site-imaging technique using high-resolution fluorescence imaging through an optical system with high optical aperture has been reported (Bakr *et al.*, 2009; Bakr *et al.*, 2010; Sherson *et al.*, 2010). In the experiments of M. Greiner and collaborators (Bakr *et al.*, 2009; Bakr *et al.*, 2010), the lattice is created by directly projecting a lithographically created holographic mask containing the lattice structure as a phase hologram. This holographic method has an advantage over the standard way of creating an optical lattice by means of standing waves along perpendicular directions: it allows for arbitrary geometries.

In the experiments reported in Bakr *et al.* (2010) and Sherson *et al.* (2010), after preparing the initial many-body state, the system is probed by ramping the optical lattice to a very high value and illuminating the atoms with an optical molasses. The atoms scatter fluorescence photons that are recollected by a high-resolution optical system. During the imaging, atom pairs on a lattice site are ejected due to light-assisted collisions and only sites occupied with an odd number of atoms before the measurement end up with one atom; the rest end up empty. Therefore, the single-atom detector indeed records the parity on each lattice site. Lattice sites with even parity are equivalent to zero occupation while those with odd parity are equivalent to a single atom. As a result of the imaging process, the many-body wave function is projected onto a number of states on each lattice site. The probing light acts for a long time ($\approx 1\text{ s}$). Since pairs of atoms in lattice sites with even occupation are expelled during the first $\approx 100\text{ }\mu\text{s}$, the remaining atoms scatter several thousand photons during the exposure time and can be detected with high fidelity. This technique has been used (Bakr *et al.*, 2010) to image, atom-by-atom, the SF–MI transition

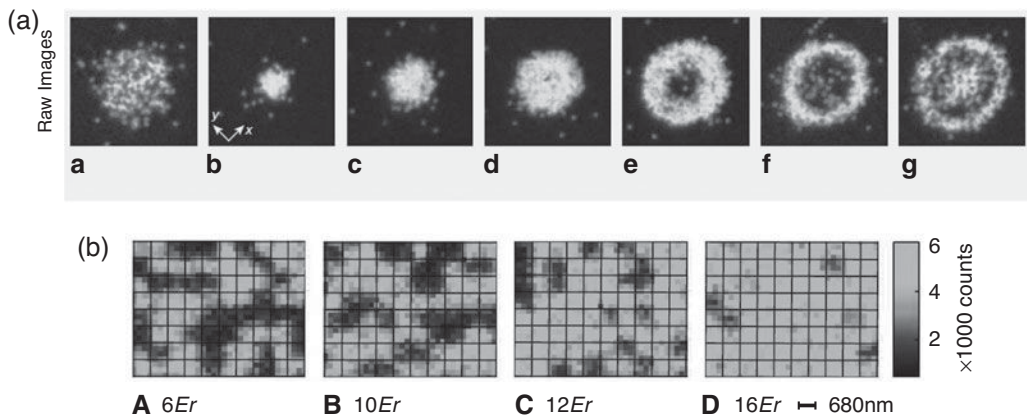


Figure 14.6 *In situ* high-resolution fluorescence images showing the atom number fluctuations for a BEC ((a) of the upper panel) and of an MI with increasing number of particles (from (b) to (g) in the upper panel). Redrawn after Sherson *et al.* (2010) by courtesy of the authors. The lower panel shows the single-site imaging of atom number fluctuations across the SF–MI transition. From Bakr *et al.* (2010).

in a 2D lattice, as shown in the lower panel of Figure 14.6. Also, measuring the defect density in the trapped MI provides precise information about the temperature and entropy (Bakr *et al.*, 2010; Sherson *et al.*, 2010). The upper panel of Figure 14.6 (from Sherson *et al.* (2010)) shows the large atom-number fluctuations in the BEC case (a) and the nearly vanishing fluctuations in the Mott regime from (b) to (g), where successive shells with step-like integer occupancy growth appear for increasing numbers of particles.

14.7. Quantum polarization spectroscopy

While optical Bragg spectroscopy (see Section 14.5) detects some magnetic ordering by coupling an off-resonant probing light to two internal states of atoms, quantum polarization spectroscopy (QPS) (Julsgaard, 2003; Hammerer *et al.*, 2010; Eckert *et al.*, 2008; Roscilde *et al.*, 2009; De Chiara *et al.*, 2011) exploits the quantum Faraday effect for such a purpose. The latter refers to the rotation experienced by the polarization of light when propagating inside a magnetic medium (polarized atomic ensemble). This interaction, moreover, can also lead to an exchange of quantum fluctuations between matter and light, i.e. a quantum interface (Hammerer *et al.*, 2010). Based on such an interface, the newly discovered technique, QPS, can provide access to measure not only the dynamic structure factors of strongly correlated systems, but also the order parameters of exotic many-body systems, leading to an unambiguous characterization of the many-body system. The method is non-demolishing and provides spatial resolution by preparing the probing light in a standing-wave configuration. It can be used both with bosonic or fermionic systems with internal spin degrees of freedom in any spatial dimension. For simplicity, in what it follows we assume a 1D optical lattice array. The technique, depicted schematically in Figure 14.7,

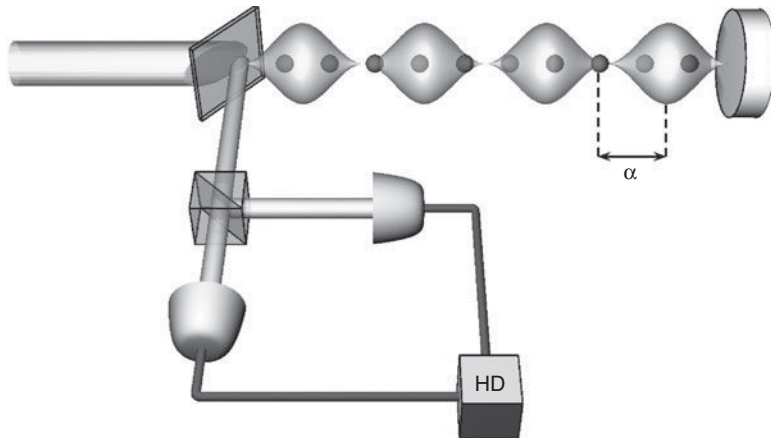


Figure 14.7 Schematic representation of the quantum polarization spectroscopy method. Atoms are loaded into an optical lattice and probed by standing wave light with wave length k_P shifted with respect to the optical lattice by α . After the interaction, a quadrature of the probing light is measured via homodyne detection. From De Chiara *et al.* (2011).

is based on the off-resonant interaction of an spin-polarized atomic sample trapped in a 1D optical lattice of spatial period $\frac{d}{2}$ oriented in the z direction with a polarized light beam with wave number k_p in standing-wave configuration along the z direction and shifted by α with respect to the optical lattice. The probe light is characterized by the Stokes operators:

$$\begin{aligned}\hat{s}_1 &= \frac{1}{2}(\hat{a}_x^\dagger \hat{a}_x - \hat{a}_y^\dagger \hat{a}_y), \\ \hat{s}_2 &= \frac{1}{2}(\hat{a}_y^\dagger \hat{a}_x + \hat{a}_x^\dagger \hat{a}_y), \\ \hat{s}_3 &= \frac{1}{2i}(\hat{a}_y^\dagger \hat{a}_x - \hat{a}_x^\dagger \hat{a}_y),\end{aligned}\quad (14.19)$$

where \hat{a}_i^\dagger ($i = x, y, z$) is the annihilation operator of a photon with i polarization. The dispersive part of the dipole-interaction Hamiltonian resulting from the adiabatic elimination of excited states (Julsgaard, 2003; Eckert *et al.*, 2008) reads:

$$\hat{H}_{\text{eff}} = -\kappa \hat{s}_3 \hat{J}_z^{\text{eff}}, \quad (14.20)$$

where κ is the coupling constant that depends on the optical depth of the atomic sample and on the spontaneous emission rate. $\hat{J}_z^{\text{eff}} = 1/\sqrt{L} \sum_n c_n \hat{S}_{z,n}$ is the z component of the effective atomic angular momentum, with L being the total number of spins of the chain, $\hat{S}_{z,n}$ being the z component of the spin at the site n , and the coefficients c_n accounting for the modification of the atom-field coupling due to the spatial modulation of the probe-beam intensity, allowing for spatial resolution. Using the Heisenberg equations of motion, the ‘effective’ angular momentum of the atomic sample \hat{J}_z^{eff} is imprinted onto the light

quadrature $\hat{X} = \int dt \hat{s}_2 / \sqrt{N_{\text{ph}}}$, with N_{ph} being the number of photons and where it has been assumed that the incoming pulse is strongly polarized along the x direction $\langle (\int dt \hat{s}_1) \rangle = N_{\text{ph}} \gg 1$. The result of the mapping is (Julsgaard, 2003):

$$\hat{X}_{\text{out}} = \hat{X}_{\text{in}} - \kappa \hat{J}_z^{\text{eff}}, \quad (14.21)$$

where \hat{X}_{out} (\hat{X}_{in}) is the quadrature of the outgoing (incoming) light. A homodyne measure of \hat{X}_{out} gives access not only to the effective angular momentum \hat{J}_z^{eff} but also to the variance (as well as the higher moments), demonstrating the inherent quantum character of the probe. Let us focus on the variance $(\Delta \hat{X}_{\text{out}}(k_P, \alpha))^2$, which reads:

$$(\Delta \hat{X}_{\text{out}}(k_P, \alpha))^2 = (\Delta \hat{X}_{\text{in}}(k_P, \alpha))^2 + \frac{\kappa^2}{L} \sum_{nm} c_m c_n (\langle \hat{S}_{zm} \hat{S}_{zn} \rangle - \langle \hat{S}_{zm} \rangle \langle \hat{S}_{zn} \rangle). \quad (14.22)$$

So the output signal is proportional to the variance of the input signal (shot-noise ratio) plus a term proportional to the variance of \hat{J}_z^{eff} , $\varepsilon(k_P, \alpha) \equiv (\Delta J_z^{\text{eff}})^2$, that corresponds to the two-point spin-correlation function. As noticed in Roscilde *et al.* (2009), the magnetic structure factor, defined as

$$S(q) = 1/L \sum_{mn} \exp[iqd(m-n)] \langle \hat{S}_{zm} \hat{S}_{zn} \rangle,$$

can be connected to the average of $\varepsilon(k_P, \alpha)$ with respect to α :

$$\bar{\varepsilon}(k_P) \equiv \int d\alpha \varepsilon(k_P, \alpha) = \frac{1}{2} S(2k_P). \quad (14.23)$$

Although the spin structure factor contains the two-body correlation functions, it does not provide the same information as order parameters, since by averaging over the phase shift α one loses some information about the correlations. Nevertheless, it has been shown (De Chiara *et al.*, 2011) that by accurately controlling the shift α , this method could provide a direct measure of local order parameters of magnetic systems.

15

Perspectives: beyond standard optical lattices

15.1. Introduction

The physics of ultracold atomic, molecular, and more recently, ionic gases has developed so rapidly, absorbed so many new topics, and created so many new challenges in recent years that it is essentially impossible to write a reasonable chapter on likely future developments. We have therefore decided to organize this chapter in a somewhat unusual way. In the fall of 2010 there was a three-month program at the Kavli Institute of Theoretical Physics (KITP) of the University of California at Santa Barbara devoted to the physics of ultracold atoms. The program, entitled ‘Beyond Standard Optical Lattices’ (BOPTILATT) (Altman *et al.*, 2010), was coordinated by E. Altman, W. V. Liu and one of us (M. L.). There was also an associated conference ‘Frontiers of Ultracold Atoms and Molecules’, which took place at KITP in mid-October 2010 (Alon *et al.*, 2010) and which was chaired by O. Alon, I. Bloch, W. V. Liu and W. D. Phillips. Finally, the program has overlapped and has had many joint activities with another two-month program ‘Disentangling Quantum Many-body Systems: Computational and Conceptual Approaches’ (COMPQCM), coordinated by M. P. A. Fisher, C. Lhuillier, S. Trebs and G. Vidal (Fisher *et al.*, 2010). All of these activities are very thoroughly documented on the web pages of the KITP: most, if not all talks and even the informal discussions are available online in the form of slides or live performances.

This material at the web pages of KITP provides a good review of the state of the art of the physics of ultracold atomic, molecular, and ionic gases at the end of 2010, as well as the state of its connections condensed-matter physics, and to the general and, in particular, numerical studies of quantum many-body systems. We have therefore decided to avoid new references in this final chapter of the book, except those to the web pages mentioned above. Instead, we have decided to provide a guide to the online talks and discussion.

There are a few very general talks, summarizing the area from the point of view of an AMO theorist (the Director’s Lunch Seminar talk by M. Lewenstein, introducing the BOPTILATT program and based on Chapters 3 and 4 of this book) and an AMO experimentalist (a talk by W. D. Phillips of atoms in optical lattices, as a novel condensed-matter system). The general viewpoint of a condensed matter theorist is represented in the conference talk of S. Das Sarma on interesting quantum phases at the frontiers of cold-atom physics. S. Trebs gave an excellent overview of the current status of numerical simulations of quantum many-body systems, also in the Director’s Lunch Seminar.

The rest of the material we have divided into two groups of subjects: those that represent new trends not yet covered in the book, and those that develop and continue the subjects of the book. The chapter is organized accordingly: the first section provides a list and a guide to some of the new trends, while the last section provides a list and guide to the more ‘standard’ subjects. There are essentially no details discussed, with two exceptions: in Section 15.2 we expand the description of the so-called orbital lattices, based on Lewenstein and Liu (2011), and in Section 15.3 we devote few paragraphs to the concept of exotic metals and in particular Bose metals, based on the talk by M. P. A. Fisher.

15.2. Beyond standard optical lattices: new trends

This section is divided into subsections in which we will describe very briefly new trends in the field, which are not discussed in this book.

15.2.1 Orbital lattices

One of the clear new trends concerns orbital lattices, and let us start by explaining why is these are so interesting. Many fascinating many-body phenomena have the roots in the degeneracy of quantum states at the single-particle level, as symmetry emerges along with it. In the standard situation, an atom without spin or any other internal degrees of freedom, loaded in an optical lattice site, occupies a single, so-called Wannier state. Exciting the atoms to the higher-energy Wannier states within the site can achieve two-fold, three-fold, or in principle multifold degeneracy.

For example, in the standard deep 3D cubic lattice, Wannier states are well described by harmonic oscillator wave functions, labeled by the quantum numbers (n_x, n_y, n_z) . The ground level is the s -orbital state $|s\rangle = |000\rangle$. The states of atoms in the next lowest level, the p -orbital, is threefold degenerate: $|p_x\rangle = |100\rangle$, $|p_y\rangle = |010\rangle$, $|p_z\rangle = |001\rangle$. If we can bring atoms to reside in p -orbitals, what consequences would that have and why is it interesting?

The system of p -orbital atoms has several salient, unique features, which do not appear in condensed-matter physics. First, with atoms one may simulate not only electrons, i.e. spin- $\frac{1}{2}$ fermions, but also bosons. The orbital physics of bosons has no direct prior analog in solids. Second, p -orbitals are anisotropic in magnitude and odd in parity, and they differ fundamentally from the electronic d -orbitals often encountered in transition metal oxides. These properties dramatically affect atomic dynamics, leading to anisotropic and frustrated tunneling (see Figure 15.1), as emphasized first in Isacsson and Girvin (2005), Kuklov (2006), and Liu and Wu (2006).

Orbital degeneracy is studied in solid-state materials, such as the transition metal oxides mentioned above. This is necessary in order to understand important material properties, including colossal magnetoresistance, ferroelectricity, unconventional superconductivity, and charge ordering. The phase diagram of transition metal oxides is rich and complex, and it is a big challenge to fully understand the role of the orbital degree of freedom in real materials.

A great advantage of the optical lattice is that one can separate the orbital degree of freedom entirely from spin and charge, for example to achieve an orbital-only model by loading single-component fermionic atoms into the p -bands. The optical lattice thus

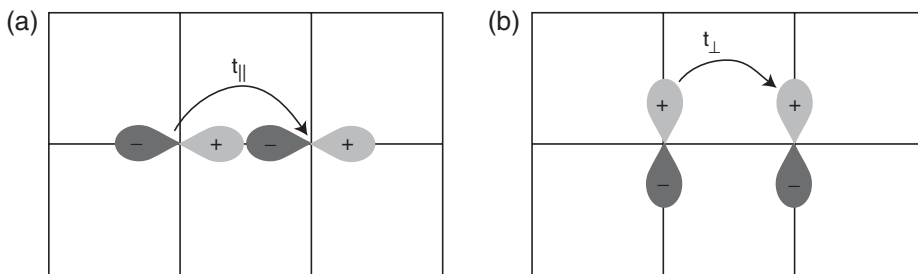


Figure 15.1 Anisotropy and odd parity of p -orbital hopping. By courtesy of W.V. Liu.

provides a unique opportunity for understanding of the effect of orbital degeneracy alone, and of the resulting novel quantum phases.

There were several talks about orbital lattices in the BOPTILATT program, starting with the talk of A. Hemmerich, who presented about the pioneering experiments of his group. These experiments are remarkable in three aspects (Wirth *et al.*, 2010). First, the authors use an ingenious superlattice method to trap bosonic ^{87}Rb atoms in s -orbitals of every second site, and then promote them to the p -orbitals using resonant tunneling to the remaining sites. Second, the lifetime of bosons in the p -orbital lattice is sufficiently long to establishing coherence and perform measurements. Third, they create novel kinds of superfluid: a striped one with a real wave function, and one with a complex wave function that spontaneously breaks the time-reversal symmetry, reminiscent of the famous π -flux phase that has been discussed thoroughly in the condensed-matter literature. The experiment reported in Wirth *et al.* (2010) marks the true beginning of the physics of orbital lattices. It is also worth mentioning here the equally pioneering and fascinating experiments of the NIST group—on square lattices of deep double wells, where the two quasi-degenerate Wannier states in the double well (even and odd) provide an analog of s - and p -orbital states. These experiments were discussed by T. Porto.

Some fascinating theoretical prospects were discussed in the talk by C. Wu on possible exotic phases, such as unconventional BEC and unconventional ferromagnetism, Fulde–Ferrell–Larkin–Ovchinnikov pairing states and others. The theory related to the double-well lattices of T. Porto was presented by Q. Zhou, who pointed out that the inter-band couplings might induce novel kinds of condensate in double-well lattices. K. Sun talked about the still more exotic possibility of achieving topological states of matter from orbital degrees of freedom. Evidently, we can expect many more fascinating experimental and theoretical developments in this area in the near future.

15.2.2 Quantum dynamics

Quantum dynamics was at the center of interest of the two programs for obvious reasons. Due to their characteristic long timescales, ultracold atoms provide a unique playground for their observation, quantum-simulation and even the control of their dynamics. On the other hand, dynamics is notoriously difficult to simulate numerically, mostly due the problems of entanglement entropy growth and the breakdown of the validity of area laws. Studying quantum dynamics would thus be a very natural domain of applications of

quantum simulators. There are several different aspects of quantum dynamics that have been intensively discussed recently and that were addressed in the BOPTILATT program.

Quantum dynamics: sudden quench and thermalization One of the questions that has been intensively studied recently concerns the physics of a sudden quench. Suppose we prepare a quantum many-body system in the equilibrium state (ground state at zero temperature, or otherwise a thermal state). Suppose that we then suddenly change some parameter (parameters) of the Hamiltonian, and let the system evolve according to the new Hamiltonian. This evolution can be considered to be Hamiltonian-like for isolated systems, or Liouville–von Neuman-like, if the systems cannot be sufficiently isolated. In the case of an isolated system at $T = 0$, a natural question to ask is if it thermalizes, i.e. if we look at the reduced density matrix of a large block of the system, can it be described by a Gibbs–Boltzmann state? What is the role of integrability and constants of motion in such dynamics?

During the fall meeting at KITP these questions were addressed by many speakers. The COMPQCM program even organized a focused week devoted to these questions. E. Altman talked about quantum phase transitions and critical dynamics far from thermal equilibrium in the colloquium talk at the Physics Department of UCSB, and also about non-equilibrium ferromagnetism and Stoner transition in an ultracold Fermi gas in the COMPQCM program. There were several talks and informal discussions about thermalization led by M. Rigol. These concerned dynamics and thermalization in isolated 1D systems, generalized thermalization in integrable systems, and the role of constants of motion. D. Huse talked about the many-body localization transition versus thermalization from the dynamical point of view at the high-temperature limit. A. Muramatsu considered specific strongly correlated quantum systems out of equilibrium.

There were also several fascinating experimental talks. J. Schmiedmayer discussed his recent experiment on probing non-equilibrium physics in 1D many-body quantum systems. D. Weiss presented his results on thermalization and heating of 1D Bose gases. Although these experiments are complementary in many respects, they have already led to new questions and unresolved puzzles.

Quantum dynamics: adiabatic dynamics and the Kibble–Żurek mechanism Another set of questions and problems associated with dynamics concerns slow adiabatic changes of the parameters of the Hamiltonian, and the resulting limits of adiabaticity and the possible non-adiabatic effects. A. Polkovnikov gave a wonderful review of universal dynamics in thermally isolated systems. B. Wu related the problems of quantum dynamics to quantum chaos theory and discussed universal behavior in quantum chaotic dynamics and its application in quantum critical gases.

Quantum dynamics: control A beautiful aspect of ultracold atoms is that the dynamics can not only be observed but can also be controlled. One can indeed realize various kinds of sudden quench and adiabatic sweeps on demand. Moreover, one can employ dynamics to realize novel states and effects.

The best example is provided by the experiments of E. Arimondo and K. Sengstock, in which shaking of the lattice allows control of effective tunneling in the lattice and influence over the MI–SF transition. In particular, one can change the sign of the tunneling and

realize in this way a very robust quantum simulator of quantum antiferromagnetism, as discussed in the conference talk by K. Sengstock. G. Refael presented a long theoretical analysis of how one can put Floquet Hamiltonians (i.e. effective Hamiltonians that describe periodically driven systems) to work in many-body systems. In particular, he has shown how it is possible to achieve superfluid enhancement and topological phases in time-periodic Hamiltonians.

Another type of control was discussed in a talk by P. Engels, who has demonstrated how one can study non-linear quantum hydrodynamics with BEC, inducing shock waves, superfluid–superfluid counterflow, and novel types of soliton.

Quantum dynamics: dynamical phase transitions In several systems people have observed novel types of quantum phase transition that involve dramatic changes of the dynamics, without affecting the statics of the ground state. A. Auerbach illustrated these ideas in the context of the transport theory of lattice bosons. S. Huber led a related discussion and gave talks on the Higgs mechanism and novel types of excitation in lattice Bose gases. Dynamical phase transitions may also occur at finite temperatures—an example in the context of a disordered system was discussed by G. Shlyapnikov.

In a somewhat different sense, the term ‘dynamical phase transitions’ is used in the context of the dissipative open-system dynamics. Here changes of ‘control parameters’ may lead both to the abrupt/dramatic change of the stationary states (analogs of the ground states), and/or may concern approach to the stationary states, without affecting the latter. Some of these subjects are discussed in the book, but the reader should listen to the joint BOPTILATT and COMPQCM introductory review talk by P. Zoller, which covered open many-body quantum systems: atoms in optical lattices. A similar recommendation applies to I. Cirac’s colloquium, held at the Physics Department of UCSM.

15.2.3 Other new trends

Cavity QED and many-body physics We briefly discussed some aspects of the physics in this area in Chapter 5, but recently there has been impressive progress. In particular, T. Esslinger (conference talk and colloquium at UCSB) presented very recent results concerning observation of the Dicke super-radiant phase transition, while H. Ritsch (BOPTILATT) talked about quantum particles in cavity-generated optical lattices from the point of view of theoretical quantum optics.

Earth alkali and $SU(N)$ physics Another hot new trend concerns the cooling of earth alkali atoms to the degenerate regime, something that has already been achieved in many laboratories. This opens the possibility of experimental realization of the exotic $SU(N)$ magnetism. Some aspects of the physics in this area are discussed in Chapters 5 and 7. We strongly recommend, however, strongly the BOPTILATT review talks by V. Gurarie, on $SU(N)$ magnetism with alkaline earth atoms and a novel kind of chiral spin liquid, and by A. Gorshkov, on quantum information processing and quantum simulations with ultracold alkaline-earth atoms in optical lattices.

Ultracold atoms and high-energy physics Apart from a lot of discussions concerning artificial gauge fields and quantum simulators of LGTs, there were interesting informal

discussions with P. Zoller and I. Cirac. There were also some talks on more exotic subjects, for example the conference lecture of M. Freedman on lattice models in which the lattice fluctuates, or F. Verstraete's COMPQCM talk on application of the variational principle and ideas related to MPS to 1+1-dimensional quantum-field theories.

Exotic lattices and traps The technology of creating novel types of lattices and traps develops rapidly. In BOPTILATT, several non-standard optical lattices and traps were discussed: G. Campbell talked on toroidal traps, M. Greiner on using holographic masks to generate whatever one wants, K. Sengstock on hexagonal and triangular lattices, I. Bloch on square lattices of square plaquettes. In a talk related to the one by Bloch, B. Paredes discussed the possibility of tailoring minimum instances of topological matter with this kind of optical superlattice.

Polarons Last, but not least, there is another very interesting subject that is completely neglected in this book, namely the subject of spin impurities in a polarized Fermi sea and their behavior close to the Feshbach resonance. Such impurities undergo crossover from polarons to molecules. At BOPTILATT there were two very pedagogical talks on this subject: one by P. Massignan and the other by H. Zhai, both discussing the question of how much the single-impurity atom problem can tell us about a many-body system.

15.3. Standard optical lattices: what's new?

This section is organized in the same way as this book. In the first subsection we go chapter by chapter, and comment on new aspects that were discussed at BOPTILATT and COMPQCM. In the second subsection we pick up one particular subject—strange metals—and discuss non-Fermi and Bose metals in a little more detail.

15.3.1 New developments: chapter by chapter

Of course, we list below only those chapters to which there were some interesting developments reported at BOPTILATT and/or COMPQCM.

Statistical physics of condensed matter: basic concepts Perhaps the most interesting developments of our understanding of quantum statistical physics in the last, say, ten years concern the novel concepts of phase transitions that clearly go beyond the Landau scenario. Such unconventional critical points and transitions were perhaps first encountered in LGTs (confinement–deconfinement transitions), but were then carried over to condensed-matter systems. During BOPTILATT and COMPQCM, L. Balents and C. Xu gave a joint set of four pedagogical lectures on this subject.

Ultracold gases in optical lattices: basic concepts There is perhaps not much to add to this subject concerning atoms. On the other hand there is an enormous effort being made in studying novel systems that can teach us something about quantum many-body physics: ultracold ions (discussed briefly in Chapter 13), Rydberg atoms, or even Bose-condensing photons in a microcavity (see the recent experiment by M. Weitz (Klaers *et al.*, 2010)). At BOPTILATT there were several talks on dipolar gases, Rydberg atoms, ions etc.

(conference talks by P. Zoller and G. Pupillo, the BOPTILATT talk by H.-P. Büchler and the discussion led by G. Shlyapnikov).

Quantum simulators of condensed matter In this context the most relevant talk is the one by M. Troyer on *ab initio* simulations of cold atoms and validation of quantum simulators.

Bose–Hubbard models: methods of treatment For the methods, the talks at COMPQCM are particularly relevant, especially the talk by M. Troyer mentioned above and the talk and discussion led by M. Rigol concerning dynamics.

Current progress in 1D methods was covered in the discussion led by P. Fendley and M. Girardeau. H.-C. Nägerl presented recent spectacular experimental results on strongly interacting quantum gases in 1D geometry, including the observation of the so-called super-Tonks regime. L. Pollet gave a very pedagogical talk on the bosonic generalizations of the dynamical mean-field theory (DMFT) and the development of a bosonic DMFT formalism. More formal aspects were discussed in the talk by G. Ortiz on the algebraic approach to dualities and its applications.

The talks discussing recent progress in numerical methods included:

- B. Svistunov on quantum Monte Carlo, the worm algorithm, and diagrammatic Monte Carlo
- A. Streltsov on non-equilibrium phenomena in attractive BECs: solitons, fragmentons, and CATons using a multi-configurational time-dependent Hartree–Bose method.

The fascinating topic of strange metals, and in particular Bose metals, was discussed in the pedagogical talk by M. P. A. Fisher. This subject is developed in more detail in the next section.

Spectacular progress on experimental studies of 2D Bose gases and Kosterlitz–Thouless–Berezinskii transitions was reported at the conference by Z. Hadzibabic, who nicely explained the current understanding of this area and pointed out open questions. Similarly, C. Chin discussed the observation of scale invariance and universality in 2D Bose gases.

On the numerical and conceptual side, there were wonderful reviews and pedagogical lectures at COMPQCM and BOPTILATT on MPS, multiscale entanglement renormalization ansatz, PEPS and the tensor network method, as well as the role of entanglement in many-body systems by M. Hastings, G. Vidal, I. Cirac, X.-G. Wen, and J. Cardy.

Fermi and Fermi–Bose Hubbard models: methods of treatment Fermi systems and related methods of treatment were also at the center of interest at KITP. One fundamental question concerned the development of quantum Monte Carlo methods that are free of or that can be controlled with respect to the celebrated sign problem. In this respect N. Prokof'ev gave a review of diagrammatic quantum Monte Carlo. B. Svistunov combined discussions of the worm algorithm and diagrammatic Monte Carlo methods. Recent progress on quantum Monte Carlo description, simulations, and emulations of fermions in optical lattices at the BCS–BEC crossover was discussed in the conference talk

by N. Trivedi. Fermionic PEPS and MERA methods were the subject of the COMPQCM talk by P. Corboz.

On the experimental side, absolutely stunning results were reported at the conference by D. Jin (on universal relations for ultracold atom gases in terms of the so-called *contact*), by R. Hulet (on spin-imbalance in a 1D Fermi gas and observation of the FFLO phase), by M. Zwierlein (on universal spin transport in strongly interacting Fermi gases), and by C. Salomon (on thermodynamics of a tunable Fermi gas). C. Kohstall (representing R. Grimm's group) discussed the recent results on Efimov physics and creation of a strongly interacting Fermi–Fermi mixture.

The most fascinating theory results on Fermi gases concerned exotic Fermi superfluids (informal discussion by A. Imambeikov, P. Massignan, M. Forbes, and R. Lutchyn). C. Boilech talked about polarized two-component Fermi gases in elongated traps and 2D optical lattices, whereas E. Zhao focused on ultracold Fermi gases in 1D and quasi-1D. M. P. A. Fisher contributed with a talk on strange metals, which for fermions are termed non-Fermi liquids. Finally, W. Zwerger discussed the search for a perfect fluid and asked the provocative question of whether string theory is relevant for ultracold atoms.

Ultracold spinor atomic gases This is another sub-area that is developing very rapidly. A. Lamacraft talked at BOPTILATT about the phase diagram of a polar (antiferromagnetic) condensate. The informal discussions on topological phases led by E. Berg, and on spinor physics, led by A. Sanpera and R. Barnett, were also very interesting. Both discussions stressed, for instance, the role and meaning of entanglement in 1D spin chains, and the relations of spinor physics to the physics of orbital lattices and double-well lattices.

On the experimental side, D. Weld from W. Ketterle's group presented a truly exciting report on thermometry and cooling with ultracold spin mixtures in optical lattices, and the search for Stoner magnetism. Several speakers talked about this from a theoretical point of view: E. Altman and, at the conference, S. Stringari, who discussed spin fluctuations and magnetic polarizability of a nearly ferromagnetic Fermi gas, and also E. Demler, who was exploring magnetism and superconductivity with Feshbach resonances.

Ultracold dipolar gases Dipolar systems have enjoyed also an explosion of popularity, according to the discussion led by G. Shlyapnikow. There were several talks on polar molecules: one by H.-P. Büchler on solid phases with cold atomic gases in one dimension, another by D. Feldman on quantum phase transitions from a liquid to a gas of cold molecules.

This subject was also strongly represented at the conference. J. Ye talked on polar molecules in the quantum regime, G. Pupillo on solids and supersolids in dipolar quantum gases, T. Pfau on coherent control of dense Rydberg gases, H.-P. Büchler on quantum critical behavior in driven and strongly interacting Rydberg gases, and M. Lukin on quantum dynamics of strongly interacting atoms and photons in dipolar systems.

Disordered ultracold atomic gases This was another of the major topics of BOPTILATT and the conference. N. Prokofiev, in his conference talk, presented the extension theorem, which leads to the solution of the dirty-boson problem. It shows that in the

disordered Bose system there is always a region of the Bose-glass phase between the Mott-insulator phase and the superfluid phases. Transition from MI to Bose glass is of the Griffith type, i.e. it is dominated by rare fluctuations, which in this particular case cause formation of islands of superfluid. G. Shlyapnikov talked about his work with B. Altshuler on phase transitions in 1D disordered Bose gases, which occur at non-zero temperature.

Experimental progress was covered in the talks by A. Aspect on ultracold atoms in optical disorder, M. Inguscio on weakly interacting bosons in a quasi-disordered lattice, and B. DeMarco on disordered insulators in optical lattices.

Frustrated models in cold atom systems Not as much interest has been devoted to frustrated ultracold atomic gases, with two important exceptions. There was a fascinating discussion, led by C. Lluillier, D. Huse, and S. White, on the current status of the understanding of the ground state of the antiferromagnetic Heisenberg model in the kagomé lattice. S. White presented impressive numerical results obtained using the DMRG method adapted to 2D cylinder geometry. Experiments with frustrated systems were reported in the talk of K. Sengstock. Last, but not least, N. Davidson talked about frustration with coupled laser arrays on kagomé lattices, and realization of a frustrated XY model in this manner.

Ultracold atomic gases in ‘artificial’ gauge fields This topic is undergoing an explosion of interest. Progress in experiments was presented at the conference by I. Spielman. Practical prospects for non-Abelian gauge fields were discussed in a pedagogical lecture by G. Juzeliūnas, who described light-induced gauge potentials for cold atoms. Finally, M. Lewenstein held an invited talk at the conference on atoms in artificial gauge fields, based on Chapter 11 of this book.

Non-Abelian gauge fields lead to physics similar to spin-orbit coupling in condensed matter, and they nearly always lead to the emergence of Dirac dispersion relations and topological insulators. In the more general theoretical plan, both L. Balents in his pedagogical lectures and J. Moore at the conference stressed the importance of topological insulators and the challenging question of the role of interactions. J. Ho described alternative ways to achieve strong interactions with ultracold atoms and pulling fluxes away from particles in quantum Hall states.

Many-body physics from a quantum information perspective New aspects of characterization of entanglement in many-body systems concern, apart from entanglement entropy, topological entropy and/or the entanglement spectrum. The entanglement spectrum in DMRG (interacting systems) was shown to characterize the topological order of the Haldane phase in one dimension, as pointed out by E. Berg during the informal discussion on topological phases. M. Ishikawa discussed differences between Haldane phases for a 1D spin chain with integer odd and even spin.

The excellent reviews of the subject, and in particular current understanding of the problem in two dimensions, was presented in the talk of I. Cirac on MPS: renormalization, gaps, and symmetries, and in that of X.-G. Wen on topological order: patterns of long-range entanglements of gapped quantum states. Last, but not least, A. Kitaev presented topological spin models in two dimensions.

Quantum information with lattice gases P. Zoller talked about novel implementations of the digital quantum simulator concept with ultracold ions in R. Blatt's group in Innsbruck. Similarly, J. I. Cirac discussed implementations of quantum information ideas in atomic ensembles, similarly to how it has been done in the experiments of E. Polzik.

Preparation and detection of quantum systems realized with ultracold atoms This also seems to be a blooming topic. At KITP there were several talks: A. Sanpera talked about witnessing order parameters and dynamics in strongly correlated systems and both M. Greiner and I. Bloch presented recent experimental breakthroughs concerning single-atom observing and addressing in optical lattices. Finally, T. Giamarchi gave a Director's Lunch Seminar, in which he discussed an overview of various detection methods and their advantages and drawbacks.

Detection as a tool for quantum metrology was covered in M. K. Oberthaler's talk. He discussed non-linear quantum atom optics with BECs and squeezing and its applications.

Exotic Fermi and Bose metals We end this chapter and the book with a slightly expanded discussion of the fascinating subject of strange metals. The interest in such phases systems, derived of course from the studies of Fermi Hubbard model (see Chapter 6). There, it is believed that, for temperatures above high T_c superconductivity and Néel order, a strange metal appears. In this subsection we present a short characterization of the concepts of a free Fermi-liquid (gas), a Fermi-liquid metal, a strange Fermi metal, and the same sequence for bosons: from ideal Bose gas to Bose metal. The discussion is based on the talk by M. P. A. Fisher at BOPTILATT.

- *2D free Fermi liquid (gas).* This system is characterized by,
 - the free Hamiltonian $\hat{H} = \sum_i \hat{\mathbf{p}}_i^2/2m = \sum_{\mathbf{k}} \epsilon_k \hat{c}_{\mathbf{k}}^\dagger \hat{c}_{\mathbf{k}}$,
 - a momentum distribution given by the Heavyside's step function, $n_{\mathbf{k}}^{\text{FF}} = \langle \hat{c}_{\mathbf{k}}^\dagger \hat{c}_{\mathbf{k}} \rangle = \Theta(k_F - |\mathbf{k}|)$,
 - a volume of the Fermi sea determined by the density of particles (Luttinger theorem) $\rho = k_F^2/4\pi$,
 - quasiparticle excitations with infinite lifetime, i.e. sharp, and given in terms of Green's function, $\text{Im}G(\mathbf{k}, \omega) = \delta(\omega - \epsilon_k)$.
- *2D Fermi-liquid metal.* Fermi liquids, the theory of which was developed by L. D. Landau, is the standard state attained by normal metals. Its simplified version is discussed in Chapter 6 in the framework of Hartree–Fock method. In general terms it is characterized by the following properties:
 - an equal time Green's function which exhibits oscillatory decay, $\langle \hat{c}^\dagger(\mathbf{r}) \hat{c}(0) \rangle \sim \cos(k_F|\mathbf{r}| - 3\pi/4)/|\mathbf{r}|^{\alpha_{\text{FL}}}$, with $\alpha_{\text{FL}} = \frac{3}{2}$,
 - a momentum distribution that still has a jump at Fermi momentum, but also contains corrections, $n_{\mathbf{k}}^{\text{FL}} = Z n_{\mathbf{k}}^{\text{FF}} + \delta n_{\mathbf{k}}^{\text{FL}}$,
 - the Luttinger theorem still holding, and the volume inside the Fermi surface is determined by the density of particles $\rho = k_F^2/4\pi$,

- there exist quasiparticle excitations that have a long (infinite) lifetime close by and at the Fermi surface, and a spectral function that contains an incoherent part, describing slow decay of quasiparticles, $A(\mathbf{k}, \omega) = Z\delta(\omega - \epsilon_k) + \delta A(\mathbf{k}, \omega)$.
- *2D strange, non-Fermi liquid metal.* There are various possibilities for systems to depart from the standard Fermi-liquid picture.
 - There are systems that exhibit a singular ‘Fermi surface’. Such a surface still satisfies Luttinger’s theorem, but there is no jump discontinuity in the momentum distribution function. An example of a similar situation appears in Luttinger liquids in one dimension (see Chapters 2 and 6).
 - There can appear singular ‘Fermi surfaces’ that violate the Luttinger’s theorem.
 - A singular ‘Fermi surface’ may consist of a disjoint arc of an oval like shape.

Various types of strange Fermi metals have been proposed and observed in condensed matter. Even more exotic is the concept of Bose metals. Below we contrast this concept with that of free and weakly interacting Bose gases.

- *2D free Bose gas.* This system is characterized by:
 - a free Hamiltonian $\hat{H} = \sum_i \hat{\mathbf{p}}_i^2/2m = \sum_{\mathbf{k}} \epsilon_k \hat{b}_{\mathbf{k}}^\dagger \hat{b}_{\mathbf{k}}$,
 - an equal time Green’s function, $G(\mathbf{r}) = \langle \hat{b}^\dagger(\mathbf{r}) \hat{b}(\mathbf{0}) \rangle$, that exhibits long-range order, $G(\mathbf{r} \rightarrow \infty) = \rho$,
 - a momentum distribution function that shows BEC, $n_{\mathbf{k}} = G(\mathbf{k}) = \langle \hat{b}_{\mathbf{k}}^\dagger \hat{b}_{\mathbf{k}} \rangle = N\delta(\mathbf{k})$.
- *2D interacting Bose gas.* This system is characterized by:
 - a Hamiltonian that includes interactions, $\hat{H} = \sum_i \hat{\mathbf{p}}_i^2/2m + \sum_{i < j} V(\hat{\mathbf{r}}_i - \hat{\mathbf{r}}_j)$,
 - a Bose Green’s function that also exhibits long-range order, $G(\mathbf{r} \rightarrow \infty) = \rho_{\text{cond}} = Z\rho$, with $Z < 1$,
 - a momentum distribution function that exhibits depletion of the Bose–Einstein condensate, and is less singular, $n_{\mathbf{k}} = ZN\delta(\mathbf{k}) + \delta n_{\mathbf{k}}$.
- *2D Bose metal.* Finally, let us consider a possible Bose metal. This system, if it exists, should be characterized by:
 - a stable fluid phase that is not superfluid,
 - real space Bose Green’s functions that should exhibit oscillatory decay, similar to Fermi liquids, $\langle b^\dagger(\mathbf{r}) b(\mathbf{0}) \rangle \sim \cos(\mathbf{k}_B(\hat{\mathbf{r}}) \cdot \mathbf{r}) / |\mathbf{r}|^{\alpha(\hat{\mathbf{r}})}$, with both $\mathbf{k}_B(\hat{\mathbf{r}})$ and $\alpha(\hat{\mathbf{r}})$ depending on the direction of momentum,
 - a momentum distribution function that should exhibit singularities for momenta at a ‘Bose surface’.

M. P. A. Fisher proposed two possible realizations of the Bose metal, with models that can potentially be realized with ultracold atoms. The first of these models is the

Bose–Hubbard model with ring exchange, also known as the boson $J - K$ model. It is similar to the one discussed in Chapter 11 in the context of simulation of LGTs and the proposal of Büchler *et al.* (2005). This model can potentially also be realized with ultracold atoms employing Rydberg blockade methods (Weimer *et al.*, 2010). Bosons in this model may represent Cooper pairs of fermions, so the model is related to the one termed the Cooper-pair ring-exchange model. The Hamiltonian, written in terms of bosonic operators, reads

$$\hat{H} = -J \sum_{\langle i,j \rangle} (\hat{b}_i^\dagger \hat{b}_j + h.c.) + K \sum_{\text{plaquettes}} \hat{b}_1^\dagger \hat{b}_2 \hat{b}_3^\dagger \hat{b}_4.$$

The $J - K$ model is expected to undergo a quantum phase transition from a superfluid phase to a Bose metal. This model is very difficult to study using exact diagonalization, so M. P. A. Fisher and collaborators (Sheng *et al.*, 2008) have been able to show the precursors of Bose-metal behavior by performing ‘exact’ DMRG calculations for two-leg ladders. As expected, the two-leg ladder exhibits the signature of a ‘Bose surface’ and a phase that is interpreted as a d -wave Bose metal.

The second candidate for observing the Bose-metal phase is the anisotropic Fermi Hubbard model with attractive interactions, which was discussed in Chapter 6:

$$\hat{H} = - \sum_{\langle i,j \rangle, \sigma} t_{ij}^\sigma (\hat{f}_{i\sigma}^\dagger \hat{f}_{j\sigma} + h.c.) - U \sum_i \hat{n}_{i\uparrow} \hat{n}_{i\downarrow}. \quad (15.1)$$

This model is conjectured to undergo a sequence of quantum phase transitions as U/t grows: from a metal to a Cooper-pair Bose metal, and then to a superconductor.

For us AMO physicists it is truly fascinating to learn from condensed-matter physicists about novel quantum phases of matter, to develop these ideas toward possible implementations in experiment, and even to open completely new avenues of quantum many-body physics. It is probable that there is a similar intellectual pleasure for condensed-matter or high-energy physicists in seeing how their sometimes very exotic ideas can be realized in a perfectly controlled way in a laboratory. Quantum physicists of all the world, unite! Long live the Third Quantum Revolution!

Bibliography

- Abo-Shaeer, J. R., Raman, C., Vogels, J. M., and Ketterle, W. (2001). *Science*, **292**, 476.
- Abrahams, E., Anderson, P. W., Licciardello, D. C., and Ramakrishnan, T. V. (1979). *Phys. Rev. Lett.*, **42**, 673.
- Abrahams, E., Kravchenko, S. V., and Sarachik, M. P. (2001). *Rev. Mod. Phys.*, **73**, 251.
- Abramowitz, M. and Stegun, I. A. (1964). *Handbook of Mathematical Functions*. National Bureau of Standards.
- Affleck, I., Kennedy, T., Lieb, E. H., and Tasaki, H. (1987). *Phys. Rev. Lett.*, **59**, 799.
- Affleck, I., Kennedy, T., Lieb, E. H., and Tasaki, H. (1988a). *Commun. Math. Phys.*, **115**, 477.
- Affleck, I., Zou, Z., Hsu, T., and Anderson, P. W. (1988b). *Phys. Rev. B*, **38**, 745.
- Affleck, I. (1989). *J. Phys. Condens. Matter*, **1**, 3047.
- Affleck, I. and Marston, J. B. (1988). *Phys. Rev. B*, **37**, 3774.
- Aharonov, D. (2000). *Phys. Rev. A*, **62**, 062311.
- Aharony, A. and Stauffer, D. (1994). *Introduction to Percolation Theory*. Taylor & Francis, London.
- Aharony, A. (1978). *Phys. Rev. B*, **18**, 3328.
- Ahufinger, V., Sanchez-Palencia, L., Kantian, A., Sanpera, A., and Lewenstein, M. (2005). *Phys. Rev. A*, **72**, 063616.
- Ahufinger, V., Sanpera, A., Pedri, P., Santos, L., and Lewenstein, M. (2004). *Phys. Rev. A*, **69**, 053604.
- Aizenman, M. and Wehr, J. (1989). *Phys. Rev. Lett.*, **62**, 2503.
- Aizenman, M. and Wehr, J. (1990). *Comm. Math. Phys.*, **130**, 489.
- Akkermans, E., Ghosh, S., and Musslimani, Z. H. (2008). *J. Phys. B: At. Mol. Opt. Phys.*, **41**, 045302.
- Alet, F., Dayal, P., Grzesik, A., Honecker, A., Körner, M., Läuchli, A., Manmana, S. R., McCulloch, I. P., Michel, F., Noack, R. M., Schmid, G., Schollwöck, U., Stöckli, F., Todo, S., Trebst, S., Troyer, M., Werner, P., , and Wessel, S. (2005). *J. Phys. Soc. Jpn. Suppl.*, **74**, 30.
- Alet, F., Walczak, A. M., and Fisher, M. P. A. (2006). *Physica A*, **369**, 122.
- Alexander, T. J., Ostrovskaya, E. A., and Kivshar, Y. S. (2006). *Phys. Rev. Lett.*, **96**, 040401.
- Alon, O. E., Streitsov, A. I., and Cederbaum, L. S. (2005). *Phys. Rev. Lett.*, **95**, 030405.
- Alon, O., Bloch, I., Liu, W. V., and Phillips, W. D. (Coord.) (2010). *KITP Conference: Frontiers of Ultracold Atoms and Molecules* (Oct. 11–15, 2010). <http://www.kitp.ucsb.edu/activities/dbdetails?acro=boptilatt-c10>.
- Altman, E., Demler, E., and Lukin, M. D. (2004). *Phys. Rev. A*, **70**, 013603.
- Altman, E., Lewenstein, M., and Liu, W. V. (Coord.) (2010). *KITP Program: Beyond Standard Optical Lattices* (Sep. 13–Dec. 10, 2010). <http://www.kitp.ucsb.edu/activities/dbdetails?acro=boptilatt10>.
- Altshuler, B. L., Aronov, A. G., and Lee, P. A. (1980). *Phys. Rev. Lett.*, **44**, 1288.
- Altshuler, B. L. and Aronov, A. G. (1979a). *Solid State Comm.*, **30**, 115.
- Altshuler, B. L. and Aronov, A. G. (1979b). *Sov. Phys. JETP*, **50**, 968.
- Alt, H. W. (1985). *Lineare Funktionalanalysis*. Springer-Verlag, Berlin.
- Al Khawaja, U. and Stoof, H. T. C. (2001a). *Phys. Rev. A*, **64**, 043612.
- Al Khawaja, U. and Stoof, H. T. C. (2001b). *Nature*, **411**, 918.
- Amico, L., Fazio, R., Osterloh, A., and Vedral, V. (2008). *Rev. Mod. Phys.*, **80**, 517.
- Amico, L. and Penna, V. (1998). *Phys. Rev. Lett.*, **80**, 2189.
- Amico, L. and Penna, V. (2000). *Phys. Rev. B*, **62**, 1224.

- Amit, D. J. (1989). *Modelling Brain Function*. Cambridge University Press, Cambridge.
- Amit, D. J. (2005). *Field Theory, the Renormalization Group and Critical Phenomena*. World Scientific, Singapore.
- Anderlini, M., Lee, P. J., Brown, B. L., Sebby-Strabley, J., Phillips, W. D., and Porto, J. V. (2007). *Nature*, **448**, 452.
- Andersen, B. M., Hirschfeld, P. J., Kampf, A. P., and Schmid, M. (2007). *Phys. Rev. Lett.*, **99**, 147002.
- Anderson, B. P. and Kasevich, M. A. (1998). *Science*, **282**, 1686.
- Anderson, M. H., Ensher, J. R., Matthews, M. R., Wieman, C. E., and Cornell, E. A. (1995). *Science*, **269**, 198.
- Anderson, P. W. and Toulouse, G. (1977). *Phys. Rev. Lett.*, **38**, 508.
- Anderson, P. W. (1951). *Phys. Rev.*, **83**, 1260.
- Anderson, P. W. (1958). *Phys. Rev.*, **109**, 1492.
- Anderson, P. W. (1961). *Phys. Rev.*, **124**, 41.
- Anderson, P. W. (1963). *Solid State Phys.*, **14**, 99.
- Anderson, P. W. (1970). *Comments Solid State Phys.*, **2**, 193.
- Anderson, P. W. (1987). *Science*, **237**, 1196.
- Ando, T. and Fukuyama, H. (ed.) (1988). *Anderson Localization*. Springer Proceedings in Physics 28. Springer, Heidelberg.
- Anker, T., Albiez, M., Gati, R., Hunsmann, S., Eiermann, B., Trombettoni, A., and Oberthaler, M. K. (2005). *Phys. Rev. Lett.*, **94**, 020403.
- Ardonne, E. and Schoutens, K. (2007). *Annals Phys.*, **322**, 201.
- Arovas, D., Schrieffer, J. R., and Wilczek, F. (1984). *Phys. Rev. Lett.*, **53**, 722.
- ARPACK (2010). <http://www.caam.rice.edu/software/ARPACK/>.
- Ashcroft, N. W. and Mermin, N. D. (1976). *Solid State Physics*. Holt, Rinehart, and Winston, Philadelphia.
- Astrakharchik, G. E., Boronat, J., Casulleras, J., and Giorgini, S. (2004). *Phys. Rev. Lett.*, **93**, 200404.
- Astrakharchik, G. E., Boronat, J., Casulleras, J., Kurbakov, I. L., and Lozovik, Yu. E. (2008a). In *Recent Progress in Many-Body Theories. Proceedings of the 14th International Conference. Series on Advances in Quantum Many-Body Theory*, Volume 11, p. 245. arXiv:0707.4630.
- Astrakharchik, G. E., Boronat, J., Kurbakov, I. L., and Lozovik, Yu. E. (2007). *Phys. Rev. Lett.*, **98**, 060405.
- Astrakharchik, G. E., Morigi, G., De Chiara, G., and Boronat, J. (2008b). *Phys. Rev. A*, **78**, 063622.
- Ates, C. and Ziegler, K. (2005). *Phys. Rev. A*, **71**, 063610.
- Aubry, S. and André, G. (1980). *Ann. Isr. Phys. Soc.*, **3**, 133.
- Audenaert, K., Plenio, M. B., and Eisert, J. (2003). *Phys. Rev. Lett.*, **90**, 027901.
- Auerbach, A. (1994). *Interacting Electrons and Quantum Magnetism*. Springer, New York.
- Augusiak, R., Cucchietti, F. M., Haake, F., and Lewenstein, M. (2010a). *New J. Phys.*, **12**, 025021.
- Augusiak, R., Cucchietti, F. M., and Lewenstein, M. (2012). *Lecture Notes in Physics*, **843**. *Many body physics from a quantum information perspective. Lectures from the Les Houches School on "Modern theories of correlated electron systems"* (eds. D. C. Cabra, A. Honecker, and P. Pujol). Springer-Verlag, Berlin. arXiv:1003.3153.
- Babujian, H. M. (1982). *Phys. Lett. A*, **90**, 479.
- Bach, R. and Rzążewski, K. (2004a). *Phys. Rev. Lett.*, **92**, 200401.
- Bach, R. and Rzążewski, K. (2004b). *Phys. Rev. A*, **70**, 063622.
- Bacry, H. (1974). *J. Math. Phys.*, **15**, 1686.
- Bagnato, V. and Kleppner, D. (1991). *Phys. Rev. A*, **44**, 7439.
- Bagnato, V., Pritchard, D. E., and Kleppner, D. (1987). *Phys. Rev. A*, **35**, 4354.
- Baig, M. and Colet, J. (1986). *Phys. Lett. B*, **176**, 149.

- Bai, Z., Demmel, J., Dongarra, J., Ruhe, A., and van der Vorst, H. (ed.) (2000). *Templates for the Solution of Algebraic Eigenvalue Problems: A Practical Guide*. SIAM, Philadelphia.
- Baker, G. A. (1999). *Phys. Rev. C*, **60**, 054311.
- Bakr, W. S., Gillen, J. I., Peng, A., Fölling, S., and Greiner, M. (2009). *Nature*, **462**, 74.
- Bakr, W. S., Peng, A., Tai, M. E., Ma, R., Simon, J., Gillen, J. I., Fölling, S., Pollet, L., and Greiner, M. (2010). *Science*, **329**, 547.
- Balian, R., Maynard, R., and Toulouse, G. (ed.) (1979). *Ill-Condensed Matter*. North-Holland, Amsterdam.
- Baranov, M. A., Dobrek, L., and Lewenstein, M. (2004). *Phys. Rev. Lett.*, **92**, 250403.
- Baranov, M. A., Fehrmann, H., and Lewenstein, M. (2008). *Phys. Rev. Lett.*, **100**, 200402.
- Baranov, M. A., Osterloh, K., and Lewenstein, M. (2005). *Phys. Rev. Lett.*, **94**, 070404.
- Baranov, M. A. (2008). *Phys. Rep.*, **464**, 71.
- Baranov, M., Dobrek, L., Góral, K., Santos, L., and Lewenstein, M. (2002). *Physica Scripta T*, **102**, 74.
- Barberán, N., Lewenstein, M., Osterloh, K., and Dagnino, D. (2006). *Phys. Rev. A*, **73**, 063623.
- Barbosa, P. H. R., Raposo, E. P., and Coutinho-Filho, M. D. (2003). *Phys. Rev. Lett.*, **91**, 197207.
- Barenco, A. (1995). *Proc. R. Soc. Lond. A*, **449**, 679.
- Barnes, S. E. (1976). *J. Phys. F: Met. Phys.*, **6**, 1375.
- Barnett, R., Petrov, D., Lukin, M., and Demler, E. (2006a). *Phys. Rev. Lett.*, **96**, 190401.
- Barnett, R., Turner, A., and Demler, E. (2006b). *Phys. Rev. Lett.*, **97**, 180412.
- Bartenstein, M., Altmeier, A., Riedl, S., Jochim, S., Chin, C., Denschlag, J. H., and Grimm, R. (2004a). *Phys. Rev. Lett.*, **92**, 203201.
- Bartenstein, M., Altmeier, A., Riedl, S., Jochim, S., Chin, C., Denschlag, J. H., and Grimm, R. (2004b). *Phys. Rev. Lett.*, **92**, 120401.
- Baskaran, G., Zou, Z., and Anderson, P. W. (1987). *Solid State Comm.*, **63**, 973.
- Batrouni, G. G., Assaad, F. F., Scalettar, R. T., and Denteneer, P. J. H. (2005). *Phys. Rev. A*, **72**, 031601(R).
- Batrouni, G. G., Rousseau, V. G., and Scalettar, R. T. (2009). *Phys. Rev. Lett.*, **102**, 140402.
- Batrouni, G. G., Rousseau, V., Scalettar, R. T., Rigol, M., Muramatsu, A., Denteneer, P. J. H., and Troyer, M. (2002). *Phys. Rev. Lett.*, **89**, 117203.
- Batrouni, G. G., Scalettar, R. T., and Zimanyi, G. T. (1990). *Phys. Rev. Lett.*, **65**, 1765.
- Bauer, D. M., Lettner, M., Vo, C., Rempe, G., and Dürr, S. (2009). *Nature Phys.*, **5**, 339.
- Baxter, R. J. (1982). *Exactly Solved Models in Statistical Mechanics*. Academic Press Inc., London.
- Beaufils, Q., Chicireanu, R., Zanon, T., Laburthe-Tolra, B., Maréchal, E., Vernac, L., Keller, J. C., and Gorceix, O. (2008). *Phys. Rev. A*, **77**, 061601.
- Becker, C., Soltan-Panahi, P., Kronjäger, J., Döscher, S., Bongs, K., and Sengstock, K. (2010). *New J. Phys.*, **12**, 065025.
- Bedaque, P. F., Caldas, H., and Rupak, G. (2003). *Phys. Rev. Lett.*, **91**, 247002.
- Bekenstein, J. D. (1973). *Phys. Rev. D*, **7**, 233.
- Bekenstein, J. D. (2004). *Contemp. Phys.*, **45**, 31.
- Bell, J. S. *Speakable and Unspeakable in Quantum Mechanics*. Cambridge University Press.
- Benenti, G., Waantal, X., and Pichard, J.-L. (1999). *Phys. Rev. Lett.*, **83**, 1826.
- Bennett, C. H., Bernstein, H., Popescu, S., and Schumacher, B. (1996a). *Phys. Rev. A*, **53**, 2046.
- Bennett, C. H., Brassard, G., Crépeau, C., Jozsa, R., Peres, A., and Wootters, W. K. (1993). *Phys. Rev. Lett.*, **70**, 1895.
- Bennett, C. H. and Brassard, G. (1984). In *IEEE Int. Conf. Comp. Sys. Sig. Proc. (Bangalore, India)*, Volume 175.
- Bennett, C. H., DiVincenzo, D. P., Smolin, J. A., and Wootters, W. K. (1996b). *Phys. Rev. A*, **54**, 3824.

- Bennett, C. H. and Wiesner, S. J. (1992). *Phys. Rev. Lett.*, **69**, 2881.
- Berezinskii, V. L. (1972). *Sov. Phys.: J. Exp. Theor. Phys.*, **34**, 610.
- Bergamini, S., Darquié, B., Jones, M., Jacubowiez, L., Browaeys, A., and Grangier, P. (2004). *J. Opt. Soc. Am. B*, **21**, 1889.
- Bermudez, A., Mazza, L., Rizzi, M., Goldman, N., Lewenstein, M., and Martin-Delgado, M. A. (2010). *Phys. Rev. Lett.*, **105**, 190404.
- Bermudez, A., Porras, D., and Martin-Delgado, M. A. (2009). *Phys. Rev. A*, **79**, 060303(R).
- Bernier, J.-S., Kollath, C., Georges, A., De Leo, L., Gerbier, F., Salomon, C., and Köhl, M. (2009). *Phys. Rev. A*, **79**, 061601(R).
- Bernu, B., Lecheminant, P., Lhuillier, C., and Pierre, L. (1994). *Phys. Rev. B*, **50**, 10048.
- Bernu, B., Lhuillier, C., and Pierre, L. (1992). *Phys. Rev. Lett.*, **69**, 2590.
- Berry, M. V. (1984). *Proc. Roy. Soc. A*, **392**, 45.
- Best, T., Will, S., Schneider, U., Hackermüller, L., van Oosten, D., Bloch, I., and Lühmann, D.-S. (2009). *Phys. Rev. Lett.*, **102**, 030408.
- Bethe, H. A. (1931). *Z. Physik*, **21**, 205.
- Bhat, R., Holland, M. J., and Carr, L. D. (2006). *Phys. Rev. Lett.*, **96**, 060405.
- Bhat, R., Krämer, M., Cooper, J., and Holland, M. J. (2007). *Phys. Rev. A*, **76**, 043601.
- Bickers, N. E., Scalapino, D. J., and White, S. R. (1989). *Phys. Rev. Lett.*, **62**, 961.
- Bilas, N. and Pavloff, N. (2006). *Eur. Phys. J. D*, **40**, 387.
- Billy, J., Josse, V., Zuo, Z., Bernard, A., Hambrecht, B., Lugan, P., Clément, D., Sanchez-Palencia, L., Bouyer, P., and Aspect, A. (2008). *Nature*, **453**, 891.
- Binder, K. and Young, A. P. (1986). *Rev. Mod. Phys.*, **58**, 801.
- Binney, J. J., Dowrick, N. J., Fisher, A. J., and Newman, M. E. J. (1992). *The Theory of Critical Phenomena: An Introduction to the Renormalization Group*. Oxford University Press, Oxford.
- Birkl, G., Buchkremer, F. B. J., Dumke, R., and Ertmer, W. (2001). *Opt. Commun.*, **191**, 67.
- Birkl, G. and Fortagh, J. (2007). *Laser and Photonics Reviews*, **1**, 12.
- Birkl, G., Gatzke, M., Deutsch, I. H., Rolston, S. L., and Phillips, W. D. (1995). *Phys. Rev. Lett.*, **75**, 2823.
- Bishop, D. J. and Reppy, J. D. (1978). *Phys. Rev. Lett.*, **40**, 1727.
- Bishop, D. J. and Reppy, J. D. (1980). *Phys. Rev. B*, **22**, 5171.
- Bishop, M. and Wehr, J. (2011). arxiv:1109.4109.
- Bissbort, U. and Hofstetter, W. (2009). *Europhys. Lett.*, **86**, 50007.
- Bissbort, U., Li, Y., Götze, S., Heinze, J., Krauser, J. S., Weinberg, M., Becker, C., Sengstock, K., and Hofstetter, W. (2011). *Phys. Rev. Lett.*, **106**, 205303.
- Blaizot, J. P. and Ripka, G. (1985). *Scaling Quantum Theory of Finite Systems*. MIT Press, Cambridge, MA.
- Bloch, F. and Rabi, I. I. (1945). *Rev. Mod. Phys.*, **17**, 237.
- Bloch, I., Dalibard, J., and Zwerger, W. (2008). *Rev. Mod. Phys.*, **80**, 885.
- Bloch, I. (2004). *Physics World*, **17**, 25.
- Bogdanovich, S., Sarachik, M. P., and Bhatt, R. N. (1999). *Phys. Rev. Lett.*, **82**, 137.
- Bogoliubov, N. (1947). *J. Phys. (Moscow)*, **11**, 23.
- Bohm, A., Mostafazadeh, A., Koizumi, H., Niu, Q., and Zwanziger, J. (2002). *The Geometric Phase in Quantum Systems*. Springer, Heidelberg.
- Bohn, J. L., Wilson, R. M., and Ronen, S. (2009). *Laser Phys.*, **19**, 547.
- Boiron, D., Michaud, A., Fournier, J. M., Simard, L., Sprenger, M., Grynberg, G., and Salomon, C. (1998). *Phys. Rev. A*, **57**, R4106.
- Bombelli, L., Koul, R. K., Lee, J., and Sorkin, R. D. (1986). *Phys. Rev. D*, **34**, 373.
- Bombin, H. and Martin-Delgado, M. A. (2008). *Phys. Rev. A*, **77**, 042322.
- Bonner, J. C. (1987). *J. Appl. Phys.*, **61**, 3941.

- Borland, R. E. (1963). *Proc. R. Soc. Lond. A*, **274**, 529.
- Bourennane, M., Eibl, M., Kurtsiefer, C., Gaertner, S., Weinfurter, H., Gühne, O., Hyllus, P., Bruß, D., Lewenstein, M., and Sanpera, A. (2004). *Phys. Rev. Lett.*, **92**, 087902.
- Bousso, R. (2002). *Rev. Mod. Phys.*, **74**, 825.
- Bouwmeester, D., Ekert, A. K., and Zeilinger, A. (2000). *The Physics of Quantum Information: Quantum Cryptography, Quantum Teleportation, Quantum Computation*. Springer, Berlin.
- Bouyer, P. (2009). *Ann. Phys.*, **18**, 844.
- Bradley, C. C., Sackett, C. A., Tollett, J. J., and Hulet, R. G. (1995). *Phys. Rev. Lett.*, **75**, 1687.
- Braungardt, S., Sen(De), A., Sen, U., and Lewenstein, M. (2007). *Phys. Rev. A*, **76**, 042307.
- Bray, A. J. and Moore, M. A. (1987). *Phys. Rev. Lett.*, **58**, 57.
- Brennen, G. K., Micheli, A., and Zoller, P. (2007). *New J. Phys.*, **9**, 138.
- Briegel, H. J. and Raussendorf, R. (2001). *Phys. Rev. Lett.*, **86**, 910.
- Browne, D. E. and Briegel, H. J. (2006). arXiv:quant-ph/0603226.
- Büchler, H. P., Demler, E., Lukin, M., Micheli, A., Prokof'ev, N., Pupillo, G., and Zoller, P. (2007a). *Phys. Rev. Lett.*, **98**, 060404.
- Büchler, H. P., Demler, E., Lukin, M., Micheli, A., Prokof'ev, N., Pupillo, G., and Zoller, P. (2007b). *Phys. Rev. Lett.*, **98**, 060404.
- Büchler, H.-P., Hermle, M., Huber, S. D., Fisher, M. P. A., and Zoller, P. (2005). *Phys. Rev. Lett.*, **95**, 040402.
- Budnik, R. and Auerbach, A. (2004). *Phys. Rev. Lett.*, **93**, 187205.
- Buluta, I. and Nori, F. (2009). *Science*, **326**, 108.
- Buonsante, P., Giampaolo, S. M., Illuminati, F., Penna, V., and Vezzani, A. (2008). *Phys. Rev. Lett.*, **100**, 240402.
- Buonsante, P., Massel, F., Penna, V., and Vezzani, A. (2009). *Phys. Rev. A*, **79**, 013623.
- Burkov, A. A. and Demler, E. (2006). *Phys. Rev. Lett.*, **96**, 180406.
- Burnell, F. J., Parish, M. M., Cooper, N. R., and Sondhi, S. L. (2009). *Phys. Rev. B*, **80**, 174519.
- Burrello, M. and Trombettoni, A. (2010). *Phys. Rev. Lett.*, **105**, 125304.
- Busch, T. and Anglin, J. R. (1999). *Phys. Rev. A*, **60**, R2669.
- Byczuk, K., Hofstetter, W., and Vollhardt, D. (2005). *Phys. Rev. Lett.*, **94**, 056404.
- Byczuk, K., Hofstetter, W., and Vollhardt, D. (2009). *Phys. Rev. Lett.*, **102**, 146403.
- Byczuk, K., Hofstetter, W., Yu, U., and Vollhardt, D. (2010). *Eur. Phys. J., Special Topics* **180**, 135.
- Calabrese, P., Cardy, J., and Doyon, B. (2009). *J. Phys. A: Math. Theor.*, **42**, 500301.
- Calabrese, P. and Cardy, J. (2009). *J. Phys. A: Math. Theor.*, **42**, 504005.
- Caldas, H. (2004). *Phys. Rev. A*, **69**, 063602.
- Campbell, G. K., Mun, J., Boyd, M., Medley, P., Leanhardt, A. E., Marcassa, L. G., Pritchard, D. E., and Ketterle, W. (2006). *Science*, **313**, 649.
- Capogrosso-Sansone, B., Trefzger, C., Lewenstein, M., Zoller, P., and Pupillo, G. (2010). *Phys. Rev. Lett.*, **104**, 125301.
- Capriotti, L., Becca, F., Parola, A., and Sorella, S. (2001). *Phys. Rev. Lett.*, **87**, 097201.
- Cardy, J. (1996). *Scaling and Renormalization in Statistical Physics*. Cambridge University Press, Cambridge.
- Carlson, J., Chang, S.-Y., Pandharipande, V. R., and Schmidt, K. E. (2003). *Phys. Rev. Lett.*, **91**, 050401.
- Carlson, J. and Reddy, S. (2005). *Phys. Rev. Lett.*, **95**, 060401.
- Carusotto, I. and Castin, Y. (2004). *Opt. Comm.*, **243**, 81.
- Casati, G., Chirikov, B., Ford, J., and Izrailev, F. M. (1979). *Lecture Notes in Physics. Stochastic Behavior of Classical and Quantum Hamiltonian systems*. Volume 93. Springer-Verlag, Berlin.

- Castro Neto, A. H., Guinea, F., Peres, N. M. R., Novoselov, K. S., and Geim, A. K. (2009). *Rev. Mod. Phys.*, **81**, 109.
- Cataliotti, F. S., Burger, S., Fort, C., Maddaloni, P., Minardi, F., Trombettoni, A., Smerzi, A., and Inguscio, M. (2001). *Science*, **293**, 843.
- Catani, J., De Sarlo, L., Barontini, G., Minardi, F., and Inguscio, M. (2008). *Phys. Rev. A*, **77**, 011603(R).
- Cazalilla, M. A., Barberán, N., and Cooper, N. R. (2005). *Phys. Rev. B*, **71**, 121303(R).
- Cazalilla, M. A., Ho, A. F., and Giamarchi, T. (2006). *New J. Phys.*, **8**, 158.
- Cazalilla, M. A., Ho, A. F., and Ueda, M. (2009). *New J. Phys.*, **11**, 103033.
- Cazalilla, M. A. (2004). *J. Phys. B: Atom. Molec. Phys.*, **37**, S1.
- Ceccatto, H. A., Gazza, C. J., and Trumper, A. E. (1992). *Phys. Rev. B*, **45**, 7832.
- Chabé, J., Lemarié, G., Grémaud, B., Delande, D., Sriftgiser, P., and Garreau, J. C. (2008). *Phys. Rev. Lett.*, **101**, 255702.
- Chang, M. S., Hamley, C. D., Barrett, M. D., Sauer, J. A., Fortier, K. M., Zhang, W., You, L., and Chapman, M. S. (2004). *Phys. Rev. Lett.*, **92**, 140403.
- Chang, M. S., Qin, Q. S., Zhang, W. X., You, L., and Chapman, M. S. (2005). *Nature Phys.*, **1**, 111.
- Chang, S. Y. (2008). *Phys. Rev. A*, **77**, 051602(R).
- Chao, K. A., Spałek, J., and Oleś, A.M. (1977). *J. Phys. C: Solid State Phys.*, **10**, L271.
- Cheneau, M. (2008). *Thése: Transition BKT et potentiels géométriques dans le gas de Bose bidimensionnel*. Université Pierre et Marie Curie.
- Chen, X., Gu, Z.-C., and Wen, X.-G. (2010). *Phys. Rev. B*, **82**, 155138.
- Chen, Y. P., Hitchcock, J., Dries, D., Junker, M., Welford, C., and Hulet, R. G. (2008). *Phys. Rev. A*, **77**, 033632.
- Chin, C., Grimm, R., Julienne, P., and Tiesinga, E. (2010). *Rev. Mod. Phys.*, **82**, 1225.
- Choi, D.-I. and Niu, Q. (1999). *Phys. Rev. Lett.*, **82**, 2022.
- Choi, M. D. (1982). *Proc. Symp. Pure Math.*, **38**, 583.
- Chowdhury, D. (1986). *Spin Glasses and other Frustrated Systems*. Wiley, New York.
- Chubukov, A. V. (1991). *Phys. Rev. B*, **43**, 3337.
- Chu, S. (1998). *Rev. Mod. Phys.*, **70**, 685.
- Ciobanu, C. V., Yip, S. K., and Ho, T.-L. (2000). *Phys. Rev. A*, **61**, 033607.
- Cirac, J. I. and Verstraete, F. (2009). *J. Phys. A: Math. Theor.*, **42**, 504004.
- Cirac, J. I. and Zoller, P. (1995). *Phys. Rev. Lett.*, **74**, 4091.
- Cirac, J. I. and Zoller, P. (2004). *Physics Today*, **57**, 38.
- Claeson, T. and Delsing, P. (2003). *Condensation and coherence in condensed matter*. Physica Scripta/The Royal Academy of Sciences/World Scientific, Singapore.
- Clark, S. R. and Jaksch, D. (2006). *New J. Phys.*, **8**, 160.
- Clément, D., Bouyer, P., Aspect, A., and Sanchez-Palencia, L. (2008). *Phys. Rev. A*, **77**, 033631.
- Clément, D., Fabbri, N., Fallani, L., Fort, C., and Inguscio, M. (2010). *J. Low Temp. Phys.*, **158**, 5.
- Clément, D., Varón, A. F., Hugbard, M., Retter, J. A., Bouyer, P., Sanchez-Palencia, L., Gangardt, D. M., Shlyapnikov, G. V., and Aspect, A. (2005). *Phys. Rev. Lett.*, **95**, 170409.
- Clément, D., Varón, A. F., Retter, J. A., Sanchez-Palencia, L., Aspect, A., and Bouyer, P. (2006). *New J. Phys.*, **8**, 165.
- Coddington, I., Engels, P., Schweikhard, V., and Cornell, E. A. (2003). *Phys. Rev. Lett.*, **91**, 100402.
- Cohen-Tannoudji, C., Dupont-Roc, J., and Grynberg, G. (1992). *Atom–Photon Interactions: Basic Processes and Applications*. Wiley, New York.
- Cohen-Tannoudji, C. (1998). *Rev. Mod. Phys.*, **70**, 707.
- Coleman, P. (1984). *Phys. Rev. B*, **29**, 3035.

- Controzzi, D. and Tsvelik, A. M. (2006). *Phys. Rev. Lett.*, **96**, 097205.
- Cooper, N. R., Rezayi, E. H., and Simon, S. H. (2005). *Phys. Rev. Lett.*, **95**, 200402.
- Cooper, N. R., Wilkin, N. K., and Gunn, J. M. F. (2001). *Phys. Rev. Lett.*, **87**, 120405.
- Cooper, N. R. (2008). *Adv. Phys.*, **57**, 539.
- Corcovilos, T. A., Baur, S. K., Hitchcock, J. M., Mueller, E. J., and Hulet, R. G. (2010). *Phys. Rev. A*, **81**, 013415.
- Cornell, E. A. and Wieman, C. E. (2002). *Rev. Mod. Phys.*, **74**, 875.
- Cornish, S. L., Claussen, N. R., Roberts, J. L., Cornell, E. A., and Wieman, C. E. (2000). *Phys. Rev. Lett.*, **85**, 1795.
- Courteille, P., Freeland, R. S., Heinzen, D. J., van Abeelen, F. A., and Verhaar, B. J. (1998). *Phys. Rev. Lett.*, **81**, 69.
- Cramer, M., Eisert, J., and Illuminati, F. (2004). *Phys. Rev. Lett.*, **93**, 190405.
- Cramer, M., Eisert, J., Plenio, M. B., and Dreissig, J. (2006). *Phys. Rev. A*, **73**, 012309.
- Crisanti, A., Paladin, G., and Vulpiani, A. (1993). *Products of Random Matrices*. Springer, Berlin.
- Cristiani, M., Morsch, O., Müller, J. H., Ciampini, D., and Arimondo, E. (2002). *Phys. Rev. A*, **65**, 063612.
- Cucchietti, F. M., Damski, B., Dziarmaga, J., and Zurek, W. H. (2007). *Phys. Rev. A*, **75**, 023603.
- Cusack, N. E. (1987). *The Physics of Structurally Disordered Matter*. Adam Hilger, Bristol.
- Dagnino, D., Barberán, N., Lewenstein, M., and Dalibard, J. (2009a). *Nature Phys.*, **5**, 431.
- Dagnino, D., Barberán, N., and Lewenstein, M. (2009b). *Phys. Rev. A*, **80**, 053611.
- Dagnino, D., Barberán, N., Osterloh, K., Riera, A., and Lewenstein, M. (2007). *Phys. Rev. A*, **76**, 013625.
- Dagotto, E., Fradkin, E., and Moreo, A. (1988). *Phys. Rev. B*, **38**, 2926.
- Dagotto, E. and Moreo, A. (1989). *Phys. Rev. Lett.*, **63**, 2148.
- Dalibard, J., Gerbier, F., Juzeliūnas, G., and Öhberg, P. (2010). *Rev. Mod. Phys.* **83**, 1523 (2011). arXiv:1008.5378.
- Damski, B., Everts, H.-U., Honecker, A., Fehrmann, H., Santos, L., and Lewenstein, M. (2005a). *Phys. Rev. Lett.*, **95**, 060403.
- Damski, B., Fehrmann, H., Everts, H.-U., Baranov, M., Santos, L., and Lewenstein, M. (2005b). *Phys. Rev. A*, **72**, 053612.
- Damski, B., Fehrmann, H., Everts, H.-U., Baranov, M., Santos, L., and Lewenstein, M. (2007). *Phys. Rev. A*, **76**, Erratum 039902.
- Damski, B., Santos, L., Tiemann, E., Lewenstein, M., Kotchigova, S., Julienne, P., and Zoller, P. (2003a). *Phys. Rev. Lett.*, **90**, 110401.
- Damski, B., Zakrzewski, J., Santos, L., Zoller, P., and Lewenstein, M. (2003b). *Phys. Rev. Lett.*, **91**, 080403.
- Damski, B. and Zakrzewski, J. (2006). *Phys. Rev. A*, **74**, 043609.
- Danzl, J. G., Mark, M. J., Haller, E., Gustavsson, M., Hart, R., Liem, A., Zellmer, H., and Nägerl, H. C. (2009). *New J. Phys.*, **11**, 055036.
- Dao, T.-L., Georges, A., Dalibard, J., Salomon, C., and Carusotto, I. (2007). *Phys. Rev. Lett.*, **98**, 240402.
- Das Sarma, S. and Pinczuk, A. (ed.) (1997). *Perspectives in Quantum Hall Effects: Novel Quantum Liquids in Low-Dimensional Semiconductor Structures*. Wiley & Sons, New York.
- Davies, J. H., Lee, P. A., and Rice, T. M. (1982). *Phys. Rev. Lett.*, **49**, 758.
- Davies, J. H., Lee, P. A., and Rice, T. M. (1984). *Phys. Rev. B*, **29**, 4260.
- Davis, K. B., Mewes, M. O., Andrews, M. R., van Druten, N. J., Durfee, D. S., Kurn, D. M., and Ketterle, W. (1995). *Phys. Rev. Lett.*, **75**, 3969.
- Davis, M. J., Morgan, S. A., and Burnett, K. (2001). *Phys. Rev. Lett.*, **87**, 160402.
- Deissler, B., Zaccanti, M., Roati, G., D'Errico, C., Fattori, M., Modugno, M., Modugno, G., and Inguscio, M. (2010). *Nature Phys.*, **6**, 354.

- Delande, D. and Zakrzewski, J. (2009). *Phys. Rev. Lett.*, **102**, 085301.
- della Pietra, L., Aigner, S., vom Hagen, C., Groth, S., Bar-Joseph, I., Lezec, H. J., and Schmiedmayer, J. (2007). *Phys. Rev. A*, **75**, 063604.
- Demler, E. and Zhou, F. (2002). *Phys. Rev. Lett.*, **88**, 163001.
- Deng, X.-L., Porras, D., and Cirac, J. I. (2005). *Phys. Rev. A*, **72**, 063407.
- Deng, X.-L., Porras, D., and Cirac, J. I. (2008). *Phys. Rev. A*, **77**, 033403.
- Denschlag, J. H., Simsarian, J. E., Häffner, H., McKenzie, C., Browaeys, A., Cho, D., Helmerson, K., Rolston, S. L., and Phillips, W. D. (2002). *J. Phys. B: At. Mol. Opt. Phys.*, **35**, 3095.
- Denteneer, P. J. H., Ulmke, M., Scalettar, R. T., and Zimanyi, G. T. (1998). *Physica A*, **251**, 162.
- Deo, N. (1974). *Graph Theory with Applications to Engineering and Computer Science*. Prentice Hall, London.
- Dettmer, S., Hellweg, D., Ryytty, P., Arlt, J. J., Ertmer, W., Sengstock, K., Petrov, D. S., Shlyapnikov, G. V., Kreutzmann, H., Santos, L., and Lewenstein, M. (2001). *Phys. Rev. Lett.*, **87**, 160406.
- Deutsch, D. and Jozsa, R. (1992). *Proc. Soc. R. Lond. A*, **493**, 553.
- Deutsch, D. (1985). *Proc. Soc. R. Lond. A*, **400**, 97.
- Deutsch, D. (1989). *Proc. Soc. R. Lond. A*, **425**, 73.
- de Almeida, J. R. L. and Thouless, D. J. (1978). *J. Phys. A*, **11**, 983.
- De Chiara, G., Lewenstein, M., and Sanpera, A. (2011). *Phys. Rev. B*, **84**, 054451.
- de Gennes, P. G. and Prost, J. (1995). *The Physics of Liquid Crystals*. Oxford University Press, Oxford.
- de Groot, S. R., Hooyman, G. J., and ten Seldam, C. A. (1950). *Proc. Soc. R. Lond. A*, **203**, 266.
- De Leo, L., Kollath, C., Georges, A., Ferrero, M., and Parcollet, O. (2008). *Phys. Rev. Lett.*, **101**, 210403.
- De Marco, B. and Jin, D. S. (1999). *Science*, **285**, 1703.
- De Martino, A., Thorwart, M., Egger, R., and Graham, R. (2005). *Phys. Rev. Lett.*, **94**, 060402.
- Diener, R. B., Georgakis, G. A., Zhong, J. X., Raizen, M., and Niu, Q. (2001). *Phys. Rev. A*, **64**, 033416.
- Diener, R. B. and Ho, T.-L. (2006). *Phys. Rev. Lett.*, **96**, 190405.
- DiVincenzo, D. P., Fuchs, C. A., Mabuchi, H., Smolin, J. A., Thapliyal, A., and Uhlmann, A. (1999). *Lecture Notes in Computer Science. Proceedings of the 1st NASA International Conference on Quantum Computing and Quantum Communication* (ed. C. S. Williams). Springer-Verlag, Berlin.
- DiVincenzo, D. P., Shor, P. W., Smolin, J. A., Terhal, B. M., and Thapliyal, A. V. (2000). *Phys. Rev. A*, **61**, 062312.
- DiVincenzo, D. P. (2000). *Fortschritte der Physik*, **48**, 771.
- Dobrek, L., Gajda, M., Lewenstein, M., Sengstock, K., Birkl, G., and Ertmer, W. (1999). *Phys. Rev. A*, **60**, 3381(R).
- Doherty, A. C., Parrilo, P. A., and Spedelieri, F. M. (2002). *Phys. Rev. Lett.*, **88**, 187904.
- Dorner, U., Fedichev, P., Jaksch, D., Lewenstein, M., and Zoller, P. (2003). *Phys. Rev. Lett.*, **91**, 073601.
- Dotsenko, V. S. and Feigelman, M. V. (1981). *J. Phys. C: Solid State Physics*, **14**, L823.
- Douçot, B., Feigelman, M. V., Ioffe, L. B., and Ioselevich, A. S. (2005). *Phys. Rev. B*, **71**, 024505.
- Drenkelforth, S., Kleine Büning, G., Will, J., Schulte, T., Murray, N., Ertmer, W., Santos, L., and Arlt, J. J. (2008). *New J. Phys.*, **10**, 045027.
- Drese, K. and Holthaus, M. (1997). *Phys. Rev. B*, **55**, R14693.
- Drummond, P. D. and Corney, J. F. (2005). *Comp. Phys. Comm.*, **169**, 412.

- Drummond, P. D. and Kheruntsyan, K. V. (2004). *Phys. Rev. A*, **70**, 033609.
- Duan, L.-M., Demler, E., and Lukin, M. D. (2003). *Phys. Rev. Lett.*, **91**, 090402.
- DuBois, J. L. and Glyde, H. R. (2001). *Phys. Rev. A*, **63**, 023602.
- Dum, R., Cirac, J. I., Lewenstein, M., and Zoller, P. (1998). *Phys. Rev. Lett.*, **80**, 2972.
- Dunlap, D. H. and Kenkre, V. M. (1986). *Phys. Rev. B*, **34**, 3625.
- Dürr, S., García-Ripoll, J. J., Syassen, N., Bauer, D. M., Lettner, M., Cirac, J. I., and Rempe, G. (2009). *Phys. Rev. A*, **79**, 023614.
- Dürr, S., Syassen, N., Bauer, D. M., Lettner, M., Volz, T., Dietze, D., García-Ripoll, J. J., Cirac, J. I., and Rempe, G. (2008). In *Atomic Physics 21. Proceedings of the XXI International Conference on Atomic Physics ICAP 2008*. arXiv:0810.2217.
- Dür, W., Cirac, J. I., Lewenstein, M., and Bruß, D. (2000). *Phys. Rev. A*, **61**, 062313.
- Dür, W., Hartmann, L., Hein, M., Lewenstein, M., and Briegel, H.-J. (2005). *Phys. Rev. Lett.*, **94**, 097203.
- Dutta, O., Eckardt, A., Hauke, P., Malomed, B., and Lewenstein, M. (2011). *New J. Phys.*, **13**, 023019.
- Dutta, O., Kanamoto, R., and Meystre, P. (2007). *Phys. Rev. Lett.*, **99**, 110404.
- Dutta, O., Kanamoto, R., and Meystre, P. (2008). *Phys. Rev. A*, **78**, 043608.
- Dutta, O. and Lewenstein, M. (2010). *Phys. Rev. A*, **81**, 063608.
- Dutta, O. and Meystre, P. (2007). *Phys. Rev. A*, **75**, 053604.
- Dutta, S. K., Teo, B. K., and Raithel, G. (1999). *Phys. Rev. Lett.*, **83**, 1934.
- Eberlein, C., Giovanazzi, S., and O'Dell, D. H. J. (2005). *Phys. Rev. A*, **71**, 033618.
- Eckardt, A., Hauke, P., Soltan-Panahi, P., Becker, C., Sengstock, K., and Lewenstein, M. (2010). *Europhys. Lett.*, **89**, 10010.
- Eckardt, A. and Lewenstein, M. (2010). *Phys. Rev. A*, **82**, 011606(R).
- Eckardt, A., Weiss, C., and Holthaus, M. (2005). *Phys. Rev. Lett.*, **95**, 260404.
- Eckert, K., Romero-Isart, O., Rodriguez, M., Lewenstein, M., Polzik, E. S., and Sanpera, A. (2008). *Nature Phys.*, **4**, 50.
- Eckert, K., Schliemann, J., Bruß, D., and Lewenstein, M. (2002). *Ann. Phys. (N.Y.)*, **299**, 88.
- Eckert, K., Zawitkowski, L., Leskinen, M. J., Sanpera, A., and Lewenstein, M. (2007). *New J. Phys.*, **9**, 133.
- Edwards, J. T. and Thouless, D. J. (1972). *J. Phys. C: Solid State Phys.*, **5**, 807.
- Edwards, S. F. and Anderson, P. W. (1975). *J. Phys. F: Met. Phys.*, **5**, 965.
- Efetov, K. (1997). *Supersymmetry in Disorder and Chaos*. Cambridge University Press, Cambridge.
- Efros, A. L. and Shklovskii, B. I. (1975). *J. Phys. C: Solid State Phys.*, **8**, L49.
- Efros, A. L. and Shklovskii, B. I. (1976). *Phys. Stat. Sol. B*, **76**, 475.
- Efros, A. L. (1981). *Sov. Phys. JETP*, **54**, 218.
- Eiermann, B., Anker, T., Albiez, M., Taglieber, M., Treutlein, P., Marzlin, K.-P., and Oberthaler, M. K. (2004). *Phys. Rev. Lett.*, **92**, 230401.
- Einarsson, T. and Schulz, H. J. (1995). *Phys. Rev. B*, **51**, 6151.
- Eisert, J., Cramer, M., and Plenio, M. B. (2010). *Rev. Mod. Phys.*, **82**, 277.
- Eisert, J. and Osborne, T. J. (2006). *Phys. Rev. Lett.*, **97**, 150404.
- Ekert, A. K. (1991). *Phys. Rev. Lett.*, **67**, 661.
- Elstner, N. and Monien, H. (1999). *Phys. Rev. B*, **59**, 12184.
- Engelhardt, M. (2004). Generation of confinement and other nonperturbative effects by infrared gluonic degrees of freedom (a talk presented at lattice2004). *hep-lat/0409023*.
- Ernst, P. T., Götze, S., Krauser, J. S., Pyka, K., Lühmann, D.-S., Pfannkuche, D., and Sengstock, K. (2010). *Nature Phys.*, **6**, 56.
- Essler, F. H. L., Frahm, H., Göhmann, F., Klümper, A., and Korepin, V. E. (2005). *The One-Dimensional Hubbard Model*. Cambridge University Press, Cambridge.
- Evenbly, G. and Vidal, G. (2010). *Phys. Rev. Lett.*, **104**, 187203.

- Ezawa, Z. F. (2000). *Quantum Hall Effects: field theoretical approach and related topics*. World Scientific, Singapore.
- Faddeev, L. and Niemi, A. J. (1997). *Nature*, **387**, 58.
- Falicov, L. M. and Kimball, J. C. (1969). *Phys. Rev. Lett.*, **22**, 997.
- Fallani, L., Fort, C., and Inguscio, M. (2008). *Adv. Atom. Molec. Opt. Phys.*, **56**, 119.
- Fallani, L., Lye, J. E., Guarnera, V., Fort, C., and Inguscio, M. (2007). *Phys. Rev. Lett.*, **98**, 130404.
- Fannes, M., Nachtergaele, B., and Werner, R. F. (1989). *Europhys. Lett.*, **10**, 633.
- Fannes, M., Nachtergaele, B., and Werner, R. F. (1992). *Comm. Math. Phys.*, **144**, 443.
- Fan, H., Korepin, V., and Roychowdhury, V. (2004). *Phys. Rev. Lett.*, **93**, 227203.
- Fáth, G. and Sólyom, J. (1991). *Phys. Rev. B*, **44**, 11836.
- Fáth, G. and Sólyom, J. (1995). *Phys. Rev. B*, **51**, 3620.
- Fedichev, P. O., Kagan, Yu., Shlyapnikov, G. V., and Walraven, J. T. M. (1996). *Phys. Rev. Lett.*, **77**, 2913.
- Fehrman, H., Baranov, M. A., Damski, B., Lewenstein, M., and Santos, L. (2004a). *Opt. Comm.*, **243**, 23.
- Fehrman, H., Baranov, M. A., Lewenstein, M., and Santos, L. (2004b). *Opt. Express*, **12**, 55.
- Feldman, D. E. (1998). *J. Phys. A: Math. Gen.*, **31**, L177.
- Ferlaino, F., Knoop, S., and Grimm, R. (2009). *Cold molecules: Theory, experiments, applications* (eds. R. V. Krems, B. Friedrich, and W. C. Stwalley). CRC Press, Boca Raton. arXiv:0809.3920.
- Fetter, A. L. and Walecka, J. D. (1971). *Quantum Theory of Many-Particle Systems*. McGraw-Hill, New York.
- Fetter, A. L. (2009). *Rev. Mod. Phys.*, **81**, 647.
- Fetter, A. and Walecka, J. (2003). *Quantum Theory of Many-Particle Systems*. Dover Publications, New York.
- Feynman, R. P. (1982). *Int. J. Theor. Phys.*, **21**, 467.
- Feynman, R. P. (1986). *Found. Phys.*, **16**, 507.
- Figueirido, F., Karlhede, A., Kivelson, S., Sondhi, S., Rocek, M., and Rokhsar, D. S. (1990). *Phys. Rev. B*, **41**, 4619.
- Fischer, U. R. (2006). *Phys. Rev. A*, **73**, 031602.
- Fisher, D. S. and Hohenberg, P. C. (1988). *Phys. Rev. B*, **37**, 4936.
- Fisher, D. S. and Huse, D. A. (1986). *Phys. Rev. Lett.*, **56**, 1601.
- Fisher, D. S. and Huse, D. A. (1988a). *Phys. Rev. B*, **38**, 373.
- Fisher, D. S. and Huse, D. A. (1988b). *Phys. Rev. B*, **38**, 386.
- Fisher, M. P. A., Lhuillier, C., Trebst, S., and Vidal, G. (Coord.) (2010). *KITP Program: Disentangling Quantum Many-body Systems: Computational and Conceptual Approaches* (Oct. 11-Dec. 17, 2010). <http://online.kitp.ucsb.edu/online/compqcm10/>.
- Fisher, M. P. A., Weichman, P. B., Grinstein, G., and Fisher, D. S. (1989). *Phys. Rev. B*, **40**, 546.
- Fölling, S., Gerbier, F., Widera, A., Mandel, O., Gericke, T., and Bloch, I. (2005). *Nature*, **434**, 481.
- Fölling, S., Widera, A., Mueller, T., Gerbier, F., and Bloch, I. (2006). *Phys. Rev. Lett.*, **97**, 060403.
- Foong, S. K. and Kanno, S. (1994). *Phys. Rev. Lett.*, **72**, 1148.
- Fort, C., Fallani, L., Guarnera, V., Lye, J. E., Modugno, M., Wiersma, D. S., and Inguscio, M. (2005). *Phys. Rev. Lett.*, **95**, 170410.
- Frahm, K., Müller-Groeling, A., Pichard, J. L., and Weinmann, D. (1995). *Europhys. Lett.*, **31**, 169.
- Freedman, M. H., Kitaev, A., Larsen, M. J., and Wang, Z. H. (2003). *Bull. Am. Math. Soc.*, **40**, 31.
- Freedman, R. and Hertz, J. A. (1977). *Phys. Rev. B*, **15**, 2384.
- Freericks, J. K. and Monien, H. (1994). *Europhys. Lett.*, **26**, 545.
- Freericks, J. K. and Monien, H. (1996). *Phys. Rev. B*, **53**, 2691.
- Friedenauer, A., Schmitz, H., Glückert, J. T., Porras, D., and Schätz, T. (2008). *Nature Phys.*, **4**, 757.

- Fukui, T., Hatsugai, Y., and Suzuki, H. (2005). *J. Phys. Soc. Jap.*, **74**, 1674.
- Fukuyama, H. (1980). *J. Phys. Soc. Jpn.*, **48**, 2169.
- Fulde, P. and Ferrell, R. A. (1964). *Phys. Rev.*, **135**, A550.
- Furstenberg, H. (1963). *Trans. Amer. Math. Soc.*, **108**, 377.
- Gaëtan, A., Miroshnychenko, Y., Wilk, T., Chotia, A., Viteau, M., Comparat, D., Pillet, P., Browaeys, A., and Grangier, P. (2009). *Nature Phys.*, **5**, 115.
- Gambetti-Césare, E., Weinmann, D., Jalabert, R. A., and Brune, P. (2002). *Europhys. Lett.*, **60**, 120.
- Gangardt, D. M. and Shlyapnikov, G. V. (2003a). *Phys. Rev. Lett.*, **90**, 010401.
- Gangardt, D. M. and Shlyapnikov, G. V. (2003b). *New J. Phys.*, **5**, 79.
- Gangardt, D. M. (2004). *J. Phys. A: Math. Gen.*, **37**, 9335.
- García-Ripoll, J. J., Dürr, S., Syassen, N., Bauer, D. M., Lettner, M., Rempe, G., and Cirac, J. I. (2009). *New J. Phys.*, **11**, 013053.
- García-Ripoll, J. J., Martin-Delgado, M. A., and Cirac, J. I. (2004). *Phys. Rev. Lett.*, **93**, 250405.
- Gardiner, C. W. and Zoller, P. (2004). *Quantum Noise : A Handbook of Markovian and Non-Markovian Quantum Stochastic Methods with Applications to Quantum Optics*. Springer, Berlin.
- Gati, R., Hemmerling, B., Fölling, J., Albiz, M., and Oberthaler, M. K. (2006). *Phys. Rev. Lett.*, **96**, 130404.
- Gavish, U. and Castin, Y. (2005). *Phys. Rev. Lett.*, **95**, 020401.
- Gebhard, F. (1997). *The Mott–Metal Insulator Transition: Models and Methods*. Springer, Heidelberg.
- Gelfand, M. P., Singh, R. R. P., and Huse, D. A. (1989). *Phys. Rev. B*, **40**, 10801.
- Gelfand, M. P., Singh, R. R. P., and Huse, D. A. (1990). *J. Stat. Phys.*, **59**, 1093.
- Gelfand, M. P. (1990). *Phys. Rev. B*, **42**, 8206.
- Gemelke, N., Sarajlic, E., and Chu, S. (2010). arXiv:1007.2677.
- Gemelke, N., Zhang, X. B., Hung, C., and Chin, C. (2009). *Nature*, **460**, 995.
- Georges, A., Parcollet, O., and Sachdev, S. (2001). *Phys. Rev. B*, **63**, 134406.
- Gerbier, F. and Dalibard, J. (2010). *New J. Phys.*, **12**, 033007.
- Gerbier, F., Widera, A., Fölling, S., Mandel, O., Gericke, T., and Bloch, I. (2005). *Phys. Rev. Lett.*, **95**, 050404.
- Gericke, T., Würtz, P., Reitz, D., Langen, T., and Ott, H. (2008). *Nature Phys.*, **4**, 949.
- Giamarchi, T. and Schulz, H. J. (1988). *Phys. Rev. B*, **37**, 325.
- Giamarchi, T. (2004). *Quantum Physics in One Dimension*. Oxford University Press, Oxford.
- Gimperlein, H., Wessel, S., Schmiedmayer, J., and Santos, L. (2005). *Phys. Rev. Lett.*, **95**, 170401.
- Gioev, D. and Klich, I. (2006). *Phys. Rev. Lett.*, **96**, 100503.
- Giorgini, S., Boronat, J., and Casulleras, J. (1999). *Phys. Rev. A*, **60**, 5129.
- Giorgini, S., Pitaevskii, L. P., and Stringari, S. (2008). *Rev. Mod. Phys.*, **80**, 1215.
- Giovanazzi, S., O'Dell, D., and Kurizki, G. (2002). *Phys. Rev. Lett.*, **88**, 130402.
- Girardeau, M. D., Wright, E. M., and Triscari, J. M. (2001). *Phys. Rev. A*, **63**, 033601.
- Girardeau, M. D. and Wright, E. M. (2000). *Phys. Rev. Lett.*, **84**, 5239.
- Girardeau, M. D. (1960). *J. Math. Phys.*, **1**, 516.
- Glauber, R. J. (1963a). *Phys. Rev.*, **130**, 2529.
- Glauber, R. J. (1963b). *Phys. Rev.*, **131**, 2766.
- Glauber, R. J. (1963c). *J. Math. Phys.*, **4**, 294.
- Gogolin, A. O., Nersesyan, A. A., and Tsvelik, A. M. (2004). *Bosonization and Strongly Correlated Systems*. Cambridge University Press, Cambridge.
- Goldman, N. and Gaspard, P. (2007). *Europhys. Lett.*, **78**, 60001.
- Goldman, N., Kubasiak, A., Bermudez, A., Gaspard, P., Lewenstein, M., and Martin-Delgado, M. A. (2009a). *Phys. Rev. Lett.*, **103**, 035301.
- Goldman, N., Kubasiak, A., Gaspard, P., and Lewenstein, M. (2009b). *Phys. Rev. A*, **79**, 023624.

- Goldman, N., Satija, I., Nikolic, P., Bermudez, A., Martin-Delgado, M. A., Lewenstein, M., and Spielman, I. B. (2010). *Phys. Rev. Lett.*, **105**, 255302.
- Goldman, N. (2009). *Quantum Transport in Lattices Subjected to External Gauge Fields: The Quantum Hall Effect in Optical Lattices and Quantum Graphs*. VDM Verlag, Saarbrücken.
- Goodman, J. W. (2007). *Speckle Phenomena in Optics: Theory and Applications*. Roberts & Co., Englewood, USA.
- Góral, K., Gajda, M., and Rzążewski, K. (2001). *Opt. Express*, **8**, 92.
- Góral, K., Gajda, M., and Rzążewski, K. (2002). *Phys. Rev. A*, **66**, 051602.
- Góral, K., Santos, L., and Lewenstein, M. (2002). *Phys. Rev. Lett.*, **88**, 170406.
- Gork'ov, L. P., Larkin, A. I., and Khmelnitskii, D. E. (1979). *JETP Lett.*, **30**, 228.
- Gor'kov, L. P. and Melik-Barkhudarov, T. K. (1961). *Sov. Phys. JETP*, **13**, 1018.
- Gorshkov, A. V., Hermele, M., Gurarie, V., Xu, C., Julienne, P. S., Ye, J., Zoller, P., Demler, E., Lukin, M. D., and Rey, A. M. (2010). *Nature Phys.*, **6**, 289.
- Grass, T., Baranov, M. A., and Lewenstein, M. (2011). *Phys. Rev. A*, **84**, 043605. arXiv:1105.0299.
- Greensite, J. (2003). *Prog. Part. Nucl. Phys.*, **51**, 1.
- Greiner, M., Bloch, I., Mandel, O., Hänsch, T. W., and Esslinger, T. (2001). *Phys. Rev. Lett.*, **87**, 160405.
- Greiner, M., Mandel, O., Esslinger, T., Hänsch, T. W., and Bloch, I. (2002). *Nature*, **415**, 39.
- Greiner, M., Regal, C. A., Stewart, J. T., and Jin, D. S. (2005). *Phys. Rev. Lett.*, **94**, 110401.
- Greiter, M., Wen, X.-G., and Wilczek, F. (1991). *Phys. Rev. Lett.*, **66**, 3205.
- Grempel, D. R., Prange, R. E., and Fishman, S. (1984). *Phys. Rev. A*, **29**, 1639.
- Gribakin, G. F. and Flambaum, V. V. (1993). *Phys. Rev. A*, **48**, 546.
- Griesmaier, A., Stuhler, J., Koch, T., Fattori, M., Pfau, T., and Giovanazzi, S. (2006). *Phys. Rev. Lett.*, **97**, 250402.
- Griesmaier, A., Werner, J., Hensler, S., Stuhler, J., and Pfau, T. (2005). *Phys. Rev. Lett.*, **94**, 160401.
- Griessner, A., Daley, A. J., Jaksch, D., and Zoller, P. (2005). *Phys. Rev. A*, **72**, 032332.
- Grimmett, G. (1999). *Percolation*. Springer, Berlin.
- Grimm, R., Weidemüller, M., and Ovchinnikov, Y. B. (2000). *Adv. Atom. Molec. Opt. Phys.*, **42**, 95.
- Grossmann, F., Dittrich, T., Jung, P., and Hänggi, P. (1991). *Phys. Rev. Lett.*, **67**, 516.
- Gross, E. P. (1961). *Nuovo Cimento*, **20**, 454.
- Gros, C. (1988). *Phys. Rev. B*, **38**, 931.
- Gühne, O., Hyllus, P., Bruß, D., Ekert, A., Lewenstein, M., Macchiavello, C., and Sanpera, A. (2002). *Phys. Rev. A*, **66**, 062305.
- Guidoni, L., Dépret, B., di Stefano, A., and Verkerk, P. (1999). *Phys. Rev. A*, **60**, R4233.
- Guidoni, L., Triché, C., Verkerk, P., and Grynberg, G. (1997). *Phys. Rev. Lett.*, **79**, 3363.
- Guidoni, L. and Verkerk, P. (1998). *Phys. Rev. A*, **57**, R1501.
- Guinea, F. (1988a). *Physica C*, **153**, 673.
- Guinea, F. (1988b). *Physica C*, **153**, 1231.
- Gulde, S., Riebe, M., Lancaster, G. P. T., Becher, C., Eschner, J., Häffner, H., Schmidt-Kaler, F., Chuang, I. L., and Blatt, R. (2003). *Nature*, **421**, 48.
- Günter, K. J., Cheneau, M., Yefsah, T., Rath, S. P., and Dalibard, J. (2009). *Phys. Rev. A*, **79**, 011604.
- Günter, K., Stöferle, T., Moritz, H., Köhl, M., and Esslinger, T. (2006). *Phys. Rev. Lett.*, **96**, 180402.
- Gurarie, V., Pollet, L., Prokof'ev, N. V., Svistunov, B. V., and Troyer, M. (2009). *Phys. Rev. B*, **80**, 214519.
- Gurarie, V. and Radzhivovsky, L. (2007a). *Ann. Phys.*, **322**, 2.
- Gurarie, V. and Radzhivovsky, L. (2007b). *Phys. Rev. B*, **75**, 212509.
- Gurvits, L. (2003). *STOC*, **69**, 448.

- Gusynin, V. P. and Sharapov, S. G. (2005). *Phys. Rev. Lett.*, **95**, 146801.
- Gygi, O., Katzgraber, H. G., Troyer, M., Wessel, S., and Batrouni, G. G. (2006). *Phys. Rev. A*, **73**, 063606.
- Haake, F. (2010). *Quantum Signatures of Chaos*. Springer, Berlin.
- Hackermüller, L., Schneider, U., Moreno-Cardoner, M., Kitagawa, T., Best, T., Will, S., Demler, E., Altman, E., Bloch, I., and Paredes, B. (2010). *Science*, **327**, 1621.
- Hadzibabic, Z. and Dalibard, J. (2010). In *Proceedings of the International School of Physics ‘Enrico Fermi’*, Varenna, Italy, Amsterdam. IOS.
- Hadzibabic, Z., Krüger, P., Cheneau, M., Battelier, B., and Dalibard, J. (2006). *Nature*, **441**, 1118.
- Hadzibabic, Z., Krüger, P., Cheneau, M., Rath, S. P., and Dalibard, J. (2008). *New J. Phys.*, **10**, 045006.
- Hadzibabic, Z., Stock, S., Battelier, B., Bretin, V., and Dalibard, J. (2004). *Phys. Rev. Lett.*, **93**, 180403.
- Haldane, F. D. M. (1983a). *Phys. Lett. A*, **93**, 464.
- Haldane, F. D. M. (1983b). *Phys. Rev. Lett.*, **50**, 1153.
- Haller, E., Hart, R., Mark, M. J., Danzl, J. G., Reichsöllner, L., Gustavsson, M., Dalmonte, M., Pupillo, G., and Nägerl, H.-C. (2010). *Nature*, **466**, 597.
- Hammerer, K., Sorensen, A. S., and Polzik, E. S. (2010). *Rev. Mod. Phys.*, **82**, 1041.
- Hanbury Brown, R. and Twiss, R. (1956). *Nature*, **177**, 27.
- Harada, K. and Kawashima, N. (2001). *J. Phys. Soc. Jpn.*, **70**, 13.
- Harada, K. and Kawashima, N. (2002). *Phys. Rev. B*, **65**, 052403.
- Harper, P. G. (1955). *Proc. Phys. Soc. A*, **68**, 874.
- Hastings, M. B. (2004). *Phys. Rev. Lett.*, **93**, 140402.
- Hastings, M. B. (2007). *J. Stat. Mech. Theory and Exp.*, P08024.
- Hastings, M. B. (2009). *Phys. Rev. Lett.*, **103**, 050502.
- Hauke, P., Cucchietti, F. M., Müller-Hermes, A., Banuls, M.-C., Cirac, J. I., and Lewenstein, M. (2010). *New J. Phys.*, **12**, 113037.
- Haussmann, R., Rantner, W., Cerrito, S., and Zwerger, W. (2007). *Phys. Rev. A*, **75**, 023610.
- Hawking, S. W. (1974). *Nature*, **248**, 30.
- Heidarian, D. and Trivedi, N. (2004). *Phys. Rev. Lett.*, **93**, 126401.
- Heidemann, R., Raitzsch, U., Bendkowsky, V., Butscher, B., Löw, R., and Pfau, T. (2008). *Phys. Rev. Lett.*, **100**, 033601.
- Heine, D., Rohringer, W., Fischer, D., Wilzbach, M., Raub, T., Loziczký, S., Liu, X. Y., Groth, S., Hessmo, B., and Schmiedmayer, J. (2010). *New J. Phys.*, **12**, 095005.
- Heiselberg, H. (2001). *Phys. Rev. A*, **63**, 043606.
- Henley, C. L. (1989). *Phys. Rev. Lett.*, **62**, 2056.
- Henny, M., Oberholzer, S., Strunk, C., Heinzel, T., Ensslin, K., Holland, M., and Schönenberger, C. (1999). *Science*, **284**, 296.
- Hering, M., Scheffler, M., Dressel, M., and Von Lohneysen, H. (2005). *Physica B*, **359**, 1469.
- Hermele, M., Fisher, M. P. A., and Balents, L. (2004). *Phys. Rev. B*, **69**, 064404.
- Hermele, M., Gurarie, V., and Rey, A. M. (2009). *Phys. Rev. Lett.*, **103**, 135301.
- Hewson, A. C. (1993). *The Kondo Problem to Heavy Fermions*. Cambridge University Press, Cambridge.
- Hilhorst, H. J., Suzuki, M., and Felderhof, B. U. (1972). *Physica*, **60**, 199.
- Hill, S. and Wootters, W. K. (1997). *Phys. Rev. Lett.*, **78**, 5022.
- Hiroshima, T. (2003). *Phys. Rev. Lett.*, **91**, 057902.
- Hirsch, J. E. (1989a). *Physica C*, **158**, 326.
- Hirsch, J. E. (1989b). *Phys. Lett. A*, **134**, 451.
- Hofferberth, S., Lesanovsky, I., Fischer, B., Verdu, J., and Schmiedmayer, J. (2006). *Nature Phys.*, **2**, 710.

- Hofstadter, D. R. (1976). *Phys. Rev. B*, **14**, 2239.
- Hofstetter, W., Cirac, J. I., Zoller, P., Demler, E., and Lukin, M. D. (2002). *Phys. Rev. Lett.*, **89**, 220407.
- Hofstetter, W. (2006). *Phil. Mag.*, **86**, 1891.
- Hohenberg, P. C. (1967). *Phys. Rev.*, **158**, 383.
- Holland, M., Kokkelmans, S. J. J. M. F., Chiofalo, M. L., and Walser, R. (2001). *Phys. Rev. Lett.*, **87**, 120406.
- Home, J. P., Hanneke, D., Jost, J. D., Amini, J. M., Leibfried, D., and Wineland, D. J. (2009). *Science*, **325**, 1227.
- Honecker, A., Cabra, D. C., Everts, H.-U., Pujol, P., and Stauffer, F. (2007). *J. Phys.: Condens. Matter*, **19**, 145249.
- Honerkamp, C. and Hofstetter, W. (2004a). *Phys. Rev. Lett.*, **92**, 170403.
- Honerkamp, C. and Hofstetter, W. (2004b). *Phys. Rev. B*, **70**, 094521.
- Hopfield, J. J. (1984). *Proc. Natl. Acad. Sci.*, **81**, 3088.
- Horn, R. A. and Johnson, C. R. (1985). *Matrix Analysis*. Cambridge University Press, Cambridge.
- Horodecki, M., Horodecki, P., and Horodecki, R. (1998). *Phys. Rev. Lett.*, **80**, 5239.
- Horodecki, M., Horodecki, P., and Horodecki, R. (1996a). *Phys. Lett. A*, **223**, 1.
- Horodecki, M. and Horodecki, P. (2000). *Phys. Rev. A*, **59**, 4206.
- Horodecki, P. (1997). *Phys. Lett. A*, **232**, 333.
- Horodecki, R., Horodecki, M., Horodecki, P., and Horodecki, K. (2009). *Rev. Mod. Phys.*, **81**, 865.
- Horodecki, R., Horodecki, P., and Horodecki, M. (1996b). *Phys. Lett. A*, **210**, 377.
- Hou, J.-M., Yang, W.-X., and Liu, X.-J. (2009). *Phys. Rev. A*, **79**, 043621.
- Ho, T.-L. and Shenoy, V. B. (1996). *Phys. Rev. Lett.*, **77**, 2595.
- Ho, T.-L. and Zhou, Q. (2009). *Proc. Nat. Acad. Sci.*, **106**, 6916.
- Ho, T.-L. (1998). *Phys. Rev. Lett.*, **81**, 742.
- Hsu, T. C., Marston, J. B., and Affleck, I. (1991). *Phys. Rev. B*, **43**, 2866.
- Huang, K. and Meng, H.-F. (1992). *Phys. Rev. Lett.*, **69**, 644.
- Huang, K. and Yang, C. N. (1957). *Phys. Rev.*, **105**, 767.
- Huang, K. (1987). *Statistical Mechanics*. Wiley, New York.
- Huang, W.-J. and Gou, S.-C. (1999). *Phys. Rev. A*, **59**, 4608.
- Hubbard, J. (1963). *Proc. R. Soc. Lond. A*, **276**, 238.
- Huber, S. D., Altman, E., Büchler, H. P., and Blatter, G. (2007). *Phys. Rev. B*, **75**, 085106.
- Hulpke, F. and Bruß, D. (2005). *J. Phys. A: Math. Theor.*, **38**, 5573.
- Hulthén, L. (1938). *Arkiv. Mat. Astron. Physik*, **26A**, 11.
- Hung, C.-L., Zhang, X., Gemelke, N., and Chin, C. (2011). *Nature*, **470**, 236.
- Idziaszek, Z. and Calarco, T. (2006). *Phys. Rev. Lett.*, **96**, 013201.
- Imambekov, A., Lukin, M., and Demler, E. (2003). *Phys. Rev. A*, **68**, 063602.
- İmamoğlu, A., Lewenstein, M., and You, L. (1997). *Phys. Rev. Lett.*, **78**, 2511.
- Imry, Y. and Ma, S.-K. (1975). *Phys. Rev. Lett.*, **35**, 1399.
- Imry, Y. (1995). *Europhys. Lett.*, **30**, 405.
- Ingold, G.-L., Wobst, A., Aulbach, Ch., and Hänggi, P. (2002). *Eur. Phys. J. B*, **30**, 175.
- Inouye, S., Andrews, M. R., Stenger, J., Miesner, H.-J., Stamper-Kurn, D. M., and Ketterle, W. (1998). *Nature*, **392**, 151.
- Ioffe, A. F. and Regel, A. R. (1960). *Prog. Semicond.*, **4**, 237.
- Isacsson, A. and Girvin, S. M. (2005). *Phys. Rev. A*, **72**, 053604.
- Iskin, M. and Sá de Melo, C. A. R. (2005). *Phys. Rev. B*, **72**, 224513.
- Itano, W. M., Bollinger, J. J., Tan, J. N., Jelenković, B., Huang, X.-P., and Wineland, D. J. (1998). *Science*, **279**, 686.
- Its, A. R., Jin, B.-Q., and Korepin, V. E. (2005). *J. Phys. A: Math. Theor.*, **38**, 2975.

- Jacak, L., Sitko, P., Wieczorek, K., and Wójs, A. (2003). *Quantum Hall Systems : Braid Groups, Composite Fermions and Fractional Charge*. Oxford University Press, Oxford.
- Jacob, A. and Santos, L. (2006). In *AMOP-Frühjahrstagung der DPG, Ver. Deutsch. Phys. Ges. 7/2006, Q2.4*.
- Jacquod, P. and Shepelyansky, D. L. (1997). *Phys. Rev. Lett.*, **78**, 4986.
- Jaksch, D., Briegel, H.-J., Cirac, J. I., Gardiner, C. W., and Zoller, P. (1999). *Phys. Rev. Lett.*, **82**, 1975.
- Jaksch, D., Bruder, C., Cirac, J. I., Gardiner, C. W., and Zoller, P. (1998). *Phys. Rev. Lett.*, **81**, 3108.
- Jaksch, D., Cirac, J. I., Zoller, P., Rolston, S. L., Côté, R., and Lukin, M. D. (2000). *Phys. Rev. Lett.*, **85**, 2208.
- Jaksch, D., Venturi, V., Cirac, J. I., Williams, C. J., and Zoller, P. (2002). *Phys. Rev. Lett.*, **89**, 040402.
- Jaksch, D. and Zoller, P. (2003). *New J. Phys.*, **5**, Art. No. 56.
- Jaksch, D. and Zoller, P. (2005). *Ann. Phys. (N.Y.)*, **315**, 52.
- Jamiołkowski, A. (1972). *Rep. Math. Phys.*, **3**, 275.
- Jaynes, E. T. and Cummings, F. W. (1963). *Proc. IEEE*, **51**, 89.
- Jiang, H. C., Weng, Z. Y., and Sheng, D. N. (2008a). *Phys. Rev. Lett.*, **101**, 117203.
- Jiang, L., Brennen, G. K., Gorshkov, A. V., Hammerer, K., Hafezi, M., Demler, E., Lukin, M. D., and Zoller, P. (2008b). *Nature Phys.*, **4**, 482.
- Jiang, L., Rey, A. M., Romero-Isart, O., García-Ripoll, J. J., Sanpera, A., and Lukin, M. D. (2009). *Phys. Rev. A*, **79**, 022309.
- Jin, B.-Q. and Korepin, V. E. (2004). *J. Stat. Phys.*, **116**, 79.
- Ji, A.-C., Liu, W. M., Song, J. L., and Zhou, F. (2008). *Phys. Rev. Lett.*, **101**, 010402.
- Jona-Lasinio, M., Morsch, O., Cristiani, M., Malossi, N., Müller, J. H., Courtade, E., Anderlini, M., and Arimondo, E. (2003). *Phys. Rev. Lett.*, **91**, 230406.
- Jördens, R., Strohmaier, N., Günter, K., Moritz, H., and Esslinger, T. (2008). *Nature*, **455**, 204.
- Jördens, R., Tarruell, L., Greif, D., Uehlinger, T., Strohmaier, N., Moritz, H., Esslinger, T., De Leo, L., Kollath, C., Georges, A., Scarola, V., Pollet, L., Burovski, E., Kozik, E., and Troyer, M. (2010). *Phys. Rev. Lett.*, **104**, 180401.
- Josephson, B. D. (1962). *Phys. Lett.*, **1**, 251.
- Josserand, C., Pomeau, Y., and Rica, S. (2007). *Phys. Rev. Lett.*, **98**, 195301.
- Jo, G.-B., Guzman, J., Thomas, C. K., Hosur, P., Vishwanath, A., and Stamper-Kurn, D. M. (2011). *Phys. Rev. Lett.*, **108**, 045305 (2012). arXiv: 1109.1591.
- Julsgaard, B. (2003). *Entanglement and Quantum Interactions with Macroscopic Gas Samples*. Ph.D. thesis, University of Aarhus.
- Juzeliūnas, G., Öhberg, P., Ruseckas, J., and Klein, A. (2005a). *Phys. Rev. A*, **71**, 053614.
- Juzeliūnas, G. and Öhberg, P. (2004). *Phys. Rev. Lett.*, **93**, 033602.
- Juzeliūnas, G., Ruseckas, J., Jacob, A., Santos, L., and Öhberg, P. (2008a). *Phys. Rev. Lett.*, **100**, 200405.
- Juzeliūnas, G., Ruseckas, J., Lindberg, M., Santos, L., and Öhberg, P. (2008b). *Phys. Rev. A*, **77**, 011802(R).
- Juzeliūnas, G., Ruseckas, J., Öhberg, P., and Fleischhauer, M. (2006). *Phys. Rev. A*, **73**, 025602.
- Juzeliūnas, G., Ruseckas, J., and Öhberg, P. (2005b). *J. Phys. B: At. Mol. Opt. Phys.*, **38**, 4171.
- Kadanoff, L. P. (2000). *Statistical Physics: Statics, Dynamics and Renormalization*. World Scientific, Singapore.
- Kagan, M. Yu., Brodsky, I. V., Efremov, D. V., and Klaptsov, A. V. (2004). *Phys. Rev. A*, **70**, 023607.
- Kagan, M. Yu., Brodsky, I. V., Efremov, D. V., and Klaptsov, A. V. (2005). *Physics of Metals and Metallography*, **99**, 225.

- Kalmeyer, V. and Laughlin, R. B. (1987). *Phys. Rev. Lett.*, **59**, 2095.
- Kantian, A. (2004). Disordered quantum phases in optical lattices. Master's thesis, Universität Hannover, Germany.
- Karbach, M., Hu, K., Müller, G., and Tobochnik, J. (1998). *Computers in Physics*, **12**, 565.
- Karbach, M. and Müller, G. (1997). *Computers in Physics*, **11**, 36.
- Karski, M., Förster, L., Choi, J. M., Alt, W., Widera, A., and Meschede, D. (2009). *Phys. Rev. Lett.*, **102**, 053001.
- Katzgraber, H. G., Körner, M., and Young, A. P. (2006). *Phys. Rev. B*, **73**, 224432.
- Katzgraber, H. G., Lee, L. W., and Campbell, I. A. (2007). *Phys. Rev. B*, **75**, 014412.
- Katzgraber, H. G. and Young, A. P. (2005). *Phys. Rev. B*, **72**, 184416.
- Kawaguchi, Y., Nitta, M., and Ueda, M. (2008). *Phys. Rev. Lett.*, **100**, 180403.
- Kawasaki, K. (1972). In *Phase Transition and Critical Phenomena* (ed. C. Domb and M. S. Green). Academic Press, New York.
- Kawashima, N. and Rieger, H. (2004). In *Frustrated Spin Systems* (ed. H. T. Diep). World Scientific, Singapore.
- Kay, A., Pachos, J. K., and Adams, C. S. (2006). *Phys. Rev. A*, **73**, 022310.
- Keating, J. P. and Mezzadri, F. (2005). *Phys. Rev. Lett.*, **94**, 050501.
- Ketterle, W. (2002). *Rev. Mod. Phys.*, **74**, 1131.
- Kibble, T. W. B. (1976). *J. Phys. A: Math. Gen.*, **9**, 1387.
- Kimura, T., Tsuchiya, S., and Kurihara, S. (2005). *Phys. Rev. Lett.*, **94**, 110403.
- Kim, Y. B. and Wen, X.-G. (1994). *Phys. Rev. B*, **49**, 4043.
- Kinast, J., Hemmer, S. L., Gehm, M. E., Turlapov, A., and Thomas, J. E. (2004). *Phys. Rev. Lett.*, **92**, 150402.
- Kinoshita, T., Wenger, T., and Weiss, D. S. (2004). *Science*, **305**, 1125.
- Kisker, J. and Rieger, H. (1997). *Phys. Rev. B*, **55**, R11981.
- Kitaev, A. Yu. (1997). arXiv:quant-ph/9707021.
- Kitaev, A. Yu. (2003). *Ann. Phys. (N.Y.)*, **303**, 2.
- Kitaev, A. Yu. (2006). *Ann. Phys. (N.Y.)*, **321**, 2.
- Kittel, C. (2004). *Introduction to Solid State Physics*. J. Wiley & Sons, New York.
- Klaers, J., Schitt, J., Lewinger, F., and Weitz, M. (2010). *Nature*, **468**, 545.
- Klein, A. and Jaksch, D. (2006). *Phys. Rev. A*, **73**, 053613.
- Klein, A. and Jaksch, D. (2009). *Europhys. Lett.*, **85**, 13001.
- Clitzing, K. Von, Dorda, G., and Pepper, M. (1980). *Phys. Rev. Lett.*, **45**, 494.
- Koashi, M. and Ueda, M. (2000). *Phys. Rev. Lett.*, **84**, 1066.
- Koch, T., Lahaye, T., Metz, J., Fröhlich, B., Griesmaier, A., and Pfau, T. (2008). *Nature Phys.*, **4**, 218.
- Koetsier, A. O., Dickerscheid, D. B. M., and Stoof, H. T. C. (2006). *Phys. Rev. A*, **74**, 033621.
- Köhler, T., Góral, K., and Julienne, P. S. (2006). *Rev. Mod. Phys.*, **78**, 1311.
- Köhl, M., Moritz, H., Stöferle, T., Günter, K., and Esslinger, T. (2005). *Phys. Rev. Lett.*, **94**, 080403.
- Kohmoto, M. (1985). *Ann. Phys. (N.Y.)*, **160**, 343.
- Kollath, C., Schollwöck, U., and Zwerger, W. (2005). *Phys. Rev. Lett.*, **95**, 176401.
- Komineas, S. and Cooper, N. R. (2007). *Phys. Rev. A*, **75**, 023623.
- Koponen, T., Kinnunen, J., Martikainen, J.-P., Jensen, L. M., and Torma, P. (2006a). *New J. Phys.*, **8**, 179.
- Koponen, T., Martikainen, J.-P., Kinnunen, J., and Torma, P. (2006b). *Phys. Rev. A*, **73**, 033620.
- Korepin, V. E., Bogoliubov, N. M., and Izergin, A. G. (1997). *Quantum Inverse Scattering Method and Correlation Functions*. Cambridge University Press, Cambridge.
- Korepin, V. E. and Essler, F. H. L. (1994). *Exactly Solvable Models of Strongly Correlated Electrons*. World Scientific, Singapore.

- Korepin, V. E. (2004). *Phys. Rev. Lett.*, **92**, 096402.
- Kosterlitz, J. M. and Thouless, D. J. (1972). *J. Phys. C: Solid State Phys.*, **5**, L124.
- Kosterlitz, J. M. and Thouless, D. J. (1973). *J. Phys. C: Solid State Phys.*, **6**, 1181.
- Kosterlitz, J. M. (1974). *J. Phys. C: Solid State Phys.*, **7**, 1046.
- Kotov, V. N., Ooitmaa, J., Sushkov, O. P., and Zheng, W. H. (1999). *Phys. Rev. B*, **60**, 14613.
- Kraemer, T., Mark, M., Waldburger, P., Danzl, J. G., Chin, C., Engeser, B., Lange, A. D., Pilch, K., Jaakkola, A., Nägerl, H. C., and Grimm, R. (2006). *Nature*, **440**, 315.
- Kramer, B. and MacKinnon, A. (1993). *Rep. Prog. Phys.*, **56**, 1469.
- Krämer, M., Pitaevskii, L., and Stringari, S. (2002). *Phys. Rev. Lett.*, **88**, 180404.
- Krauth, W., Caffarel, M., and Bouchaud, J.-P. (1992). *Phys. Rev. B*, **45**, 3137.
- Krauth, W., Trivedi, N., and Ceperley, D. (1991). *Phys. Rev. Lett.*, **67**, 2307.
- Krauth, W. (1991). *Phys. Rev. B*, **44**, 9772.
- Krems, R. V., Doyle, J., Friedrich, B., and Meijer, G. (2009). *Cold Molecules: Theory, Experiment, Applications* (eds. R. V. Krems, B. Friedrich, and W. C. Stwalley). CRC, Boca Raton.
- Kronjäger, J., Becker, C., Brinkmann, M., Walser, R., Navez, P., Bongs, K., and Sengstock, K. (2005). *Phys. Rev. A*, **72**, 063619.
- Krüger, F., Wu, J. S., and Phillips, P. (2009). *Phys. Rev. B*, **80**, 094526.
- Krutitsky, K. V., Thorwart, M., Egger, R., and Graham, R. (2008). *Phys. Rev. A*, **77**, 053609.
- Krzakala, F. and Bouchaud, J.-P. (2005). *Europhys. Lett.*, **72**, 472.
- Kubo, R. (1952). *Phys. Rev.*, **87**, 568.
- Kühner, T. D. and Monien, H. (1998). *Phys. Rev. B*, **58**, R14741.
- Kühner, T. D., White, S. R., and Monien, H. (2000). *Phys. Rev. B*, **61**, 12474.
- Kuhn, R. C., Miniatura, C., Delande, D., Sigwarth, O., and Müller, C. A. (2005). *Phys. Rev. Lett.*, **95**, 250403.
- Kuklov, A. B. and Svistunov, B. V. (2003). *Phys. Rev. Lett.*, **90**, 100401.
- Kuklov, A. B. (2006). *Phys. Rev. Lett.*, **97**, 110405.
- Laburthe Tolra, B., O'Hara, K. M., Huckans, J. H., Phillips, W. D., Rolston, S. L., and Porto, J. V. (2004). *Phys. Rev. Lett.*, **92**, 190401.
- Laflorencie, N. and Poilblanc, D. (2004). *Lecture Notes in Physics*, **645**, 227.
- Lahaye, T., Menotti, C., Santos, L., Lewenstein, M., and Pfau, T. (2009). *Rep. Prog. Phys.*, **72**, 126401.
- Lai, C. K. (1974). *J. Math. Phys.*, **15**, 1675.
- Lamporesi, G., Catani, J., Barontini, G., Nishida, Y., Inguscio, M., and Minardi, F. (2010). *Phys. Rev. Lett.*, **104**, 153202.
- Landau, L. D. and Lifshitz, E. M. (1987). *Quantum Mechanics*. Pergamon, New York.
- Landau, L. D. (1957a). *Sov. Phys. JETP*, **3**, 920.
- Landau, L. D. (1957b). *Sov. Phys. JETP*, **5**, 101.
- Landau, L. D. (1959). *Sov. Phys. JETP*, **8**, 70.
- Larkin, A. J. and Ovchinnikov, Yu. N. (1964). *Zh. Eksp. Teor. Fiz.*, **47**, 1136.
- Larkin, A. J. and Ovchinnikov, Yu. N. (1965). *Sov. Phys. JETP*, **20**, 762.
- Larson, J., Damski, B., Morigi, G., and Lewenstein, M. (2008). *Phys. Rev. Lett.*, **100**, 050401.
- Latorre, J. I., Rico, E., and Vidal, G. (2004). *Quantum Inf. Comput.*, **4**, 48.
- Latorre, J. I. and Riera, A. (2009). *J. Phys. A: Math. Theor.*, **42**, 504002.
- Läuchli, A. (2008). *Highly Frustrated Magnetism*, **739**, 529.
- Laughlin, R. B. (1983). *Phys. Rev. Lett.*, **50**, 1395.
- Laustsen, T., Verstraete, F., and van Enk, S. J. (2003). *Quantum Inf. Comput.*, **3**, 64.
- Lavis, D. A., Bell, G. M., and Balian, R. (ed.) (1999). *Statistical Mechanics of Lattice Systems: Volume 1: Closed-Form and Exact Solutions (Theoretical and Mathematical Physics)*. Springer, Berlin.

- Lavis, D. A. and Bell, G. M. (1999). *Statistical Mechanics of Lattice Systems: Volume 2: Exact, Series and Renormalization Group Methods (Theoretical and Mathematical Physics)*. Springer, Berlin.
- Law, C. K., Pu, H., and Bigelow, N. P. (1998). *Phys. Rev. Lett.*, **81**, 5257.
- Leanhardt, A. E., Görlitz, A., Chikkatur, A. P., Kielpinski, D., Shin, Y., Pritchard, D. E., and Ketterle, W. (2002). *Phys. Rev. Lett.*, **89**, 190403.
- Lecheminant, P., Bernu, B., Lhuillier, C., Pierre, L., and Sindzingre, P. (1997). *Phys. Rev. B*, **56**, 2521.
- Lecheminant, P., Boulat, E., and Azaria, P. (2005). *Phys. Rev. Lett.*, **95**, 240402.
- Lee, D. K. K. and Gunn, J. M. F. (1990). *J. Phys. C: Condens. Matter*, **2**, 7753.
- Lee, H.-L., Carini, J. P., Baxter, D. V., and Gruner, G. (1998). *Phys. Rev. Lett.*, **80**, 4261.
- Lee, H.-L., Carini, J. P., Baxter, D. V., Henderson, W., and Gruner, G. (2000). *Science*, **287**, 633.
- Lee, P. A., Nagaosa, N., and Wen, X.-G. (2006). *Rev. Mod. Phys.*, **78**, 17.
- Lee, P. A. and Nagaosa, N. (1992). *Phys. Rev. B*, **45**, 5621.
- Lee, P. A. and Ramakrishnan, T. V. (1985). *Rev. Mod. Phys.*, **57**, 287.
- Lee, P. A. (2008). *Rep. Prog. Phys.*, **71**, 012501.
- Leggett, A. J., Chakravarty, S., Dorsey, A. T., Fisher, M. P. A., and Zwerger, W. (1987). *Rev. Mod. Phys.*, **59**, 1.
- Lenard, A. (1964). *J. Math. Phys.*, **5**, 930.
- Leung, P. W. and Elser, V. (1993). *Phys. Rev. B*, **47**, 5459.
- Levinson, J. and Gurarie, V. (2006). *Phys. Rev. A*, **73**, 053607.
- Levin, M. and Wen, X.-G. (2005). *Rev. Mod. Phys.*, **77**, 871.
- Lewenstein, M., Kraus, B., Cirac, J. I., and Horodecki, P. (2000). *Phys. Rev. A*, **62**, 052310.
- Lewenstein, M. and Liu, W. V. (2011). *Nature Phys.*, **7**, 101.
- Lewenstein, M., Sanpera, A., Ahufinger, V., Damski, B., Sen(De), A., and Sen, U. (2007). *Adv. Phys.*, **56**, 243.
- Lewenstein, M., Santos, L., Baranov, M. A., and Fehrmann, H. (2004). *Phys. Rev. Lett.*, **92**, 050401.
- Lewenstein, M. and You, L. (1996). *Phys. Rev. Lett.*, **77**, 3489.
- Lewenstein, M. (2006). *Nature Phys.*, **2**, 289.
- Lhuillier, C. (2005). arXiv:cond-mat/0502464.
- Liang, S., Doucot, B., and Anderson, P. W. (1988). *Phys. Rev. Lett.*, **61**, 365.
- Liao, Y. A., Rittner, A. S. C., Paprotta, T., Li, W., Partridge, G. B., Hulet, R. G., Baur, S. K., and Mueller, E. J. (2010). *Nature*, **467**, 567.
- Licciardello, D. C. and Thouless, D. J. (1975). *J. Phys. C: Solid State Phys.*, **8**, 4157.
- Lieb, E. H. and Liniger, W. (1963). *Phys. Rev.*, **130**, 1605.
- Lieb, E. H. and Robinson, D. W. (1972). *Comm. Math. Phys.*, **28**, 251.
- Lieb, E. H. (1992). *Helv. Phys. Acta*, **65**, 247.
- Lieb, E. H. (1994). *Phys. Rev. Lett.*, **73**, 2158.
- Lifshits, I. M., Gredeskul, S. A., and Pastur, L. A. (1988). *Introduction to the Theory of Disordered Systems*. Wiley and Sons, New York.
- Lignier, H., Sias, C., Ciampini, D., Singh, Y., Zenesini, A., Morsch, O., and Arimondo, E. (2007). *Phys. Rev. Lett.*, **99**, 220403.
- Lim, L.-K., Smith, C. M., and Hemmerich, A. (2008). *Phys. Rev. Lett.*, **100**, 130402.
- Lin, H. Q. and Hirsch, J. E. (1995). *Phys. Rev. B*, **52**, 16155.
- Lin, Y.-J., Compton, R. L., Perry, A. R., Phillips, W. D., Porto, J. V., and Spielman, I. B. (2009a). *Phys. Rev. Lett.*, **102**, 130401.
- Lin, Y.-J., Compton, R. L., Jiménez-García, K., Porto, J. V., and Spielman, I. B. (2009b). *Nature*, **462**, 628.
- Little, W. A. (1974). *Math. Biosci.*, **19**, 101.
- Liu, W. V., Wilczek, F., and Zoller, P. (2004). *Phys. Rev. A*, **70**, 033603.

- Liu, W. V. and Wilczek, F. (2003). *Phys. Rev. Lett.*, **90**, 047002.
- Liu, W. V. and Wu, C. (2006). *Phys. Rev. A*, **74**, 013607.
- Lącki, M., Paganelli, S., Ahufinger, V., Sanpera, A., and Zakrzewski, J. (2011). *Phys. Rev. A*, **83**, 013605.
- Löw, R., Gati, R., Stuhler, J., and Pfau, T. (2005). *Europhys. Lett.*, **71**, 214.
- Lubkin, E. (1978). *J. Math. Phys.*, **19**, 1028.
- Lugan, P., Clément, D., Bouyer, P., Aspect, A., Lewenstein, M., and Sanchez-Palencia, L. (2007). *Phys. Rev. Lett.*, **98**, 170403.
- Lühmann, D.-S., Bongs, K., Sengstock, K., and Pfannkuche, D. (2008). *Phys. Rev. Lett.*, **101**, 050402.
- Luttinger, J. M. (1951). *Phys. Rev.*, **84**, 814.
- Lu, M., Youn, S. H., and Lev, B. L. (2011). *Phys. Rev. A*, **83**, 012510.
- Lye, J. E., Fallani, L., Fort, C., Guarnera, V., Modugno, M., Wiersma, D. S., and Inguscio, M. (2007). *Phys. Rev. A*, **75**, 061603(R).
- Lye, J. E., Fallani, L., Modugno, M., Wiersma, D. S., Fort, C., and Inguscio, M. (2005). *Phys. Rev. Lett.*, **95**, 070401.
- Macris, N. and Nachtergale, B. (1996). *J. Stat. Phys.*, **85**, 754.
- Madison, K. W., Chevy, F., Wohlleben, W., and Dalibard, J. (2000). *Phys. Rev. Lett.*, **84**, 806.
- Mahan, G. D. (1993). *Many-Particle Physics*. Plenum Press, New York.
- Maier, T. A., Jarrel, M., and Scalapino, D. J. (2006). *Phys. Rev. Lett.*, **96**, 047005.
- Majorana, E. (1932). *Nuovo Cimento*, **9**, 43.
- Majumdar, C. K. and Ghosh, D. K. (1969). *J. Math. Phys.*, **10**, 1388.
- Mäkelä, H. and Suominen, K.-A. (2007). *Phys. Rev. Lett.*, **99**, 190408.
- Mäkelä, H., Zhang, Y., and Suominen, K.-A. (2003). *J. Phys. A: Math. Gen.*, **36**, 8555.
- Mambrini, M. and Mila, F. (2000). *Eur. Phys. J. B*, **17**, 651.
- Mandel, O., Greiner, M., Widmer, A., Rom, T., Hänsch, T. W., and Bloch, I. (2003). *Nature*, **425**, 937.
- Manousakis, E. (1991). *Rev. Mod. Phys.*, **63**, 1.
- Marinescu, M. and You, L. (1998). *Phys. Rev. Lett.*, **81**, 4596.
- Marini, M., Pistolesi, F., and Strinati, G. C. (1998). *Eur. Phys. J. B*, **1**, 151.
- Marshall, W. and Olkin, I. (1979). *Inequalities: Theory of Majorization and Its Applications*. Academic Press, New York.
- Marston, J. B. and Affleck, I. (1989). *Phys. Rev. B*, **39**, 11538.
- Martikainen, J.-P., Collin, A., and Suominen, K.-A. (2002a). *Phys. Rev. A*, **66**, 053604.
- Martikainen, J.-P., Collin, A., and Suominen, K.-A. (2002b). *Phys. Rev. Lett.*, **88**, 090404.
- Martikainen, J.-P. and Suominen, K.-A. (2001). *J. Phys. B: At. Mol. Opt. Phys.*, **34**, 4091.
- Martin, T., Montambaux, G., and Trân Thanh Vân, J. (ed.) (1996). *Correlated Fermions and Transport in Mesoscopic Systems*. Editions Frontières, Gif-sur-Yvette.
- Marzlin, K.-P., Zhang, W., and Sanders, B. C. (2000). *Phys. Rev. A*, **62**, 013602.
- Masanes, Ll. (2009). *Phys. Rev. A*, **80**, 052104.
- Maschler, C. and Ritsch, H. (2005). *Phys. Rev. Lett.*, **95**, 260401.
- Massignan, P. and Castin, Y. (2006). *Phys. Rev. A*, **74**, 013616.
- Massignan, P., Sanpera, A., and Lewenstein, M. (2010). *Phys. Rev. A*, **81**, 031607.
- Matthews, M. R., Anderson, B. P., Haljan, P. C., Hall, D. S., Wieman, C. E., and Cornell, E. A. (1999). *Phys. Rev. Lett.*, **83**, 2498.
- Mazza, L., Bermudez, A., Goldman, N., Rizzi, M., Martin-Delgado, M. A., and Lewenstein, M. (2011). *New J. Phys.*, **14**, 015007 (2012). arXiv:1105.0932.
- Mazza, L., Rizzi, M., Lewenstein, M., and Cirac, J. I. (2010). *Phys. Rev. A*, **82**, 043689.
- McCoy, B. M. and Wu, T. T. (1973). *The Two-Dimensional Ising Model*. Harvard University Press, Cambridge, MA.

- McKay, D., White, M., Pasienski, M., and DeMarco, B. (2008). *Nature*, **453**, 76.
- McMillan, W. L. (1981). *Phys. Rev. B*, **24**, 2739.
- Mehring, A., Schollwöck, U., and Fleischhauer, M. (2005). In *Ver. der Deutsch. Phys. Ges., 69 Jahrestagung Berlin 2005, Kurzfassungen der Vorträge, Q32.6*.
- Melzi, R., Carretta, P., Lascialfari, A., Mambrini, M., Troyer, M., Millet, P., and Mila, F. (2000). *Phys. Rev. Lett.*, **85**, 1318.
- Menotti, C., Lewenstein, M., Lahaye, T., and Pfau, T. (2008). In *AIP Conf. Proc., Proceedings of the Workshop Dynamics and Thermodynamics of Systems with Long Range Interactions (Assisi, July 2007)*, p. 332.
- Menotti, C. and Lewenstein, M. (2008). In *Proceedings of the 14th International Conference Recent Progress in Many-body Theories (Barcelona 2007)*, p. 79. World Scientific, Singapore.
- Menotti, C., Smerzi, A., and Trombettoni, A. (2003). *New J. Phys.*, **5**, 112.
- Menotti, C., Trefzger, C., and Lewenstein, M. (2007). *Phys. Rev. Lett.*, **98**, 235301.
- Menotti, C. and Trivedi, N. (2008). *Phys. Rev. B*, **77**, 235120.
- Mering, A. and Fleischhauer, M. (2008). *Phys. Rev. A*, **77**, 023601.
- Mermin, N. D. and Ho, T.-L. (1976). *Phys. Rev. Lett.*, **36**, 594.
- Mermin, N. D. and Wagner, H. (1966). *Phys. Rev. Lett.*, **17**, 1133.
- Mermin, N. D. (1979). *Rev. Mod. Phys.*, **51**, 591.
- Messiah, A. (1961). *Quantum Mechanics, vol. 2*. North-Holland, Amsterdam.
- Messio, L., Lhuillier, C., and Misguich, G. (2011). *Phys. Rev. B*, **83**, 184401.
- Metcalf, H. J. and van der Straten, P. (2001). *Laser Cooling and Trapping*. Springer, Berlin.
- Meyrath, T. P., Schreck, F., Hanssen, J. L., Chu, C.-S., and Raizen, M. G. (2005). *Phys. Rev. A*, **71**, 041604(R).
- Meystre, P. (2001). *Atom Optics*. American Institute of Physics, Ridge, NY.
- Mézard, M., Parisi, G., and Virasoro, M. A. (1987). *Spin Glass Theory and Beyond*. World Scientific, Singapore.
- Micheli, A., Brennen, G. K., and Zoller, P. (2006). *Nature Phys.*, **2**, 341.
- Micnas, R., Ranninger, J., and Robaszkiewicz, S. (1989). *Phys. Rev. B*, **39**, 11653.
- Micnas, R., Ranninger, J., and Robaszkiewicz, S. (1990). *Rev. Mod. Phys.*, **62**, 113.
- Mila, F. (1998). *Phys. Rev. Lett.*, **81**, 2356.
- Minchau, B. J. and Pelcovits, R. A. (1985). *Phys. Rev. B*, **32**, 3081.
- Mintert, F. and Wunderlich, C. (2001). *Phys. Rev. Lett.*, **87**, 257904.
- Miroshnychenko, Y., Alt, W., Dotsenko, I., Förster, L., Khudaverdyan, M., Meschede, D., Schrader, D., and Rauschenbeutel, A. (2006). *Nature*, **442**, 151.
- Misguich, G. and Lhuillier, C. (2003). In *Frustrated Spin Systems* (ed. H. T. Diep). World Scientific, Singapore.
- Mitchell, T. B., Bollinger, J. J., Dubin, D. H. E., Huang, X.-P., Itano, W. M., and Baughman, R. H. (1998). *Science*, **282**, 1290.
- Mizushima, T., Kobayashi, N., and Machida, K. (2004). *Phys. Rev. A*, **70**, 043613.
- Mizushima, T., Machida, K., and Kita, T. (2002). *Phys. Rev. Lett.*, **89**, 030401.
- Modugno, M. (2006). *Phys. Rev. A*, **73**, 013606.
- Modugno, M. (2009). *New J. Phys.*, **11**, 033023.
- Moessner, R., Sondhi, S. L., and Chandra, P. (2000). *Phys. Rev. Lett.*, **84**, 4457.
- Moessner, R. and Sondhi, S. L. (2001a). *Phys. Rev. B*, **63**, 224401.
- Moessner, R. and Sondhi, S. L. (2001b). *Phys. Rev. Lett.*, **86**, 1881.
- Møller, D., Madsen, L. B., and Mølmer, K. (2008). *Phys. Rev. Lett.*, **100**, 170504.
- Mompart, J., Eckert, K., Ertmer, W., Birk, G., and Lewenstein, M. (2003). *Phys. Rev. Lett.*, **90**, 147901.
- Montvay, I. and Münster, G. (1997). *Quantum Fields of a Lattice*. Cambridge University Press, Cambridge.

- Monz, T., Schindler, P., Barreiro, J. T., Chwalla, M., Nigg, D., Harlander, M., Hänsel, W., Hennrich, M., and Blatt, R. (2011). *Phys. Rev. Lett.*, **106**, 130506.
- Moore, F. L., Robinson, J. C., Bharucha, C. F., Sundaram, B., and Raizen, M. G. (1995). *Phys. Rev. Lett.*, **75**, 4598.
- Moore, G. and Read, N. (1991). *Nucl. Phys. B*, **360**, 362.
- Mora, C. and Castin, Y. (2003). *Phys. Rev. A*, **67**, 053615.
- Mora, C., Parcollet, O., and Waintal, X. (2007). *Phys. Rev. B*, **76**, 064511.
- Moritz, H., Stöferle, T., Köhl, M., and Esslinger, T. (2003). *Phys. Rev. Lett.*, **91**, 250402.
- Morrison, S., Kantian, A., Daley, A. J., Katzgraber, H. G., Lewenstein, M., Büchler, H. P., and Zoller, P. (2008). *New J. Phys.*, **10**, 073032.
- Morris, A. G. and Feder, D. L. (2006). *Phys. Rev. A*, **74**, 033605.
- Morsch, O., Müller, J. H., Cristiani, M., Ciampini, D., and Arimondo, E. (2001). *Phys. Rev. Lett.*, **87**, 140402.
- Morsch, O. and Oberthaler, M. (2006). *Rev. Mod. Phys.*, **78**, 179.
- Motrunich, O. I. and Senthil, T. (2002). *Phys. Rev. Lett.*, **89**, 277004.
- Mott, N. F. and Twose, W. D. (1961). *Adv. Phys.*, **10**, 107.
- Mott, N. F. (1949). *Proc. Phys. Soc. A*, **62**, 416.
- Mott, N. F. (1968a). *Rev. Mod. Phys.*, **40**, 677.
- Mott, N. F. (1968b). *J. Non-Cryst. Solids*, **1**, 1.
- Moyal, J. E. (1949). *Proc. Camb. Phil. Soc.*, **45**, 99.
- Mueller, E. J. (2004). *Phys. Rev. A*, **70**, 041603.
- Mukerjee, S., Xu, C., and Moore, J. E. (2006). *Phys. Rev. Lett.*, **97**, 120406.
- Murthy, G. and Sachdev, S. (1990). *Nucl. Phys. B*, **344**, 557.
- Mur-Petit, J., Guilleumas, M., Polls, A., Sanpera, A., Lewenstein, M., Bongs, K., and Sengstock, K. (2006). *Phys. Rev. A*, **73**, 013629.
- Mussardo, G. (2010). *Statistical Field Theory*. Oxford University Press, Oxford.
- Myatt, C. J., Burt, E. A., Ghrist, R. W., Cornell, E. A., and Wieman, C. E. (1997). *Phys. Rev. Lett.*, **78**, 586.
- Nagaoka, Y. and Fukuyama, H. (1982). *Anderson Localization*. Springer Series in Solid State Sciences 39. Springer, Heidelberg.
- Nakamura, T. and Miyashita, S. (1995). *Phys. Rev. B*, **52**, 9174.
- Nayak, C., Simon, S. H., Stern, A., Freedman, M., and Das Sarma, S. (2008). *Rev. Mod. Phys.*, **80**, 1083.
- Negele, J.W. and Orland, H. (1998). *Quantum Many-Particle Systems (Advanced Books Classics)*. Westview Press, Boulder, CO.
- Nelson, D. R. and Kosterlitz, J. M. (1977). *Phys. Rev. Lett.*, **39**, 1201.
- Nelson, K. D., Li, X., and Weiss, D. S. (2007). *Nature Phys.*, **3**, 556.
- Newman, C. M. and Stein, D. L. (2003). *J. Phys: Condens. Mat.*, **15**, R1319.
- Niederberger, A., Rams, M. M., Dziarmaga, J., Cucchietti, F., Wehr, J., and Lewenstein, M. (2010). *Phys. Rev. A*, **82**, 013630.
- Niederberger, A., Schulte, T., Wehr, J., Lewenstein, M., Sanchez-Palencia, L., and Sacha, K. (2008). *Phys. Rev. Lett.*, **100**, 030403.
- Niederberger, A., Wehr, J., Lewenstein, M., and Sacha, K. (2009). *Europhys. Lett.*, **86**, 26004.
- Nielsen, M. A. and Chuang, I. L. (2000). *Quantum Computation and Quantum Information*. Cambridge University Press, Cambridge.
- Nielsen, M. A. and Kempe, J. (2001). *Phys. Rev. Lett.*, **86**, 5184.
- Niemeijer, T. and van Leeuwen, J. M. J. (1973). *Phys. Rev. Lett.*, **31**, 1411.
- Nihsida, Y. and Son, D. T. (2007). *Phys. Rev. A*, **75**, 063617.
- Nikolić, P. and Sachdev, S. (2007). *Phys. Rev. A*, **75**, 033608.

- Nilsen, J. K., Mur-Petit, J., Guilleumas, M., Hjorth-Jensen, M., and Polls, A. (2005). *Phys. Rev. A*, **71**, 053610.
- Ni, K.-K., Ospelkaus, S., de Miranda, M. H. G., Pe'er, A., Neyenhuis, B., Zirbel, J. J., Kotochigova, S., Julienne, P. S., Jin, D. S., and Ye, J. (2008). *Science*, **322**, 231.
- Noack, R. M. and Manmana, S. R. (2005). In *AIP Conf. Proc.*, Volume 789, p. 93.
- Novoselov, K. S., Geim, A. K., Morozov, S. V., Jiang, D., Katsnelson, M. I., Grigorieva, I. V., Dubonos, S. V., and Firsov, A. A. (2005). *Nature*, **438**, 197.
- O'Dell, D. H. J., Giovanazzi, S., Kurizki, G., and Akulin, V. M. (2000). *Phys. Rev. Lett.*, **84**, 5687.
- O'Dell, D. H. J., Giovanazzi, S., and Kurizki, G. (2003). *Phys. Rev. Lett.*, **90**, 110402.
- Oguchi, T. (1960). *Phys. Rev.*, **117**, 117.
- Ohashi, Y. and Griffin, A. (2002). *Phys. Rev. Lett.*, **89**, 130402.
- Öhberg, P., Juzeliūnas, G., Ruseckas, J., and Fleischhauer, M. (2005). *Phys. Rev. A*, **72**, 053632.
- Öhberg, P. and Santos, L. (2002). *Phys. Rev. Lett.*, **89**, 240402.
- Ohmi, T. and Machida, K. (1998). *J. Phys. Soc. Jpn.*, **67**, 1822.
- Oitmaa, J. and Weihong, Z. (1996). *Phys. Rev. B*, **54**, 3022.
- Oliver, W. D., Kim, J., Liu, R. C., and Yamamoto, Y. (1999). *Science*, **284**, 299.
- Olshanii, M. (1998). *Phys. Rev. Lett.*, **81**, 938.
- Ong, N.-P and Bhatt, R. N. (ed.) (2001). *More is Different*. Princeton University Press, Princeton, NJ.
- Onsager, L. (1944). *Phys. Rev.*, **65**, 117.
- Oppermann, R. and Rosenow, B. (1999). *Phys. Rev. B*, **60**, 10325.
- Oppermann, R. and Sherrington, D. (2003). *Phys. Rev. B*, **67**, 245111.
- Orus, R. and Lattore, J. I. (2004). *Phys. Rev. A*, **69**, 052308.
- Osborne, T. J. and Nielsen, M. A. (2002a). *Quantum Inf. Process.*, **1**, 45.
- Osborne, T. J. and Nielsen, M. A. (2002b). *Phys. Rev. A*, **66**, 032110.
- Ospelkaus, S., Ni, K.-K., de Miranda, M. H. G., Neyenhuis, B., Wang, D., Kotochigova, S., Julienne, P. S., Jin, D. S., and Ye, J. (2009). *Farad. Discuss.*, **142**, 351.
- Ospelkaus, S., Ospelkaus, C., Wille, O., Succo, M., Ernst, P., Sengstock, K., and Bongs, K. (2006). *Phys. Rev. Lett.*, **96**, 180403.
- Ospelkaus, S., Pe'er, A., Ni, K.-K., Zirbel, J. J., Neyenhuis, B., Kotochigova, S., Julienne, P. S., Ye, J., and Jin, D. S. (2008). *Nature Phys.*, **4**, 622.
- Osterloh, A., Amico, L., Falci, G., and Fazio, R. (2002). *Nature*, **416**, 608.
- Osterloh, K., Baig, M., Santos, L., Zoller, P., and Lewenstein, M. (2005). *Phys. Rev. Lett.*, **95**, 010403.
- Osterloh, K., Barberán, N., and Lewenstein, M. (2007). *Phys. Rev. Lett.*, **99**, 160403.
- Östlund, S. and Rommer, S. (1995). *Phys. Rev. Lett.*, **75**, 3537.
- Paalanen, M. A., Rosenbaum, T. F., Thomas, G. A., and Bhatt, R. N. (1983). *Phys. Rev. Lett.*, **51**, 1896.
- Pachos, J. K. and Rico, E. (2004). *Phys. Rev. A*, **70**, 053620.
- Page, D. N. (1993). *Phys. Rev. Lett.*, **71**, 1291.
- Pai, R. V., Pandit, R., Krishnamurthy, H. R., and Ramasesha, S. (1996). *Phys. Rev. Lett.*, **76**, 2937.
- Palmer, R. N. and Jaksch, D. (2006). *Phys. Rev. Lett.*, **96**, 180407.
- Palmer, R. N., Klein, A., and Jaksch, D. (2008). *Phys. Rev. A*, **78**, 013609.
- Pao, C.-H., Wu, S.-T., and Yip, S.-K. (2006). *Phys. Rev. B*, **73**, 132506.
- Papanicolaou, N. (1986). *Phys. Lett. A*, **116**, 89.
- Papanicolaou, N. (1988). *Nucl. Phys. B*, **305**, 367.
- Papoulias, D. J., Shlyapnikov, G. V., and Dalibard, J. (2010). *Phys. Rev. A*, **81**, 041603(R).
- Paredes, B. and Bloch, I. (2008). *Phys. Rev. A*, **77**, 023603.
- Paredes, B. and Cirac, J. I. (2003). *Phys. Rev. Lett.*, **90**, 150402.

- Paredes, B., Fedichev, P., Cirac, J. I., and Zoller, P. (2001). *Phys. Rev. Lett.*, **87**, 010402.
- Paredes, B., Tejedor, C., and Cirac, J. I. (2005a). *Phys. Rev. A*, **71**, 063608.
- Paredes, B., Verstraete, F., and Cirac, J. I. (2005b). *Phys. Rev. Lett.*, **95**, 140501.
- Paredes, B., Widera, A., Murg, V., Mandel, O., Fölling, S., Cirac, J. I., Shlyapnikov, G. V., Hänsch, T. W., and Bloch, I. (2004). *Nature*, **429**, 277.
- Parish, M. M., Marchetti, F. M., Lamacraft, A., and Simons, B. D. (2007). *Nature Phys.*, **3**, 124.
- Partridge, G. B., Li, W., Kamar, R. I., Liao, Y. A., and Hulet, R. G. (2006). *Science*, **311**, 503.
- Pasienski, M., McKay, D., White, M., and DeMarco, B. (2010). *Nature Phys.*, **6**, 667.
- Paul, T., Leboeuf, P., Pavloff, N., Richter, K., and Schlagheck, P. (2005). *Phys. Rev. A*, **72**, 063621.
- Pázmándi, F., Zimányi, G., and Scalettar, R. (1995). *Phys. Rev. Lett.*, **75**, 1356.
- Peierls, R. (1936). *Proc. Camb. Phil. Soc.*, **32**, 477.
- Pelissetto, A. and Vicari, E. (2002). *Phys. Rep.*, **368**, 549.
- Peres, A. (1993). *Quantum Theory: Concepts and Methods*. Kluwer Academic Publishers, Dordrecht.
- Peres, A. (1996). *Phys. Rev. Lett.*, **77**, 1413.
- Perez-García, D., Verstraete, F., Wolf, M. M., and Cirac, J. I. (2007). *Quantum Inf. Comput.*, **7**, 401.
- Pérez-García, V. M., Michinel, H., Cirac, J. I., Lewenstein, M., and Zoller, P. (1996). *Phys. Rev. Lett.*, **77**, 5320.
- Pérez-García, V. M., Michinel, H., Cirac, J. I., Lewenstein, M., and Zoller, P. (1997). *Phys. Rev. A*, **56**, 1424.
- Pethick, C. J. and Smith, H. (2008). *Bose-Einstein Condensation in Dilute Gases*. Cambridge University Press, Cambridge.
- Petrov, D. S., Gangardt, D. M., and Shlyapnikov, G. V. (2004). *J. Phys. IV France*, **116**, 3.
- Petrov, D. S., Holzmann, M., and Shlyapnikov, G. V. (2000a). *Phys. Rev. Lett.*, **84**, 2551.
- Petrov, D. S., Shlyapnikov, G. V., and Walraven, J. T. M. (2000b). *Phys. Rev. Lett.*, **85**, 3745.
- Petrov, D. S., Shlyapnikov, G. V., and Walraven, J. T. M. (2001). *Phys. Rev. Lett.*, **87**, 50404.
- Petrov, D. S. and Shlyapnikov, G. V. (2001). *Phys. Rev. A*, **64**, 012706.
- Pezzoli, M. E., Becca, F., Fabrizio, M., and Santoro, G. (2009). *Phys. Rev. B*, **79**, 033111.
- Phillips, W. D. (1998). *Rev. Mod. Phys.*, **70**, 721.
- Pietilä, V. and Möttönen, M. (2009). *Phys. Rev. Lett.*, **102**, 080403.
- Pietilä, V. (2010). *Topological defects and phase transitions in dilute Bose gases*. Ph.D. thesis, Aalto University School of Science and Technology, Espoo.
- Pilati, S., Boronat, J., Casulleras, J., and Giorgini, S. (2005). *Phys. Rev. A*, **71**, 023605.
- Pilati, S., Sakkos, K., Boronat, J., Casulleras, J., and Giorgini, S. (2006). *Phys. Rev. A*, **74**, 043621.
- Pitaevskii, L. P. (1961). *Sov. Phys. JETP*, **13**, 451.
- Pitaevskii, L. and Stringari, S. (2003). *Bose-Einstein Condensation*. Clarendon Press, Oxford.
- Plenio, M. B., Eisert, J., Dreissig, J., and Cramer, M. (2005). *Phys. Rev. Lett.*, **94**, 060503.
- Poilblanc, D., Gagliano, E., Bacci, S., and Dagotto, E. (1991). *Phys. Rev. B*, **43**, 10970.
- Polini, M., Fazio, R., MacDonald, A. H., and Tosi, M. P. (2005). *Phys. Rev. Lett.*, **95**, 010401.
- Polini, M., Fazio, R., Tosi, M. P., Sinova, J., and MacDonald, A. H. (2004). *Laser Phys.*, **14**, 603.
- Pollak, M. and Ortuño, M. (1985). In *Electron-Electron Interactions in Disordered Systems* (ed. A. L. Efros and M. Pollak), p. 287. North Holland, Amsterdam.
- Pollet, L., Prokof'ev, N. V., Svistunov, B. V., and Troyer, M. (2009). *Phys. Rev. Lett.*, **103**, 140402.
- Pollock, E. L. and Ceperley, D. M. (1987). *Phys. Rev. B*, **36**, 8343.
- Polyakov, A. M. (1974). *JETP Lett.*, **20**, 194.
- Pomeau, Y. and Rica, S. (1994). *Phys. Rev. Lett.*, **72**, 2426.
- Pons, M., Ahufinger, V., Wunderlich, C., Sanpera, A., Braungardt, S., Sen(De), A., Sen, U., and Lewenstein, M. (2007). *Phys. Rev. Lett.*, **98**, 023003.

- Popov, V. N. (1983). *Functional Integrals in Quantum Field Theory and Statistical Physics*. D. Reidel, Dordrecht.
- Popp, M., García-Ripoll, J. J., Vollbrecht, K. G. H., and Cirac, J. I. (2006a). *Phys. Rev. A*, **74**, 013622.
- Popp, M., García-Ripoll, J.-J., Vollbrecht, K. G. H., and Cirac, J. I. (2006b). *New J. Phys.*, **8**, 164.
- Popp, M., Paredes, B., and Cirac, J. I. (2004). *Phys. Rev. A*, **70**, 053612.
- Porras, D. and Cirac, J. I. (2004a). *Phys. Rev. Lett.*, **92**, 207901.
- Porras, D. and Cirac, J. I. (2004b). *Phys. Rev. Lett.*, **93**, 263602.
- Porras, D. and Cirac, J. I. (2006). *Phys. Rev. Lett.*, **96**, 250501.
- Porras, D., Marquardt, F., von Delft, J., and Cirac, J. I. (2008). *Phys. Rev. A*, **78**, 010101.
- Porras, D., Verstraete, F., and Cirac, J. I. (2006). *Phys. Rev. B*, **73**, 014410.
- Prange, R. E. and Girvin, S. M. (1987). *The Quantum Hall Effect*. Springer-Verlag, New York.
- Preskill, J. (2004). *Lecture Notes for Physics 219*, **47**, 127.
- Press, W. H., Flannery, B. P., Teukolsky, S. A., and Vetterling, W. T. (1987). *Numerical Recipes*. Cambridge University Press, Cambridge.
- Prokof'ev, N. V., Ruebenacker, O., and Svistunov, B. V. (2001). *Phys. Rev. Lett.*, **87**, 270402.
- Prokof'ev, N. V., Svistunov, B. V., and Tupitsyn, I. S. (1998a). *Phys. Lett. A*, **238**, 253.
- Prokof'ev, N. V., Svistunov, B. V., and Tupitsyn, I. S. (1998b). *JETP*, **87**, 310.
- Prokof'ev, N. V. and Svistunov, B. V. (2004). *Phys. Rev. Lett.*, **92**, 015703.
- Pupillo, G., Griessner, A., Micheli, A., Ortner, M., Wang, D.-W., and Zoller, P. (2008). *Phys. Rev. Lett.*, **100**, 050402.
- Pupillo, G., Micheli, A., Büchler, H. P., and Zoller, P. (2009). In *Cold molecules: Creation and Applications* (ed. R. V. Krems, B. Friedrich, and W. C. Stwalley). Taylor & Francis, London.
- Pupillo, G., Rey, A. M., and Batrouni, G. G. (2006). *Phys. Rev. A*, **74**, 013601.
- Rabl, P., Daley, A. J., Fedickev, P. O., Cirac, J. I., and Zoller, P. (2003). *Phys. Rev. Lett.*, **91**, 110403.
- Radzhivovsky, L. and Sheehy, D. E. (2010). *Rep. Prog. Phys.*, **73**, 076501.
- Rapp, A., Hofstetter, W., and Zaránd, G. (2008). *Phys. Rev. B*, **77**, 144520.
- Rapp, A., Zaránd, G., Honerkamp, C., and Hofstetter, W. (2007). *Phys. Rev. Lett.*, **98**, 160405.
- Rapsch, S., Schollwöck, U., and Zwerger, W. (1999). *Europhys. Lett.*, **46** (5), 559.
- Rasolt, M. and Tesanović, Z. (1992). *Rev. Mod. Phys.*, **64**, 709.
- Raussendorf, R. and Briegel, H.-J. (2001a). *Phys. Rev. Lett.*, **86**, 5188.
- Raussendorf, R. and Briegel, H.-J. (2001b). *Phys. Rev. Lett.*, **86**, 910.
- Read, N. and Green, D. (2000). *Phys. Rev. B*, **61**, 10267.
- Read, N. and Moore, G. (1992). *Prog. Theor. Phys. Suppl.*, **107**, 157.
- Read, N. and Rezayi, E. (1996). *Phys. Rev. B*, **54**, 16864.
- Read, N. and Rezayi, E. (1999). *Phys. Rev. B*, **59**, 8084.
- Read, N. and Sachdev, S. (1989). *Phys. Rev. Lett.*, **62**, 1694.
- Read, N. and Sachdev, S. (1991). *Phys. Rev. Lett.*, **66**, 1773.
- Recati, A., Fedickev, P. O., Zwerger, W., von Delft, J., and Zoller, P. (2005). *Phys. Rev. Lett.*, **94**, 040404.
- Recati, A., Fedickev, P. O., Zwerger, W., and Zoller, P. (2003). *Phys. Rev. Lett.*, **90**, 020401.
- Regal, C. A., Greiner, M., and Jin, D. S. (2004). *Phys. Rev. Lett.*, **92**, 040403.
- Regal, C. A. and Jin, D. S. (2003). *Phys. Rev. Lett.*, **90**, 230404.
- Regnault, N. and Jolicœur, T. (2004a). *Mod. Phys. Lett. B*, **18**, 1003.
- Regnault, N. and Jolicœur, T. (2004b). *Phys. Rev. B*, **70**, 241307.
- Rezayi, E. H., Read, N., and Cooper, N. R. (2005). *Phys. Rev. Lett.*, **95**, 160404.
- Richter, J. (1993). *Phys. Rev. B*, **47**, 5794.
- Rieger, T., Junglen, T., Rangwala, S. A., Pinkse, P. W. H., and Rempe, G. (2005). *Phys. Rev. Lett.*, **95**, 173002.

- Riera, A. and Latorre, J. I. (2006). *Phys. Rev. A*, **74**, 052326.
- Rivest, R. L., Shamir, A., and Adelman, L. M. (1979). On digital signatures and public key cryptosystems. Technical Report MIR/LCS/TR-212, MIT Laboratory for Computer Science.
- Rizzi, M., Rossini, D., De Chiara, G., Montangero, S., and Fazio, R. (2005). *Phys. Rev. Lett.*, **95**, 240404.
- Roati, G., D'Errico, C., Fallani, L., Fattori, M., Fort, C., Zaccanti, M., Modugno, G., Modugno, M., and Inguscio, M. (2008). *Nature*, **453**, 895.
- Rodriguez, K., Argüelles, A., Kolezhuk, A. K., Santos, L., and Vekua, T. (2011). *Phys. Rev. Lett.*, **106**, 105302.
- Rokhsar, D. S. and Kotliar, B. G. (1991). *Phys. Rev. B*, **44**, 10328.
- Romanovsky, I., Yannouleas, C., Baksmaty, L. O., and Landman, U. (2006). *Phys. Rev. Lett.*, **97**, 090401.
- Romanovsky, I., Yannouleas, C., and Landman, U. (2004). *Phys. Rev. Lett.*, **93**, 230405.
- Romero-Isart, O., Eckert, K., and Sanpera, A. (2007). *Phys. Rev. A*, **75**, 050303(R).
- Rommer, S. and Östlund, S. (1997). *Phys. Rev. B*, **55**, 2164.
- Rom, T., Best, T., Mandel, O., Widera, A., Greiner, M., Hänsch, T. W., and Bloch, I. (2004). *Phys. Rev. Lett.*, **93**, 073002.
- Rom, T., Best, T., Van Oosten, D., Schneider, U., Fölling, S., Paredes, B., and Bloch, I. (2006). *Nature*, **444**, 733.
- Ronen, S., Bortolotti, D. C. E., and Bohn, J. L. (2007). *Phys. Rev. Lett.*, **98**, 030406.
- Roscilde, T. and Cirac, J. I. (2007). *Phys. Rev. Lett.*, **98**, 190402.
- Roscilde, T., Rodriguez, M., Eckert, K., Romero-Isart, O., Lewenstein, M., Polzik, E., and Sanpera, A. (2009). *New J. Phys.*, **11**, 055041.
- Roscilde, T. (2008). *Phys. Rev. A*, **77**, 063605.
- Rothe, H. J. (1998). *Lattice Gauge Theories*. World Scientific, Singapore.
- Rothe, H. J. (2005). *Lattice Gauge Theories, An Introduction*. World Scientific, Singapore.
- Roth, R. and Burnett, K. (2003a). *Phys. Rev. A*, **68**, 023604.
- Roth, R. and Burnett, K. (2003b). *J. Opt. B: Quantum Semiclass. Opt.*, **5**, S50.
- Roth, R. and Burnett, K. (2004). *J. Phys. B: At. Mol. Opt. Phys.*, **37**, 3893.
- Roux, G., Barthel, T., McCulloch, I. P., Kollath, C., Schollwöck, U., and Giamarchi, T. (2008). *Phys. Rev. A*, **78**, 023628.
- Rubakov, V. (2002). *Classical Theory of Gauge Fields*. Princeton University Press, Princeton.
- Rudolph, O. (2003). *Phys. Rev. A.*, **67**, 032312.
- Runge, K. J. (1992). *Phys. Rev. B*, **45**, 12292.
- Ruostekoski, J. and Anglin, J. R. (2003). *Phys. Rev. Lett.*, **91**, 190402.
- Ruseckas, J., Juzeliūnas, G., Öhberg, P., and Fleischhauer, M. (2005). *Phys. Rev. Lett.*, **95**, 010404.
- Sachdev, S. (1999). *Quantum Phase Transitions*. Cambridge University Press, Cambridge.
- Sachdev, S. (2008). *Nature Phys.*, **4**, 173.
- Sadler, L. E., Higbie, J. M., Leslie, S. R., Vengalattore, M., and Stamper-Kurn, D. M. (2006). *Nature*, **443**, 312.
- Saffman, M., Walker, T. G., and Mølmer, K. (2010). *Rev. Mod. Phys.*, **82**, 2313.
- Saito, H., Kawaguchi, Y., and Ueda, M. (2006). *Phys. Rev. Lett.*, **96**, 065302.
- Saito, H., Kawaguchi, Y., and Ueda, M. (2007). *Phys. Rev. A*, **75**, 013621.
- Sanchez-Palencia, L., Clément, D., Lugan, P., Bouyer, P., and Aspect, A. (2008). *New J. Phys.*, **10**, 045019.
- Sanchez-Palencia, L., Clément, D., Lugan, P., Bouyer, P., Shlyapnikov, G. V., and Aspect, A. (2007). *Phys. Rev. Lett.*, **98**, 210401.
- Sanchez-Palencia, L. and Lewenstein, M. (2010). *Nature Phys.*, **6**, 87.
- Sanchez-Palencia, L. and Santos, L. (2005). *Phys. Rev. A*, **72**, 053607.
- Sanchez-Palencia, L. (2006). *Phys. Rev. A*, **74**, 053625.

- Sandvik, A. W. (1997). *Phys. Rev. B*, **56**, 11678.
- Sanpera, A., Kantian, A., Sanchez-Palencia, L., Zakrzewski, J., and Lewenstein, M. (2004). *Phys. Rev. Lett.*, **93**, 040401.
- Sanpera, A., Tarrach, R., and Vidal, G. (1998). *Phys. Rev. A*, **58**, 826.
- Santos, L., Baranov, M. A., Cirac, J. I., Everts, H.-U., Fehrmann, H., and Lewenstein, M. (2004). *Phys. Rev. Lett.*, **93**, 030601.
- Santos, L. and Pfau, T. (2006). *Phys. Rev. Lett.*, **96**, 190404.
- Santos, L., Shlyapnikov, G. V., and Lewenstein, M. (2003). *Phys. Rev. Lett.*, **90**, 250403.
- Santos, L., Shlyapnikov, G. V., Zoller, P., and Lewenstein, M. (2000). *Phys. Rev. Lett.*, **85**, 1791.
- Sarajlic, E., Gemelke, N., Chiow, S.-W., Herrman, S., Müller, H., and Chu, S. (2009). In *Pushing the Frontiers of Atomic Physics: Proceedings of the XXI International Conference on Atomic Physics* (ed. M. R. R. Côté, P. L. Gould and W. W. Smith). World Scientific, New Jersey.
- Sarma, G. (1963). *J. Phys. Chem. Solids*, **24**, 1029.
- Satija, I. I., Dakin, D. C., and Clark, C. W. (2006). *Phys. Rev. Lett.*, **97**, 216401.
- Scalapino, D. J. (1995). *Phys. Rep.*, **250**, 329.
- Scalettar, R. T., Batrouni, G. G., and Zimanyi, G. T. (1991). *Phys. Rev. Lett.*, **66**, 3144.
- Scarola, V. W., Demler, E., and Das Sarma, S. (2006). *Phys. Rev. A*, **73**, 051601(R).
- Scheffler, M., Dressel, M., Jourdan, M., and Adrian, H. (2005). *Nature*, **438**, 1135.
- Schellekens, M., Hoppeler, R., Perrin, A., Gomes, J. V., Boiron, D., Aspect, A., and Westbrook, C. I. (2005). *Science*, **310**, 648.
- Scheunemann, R., Cataliotti, F. S., Hänsch, T. W., and Weitz, M. (2000). *Phys. Rev. A*, **62**, 051801(R).
- Schmaljohann, H., Erhard, M., Kronjäger, J., Kottke, M., van Staa, S., Cacciapuoti, L., Arlt, J. J., Bongs, K., and Sengstock, K. (2004). *Phys. Rev. Lett.*, **92**, 040402.
- Schmidt-Kaler, F., Häffner, H., Riebe, M., Gulde, S., Lancaster, G. P. T., Deuschle, T., Becher, C., Roos, C. F., Eschner, J., and Blatt, R. (2003). *Nature*, **422**, 408.
- Schmied, R., Roscilde, T., Murg, V., Porras, D., and Cirac, J. I. (2008). *New J. Phys.*, **10**, 045017.
- Schmitteckert, P., Jalabert, R. A., Weinmann, D., and Pichard, J.-L. (1998). *Phys. Rev. Lett.*, **81**, 2308.
- Schneider, U., Hackermüller, L., Will, S., Best, T., Bloch, I., Costi, T. A., Helmes, R. W., Rasch, D., and Rosch, A. (2008). *Science*, **322**, 1520.
- Schollwöck, U. (2005). *Rev. Mod. Phys.*, **77**, 259.
- Schreck, F., Khaykovich, L., Corwin, K. L., Ferrari, G., Bourdel, T., Cubizolles, J., and Salomon, C. (2001). *Phys. Rev. Lett.*, **87**, 80403.
- Schroll, C., Marquardt, F., and Bruder, C. (2004). *Phys. Rev. A*, **70**, 053609.
- Schuch, N., Cirac, J. I., and Perez-García, D. (2010). *Ann. Phys. (N.Y.)*, **325**, 2153.
- Schuch, N., Wolf, M. M., Verstraete, F., and Cirac, J. I. (2007). *Phys. Rev. Lett.*, **98**, 140506.
- Schulte, T., Drenkelforth, S., Kruse, J., Ertmer, W., Arlt, J. J., Sacha, K., Zakrzewski, J., and Lewenstein, M. (2005). *Phys. Rev. Lett.*, **95**, 170411.
- Schulte, T., Drenkelforth, S., Kruse, J., Tiemeyer, R., Sacha, K., Zakrzewski, J., Lewenstein, M., Ertmer, W., and Arlt, J. J. (2006). *New J. Phys.*, **8**, 230.
- Schulz, H. J., Ziman, T. A. L., and Poilblanc, D. (1996). *J. Phys. I*, **6**, 675.
- Schulz, H. J. and Ziman, T. A. L. (1992). *Europhys. Lett.*, **18**, 355.
- Schulz, H. (2000). The 3D Yang-Mills system. Lecture notes on the Karabali-Nair theory. arXiv:hep-ph/0008239.
- Schweikhard, V., Coddington, I., Engels, P., Mogendorff, V. P., Cornell, E. A., and Ballagh, R. J. (2004a). *Phys. Rev. Lett.*, **92**, 040404.
- Schweikhard, V., Coddington, I., Engels, P., Tung, S., and Cornell, E. A. (2004b). *Phys. Rev. Lett.*, **93**, 210403.
- Semenoff, G. W. (1984). *Phys. Rev. Lett.*, **53**, 2449.

- Senechal, D., Lavertu, P.-L., Marois, M.-A., and Tremblay, A.-M. S. (2005). *Phys. Rev. Lett.*, **94**, 156404.
- Sengupta, P., Pryadko, L. P., Alet, F., Troyer, M., and Schmid, G. (2005a). *Phys. Rev. Lett.*, **94**, 207202.
- Sengupta, P., Rigol, M., Batrouni, G. G., Denteneer, P. J. H., and Scalettar, R. T. (2005b). *Phys. Rev. Lett.*, **95**, 220402.
- Senthil, T., Vishwanath, A., Balents, L., Sachdev, S., and Fisher, M. P. A. (2004). *Science*, **303**, 1490.
- Sen, S. (1996). *Phys. Rev. Lett.*, **77**, 1.
- Shapere, A. and Wilczek, F. (1989). *Geometric Phases in Physics*. World Scientific, Singapore.
- Shapiro, B. (2007). *Phys. Rev. Lett.*, **99**, 060602.
- Sheehy, D. E. and Radzihovsky, L. (2007a). *Ann. Phys. (N.Y.)*, **322**, 1790.
- Sheehy, D. E. and Radzihovsky, L. (2007b). *Phys. Rev. B*, **75**, 136501.
- Shender, E. F. and Holdsworth, P. C. W. (1994). In *Fluctuations and Order: The New Synthesis* (ed. M. Millonas). MIT Press, New York.
- Sheng, D. N., Trebst, O. I. Motrunich S., Gull, E., and Fisher, M. P. A. (2008). *Phys. Rev. B*, **78**, 54520.
- Shepelyansky, D. L. (1994). *Phys. Rev. Lett.*, **73**, 2607.
- Sherrington, D. and Kirkpatrick, S. (1975). *Phys. Rev. Lett.*, **35**, 1792.
- Sherrington, D. (1998). arXiv:cond-mat/9806289.
- Sherson, J. F., Weitenberg, C., Endres, M., Cheneau, M., Bloch, I., and Kuhr, S. (2010). *Nature*, **467**, 68.
- Sheshadri, K., Krishnamurthy, H. R., Pandit, R., and Ramakrishnan, T. V. (1993). *Europhys. Lett.*, **22**, 257.
- Shiba, H. and Kuramoto, Y. (ed.) (2005). *Kondo Effect – 40 Years after the Discovery*. J. Phys. Soc. Jpn., Vol.74, No.1.
- Shih, C. T., Chen, Y. C., Lin, H. Q., and Lee, T.-K. (1998). *Phys. Rev. Lett.*, **81**, 1294.
- Shih, C. T., Lee, T. K., Eder, R., Mou, C.-Y., and Chen, Y. C. (2004). *Phys. Rev. Lett.*, **92**, 227002.
- Shin, Y., Zwierlein, M. W., Schunck, C. H., Schirotzek, A., and Ketterle, W. (2006). *Phys. Rev. Lett.*, **97**, 030401.
- Shirmai, E. and Lewenstein, M. (2011). *Europhys. Lett.*, **93**, 66005.
- Shor, P. W. (1994). In *Proceedings of 35th Annual Symposium on Foundations of Computer Science*. IEEE Press, Los Alamitos.
- Shor, P. W. (1995). *Phys. Rev. A*, **52**, R2493.
- Sigrist, M. and Rice, T. M. (1995). *Rev. Mod. Phys.*, **67**, 503.
- Simula, T. P., Engels, P., Coddington, I., Schweikhard, V., Cornell, E. A., and Ballagh, R. J. (2005). *Phys. Rev. Lett.*, **94**, 080404.
- Sinatra, A., Lobo, C., and Castin, Y. (2002). *J. Phys. B: At. Mol. Opt. Phys.*, **35**, 3599.
- Sindzingre, P., Lecheminant, P., and Lhuillier, C. (1994). *Phys. Rev. B*, **50**, 3108.
- Singh, A., Ulmke, M., and Vollhardt, D. (1998). *Phys. Rev. B*, **58**, 8683.
- Singh, K. G. and Rokhsar, D. S. (1992). *Phys. Rev. B*, **46**, 3002.
- Singh, K. G. and Rokhsar, D. S. (1994). *Phys. Rev. B*, **49**, 9013.
- Singh, R. R. P. and Huse, D. A. (1992). *Phys. Rev. Lett.*, **68**, 1766.
- Singh, R. R. P. and Narayanan, R. (1990). *Phys. Rev. Lett.*, **65**, 1072.
- Singh, R. R. P., Weihong, Z., Hamer, C. J., and Oitmaa, J. (1999). *Phys. Rev. B*, **60**, 7278.
- Sinova, J., Hanna, C. B., and MacDonald, A. H. (2002). *Phys. Rev. Lett.*, **89**, 030403.
- Skyrme, T. H. R. (1961). *Proc. R. Soc. Lond. A*, **260**, 127.
- Skyrme, T. H. R. (1962). *Nucl. Phys.*, **31**, 556.
- Smerzi, A., Trombettoni, A., Kevrekidis, P. G., and Bishop, A. R. (2002). *Phys. Rev. Lett.*, **89**, 170402.

- Snoek, M., Vandoren, S., and Stoof, H. T. C. (2006). *Phys. Rev. A*, **74**, 033607.
- Soltan-Panahi, P., Struck, J., Hauke, P., Bick, A., Plenkers, W., Meineke, G., Becker, C., Windpassinger, P., Lewenstein, M., and Sengstock, K. (2011). *Nature Phys.*, **7**, 434.
- Sondhi, S. L., Karlhede, A., Kivelson, S. A., and Rezayi, E. H. (1993). *Phys. Rev. B*, **47**, 16419.
- Sorella, S., Martins, G. B., Becca, F., Gazza, C., Capriotti, L., Parola, A., and Dagotto, E. (2002). *Phys. Rev. Lett.*, **88**, 117002.
- Sørensen, A. S., Demler, E., and Lukin, M. D. (2005). *Phys. Rev. Lett.*, **94**, 086803.
- Sørensen, A. S. and Mølmer, K. (1999). *Phys. Rev. Lett.*, **83**, 2274.
- Spalek, J. and Oleś, A. M. (1977). *Physica B*, **86–88**, 375.
- Spalek, J. (2007). *Acta Phys. Polon.*, **111**, 409.
- Srednicki, M. (1993). *Phys. Rev. Lett.*, **71**, 66.
- Stamper-Kurn, D. M., Andrews, M. R., Chikkatur, A. P., Inouye, S., Miesner, H. J., Stenger, J., and Ketterle, W. (1998). *Phys. Rev. Lett.*, **80**, 2027.
- Stamper-Kurn, D. M., Chikkatur, A. P., Görlitz, A., Inouye, S., Gupta, S., Pritchard, D. E., and Ketterle, W. (1999). *Phys. Rev. Lett.*, **83**, 2876.
- Stamper-Kurn, D. M. and Ketterle, W. (2001). *Coherent Atomic Matter Waves, Les Houches Summer School Session LXXII in 1999* (eds. R. Kaiser, C. Westbrook, and F. David). Springer, New York. arXiv:cond-mat/0005001.
- Stasińska, J., Massignan, P., Bishop, M., Wehr, J., Sanpera, A., and Lewenstein, M. (2011). arXiv:1111.3494.
- Steane, A. M. (1996). *Proc. R. Soc. Lond. A*, **452**, 2551.
- Steel, M. J., Olsen, M. K., Plimak, L. I., Drummond, P. D., Tan, S. M., Collett, M. J., Walls, D. F., and Graham, R. (1998). *Phys. Rev. A*, **58**, 4824.
- Stenger, J., Inouye, S., Chikkatur, A. P., Stamper-Kurn, D. M., Pritchard, D. E., and Ketterle, W. (1999). *Phys. Rev. Lett.*, **82**, 4569.
- Stenger, J., Inouye, S., Stamper-Kurn, D. M., Miesner, H. J., Chikkatur, A. P., and Ketterle, W. (1998). *Nature*, **396**, 345.
- Stewart, J. T., Gaebler, J. P., and Jin, D. S. (2008). *Nature*, **454**, 744.
- Stock, S., Battelier, B., Bretin, V., Hadzibabic, Z., and Dalibard, J. (2005). *Laser Phys. Lett.*, **2** (6), 275.
- Stöferle, T., Moritz, H., Günter, K., Köhl, M., and Esslinger, T. (2006). *Phys. Rev. Lett.*, **96**, 030401.
- Stöferle, T., Moritz, H., Schori, Ch., Köhl, M., and Esslinger, T. (2004a). *Phys. Rev. Lett.*, **92**, 130403.
- Stöferle, T., Moritz, H., Schori, Ch., Köhl, M., and Esslinger, T. (2004b). *Phys. Rev. Lett.*, **93**, 240402.
- Stoll, M. and Köhler, T. (2005). *Phys. Rev. A*, **72**, 022714.
- Stone, M. (1992). *Quantum Hall Effect*. World Scientific, London.
- Stoof, H. T. C., Vliegen, E., and Al Khawaja, U. (2001). *Phys. Rev. Lett.*, **87**, 120407.
- Struck, J., Ölschläger, C., Le Targat, R., Soltan-Panahi, P., Eckardt, A., Lewenstein, M., Windpassinger, P., and Sengstock, K. (2011). *Science*, **333**, 996. arXiv:1103.5944.
- Stuhler, J., Griesmaier, A., Koch, T., Fattori, M., Pfau, T., Giovanazzi, S., Pedri, P., and Santos, L. (2005). *Phys. Rev. Lett.*, **95**, 150406.
- Sudarshan, E. C. G. (1963). *Phys. Rev. Lett.*, **10**, 277.
- Sushkov, O. P., Oitmaa, J., and Weihong, Z. (2001). *Phys. Rev. B*, **63**, 104420.
- Sutherland, B. (1975). *Phys. Rev. B*, **12**, 3795.
- Syassen, N., Bauer, D. M., Lettner, M., Volz, T., Dietze, D., García-Ripoll, J. J., Cirac, J. I., Rempe, G., and Dürr, S. (2008). *Science*, **320**, 1329.
- Szirmai, E. and Lewenstein, M. (2011). *Europhys. Lett.*, **93**, 66005.

- Takhtajan, L. A. (1982). *Phys. Lett. A*, **87**, 479.
- Teichmann, N., Hinrichs, D., Holthaus, M., and Eckardt, A. (2009). *Phys. Rev. B.*, **79**, 224515.
- Temme, K., Wolf, M. M., and Verstraete, F. (2009). arXiv:0912.0858.
- Terhal, B. M. (2001). *Lin. Alg. Appl.*, **323**, 61.
- Tewari, S., Das Sarma, S., Nayak, C., Zhang, C. W., and Zoller, P. (2007). *Phys. Rev. Lett.*, **98**, 010506.
- Tewari, S., Scarola, V. W., Senthil, T., and Das Sarma, S. (2006). *Phys. Rev. Lett.*, **97**, 200401.
- Thalhammer, G., Barontini, G., De Sarlo, L., Catani, J., Minardi, F., and Inguscio, M. (2008). *Phys. Rev. Lett.*, **100**, 210402.
- Thalhammer, G., Theis, M., Winkler, K., Grimm, R., and Denschlag, J. H. (2005). *Phys. Rev. A*, **71**, 033403.
- Theis, M., Thalhammer, G., Winkler, K., Hellwig, M., Ruff, G., Grimm, R., and Denschlag, J. H. (2004). *Phys. Rev. Lett.*, **93**, 123001.
- Thouless, D. J. (1974). *Phys. Rep.*, **13C**, 93.
- Thouless, D. J. (1983). *Phys. Rev. B*, **28**, 4272.
- Timmermans, E., Furuya, K., Milonni, P. W., and Kerman, A. K. (2001). *Phys. Lett. A*, **285**, 228.
- Timmermans, E., Tommasini, P., Hussein, M., and Kerman, A. (1999). *Phys. Rep.*, **315**, 199.
- Töke, C. and Jain, J. K. (2006). *Phys. Rev. Lett.*, **96**, 246805.
- Tonks, L. (1936). *Phys. Rev.*, **50**, 955.
- Trefzger, C., Menotti, C., Capogrosso-Sansone, B., and Lewenstein, M. (2011). *J. Phys. B: At. Mol. Opt. Phys.*, **44**, 193001.
- Trefzger, C., Menotti, C., and Lewenstein, M. (2008). *Phys. Rev. A*, **78**, 043604.
- Trefzger, C. and Sengupta, K. (2011). *Phys. Rev. Lett.*, **106**, 095702.
- Trefzger, C. (2010). *Thesis: Ultracold Dipolar Gases*. ICFO – Institute of Photonic Sciences, Barcelona.
- Tremblay, A.-M. S., Kyung, B., and Senecal, D. (2006). *Low Temp. Phys.*, **32**, 424.
- Trivedi, N. and Ceperley, D. M. (1989). *Phys. Rev. B*, **40**, 2737.
- Trombettoni, A. and Smerzi, A. (2001). *Phys. Rev. Lett.*, **86**, 2353.
- Trombettoni, A. and Smerzi, A. (2003). *Phys. Rev. A*, **68**, 023613.
- Trotzky, M. S., Pollet, L., Gerbier, F., Schnorrberger, U., Bloch, I., Prokof'ev, N. V., Svistunov, B., and Troyer, M. (2010). *Nature Phys.*, **6**, 998.
- Trotzky, S., Cheinet, P., Fölling, S., Feld, M., Schnorrberger, U., Rey, A. M., Polkovnikov, A., Demler, E. A., Lukin, M. D., and Bloch, I. (2008). *Science*, **319**, 295.
- Truscott, A. G., Strecker, K. E., McAlexander, W. I., Partridge, G. B., and Hulet, R. G. (2001). *Science*, **291**, 2570.
- Tsomokos, D. I., Hamma, A., Zhang, W., Haas, S., and Fazio, R. (2009). *Phys. Rev. A*, **80**, 060302.
- Tsuchiya, S. and Kurihara, S. (2001). *J. Phys. Soc. Jpn.*, **70**, 1182.
- Tsuchiya, S., Kurihara, S., and Kimura, T. (2004). *Phys. Rev. A*, **70**, 043628.
- Tsunetsugu, H., Sigrist, M., and Ueda, K. (1997). *Rev. Mod. Phys.*, **69**, 809.
- Tsvetkov, A. M. (2003). *Quantum Field Theory in Condensed Matter Physics*. Cambridge University Press, Cambridge.
- Tung, S., Schweikhard, V., and Cornell, E. A. (2006). *Phys. Rev. Lett.*, **97**, 240402.
- Tusch, M. A. and Logan, D. E. (1993). *Phys. Rev. B*, **48**, 14843.
- 't Hooft, G. (1974). *Nucl. Phys. B*, **79**, 276.
- Ueda, M. and Kawaguchi, Y. (2010). arXiv:1001.2072.
- Ueda, M. and Koashi, M. (2002). *Phys. Rev. A*, **65**, 063602.
- Uimin, G. V. (1970). *JETP Lett.*, **12**, 225.
- Ulmke, M., Janiš, V., and Vollhardt, D. (1995). *Phys. Rev. B*, **51**, 10411.
- Umucalilar, R. O., Zhai, H., and Oktel, M. Ö. (2008). *Phys. Rev. Lett.*, **100**, 070402.

- Urban, E., Johnson, T. A., Henage, T., Isenhower, L., Yavuz, D. D., Walker, T. G., and Saffman, M. (2009). *Nature Phys.*, **5**, 110.
- Vaidya, H. G. and Tracy, C. A. (1979). *Phys. Rev. Lett.*, **42**, 3.
- Van den Nest, M., Dür, W., Miyake, A., and Briegel, H. J. (2007). *New J. Phys.*, **9**, 204.
- van Enter, A. C. D. and van Hemmen, J. L. (1983). *J. Stat. Phys.*, **32**, 141.
- van Enter, A. C. D. and van Hemmen, J. L. (1984). *Phys. Rev. A*, **29**, 355.
- van Oosten, D., van der Straten, P., and Stoof, H. T. C. (2001). *Phys. Rev. A*, **63**, 053601.
- Veillette, M. Y., Sheehy, D. E., and Radzihovsky, L. (2007). *Phys. Rev. A*, **75**, 043614.
- Veillette, M., Moon, E. G., Lamacraft, A., Radzihovsky, L., Sachdev, S., and Sheehy, D. E. (2008). *Phys. Rev. A*, **78**, 033614.
- Venkatesh, B. P., Trupke, M., Hinds, E. A., and O'Dell, D. H. J. (2009). *Phys. Rev. A*, **80**, 063834.
- Verstraete, F., Cirac, J. I., and Murg, V. (2008). *Adv. Phys.*, **57**, 143.
- Verstraete, F. and Cirac, J. I. (2004). arXiv:cond-mat/0407066.
- Verstraete, F. and Cirac, J. I. (2005). *J. Stat. Mech.*, P09012.
- Verstraete, F. and Cirac, J. I. (2006). *Phys. Rev. B*, **73**, 094423.
- Verstraete, F., Martin-Delgado, M. A., and Cirac, J. I. (2004a). *Phys. Rev. Lett.*, **92**, 087201.
- Verstraete, F., Popp, M., and Cirac, J. I. (2004b). *Phys. Rev. Lett.*, **92**, 027901.
- Verstraete, F., Porras, D., and Cirac, J. I. (2004c). *Phys. Rev. Lett.*, **93**, 227205.
- Verstraete, F., Wolf, M. M., Pérez-García, D., and Cirac, J. I. (2006). *Phys. Rev. Lett.*, **96**, 220601.
- Vidal, G., Latorre, J. I., Rico, E., and Kitaev, A. (2003). *Phys. Rev. Lett.*, **90**, 227902.
- Vidal, G. and Werner, R. F. (2002). *Phys. Rev. A*, **65**, 032314.
- Vidal, G. (2003). *Phys. Rev. Lett.*, **91**, 147902.
- Vidal, G. (2007a). *Phys. Rev. Lett.*, **98**, 070201.
- Vidal, G. (2007b). *Phys. Rev. Lett.*, **99**, 220405.
- Vidal, G. (2008). *Phys. Rev. Lett.*, **101**, 110501.
- Vidal, G. (2010). *Understanding Quantum Phase Transitions* (ed. L. D. Carr). Taylor and Francis, Boca Raton. arXiv:0912:1651.
- Villain, J., Bidaux, R., Carton, J. P., and Conte, R. J. (1980). *J. Phys. (Paris)*, **41**, 1263.
- Vogt, T., Viteau, M., Zhao, J. M., Chotia, A., Comparat, D., and Pillet, P. (2006). *Phys. Rev. Lett.*, **97**, 083003.
- Volz, T., Syassen, N., Bauer, D. M., Hansis, E., Dürr, S., and Rempe, G. (2006). *Nature Phys.*, **2**, 692.
- von Oppen, F., Wettig, T., and Müller, J. (1996). *Phys. Rev. Lett.*, **76**, 491.
- Waintal, X., Benenti, G., and Pichard, J.-L. (2000). *Europhys. Lett.*, **49**, 466.
- Walldtmann, C., Everts, H.-U., Bernu, B., Lhuillier, C., Sindzingre, P., Lecheminant, P., and Pierre, L. (1998). *Eur. Phys. J. B*, **2**, 501.
- Wallin, M., Sørensen, E. S., Girvin, S. M., and Young, A. P. (1994). *Phys. Rev. B*, **49**, 12115.
- Walls, D. F. and Milburn, G. J. (2006). *Quantum Optics*. Springer, Berlin.
- Wegner, F. J. (1976). *Z. Phys.*, **25**, 327.
- Wehr, J., Niederberger, A., Sanchez-Palencia, L., and Lewenstein, M. (2006). *Phys. Rev. B*, **74**, 224448.
- Weidemüller, M., Hemmerich, A., Görlitz, A., Esslinger, T., and Hänsch, T. W. (1995). *Phys. Rev. Lett.*, **75**, 4583.
- Weimer, H., Müller, M., Lesanovsky, I., Zoller, P., and Büchler, H. P. (2010). *Nature Phys.*, **6**, 382.
- Weinmann, D., Müller-Groeling, A., Pichard, J. L., and Frahm, K. (1995). *Phys. Rev. Lett.*, **75**, 1598.
- Weisse, A. and Fehske, H. (2008). *Lecture Notes in Physics*, **739**, 529.
- Wen, X.-G. and Lee, P. A. (1996). *Phys. Rev. Lett.*, **76**, 503.
- Wen, X.-G., Wilczek, F., and Zee, A. (1989). *Phys. Rev. B*, **39**, 11413.

- Wen, X.-G. (2004). *Quantum Field Theory of Many-body Systems*. Oxford University Press, Oxford.
- Werner, F., Parcollet, O., Georges, A., and Hassan, S. R. (2005). *Phys. Rev. Lett.*, **95**, 056401.
- Werner, R. F. (1989). *Phys. Rev. A*, **40**, 4277.
- Wessel, S., Alet, F., Troyer, M., and Batrouni, G. G. (2004). *Phys. Rev. A*, **70**, 053615.
- White, M., Pasienski, M., McKay, D., Zhou, S. Q., Ceperley, D., and DeMarco, B. (2009). *Phys. Rev. Lett.*, **102**, 055301.
- White, S. R. and Scalapino, D. J. (1999). *Phys. Rev. B*, **60**, R753.
- White, S. R. (1992). *Phys. Rev. Lett.*, **69**, 2863.
- White, S. R. (1998). *Phys. Rep.*, **301**, 187.
- Widera, A., Gerbier, F., Fölling, S., Gericke, T., Mandel, O., and Bloch, I. (2005). *Phys. Rev. Lett.*, **95**, 190405.
- Wigner, E. P. (1931). *Gruppentheorie und ihre Anwendung auf die Quantenmechanik der Atomspektren*. F. Vieweg und Sohn, Braunschweig. English translation (1959): *Group Theory and its Application to the Quantum Mechanics of Atomic Spectra (expanded and improved edition)*. Academic Press, New York.
- Wigner, E. P. (1932). *Phys. Rev.*, **40**, 749.
- Wilczek, F. and Zee, A. (1984). *Phys. Rev. Lett.*, **52**, 2111.
- Wilczek, F. (1982a). *Phys. Rev. Lett.*, **48**, 1144.
- Wilczek, F. (1982b). *Phys. Rev. Lett.*, **48**, 1146.
- Wilkin, N. K., Gunn, J. M. F., and Smith, R. A. (1998). *Phys. Rev. Lett.*, **80**, 2265.
- Wilkin, N. K. and Gunn, J. M. F. (2000). *Phys. Rev. Lett.*, **84**, 6.
- Wilson, K. G. (1970a). *Phys. Rev. D*, **2**, 1438.
- Wilson, K. G. (1970b). *Phys. Rev. D*, **2**, 1473.
- Wilson, K. G. (1970c). *Phys. Rev. D*, **2**, 1478.
- Wilson, K. G. (1975). *Rev. Mod. Phys.*, **47**, 773.
- Winkler, K., Thalhammer, G., Lang, F., Grimm, R., Denschlag, J. H., Daley, A. J., Kantian, A., Büchler, H.-P., and Zoller, P. (2006). *Nature*, **441**, 853.
- Wirth, G., Ölschlägel, M., and Hemmerich, A. (2010). *Nature Phys.*, **7**, 147.
- Wolf, M. M., Ortiz, G., Verstraete, F., and Cirac, J. I. (2006). *Phys. Rev. Lett.*, **97**, 110403.
- Wolf, M. M., Verstraete, F., Hastings, M. B., and Cirac, J. I. (2008). *Phys. Rev. Lett.*, **100**, 070502.
- Wolf, M. M. (2006). *Phys. Rev. Lett.*, **96**, 010404.
- Wootters, W. K. (1998). *Phys. Rev. Lett.*, **80**, 2245.
- Woronowicz, S. L. (1976). *Comm. Math. Phys.*, **51**, 243.
- Wright, E. M., Walls, D. F., and Garrison, J. C. (1996). *Phys. Rev. Lett.*, **77**, 2158.
- Wunderlich, C. and Balzer, C. (2003). *Adv. Atom. Mol. Phys.*, **49**, 295.
- Wunderlich, C. (2002). In *Laser Physics at the Limit*, p. 261. Springer Verlag, Heidelberg. arXiv:quant-ph/0111158.
- Würtz, P., Langen, T., Gericke, T., Koglbauer, A., and Ott, H. (2009). *Phys. Rev. Lett.*, **103**, 080404.
- Wu, C. (2005). *Phys. Rev. Lett.*, **95**, 266404.
- Wu, C. (2006). *Mod. Phys. Lett. B*, **20**, 1707.
- Wu, J. S. and Phillips, P. (2008). *Phys. Rev. B*, **78**, 014515.
- Wu, Y. (1996). *Phys. Rev. A*, **54**, 4534.
- Yang, C. N. and Yang, C. P. (1966a). *Phys. Rev.*, **150**, 321.
- Yang, C. N. and Yang, C. P. (1966b). *Phys. Rev.*, **150**, 327.
- Yannouleas, C. and Landman, U. (2004). *Phys. Rev. B*, **70**, 235319.
- Yan, S., Huse, D. A., and White, S. R. (2011). *Science*, **332**, 1173. arXiv:1011.6114.
- Yavuz, D. D., Kulatunga, P. B., Urban, E., Johnson, T. A., Proite, N., Henage, T., Walker, T. G., and Saffman, M. (2006). *Phys. Rev. Lett.*, **96**, 063001.
- Yip, S.-K. (1999). *Phys. Rev. Lett.*, **83**, 4677.

- Yip, S.-K. (2003a). *Phys. Rev. Lett.*, **90**, 250402.
Yip, S.-K. (2003b). *J. Phys.: Condens. Matter*, **15**, 4583.
Yi, S. and You, L. (2000). *Phys. Rev. A*, **61**, 041604.
Yi, S. and You, L. (2001). *Phys. Rev. A*, **63**, 053607.
Young, A. P. and Katzgraber, H. G. (2004). *Phys. Rev. Lett.*, **93**, 207203.
Zakrzewski, J. (2005). *Phys. Rev. A*, **71**, 043601.
Zanardi, P. and Wang, X. (2002). *J. Phys. A: Math. Theor.*, **35**, 7947.
Zanardi, P. (2002). *Phys. Rev. A*, **65**, 042101.
Zenesini, A., Lignier, H., Ciampini, D., Morsch, O., and Arimondo, E. (2009). *Phys. Rev. Lett.*, **102**, 100403.
Zeng, C. and Elser, V. (1990). *Phys. Rev. B*, **42**, 8436.
Zeng, C. and Elser, V. (1995). *Phys. Rev. B*, **51**, 8318.
Zhang, F. C., Gros, C., Rice, T. M., and Shiba, H. (1988). *Supercond. Sci. Tech.*, **1**, 36.
Zhang, L. and Ma, M. (1992). *Phys. Rev. B*, **45**, 4855.
Zhang, L. and Wang, X.-Q. (1993). *Phys. Rev. B*, **47**, 11518.
Zhang, L. (1993). *Phys. Rev. B*, **47**, 14364.
Zhang, Y. B., Tan, Y. W., Störmer, H. L., and Kim, P. (2005). *Nature*, **438**, 201.
Zhou, F. and Semenoff, G. W. (2006). *Phys. Rev. Lett.*, **97**, 180111.
Zhu, S.-L., Wang, B. G., and Duan, L.-M. (2007). *Phys. Rev. Lett.*, **98**, 260402.
Ziegler, K. (2006). *Laser Phys.*, **16**, 699.
Zoller, P., Beth, T., Binosi, D., Blatt, R., Briegel, H., Bruss, D., Calarco, T., Cirac, J. I., Deutsch, D., Eisert, J., Ekert, A., Fabre, C., Gisin, N., Grangier, P., Grassl, M., Haroche, S., Imamoglu, A., Karlson, A., Kempe, J., Kouwenhoven, L., Kröll, S., Leuchs, G., Lewenstein, M., Loss, D., Lütkenhaus, N., Massar, S., Mooij, J. E., Plenio, M. B., Polzik, E., Popescu, S., Rempe, G., Sergienko, A., Suter, D., Twamley, J., Wendin, G., Werner, R., Winter, A., Wrachtrup, J., and Zeilinger, A. (2005a). *Eur. Phys. J. D*, **36**, 203.
Zoller, P., Büchler, H. P., and Bloch, I. (2005b). private communication.
Żukowski, M., Zeilinger, A., Horne, M. A., and Ekert, A. (1993). *Phys. Rev. Lett.*, **71**, 4287.
Żurek, W. H. (1985). *Nature*, **317**, 505.
Zwerger, W. (2003). *J. Opt. B*, **5**, S9.
Zwierlein, M. W., Schirotzek, A., Schunck, C. H., and Ketterle, W. (2006). *Science*, **311**, 492.
Zwierlein, M. W., Stan, C. A., Schunck, C. H., Raupach, S. M. F., Kerman, A. J., and Ketterle, W. (2004). *Phys. Rev. Lett.*, **92**, 120403.
Życzkowski, K., Horodecki, P., Sanpera, A., and Lewenstein, M. (1998). *Phys. Rev. A*, **58**, 883.

Index

- absorption imaging, 415
Affleck–Kennedy–Lieb–Tasaki (AKLT)
Hamiltonian, 143, 374
model, 361, 379
state, 266
valence bond solid, 358
Aharonov–Bohm effect, 307, 308
Almeida–Thouless plane, 254
Anderson
glass, 6
Hamiltonian, 247
localization, 6, 7, 207, 208, 210
model, 209
anyons
excitations, 203
fractional statistics, 398
fusion rules, 399
interferometry, 399
non-Abelian, 323, 399, 402
p-wave superfluidity, 406
area law
1D systems, 367
classical Gibbs states, 370
classical systems, 369
critical systems, 368
generic, 51, 90, 363, 366, 372
quantum thermal states at $T > 0$
 $(\beta < \infty)$, 371
simulability, 90
ARPES (angle-resolved photoemission spectroscopy), 413
artificial gauge fields
Abelian, 293, 310
basic concepts, 10, 293
for neutral atoms, 312
gauge symmetry, 304
generation of, 328
laser-induced, 9, 335
new trends, 435
non-Abelian, 314, 435
electromagnetically induced transparency, 331
 $SU(2)$, 117
 $SU(N)$, 294
rotating traps, 334
rotating ultracold gas, 9, 329
tunneling control, 9
- Baker–Hausdorff formula, 119
band structure, 41
Bardeen–Cooper–Schrieffer (BCS)
equations, 181
- finite T, 105
gap equation, 100
theory, 1, 98, 99, 103
transition, 8
wave function, 112
BCS–BEC
crossover, 1, 8, 106, 433
balanced, 101
imbalanced, 106
Berezinskii–Kosterlitz–Thouless (BKT)
phase, 22
transition, 19, 34
Bernoulli
potential, 209, 237
Berry phase, 331, 399
Bethe ansatz, 5, 87, 111
bilinear biquadratic Hamiltonian, 58, 141
Bloch
functions, 41, 53
oscillations, 44, 46
theorem, 41
wall, 211
Bogoliubov
approach, 60, 62, 281
modes, 421
spectrum, 173
Bogoliubov–de Gennes (BdG)
approach, 3, 26, 98
equations, 32, 179, 407
fermions, 100
finite T approach, 33
non-local approach, 178
quasiparticles, 24
time dependent method, 64
transformation, 63
Bose systems
2D interacting gas, 437
Bose glass, 6, 218, 240, 435
Bose metal, 111, 437
dipolar, 187
hard-core limit, 29, 57, 84, 197, 222
ideal gas, 437
spinor, 58
spinors in optical lattices, 137
Bose–Bose mixtures, 4, 248
Bose–Einstein condensation (BEC)
alkalines, 1, 3
box, 21
depletion, 437
dipolar, 10, 166
disordered systems, 228
interacting systems, 24

- Bose–Einstein condensation (BEC) (*cont.*)
 mean-field spinor phases, 128
 molecules, 8
 non-interacting systems, 21
 optical lattices, 45
 photons, 432
 topological defects, 133
 trap, 22
 unconventional, 429
 Bose–Einstein statistics, 22, 64
 Bose–Fermi mixtures
 composite fermions, 121, 122
 disordered Hamiltonian, 248
 model, 4, 7, 8, 101, 102, 121, 181,
 248, 406
 Bose–Hubbard model, 50, 60–62, 67, 75, 84
 bosonic dynamical mean-field theory (BDMFT),
 433
 bosonic pair creation operator, 100
 bosonization, 5, 29, 87, 111
 Bragg scattering, 418
 bunching and antibunching effect, 418
- CATons, 433
 cavity electrodynamics QED, 431
 charge ordering, 428
 chemical potential, 56
 Chern number, 320
 chirality, 58
 chirality factor, 408
 classical
 field method, 83
 kinetic models, 382
 phase transitions, 13
 simulator, 52
 spin models, 14
 coherent momentum transfer mapping
 (CMTM), 421
 coherent on-site transitions, 56
 collective modes, 412
 collisions
 binary elastic, 45
 control, 6, 396
 instability, 406
 light-assisted, 423
 quantum information, 388
 spin relaxation, 126
 two-body short-range, 126
 computational basis, 386
 confinement–deconfinement transitions, 432
 conformal field theory (CFT), 5, 358, 369
 cooling
 evaporative, 3
 laser, 3
 Cooper pair, 8, 100, 111, 438
 correlation
 $g^{(2)}$ function, 418
 1D systems, 5
 density–density, 413, 417
 first-order, 413, 415
 in momentum, 417
 length, 15
 one-particle, 413
 second-order, 413, 417
 spin–spin, 413
 two-point, 28, 426
 Coulomb
 crystal, 4, 11
 interactions, 11
 counterflow superfluidity, 121
 critical dimension
 lower, 19
 upper, 18
 crystal order, 167, 203
- d*-wave
 Bose metal, 438
 pairing, 113, 116
 superconductivity, 110, 116
 de Broglie wavelength, 21
 degenerate perturbation theory, 119
 density matrix renormalization group (DMRG), 5,
 51, 89, 113, 435, 438
 density of states (DOS), 22
 detection
 Bragg scattering, 418
 density distribution, 200
 noise correlations, 417
 optical Bragg diffraction, 421
 particle–particle correlations, 200
 quantum polarization spectroscopy (QPS), 424
 single-atom resolution, 423
 ultracold quantum systems, 412
 Deutsch–Jozsa algorithm, 384
 devil’s staircase, 198
 Dicke super-radiant phase transition, 431
 diffeomorphisms, 399
 differential scattering cross-section, 422
 dimensional ϵ expansions, 106
 dipolar gases
 quantum Monte Carlo (QMC) methods, 196
 dipolar systems
 action and tunneling time, 196
 anisotropic interactions, 166, 167
 basic concepts, 10, 165
 BEC, 10
 bosons, 10, 171, 182, 187, 197
 bouncing point, 196
 crystallization, 202
 dipole phases, 198, 201
 dipole–dipole interactions, 287
 excitations, 173
 fermions, 8, 181
 geometrical stabilization, 174
 ground state, 173
 Hamiltonian, 182
 interactions, 11, 196
 metastable states, 191
 new trends, 432
 quantum phases, 197
 rotating, 330
 self-assembled structures, 203

- ultracold gases, 169
 - with ultracold atoms, 434
- dipole
 - electric moment, 167
 - light-induced, 170
 - magnetic moment, 167, 171
- Dirac
 - dispersion relation, 435
 - equation, 408
 - fermions, 316, 318
 - relativistic massless fermion, 117
- dirty
 - bosons, 218, 434
 - superconductors, 6
- disordered systems
 - Anderson localization, 228
 - basic concepts, 205
 - BEC, 228
 - Bernoulli potentials, 237
 - Bose–Fermi mixtures, 248
 - bosons, 4
 - correlation length, 232
 - critical temperature, 58
 - disorder-induced order (DIO), 258
 - fermions, 246
 - interplay localization-interactions, 6
 - quantum computation, 410
 - spin glass, 7
 - stochastic approach, 243
 - ultracold atoms, 434
 - ultracold gases, 224
- dissipative
 - open system, 431
 - processes, 5
- DiVincenzo criteria, 385
- droplet model, 7
- dynamical phase transitions, 431
- effective mass, 44
- effective mobility edge, 6
- Efimov effects, 10, 434
- electronic conductivity, 213
- energy functional, 174
- entanglement
 - bound, 345
 - concurrence, 355
 - criteria, 343
 - ebit, 354
 - entropy, 358, 435
 - formation, 354
 - length, 361
 - localizable (LE), 358
 - logarithmic negativity, 355
 - majorization criterion, 345
 - measures, 354
 - of assistance, 359
 - positive partial transposition (PPT), 344
 - scaling, 356
 - short correlations, 51
 - spectrum, 435
 - witness, 346, 347
- entropy
 - Bekenstein–Hawking, 363
 - block, 369
 - control, 58
 - Rényi, 368, 378
 - Shannon, 369, 371
 - von Neumann, 345, 371
- exact diagonalization, 72
- excitation blockade, 170
- Falicov–Kimball model, 110
- Faraday effect, 424
- Fermi systems
 - 2D exotic metal, 111
 - antiferromagnetism, 57
 - asymmetric model, 110
 - band insulator, 101, 418
 - BCS theory, 98
 - degenerated gas, 1
 - dipolar gas, 8
 - disorder, 246
 - exotic superfluids, 181, 434
 - Fermi liquid metal, 436
 - Fermi liquid phase, 98, 116
 - fermionic flavor, 103, 106
 - Feshbach resonances, 101
 - free Fermi-liquid, 436
 - frustrated gas, 51
 - glass, 216, 217, 249
 - Hartree–Fock theory, 98
 - imbalanced two-component gas, 109
 - kagomé lattice, 275
 - Landau–Fermi liquid theory, 98, 216
 - non-Fermi-liquid metal, 437
 - polarized gas, 7, 101
 - polarons, 432
 - quasi-Majorana fermion excitation, 408
 - resonant superfluidity theory, 101
 - spin- $\frac{3}{2}$ gas, 160
 - spinor gas, 156
 - strong coupling expansion, 98
 - strongly interacting, 434
 - superfluidity, 1
 - unitarity limit, 105
 - unpolarized gas, 7, 57
 - weakly interacting gas, 98
- Fermi–Hubbard model, 60, 98, 99, 406, 433
- fermionization, 29
- ferromagnetism
 - non-equilibrium, 430
 - unconventional, 429
- Feshbach resonances, 3, 8, 10, 101, 165, 166, 434
- Feynman's path integral, 24, 76
- Floquet Hamiltonian, 431
- fluctuations
 - of the phase in quasi-1D BEC, 82
 - phase, 25, 27, 32
 - quantum, 5, 23, 25
 - thermal, 13
- Fourier transform, 168

- fractional quantum Hall effect (FQHE), 9, 266, 267, 293, 322, 330, 331, 406
 fragmentons, 433
 free-particle spectrum, 180
 frustrated systems
 basic concepts, 264
 classical, 264
 geometrical, 264
 lattice topologies, 202
 polar molecules, 286
 quantum antiferromagnets, 8, 264, 270, 271, 279
 sign problem, 75
 spin liquids, 8
 ultracold atoms, 435
 Fulde–Ferrell–Larkin–Ovchinnikov (FFLO)
 pairing state, 429
 phase, 106, 109, 434
 state, 8, 107
 functional-integral formulation, 114
 Furstenberg theorem, 210

 gate
 Boolean operation, 386
 controlled-NOT (CNOT), 387
 Hadamard, 387
 logical operation, 386
 one-qubit, 387
 square root of SWAP, 392
 SWAP, 388, 392
 two-qubit, 387
 unitary phase, 388
 universal, 385, 387
 gauge fields
 Abelian, 304, 306
 classical, 304
 in a lattice, 115
 invariance, 305
 non-Abelian, 305, 307, 308
 SU(N), 339
 Gibbs–Boltzmann state, 430
 Glauber’s model, 382
 graph states, 395
 Green function, 28, 197
 Green’s function, 415
 Greenberger–Horne–Zeilinge (GHZ)
 states, 380
 Gross–Pitaevskii equation (GPE)
 rotating gas, 294
 stationary, 24
 time evolution, 46
 time-dependent, 25
 weakly interacting regime, 228
 Gutzwiller
 ansatz, 98, 244
 dynamical mean-field, 70
 mean-field approach, 69, 184
 projective method, 112

 Haar measure, 364
 Hahn–Banach theorem, 346

 Haldane
 conjecture, 9, 271
 phase, 143, 203, 435
 Hall conductivity, 320
 Hanbury Brown and Twiss effect, 418
 hard-core bosons, 29, 57, 84, 222
 Harper equation, 311, 314
 Hartree–Bose multi-configurational method, 433
 Hartree–Fock (HF)
 mean-field theory, 98, 99
 multi-orbital, 239
 wave function, 112
 Hastings’ theorem, 94
 heavy fermion compounds, 113
 Hebb’s learning rule, 410
 Heisenberg
 $J_1 - J_2$ model, 272, 379
 antiferromagnetic model, 112, 267, 271, 435
 exchange term, 114
 ferromagnetic model, 271
 generalized Hamiltonian, 9
 model, 14, 19, 57, 58, 87, 112, 141, 211, 212, 270, 273, 274, 285
 point, 144
 superexchange interactions, 397
 Higgs
 mechanism, 431
 mode, 421
 high T_c superconductivity, 7, 8, 52, 109, 110
 high-resolution fluorescence imaging, 423
 Hofstadter spectrum, 311, 315
 hole doping, 110, 117
 holographic masks, 432
 holographic principle, 363
 Hopfield model, 409, 410
 hopping
 laser-assisted, 54
 Hubbard model
 Anderson disordered, 216
 asymmetric Fermi systems, 110
 basic concepts, 6, 53
 Bose ring-exchange, 438
 Bose systems, 50, 60, 61, 67, 151, 197, 243
 Bose–Fermi systems, 98, 121
 disordered Fermi systems, 246
 effective Hamiltonians, 118
 extended, 10, 55
 extended dipolar, 182
 Fermi systems, 60, 98, 99, 406, 433, 438
 Fermi–Bose systems, 433
 spin models, 56
 spin- $\frac{1}{2}$ fermions, 109
 spin-1, 138
 spinless bosons, 57
 SU(N), 156
 SU(N) symmetric, 111
 Hubbard–Stratonovich (HS) transformation, 114, 256
 hydrodynamic approach, 26, 32, 173

- Imry–Ma argument, 211
infrared fixed point, 16
instanton theory, 191
integer quantum Hall effect (IQHE), 293, 294, 316, 319, 331
interactions
 boson mediated, 7, 181
 contact, 54
 cooling, 57
 Coulomb, 11
 dipolar, 11
 dipolar anisotropic, 166, 167
 dipole–dipole, 54, 165, 167, 287
 exchange, 6, 39
 hopping-assisted, 55
 long-range, 54, 167
 phonon-mediated, 203
 ring exchange, 10, 111
 short-range, 54, 165
 superexchange, 6, 7, 57, 397
ions, 432
Ising model
 classical ϕ^4 models, 19
 critical, 369
 domain wall, 211
 in 2D, 16, 19
 in random fields, 7, 259
 in transverse field, 15, 23
 kinetic, 382
 properties, 381
 spin glass, 7
 with discrete Z_2 symmetry, 14
 $J - K$ boson model, 438
Jamiolkowski isomorphism, 352
Jaynes–Cumming model, 321
Jordan–Wigner transformation, 23, 57–59, 84, 98, 221, 222
Josephson junctions, 47
Kato expansion, 65
Kepler radius, 170
Kibble–Żurek mechanism, 64, 430
kicked rotor model, 230
Kitaev
 honeycomb code, 286, 400, 402
 toric code, 328, 400
Klein–Gordon equation, 363
Kondo effect, 5, 113, 247
Kosterlitz–Thouless–Berezinskii (KTB) transition, 5, 200, 433
Lagrange multipliers, 193
Lanczos algorithm, 74
Landau
 Fermi liquid theory, 98, 216
 Hamiltonian, 295
 level filling factor, 330
 levels, 295, 322, 330
 Landau–Ginsburg mean-field theory, 18
Landau–Ginsburg–Wilson energy functional, 19
Landau–Zener tunneling, 44, 46
Laplace’s saddle point method, 20
lattice
 d -dimensional hypercubic, 19
 2D dimerized, 58
 Abrikosov, 329
 acceleration, 290
 bipartite, 266, 271
 geometry, 9, 283
 hexagonal, 432
 kagomé, 8, 273, 275, 283
 kagomé trimerized, 58
 of square plaquettes, 432
 orbital, 428
 polymerized, 58
 square quadrumerized, 58
 superlattice, 283
 triangular, 8, 10, 432
 vortex, 10
lattice gauge theories (LGT), 9, 10, 12, 326, 432
Laughlin
 liquid, 10
 state, 10, 297, 299, 322, 406
length
 correlation, 15, 361
 dipolar, 169
 disorder correlation, 232
 entanglement, 361
 harmonic oscillator, 174
 healing, 33, 34, 233
 participation, 234
 phase coherence, 29
 scattering, 172
Lieb–Robinson bound, 368
Lifshits
 glass, 7, 231, 237
 tail, 7
 tails, 231
linear response, 413, 421
liquid crystals, 166
local density approximation, 202
low-dimensional systems
 1D
 analytic methods, 84
 Luttinger liquid, 29
 MPS representation, 378
 phase fluctuations, 27
 quantum fluctuations, 5
 renormalization approaches, 89
 Tonks–Girardeau, 29
 2D
 continuous symmetry, 5
 phase fluctuations, 32
 renormalization approach, 94
Luttinger
 liquid, 5, 29, 87, 437
 model, 86
 parameter, 5, 27
 theorem, 436

- Majorana
 excitations, 406
 fermions, 403, 406
 representation, 403
- Majumdar–Gosh model, 379
- map
 completely positive, 350
 linear, 350
 positive, 349, 351
- Mathieu equation, 42
- matrix product states (MPS), 51, 90, 375, 377, 379, 380, 433
- Matsubara Green functions, 80
- mean-field theory
 BCS–BEC, 106
 dynamical (DMFT), 217
 dynamical cluster, 113
 exotic fermionic phases, 160
 Gutzwiller approach, 69, 149, 184
 Mézard–Parisi, 252
 of slave-boson model, 116
 perturbative approach, 68, 185
 SF–MI transition, 146
 stochastic, 243
- Melik–Bakhudarov corrections, 105
- Mermin–Wagner–Hohenberg theorem, 5, 19
- mobility edge, 209, 215
- molecules
 frustrated models, 286
 polar, 8, 166, 170, 202, 434
 supersolid phase, 434
- Mott insulator (MI)
 solid lobes, 198
 basic concepts, 417
 bosons, 418
 Fermi–Bose mixtures, 122
 fermions, 4, 7, 110, 112
 lobes, 61, 197
 molecular, 10
 molecules, 4
 stability, 188
- multiscale entanglement renormalization ansatz (MERA), 95, 433
- mutual information, 369
- Néel order, 8, 113, 266, 422
- Nambu–Goldstone mode, 24, 25
- Nernst effect, 110
- neural network models, 409
- one-body density matrix, 415
- operator
 linear, 347
 plaquette, 400
 star, 400
- optical Bragg diffraction, 421
- optical lattices
 basic concepts, 36, 37
 cubic, 53
 geometry, 39
- spin-dependent, 40
- superlattice, 6, 39
- orbital lattices
 ferroelectricity, 428
 magneto-resistance, 428
 unconventional superconductivity, 428
- order parameter
 algebraic decay, 270
 basic concepts, 13, 412
 BCS, 116
 BEC, 34, 47
 bond, 161
 dimer phase, 142
 magnetization, 14
 spin-glass, 251
 spinor gas, 130
 superfluid, 68, 70, 146
 topological phases, 266
- p*-wave
 pairing, 181
 superconductivity, 406
 superfluidity, 406
- pair correlation operator, 298
- Parisi–Mézard model, 253
- particle–hole (P–H)
 exchange, 196
 excitations, 188, 197
 transformation, 117
- path integral
 approach, 26
 imaginary time, 191
- Pauli exclusion principle, 110
- Pfaffian state, 202
- phase-space methods, 81
- phonon
 instability, 173, 180
 ions, 4
 mediated interactions, 203
 optical lattices, 39, 53
 spectrum, 180
- photoassociation, 10, 166
- plaquettes, 59
- polarons, 432
- potential
 Bernoulli, 209, 237
 dipole, 36
 geometric light, 335
 speckle, 6
 zero-range pseudo-potentials, 54
- projected entangled pair states (PEPS), 51, 94, 433
- quantum antiferromagnets
 super-exchange interactions, 284
- quantum circuit model, 385
- quantum computation
 cluster states, 380, 385, 394
 decoherence-free schemes, 396
 disordered systems, 410
 error-resistant, 411

- fault-tolerant method, 385
 ions proposal, 3, 4
 measurement-based, 385
 one-way quantum computer, 285, 385, 394
 quantum circuit model, 386
 topological, 8, 286, 385, 398
 topological braiding group, 398
 topological excitations, 401
 topological fusion rules, 398, 399
 topological stabilizers, 401
 quantum correlations, 3, 359
 quantum dynamics, 429, 430
 quantum field theory (QFT), 19, 24, 83, 99
 quantum information
 adiabatic processing, 4
 basic concepts, 340, 341
 decoherence, 385
 decoherence time, 394
 distributed, 409
 DMRG, 89
 lattice gases, 384
 majorization criterion, 345
 quantum phase transition (QPT), 355
 separability, 342
 quantum interface, 424
 quantum inverse scattering theory, 5
 quantum melting, 10
 quantum metrology, 436
 quantum Monte Carlo (QMC)
 basic concepts, 51
 diagrammatic, 433
 dipolar gases, 196
 kinks, 80
 method, 75, 98, 106
 path integral, 75, 196
 sign problem, 75
 world line, 78
 worm algorithm, 80, 196, 199
 quantum neural networks, 4, 410
 quantum phase transitions (QPT)
 critical exponents, 15, 67
 criticality, 15
 entanglement, 355
 first order, 203
 quantum fluctuations, 23
 scaling behavior, 15
 scaling theory, 21
 second order, 13
 universality, 16, 52
 universality classes, 20
 quantum phases
 checkerboard (CB), 10, 190, 191, 198, 199, 249
 delocalized metallic, 6
 emulsion, 196
 Haldane, 143
 non-Abelian topological, 202
 normal (Fermi liquid), 101, 109, 111
 paired superfluid, 111
 pseudogap metallic state, 110
 separation, 109
 spin gap, 116
 star solid (SR), 198, 202
 stripe (ST), 198, 201, 429
 superfluid (SF), 101, 109, 196, 199
 supersolid (SS), 10, 167, 181, 190, 191,
 197–199, 201
 valence-bond crystal (VBC), 266
 valence-bond solids (VBS), 8, 266
 quantum polarization spectroscopy (QPS), 424
 quantum pressure effects, 178
 quantum register, 386
 quantum simulator
 antiferromagnetism, 431
 basic concepts, 3, 51, 384
 definition, 52
 fermionic atoms, 7
 ion systems, 4
 spin models, 287
 quantum spin-liquid crystal, 8, 269
 qubit
 control, 387
 definition, 386
 error-resistant encoding, 203
 spatially delocalized, 57
 supercoherent, 397
 target, 387
 real-space renormalization group (RG), 16,
 20, 89
 renormalization approach
 2D, 94
 replica symmetry breaking picture, 7
 replica trick, 255
 resonating valence-bond (RVB) states, 8, 406
 retardation effects, 170
 ring-exchange models, 202
 roton
 basic concept, 180
 gap, 180
 instability, 180
 roton–maxon spectrum, 178
 Rydberg
 atoms, 170, 432, 434
 blockade, 438
s-wave scattering, 165
 saddle-point method, 115
 scaling theory of localization, 214
 scattering length, 172
 Schmidt
 decomposition, 90, 91, 341
 rank, 91, 97
 Schrödinger equation
 discrete non-linear, 47
 Schur complement, 360
 self-annealing, 201
 SF-MI phase transition, 1, 4, 50, 61, 62, 146, 417,
 423, 430
 shock waves, 431
 Shor’s factorization algorithm, 384
 single atom
 resolution, 436

- single-particle density matrix, 299
 single-particle spectral function, 413
 singular value decomposition (SVD), 91
 slave-boson model, 98, 113, 116
 solitons, 431, 433
 sound velocity, 27, 421
 spin
 glass, 7
 imbalance mixtures, 8
 impurities, 432
 models, 6, 18, 56, 58, 203, 204, 265, 287,
 289, 328
 transport, 434
 waves, 266
 spin fluctuations, 434
 spin glass, 251
 spin liquid, 281
 chiral, 267, 431
 critical, 8
 gapped, 280
 resonating valence-bond
 (RVB), 266
 topological, 8
 type I, 8, 266
 type II, 8, 268
 spin- $\frac{3}{2}$
 effective Hamiltonian, 157, 159
 mean-field Hamiltonian, 160
 spin–charge separation, 29
 spin–orbit coupling, 435
 spin-1
 Bose–Hubbard Hamiltonian, 138
 energy functional, 129
 ferromagnetic phase, 129
 knots, 136
 mean-field, 128
 monopoles, 134
 polar phase, 129
 SF–MI phase transition, 146
 skyrmions, 135
 vortices, 133
 spin-2
 Bose–Hubbard Hamiltonian, 151
 cyclic phase, 132
 effective Hamiltonian, 151
 energy functional, 130
 ferromagnetic phase, 131
 mean field, 130
 polar phase, 131
 spin–boson model, 4, 5
 spinons, 266
 spinor
 Fermi gases, 156
 interactions, 126
 Majorana representation, 132
 textures, 133
 topological defects, 133
 spinor gases, 9, 125, 434
 spiral long-range order, 280
 Spontaneous symmetry-breaking, 25
 stability threshold, 176
 staggered
 flux states, 117
 long-range order, 280
 Stoner
 magnetism, 434
 transition, 430
 strange metals, 116, 436, 437
 string-net-condensed states, 406
 strong coupling expansion, 64
 strong coupling limit, 118
 strongly correlated regime, 48
 structure factor, 198
 crystalline, 422
 dynamical, 413, 418
 magnetic, 426
 spin, 422
 SU(N)
 Hubbard model, 111
 magnetism, 431
 superfluid
 fraction, 199
 parameter, 191
 stiffness, 80
 superfluid counterflow, 431
 $t - J$ model, 98, 111, 112, 284
 T-matrix approximation, 102
 temperature annealing, 201
 tensor network structure (TNS),
 374, 433
 thermalization, 430
 thermodynamic limit, 13, 22
 Thomas–Fermi limit, 26, 178
 Thouless
 conductance, 208, 212
 number, 214
 tight-binding approximation, 47,
 48, 53
 time of flight, 415, 417
 time-evolving block decimation
 (TEBD), 92
 Tonks
 super regime, 433
 Tonks parameter, 30
 Tonks–Girardeau gas, 5, 29
 topological
 entropy, 435
 excitations, 399, 400
 insulators, 435
 order, 8, 203, 286, 399
 phase, 431, 434, 435
 phase factor, 403
 spin models, 435
 transport theory of lattice
 bosons, 431
 trap
 aspect ratio, 171, 174
 Fermi dipolar gas, 181
 ions, 4, 203
 toroidal, 432
 Trotter expansion, 92

- tunneling, 39
 - anisotropic, 428
 - frustrated, 428
- tunneling time, 196
- unitarity limit, 105
- universality, 105
- Van der Waals forces, 54
- vortex
 - Abrikosov lattice, 329
 - mean-field, 301
 - nucleation, 294, 300
 - vortices, 34
- Wannier functions, 43, 53, 182, 416
- Wigner
 - crystal, 10, 11
 - truncated approach, 82
- Wilson loop, 306, 308, 309, 317
- Wilson–Fisher fixed point, 21
- winding numbers, 80
- XX model, 368
- XXZ model, 58, 358
- XY model, 14, 19, 27, 57, 211,
 - 212, 258, 280, 290, 356,
 - 368, 435
- XYZ model, 289